Physics of the Solid State, Vol. 44, No. 4, 2002, pp. 601–602. Translated from Fizika Tverdogo Tela, Vol. 44, No. 4, 2002, pp. 579–580.

PROCEEDINGS OF THE V INTERNATIONAL WORKSHOP "FULLERENES AND ATOMIC CLUSTERS"

(St. Petersburg, Russia, July 2–6, 2001)

Synthesis of Fullerene Derivatives

G. N. Churilov*, V. G. Isakova*, R. B. Weisman, N. V. Bulina*, S. M. Bachilo**, D. Cybulski**, G. A. Glushchenko*, and N. G. Vnukova***

** Kirensky Institute of Physics, Siberian Division, Russian Academy of Sciences, Akademgorodok, Krasnoyarsk, 660036, Russia*

e-mail: churilov@iph.krasn.ru

*** Rice University, Houston, TX 77005 USA*

e-mail: weisman@rice.edu

Received April 1, 1999

Abstract—This paper presents the results of plasmochemical synthesis of fullerene derivatives with hydrogen, iodine, iridium, platinum, and scandium. The synthesis is carried out under atmospheric pressure in a carbon–helium plasma stream formed by an ac arc in the rf range. © *2002 MAIK "Nauka/Interperiodica".*

The synthesis of fullerene derivatives with H_2, I_2, Sc, Ir, and Pt was carried out in a plasmochemical reactor developed earlier in [1, 2]. The reactor differs considerably from the widely used Kretschmer reactor in that the synthesis occurs under atmospheric pressure in a stream of carbon–helium plasma generated by an ac arc in the rf range. The reactor makes it possible for particles of the introduced substance to stay for a long time in the carbon plasma jet and, hence, become atomized completely. Consequently, this reactor can be used for the synthesis of fullerenes both with light elements and with refractory metals.

In accordance with the concept of the effect of the electron concentration on the formation of fullerenes and fullerene derivatives in a carbon plasma, which was developed in our earlier work [3], we synthesized fullerene derivatives by adding both donors and acceptors of electrons (hydrogen, iodine, scandium, iridium, and platinum). The initial metallic powder or metal wire was placed in a hole (d = 1.2 mm) made in one of the electrodes between which the plasma jet of carbon with a metal was formed. Hydrogen and iodine were introduced into the reactor in the form of a gas flow and vapor, respectively, in different temperature regions of the plasma. We tested fullerene-containing soot and fullerenes extracted from it.

An analysis of the x-ray spectra revealed that Ir, Pt, and Sc metals are present in a fullerene-containing soot only in the amorphous state.

The fullerene yield increased upon the introduction of a metal from 4 to 12%. The introduction of iodine virtually nullifies the concentration of fullerenes in the soot.

The electronic absorption spectra for the fullerene extract from soots obtained during the synthesis with the introduction of hydrogen exhibited the following changes (as compared to the spectrum for a fullerene mixture): a new band appeared at 434 nm and the band at 334 nm was displaced to the UV region by 17 nm. This variation is usually attributed to fullerene complexes with hydrogen of the $C_{60}H_2$ type [4, 5].

Emission spectroscopy revealed the presence of Sc at a content of the order of 10^{-3}% in the fullerene-containing extract.

Highly effective chromatographic separation of the fullerene mixture prepared by extraction from Ir- and Pt-containing soots was carried out in a Cosmosil Buckyprep column. The mass spectra of the separated fractions were measured. It was found that the given extract contains 55% C_{60}, 25% C_{70}, 15% higher fullerenes (mainly, C_{76}, C_{78}, C_{82}, C_{84}, and C_{86}), and 5% oxidized fullerenes C_{60} and C_{70}.

Mass spectrometry did not reveal the presence of any platinum or iridium derivatives in the extracts separated from Ir- and Pt-containing soots. This can be due to poor volatility of the formed metal compounds. Moreover, Pt- and Ir-containing derivatives involved in soots may be insoluble in organic solvents. In this connection, we made an attempt to convert them into volatile chelate complexes of metals, which are soluble in organic solvents and similar to those described in [6]. Fullerene-containing soots with Pt and Ir (samples I and II, respectively) were treated with acetylacetone (*Hacac*) in solutions of HF (a) and HCl (b) acids during heating, and, then, reaction products (**Ia**, **IIa**, **Ib**, and **IIb**) soluble in organic solvents were extracted from the reaction systems.

The electronic absorption spectra of products **Ia** and **IIa** are shifted to the UV region as compared to samples I and II. The x-ray diffraction pattern of the toluene extract of the Ir-containing product **IIa** contains reflections of fullerene (for small angles) and reflections of

an unknown substance (for large angles); the latter reflections can be associated with Ir complexes.

Toluene extracts of the synthesis products contained fractions of greenish yellow and yellow color which were soluble in protogenic solvents (acetone and alcohol). The electronic absorption spectra of compounds obtained from fullerene-containing soots and the spectra of halogenated iridium acetylacetonates contain bands at 270–280 nm, which are similar to the bands of iridium γ-fluoroacetylacetones but are displaced by 10–15 nm toward the long-wavelength range. The presence of other bands can be associated with the presence of fullerenes in the metal complexes; in addition, the formation of carbon-bonded acetylacetonates and mixed halogenacetylacetonates of metals is also possible.

The results obtained demonstrate that, in the iridium- and platinum-based fullerene-containing soots, iridium and platinum are in the chemically active form. This follows from the fact that the aforementioned reactions with acetylacetone do not occur with the familiar metallic forms of iridium and platinum (compact metal, metallic sponges, and powders). It can be assumed that the active form of Ir and Pt is their oxidized state in the form of insoluble fullerides; however, the results of x-ray diffraction analysis indicate the presence of amorphous particles of a metal in soots, which probably exhibit a high chemical activity.

The experiments described here indicate that the synthesis of metallocomplexes of fullerenes in preparation amounts is a complex problem associated with the donor and acceptor properties of the substances being introduced. Further investigations are required for determination of the relation between the magnitude and the variation of the electron concentration in a plasma upon the introduction of various elements, on the one hand, and the yield of the resulting fullerene derivatives, on the other. This will be the next step toward the controlled synthesis of fullerene derivatives.

ACKNOWLEDGMENTS

This work was supported by the American Foundation CRDF, grant no. RE1-2231. The foundation is not responsible for the concepts, ideas, and results presented in this paper. This work was also partly supported by the Russian State Program "Fullerenes and Atomic Clusters" (project no. 5-3-00) and the Program "University Research Work in Priority Trends of Science and Technology," the Ministry of Education of the Russian Federation (project nos. 201.05.01.001 and 203.02.05.007).

REFERENCES

1. G. H. Churilov, L. A. Soloviev, Ya. N. Churilova, *et al.*, Carbon **37**, 427 (1999).
2. G. N. Churilov, Prib. Tekh. Éksp., No. 1, 5 (2000).
3. G. N. Churilov, P. V. Novikov, and N. G. Vnukova, in *Proceedings of the XV International Winterschool on Electronic Properties of Novel Materials "Molecular Nanostructures," Kirchberg, Austria, 2001.*
4. D. Mandrus, M. Kele, R. L. Hettich, *et al.*, J. Phys. Chem. B **101**, 123 (1997).
5. C. C. Henderson and P. A. Cahill, Science **259**, 1885 (1993).
6. V. G. Isakova, I. A. Baidina, N. B. Morozova, and I. K. Igumenov, Polyhedron **19**, 1097 (2000).

Translated by N. Wadhwa

Physics of the Solid State, Vol. 44, No. 4, 2002, pp. 603–606. From Fizika Tverdogo Tela, Vol. 44, No. 4, 2002, pp. 581–584.

PROCEEDINGS OF THE V INTERNATIONAL WORKSHOP "FULLERENES AND ATOMIC CLUSTERS"

(St. Petersburg, Russia, July 2–6, 2001)

Synthesis of Multishell Fullerenes by Laser Vaporization of Composite Carbon Targets[1]

V. Z. Mordkovich, Yosuke Shiratori, H. Hiraoka, and Yoshimasa Takeuchi

International Center for Materials Research, East 601, KSP, Takatsuku, Kawasaki, 213-0012 Japan

e-mail: vladimir@icmr.co.jp

Abstract—Multishell fullerenes are the smallest among multishell carbon clusters, such as the larger graphitic onions or multishell nanotubes. Unlike classical fullerenes, which have a cage structure and are known to have been synthesized in a variety of sizes (C_{60}, C_{70}, C_{84}, C_{102}, etc.), multishell fullerenes have a cage-inside-cage concentric structure, such as double-shell $C_{60}@C_{240}$ or triple-shell $C_{60}@C_{240}@C_{560}$. We report on the synthesis of multishell fullerenes by laser vaporization of C_{60}-containing composite carbon targets. Transmission electron microscopy, Raman scattering spectroscopy, and other methods were used for characterization of the product. The yield of the process reaches up to 40%, which permits production in gram amounts even in laboratory conditions. © *2002 MAIK "Nauka/Interperiodica".*

Multishell fullerenes are the smallest among multishell carbon clusters, such as the larger graphitic onions [1, 2] or multiwall nanotubes [2, 3]. Unlike classical fullerenes, which have a cage structure and are known to have been synthesized in a variety of sizes (C_{60}, C_{70}, C_{84}, etc.), multishell fullerenes have a cage-inside-cage concentric structure, such as double-shell $C_{60}@C_{240}$ or triple-shell $C_{60}@C_{240}@C_{560}$. These cage-inside-cage structures were foreseen by Kroto *et al.* [4] as early as in 1988, i.e., shortly after his pioneering discovery of the basic buckminster fullerene C_{60} [5]. The first observation of several double-shell and triple-shell molecules was, however, reported only recently [6, 7]. In works [6, 7], the double-shell $C_{60}@C_{240}$, double-shell $C_{240}@C_{560}$, and triple-shell $C_{80}@C_{240}@C_{560}$ were found as products of 3000°C high-temperature treatment of laser pyrolysis carbon blacks. The content of multishell fullerenes was less than 0.01%, while most of the material was dominated by hollow graphitic particles ~20 nm in size and ordinary, single-shell fullerenes.

Though multishell fullerenes possibly possess interesting and attractive properties [7], no measurements could be performed until these fullerenes had been isolated in, at least, milligram amounts. Therefore, the first priority of the research in this field was to find an efficient synthetic route of the production of multishell fullerenes.

It is difficult to improve the method of high-temperature treatment of laser pyrolysis carbon black [7]. Also, it seems reasonable to suggest that the actual growth of additional shells around C_{60} cores takes place not during 3000°C treatment but during the cooldown after the heat treatment. If this suggestion is correct, the successful synthetic route should be comprised of at least two steps: (1) the formation of carbon vapor containing many C_{60} molecules and (2) cooling down at the appropriate substrate. A hypothetical growth sequence is shown in Fig. 1. We hypothesized that the method of laser vaporization would meet the above conditions. Another attractive feature of this method is that it allows flexible control of different key parameters of the process.

The purpose of the present work was to find an efficient synthetic route to the creation of multishell fullerenes using the laser vaporization method.

1. EXPERIMENTAL

For laser vaporization, a KrF excimer pulse laser (λ = 248 nm) was used. The typical laser fluence and repetition rate were 1.5 J/cm^2 and 10 Hz, respectively. Two different targets were used for vaporization. Both targets contained 40 wt % fullerene C_{60}, but the remaining components were different: amorphous laser pyrolysis carbon black or, alternatively, carbon nanofibers. The carbon nanofibers were vapor-grown carbon fibers with a nanotube-like concentric multishell structure [3]. The experiment was performed in a helium atmosphere, with the He pressure varying in the range from 1 to 200 Torr. Substrates of stainless steel SUS304, quartz glass, and pyrolytic graphite were used to collect

[1] This article was submitted by the authors in English.

1063-7834/02/4404-0603$22.00 © 2002 MAIK "Nauka/Interperiodica"

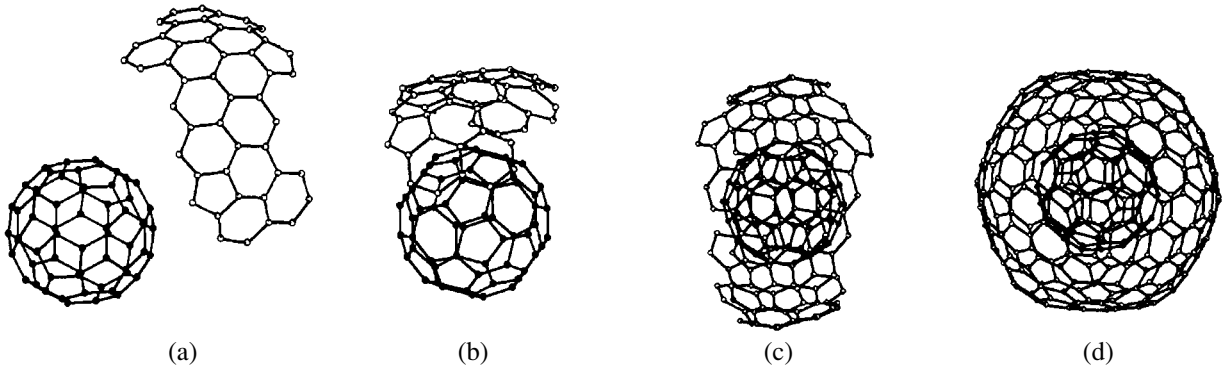

Fig. 1. Hypothetical growth sequence of multishell fullerene evolving from (a) a fullerene molecule and a fullerene/nanotube fragment, through (b) and (c), in which the shell fragment deposited onto a fullerene forms the embryo in which the second shell forms. The sequence leads, in a natural way, to multishell fullerenes (d).

the deposit. The substrate temperature was 300°C. The deposits were studied by transmission electron microscopy (TEM), Raman spectroscopy, and other methods. Vacuum sublimation was used to separate the fractions of the deposit. The details of the vacuum sublimation technique can be found elsewhere [7].

2. RESULTS AND DISCUSSION

The deposits obtained by vaporization of either of the targets at different He pressures were thin yellow films (~500 nm thick after 20 000 pulses). The films could not be dissolved in organic solvents such as toluene, xylene, or chloroform. Though the yellow color implies the absence of graphite or graphitic particles, the TEM study showed that the latter actually did occur in small amounts in the deposits.

The main result of the TEM study was, however, the observation of large amounts of double and triple fullerenes. The yield was higher at lower He pressure, in the range of 1–4 Torr. Vaporization of C_{60}/nanofiber targets always gave a 3- to 5-times higher yield than that of C_{60}/carbon black targets. The best samples, received by vaporization of a C_{60}/nanofiber target at 1 Torr, contained 40% multishell fullerenes. At least two varieties were observed: two-shell 14 Å in size, and three-shell 20 Å in size. The two-shell fullerenes are easily seen in Fig. 2. From the fullerene diameter it is possible to calculate mass [2], though the uncertainty in the carbon–carbon bond length and other factors produce an inevitable error, which we estimate as ±5%. As a result, it is possible to assign the following chemical formulae to the observed fullerenes: $C_{60}@C_{240}$ to the double fullerene 14 Å in size, and $C_{60}@C_{240}@C_{560}$ to the triple fullerene 20 Å in size.

The multishell fullerene fraction can be easily separated by vacuum sublimation, though this requires at least 1200°C in a vacuum of 10^{-7} Torr. Therefore, the high sublimation temperature is in sharp contrast with that of C_{60}, which can be easily sublimated at 400°C. The sublimate film has a yellow color and predominantly contains multishell fullerenes.

The comparison of Raman scattering spectra of laser vaporization deposits and the sublimated films (Fig. 3) shows how the strong "disordered graphite" features at 1360 and 1590 cm^{-1} disappear after sublimation. The sublimated film does not contain graphitic nanoparticles with strong, overwhelming spectral lines, and its spectra (Fig. 3b) clearly display three strong broad peaks at 1430, 1464, and 1569 cm^{-1} and a number of weaker peaks below 1000 cm^{-1}. This pattern is very similar to that of C_{60} (1426, 1469, and 1573 cm^{-1} features) [8]. Four of the weaker peaks, 530, 737, 757, and 880 cm^{-1}, cannot be identified with the vibrations of the C_{60} molecule, even though the peaks at 730 and 757 cm^{-1} were earlier observed in the spectra of a "phototransformed" C_{60} solid [8], i.e., the C_{60} solid after photoinduced immobilization of C_{60} molecules in the polymer network.

It is reasonable to suppose that most of the peaks in Fig. 3b are produced by the core C_{60} molecules immobilized inside the multishell fullerenes. No peaks, with the possible exception of the 530 and 880 cm^{-1} features, can be assigned to the outer shells, because the latter produce many weak Raman peaks due to their generally lower symmetry, larger number of degrees of freedom, and/or possible isomers. Also, it was predicted by Iglesias-Groth *et al.* [9] that the strongest vibrational lines of the outer shells lie at much lower frequencies, 65–120 cm^{-1}.

The growth of the outer shells is probably determined by the mechanism shown in Fig. 1 and discussed above. This hypothesis is supported by the above-mentioned fact that laser vaporization of the C_{60}/nanofiber targets gave a much higher yield of multishell fullerenes than that of the C_{60}/carbon black targets. Indeed, the difference between the targets is in the pres-

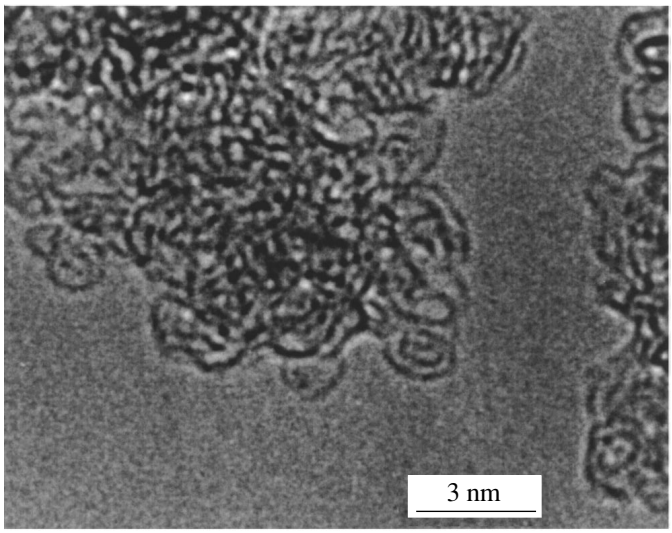

Fig. 2. TEM images show multishell fullerenes in large amounts. The concentric dark rings are the electron images of multishell fullerenes.

ence of nanofibers. Those nanofibers, comprised of multiple curved shells, are a good source of shell fragments for initiation of the multishell fullerene growth process according to Figs. 1a, 1b. On the other hand, the vaporization of the C_{60}/carbon black target cannot produce the shell fragments; hence, even if the embryos of multishell fullerenes do appear, this happens due to the much less probable process of spontaneous nucleation of corannulene-like carbon networks from the carbon vapor, as was suggested by Kroto *et al.* [4].

Apparently, the uncertain stage of the hypothetical growth mechanism is the shell closure (Figs. 1c, 1d). The growth may well lead to elongation of the outer shell with the formation of a tubulene, as shown in Fig. 4a. Indeed, we observed such objects more than once in the laser vaporization deposits; see, for example, Fig. 4b. This kind of nanocluster, called a "buckyshuttle," represents a nanometer-sized, two-level system which can be used as a computer memory element and was recently discovered in the products of heat treatment of nanodiamond [10]. We have good reason to believe that the laser vaporization method can be controlled so as to selectively synthesize buckyshuttles in high yields.

In conclusion, a method of large-scale synthesis of multishell fullerenes was found. The method of laser vaporization of composite C_{60}-containing carbon targets gives a yield of up to 40%, which permits production in gram amounts even under laboratory conditions. The results suggest that the method can be controlled so as to selectively synthesize certain types of multishell fullerenes and other multishell carbon clusters.

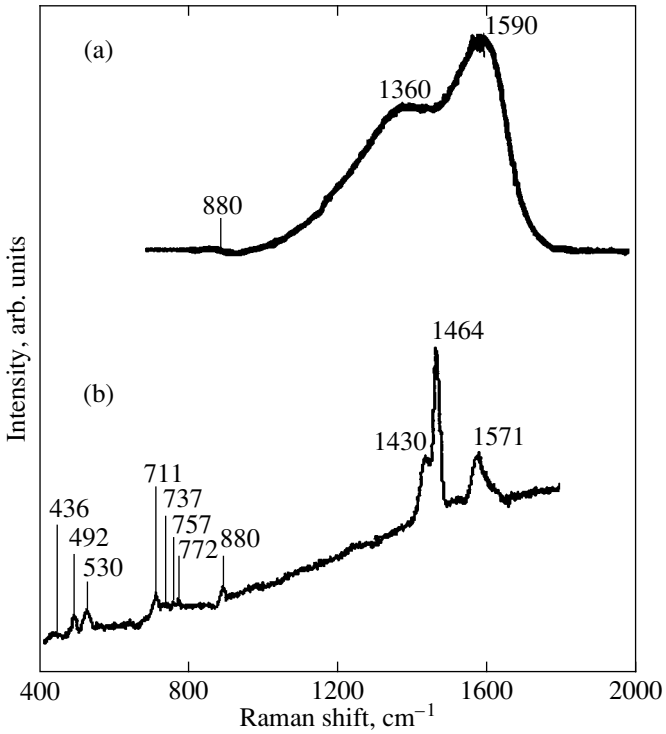

Fig. 3. Raman scattering spectra: (a) laser vaporization deposit on stainless steel; (b) sublimated film. The spectrum of the deposit (a) is dominated by two overwhelming "disordered graphite" features: the peak at 1590 cm^{-1} is identified with the well-known E_{2g} vibrational mode of graphite, upshifted by ~10 cm^{-1} from the position 1582 cm^{-1} reported for single-crystal graphite [2]; the peak at 1360 cm^{-1} is identified with symmetry-forbidden modes associated with the maximum in the graphite density of states (activated lattice disorder and/or small crystalline size) [2]. For features of the (b) spectrum, see comments in the text.

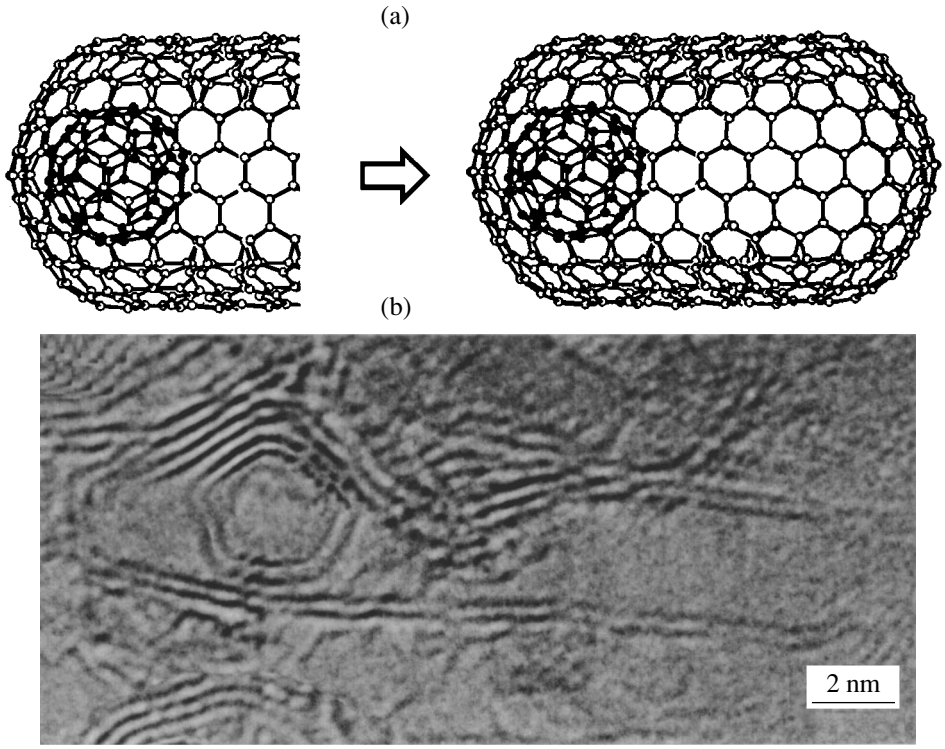

Fig. 4. A buckyshuttle (fullerene molecule enclosed in a tubulene) as a result of deviation from the normal growth sequence of a multishell fullerene: (a) hypothetical growth sequence after deviation from the path, which is shown in Figs. 1c, 1d; (b) TEM image of a deposit, showing a buckyshuttle.

ACKNOWLEDGMENTS

We are grateful to Dr. T. Sasaki and Dr. F. Imaizumi for their continuous support and helpful discussions. Laser vaporization experiments were carried out through the courtesy of the Quantum Design Japan Co. with valuable assistance from Dr. M. Nakamura and Dr. M. Sawada.

REFERENCES

1. S. Iijima, J. Phys. Chem. **91**, 3466 (1987).
2. M. S. Dresselhaus, G. Dresselhaus, and P. C. Eklund, *Science of Fullerenes and Carbon Nanotubes* (Academic, London, 1996).
3. *Carbon Nanotubes*, Ed. by M. Endo (CRC, New York, 1997), pp. 35–100.
4. H. W. Kroto and K. McKay, Nature **331**, 328 (1988).
5. H. W. Kroto, J. R. Heath, S. C. O'Brien, *et al.*, Nature **318**, 162 (1985).
6. V. Z. Mordkovich, A. G. Umnov, T. Inoshita, and M. Endo, Carbon **37** (10), 1855 (1999).
7. V. Z. Mordkovich, Chem. Mater. **12** (9), 2813 (2000).
8. A. M. Rao, P. Zhou, K.-A. Wans, *et al.*, Science **259**, 955 (1993).
9. S. Iglesias-Groth and J. Breton, Astron. Astrophys. **357**, 782 (2000).
10. Y.-K. Kwon, D. Tomanek, and S. Iijima, Phys. Rev. Lett. **82**, 1470 (1999).

Physics of the Solid State, Vol. 44, No. 4, 2002, pp. 607–611. From Fizika Tverdogo Tela, Vol. 44, No. 4, 2002, pp. 585–588.

PROCEEDINGS OF THE V INTERNATIONAL WORKSHOP "FULLERENES AND ATOMIC CLUSTERS"

(St. Petersburg, Russia, July 2–6, 2001)

A New Nanocluster Carbyne-Based Material Synthesized under High Pressure[1]

S. V. Demishev*, A. A. Pronin*, N. E. Sluchanko*, N. A. Samarin*, V. V. Glushkov*, A. G. Lyapin, M. V. Kondrin**, V. V. Brazhkin**, T. D. Varfolomeeva**, S. V. Popova**, and H. Ohta*****

** General Physics Institute, Russian Academy of Sciences, Moscow, 117942 Russia*

e-mail: demis@lt.gpi.ru

*** Institute of High Pressure Physics, Russian Academy of Sciences, Troitsk, Moscow oblast, 142092 Russia*

**** Molecular Photoscience Research Center and Department of Physics, Kobe University, Rokkodai, Nada, Kobe 657-8501 Japan*

Abstract—The DC and AC conductivities and the magnetoresistance and thermopower of carbyne samples were studied over the temperature range 1.8–300 K at frequencies 10 MHz–1 GHz. It was established that a variation in the fraction of sp^2 bonds in carbynes induces a transition from one- to two- and then to three-dimensional conduction. The physical properties of the new carbyne-based solids may be understood within the model treating carbyne as a nanocluster material based on linear carbon chains and having a characteristic cluster size of 1 to 10 nm. *© 2002 MAIK "Nauka/Interperiodica".*

1. Carbyne is an allotropic carbon form based on *sp*-type bonds and possesses a pronounced linear-chain structure [1–3]. Contrary to other allotropic modifications with sp^2 (graphite) or sp^3 (diamond) bonds, carbyne cannot be synthesized as a perfect crystal, because its chains contain "built-in" disorder, probably due to the instability of large linear carbon clusters [3]. Although to date there is no commonly accepted model structure of carbyne, it is customarily believed that linear *sp* segments of the polymeric carbon molecule in carbyne alternate with sp^2-hybridized carbon atoms [1–3]. The sp^2-centers give rise to chain kinks, and the dangling bonds appearing at the kinks may attach to impurity atoms or form interchain links (in the absence of sp^2-defects, the carbon chains are bonded by weak van der Waals forces). As a result, the carbon chains may form complex globular structures.

The fraction of sp^2-bonds in carbyne can be varied smoothly by applying high pressure and temperature [1]. An increase in the synthesis temperature T_{syn} under pressure induces the $sp \longrightarrow sp^2$ transition, i.e., the formation of a disordered 2*D* graphite-like network from the structure dominated by 1*D* chains. Therefore, carbynes synthesized under high pressure open an intriguing opportunity of creating experimental systems with variable dimensionality [4]. In the present work, we report on results of studying DC and AC conductivity and magnetoresistance and thermopower measured in the temperature, frequency, and magnetic field domain $1.8 < T < 300$ K, 1 MHz $< \nu <$ 1 GHz, and $B < 7$ T.

2. A carbyne with chains …=C=C=C=C=… of the cumulene type was synthesized at the Nesmeyanov Institute of Organoelement Compounds, Russian Academy of Sciences, and used as the starting material. Samples were prepared by the method used in [1]. Synthesis was carried out at a pressure of 7.7 GPa. At different T_{syn} values, the sample structure was identical to that described in [1]. The temperature dependences $\rho(T)$ for different T_{syn} temperatures are shown in Fig. 1a. In the coordinates $\log(\rho) = f(T^{-\alpha})$, linear segments characteristic of the variable range hopping (VRH) conductivity are clearly seen in the curves at $T < T^* \sim 40$ K down to $T \sim 1.8$ K. The index α, which, for a constant density of states and space dimension *d*, is given by [5]

$$\alpha = 1/(d + 1), \qquad (1)$$

increases with decreasing synthesis temperature (Fig. 1). The value of 1/4 found for this parameter for $T_{syn} = 890$°C corresponds to the 3*D* Mott's law, while the reduction in T_{syn} to 800°C increases α to 1/3, which is characteristic of 2*D* hopping conduction (Eq. (1)). In the vicinity of $T_{syn} \sim 700$°C, the exponent changes to 1/2 (Fig. 1, $T_{syn} = 690$°C), which suggests a transition to 1*D* hopping transport.

Thus, one can assume that the rise in the temperature of synthesis under pressure induces a crossover from 1*D* to 3*D* hopping conduction. In the transition region $700 < T_{syn} < 800$°C, the carbyne matrix repre-

[1] This article was submitted by the authors in English.

1063-7834/02/4404-0607$22.00 © 2002 MAIK "Nauka/Interperiodica"

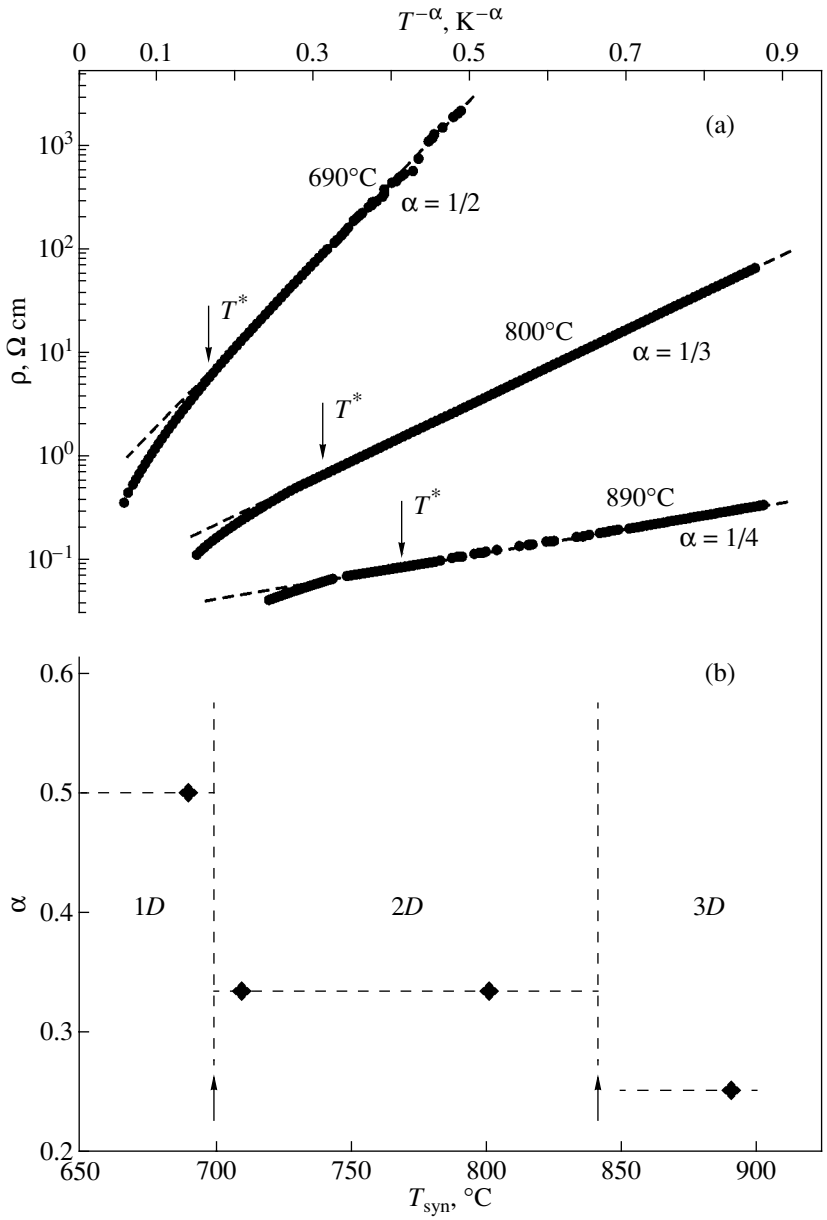

Fig. 1. Temperature dependence of the conductivity (a) and hopping conduction exponent (b) for carbyne samples synthesized at different temperatures.

sents a set of mutually noninteracting 2*D* carbon layers. Such an interpretation qualitatively agrees with the data [1] on the $sp \longrightarrow sp^2$ transition, because the "degree of crosslinking" between the carbon chains increases with T_{syn} and the effective dimensionality of the system should increase. Note that, according to [1], carbyne samples undergo "graphitization" at $T_{syn} \sim 700$°C, so that the crossover first to 2*D* and than to 3*D* conduction at $T_{syn} > 700$°C seems to be quite natural.

At the same time, it was assumed in [1] that a quasi-one-dimensional structure occurs in carbyne at $T_{syn} < 500$°C, while in the samples obtained at higher temperatures, the fraction of sp^2-bonds is appreciable. Because of this, the interpretation of the data in Fig. 1 as a $1D \longrightarrow 2D \longrightarrow 3D$ transition is not unique. For example, the $\alpha = 1/2$ value may be explained by the appearance of a Coulomb gap in a 2*D* hopping system [4, 5].

The latter possibility is eliminated from analyzing the AC conductivity data. In the 2*D* or 3*D* case with Coulomb correlations, the hopping conductivity $\sigma(\omega) = \sigma_1(\omega) + i\sigma_2(\omega)$ at frequency ω is given by [4, 6]

$$\sigma_1, \sigma_2 \sim \omega^s T^\alpha, \qquad (2)$$

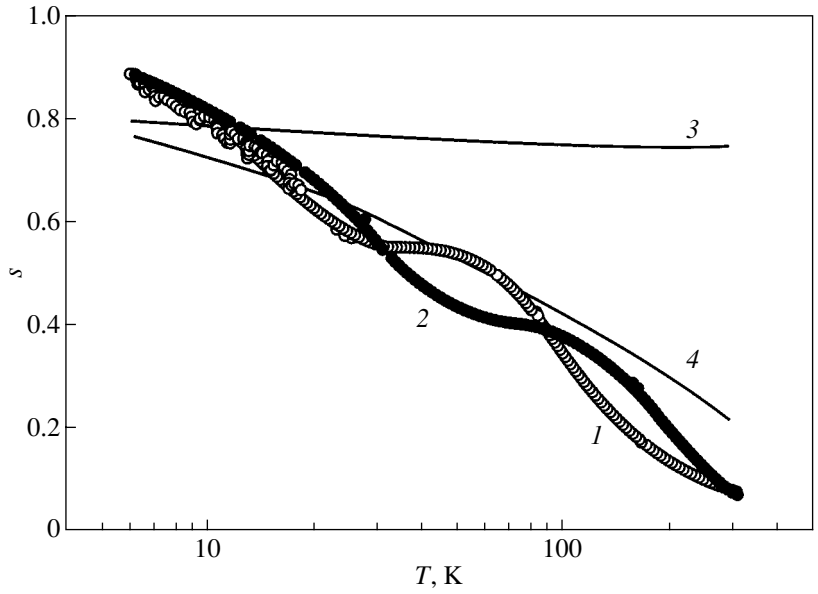

Fig. 2. Temperature-dependent exponent s: (*1*) experiment with 100 MHz, (*2*) experiment with 500 MHz, (*3*) model of Coulomb correlations for $d = 2$, and (*4*) Hunt's model for $d = 1$.

with an effectively temperature-independent index s. Contrary to this expectation, the experiment shows a strong $s(T)$ dependence (Fig. 2) characteristic of 1*D* systems. Indeed, according to Hunt's calculation for the 1*D* system [7, 8],

$$s(T) = [(AT_0/T)^{1/2} - 2]/[(AT_0/T)^{1/2} + 2], \qquad (3)$$

where T_0 is the same as in the temperature dependence of DC conductivity $\ln\sigma \sim -(T_0/T)^{\alpha}$ while parameter A depends on the length of linear hopping chain L and localization radius a: $A \approx \exp(2)L/a$. Comparison of Eq. (3) with the experiment shows that Hunt's theory well describes the observed $s(T)$ data, assuming the reasonable value $L/a \sim 680$ (curve *4* in Fig. 2).

An additional argument against opening of the Coulomb gap in carbynes obtained at $T_{syn} < 700$°C is provided by thermopower measurements. In the VRH regime at $T < T^*$, thermopower is proportional to the first derivative of the density of states (DOS) [6]. Therefore, for the Coulomb gap regime where DOS is symmetric with respect to the Fermi level, the Seebeck coefficient should be equal to zero. At the same time, we find that for all the samples studied, including those with $\alpha = 1/2$, the thermopower remains finite in the hopping region. The observed behavior is consistent with the above explanation of the values $a > 1/4$ in terms of the $1D \longrightarrow 3D$ crossover and disagrees with the opening of the correlation gap at the Fermi level.

3. Study of the VRH regime opens the opportunity of determining the localization radius. The shrinkage of the wave function in a magnetic field gives rise to positive magnetoresistance:

$$\ln[\rho(B)/\rho(0)] = t_d a^4 B^2 (T_0/T)^{3\alpha}/c^2\hbar^2, \qquad (4)$$

where coefficient t_d depends on the space dimension: in 2*D*, $t_2 = 1/360$ [9], and in 3*D*, $t_3 = 5/2016$ [10]. Experimental $\rho(B)$ data at $T = 4.2$ K are shown in Fig. 3a; it is seen that Eq. (4) provides a good approximation of the magnetoresistance of carbynes synthesized at different T_{syn}. Taking slopes of linear parts in the coordinates $\ln\rho = f(B^2)$ together with the T_0 values calculated from Fig. 1a, we found localization radius values for $T_{syn} > 700$°C (see Fig. 3b, regions 2*D*, 3*D*). In the 1*D* case (i.e., at $T_{syn} < 700$°C), the exact value of t_d is unknown; therefore, we used t_2 to get an estimate (Fig. 3b).

The obtained $a(T_{syn})$ data demonstrate a clear increase in localization radius with synthesis temperature. In the 1*D* case, we find $a \sim 60$ Å, whereas for the 2*D* case, the localization radius reaches ~80 Å. The region of 3*D* VRH ($T_{syn} > 840$°C) is described by $a \sim 140$ Å; it is 2.3 times higher than in 1*D* (Fig. 3b). It is worth comparing the obtained data on the localization radius with the structural characteristics of the disordered carbyne matrix. X-ray structural analysis gives a medium range order length $L_{MRO} \sim 8$–10 Å for the initial carbyne powder, and, for the samples studied in the present work, L_{MRO} is about 10–12 Å. These values are of the same order of magnitude as expected for the maximal stable linear cumulene fragments in the carbyne structure [2, 3] but are 5–14 times lower than the observed values of the localization radius. Therefore, the localization in the disordered potential of the carbyne matrix has a multicenter nature.

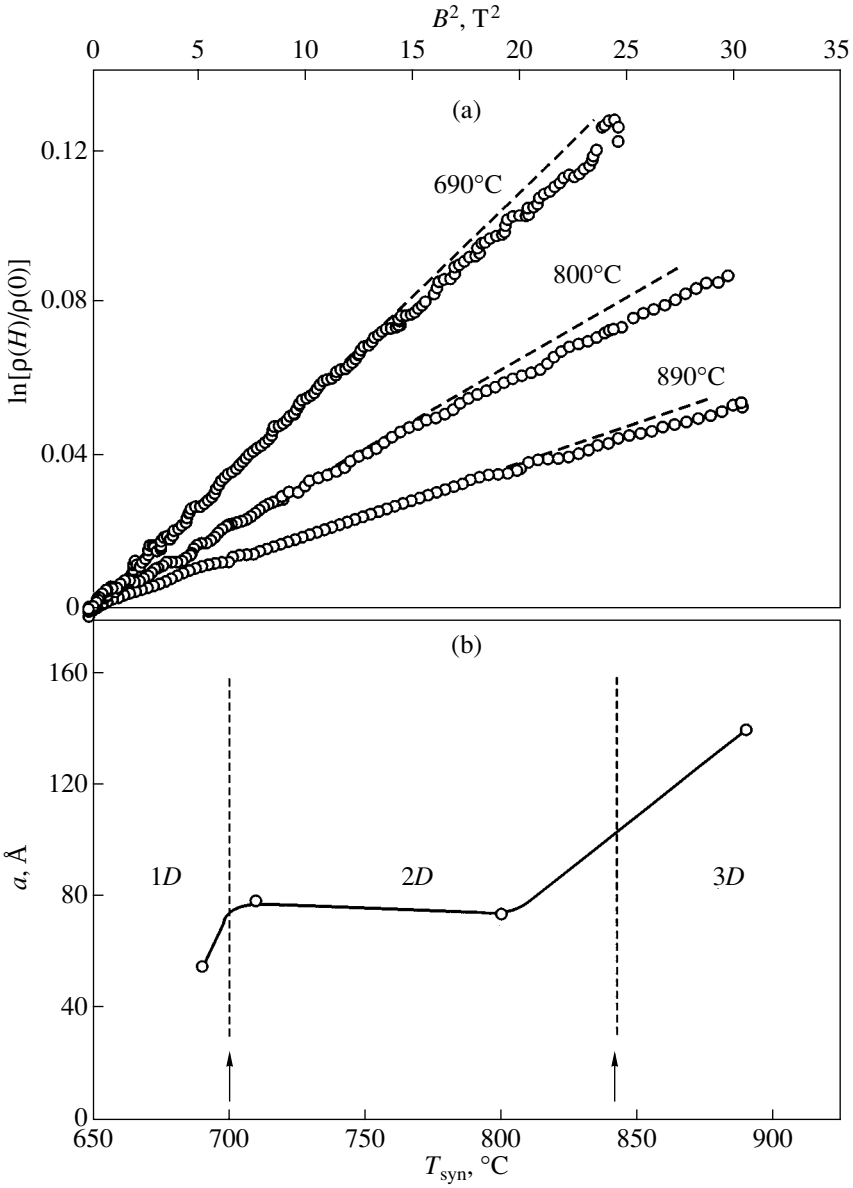

Fig. 3. Magnetoresistance (a) and localization (b) for carbyne samples synthesized at different temperatures.

On the other hand, in a strongly disordered solid, like carbyne, the spatial scale $a \gg L_{MRO}$ may be relevant to some structural elements of the disordered network [11]; for instance, it may correspond to clusters or physical inhomogeneties of size ~a with a higher conductivity formed from linear fragments of size ~L_{MRO}. Verification of this hypothesis requires further structural study of carbynes synthesized under high pressure.

The obtained results allow one to refine the scenario of the $sp \longrightarrow sp^2$ transition [1]. Since the 1*D* conduction persists up to $T_{syn} \sim 700$°C, the appearance of new sp^2-centers likely leads to the disorder and bending of individual chains in this range of synthesis temperatures. At $T_{syn} > 700$°C, the increase in the fraction of the sp^2-bonds induces crosslinking between the chains, rendering the conduction two-dimensional. With a further increase in T_{syn} raising the concentration of sp^2-centers in the carbyne matrix, the topology of quasi-two-dimensional carbon layers becomes more complicated and they start to interact with each other, leading to the 3*D* character of conduction.

The obtained values of the localization radius and x-ray structural data suggest that the carbyne matrix can be likely treated as a nanocluster material with a characteristic cluster size of 1 to 10 nm and based on linear fragments of carbon chains. The complicated spatial hierarchy of the disordered carbyne matrix together with the intriguing possibility of varying the effective dimension of space where charge carriers

move from 1*D* to 3*D* via 2*D* makes future fundamental and applied studies of these solids prospective.

ACKNOWLEDGMENTS

This work was supported by the Russian Foundation for Basic Research (project nos. 00-02-16403 and 99-02-17408), INTAS (grant no. 00-807), and the programs of the Ministry of Industry, Science, and Technology "Fullerenes and Atomic Clusters," "Physics of Microwaves," and "Fundamental Spectroscopy."

REFERENCES

1. A. G. Lyapin *et al.*, Phys. Status Solidi B **211**, 401 (1999).
2. Yu. P. Kudryavtsev *et al.*, Izv. Ross. Akad. Nauk, Ser. Khim., No. 3, 450 (1993).
3. B. M. Bulychev and I. A. Udod, Ross. Khim. Zh. **39**, 9 (1995).
4. S. V. Demishev *et al.*, Pis'ma Zh. Éksp. Teor. Fiz. **72**, 547 (2000) [JETP Lett. **72**, 381 (2000)].
5. N. F. Mott and E. A. Davis, *Electronic Processes in Non-Crystalline Materials* (Clarendon, Oxford, 1979; Mir, Moscow, 1974), Vol. 1.
6. I. P. Zvyagin, *Kinetic Phenomena in Disordered Semiconductors* (Mosk. Gos. Univ., Moscow, 1984).
7. A. Hunt, Solid State Commun. **86**, 765 (1993).
8. A. Hunt, in *Proceedings of the 5th International Conference on Hopping and Related Phenomena, Glasgow, 1993*, Ed. by C. J. Adkins, A. R. Long, and J. A. McInnes (World Scientific, Singapore, 1994), p. 65.
9. M. E. Raikh *et al.*, Phys. Rev. B **45**, 6015 (1992).
10. B. I. Shklovskii and A. L. Efros, *Electronic Properties of Doped Semiconductors* (Nauka, Moscow, 1979; Springer, New York, 1984).
11. S. V. Demishev *et al.*, Zh. Éksp. Teor. Fiz. **110**, 334 (1996) [JETP **83**, 180 (1996)].

Physics of the Solid State, Vol. 44, No. 4, 2002, pp. 612–614. From Fizika Tverdogo Tela, Vol. 44, No. 4, 2002, pp. 589–591.

PROCEEDINGS OF THE V INTERNATIONAL WORKSHOP "FULLERENES AND ATOMIC CLUSTERS"

(St. Petersburg, Russia, July 2–6, 2001)

Syntheses, Structures, and Properties of Novel Molybdenum and Tungsten Complexes of Fullerenes[1]

Kaluo Tang, Xianglin Jin, and Youqi Tang

Institute of Physical Chemistry, Peking University, Beijing, 100871 P. R. China
e-mail: jt1939@pku.edu.cn

Abstract—The synthesis and characterization of several fullerene-based organometallic complexes containing Mo and W is reported. © *2002 MAIK "Nauka/Interperiodica".*

Since the time the crystal structure of the first organometallic complex of fullerene $(\eta^2\text{-}C_{60})Pt(PPh_3)_2 \cdot C_4H_8O$ was first reported in [1], several other complexes have been synthesized and characterized by the x-ray diffraction method. However, among them, most are metals from group VIII, such as Pt, Ir, Pd, Rh, etc. Only a few molybdenum or tungsten complexes of C_{60} have been described in the literature, such as $[M(\eta^2\text{-}C_{60})(CO)_3(dppb)]$ (M = Mo, W) [2], $[M(\eta^2\text{-}C_{60})(CO)_3(dppe)]$ (M = Mo, W) [3], $[Mo(\eta^2\text{-}C_{70})(CO)_3(dppe)]$[3], etc. with phosphorous-containing ligands.

The key problems in growing single crystals of fullerene-based complexes are the instability of their solution and low solubility. We synthesized four airtable organometallic C_{60} derivatives of molybdenum (0) and tungsten (0) with nitrogen-containing ligands $(\eta^2\text{-}C_{60})M(CO)_3LL$ (M = Mo, W, LL = 2,2'-bipyridine or 1,10-phenanthroline) [4]. They are only slightly soluble in chlorobenzene and *o*-dichlorobenzene. No crystals suitable for x-ray diffraction studies were obtained. However, when one carbonyl group of $(\eta^2\text{-}C_{60})M(CO)_3$(*o*-phen) was displaced by dibutyl fumarate (dbf), the resulting complexes had good solubility in a number of organic solvents, even much better than C_{60} itself. Here, we report on the syntheses, crystal structure, and properties of novel molybdenum and tungsten complexes of C_{60} and C_{70}.

A series of Mo/W complexes of fullerenes $(\eta^2\text{-}C_x)[M(CO)_2$(*o*-phen)(dbf)$]_n$ (x = 60 or 70, M = Mo or W, n = 1, 2, 3, phen = 1,10-phenanthroline) were synthesized by heating a solution of fullerene (C_{60} or C_{70}) with $[M(CO)_2$(*o*-phen)$(dbf)_2]$ in toluene followed by column chromatography over silica gel. They are remarkably stable in air and have unusually good solubility. The complexes were characterized by chemical analysis, IR, UV/vis, ^{1}H, and ^{13}C NMR spectroscopy and single crystal x-ray diffraction analysis [5, 6].

The x-ray structure analysis indicates that molybdenum and tungsten complexes of C_{60} are isomorphous compounds, $(\eta^2\text{-}C_{60})M(CO)_2$(*o*-phen)(dbf) $\cdot$ $2C_6H_6 \cdot C_5H_{12}$ (M = Mo (1) or W (2)). The molecular structure of unsolvated complexes is shown in Fig. 1 [5].

In the molecules of complexes (1) and (2), the Mo or W atom coordination is distorted octahedrally with the two CO groups *cis* to each other and each *trans* to a nitrogen atom of *o*-phenanthroline. The metal (M) atom, two CO groups, and *o*-phen are in the equatorial plane. They are coplanar within 0.050 Å. The M atom binds in an η^2 fashion to the C–C bond [C(1)–C(2)] between two six-member rings of C_{60}. The distances of W–C(1) and W–C(2) are almost equal (2.30(2), 2.30(3) Å). The M atom binds also in an η^2 fashion to the C–C bond [C(85)–C(91)] of dibutyl fumarate (W–C(85) 2.28(3) Å and W–C(91) 2.29(3) Å). The two C–C bonds (C(1)–C(2) and C(85)–C(91)) are almost orthogonal, and each alkene ligand eclipses an N–M–CO vector (av. 171.4°). The coordination about the metal atom closely resembles that observed in the molybdenum complex of methyl acrylate $(\eta^2\text{-}CH_2{=}CHCOOMe)_2Mo(CO)_2$(bipy) (3), the structure of which has been determined by us. Actually, we prepared complex (3) as an electronic model for the corresponding C_{60} compound [7].

The molecular structure of the molybdenum complex of C_{70} $(\eta^2\text{-}C_{70})Mo(CO)_2$(*o*-phen)(dbf) $\cdot$ $2C_3H_8O \cdot 2.5H_2O$ (4) is shown in Fig. 2 [6]. The Mo atom binds in an η^2 fashion to the Ca–Cb bond of C_{70} (C(1)–C(2)), and the distances of Mo–C(1) and Mo–C(2) bonds are very close (2.29 and 2.28 Å). Typical distances can also been found in other molybdenum complexes of fullerenes. For example, the distances of Mo–C(1) and Mo–C(2) are 2.31 and 2.32 Å in complex (1), 2.33 and 2.31 Å in $[Mo(\eta^2\text{-}C_{60})(CO)_3(dppb)]$ [2], 2.31 and 2.31 Å in $[Mo(\eta^2\text{-}C_{60})(CO)_3(dppe)]$ [3], and 2.29 and

[1] This article was submitted by the authors in English.

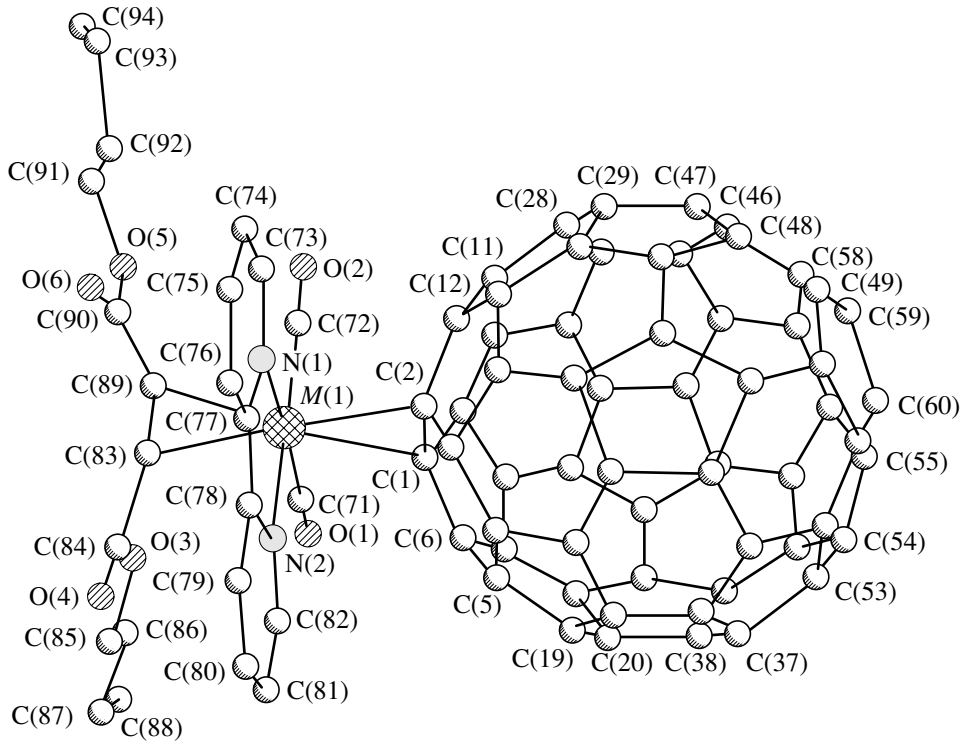

Fig. 1. Perspective view of the structure of [$M(\eta^2\text{-}C_{60})(CO)_2$(phen)(dbf)] ($M$ = Mo, W).

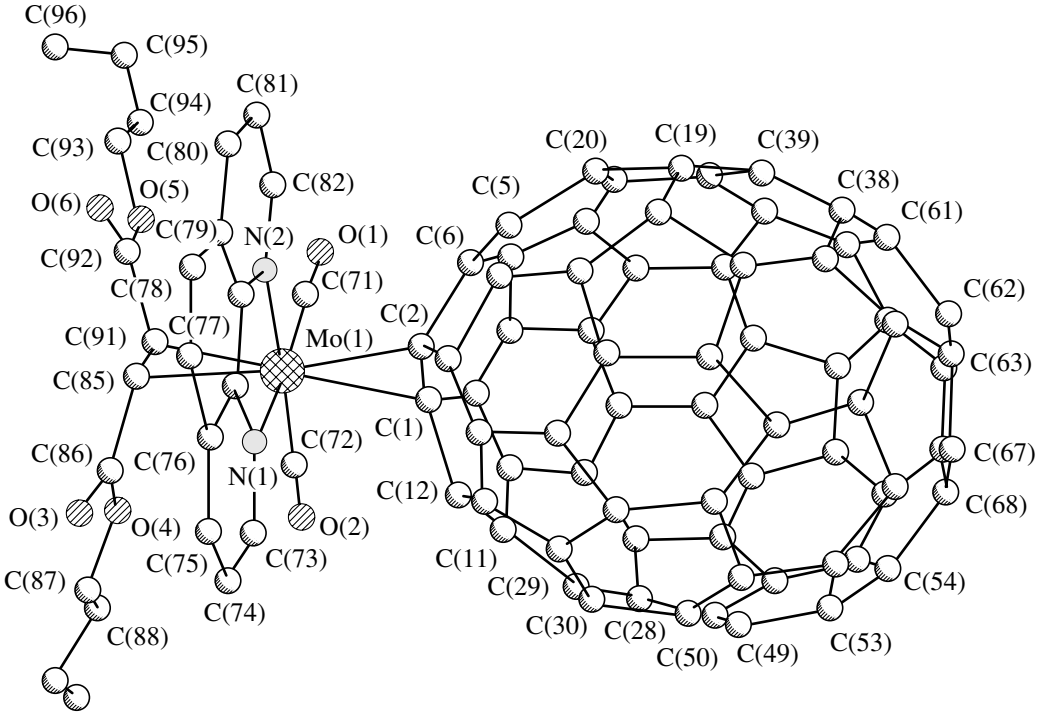

Fig. 2. Perspective view of the structure of [Mo($\eta^2\text{-}C_{70}$)$(CO)_2$(phen)(dbf)].

2.28 Å in [Mo(η^2-C_{70})$(CO)_3$(dppe)] [3]. Crystal structure analysis indicates that the molecular configuration of complex (4) is similar to that of Mo–C_{60} of complex (1).

The electrochemical behavior of these complexes has been studied in a dichloromethane solution, and the EPR spectra of electrogenerated monoanions have also been studied [8, 9]. The electrochemistry of complexes (1) and (2) shows that they undergo four sequential reduction processes. As with free C_{60}, the first three electrons add reversibly (even if the relevant potentials are shifted *ca.* 0.15 V toward negative values), whereas the fourth reduction features chemical irreversibility [8]. Comparison with the redox behavior of the C_{70}-analog reveals significant differences, namely, complex (4) exhibits two reversible one-electron reductions followed by a single two-electron reduction, all of these reductions being centered on the fullerene ligand. A further cathodic step centered on the metallic fragment is present, which, also in this case, causes framework destruction, which releases the C_{70} ligand. Under the same experimental conditions, the cathodic shift induced by appending the $Mo(CO)_2$(phen)(dbf) unit to C_{70} is lower than for C_{60} (0.10 vs. 15 V), thus suggesting that the extent to which the double bond conjugation is broken by the coordination to C_{70} should be lower than that with C_{60} [9].

The optical limiting property of molybdenum complexes of fullerenes C_{60} and C_{70} was investigated under irradiation of a 10-ns laser pulse at 532 nm. The experimental results demonstrated that the complexes performed with better optical limiting behavior than the parents C_{60} or C_{70}. The absorption of each (η^2-C_{60})[$Mo(CO)_2$(phen)(dbf)] molecule was as much as 3 times that of a C_{60} C_{60} molecule [10], whereas each (η^2-C_{70})[$Mo(CO)_2$(phen)(dbf)] molecule absorbed as much as 1.7 times more than a C_{70} molecule [11]. An explanation based on the enhanced triplet-state absorption being caused by the intramolecular charge transfer was put forward.

ACKNOWLEDGMENTS

We wish to express our gratitude for the financial support of this work by China's National Natural Science Foundation (project nos. 29873080, 29873001).

REFERENCES

1. P. J. Fagan, J. C. Calabrese, and B. Malone, Science **252**, 1160 (1991).
2. L. C. Song, J. T. Liu, Q. M. Hu, *et al.*, Organometallics **19**, 1643 (2000).
3. Hsiu-Fu Hsu, Yuhua Du, T. E. Albrecht-Schmitt, *et al.*, Organometallics **17**, 1756 (1998).
4. K. Tang, X. Jin, H. Zeng, *et al.*, in *Abstracts of the 17th International Conference on Organometallic Chemistry, Brisbane, Australia, 1996*, p. 194.
5. K. Tang, S. Zheng, X. Jin, *et al.*, J. Chem. Soc., Dalton Trans., 3585 (1997).
6. P. Cui, X. Jin, X. Xie, and K. Tang, J. Chem. Res., Synop. (in press).
7. X. Jin, K. Tang, H. Zeng, *et al.*, Chem. J. Chin. Univ. **7**, 995 (1997).
8. P. Zanello, F. Laschi, M. Fortani, *et al.*, J. Chem. Soc., Dalton Trans., 965 (1999).
9. P. Zanello, F. Laschi, A. Cinquantini, *et al.*, Eur. J. Inorg. Chem., 1345 (2000).
10. T. Zhang, J. Li, P. Gao, *et al.*, Opt. Commun. **150**, 201 (1998).
11. C. Liu, G. Zhao, Q. Gong, *et al.*, Opt. Commun. **184**, 309 (2000).

Physics of the Solid State, Vol. 44, No. 4, 2002, pp. 615–616. Translated from Fizika Tverdogo Tela, Vol. 44, No. 4, 2002, pp. 592–593.

PROCEEDINGS OF THE V INTERNATIONAL WORKSHOP "FULLERENES AND ATOMIC CLUSTERS"

(St. Petersburg, Russia, July 2–6, 2001)

Synthesis of Fullerene-Containing Polymer Composites and Investigation of Interactions in These Systems

V. N. Zgonnik, L. V. Vinogradova, E. Yu. Melenevskaya, K. Yu. Amsharov, O. V. Ratnikova, Yu. F. Biryulin, A. V. Novoselova, and P. N. Lavrenko

Institute of Macromolecular Compounds, Russian Academy of Sciences, Bol'shoĭ proezd 31, St. Petersburg, 199004 Russia

e-mail: melen@hq.macro.ru

Abstract—The methods of synthesizing fullerene-containing polymer composites are analyzed. It is established that the technique of determining the intrinsic viscosity can be used for evaluating the effect of the fullerene involved in the polymer composite on the polymer chains. The influence of the synthesis procedure on the fullerene content in a water-soluble fraction is demonstrated using the poly(*N*-vinylpyrrolidone)–C_{60} (PVP–C_{60}) system as an example. © *2002 MAIK "Nauka/Interperiodica".*

1. INTRODUCTION

Synthesis of fullerene-containing polymers is a new line in the production of polymer materials. The increasing urgency of this method is due to the fact that composites, for example, of polyconjugated polymers with a fullerene, possess electron conduction, magnetic properties, and photoinduced charge transfer [1–3]. The basic problem concerning the production of composites is associated with the dispersion and mixing of initial components on the molecular level. It is found that fullerenes manifest the highest activity when they are introduced into composites without aggregation. The development of special techniques providing a means for the molecular dispersion of fullerenes in composites is a topical problem. Moreover, it remains unclear how the complex formation in polymer–fullerene systems affects the flexibility of polymer chains, the segment dynamics, the ball size, and the ability to associate and form supramolecular structures.

2. SAMPLES AND EXPERIMENTAL TECHNIQUE

In this work, the polymer–fullerene composites were synthesized from widely used initial polymers, such as poly(2,6-dimethyl-1,4-phenylene oxide) (PPhO), linear and cyclic poly(acrylonitriles) (PAN) and their copolymers, poly(methyl methacrylate) (PMMA), and poly(*N*-vinylpyrrolidone) (PVP). The synthesis was performed according to two basic methods: (1) vacuum evaporation of a mixture of solvents from a solution of the components or their sedimentation and (2) the solid-phase reaction between the components under vacuum.

3. RESULTS AND DISCUSSION

The low solubility of C_{60} fullerenes, as a rule, leads to the formation of aggregates when using synthesis method *1*. In method *2*, as was shown in [4], the dispersion can proceed up to the formation of small-sized aggregates.

The PPhO composites with C_{60} at a fullerene content in the range from 0.5 to 4% were studied using IR spectroscopy (a shift of the 525- and 575-cm^{-1} absorption bands by 1.5 cm^{-1}) and photoluminescence (a shift in the maximum toward the high-energy range). These measurements revealed the complex formation in the given system. In recent works [5, 6], the PPhO complex with C_{60} (0.5 wt %) in benzene was examined by high-rate sedimentation, free diffusion, and viscometry. It was demonstrated that, in this system, the complex formation manifests itself in a decrease in the intrinsic viscosity of the initial PPhO polymer by approximately 14%. This finding agrees with the inferences regarding both the local nature of the interaction within a single macromolecule and the lack of association of the polymer complexes in the solution. It can be stated that the C_{60} fullerene has a restructuring effect on the PPhO chain units (distant chain units included), for which the hydrodynamic radius of the equivalent sphere in an isolated state is almost 50 times larger than the radial size of the C_{60} molecule.

The simplest method of testing for the formation of polymer composites turned out to be viscometry. In the case when the composites were examined by viscometry, the dilution was accomplished with both a solvent and a fullerene solution in the solvent in order to displace the equilibrium toward complex formation (see table). The observed decrease in the intrinsic viscosity of the studied composites permits intramolecular com-

1063-7834/02/4404-0615$22.00

Viscometric characteristics of polymers and their complexes with C_{60} fullerene

No.	Sample	Solvent	[η], cm^3/g
1	PMMA	Toluene	0.34
2	PMMA–C_{60}	Toluene (+C_{60})	0.25
3	PAN	Methylpyrrolidone	1.55
4	PAN–C_{60}	Methylpyrrolidone (+C_{60})	1.40
5	PAN (cyclization)	Methylpyrrolidone	0.25
6	PAN (cyclization)–C_{60}	Methylpyrrolidone (+C_{60})	0.25
7	Copolymer (PAN–BA)*	Methylpyrrolidone	2.70
8	Copolymer (PAN–BA)*–C_{60}	Methylpyrrolidone (+C_{60})	2.00
9	PAN	Dimethylformamide	3.70
10	(PAN–C_{60})**	"	2.90

* The copolymer (PAN–BA) contained 8 mol % butyl acrylate.

** The composite was preliminarily prepared by precipitation in water from a dimethylformamide–toluene solution with the volume ratio 5 : 1.

plex formation, a decrease in asymmetry, and compaction of the polymer chain involved in the complex. The lack of the effect for the cyclic PAN and a weaker effect for the homo-PAN indicate a larger inflexibility in this polymer. A comparison of the results of the dilution (when determining the intrinsic viscosity) with the solvent and the fullerene solution allows us to make an inference regarding the relative intensity of the interaction between the components in the system under investigation.

It was found that the PAN composites with C_{60} (0.5 wt %) in solutions of dimethylformamide in the form of films are capable of decreasing laser radiation (by 5–7%) and retain no less than 50% of their transparency in the process. At a higher content of the fullerene, the ability to limit laser radiation decreases, which indicates the presence of C_{60} aggregates in these systems.

It should be noted that a system such as water-soluble complexes of PVP and C_{60} is of considerable interest both from the practical standpoint (this system is capable of suppressing virus activity [7]) and with respect to investigation of the properties of C_{60} fullerenes. The use of porphyrine (TPhP) admixtures in the preparation of PVP–C_{60} complexes according to method *1* makes it possible to increase the relative content of the fullerene (6 wt %). Elucidation of the mechanism of the interaction in the ternary PVP–C_{60}–TPhP system demonstrated that an increase in the fraction of C_{60} in this system is achieved at an optimum content of water that is strongly bound to PVP and affects the polymer conformation. Apparently, TPhP prevents aggregation of the fullerene during the synthesis of the composites. ^{13}C NMR solid-state spectroscopy revealed the formation of complexes between C_{60} and TPhP in the ternary system (a shift of the C_{60} signal from 143 to 142 ppm). In the solution free of PVP, the C_{60}–TPhP complex was not detected by the NMR technique. The preparation of PVP–C_{60} composites according to method *2* in a vacuum system with an admixture of anhydrous KBr increases the relative fraction of the fullerene in the water-soluble fraction to 3%. The introduction of KBr favors a decrease in the fraction of fullerene aggregates in the composite. This can be judged from a comparison of the electronic spectra of water solutions of the PVP–C_{60} and PVP–C_{60}–KBr composites.

ACKNOWLEDGMENTS

This work was supported by the Russian Scientific and Technical Program "Fullerenes and Atomic Clusters," project no. 98076.

REFERENCES

1. M. Prato, Top. Curr. Chem. **199**, 173 (1999).
2. C. J. Brabec, N. S. Saricifici, and J. C. Hummelen, Adv. Funct. Mater. **11**, 15 (2001).
3. S-A. Chen, K-R. Chuang, C-I. Chao, and H-T. Lee, Synth. Met. **32**, 207 (1996).
4. V. A. Reznikov, E. Yu. Melenevskaya, L. S. Litvinova, and V. N. Zgonnik, Vysokomol. Soedin., Ser. A **42** (2), 229 (2000).
5. N. P. Evlampieva, P. N. Lavrenko, L. V. Vinogradova, *et al.*, in *Proceedings of the 3rd International Conference "Chemistry of Highly Organized Substances and Scientific Principles of Nanotechnologies," 2001*, p. 237.
6. P. N. Lavrenko, N. P. Evlampieva, D. M. Volokhova, *et al.*, Vysokomol. Soedin. (in press).
7. O. I. Kiselev, K. N. Kozeletskaya, L. V. Vinogradova, *et al.*, Mol. Mater. **11**, 121 (1998).

Translated by O. Moskalev

Physics of the Solid State, Vol. 44, No. 4, 2002, pp. 617–622. From Fizika Tverdogo Tela, Vol. 44, No. 4, 2002, pp. 594–598.

PROCEEDINGS OF THE V INTERNATIONAL WORKSHOP "FULLERENES AND ATOMIC CLUSTERS"

(St. Petersburg, Russia, July 2–6, 2001)

Phosphorus Clusters: Synthesis in the Gas-Phase and Possible Cagelike and Chain Structures[1]

A. V. Bulgakov*, O. F. Bobrenok*, V. I. Kosyakov, I. Ozerov***, W. Marine***, M. Hedén***, F. Rohmund****, and E. E. B. Campbell******

** Institute of Thermophysics, Siberian Branch of Russian Academy of Sciences, Novosibirsk, 630090 Russia*

e-mail: bulgakov@itp.nsc.ru

*** Institute of Inorganic Chemistry, Novosibirsk, 630090 Russia*

**** Université de la Méditerranée, GPEC, UMR CNRS 6631, Marseille, France*

***** Göteborg University, Chalmers University of Technology, Göteborg, Sweden*

Abstract—Experimental results on the gas-phase formation of neutral and cationic phosphorus clusters are presented. The clusters were synthesized by visible (532 nm) or UV (193 nm) laser ablation of crystalline red phosphorus under high vacuum conditions and were analyzed using TOF mass spectrometry. Neutral P_n clusters produced by 532-nm ablation are found to be even-numbered while P_n^+ cations are mainly odd-numbered, with P_7^+ and P_{21}^+ being the most abundant ions. For UV laser ablation, stable compound clusters, neutral P_7H_3 and $P_{23}H_5$, and cations $P_{23}H_6^+$ were synthesized for the first time. The formation of P_n clusters by thermal vaporization of red phosphorus into a cold He gas was also investigated and only small clusters ($n < 6$) were found. Possible structures of the observed phosphorus clusters, as well as their formation mechanisms under different conditions, are discussed. © *2002 MAIK "Nauka/Interperiodica".*

The discovery of fullerenes has naturally raised the question as to whether carbon is unique or other elements can also form stable closed cages. Recently, there has been renewed interest in the study of phosphorus clusters [1–3], which are expected to display a variety of structural forms. Two main structural families have been considered theoretically, chains and cages (polyhedra) [1, 3–9]. A number of closed-shell structures for P_n clusters have been proposed to be probably energetically more stable then tetrahedral P_4. Also, the viability of phosphorus nanotubes has been theoretically predicted [10].

These theoretical suggestions, however, still have not been confirmed by experiment. Only a few experiments have been performed on clusters larger than P_4 [11–13]. Recently, a wide spectrum of neutral and cationic phosphorus clusters were synthesized in the gas phase by visible laser ablation of crystalline red phosphorus [2]. The cationic P_{21}^+ cluster was found to be the most abundant ion. Based on a topological analysis, it was suggested that dodecahedral fullerene-like P_{20}, stabilized with an additional phosphorus ion in the laser plasma, could be particularly stable. It was also speculated that the efficient generation of cagelike P_n clusters could be explained by the presence, in the laser plume, of their building blocks, which are already formed in the target and ejected from its surface under irradiation.

In this paper, we continue our investigations on the gas phase formation of phosphorus clusters. This work is focused mainly on the role played by particles directly ejected (vaporized) from red phosphorus. Three vaporization regimes, principally different in terms of their particle ejection mechanisms, were studied: ablation by visible (532 nm) and UV (193 nm) laser light and thermal vaporization in a carrier gas. Possible structures of the observed P_n clusters, as well as their formation mechanisms under different conditions, are discussed.

1. EXPERIMENTAL

The apparatus used for laser ablation and cluster generation and detection was described earlier in [14–16]. In brief, the target was placed in a rotating holder in a vacuum chamber (base pressure 10^{-5} Pa) and irradiated at normal incidence by a 13-ns FWHM laser pulse at 532 nm (the second harmonic of a Nd:YAG laser) or at an incidence angle of 45° by a 15-ns FWHM ArF laser pulse at 193 nm. Crystalline red phosphorus (also called Hittorf's phosphorus) of 99.999% purity

[1] This article was submitted by the authors in English.

(with respect to metals) was used as the target. The laser fluence on the target was varied in the range 0.02–0.8 J/cm^2 at a fixed spot area of about 0.4 mm^2 with the Nd:YAG laser and about 6 mm^2 with the ArF laser.

The relative abundance of neutral and positively charged particles in the laser-ablation plume was analyzed using a reflection time-of-flight mass spectrometer (RETOF MS). When ions were studied, the plume was allowed to expand under field-free conditions, while the neutral particles of the plume were analyzed using a simple plasma suppressor [14]. The latter consisted of a pair of deflection plates placed along the plume axis in front of the ion source of the MS, where neutral particles were pulse-ionized by 90-eV electrons. The 900 V/cm deflection field was sufficient for removal of the plasma ions throughout the studied laser fluence range. At a distance of 6 cm (with 532-nm ablation) or 7 cm (with 193-nm ablation) from the target, the ions, either ablated or post-ionized, were sampled perpendicular (at 532 nm) or parallel (at 193 nm) to the plume axis by a 500-V repeller pulse after a time delay t_d following the laser pulse.

P_n cluster formation during thermal vaporization in a gas aggregation source [17, 18] has also been investigated. In this source, phosphorus vapor was created in an oven at 570–620 K and quenched in an aggregation chamber in a cold He gas at a pressure of about 1 Torr. The outer mantel of the chamber was cooled with liquid nitrogen. The high efficiency of this type of cluster source has been demonstrated previously for a number of materials [11, 17–19]. The clusters condensed out in the quenched vapor were transported by the gas stream through a nozzle at a temperature of 80–100 K. They crossed a differentially pumped region and were then pulse-ionized with 90-eV electrons and analyzed with a RETOF MS.

All spectra reported here represent an average over ~200 pulses.

2. RESULTS AND DISCUSSION

Figure 1a shows the TOF mass spectra of cation species in the plume with 532-nm ablation under "optimum" conditions corresponding to the maximum yield of large P_n^+ clusters ($n > 9$). Figures 1b, 1c illustrate typical mass spectra of P_n^+ cations obtained with 193-nm ablation. Clearly, the spectra are quite different. With visible laser ablation, large P_n clusters are generated in abundance and their concentration in the plume is found to be comparable to that of molecules and small clusters. The mass distribution comprises mainly odd-numbered P_n^+ clusters and is rather smooth with few magic numbers (Fig. 1a). The strongest peaks correspond to P_7^+ and P_{21}^+ cations.

In contrast, with UV laser ablation, P_n clusters are presented in minor amounts in the plume. Even under "optimum" conditions, the intensities of the strongest cluster peaks are less by about two orders of magnitude than those of molecular peaks ($n = 2$–5). The abundance spectra represent only a few individual peaks corresponding, presumably, to the most stable clusters under these conditions. These stable species consist mainly of compound (oxidized and phosphane) clusters, again in contrast to 532-nm ablation in which pure P_n clusters dominate. The O and H atoms appear to come from trace impurities in the red phosphorus. More efficient generation of compound clusters under UV light irradiation may be attributed to photodissociation and photodissociative ionization of the surface impurities in this case. The generated O and H atoms and ions react in the near-surface region with the ablated P_n clusters, which leads to the formation of stable structures.

The most intriguing feature of the mass spectra obtained with UV laser pulses is the strong dominance of the $P_{23}H_6^+$ cluster cation, which was not observed with visible lasers. It is particularly abundant at a very low fluence of 0.06 J/cm^2 (Fig. 1b) and is the only cluster that survives in the $n > 15$ range when the laser fluence is doubled (Fig. 1c).

A study of the ablation plume dynamics by varying the time delay t_d also revealed different cluster expansion behavior for the two considered cases. With 532-nm ablation, large clusters ($n > 9$) are found to have approximately the same expansion velocity (about 1.6 km/s for the conditions shown in Fig. 1a) in spite of the large difference in their mass. This implies a gas-phase condensation mechanism of cluster formation rather than their direct ejection. In the latter case, one would expect the same kinetic energy of the plume particles rather than the same velocity. However, smaller P_n species ($n < 9$), and also oxidized clusters, are mainly ejected directly from the target [2]. With 193-nm ablation, the most probable velocities of the observed clusters (Figs. 1b, 1c) are found to decrease gradually with increasing cluster size, implying the direct ejection mechanism of cluster generation. The ejection of "building blocks" (P_7–P_9) of larger P_n clusters is much less efficient than in the case of 532-nm ablation and does not seem to be sufficient for gas-phase cluster growth.

Figure 2 shows mass spectra of neutral clusters obtained for the three experimental situations considered. Relatively large P_n clusters are generated in abundance during visible laser ablation (Fig. 2a). The clusters are mainly even-numbered with "magic sizes" at $n = 10$, 14, and 40 (the latter is not shown in Fig. 2a). In the $n = 16$–26 range, there is a prominent local minimum at $n = 22$. The analysis of cluster velocity distributions indicates again the gas-phase condensation mechanism of their formation. For UV laser ablation,

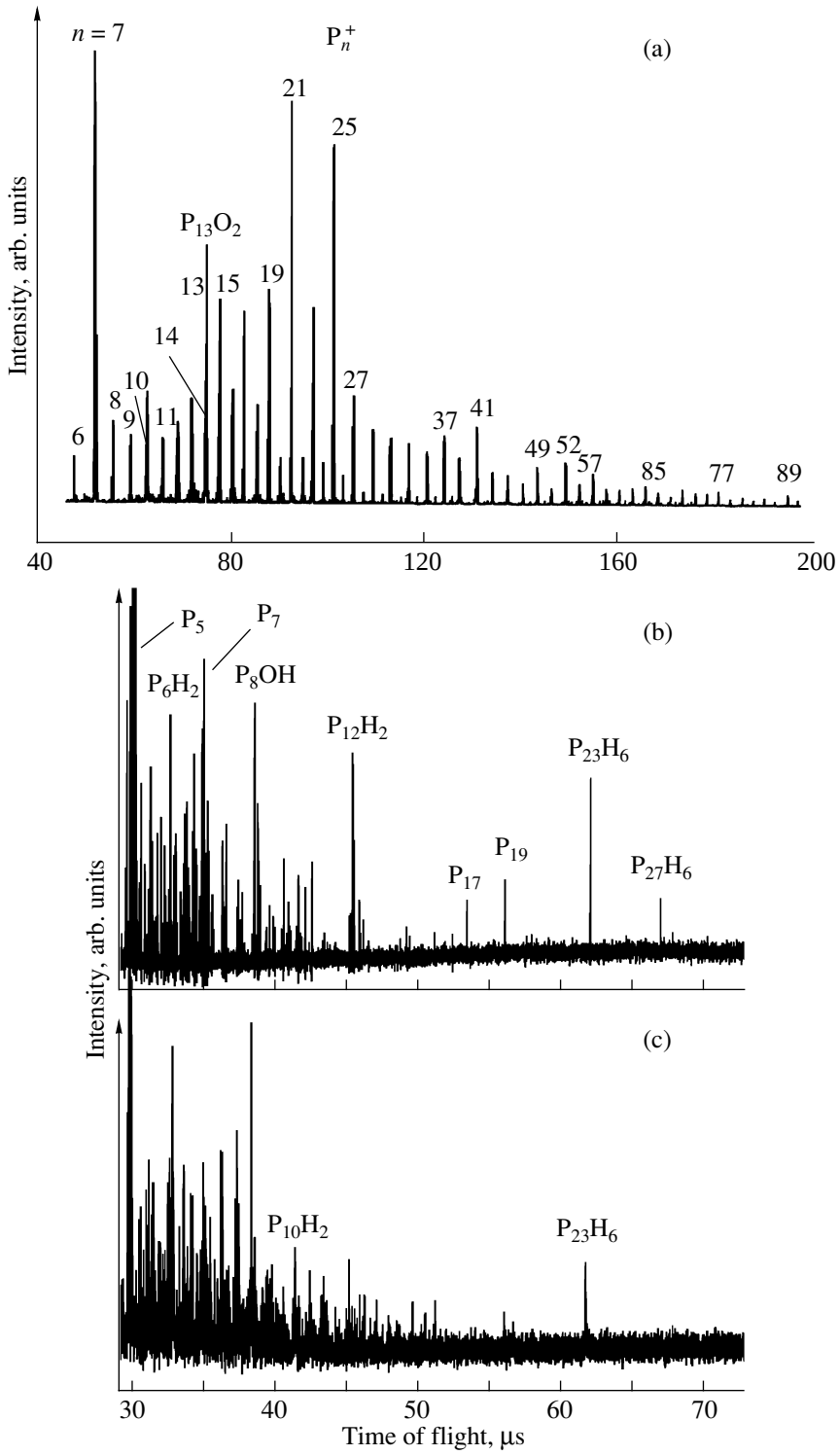

Fig. 1. TOF mass spectra of phosphorus cluster cations produced by laser ablation: (a) 532-nm laser ablation, laser fluence E = 0.3 J/cm^2, time delay t_d = 37 μs; (b) 193-nm laser ablation, E = 0.06 J/cm^2, t_d = 62 μs; and (c) same as (b) but E = 0.13 J/cm^2.

the plume consists mostly of atoms and small molecules, among which P_2 dominates (Fig. 2b). In the larger mass region, only two neutral compound clusters P_7H_3 and $P_{23}H_5$ were registered.

Figure 2c shows a mass spectrum of particles produced during thermal vaporization of red phosphorus in the gas aggregation source. Only atoms and small molecules have been registered with such a source when the

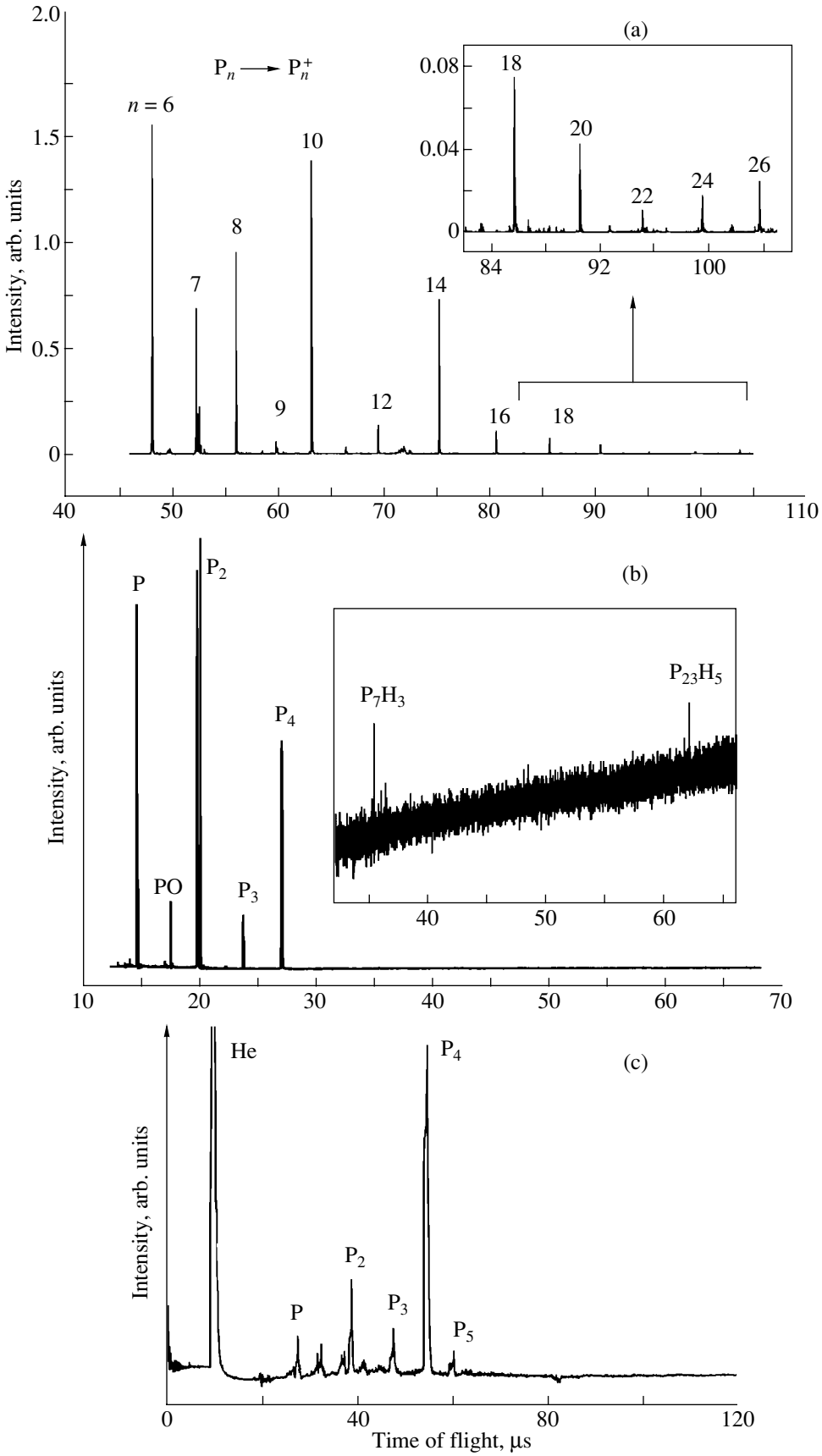

Fig. 2. TOF mass spectra of neutral phosphorus cluster produced under different conditions; (a) 532-nm laser ablation, E = 0.3 J/cm^2, t_d = 37 μs; (b) 193-nm laser ablation, E = 0.06 J/cm^2, t_d = 62 μs; and (c) gas aggregation source, oven temperature of 590 K.

initial vapor consists mainly of P_2 dimers [4]. The strongest peak corresponds to the P_4 molecule. Obviously, the aggregation process in this case is terminated by the formation of the stable tetrahedral P_4. The key role of the ejection of small P_n clusters (n = 7–9) for the gas-phase growth of larger clusters is thus again demonstrated. It also seems likely that such a termination of the aggregation process can be avoided by adding a reactant gas into the chamber [11].

Of particular interest is the question of the possible structures of the observed phosphorus clusters and, specifically, of the abundant P_{21}^+ and $P_{23}H_6^+$ cations and P_7H_3 and $P_{23}H_5$ neutrals. Note that the availability of compound clusters, both neutral and ionized, can provide additional information on the structures of the phosphorus skeletons. In particular, the presence of an additional H atom in cationic $P_{23}H_6^+$, as compared to the corresponding neutral cluster, support recent calculations [1, 3, 12] suggesting that P_n^+ cations adopt structures with one four-coordinated atom.

The local abundance minimum at n = 22 for neutral phosphorus clusters (Fig. 2a) provides convincing circumstantial evidence of the presence of fullerene-like P_n clusters in the plume induced by a 532-nm laser pulse. In fact, all the even-numbered polyhedra can be geometrically realized from P_{20} up to P_{60} (some in more than one form) except P_{22} [20]. The chain structure is still possible for P_{22} [7] (a plausible stable structure is shown in Fig. 3a). One would thus speculate that dodecahedral fullerene-like P_{20}, stabilized in the plasma with an additional fourfold coordinated atom (as shown in Fig. 3b), could be especially stable and explain the magic number of 21 in the cation spectra obtained from visible laser ablation (Fig. 1a).

Since the observed compound clusters are ejected directly from the target, they should adopt structures with skeletons corresponding to the structural groups of red phosphorus. We believe that the stable P_7H_3 neutral is a cagelike cluster constituting 3 five-membered rings and a triangle with three bridge P atoms and three H atoms satisfying the dangling bonds (Fig. 3c). This structure has been identified by x-ray spectroscopy as the most stable P_7-based skeleton in polyphosphides [5]. Assuming the direct ejection mechanism to be in effect, one can also easily design the structure of the magic clusters $P_{23}H_6^+$ and $P_{23}H_5$. Their phosphorus skeleton should represent the main unit of an infinite double "tube" of crystalline red phosphorus built from successive translation of the chain P_{23} cluster [21]. Figure 3d shows a plausible structure for the $P_{23}H_6^+$ ion, which needs six H atoms to satisfy the dangling bonds (assuming that one P atom is four-connected). In the neutral $P_{23}H_5$ cluster, all P atoms are threefold.

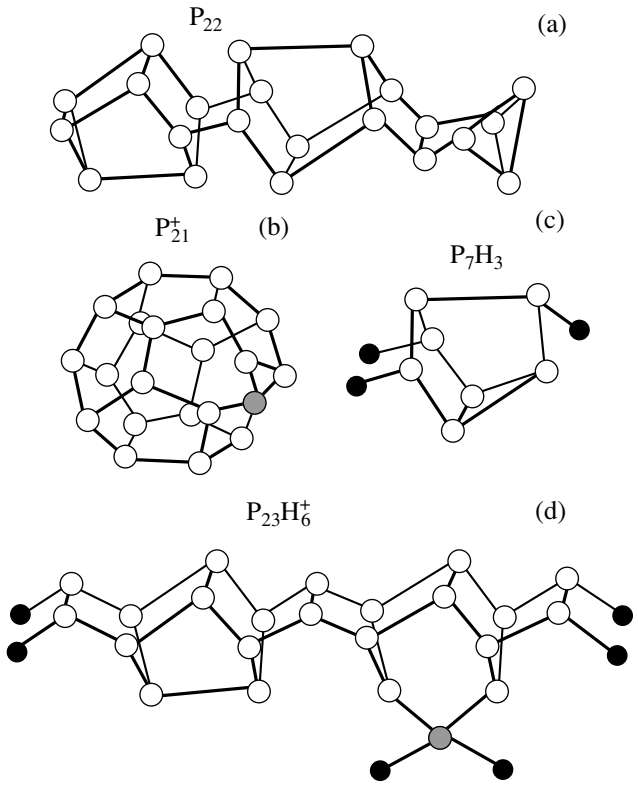

Fig. 3. Possible structures of some phosphorus clusters observed in laser ablation plumes. Grey circles in (b) and (d) show a four-coordinated P atom. Closed circles in (c) and (d) stand for hydrogen atoms.

ACKNOWLEDGMENTS

This work was supported by the Russian Foundation for Basic Research (project no. 99-03-33372), by the Russian Scientific and Technical Program "Fullerenes and Atomic Clusters" (project no. 5-4-99), and by the Royal Swedish Academy of Sciences.

REFERENCES

1. M. D. Chen, J. T. Li, R. B. Huang, *et al.*, Chem. Phys. Lett. **305**, 439 (1999).
2. A. V. Bulgakov, O. F. Bobrekov, and V. I. Kosyakov, Chem. Phys. Lett. **320**, 19 (2000).
3. M. D. Chen, R. B. Huang, L. S. Zheng, *et al.*, Chem. Phys. Lett. **325**, 22 (2000).
4. D. E. C. Corbridge, *The Structural Chemistry of Phosphorus* (Elsevier, Amsterdam, 1974).
5. V. I. Kosyakov, Izv. Sib. Otd. Akad. Nauk SSSR, Ser. Khim. Nauk, No. 9, 96 (1982).
6. R. O. Jones and G. Seifert, J. Chem. Phys. **96**, 7564 (1992).

7. M. Häser, U. Schneider, and R. Ahlrichs, J. Am. Chem. Soc. **114**, 9551 (1992).
8. M. Häser and O. Treutler, J. Chem. Phys. **102**, 3703 (1995).
9. C.-H. Hu, M. Shen, and H. F. Schaefer, III, Theor. Chim. Acta **88**, 29 (1994).
10. G. Seifert and E. Hernández, Chem. Phys. Lett. **318**, 355 (2000).
11. T. P. Martin, Z. Phys. D **3**, 211 (1986).
12. R. Huang, H. Li, Z. Lin, and S. Yang, J. Phys. Chem. **99**, 1418 (1995).
13. Z. Liu, R. Huang, and L. Zheng, Z. Phys. D **38**, 171 (1996).
14. B. N. Kozlov, I. I. Pilyugin, V. G. Shchebelin, *et al.*, Zh. Tekh. Fiz. **64** (9), 155 (1994) [Tech. Phys. **39**, 944 (1994)].
15. A. V. Bulgakov, M. R. Predtechensky, and A. P. Mayorov, Appl. Surf. Sci. **96–98**, 159 (1996).
16. L. Patrone, D. Nelson, V. I. Safarov, *et al.*, Appl. Phys. A **69**, S217 (1999).
17. K. Hansen, H. Hohmann, R. Müller, and E. E. B. Campbell, J. Chem. Phys. **105**, 6088 (1996).
18. K. Hansen, R. Müller, H. Hohmann, and E. E. B. Campbell, Z. Phys. D **40**, 361 (1997).
19. T. P. Martin, U. Näher, H. Schaber, and U. Zimmermann, Phys. Rev. Lett. **70**, 3079 (1993).
20. A. F. Wells, *Structural Inorganic Chemistry* (Clarendon, Oxford, 1984, 5th ed.).
21. H. Turn and H. Krebs, Acta Crystallogr. B **25**, 125 (1969).

Physics of the Solid State, Vol. 44, No. 4, 2002, pp. 623–624. Translated from Fizika Tverdogo Tela, Vol. 44, No. 4, 2002, pp. 599–600.

PROCEEDINGS OF THE V INTERNATIONAL WORKSHOP "FULLERENES AND ATOMIC CLUSTERS"

(St. Petersburg, Russia, July 2–6, 2001)

A Novel Covalent Crystal Formed by Carbon (6, 0) Nanotubes: Structure and Electronic Properties

E. G. Gal'pern[1], A. R. Sabirov[1, 2], I. V. Stankevich[1], A. L. Chistyakov[1], and L. A. Chernozatonskiĭ[2]

[1] *Nesmeyanov Institute of Organoelement Compounds, Russian Academy of Sciences, ul. Vavilova 28, Moscow, 119991 Russia*

[2] *Émanuel Institute of Biochemical Physics, Russian Academy of Sciences, ul. Kosygina 4, Moscow, 119991 Russia*

e-mail: stan@ineos.ac.ru

Abstract—The structure of a carbon crystal formed by (6, 0) nanotubes is simulated. The electronic spectrum of the crystal is calculated by the crystalline-orbital method in the valence approximation. The band gap of the studied crystal is found to be equal to 1.3 eV. © *2002 MAIK "Nauka/Interperiodica".*

1. INTRODUCTION

The discovery of single-walled carbon nanotubes (SWNTs) and their synthesis in large amounts [1, 2] have lent impetus to a great number of interdisciplinary investigations. Quite recently, Schlittler *et al.* [3] prepared molecular crystals with close-packed SWNTs according to a special technology using SWNTs of the same diameter D ($1.4 \le D \le 2.3$ nm in each crystalline stack). In recent works [4–6], the properties of similar materials were investigated under high pressure. Popov *et al.* [6] synthesized a material consisting of polymerized nanotubes in a diamond chamber under shear load (~10–20 GPa).

The possible formation of the dimer and trimer SWNT structures connected by covalent bonds was considered already in the first works concerning the structure of SWNTs [7, 8]. Some variants of the formation of crystal phases from polymerized SWNTs were analyzed in [9].

Since the synthesis of bundles of small-diameter ($D < 1$ nm) nanotubes has already been reported in [2], in the present communication, the primary attention is focused on the polymerization of SWNTs that should polymerize at relatively low pressures and temperatures owing to a large surface curvature. This assumption is based on the fact that the layered polymer structures were synthesized from C_{60} fullerenes with a diameter $D = 0.7$ nm under a pressure of 2–5 GPa at temperatures ranging from 200 to 300°C [10]. The main structural transformations in these materials occur through a simple reaction widely known in organic chemistry, namely, the (2 + 2) cycloaddition.

2. SIMULATION TECHNIQUE AND RESULTS

In this work, we simulated the structure and electronic properties of a covalent crystal composed of (6, 0) nanotubes of the zigzag type with a hexagonal unit cell (Fig. 1a). Single-walled carbon nanotubes are aligned parallel to each other. Each nanotube is connected to its six neighbors through covalent bonds. In the crystal structure, four-membered and six-membered rings alternate along the bonds between the nanotubes. The cross sections of the nanotubes in the plane perpendicular to the tube axes form a close-packed structure. This crystal structure is described by the space group $P6/mmm$ with 24 atoms per unit cell.

The unit cell of the crystal was simulated in the framework of the MNDO/PM3 quantum-chemical method using the GAMESS software package [11]. Note that, in our earlier work [12], we applied this method to the description of the structure of a covalent crystal consisting of (D_{6h})–C_{36} fullerenes. The parameters of the hexagonal unit cell of the nanotube structure and atomic coordinates were chosen by optimizing the energy of a $C_{252}H_{108}$ hydrocarbon molecule with D_{6h} symmetry. This fragment of the lattice was cut out from the crystal structure by a cylinder, whose axis coincided with the symmetry axis of the central nanotube, and two planes perpendicular to the axis of the cylinder. The C–C dangling bonds were replaced by the C–H bonds. The coordinates of the nonequivalent atoms in the crystal unit cell were found to be as follows (in Å): 0.402, 0, 0.181 for C(1) and 0, 0.359, 0.340 for C(2). The unit cell parameters of the hexagonal lattice are $a = 6.684$ Å and $c = 4.206$ Å (the c axis is aligned parallel to the tube axes). This structure has four nonequivalent types of C–C bonds: (i) the C_1–$C_{1'}$ bonds (1.522 Å) are aligned par-

1063-7834/02/4404-0623$22.00 © 2002 MAIK "Nauka/Interperiodica"

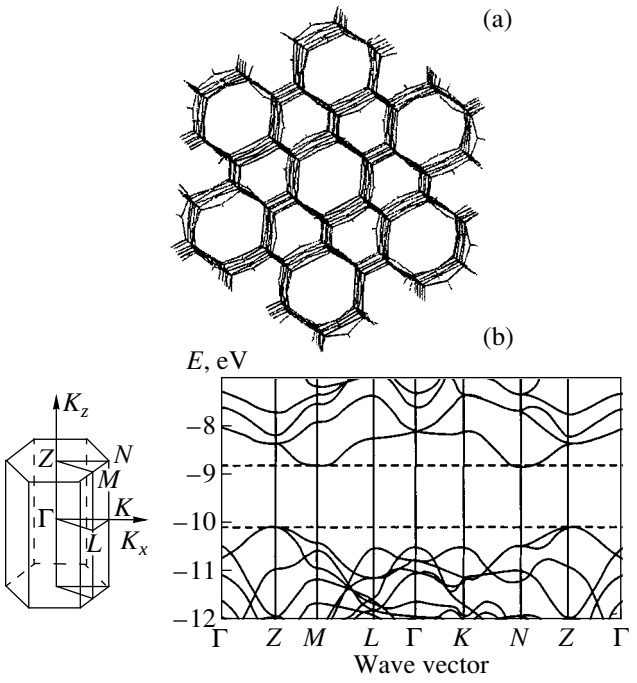

Fig. 1. (a) Crystal structure consisting of polymerized carbon (6, 0) nanotubes and (b) the Brillouin zone and the electronic spectrum of the crystal.

allel to the tube axes and participate in the formation of the four-membered ring, (ii) the C_2–$C_{2'}$ bonds (1.350 Å) are aligned parallel to the tube axes and are involved in the formation of the six-membered ring, (iii) the C_1–C_2 bonds (1.503 Å) are perpendicular to the tube axes, and (iv) the C_1–$C_{1''}$ bonds (1.605 Å) link the atoms of the adjacent tubes.

The electronic spectrum of the crystal structure was calculated in the valence approximation of the extended Hückel method within the crystalline-orbital formalism according to the program described earlier in [13]. Figure 1b represents the band structure of the energy spectrum and the Brillouin zone of the crystal. As is seen from Fig. 1, this crystal is a semiconductor with a band gap of ≈1.27 eV.

3. CONCLUSIONS

Thus, we simulated the geometric and electronic structures of a new crystalline carbon form (D_{6h} symmetry) composed of covalently bonded (6, 0) nanotubes. It was demonstrated that, upon changing over from isolated nanotubes in a molecular crystal to the polymer structure, the electronic spectrum of the semimetal transforms into the spectrum of a semiconductor. Since half the total number of atoms in the crystal structure under consideration are bound by double bonds, the crystal should exhibit high values of the elastic constants; consequently, the hardness should also be high (comparable to the diamond hardness), as is the case with the three-dimensional polymerization of C_{60} [14].

ACKNOWLEDGMENTS

This work was supported by the Russian Foundation for Basic Research, the State Scientific and Technical Program "Fullerenes and Atomic Clusters," and the International Association of Assistance for the promotion of cooperation with scientists from the New Independent States of the former Soviet Union, project INTAS no. 00-279.

REFERENCES

1. A. Thess, R. Lee, P. Nikolaev, *et al.*, Science **273**, 483 (1996).
2. C. Journet, W. K. Maser, P. Bernier, *et al.*, Nature (London) **388**, 756 (1997).
3. R. R. Schlittler, J. W. Seo, J. K. Gimezewski, *et al.*, Science **292**, 1136 (2001).
4. S. A. Chesnokov, V. A. Nalimova, A. G. Rinzler, *et al.*, Phys. Rev. Lett. **82**, 343 (1999).
5. J. Tang, Lu-Chang Qin, T. Sasaki, *et al.*, Phys. Rev. Lett. **85**, 1887 (2000).
6. M. Popov, M. Kyotani, Y. Koga, and R. J. Nemanich, Phys. Rev. B (2001) (in press).
7. L. A. Chernozatonskii, Phys. Lett. A **209**, 229 (1992).
8. Z. Ya. Kosakovskaya, L. A. Chernozatonskiĭ, and E. P. Fedorov, Pis'ma Zh. Éksp. Teor. Fiz. **56**, 26 (1992) [JETP Lett. **56**, 26 (1992)].
9. L. A. Chernozatonskii, E. G. Gal'pern, N. R. Serebryanaya, and I. V. Stankevich, in *Electronic Properties of Novel Materials—Science and Technology of Molecular Nanostructures: Proceedings of the XIII International Winterschool, Kirchberg, Tirol, Austria, 1999*, Ed. by H. Kuzmany, J. Fink, M. Mehring, and S. Roth, AIP Conf. Proc. **486**, 284 (1999).
10. M. Nunez-Regueiro, L. Marques, J.-L. Hodeau, *et al.*, Phys. Rev. Lett. **74** (2), 278 (1995).
11. M. W. Schmidt, K. K. Baldridge, J. A. Boatz, *et al.*, J. Comput. Chem. **14**, 1347 (1993).
12. E. G. Gal'pern, A. R. Sabirov, V. V. Stankevich, *et al.*, Pis'ma Zh. Éksp. Teor. Fiz. **73**, 556 (2001) [JETP Lett. **73**, 491 (2001)].
13. D. A. Bochvar, E. G. Gal'pern, and V. V. Stankevich, Zh. Strukt. Khim. **29**, 26 (1988).
14. L. Chernozatonskii, N. Serebryanaya, and B. Mavrin, Chem. Phys. Lett. **316** (3–4), 199 (2000).

Translated by O. Moskalev

Physics of the Solid State, Vol. 44, No. 4, 2002, pp. 625–628. From Fizika Tverdogo Tela, Vol. 44, No. 4, 2002, pp. 601–604.

PROCEEDINGS OF THE V INTERNATIONAL WORKSHOP "FULLERENES AND ATOMIC CLUSTERS"

(St. Petersburg, Russia, July 2–6, 2001)

Pressure-Induced Transformations in Two-Dimensional Polymeric Phases of C_{60}[1]

K. P. Meletov*, **, J. Arvanitidis*, S. Assimopoulos*, and G. A. Kourouklis*

** Physics Division, School of Technology, Aristotle University of Thessaloniki, GR-540 06 Thessaloniki, Greece*

*** Institute of Solid State Physics, Russian Academy of Sciences, Chernogolovka, Moscow oblast, 142432 Russia*

e-mail: mele@issp.ac.ru

Abstract—The structural stability of the tetragonal and rhombohedral two-dimensional (2D) polymeric phases of C_{60} was studied under pressures up to 27 GPa at room temperature by means of in situ Raman scattering spectroscopy. The results show that the tetragonal 2D phase undergoes an irreversible transformation in the region of 20 GPa while no pressure-induced transitions were observed for the rhombohedral 2D phase. The obtained data are discussed within the framework of recent numerical calculations, which predict the pressure-induced transformation of the 2D polymeric phases of C_{60} into three-dimensional (3D) polymers in the pressure range 14–20 GPa. © *2002 MAIK "Nauka/Interperiodica".*

Pristine C_{60} in the condensed phase has great potential for polymerization due to the existence of 30 double C=C bonds in the fullerene molecular cage. Covalent polymeric bonds between adjacent molecules are usually built up by the [2 + 2] cycloaddition mechanism, which results in an sp^3-like four-fold coordination of a number of carbon atoms of the molecular cage [1]. The crystal structures of the known polymeric phases of C_{60} were identified as one-dimensional (1D) orthorhombic, 2D tetragonal, 2D rhombohedral, and 3D cubic [2–4]. These phases, as well as the so-called hard fullerite phases of 3D polymeric nature [5], can be prepared under various conditions of high pressure and high temperature treatment. Recent theoretical calculations have predicted that the 2D polymeric phase of C_{60} can be transformed, at room temperature, by uniaxial compression into a 3D polymeric phase [6]. This polymerization will take place at $P \approx 20$ GPa and results in the formation of a stable metallic phase having 24 sp^3- and 36 sp^2-like coordinated carbon atoms in each C_{60} molecule. Another theoretical study [7] predicts that uniaxial compression up to ~14 GPa perpendicular to the chains in 1D or the planes in 2D polymers of C_{60} leads to 3D polymerization with 52, 56, or even 60 sp^3-like coordinated carbon atoms per molecule. To explore these predictions, we studied the pressure response of the 2D tetragonal and rhombohedral polymeric phases of C_{60} at pressures up to ~27 GPa by means of in situ Raman scattering using the diamond anvil cell (DAC) technique.

[1] This article was submitted by the authors in English.

1. EXPERIMENTAL

The 2D polymeric phases of C_{60} were obtained by high pressure and high temperature treatment of 99.99% pure pristine C_{60} at $T = 820$ K, $P \approx 2.5$ GPa and $T = 773$ K, $P \approx 5$ GPa for the tetragonal and rhombohedral polymers, respectively. Raman spectra were recorded using a triple monochromator (DILOR XY-500) equipped with a CCD liquid-nitrogen-cooled detector system. The 514.5 nm line of an Ar^+ laser with a beam power of 2–10 mW, measured before the cell, was used for excitation. Measurements of the Raman spectra at high pressure were carried out using a DAC of the Mao–Bell type. A 4 : 1 methanol-ethanol mixture was used as the pressure transmitting medium, and the ruby fluorescence technique was used for pressure calibration. The specimens had dimensions of ~100 μm and were selected from a batch material by checking their Raman spectrum such that they were spatially uniform and typical of the corresponding phase.

2. RESULTS AND DISCUSSION

The Raman spectra of the 2D tetragonal polymer of C_{60} at pressures up to ~27 GPa and room temperature are illustrated in Fig. 1. The initial spectrum (Fig. 1a), taken under normal conditions, is identical to the spectra of this material reported earlier [8]. The spectrum is richer than that of the pristine C_{60} due to the lower symmetry of the molecule, which, in turn, results in the splitting of degenerate phonon modes and/or the activation of silent modes. As the pressure increases, the Raman peaks shift to higher energies and their bandwidth gradually increases (Fig. 1b, $P \approx 14.1$ GPa). Dra-

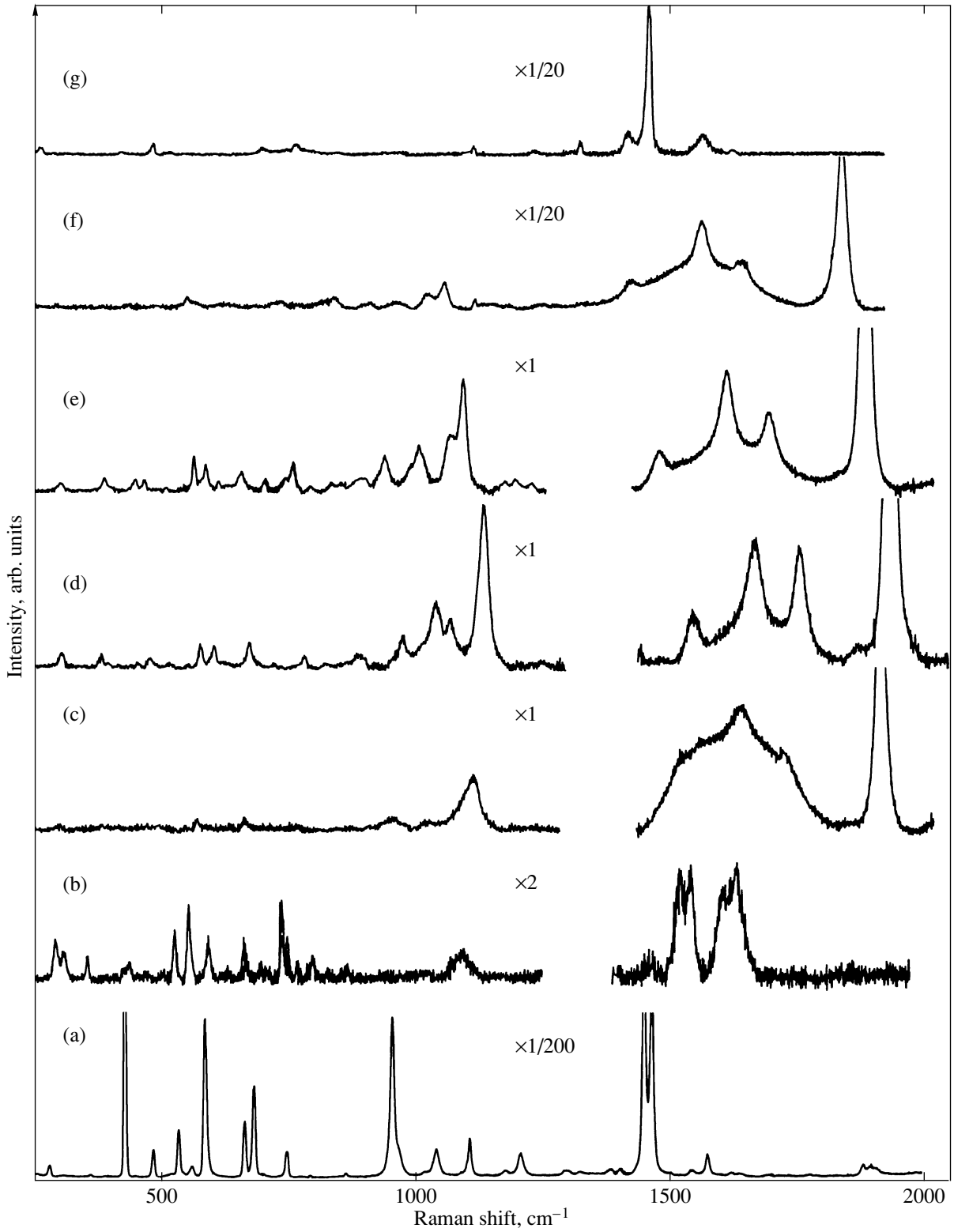

Fig. 1. Raman spectra of the tetragonal 2D polymeric phase of C_{60} at high pressure and room temperature. Spectra (a), (b), (c), (d) are related to an increase in pressure from ambient to 14.1, 20.7, and 27.5 GPa, respectively. Spectra (e) and (f) are related to a decrease in pressure from 12 GPa to ambient. Spectrum (g) is related to the principal part of the detonated sample after the pressure is released.

matic changes are first recorded at a pressure of ~20.7 GPa (Fig. 1c). New features appear which grow rapidly in intensity with increasing pressure up to the highest pressure attained in this study (Fig. 1d, $P \approx$ 27.5 GPa). The transformation of the Raman spectrum is associated with the appearance of new intense peaks near ~1000 and ~1920 cm^{-1}, as well as the disappearance of some old ones. The total number of Raman active modes in the new spectrum is smaller than, whereas the intensity and position of other peaks differ considerably from, those in the initial spectrum. The majority of the peaks can be tracked back to the peaks observed in the tetragonal polymeric phase of C_{60} and may be related to the fullerene molecular cage. The decrease in pressure (Fig. 1e, $P \approx 12$ GPa) up to its total release to ambient pressure (Fig. 1f) results in a gradual shift of the Raman peaks to lower energies, as well as in preservation of the spectrum to ambient pressure. The pressure dependence of the Raman modes of the tetragonal 2D polymeric phase of C_{60} in the high-energy region is shown in Fig. 2. The shaded area marks the pressure region around ~20 GPa where drastic changes in the Raman spectrum took place. Similar changes, at ~20 GPa, are shown also in the pressure dependence of almost all Raman modes. The decrease in pressure from ~27 GPa to ambient pressure, in a time period of about two weeks, does not lead to any observable changes in the Raman intensity distribution, and the new high-pressure phase remains stable. It is important to note that the recovered sample was in fact in a metastable phase, which was detonated by the probing laser beam during the Raman measurements after a time period of a few days from the moment of its exposure to air. The main part of the detonated sample is related to pristine or partially dimerized C_{60} (Fig. 1g), but there was also a small part related to "diamond-like graphite" that has strong Raman peaks at 1339 and 1595 cm^{-1} resembling those of diamond and graphite, respectively.

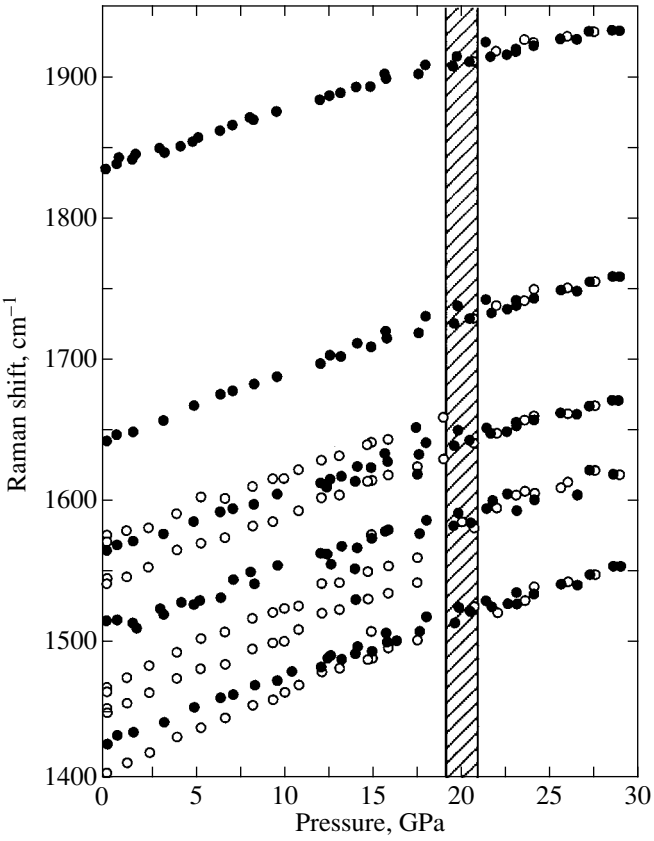

Fig. 2. Pressure dependence of the Raman frequencies of the 2D tetragonal polymeric phase of C_{60} in the high-energy region. Open (closed) symbols are related to the increase (decrease) in pressure. The shaded area near 20 GPa indicates the pressure region of the irreversible transformation of the material.

The Raman spectrum of the rhombohedral 2D polymeric phase of C_{60}, under normal conditions, is shown in Fig. 3. As in the case of the other polymeric phases of C_{60}, the lowering in symmetry results in a very rich Raman spectrum, especially in the low energy region [9]. The spectrum differs in many details from that of the tetragonal 2D polymer of C_{60}. An important difference is related to the frequency of the pentagonal-pinch (PP) mode, which is gradually softened in the polymeric phases of C_{60} in accordance with the increasing number of sp^3-like coordinated carbon atoms per C_{60} molecule. Thus the frequency of the PP-mode decreases from 1469 cm^{-1} for pristine C_{60} to 1465, 1450, and 1408 cm^{-1} for dimerized C_{60}, tetragonal, and rhombohedral polymeric phases, respectively. The pressure dependence of the Raman modes of the rhombohedral polymeric phase of C_{60}, studied up to 10 GPa, is shown in the insert to Fig. 3. The behavior of the material is reversible with pressure (open and closed symbols indicate increases and decreases in pressure, respectively) and does not show any peculiarity in the pressure range investigated.

The obtained experimental data provide a strong indication that the tetragonal 2D polymeric phase of C_{60} undergoes a phase transition at ~20 GPa. The transformation is irreversible and takes place via an intermediate disordered pretransitional state. The retention of the phonon modes of the C_{60} cage and the reduction of the total number of Raman active modes in the high-pressure phase are indications that this phase may be related to a 3D polymerized phase. This agrees well with the expected higher symmetry for the 3D polymeric phase. Another argument in favor of the 3D polymerization is the metastability of the high-pressure phase, which is transformed after a period of time into pristine or partially dimerized C_{60}. The most intriguing feature of the new phase in its Raman spectrum is the presence of a very intense peak at ~1840 cm^{-1}, which cannot be related to any of the fullerene molecular cage modes. The appearance of this peak may be associated

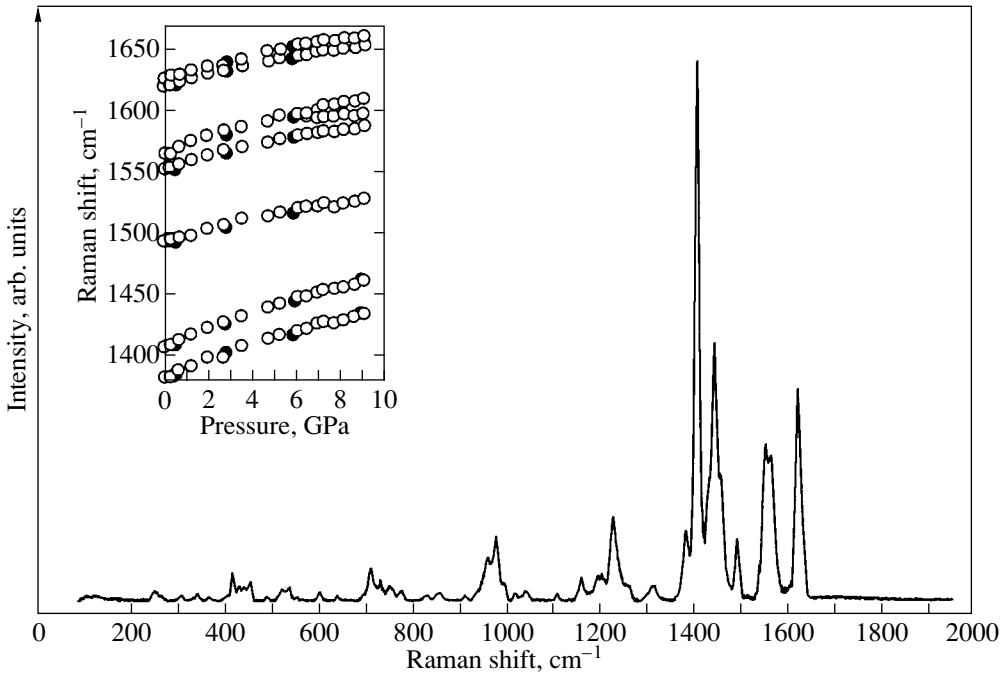

Fig. 3. Raman spectrum of the rhombohedral 2D polymeric phase of C_{60} under normal conditions. Insert shows the pressure dependence of Raman frequencies; open (closed) symbols are related to an increase (decrease) in pressure.

with the considerable distortion of the PP-mode of the pristine C_{60} molecule due to the breakdown of a large number of double C=C bonds and the sp^3-like hybridization of the carbon atoms involved in the intermolecular covalent bonding. The similar strong Raman peak near 1840 cm^{-1}, in some chemical compounds of carbon, is related to the stretching vibration of the isolated double $\rangle$C=C$\langle$ bond [10]. The existence of the 1840 cm^{-1} mode in the high-pressure phase is not compatible with the theoretical calculations in [7], as they predict no phonon mode above 1600 cm^{-1}. On the other hand, the observed transition pressure near ~20 GPa agrees well with the theoretical predictions in [6]; therefore, our results point to the polymerization mechanism predicted in that study.

In conclusion, the pressure-induced irreversible transformation of the 2D tetragonal polymeric phase of C_{60} was observed at ~20 GPa by means of in situ Raman scattering. The data obtained provide a strong indication that the new phase is related to a 3D polymeric phase of C_{60}. The Raman study of the rhombohedral polymeric phase of C_{60} at pressures up to 10 GPa does not show any structural phase transition or irreversible transformation of the material.

ACKNOWLEDGMENTS

The authors thank Mrs. I. Tsilika for her assistance and Profs. Y. Iwasa, K. Prassides, and B. Sundqvist for providing the 2D polymeric samples of C_{60}.

This work was supported, in part, by the Russian Foundation for Basic Research (project no. 99-02-17555). The support of the General Secretariat for Research and Technology (GSRT), Greece (grant no. ΠΕΝΕΔ99, 99ΕΔ/62), is acknowledged.

REFERENCES

1. A. M. Rao, P. Zhou, K.-A. Wans, *et al.*, Science **259**, 955 (1993).
2. Y. Ivasa, T. Arimo, R. M. Fleming, *et al.*, Science **264**, 1570 (1994).
3. M. Nunez-Regueiro, L. Marques, J.-L. Hodeau, *et al.*, Phys. Rev. Lett. **74** (2), 278 (1995).
4. V. V. Brazhkin, A. G. Lyapin, and S. V. Popova, Pis'ma Zh. Éksp. Teor. Fiz. **64** (11), 755 (1996) [JETP Lett. **64**, 802 (1996)].
5. L. Marques, M. Mezouar, J.-L. Hodeau, *et al.*, Science **283**, 1720 (1999).
6. S. Okada, S. Saito, and A. Oshiyama, Phys. Rev. Lett. **83** (10), 1986 (1999).
7. E. Burgos, E. Halac, R. Weht, *et al.*, Phys. Rev. Lett. **85** (11), 2328 (2000).
8. K. P. Meletov, J. Arvanitidis, I. Tsilika, *et al.*, Phys. Rev. B **63** (5), 54106 (2001).
9. J. Arvanitidis, K. P. Meletov, K. Papagelis, *et al.*, Phys. Status Solidi B **215** (1–2), 443 (1999).
10. D. A. Long, *Raman Spectroscopy* (McGraw-Hill, London, 1978), p. 152.

Physics of the Solid State, Vol. 44, No. 4, 2002, pp. 629–630. Translated from Fizika Tverdogo Tela, Vol. 44, No. 4, 2002, pp. 605–606.

PROCEEDINGS OF THE V INTERNATIONAL WORKSHOP "FULLERENES AND ATOMIC CLUSTERS"

(St. Petersburg, Russia, July 2–6, 2001)

Fluorination of the Cubic and Hexagonal C_{60} Modifications by Crystalline Manganese Trifluoride

V. É. Aleshina, A. Ya. Borshchevskiĭ, E. V. Skokan, I. V. Arkhangel'skiĭ, A. V. Astakhov, and N. B. Shustova

Moscow State University, Vorob'evy gory, Moscow, 119899 Russia

Abstract—This paper reports on a comparative study of the solid-state fluorination of the cubic and hexagonal fullerene C_{60} modifications by crystalline manganese trifluoride. It is shown that the variation of the fullerene crystal structure does not noticeably affect the composition of the fluorination products. The enthalpy and entropy of sublimation of the C_{60} hexagonal phase are experimentally determined for the first time. © *2002 MAIK "Nauka/Interperiodica".*

C_{60} molecules crystallizing from a solution or resublimating from the gas phase form, as a rule, a three-layer stack corresponding to the fcc phase, whereas the two-layer stack corresponding to the hcp phase was detected as an impurity forming in crystallization from a solution or in structural transformation of the fcc phase acted upon by an external factor and, therefore, was less available until recently. The technique proposed in [1] for the preparation of the hexagonal phase in macroscopic amounts permits a systematic study of its properties to be made.

This work was aimed at a comparative investigation of the solid-state fluorination of the cubic and hexagonal modifications of crystalline C_{60}.

In the experiments, we used the hexagonal modification of C_{60} prepared by the technique described in [1]. X-ray characterization did not reveal any sign of the cubic phase in the sample. Crystalline manganese trifluoride was employed as the fluorinating agent; its fluorinating properties have been studied most comprehensively for selective preparation of $C_{60}F_{36}$.

The fluorination process was studied by Knudsen mass spectrometry. The starting samples of C_{60} and MnF_3, mixed and ground properly, were placed in a Knudsen cell heated by a W/Re Ohmic resistor. The temperature was measured with a Pt–Pt/Rh thermocouple to within 1–2 K. The mixtures contained a molar excess of the fullerene. The molecular beam effusing from the cell was ionized by 75-eV electrons, and the ions thus produced were measured in an MI-1201 commercial mass spectrometer modified for use in high-temperature studies. Information on the conditions under which the solid-phase fluorination reactions (1) were performed is specified in Table 1.

$$C_{60}(\text{g.}) + n\text{MnF}_3(\text{cr.}) = C_{60}F_n(\text{g.}) + n\text{MnF}_2(\text{cr.}). \quad (1)$$

During the first 10 h, $C_{60}F_{36}$ was the main product of the reaction in both cases. After 20 h of fluorination, the main component in the mass spectrum became $C_{60}F_{18}$. Nevertheless, in contrast to the case of the cubic phase, the products of fluorination of the hexagonal phase contained an excess of intermediate fluorofullerenes, from $C_{60}F_{32}$ to $C_{60}F_{26}$. Although their content in the total reaction product did not exceed 1%, the total fraction of these products in the mass spectrum 14 h after the beginning of the experiment at 644 K was as high as 10%. The final composition of the condensate formed in the reaction is given in Table 2. One readily sees that variation of the C_{60} crystal structure did not noticeably affect the final composition of the reaction products, which may be considered an additional argument for the fluorination process taking place at the interface between the reacting phases without involving deep layers of the interacting products.

Table 1. Experimental conditions in which the solid-phase fluorination was performed

	Total sample weight, mg	C_{60} mass, mg	Molar composition $n(MnF_3)/n(C_{60})$	Effusion hole diameter, mm	Fluorination time, h	Temperature range, K	Sample weight loss, mg	
							calc.*	exp.
C_{60} (fcc)	213.10	46.98	22.74	0.36	26.92	354–786	57.9	57.0
C_{60} (hcp)	184.35	37.32	25.33	0.37	24.92	524–761	51.2	47.8

*Assuming only the main $C_{60}F_{36}$ product to form, and taking into account detachment of one fluorine atom from MnF_3 per formula unit.

1063-7834/02/4404-0629$22.00 © 2002 MAIK "Nauka/Interperiodica"

Table 2. Integrated results of the fluorination experiment

n[a]	C_{60} (fcc)/MnF_3		C_{60} (hcp)/MnF_3	
	J_n[b]	m_n/m, %[c]	J_n	m_n/m, %
0	80795	6.7	8553	1.4
18	28762	2.5	51183	9.0
34	71318	6.3	52400	9.3
36	945697	83.2	451030	80.0
38	15602	1.4	2224	0.39
k_1[d] =	2.48×10^{-5}		1.11×10^{-4}	
k_2[e] =	2.50×10^{-5}		5.73×10^{-5}	

[a] Number of fluorine atoms in the $C_{60}F_n$ fluorofullerene molecule.

[b] Integrals of the ionic currents $I(C_{60}F_n^+)$ of the type $J_n = \int_0^\tau I_n\sqrt{T(t)}dt$ taken over the total reaction time τ.

[c] Weight fraction of the $C_{60}F_n$ product in the total amount of the condensate formed in the reaction.

[d] Mass-spectrometer sensitivity constant derived from sample weight loss m.

[e] Mass-spectrometer sensitivity constant derived from the ionic currents $I(C_{60}^+)$ measured on completion of the reaction.

The C_{60} fullerene was in excess in both cases, so that, after the completion of the solid-phase reactions, the effusion cell had to contain some unreacted fullerene and manganese difluoride: a product of MnF_3 decomposition by reaction (1), whose presence was subsequently confirmed from x-ray diffraction data. Because these components do not interact with each other, we measured the temperature dependence of the partial pressures of the C_{60} fullerene and determined the thermodynamic characteristics of sublimation of the cubic and hexagonal phases. The figure plots the logarithm of the partial pressure of C_{60} as a function of inverse temperature. These data were used to derive temperature dependences for the saturated vapor pressure of both C_{60} modifications:

$$\ln[P(C_{60}, \text{fcc}), \text{Pa}] = -(19793 \pm 685)/T + (24.6 \pm 0.9), \quad (2)$$

$$\ln[P(C_{60}, \text{hcp}), \text{Pa}] = -(23778 \pm 1010)/T + (30.4 \pm 1.4). \quad (3)$$

The enthalpy and entropy of sublimation of the fcc phase calculated from Eq. (2) were found to be

$$\Delta_{sub}H_T^0 = 165 \pm 6 \text{ kJ/mol},$$

$$\Delta_{sub}S_T^0 = 108 \pm 8 \text{ kJ/mol},$$

which coincide with literature data [2] and can be considered additional support of the fullerene having unity activity in a mixture with MnF_2. This gives us grounds to recommend the respective values calculated from Eq. (3),

$$\Delta_{sub}H_T^0 = 198 \pm 8 \text{ kJ/mol},$$

$$\Delta_{sub}S_T^0 = 157 \pm 12 \text{ kJ/mol},$$

as the first preliminary data on the thermodynamics of sublimation of the hexagonal phase.

The differences in the enthalpy and entropy of sublimation between the two phases are seen to lie outside the experimental error. This result comes as a surprise, because the reasons for which molecular interactions in crystals of the hexagonal and cubic modifications could differ noticeably are unclear. Nevertheless, this result suggests the possible existence of a temperature range over which the formation of the hexagonal phase would be preferable to that of the cubic one.

This issue obviously requires further investigation.

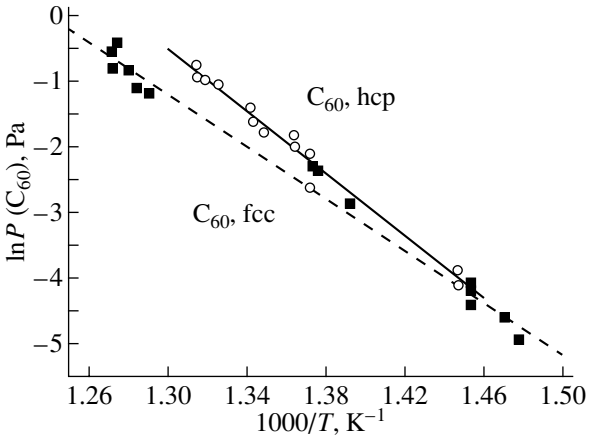

Experimental values of ln$P(C_{60})$ for different $1/T$ obtained for the cubic (squares) and hexagonal (circles) modifications of the C_{60} fullerene. The data were treated using the second law of thermodynamics. The dashed line is a plot of Eq. (2); the solid line, a plot of Eq. (3).

ACKNOWLEDGMENTS

The support of the Russian Foundation for Basic Research (project no. 00-03-32703a), INTAS-RBRF (grant IR 97-1015), and of the Russian Research Program "Fullerenes and Atomic Clusters" (grant no. 98046, "Sphere") is gratefully acknowledged.

REFERENCES

1. I. V. Arkhangel'skiĭ, E. V. Skokan, Yu. A. Velikodnyĭ, *et al.*, Dokl. Akad. Nauk **363** (4), 494 (1998).
2. V. Yu. Markov, O. V. Boltalina, and L. N. Sidorov, Zh. Fiz. Khim. **75**, 5 (2001).

Translated by G. Skrebtsov

Physics of the Solid State, Vol. 44, No. 4, 2002, pp. 631–633. From Fizika Tverdogo Tela, Vol. 44, No. 4, 2002, pp. 607–609.

PROCEEDINGS OF THE V INTERNATIONAL WORKSHOP "FULLERENES AND ATOMIC CLUSTERS"

(St. Petersburg, Russia, July 2–6, 2001)

Glass and Phase Transitions in Solid C_{60} Charged with Ar, Ne, He, and O_2[1]

Tong B. Tang* and Min Gu*, **

** Department of Physics, Hong Kong Baptist University, Kowloon, Hong Kong SAR, P. R. China*

*** National Laboratory of Solid State Microstructures, Nanjing University, Nanjing, P. R. China*

Abstract—C_{60} pellets, charged respectively with He, Ne, Ar, and O_2 under high pressure, were studied with complex impedance spectroscopy. The latter two were found to depress the temperatures for both the phase change (T_c) and glass transition (T_g), although in time shifts, they stayed almost constant in the Ar, but decreased in the O_2, case. The effective barriers for the glass transition were determined as 218 ± 15 meV in $Ar_{0.49}C_{60}$ and 182 ± 20 meV in $(O_2)_{0.5}C_{60}$. In contrast, neither He nor Ne had a discernible influence on these material parameters. These observations could be explained as follows. (1) Interstitial Ar causes a reduction in the energy barrier and a weakening in the restorative force of the cage libration mode, thereby depressing T_c. (2) For $(O_2)_{0.5}C_{60}$, coupling between the cage libration and the tumbling of an O_2 diatomic molecule further weakens the restorative force, so that a larger temperature shift results. (3) Its tumbling motion makes O_2 more susceptible to the "paddle wheel" action of rotating C_{60} and more easy to diffuse even under ambient conditions.

C_{60} fullerite displays a first-order phase transition [1] from face-centered cubic (fcc) symmetry above T_c = 260 K to simple cubic (sc) when the random rotations of C_{60} lock into specific orientations. In the ordered phase, two possible orientations can be obtained by rotating the molecules by either 38° or 98° around the unit cell diagonal [1]. Further freezing of reorientational jumps leads to an orientational glass; dielectric measurements revealed a Debye-like relaxational peak near 165 K at 10 kHz [2].

Gases doped interstitially offer the advantage of not altering the structure of the host lattice significantly to affect the C_{60} interaction potential. In the case of argon, T_c is shifted by $\Delta T = -10$ K [3], whereas for oxygen, $\Delta T = -20$ K [4, 5]. The glass transition is also highly sensitive to the details of the potential; however, its relation to gas intercalation has been little studied. We have therefore selected the van der Waals gases He, Ne, and Ar, as well as the diatomic gas O_2, as guest molecules and correlated the phase and the glass transition temperatures with the potential barriers as determined with complex impedance spectroscopy.

1. EXPERIMENTAL

C_{60} of 3*N* purity was annealed at 510 K in dynamic vacuum for 60 h before being compacted uniaxially under 6.5 kbar in an evacuated mold for 15 min. The rigid pellets thus produced measured $6 \times 7 \times 0.7$ mm. One batch was charged with He at 0.115 kbar after storage for 3 days inside a steel vessel at room temperature, the other, with Ne at 0.12 kbar. The molar concentration (octahedral site occupancy) as calculated from the fractional mass increase was $x = 1.00 \pm 0.01$ for He and $x = 0.62 \pm 0.01$ for Ne. A third batch was treated with Ar for 3 days at 300°C, the gas pressure reaching 0.16 kbar at that temperature, to reach $x = 0.49 \pm 0.01$, which remained constant for months at room temperature, even in vacuum, as indicated by weighing. The last batch of pellets was charged with 0.15-kbar O_2 for 7 days at room temperature, whence $x = 0.50 \pm 0.01$.

Silver films were evaporated onto the two large surfaces of each pellet. The AC impedance was recorded using the three-terminal method on an HP 4284A precision multimeter under computer control as the pellet was heated at a rate of 1 K min^{-1}.

2. RESULTS

Figure 1a represents the reduced dielectric constant $\varepsilon' \equiv (\varepsilon - \varepsilon_0)/\varepsilon_0$ and Fig. 1b shows the conductance *G* of a representative sample from each batch, ε_0 denoting the minimum value obtained for ε. The position of $\varepsilon = \varepsilon_0$ or $\varepsilon' = 0$ corresponds to the fcc-sc phase transition. For HeC_{60} and $Ne_{0.62}C_{60}$ (curves *2*, *3*), T_c remained unchanged from the undoped case (curve *1*) but the intercalation of Ar (curve *4*) shifted it by –13 K and ΔT remained the same after exposure of the pellet to vacuum at room temperature for up to 50 days (curve omitted for clarity). In $(O_2)_{0.5}C_{60}$ (curve *5*), there was a larger shift of –20 K, but ΔT decreased as the pellet spent a longer time in vacuum. These indications are

[1] This article was submitted by the authors in English.

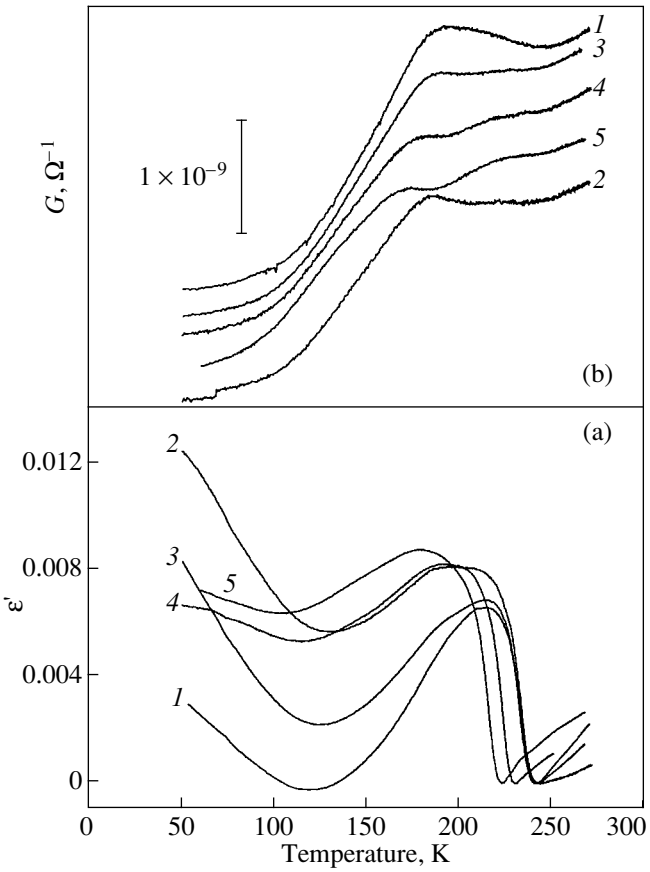

Fig. 1. Reduced dielectric constant (a) and conductance (b) at 50 kHz for (*1*) undoped C_{60}, (*2*) HeC_{60}, (*3*) $Ne_{0.62}C_{60}$, (*4*) $Ar_{0.49}C_{60}$, and (5) $(O_2)_{0.5}C_{60}$.

consistent with our previous observation [4] that, at room temperature, Ar does not diffuse out of C_{60} significantly but O_2 does.

The curves also show a peak in conductivity and a jump in the dielectric constant at almost the same temperature for each sample, which increased with frequency ω of the applied field. This relaxational feature points to the glass transition, and its activation energy may be calculated from respective Arrhenius plots of logω. Again, our data indicate that charging with He or Ne did not shift T_g, but with Ar and O_2 T_g it was depressed, and that the activation energy was virtually identical to that for undoped C_{60} in the first two cases but much smaller for Ar and O_2 (see table).

Effective barrier energy

Sample	Barrier, meV
Pristine C_{60}	291 ± 10
HeC_{60}	314 ± 30
$Ne_{0.62}C_{60}$	282 ± 30
$Ar_{0.49}C_{60}$	218 ± 15
$(O_2)_{0.5}C_{60}$	182 ± 20

3. DISCUSSION

In fcc solid C_{60}, the voids belong to geometrical categories, octahedral (radius 2.06 Å) and tetrahedral (1.13 Å); the latter lacks room for a rare-gas atom [6, 7]. Ar atoms (1.54 Å) are charged into the octahedral sites under high pressure [8]. Neutron-diffraction reveals no modification in the lattice symmetry but reveals an expansion in lattice parameter from 14.218 to 14.230 Å [3]. The resulting extra "free volume" enables the C_{60} molecules to rotate more easily. Indeed, $Ar_{0.49}C_{60}$ has an effective barrier determined as 218 ± 15 meV, approximately 70 meV lower than that in pristine C_{60}. That explains our observation that its T_g is depressed. For T_c, the suppression is usually attributed to negative "chemical pressure." However, $\Delta T = -13$ K would invoke a pressure of 1.2 kbar [9], whereas the pressure actually applied reached merely 0.16 kbar. We therefore propose that the suppression is enhanced by the reduction in effective barrier for molecule reorientation. The consequential weakening in the restorative force for the cage libration mode decreases T_c beyond what is expected from the negative pressure.

Being a diatomic molecule, O_2 has additional degrees of freedom in rotation and vibration. It executes a tumbling motion inside the octahedral void [6] with a frequency close to that of the cage libration mode [10]; thereby, the two may couple below T_c. This interaction will further weaken the restorative force in cage libration. Indeed, the largest $\Delta T = -20$ K and the lowest effective barrier = 182 ± 20 meV were determined for $(O_2)_{0.5}C_{60}$.

In molecular weight and radius, oxygen differs little from argon (32 vs. 39; 1.40 Å vs. 1.54 Å), but the former diffuses readily whereas the latter does not. Our explanation is as follows. The intercalation of a gas involves its passage through a channel of radius ~0.82 Å between adjacent octahedral sites [8]. The center of each pentagonal face on C_{60} molecules is ~0.29 Å inside the surface defined by the molecular radius and can increase to ~1.11 Å as molecules rotate the channel size. This still suffices for argon or oxygen to pass, but there is a further consideration. They are envisaged to undergo random-walk rotational diffusion uncorrelated with the motion of neighbors [1]; based on this picture, a paddle wheel model was proposed for the intercalation of Ne [8]. For oxygen, its tumbling will accentuate the paddling and accounts for its fast diffusion at room temperature. This diffusitivity has significant implications for the practical applicability of fullerenes.

ACKNOWLEDGMENTS

Tong B. Tang was supported by the Hong Kong Baptist University under FRG/97-98/II-70; Gu Min, by a Croucher Fellowship at HKBU and in Nanjing by the NSF of China under grant no. 10074031.

REFERENCES

1. M. S. Dresselhaus, G. Dresselhaus, and P. C. Eklund, *Science of Fullerenes and Carbon Nanotubes* (Academic, London, 1996).
2. G. B. Alers, B. Golding, A. R. Kortan, *et al.*, Science **257**, 511 (1992).
3. G. E. Gadd, S. J. Kennedy, S. Moricca, *et al.*, Phys. Rev. B **55**, 14794 (1997).
4. M. Gu, T. B. Tang, C. Hu, and D. Feng, Phys. Rev. B **58**, 659 (1998).
5. B. Renker, H. Schober, M. T. Fermandez-Diaz, and R. Heid, Phys. Rev. B **61**, 13960 (2000).
6. R. A. Assink, J. E. Schirber, D. A. Loy, *et al.*, J. Mater. Res. **7**, 2136 (1992).
7. B. Sundqvist, Adv. Phys. **48**, 1 (1999).
8. B. Morosin, Z. Hu, J. D. Jorgensen, *et al.*, Phys. Rev. B **59**, 6051 (1999).
9. G. A. Samara, I. V. Hansin, R. A. Assink, *et al.*, Phys. Rev. B **47**, 4756 (1993).
10. D. A. Neumann, J. R. D. Copley, W. A. Kamitakahara, *et al.*, J. Chem. Phys. **96**, 8631 (1992).

Physics of the Solid State, Vol. 44, No. 4, 2002, pp. 634–636. From Fizika Tverdogo Tela, Vol. 44, No. 4, 2002, pp. 610–611.

PROCEEDINGS OF THE V INTERNATIONAL WORKSHOP "FULLERENES AND ATOMIC CLUSTERS"

(St. Petersburg, Russia, July 2–6, 2001)

Complete Pentagon Orientational Ordering in C_{60} Fullerite Charged with NO[1]

Min Gu*, ** and Tong B. Tang**

** National Laboratory of Solid State Microstructures, Nanjing University, Nanjing, 210093 P. R. China*

*** Department of Physics, Hong Kong Baptist University, Kowloon, Hong Kong SAR, P. R. China*

Abstract—Solid C_{60} was stored in NO under high pressure, and the gas molecules NO were found to diffuse into the octahedral interstitial sites in its fcc crystal lattice. Its ^{13}C NMR MAS spectra are composed of a primary resonance at 143.7 ppm accompanied by two minor peaks shifted 0.4 and 0.8 ppm downfield, respectively. The dopant was found to depress its phase transition temperature at 260 K in pure C_{60} and to substantially reduce the drop $\Delta\varepsilon'$ at the phase transition temperature. Furthermore, the spectral features associated with relaxation during glass transition at lower temperature, as observed in impedance spectra, were smeared. The fraction of *P*-orientation below T_c was calculated to be larger than 11/12. These results show that a completely *P*-oriented phase occurred in $(NO)_{0.1}C_{60}$ and that this phase is favored by a negative pressure on the C_{60} lattice exerted by NO, as well as by the electrostatic interaction between the two. © *2002 MAIK "Nauka/Interperiodica".*

Gases accommodated interstitially in C_{60} fullerite have exerted significant influence on its order-disorder phase transition [1–4]. As we known, the C_{60} fullerite accommodates a rotational disorder of C_{60} molecules and adopts a face-centered cubic (fcc) lattice, but below T_c = 260 K, the structure changes to simple-cubic (sc) when the random rotations lock into specific orientations with fluctuations characterized by discrete jumps over an energy barrier. After C_{60} fullerite was charged with gases under high pressure conditions, the consequential changes in the critical temperature for the ordered phase were examined. In the case of argon, the shift is ΔT = –10 K [2], and oxygen produces a large shift of –20 K [1, 3]. CO was also found to depress the fcc-sc transition temperature T_c from its normal value by as much as 12 K [5–7]. Likewise, CO causes a slight expansion of the lattice [8]. However, no subsequent changes in the lattice symmetry have yet been observed. Being a paramagnetic molecule with a permanent electronic-dipole moment, NO was selected as the dopant to form a candidate system, C_{60} doped with NO. To better clarify the roles played by foreign molecules in the lattice, we further studied the dielectric responses vs. temperature of C_{60} solids charged with NO; these characteristics are sensitive to the orientation order. Meanwhile, the amount of NO in the C_{60} solids was estimated from the solid ^{13}C NMR of C_{60}. These experimental findings may also contribute to a deeper understanding of the order-disorder transition phenomenon itself.

[1] This article was submitted by the authors in English.

1. EXPERIMENTAL DETAILS

C_{60}, of better than 99.9% purity, was annealed at 280°C in dynamic vacuum for 72 h to remove solvent. Rigid pellets $6 \times 7 \times 0.7$ mm in dimension were then fabricated by uniaxial compaction in an evacuated mold under a pressure of 7 kbar for 10 min. Some powder was crushed from the pellets for ^{13}C NMR and DSC experiments. One batch, each of powder and pellets, was subjected to NO at 30 bar for 24 h at 200°C.

^{13}C NMR measurements proceeded at room temperature in a Bruker MSL-300 spectrometer equipped with a 7-T field with a resonance frequency of 75 MHz under the condition of magic-angle spinning (MAS) at a rate of 2.0 kHz and with a delay time of 60 s. In dielectric spectral studies, silver films were evaporated onto the two surfaces of the pellet in question for measurement using the three-terminal method on an HP 4284 A multimeter. For DSC, two batches were studied. The first consisted of powder prepared from crushing pellets; the second, from pellets that had been subjected to high-pressure NO. Samples 25–30 mg in mass were examined at a same scanning rate of 10 K min^{-1} on a Setaram DSC 92 instrument.

2. RESULTS

The high-resolution ^{13}C NMR spectrum of pristine crushed powder exhibited a primary resonance at 143.7 ppm related to freely rotating C_{60}, which is in agreement with previous studies [3, 9]. Furthermore, charging with NO at 30 bar and 200°C for 24 h led to the introduction of two secondary resonances which shifted 0.4 and 0.8 ppm downfield, respectively. Calcu-

1063-7834/02/4404-0634$22.00 © 2002 MAIK "Nauka/Interperiodica"

lated from the height of each resonance [9], the value of the octahedral occupancies of NO reached 0.10. After exposure to air for over 800 h, however, their intensities remained the same.

Figure 1 depicts the dielectric constant and conductivity, $\varepsilon' \propto (\varepsilon' - \varepsilon'_0)/\varepsilon'_0$ and G, respectively, in a representative pellet charged with NO; here, ε'_0 stands for the minimum value obtained for ε' indicative of the fcc-sc structure transition. The measurement was repeated after the pellet had sat in air for various lengths of time. The permittivity in the "fresh" pellet, upon heating, dropped to a minimum value at 230 K, as curve (*2*) in Fig. 1 shows, and with longer exposure, this minimum remained the same (curves *3*, *4*).

The conductivity G of the pellet, in its pristine state, exhibited a peak at 170 K upon heating, and its dielectric constant ε' showed a step at the same temperature T_p (curves *1* in Fig. 1). These relaxation features related to a glass transition disappeared entirely after the sample was charged with NO at 30 bar and 200°C for 24 h (curves *2–4* in Fig. 1b). Meanwhile, the magnitude of the drop in $\Delta\varepsilon' = (\varepsilon' - \varepsilon'_0)$ induced by the fcc-sc transition reduced substantially.

The DSC scan for a freshly NO charged sample shows a broad endothermic peak whose position shifted down 20 K compared with that of pristine C_{60}.

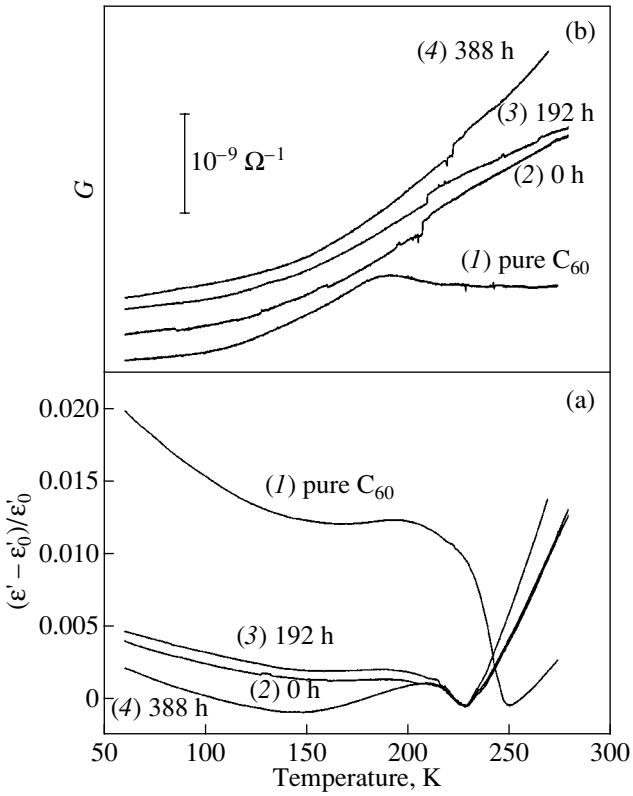

Fig. 1. Reduced dielectric constant (a) and conductivity (b) at 50 kHz measured for pristine C_{60} (curves *1*) and the pellet charged with NO after various lapses of time: 0 (*2*), 192 (*3*), and 388 h (*4*).

3. DISCUSSION

In the low-temperature phase, C_{60} molecules have two possible orientations, their difference in energy is very small, and the fraction of molecules in the more stable orientation *P* is only about 60% near 260 K, increasing to about 84% near T_g = 90 K. Below T_g, the reorientational jumps of molecules are frozen and an orientation glass is formed. A Debye-like relaxational peak from this glass transition, probed by the dielectric method [10], was observed and confirms that there exists orientational disorder of the C_{60} molecules in the sc phase and that these molecules adopt both H and P orientations following the usual thermal distribution.

In our case, solid C_{60} was stored in NO under high pressure and the gas molecules NO were found to diffuse into the octahedral interstitial sites in its fcc crystal lattice. The downfield shifts of the two minor peaks in its ^{13}C NMR MAS spectra were attributed to the Fermi-contact interaction between paramagnetic NO and the carbon atoms of the nearest neighbor C_{60}. The shift in temperature of the DSC peak for $(NO)_{0.1}C_{60}$, compared with that for pristine C_{60}, arises solely from the doping of these gas molecules. Moreover, the dielectric spectrum in Fig. 1 was seen to be virtually identical to that of DSC. Furthermore, the spectral features of the pristine C_{60} at 170 K (curves *1* in Fig. 1) were smeared by the interstitial NO (curves *2–4* in Fig. 1).

In the sample of $(NO)_{0.1}C_{60}$, the interstitial NO may exert a negative pressure on the C_{60} lattice, in analogy to a dilated lattice of $(CO)_xC_{60}$ by CO. Furthermore, the interstitial NO would change the orientation of the nearest C_{60} molecules to *P*-orientation and decrease the quantity of intrinsic permanent dipoles. This viewpoint is testified to by our experimental data. We calculated the fraction of *P*-orientation for a sample charged with NO from the drop in the dielectric constant near T_c and found that to fraction of *P*-orientation reached to over 93%. Because the fraction of orientational defects is lower than 1/12, it is insufficient to induce a dipole on essentially all molecules; therefore, there are too few dipoles (density n) to contribute to the dielectric response. That is the reason why the peak at T_p = 170 K disappeared after the sample was charged with NO. Meanwhile, below T_c, the fraction of *P*-orientation is larger than 11/12; therefore, a completely *P*-oriented phase occurred in $(NO)_{0.1}C_{60}$.

Thus, a phase with almost completely *P*-oriented molecules exists in solid C_{60} containing NO with a molar ratio exceeding 0.10.

ACKNOWLEDGMENTS

This work was supported by grants from the NSF of China (grant no. 10074031) and from The Jiangsu Province Foundation of Natural Science (grant no. BK2001027). M. Gu thanks the Crocher Foundation of Hong Kong for his fellowship at HKBU.

REFERENCES

1. M. S. Dresselhaus, G. Dresselhaus, and P. C. Eklund, *Science of Fullerenes and Carbon Nanotubes* (Academic, London, 1996).
2. G. B. Alers, B. Golding, A. R. Kortan, *et al.*, Science **257**, 511 (1992).
3. G. E. Gadd, S. J. Kennedy, S. Moricca, *et al.*, Phys. Rev. B **55**, 14794 (1997).
4. M. Gu, T. B. Tang, C. Hu, and D. Feng, Phys. Rev. B **58**, 659 (1998).
5. B. Renker, H. Schober, M. T. Fermandez-diaz, and R. Heid, Phys. Rev. B **61**, 13 960 (2000).
6. R. A. Assink, J. E. Schirber, D. A. Loy, *et al.*, J. Mater. Res. **7**, 2136 (1992).
7. B. Subdqvist, Adv. Phys. **48**, 1 (1999).
8. B. Morosin, Z. Hu, J. D. Jorgensen, *et al.*, Phys. Rev. B **59**, 6051 (1999).
9. G. A. Samara, I. V. Hansin, R. A. Assink, *et al.*, Phys. Rev. B **47**, 4756 (1993).
10. D. A. Neumann, J. R. D. Copley, W. A. Kamitakahara, *et al.*, J. Chem. Phys. **96**, 8631 (1992).

Physics of the Solid State, Vol. 44, No. 4, 2002, pp. 637–640. Translated from Fizika Tverdogo Tela, Vol. 44, No. 4, 2002, pp. 612–615.

PROCEEDINGS OF THE V INTERNATIONAL WORKSHOP "FULLERENES AND ATOMIC CLUSTERS"

(St. Petersburg, Russia, July 2–6, 2001)

Fast-Ion Channeling in Fullerene Crystals

V. V. Afrosimov, R. N. Il'in, V. I. Sakharov, and I. T. Serenkov

Ioffe Physicotechnical Institute, Russian Academy of Sciences, ul. Politekhnicheskaya 26, St. Petersburg, 194021 Russia

e-mail: r.ilin@pop.ioffe.rssi.ru

Abstract—The motion of H^+ and He^+ ions with energies of 230 and 2000 keV in C_{60} and K_3C_{60} crystals was calculated by the Monte Carlo method. Ion channeling was shown to occur in the ⟨100⟩ and ⟨111⟩ directions. The main parameters characterizing channeling were determined. Medium-energy ions were found to be preferable in the detection of channeling in C_{60} films. © *2002 MAIK "Nauka/Interperiodica".*

Channeling of ions with energies on the order of 1–0.1 MeV offers an efficient way of studying the perfection of crystal films. It is, however, only very rarely used to investigate films of fullerenes and of fullerene-based compounds. This may be due to the fact that, at 260 K, C_{60} crystals undergo a phase transition from the fixed state, in which the fullerenes in a crystal are oriented with respect to one another and the carbon atoms form atomic chains, to a free state, where the fullerenes rotate freely. Thus, at room temperature, chains of fullerenes rather than those of atoms are formed, as a result of which the occurrence of channeling and its possible use for structural diagnostics become problematic.

To explore the possibility and optimum conditions of the channeling of fast ions in fullerene crystals, we performed a numerical simulation of fast-ion motion in such structures. The program used in the calculations, based on the Monte Carlo method and the pair-collision model, was similar to the one described in [1].

We considered the propagation of H^+ and He^+ ions with energies of 230 or 2000 keV in an fcc cubic C_{60} crystal (lattice constant a = 1.41 nm) in the ⟨100⟩ and ⟨111⟩ directions and in a K_3C_{60} crystal in the ⟨100⟩ direction.

The calculations produced the yield of backscattered ions Y as a function of the angle ψ between the beam direction and the chosen crystal axis. The main characteristics of the angular dependence of the yield $Y(\psi)$ are the characteristic channeling angle $\psi_{1/2}$ [equal to the halfwidth at half-maximum of $Y(\psi)$], the minimum yield $Y(0)$, the yield Y_r for a random orientation ($\psi \gg \psi_{1/2}$), and the minimum relative yield $\chi = Y(0)/Y_r$.

The calculations were carried out using three different programs: FS (fixed state), FSA (free state, atoms), and FSM (free state, molecules).

In the FS program, the fullerenes were assumed to be oriented such that the twofold axes were parallel to the principal crystallographic axes. In the calculation, the crystal was separated into layers containing only atoms located in the plane perpendicular to the chosen crystallographic direction. The interaction of a carbon atom with a fast ion was described by a universal potential [2],

$$V(r) = Z_1 Z_2 e^2 r^{-1} \sum_{i=1}^{4} \alpha_i \exp(-\beta_i r/a), \qquad (1)$$

where α_i = {0.1818, 0.5099, 0.2802, 0.02817}, β_i = {3.2, 0.9423,0.4029, 0.2106}, and $a = 0.8853a_0/(Z_1^{0.23} + Z_2^{0.23})$.

The nuclear-collision probability was calculated from the relation

$$p = KZ_1^2 Z_2^2 E^{-2} (2\pi\sigma^2)^{-1} \exp[-b^2/(2\sigma^2)], \qquad (2)$$

where K is a constant assumed to be unity; b is the impact parameter; Z_1 and Z_2 are the ion and atom charges, respectively; E is the ion energy at the instant of collision; and σ is the rms amplitude of thermal vibrations.

After each crossing of a layer by the ion, the program calculated the deflection of the latter suffered in scattering from the nearest atoms and the probability of a nuclear collision with the nearest atom displaced from the lattice site by thermal vibrations.

Straightforward calculation of channeling using Eqs. (1) and (2) under free rotation of the C_{60} molecules also required selection of an arbitrary orientation of each fullerene, as well as a calculation over 240 layers in each cell in place of 30 layers, which was sufficient for the FS case. Such a program, FSA, was prepared; however, because of the very long computational time needed, it was used only to compare channeling in the ⟨100⟩ and ⟨111⟩ directions.

1063-7834/02/4404-0637$22.00 © 2002 MAIK "Nauka/Interperiodica"

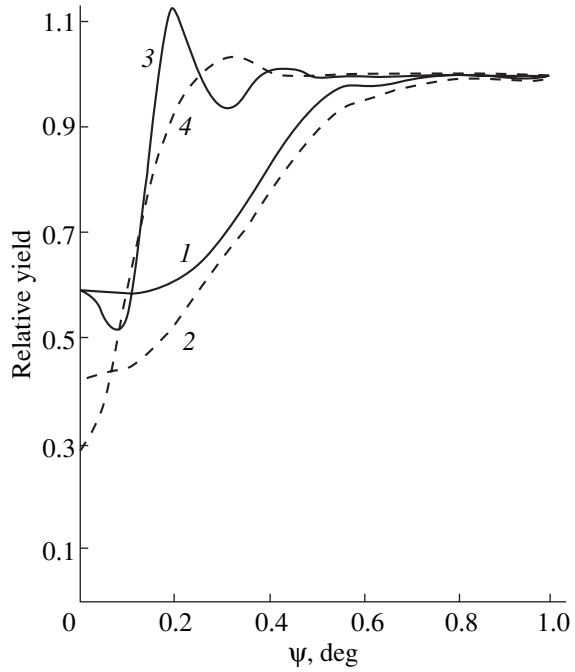

Fig. 1. Calculated angular relations $Y(\psi)$ for the He^+–$C_{60}\langle 111\rangle$ system. (*1*, *3*) FSM calculation; (*2*, *4*) FS program. Ion energy is (*1*, *2*) 0.23 and (*3*, *4*) 2 MeV.

To compare the results obtained with different ions and energies in the case of free molecule rotation, a faster program was developed, FSM, in which each fullerene molecule was approximated by a sphere of radius R_f equal to that of the C_{60} molecule. The ion–atom interaction was replaced by the interaction of the ion with a spherical-surface element *dS*. The dependence of potential energy on the distance between the ion and the element *dS* was calculated from Eq. (1). Integration over the surface of the sphere yielded the following expression for the potential function:

$$V_f(R) = Z_1 Z_2 e^2 R^{-1} \sum_{i=1}^{4} \gamma_i \exp(-\beta_i R/a), \quad R \geq R_f,$$
$$V_f(R) = Z_1 Z_2 e^2 R^{-1} \sum_{i=1}^{4} \delta_i \sinh(\beta_i R/a), \quad R \leq R_f, \tag{3}$$

Minimum relative yield

Ion	Energy, keV	Program					
		FSA		FS		FSM	
		⟨100⟩	⟨111⟩	⟨100⟩	⟨111⟩	⟨100⟩	⟨111⟩
H^+	230	0.80	0.78	0.32	0.42	0.72	0.73
He^+	230			0.33	0.42	0.68	0.70
He^+	2000			0.32	0.44	0.67	0.68

where $\gamma_i = \alpha_1 a N R_f^{-1} \beta_i^{-1} \sinh(\beta_i R_f/a)$, $\delta_i = \alpha_i a N R_f^{-1} \beta_i^{-1} \exp(-\beta_i R_f/a)$, $Z_2 = 6$, $N = 60$ (the number of atoms in the fullerene molecule), and R is the distance between the ion and the center of the sphere.

The nuclear-collision probability P was calculated in this case as follows. First, the contribution dP due to each element dS of the sphere was determined from Eq. (2) and then multiplied by the probability of a carbon atom being within the element dS:

$$dP = K Z_1^2 Z_2^2 E^{-2} (2\pi\sigma^2)^{-1} \times \exp[-\rho^2/(2\sigma^2)] N (4\pi R_f^2)^{-1} dS, \tag{4}$$

$$\rho^2 = B^2 + R_f^2 \sin^2\theta - 2BR_f \sin\theta\cos\varphi,$$
$$dS = R_f^2 \sin\theta d\theta d\varphi, \tag{5}$$

where ρ is the impact parameter in the ion- and dS-center system, B is the impact parameter in the ion- and sphere-center system, and θ and φ are the polar and azimuthal angles, respectively ($\theta = 0$ is the axis parallel to the ion trajectory). The $P(B)$ relation was obtained by integrating Eq. (4) over the sphere surface with due account of Eqs. (5).

The dependence of the ion deflection angle θ on the parameter B was calculated as

$$\theta(B) = -E^{-1} \int_0^\infty \frac{\partial}{\partial B} V_f(\sqrt{z^2 + B^2})\, dz, \tag{6}$$

where $V_f(R)$ is defined by Eqs. (3).

A comparison of the $V_f(R)$, $P(B)$, and $\theta(B)$ functions calculated from Eqs. (3), (4), and (6) with the respective Monte Carlo calculations for real C_{60} molecules on averaging over 10000 different orientations showed them to practically coincide.

In all the programs (FS, FSA, FSM), the total backscattering probability for an ion having crossed a 50-nm-thick layer was calculated as the sum of nuclear-collision probabilities over the whole ion path inside this layer for each incidence angle ψ. The calculations were carried out for a film 350 nm thick.

The rms thermal-vibration amplitudes σ used in the calculations were 0.019 nm for carbon and 0.022 nm for potassium [3].

The $Y(\psi)$ relation was calculated for 230-keV protons by the FS, FSA, and FSM programs and for He^+ ions (230 and 2000 keV) in a C_{60} crystal and H^+ (230 keV) in a K_3C_{60} crystal by the FS program. Figure 1 shows some of the calculated $Y(\psi)/Y_r$ relations. The relative minimum yield after the passage through a 100-nm thick layer is given in the table.

Channeling was observed to occur in all the cases studied. Because the particle flux passing through C_{60} molecules in the fixed state is governed by stable car-

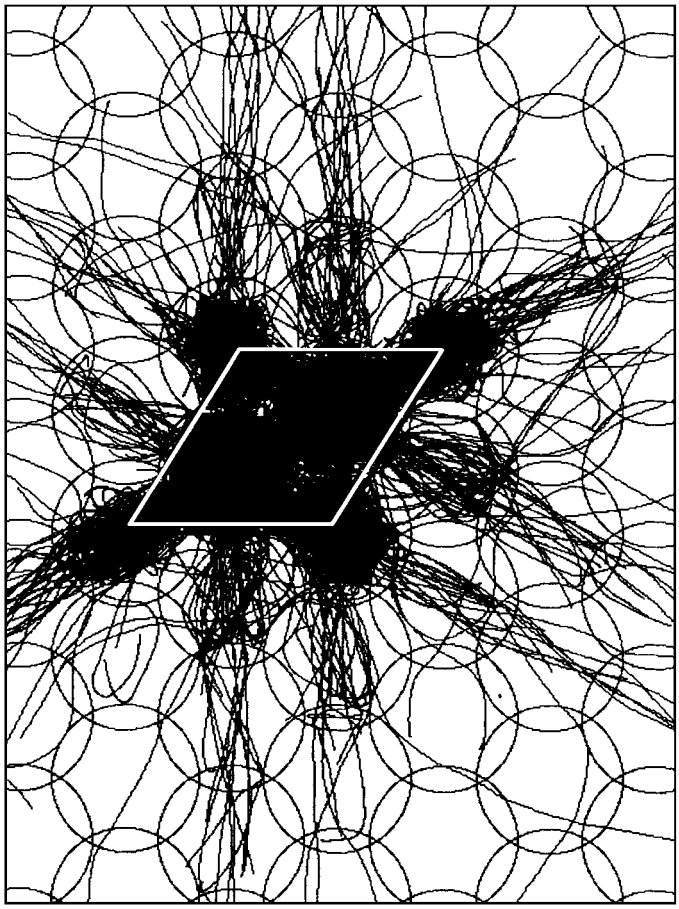

Fig. 2. Visualization of the FSM program operation for the ⟨111⟩ orientation. Ions are H^+: energy 230 keV, $\psi = 0$. Circles are C_{60} molecule projections on the (111) plane; lines are ion trajectory projections. The rhomboid is the region on the surface populated by particles of the incident beam.

bon-atom chains, the decrease in χ in this case is observed to be larger than that in the case of free molecule rotation. An analysis of the particle flow in the case of free rotation shows that, for the ⟨100⟩ orientation, the ion beam is focused both into the channels between the C_{60} rows (focusing of the first type) and in the vicinity of the axes passing through the centers of molecules in these rows (focusing of the second type). The first type is standard channeling, which is characterized by a small minimum yield, whereas the minimum yield reached in focusing of the second type is close to Y_r; therefore, the value of χ obtained in the calculations is a weighted mean over the two types of focusing. For the ⟨111⟩ direction, the fullerene projections on the (111) plane overlap it fully and channeling appears impossible, because only focusing of type two should exist in this case. However, the calculations revealed that the values of χ obtained for the ⟨111⟩ and ⟨100⟩ orientations are close in magnitude. This is accounted for by the fact that, in the case of the ⟨111⟩ orientation, the beam focusing is enhanced near the axes passing through the fullerene centers, which is associated with the geometry of the structure (Fig. 2). This is also buttressed by the trapping of the particle flux observed to occur into the planes perpendicular to the crystal surface. The projections of these planes lie between the chains of intersecting segments of the C_{60} projections. Note that, in the case of the ⟨100⟩ orientation, particle trapping into planes is only weakly pronounced.

The minimum relative yields for different probing ions (H^+, He^+) were found to be similar. As for the beam particle energy, its increase from 230 keV to 2 MeV reduces $\psi_{1/2}$ from 0.4° to 0.12° (Fig. 1), which makes the requirements on the probing beam divergence more stringent (it should be substantially smaller than $\psi_{1/2}$) and, moreover, hampers experimental observation of channeling in the presence of disordered crystallites, because the average misorientation angle should also meet the condition of its smallness compared to $\psi_{1/2}$. Thus, the use of medium-energy ions is advantageous to the use of ions in the megaelectronvolt energy range.

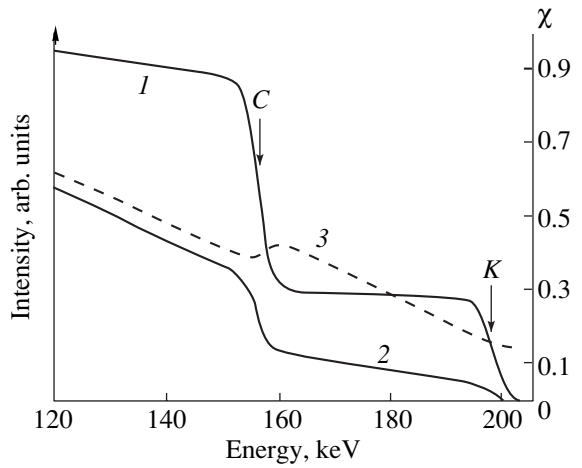

Fig. 3. Calculated ion backscattering spectra for the H^+–K_3C_{60} system: (*1*) $Y_r(E)$, (*2*) $Y_c(E)$, and (*3*) $\chi(E)$. Incident ion energy 230 keV. The arrows identify the leading edges of the carbon and potassium signals.

The results of channeling experiments are usually presented in the form of spectra of backscattered ions for a beam aligned with the channel and for a randomly oriented beam ($\psi \gg \psi_{1/2}$). Such a spectrum is displayed in Fig. 3 for the K_3C_{60} compound. The part of the spectrum corresponding to the potassium sublattice is shifted toward higher energies and has a minimum yield $\chi \approx 0.3$. This means that the quality of the lattice of intercalated fullerenes can be judged from the scattering spectrum from the impurity atoms [4].

Calculations also permit one to reveal relations that are difficult to observe experimentally. In particular, we carried out calculations for individual sublattices in the K_3C_{60} crystal. It was found that the characteristic channeling angles for the potassium atoms are $\psi_{1/2} = 0.35°$ and 0.45° for the octahedral and tetrahedral sites, respectively; therefore, it is possible to derive the position of intercalated atoms from the $Y(\psi)$ relation.

In conclusion, we have studied specific features of fast-ion propagation through fullerene crystals by the Monte Carlo method. The calculations revealed that channeling of fast H^+ and He^+ ions in ordered fullerene films occurs in both the ⟨100⟩ and ⟨111⟩ directions, and we determined the main parameters characterizing the channeling. It was also shown that medium-energy ions are preferable for studying channeling in fullerene crystals. Thus, fast-ion channeling can be employed to advantage in the determination of the structure of films consisting of fullerenes and atomic clusters.

ACKNOWLEDGMENTS

This study was supported by the Russian Foundation for Basic Research (project no. 99-02-18170) and the State Research and Development Program “Fullerenes and Atomic Clusters” (project “Film”).

REFERENCES

1. V. V. Afrosimov, G. O. Dzyuba, R. N. Il’in, *et al.*, Zh. Tekh. Fiz. **66** (12), 76 (1996) [Tech. Phys. **41**, 1240 (1996)].
2. J. F. Ziegler, J. P. Biersack, and U. Littmark, *The Stopping and Range of Ions in Solids* (Pergamon, New York, 1985), Vol. 1.
3. Y. M. Guerro, R. L. Cappeletti, D. A. Neumann, and T. Yildirim, Chem. Phys. Lett. **297** (3–4), 265 (1998).
4. V. V. Afrosimov, R. N. Il’in, S. F. Karmanenko, *et al.*, Fiz. Tverd. Tela (St. Petersburg) **41** (4), 588 (1999) [Phys. Solid State **41**, 527 (1999)].

Translated by G. Skrebtsov

Physics of the Solid State, Vol. 44, No. 4, 2002, pp. 641–643. Translated from Fizika Tverdogo Tela, Vol. 44, No. 4, 2002, pp. 616–617.

PROCEEDINGS OF THE V INTERNATIONAL WORKSHOP "FULLERENES AND ATOMIC CLUSTERS"

(St. Petersburg, Russia, July 2–6, 2001)

Magnetic-Field-Induced Slowing-Down of Molecular Rotation in C_{60} Crystals

V. T. Lebedev*, Gy. Török, L. Cser**, V. P. Budtov***, and A. I. Sibilev***

** St. Petersburg Nuclear Physics Institute, Russian Academy of Sciences, Gatchina, Leningrad oblast, 188300 Russia*

e-mail: vlebedev@mail.pnpi.spb.ru

*** Research Institute for Solid State Physics and Optics, Budapest, Hungary*

e-mail: torok@power.szfki.kfki.hu

**** Scientific Evaluation Center, pr. Elizarova 14, Office 45, St. Petersburg, 193029 Russia*

e-mail: cnir@city.com.ru

Abstract—The molecular dynamics of C_{60} crystals was studied by inelastic neutron scattering at $T = 290$ K, i.e., above the first-order phase transition temperature ($T_C \approx 260$ K), in the region of free C_{60}-spheroid rotation in the lattice. The energy broadening of the original neutron spectrum $2\Gamma_0 \approx 0.1$ meV for a momentum transfer $q = 2$ Å^{-1} is in agreement with NMR data on the rotational relaxation time of the molecule $\tau \sim 10^{-11}$ s $\sim \hbar/\Gamma_0$. This effect was observed to decrease in magnetic fields $H = 2.5$–4.5 kOe applied along the scattering vector: $\Gamma_H = 0.7\Gamma_0$. The slowing-down of the molecular rotation is discussed in connection with the interaction of a magnetic field with the molecular currents, which fluctuate when the C_{60} cage rotates. © *2002 MAIK "Nauka/Interperiodica".*

1. INTRODUCTION

The molecular dynamics of C_{60} undergoes a qualitative change in the first-order phase transition ($T_C \approx 260$ K) when the low-temperature phase transforms from the simple cubic to an fcc lattice [1–3]. The fcc phase is characterized by a high rotational mobility of the molecules, because a molecule in this structure resides in a spherically symmetric potential. Neutron experiments [4, 5] have shown that, above T_C, the libration excitation spectrum collapses into a single broad quasi-elastic peak, which can be described in terms of the orientational random-walk approximation, i.e., rotational diffusion, with a constant $D \sim 1 \times 10^{10}$ s^{-1} and the corresponding relaxation time $\tau \sim 1/6D \sim 10$ ps. This behavior is observed at high momentum transfers $q \sim 5$ Å^{-1}, conditions under which the dynamics is dominated by temporal self-correlations of atoms in a molecule. Much less information is known about local displacements for transfer momenta q lying in the range from $2\pi/a \sim 0.5$ Å^{-1} to $2\pi/R_F \approx 1.8$ Å^{-1} ($R_F = 3.5$ Å is the fullerene radius, and $a \approx 14$ Å is the lattice constant). At the same time, scattering in this momentum transfer region contains most of the information on short-range molecular interactions. In this region, the dynamics is particularly sensitive to external factors (temperature, fields). For instance, if a macroscopic perturbation (field) breaks the symmetry of the system, a transition to correlated rotation of the molecules is possible.

The effect of a magnetic field on the dynamics is very specific, because this field can interact with molecular currents in the fullerene shell. The diamagnetic response of C_{60} crystals to a static field does not differ noticeably from that for aromatic molecules [6]. When considering a C_{60} cage rotating rapidly in thermal motion, one should not neglect the π-electron delocalization in the shell. Rotation can generate circular currents that screen the external field, whose interaction with the currents slows down the rotation. The purpose of our experiment was to investigate the weak magnetic properties of fullerenes, which are presently discussed in the literature in connection with the van Vleck paramagnetism [6] and possible antiferromagnetic spin correlations [7].

2. NEUTRON-SCATTERING EXPERIMENTS

Experiments on inelastic neutron scattering from crystalline C_{60} powder were carried out at the Budapest Neutron Center with a triple-axis spectrometer (wavelength $\lambda = 3$ Å, momentum transfer $q = 1.5$–2 Å^{-1}). A magnetic field $H = 2.5$–4.5 kOe directed along the momentum transfer was applied to a sample at $T = 290$ K in order to observe dynamic correlations in molecular chains oriented along the field; these correlations may be created through the interaction of the moments induced by the field in the molecules. Reference measurements were performed without field application. The instrument resolution $W_0 = 150$ μeV

was determined using vanadium, which is an incoherent scatterer. We used samples containing 96 at. % C_{60} prepared by a standard technique at the St. Petersburg Scientific Evaluation Center.

3. RESULTS

Figure 1 presents typical quasi-elastic scattering spectra obtained on fullerene in the range of energy transfers E from –0.5 to 0.5 meV in comparison with the corresponding distributions for vanadium. In all experiments, the lines have a Gaussian shape, $I(E)/I_0 = \exp(-2E^2/W^2)$, where I_0 is the intensity at the maximum and W is the total linewidth. Assuming a Gaussian distribution for the inelastic scattering function of the fullerene, $S(\omega) \sim \exp[-(\hbar\omega)^2/2\Gamma^2]$ ($\hbar\omega$ is the energy transfer in scattering), we found the characteristic energy for the observed broadening of initial line (width W_0, vanadium) determined by the C_{60} dynamics: $2\Gamma = (W^2 - W_0^2)^{1/2}$, where W is the linewidth measured for the sample (Fig. 1a). In the case where the fullerene is not perturbed by any magnetic field, the characteristic energy is $2\Gamma_0 = 102 \pm 10$ μeV, which indeed agrees with the rotational diffusion rate and the relaxation time $\tau \sim \hbar/\Gamma_0 \sim 10^{-11}$ s for C_{60} [4, 5]. At the same time, the data available for the fullerene in a magnetic field (Fig. 1b) reveal a noticeable decrease in the linewidth compared with that for the sample in a zero field. For $H = 2.5$ kOe, the broadening is $2\Gamma_H = 77 \pm 10$ μeV, which is ~25% less than the value for $H = 0$. This slowing-down of the rotation indicates field-induced ordering of the system, which can be due, for example, to the interaction between the induced dipoles of the fullerenes. In order to estimate the greatest possible magnitude of this effect, we assume that the molecular currents completely screen the external magnetic field at any interior point of the fullerene. In this case, the magnetization of the molecule is $M \sim -B_{ext}/4\pi$, its magnetic moment is

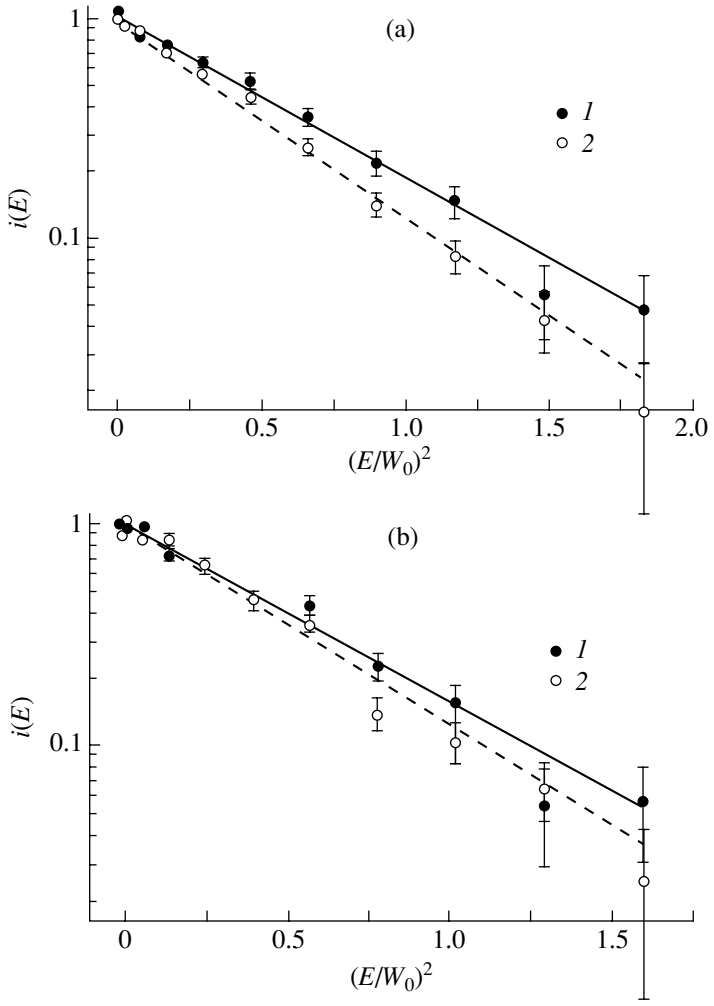

Fig. 1. Broadening of the neutron energy spectrum $i(E) = I(E)/I_0$ in scattering from C_{60} crystals: (a) no field applied and (b) H = 2.5 kOe; (*1*) data for C_{60} (solid line is a Gaussian fit) and (*2*) data for vanadium.

equal to $M_F = M(4\pi/3)R_F^3$, and the interaction energy between the moment and the external field equals $E_d \sim M_F B_{\text{ext}} \sim 10$ μeV, which is comparable to the experimentally observed inelastic effect. Therefore, this mechanism of slowing down can be operative. Another reason for the slowing-down may be field-induced lattice distortions, which make the potential in which the molecule rotates anisotropic. Further experiments carried out within a broad range of fields and in the temperature range including T_C will hopefully shed light on the nature of the molecular magnetism and the specific features of its effect on fullerite dynamics in magnetic fields.

ACKNOWLEDGMENTS

The authors are grateful to I.N. Ivanova and S.M. Bogdanovich (PNPI) for their assistance in preparing the material for publication.

This study was supported by the Russian Foundation for Basic Research (project no. 00-15-96814), the Ministry of Industry and Science of the Russian Federation (project "Fullerene Stars"), and the program "Neutron Studies of Condensed Media."

REFERENCES

1. P. A. Heiney, J. E. Fischer, A. R. McGhie, *et al.*, Phys. Rev. Lett. **66**, 2911 (1991).
2. R. Sachidanandam and A. B. Harris, Phys. Rev. Lett. **67**, 1467 (1991).
3. W. I. F. David, R. M. Ibberson, J. C. Matthewman, *et al.*, Nature **353**, 147 (1991).
4. D. A. Neumann, J. R. D. Copley, W. A. Kamitakahara, *et al.*, J. Chem. Phys. **96**, 8631 (1992).
5. C. Christides, T. J. S. Dennis, and K. Prassides, Phys. Rev. B **49**, 2897 (1994).
6. V. Elser and R. C. Haddon, Phys. Rev. A **36**, 4579 (1987).
7. D. Coffey and S. A. Trugman, Phys. Rev. Lett. **69**, 176 (1992).

Translated by G. Skrebtsov

Physics of the Solid State, Vol. 44, No. 4, 2002, pp. 644–646. Translated from Fizika Tverdogo Tela, Vol. 44, No. 4, 2002, pp. 618–620.

PROCEEDINGS OF THE V INTERNATIONAL WORKSHOP "FULLERENES AND ATOMIC CLUSTERS"

(St. Petersburg, Russia, July 2–6, 2001)

Comparative Study of the High-Pressure Conductivity of Graphite and Fullerene

G. V. Tikhomirova and A. N. Babushkin

Ural State University, pr. Lenina 51, Yekaterinburg, 620083 Russia
e-mail: Galina.Tikhomirova@usu.ru

Abstract—The electrical resistance of polycrystalline fullerene and graphite was studied at pressures up to 50 GPa within the temperature range 77–450 K. The temperature dependences of the resistance of both materials behave in a qualitatively similar manner. However, the resistances of these materials differ by several orders of magnitude. This shows that fullerene and graphite retain some specific features of their microstructure in the pressure and temperature ranges covered. © *2002 MAIK "Nauka/Interperiodica".*

1. The physical properties and electronic structure of C_{60} at high pressures have been studied in considerable detail (see, e.g., [1–4]). Orientational phase transformations were found to occur at relatively low pressures. At higher pressures, fullerene was observed to transform to diamond, graphite, and amorphous states. It is maintained, in particular in [1], that C_{60} molecules become unstable at pressures above 20–25 GPa, with the fullerene converting primarily to graphite. It has been shown that, in intermediate stages of the transformation, covalent bonds may form between molecules (one-, two-, and three-dimensional polymerization). Some authors came to the conclusion that the elastic moduli and the hardness of the high-pressure phases of fullerene may be larger than those of diamond [4]. The electrical characteristics of polycrystalline C_{60} samples were studied at pressures not exceeding 20 GPa (see, e.g., [1, 4]). In addition, we are not aware of any investigations into the electrophysical properties of fullerene at higher pressures.

This paper reports on a comparative study of the conductivity of the polycrystalline C_{60} fullerene and graphite at pressures of 15–50 GPa.

2. To obtain pressures of up to 50 GPa, we used a high-pressure chamber (HPC) with Vereshchagin–Yakovlev anvils of the rounded-cone and plane type made of synthetic polycrystalline black diamonds [5]. These diamonds are good electrical conductors and can be employed as electric contacts for samples. The resistance of the short-circuited anvils is 7–12 Ω and varies little with temperature. The pressure was derived from the expression $P = AF/\pi a^2$, where F is the applied force, a is the radius of the contact area, and A is an empirical factor (in our case, $A = 1.51$). This method of pressure determination was checked on a large number of various materials over broad temperature and pressure ranges [6, 7]. The technique used permits one to study the same sample under a successive increase and decrease in pressure. The samples under study, prepared by compression in a HPC, were ≈0.2 mm in diameter and 10–30 μm thick. The sample resistance was measured at temperatures from 77 to 450 K. The ac measurements were conducted at room temperature. The HPC temperature was monitored with a copper–constantan thermocouple.

3. Figure 1 plots the room-temperature resistance of the C_{60} fullerene as a function of pressure. In the range 15–50 GPa, the pressure dependence exhibited a hysteresis whose magnitude is dependent on the number of pressure application–removal cycles involved. The applied pressure was increased smoothly up to the maximum value and, afterwards, reduced as smoothly to

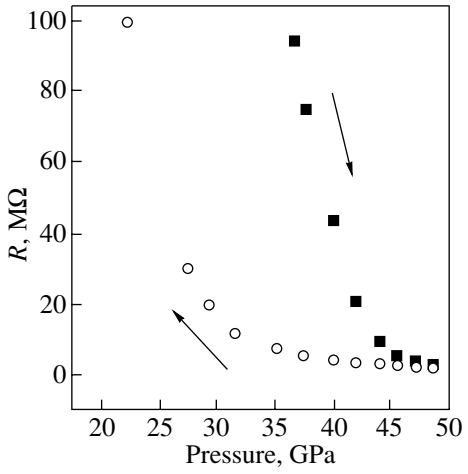

Fig. 1. Pressure dependences of the electrical resistance of fullerene at room temperature obtained under the first application of pressure. The arrows specify the direction of the pressure variation.

1063-7834/02/4404-0644$22.00 © 2002 MAIK "Nauka/Interperiodica"

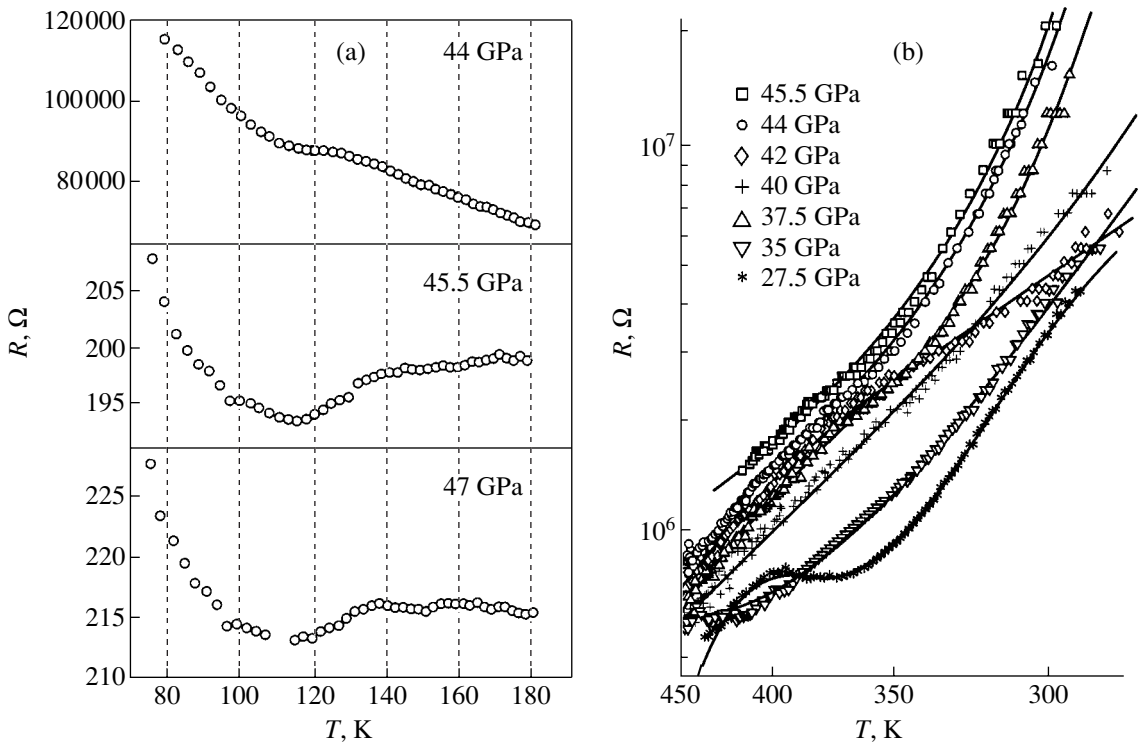

Fig. 2. Temperature dependences of the fullerene resistance measured at various pressures: (a) at the first application of pressure and (b) after stabilization reached in a few successive pressure application runs.

zero. When loaded for the first time, the fullerene resistance dropped sharply (at pressures above 45 GPa) by two orders of magnitude at room temperature and by nearly three orders of magnitude at liquid-nitrogen temperature. After a few cycles of successive application and removal of pressure, the fullerene resistance stabilized and the hysteresis decreased considerably in magnitude. No hysteresis of resistance as a function of pressure was observed in graphite.

Figure 2 shows temperature dependences of the C_{60} fullerene resistance $R(T)$ obtained at various pressures. In the first loading of the sample, the temperature dependences measured below 44 GPa exhibit an activation character with two activation energies. The slope changes at a temperature of approximately 110 K. When the pressure is increased, in the same temperature interval, the $R(T)$ dependence passes through a minimum. Metal-like conduction is observed at temperatures above 115–125 K (for various pressures). We attribute this semiconductor–metal transformation to the orientational phase transition observed to occur in [1, 3] at 90 K under atmospheric pressure.

After a few successive pressure application cycles, the temperature dependence of the C_{60} resistance acquires an activation character throughout the temperature interval studied, with the sample resistance growing strongly. This is seen from the plot in Fig. 2b constructed in the $\log R$–$1/T$ coordinates. The activation energy changes at temperatures from 325 to 345 K for various pressures. At the same temperatures, a sharp change is observed in the character of the temperature dependences within the range 37–44 GPa (compare with the changes in the $R(T)$ curves observed to occur at 35, 37.5, 42, and 44 GPa in Fig. 2b). This indicates the occurrence of a structural phase transition at these pressures.

The temperature dependences of the graphite resistance measured at high pressures follow qualitatively the same course as the resistance of fullerene; namely, when loaded for the first time, the sample passes through a minimum in the $R(T)$ dependence (at $T \approx 330$ K), and after a few successive runs of increasing and decreasing pressure, the $R(T)$ plot (Fig. 3) becomes monotonic and, unlike the situation with the fullerene (Fig. 2), does not exhibit any features in the pressure interval studied. Furthermore, the resistance of the graphite samples did not exceed 100 Ω, which is four to five orders of magnitude lower than that of the fullerene samples (Fig. 2b).

The activation character of the resistance of both the fullerene and graphite is apparently associated with the percolation nature of conduction in polycrystalline samples. This is supported by the measured frequency dependence of the impedance $Z \propto f^{\nu}$ with the value $\nu \approx 1$ characteristic of randomly inhomogeneous media [8].

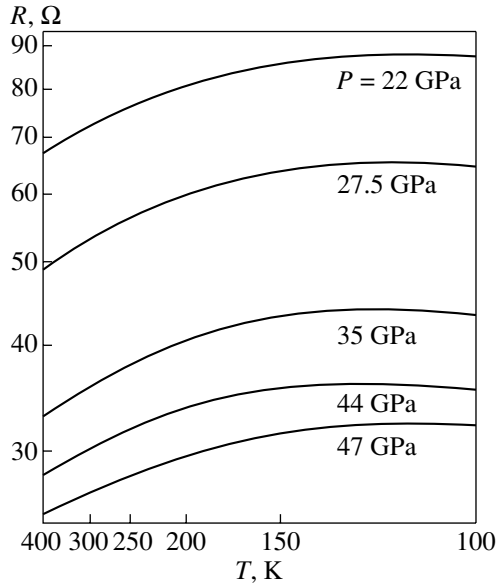

Fig. 3. log$R$ vs. 1/T plots obtained on graphite at various pressures.

The high resistance of the fullerene (compared to that of graphite) at high pressures indicates that (i) fullerene graphitization does not occur at pressures up to 50 GPa in the temperature interval studied and (ii) both the fullerene and graphite retain some features in their microstructure in this pressure range.

In conclusion, we note that while conductivity measurements can provide information on the onset of phase transitions of various types, their microscopic nature can be established only in structural (for instance, x-ray diffraction) studies. On the other hand, the critical behavior of resistance at a phase transition point indicates that the phase transition occurs throughout the volume of the substance under investigation, whereas structural studies detect only local phase transformations. Therefore, as follows from the above results, investigation of transport phenomena can provide additional important information on critical phenomena taking place at high pressures.

ACKNOWLEDGMENTS

This study was partially supported by the CRDF foundation (grant no. REC-005) within the frame of the Ural Research and Education Center “Promising Materials.”

REFERENCES

1. A. V. Eletskiĭ and B. M. Smirnov, Usp. Fiz. Nauk **165** (9), 977 (1995) [Phys. Usp. **38**, 935 (1995)].
2. V. V. Brazhkin and A. G. Lyapin, Usp. Fiz. Nauk **166** (8), 893 (1996) [Phys. Usp. **39**, 837 (1996)].
3. M. S. Dresselhaus, G. Dresselhaus, and P. C. Eklund, *Science of Fullerenes and Carbon Nanotubes* (Academic, London, 1996).
4. S. G. Buga, V. D. Blank, G. A. Dubitsky, *et al.*, J. Phys. Chem. Solids **61**, 1009 (2000).
5. L. F. Vereshchagin, E. N. Yakovlev, T. N. Stepanov, *et al.*, Pis’ma Zh. Éksp. Teor. Fiz. **16** (4), 240 (1972) [JETP Lett. **16**, 169 (1972)].
6. A. N. Babushkin, G. I. Pilipenko, and F. F. Gavrilov, J. Phys.: Condens. Matter **5**, 8659 (1993).
7. A. N. Babushkin, G. V. Babushkina, and O. A. Ignatchenko, J. High Press. School **1**, 32 (1999).
8. N. F. Mott and E. A. Davis, *Electronic Processes in Non-Crystalline Materials* (Clarendon, Oxford, 1979; Mir, Moscow, 1982), Vol. 1.

Translated by G. Skrebtsov

Physics of the Solid State, Vol. 44, No. 4, 2002, pp. 647–651. From Fizika Tverdogo Tela, Vol. 44, No. 4, 2002, pp. 621–625.

PROCEEDINGS OF THE V INTERNATIONAL WORKSHOP "FULLERENES AND ATOMIC CLUSTERS"

(St. Petersburg, Russia, July 2–6, 2001)

Potential of Fullerene-Based Materials for the Utilization of Solar Energy[1]

E. A. Katz

Departament of Solar Energy and Environmental Physics, J. Blaustein Institute for Desert Research, Ben-Gurion University of the Negev, Sede Boqer, 84990 Israel

e-mail: keugene@bgumail.bgu.ac.il

Abstract—This paper reviews the prospects of fullerene-based materials for photovoltaics. The device structure and parameters of inorganic and organic fullerene-based solar cells are presented. An additional promising direction of solar energy utilization—the production of fullerenes and carbon nanotubes by concentrated sunlight—is also discussed. © *2002 MAIK "Nauka/Interperiodica".*

Pristine solid C_{60} is known to exhibit semiconductor-like behavior in its optical and electronic properties, while that of doped fullerenes can be "tuned" between semiconductors, conductors, and even superconductors [1]. There are, accordingly, great expectations that fullerene-based materials will find practical applications in electronic and optoelectronic devices and, in particular, in photovoltaic solar cells.

This paper reviews the prospects of fullerene-based materials for photovoltaics. However, we start with another promising direction of solar energy utilization, the production of fullerenes by concentrated sunlight.

1. PRODUCTION OF FULLERENES AND CARBON NANOTUBES BY CONCENTRATED SUNLIGHT

In 1990, Krätschmer *et al.* [2] discovered a simple technique to produce fullerenes. The method uses arc discharge between two graphite electrodes in a helium atmosphere to vaporize graphite and produce fullerene-containing soot, the subsequent extraction of soluble fullerenes from insoluble species of the soot by an organic solvent (e.g., toluene), and final chromatographic separation of the isolated fullerenes (C_{60}, C_{70}, …). At present, the most efficient methods of fullerene production involve different modifications of thermal evaporation of graphite in an inert atmosphere (e.g., ac or dc arc discharge between graphite electrodes, laser ablation of graphite) [1].

The electric arc process requires the use of high quality, electrically conductive graphite rods. On the other hand, the yield of fullerene production from the collected soot is low (5–10%) due to the photodestriction of fullerene molecules by UV radiation of the electric arc [3]. Furthermore, because the yield is low, excessive amounts of toluene are required to separate the fullerenes from the soot. These factors present serious limitations on the minimum cost obtainable with this process.

Even though the yield from the laser ablation process can be high, it is generally accepted that this process will not be cost effective on large production levels [4]. The search for a more efficient and environmentally safe method led to the use of concentrated solar energy to evaporate the carbon and efficiently produce fullerenes [3–8] and carbon nanotubes [8–10].

In all reported solar techniques, concentrated ($\geq$1100 W/cm^2) sunlight is focused onto a graphite target, resulting in its heating up to temperatures in excess of 3500 K. Controlling the vaporization and condensation conditions leads to the formation of fullerene-rich soot or/and carbon nanotubes (if the target consists of a mixture of graphite and metal catalysts).

The UV component in sunlight is very small (compared with the irradiation of an electric arc). Therefore, the photodestruction process is very weak and the yield of fullerenes is as high as 20% [8]. Increased yield leads to less solvent use, which reduces cost. Furthermore, the relaxation of the requirement of using conductive graphite rods opens the possibility of employing less expensive forms of graphite, including mineral graphite powders. A preliminary cost analysis [5] suggested that solar production can be less expensive than the arc process by at least a factor of four.

Fullerenes have been demonstrated to be purified and crystallized via differential sublimation [1]. These technological steps are certainly possible to perform in a similar solar furnace.

[1] This article was submitted by the author in English.

1063-7834/02/4404-0647$22.00 © 2002 MAIK "Nauka/Interperiodica"

2. FULLERENE-BASED PHOTOVOLTAIC SOLAR CELLS

2.1. Why are Fullerenes So Promising for Photovoltaics?

We consider the following reasons that make C_{60} unique among all known semiconductors and, in particular, promising for photovoltaic application.

(1) There is probably no more environmentally benign semiconductor than C_{60} in that it can be sythesized from graphite using nothing more than a beam of concentrated solar energy and subsequently purified and crystallized using the same energy source (as described above).

(2) Early studies of C_{60} as a material for inorganic solar cells were instigated by the theoretical prediction [11] that a C_{60} crystal has a direct band gap of 1.5 eV. On one hand, this value is close to the experimental value of about 1.6 eV for the fundamental edge in the optical absorption spectra [12] and that of 1.7 eV for the photoconductivity spectra [13] of C_{60} thin films. On the other hand, this is the optimal value for high efficiency photovoltaic devices of the single junction type [14]. Recent experimental studies [15, 16] have demonstrated that the electronic structure of a C_{60} crystal is more complicated. Specifically, the band gap value is suggested to be about 2.3 eV (the mobility gap), but the optical absorption extends from the gap energy to the lower energy side (the optical gap is of ~1.6 eV). These experimental works stimulated new theoretical calculations of the band gap value of 2.15 eV using a "many-body" approach [17]. However, even if this is true, the electronic structure and optical properties of C_{60} thin films are suitable for the use of this material in efficient heterojunction solar cells (such as C_{60}/Si devices).

(3) If one contrasts a C_{60} molecular crystal unit cell with the corresponding Si cell, the former has 240 atoms to the latter's 8. This allows the possibility of doping to a much greater percent than would be possible with conventional semiconductors. Furthermore, unlike the case of conventional semiconductors, for which doping is only possible via the substitution of atoms (e.g., P or B for Si), fullerenes may be doped in three additional, distinct ways: intercalation of dopants between the buckyballs, endohedral doping within the buckyballs themselves, and adductive doping to the outside of the buckyballs [1]. The spectrum of resultant doping energy levels will naturally differ for each manner of doping, thus greatly increasing the probability of finding successful dopants for high efficiency photovoltaic devices.

(4) For organic donor-acceptor solar cells, a C_{60} molecule is an ideal candidate as an acceptor because of its high electron affinity (2.65 eV [1]). Such cells are now becoming a serious alternative to conventional inorganic photovoltaic devices due to a number of potential advantages, such as their light weight, flexibility, and low cost of fabrication of large areas. The efficient photoresponse of donor-acceptor cells consisting of conjugated polymers and fullerenes [18–22] originates from an ultrafast (subpicosecond) photoinduced electron transfer from the conjugated polymer (as a donor) to a nearby C_{60} molecule (as an acceptor) [23]. Since this process is faster than any other relaxation mechanism in the conjugated polymer, the quantum efficiency of this process is estimated to be close to unity. Accordingly, the best photovoltaic parameters ever reported for organic solar cells—in particular, the energy conversion efficiencies of 2.5% [24]—were for bulk heterojunction fullerene/polymer devices.

2.2. Inorganic Photovoltaic Devices

In 1992, Hebard *et al.* patented an idea for the utilization of the photoconductivity of fullerides in the fabrication of fullerene-based solar cells [25]. The photovoltaic response of most device structures originates from their rectifying properties. However, in that patent publication, the authors described a symmetrical (nonrectifying) Ag/C_{60}/Ag device structure which exhibited photoconductivity but no photovoltaic effect.

For the first time, a fullerene-based device displaying a remarkable rectifying effect in the dark and photoresponse under illumination was demonstrated with a sandwich cell consisting of a C_{60} thin film (of 100 nm thickness) and two Al electrodes [26]. The devices without any exposure of the front electrode to oxygen exhibited no rectification and photoresponse. The devices with a front Al electrode exposed to oxygen (before C_{60} film deposition) exhibited a rectification ratio of 66 (at ±2 V) and a greatly enhanced photocurrent (the quantum yield of the photocurrent for a monochromatic irradiation of $\lambda = 400$ nm was about 53%). The observed excitation profile of the photocurrent closely follows the optical absorption of a C_{60} film. The authors interpreted the results as the formation of an oxide layer at the front Al electrode interface and the Metal–Insulator–Semiconductor (MIS) configuration rather than the Schottky barrier device. The Schottky barrier solar cells based on C_{60} crystals and films were demonstrated later [27, 28].

A heterojunction behavior with a high rectifying ratio in the dark ($>10^4$ at ±2 V) [29] and photovoltage generation [30] were demonstrated, first, for a C_{60}/*p*-Si interface. The properties of such a heterojunction were then extensively studied in the dark and under irradiation of various light sources [27–34]. Although different groups studied various device configurations (Nb/C_{60}/Si, Ti/C_{60}/Si [29, 31], Au/C_{60}/Si, ITO/C_{60}/Si [30, 34], Al/C_{60}/Si [27, 28, 32, 33]), all authors seem to agree that potential barrier formation at the C_{60}/*p*-Si rather than metal/C_{60} interfaces is responsible for the strong rectifying properties of the heterostructures.

Detailed study of the photovoltaic properties was performed for highly crystalline C_{60} thin film/*p*-Si het-

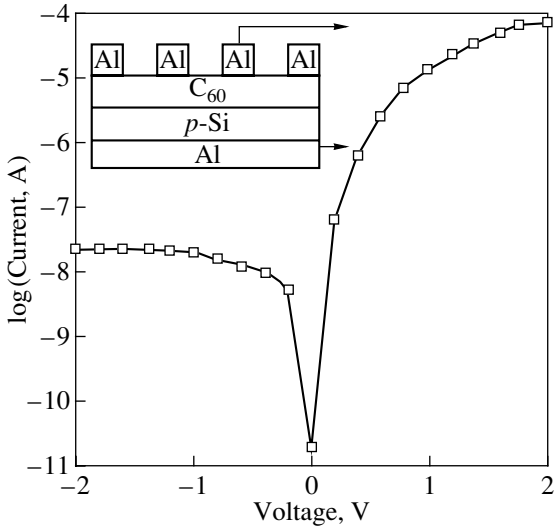

Fig. 1. Dark *I–V* curve of the Al/C_{60}/p-Si/Al heterojunction solar cell (inset shows a schematic diagram of the device) [32].

erojunction solar cells [28, 32]. The dark *I–V* curve is shown in Fig. 1, which exhibits strongly rectifying properties: the rectification ratio being approximately 10^4 at ±2 V. Under sun irradiation (AM 1.5), the short-circuit current density J_{sc} was found to be 42 μA/cm^2, open-circuit voltage V_{oc} = 322 mV, and fill-factor FF = 0.3. The low values of J_{sc} and FF = 0.3 are attributable to the high resistivity of pristine C_{60} films. SPV spectroscopy characterization of the devices (Fig. 2a) suggested that the C_{60} film acts as an active layer in the device, in particular, for the conversion of short-wavelength components of sunlight. This conclusion is consistent with the spectral response of similar Al/C_{60}/*p*-Si/Al solar cells (Fig. 2b) and that calculated using the published optical absorption coefficient values for C_{60} and Si (Fig. 2c) [33].

The maximum V_{oc} of a heterojunction corresponds to its built-in potential, i.e., the difference between the Fermi levels of both semiconductors forming the junction, the C_{60} thin film and Si in this case. The Fermi level of Si can be controlled by changing the kind and concentration of the dopant. Photovoltage generation by a C_{60}/Si heterojunction was studied with four different types of Si substrates: heavily doped *p*-Si (8×10^{18} cm^{-3} of B), lightly doped *p*-Si (1.5×10^{15} cm^{-3} of B), lightly doped *n*-Si (5×10^{14} cm^{-3} of P), and heavily doped *n*-Si (5×10^{18} cm^{-3} of P) [34]. The lightly doped *n*-Si/C_{60} junction was measured to have the highest V_{oc} (0.4 V), while the lightly doped *p*-Si/C_{60} junction was measured to have the lowest, 0.12 V (Fig. 3). This result implies that the Fermi level of C_{60} should be more than 0.4 eV below the Fermi level of lightly doped *n*-Si and more than 0.12 eV above that of lightly doped *p*-Si. The Fermi level of C_{60} was estimated to be at about 4.7 eV

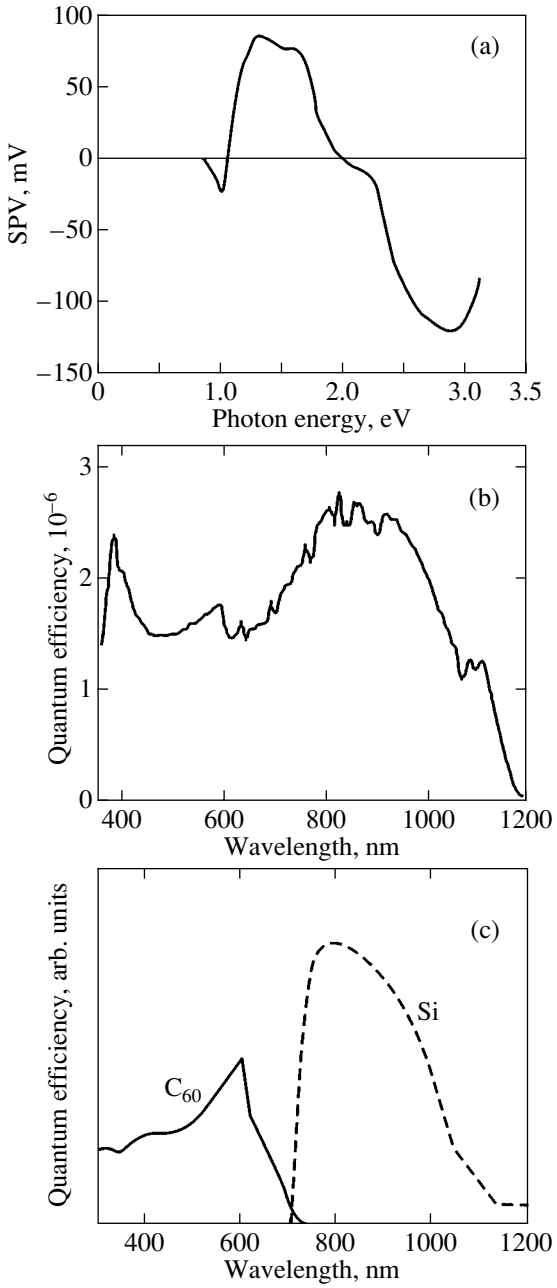

Fig. 2. Spectral characteristics of the Al/C_{60}/*p*-Si/Al solar cells: Surface Photovoltage Spectrum [32] (a); experimental (b) and calculated (c) spectral response [33].

below the vacuum level. In our opinion, further research is needed to understand the true electronic structure of such heterojunctions.

The very intrinsic conductivity of a C_{60} solid is considered by most authors to be one of the main limiting factors to solar-cell efficiency. Therefore, doping of C_{60} is one of the central challenges in high efficiency fullerene-based solar cell production. Photovoltaic cells based on doped C_{60} films were reported, for the first time, in [35]. *p*-Type conductivity was observed for C_{60} films doped with Al in its simultaneous sputtering

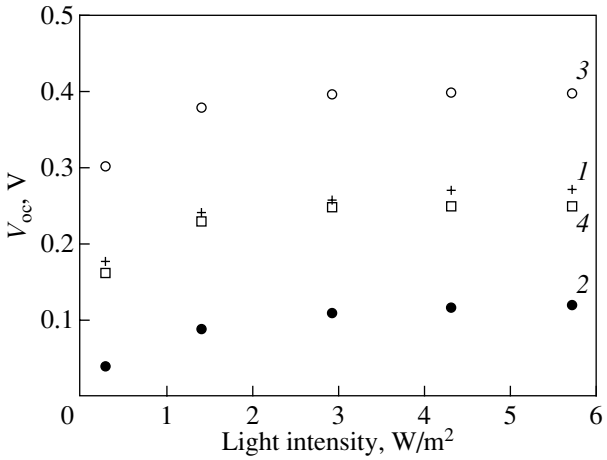

Fig. 3. Irradiance dependence of open-circuit voltage of the solar cells based on a heterojunction between a C_{60} thin film and different types of Si substrates [34]: (*1*) heavily doped *p*-Si, (*2*) lightly doped *p*-Si, (*3*) lightly doped *n*-Si, and (*4*) heavily doped *n*-Si.

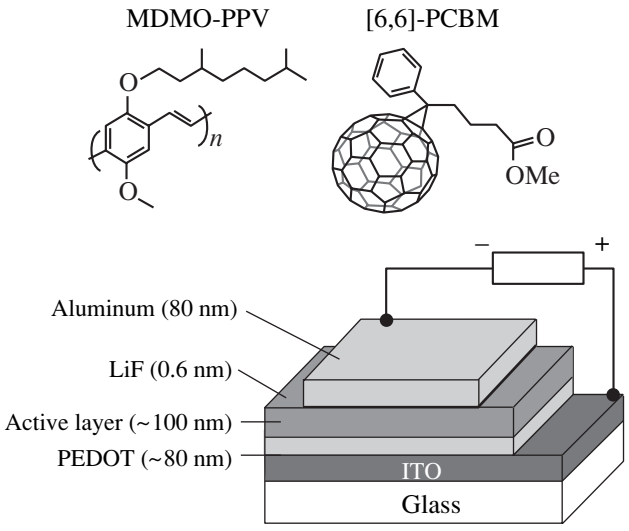

Fig. 4. Schematic device structure of the bulk heterojunction fullerene/polymer solar cells, together with the chemical structure of compounds used for the cell active layer [24]. Poly[2-methoxy, 5-(3',7'-dimethyl-octyloxy)]-*p*-phenylene-vinelyne (MDMO-PPV) was used as the electron donor, while the electron acceptor was [6,6]-phenyl C_{61}-butyric acid methyl ester (PCBM). The enhanced solubility of PCBM compared to C_{60} allows a high fullerene-conjugated polymer ratio and strongly supports the formation of bulk donor-acceptor heterojunctions. As electrodes, a transparent indium–tin–oxide (ITO) film on one side and an LiF/Al bi-layer contact on the other side were used. For improvement of the ITO contact, the ITO was coated with a thin layer of poly(ethylene dioxythiphene) (PEDOT).

during film deposition. Photovoltaic parameters of C_{60}/Si solar cells were found to be improved by doping. In the same paper, an ion implantation of P was demonstrated to result in an increase in *n*-type conductivity of C_{60} films.

The idea of ion implantation of P and B in C_{60} films was then developed and applied to solar-cell production [36–38]. Implantation of B^+ (with an energy of 50–80 keV and a dose of 10^{14} cm^{-2}) into C_{60} films, grown on an *n*-Si substrate, was shown to lead to structural changes from crystalline C_{60} to amorphous carbon and a dramatic increase in the C_{60} film conductivity. The Hall effect measurements of the implanted films indicate *p*-type conduction. Boron implantation significantly improved the parameters of the resultant *p*-C/*n*-Si solar cells [36]. In particular, the cell series resistance R_s was improved by the implantation from 35 kΩ to 370 Ω. J_{sc} for the implanted cells was found to be 0.33 mA/cm^2; V_{oc} = 0.17 V, fill-factor FF = 0.415, and efficiency η = 0.023%. (The latter is the highest value reported for inorganic C_{60}-based solar cells.)

The spectral response of these cells (not shown) includes two broad features: 370–600 nm due to α-C layers and 700–1150 nm due to Si [36]. This result is in agreement with the experimental finding that the optical gap of the C_{60} films decreases after B^+ implantation [37]. Furthermore, it is possible to control this value by varying the implantation dose. The optical gap was found to decrease gradually with the ion dose. For example, the gap was reported to be reduced continuously from 1.6 eV for nonimplanted C_{60} films to 0.8 eV after implantation with a dose of 8×10^{14} cm^{-2} [37]. The authors explained this effect in terms of the structural transformation from C_{60} to α-C. We may attribute the intermediate optical gap values to a composite with various concentrations of C_{60} and α-C. In our opinion, this result is even more important than the improvement of the solar-cell parameters (which are still not high). Indeed, using this effect, together with the control of the depth-implantation profile in the ion energy variation [38], it might be possible to produce a C_{60}/α-C composite with a nonhomogeneous depth-profile optimized for maximum sunlight absorption and cell efficiency. We may predict that the next step in this direction will be the production of efficient multijunction C_{60}/α-C/Si solar cells.

2.3. Organic Photovoltaic Devices

Over the last decade, tremendous progress has been achieved in organic donor-acceptor solar cells and fullerene/conjugated polymer devices in particular. A number of detailed reviews are devoted to this topic [20–22]. Thus, we will discuss it here very briefly.

Immediately after the discovery of the photoinduced electron transfer from the conjugated polymer to the C_{60} molecule [23], this molecular effect was used for the preparation of a heterojunction between methyl-ethyl-hydroxyl-polypropylvinyl (MEH-PPV) and a C_{60} thin film [18]. The dark rectification ratio of 10^4 (at ±2%) and the following photovoltaic parameters (measured under illumination of an argon ion laser with

wavelength λ = 514.5 nm and a light power of 1 mW/cm^2) were reported: J_{sc} = 2 μA cm^{-2}, V_{oc} = 0.5 V, FF = 0.48, and η = 0.04%. The spectral response measurements revealed a clear minimum at a photon energy of 2.5 eV. This minimum corresponds to the region of maximum absorption in the polymer layer. Since the light was incident from the polymer side of the device, this result implies that the diffusion of charge carriers in the devices is limited and the photoactive region is a very thin layer adjacent to the heterojunction interface.

Significant improvement of the relatively low collection efficiency has been achieved using a composite material with a network of internal heterojunctions between fullerene and conjugated polymer, forming so-called bulk heterojunctions. Using this principle of material construction, a solar cell without any macrojunction (!) has been demonstrated [19]. The electric field was created by asymmetric (with different work functions) metallic contacts, one of which was transparent ITO. Photogeneration resulting in separated charge carriers may occur over the whole depth of such a device. Very recently [24], flexible and inexpensive bulk heterojunction fullerene/polymer solar cells (Fig. 4) with tremendously improved efficiency (2.5% under AM 1.5 sunlight) were reported. The other parameters were J_{sc} = 5.25 mA/cm^2, V_{oc} = 0.82 V, and FF = 0.61. These results strongly demonstrate that fullerene/polymer solar cells can be a viable technology for future power generation, although further work is needed to improve the stability of such devices.

ACKNOWLEDGMENTS

The author thanks the Israel Ministry of National Infrastructures and the Ministry of Immigrant Absorption for their financial support.

REFERENCES

1. M. S. Dresselhaus, G. Dresselhaus, and P. C. Eklund, *Science of Fullerenes and Carbon Nanotubes* (Academic, London, 1996).
2. W. Krätschmer, L. D. Lamb, K. Fostipoulos, and D. R. Huffman, Nature **347**, 354 (1990).
3. L. F. P. Chibante, A. Tess, J. Alford, *et al.*, J. Phys. Chem. **97**, 8696 (1993).
4. J. R. Pitts, D. Mischler, C. L. Fields, *et al.*, Sol. Chem. News, No. 6, 2 (1998).
5. C. L. Fields, D. H. Parker, J. R. Pitts, *et al.*, J. Phys. Chem. **97**, 8701 (1993).
6. D. Laplaze, P. Bernier, G. Flamant, *et al.*, J. Phys. B **29**, 4843 (1996).
7. D. Laplaze, P. Bernier, C. Journet, *et al.*, Synth. Met. **86**, 2295 (1997).
8. G. Flamant, A. Ferriere, D. Laplaze, and C. Monty, Sol. Energy **66**, 117 (1999).
9. M. J. Heben, T. A. Bekkedahl, D. L. Schulz, *et al.*, in *Recent Advances in the Chemistry and Physics of Fullerenes and Related Materials III* (Electrochemical Society, Pennington, 1996), p. 803.
10. D. Laplaze, P. Bernier, W. K. Maser, *et al.*, Carbon **36**, 685 (1998).
11. S. Saito and A. Oshiyama, Phys. Rev. Lett. **66**, 2637 (1991).
12. A. Skumanich, Chem. Phys. Lett. **182**, 486 (1991).
13. M. Hosoya, K. Ichimura, Z. H. Wang, *et al.*, Phys. Rev. B **49**, 4981 (1994).
14. J. J. Loferski, J. Appl. Phys. **27**, 777 (1956).
15. R. W. Lof, M. A. van Leenendaal, B. Koopmans, *et al.*, Phys. Rev. Lett. **68**, 3924 (1992).
16. B. Mishori, E. A. Katz, D. Faiman, and Y. Shapira, Solid State Commun. **102**, 489 (1997).
17. E. L. Shirley and S. G. Louie, Phys. Rev. Lett. **71**, 133 (1993).
18. N. S. Sariciftci, D. Braun, C. Zhang, *et al.*, Appl. Phys. Lett. **62**, 585 (1993).
19. G. Yu, J. Gao, J. C. Hummelen, *et al.*, Science **270**, 1789 (1995).
20. N. S. Sariciftci and A. J. Heeger, in *Handbook of Organic Conductive Molecules and Polymers*, Ed. by H. S. Nalwa (Wiley, New York, 1997), Vol. 1, p. 413.
21. K. Yoshino, K. Tada, A. Fujii, *et al.*, IEEE Trans. Electron Devices **4**, 1315 (1997).
22. N. S. Saticiftci, in *Optical and Electronic Properties of Fullerenes and Fullerene-based Materials*, Ed. by J. Shinar, Z. V. Vardeny, Z. H. Kafafi (Marcel Dekker, New York, 2000), p. 367.
23. N. S. Sariciftci, L. Smilowitz, A. J. Heeger, and F. Wudl, Science **258**, 1474 (1992).
24. S. E. Shaheen, C. J. Brabec, N. S. Sariciftci, *et al.*, Appl. Phys. Lett. **78**, 841 (2001).
25. A. F. Hebard, B. Miller, J. M. Rosamilia, and W. L. Wilson, U.S. Patent No. 5171373 (1992).
26. H. Yohehara and Ch. Pac, Appl. Phys. Lett. **61**, 575 (1992).
27. D. Faiman, S. Goren, E. Katz, *et al.*, in *Proceedings of the 13th European Photovoltaic Solar Energy Conference, 1995*, Ed. by W. Freieslenben, W. Palz, H. A. Ossenbring, P. Helm, and H. S. Stephens & Associates, Vol. 2, p. 1284.
28. E. A. Katz, D. Faiman, S. Shtutina, *et al.*, Mater. Res. Soc. Symp. Proc. **485**, 113 (1997).
29. K. M. Chen, Y. Q. Jia, S. X. Jin, *et al.*, J. Phys.: Condens. Matter **6**, L367 (1994).
30. C. Wen, T. Aida, I. Honma, *et al.*, Denki Kagaku **62**, 264 (1994).
31. K. M. Chen, Y. Q. Jia, S. X. Jin, *et al.*, J. Phys.: Condens. Matter **7**, L201 (1995).
32. E. A. Katz, D. Faiman, S. Goren, *et al.*, Fullerene Sci. Technol. **6**, 103 (1998).
33. N. Kojima, M. Yamaguchi, and N. Ishikawa, Jpn. J. Appl. Phys., Part 1 **39**, 1176 (2000).
34. K. Kita, C. Wen, M. Ihara, and K. Yamada, J. Appl. Phys. **79**, 2798 (1996).
35. D. J. Fu, Y. Y. Lei, J. C. Li, *et al.*, Appl. Phys. A **67**, 441 (1998).
36. K. L. Narayanan and M. Yamaguchi, Appl. Phys. Lett. **75**, 2106 (1999).
37. N. Dharmasu, T. Sakai, N. Kojima, *et al.*, J. Appl. Phys. **89**, 318 (2001).
38. K. L. Narayanan, O. Goetzberger, A. Khan, *et al.*, Sol. Energy Mater. Sol. Cells **65**, 29 (2001).

Physics of the Solid State, Vol. 44, No. 4, 2002, pp. 652–655. Translated from Fizika Tverdogo Tela, Vol. 44, No. 4, 2002, pp. 626–629.

PROCEEDINGS OF THE V INTERNATIONAL WORKSHOP "FULLERENES AND ATOMIC CLUSTERS"

(St. Petersburg, Russia, July 2–6, 2001)

Gas-Phase Synthesis of Nitrogen-Containing Carbon Nanotubes and Their Electronic Properties

A. G. Kudashov*, A. V. Okotrub*, N. F. Yudanov*, A. I. Romanenko*, L. G. Bulusheva*, O. G. Abrosimov, A. L. Chuvilin**, E. M. Pazhetov**, and A. I. Boronin****

** Institute of Inorganic Chemistry, Siberian Division, Russian Academy of Sciences, pr. Akademika Lavrent'eva 3, Novosibirsk, 630090 Russia*

*** Institute of Catalysis, Siberian Division, Russian Academy of Sciences, pr. Akademika Lavrent'eva 5, Novosibirsk, 630090 Russia*

e-mail: spectrum@che.nsk.su

Abstract—Nitrogen-containing carbon nanotubes are synthesized using a gas-phase reaction. The synthesis of nitrogen-doped carbon nanotubes from 100 to 500 Å in diameter is accomplished through pyrolysis of acetonitrile (CH_3CN) at a temperature of 800°C. Cobalt and nickel metallic particles formed upon thermal decomposition of a mixture of maleate salts are used as catalysts. The materials synthesized are investigated by scanning and transmission electron microscopy. Analysis of the x-ray photoelectron spectra demonstrates that the content of nitrogen atoms in three nonequivalent charge states is approximately equal to 3%. A comparison of the CK_α x-ray fluorescence spectrum of the carbon nanotubes synthesized through electric-arc evaporation of graphite and the x-ray fluorescence spectrum of the nitrogen-containing carbon nanotubes prepared by catalytic decomposition of acetonitrile indicates that, in the latter case, the spectrum contains a certain contribution from the sp^3 states of carbon atoms. The temperature dependences of the electrical conductivity for different types of multi-walled carbon nanotubes are compared. The difference observed in the temperature dependences of the electrical conductivity is associated with the presence of additional scattering centers in nitrogen-containing carbon nanotubes. © *2002 MAIK "Nauka/Interperiodica".*

1. INTRODUCTION

Multi-walled carbon nanotubes (MWNTs) synthesized by different methods substantially differ in morphology and microstructure. The structure with the lowest content of defects is observed in carbon nanotubes produced in an electric arc [1]. Multi-walled carbon nanotubes prepared using different-type initial organic compounds and catalysts at different temperatures and pressures are characterized by different degrees of ordering of the graphite layers. For example, carbon nanotubes synthesized from gaseous acetylene at a temperature of 700°C with the use of an iron–nickel catalyst supported on zeolite contain a considerable amount of defects in the form of holes (formed instead of atoms) in the network of carbon hexagons [2, 3].

The electrical properties of carbon nanotubes can be controlled by modifying their structure through doping with atoms of different types. In turn, this makes it possible to execute control over the electronic states in the vicinity of the valence band and conduction band edges. It can be assumed that nitrogen atoms incorporated into graphite layers of the carbon nanotube walls serve as electron donors and, hence, bring about an increase in the electrical conductivity of the nanotubes.

At present, nitrogen-containing carbon nanotubes (CN_x nanotubes) can be synthesized using different techniques. In particular, the nitrogen content in the graphite layers of carbon nanotubes produced through electric-arc evaporation of graphite in a nitrogen atmosphere does not exceed 5% [4]. It was found that, in this case, the inner core of multi-walled carbon nanotubes is filled with gaseous nitrogen [5]. The nitrogen content in CN_x nanotubes prepared by low-temperature gas-phase pyrolysis (magnetron sputtering) can be as high as 30% [6].

In the present work, we devised a procedure for gas-phase synthesis of nitrogen-containing carbon nanotubes and examined the nanotube structure by using scanning and transmission electron microscopy. Moreover, we determined the electronic structure of carbon nanotubes from an analysis of the x-ray photoelectron and x-ray fluorescence spectra and investigated the conducting properties of carbon nanotube samples.

2. SYNTHESIS AND CHARACTERIZATION OF CARBON NANOTUBE SAMPLES

The catalytic pyrolysis of hydrocarbons and synthesis of carbon nanotubes were performed in a tube stainless steel furnace 1000 mm long and 36 mm in diameter. The furnace temperature was varied from 200 to 1000°C with the use of a RIF 101 thermoregulator.

1063-7834/02/4404-0652$22.00 © 2002 MAIK "Nauka/Interperiodica"

Gaseous argon at atmospheric pressure served as a buffer gas. The rate of gas flow was 3 l/min. Acetonitrile vapor entered the reactor through a bubbler, and the stream consumption was controlled by choosing the appropriate temperature of the bubbler.

A mixture of cobalt and nickel maleate salts in the form of a brown solid crystalline substance with 0.5- to 3-mm grains was used as a catalyst. The catalyst in an alundum boat was placed at the center of the reactor. Then, the reaction zone was blown with an argon stream and heated to 450°C for the purpose of decomposing the catalyst into nanoparticles of the cobalt–nickel alloy. Thereafter, the temperature inside the reactor was raised to the synthesis temperature and acetonitrile was added to the argon stream. The duration of the synthesis was 1 h. The catalytic pyrolysis resulted in the formation of a dark gray substance whose volume was three or five times greater than the volume of the crystalline grains of the initial salt (Fig. 1a). Crystalline grains of the product collapsed into powder under an even insignificant mechanical action.

The electronic properties of catalytic nitrogen-containing carbon nanotubes were compared with those of carbon nanotubes synthesized through electric-arc evaporation of graphite according to the procedure described in our recent work [7].

The CK_α x-ray fluorescence spectra of carbon nanotube samples were recorded on a Stearat laboratory x-ray spectrometer. The spectral resolution was ~0.4 eV. The spectra were measured using an NH_4AP ammonium biphthalate single crystal as an analyzing crystal [8].

The x-ray photoelectron spectra were recorded on a VG ESCALAB electron spectrometer (VG Scientific Co.). Electron emission was excited using x-ray radiation of the AlK_α line. The instrumental broadening was equal to 0.3 eV.

The electrical conductivity of bulk carbon-nanotube samples synthesized through catalytic decomposition of acetonitrile and electric-arc evaporation of graphite was measured by the four-point probe method in the temperature range 4.2–300 K.

3. RESULTS AND DISCUSSION

We performed a series of syntheses of carbon nanotubes at different temperatures in the range from 700 to 1000°C and revealed that the highest efficiency of the formation of carbon nanotubes is observed at synthesis temperatures ranging from 800 to 850°C (Fig. 1b). An increase (or decrease) in the synthesis temperature by 100°C leads to a substantial decrease in the nanotube yield due to carbonization and the formation of large-sized (more than 1000 Å) particles in the sample. These particles undergo graphitization at a temperature above 900°C and do not exhibit a visible texture at low temperatures. The carbon nanotubes synthesized at an optimum temperature are oriented in a random manner and contain virtually no impurities and amorphous carbon. The nanotube diameter falls in the range 10–50 nm. Judging from the electron microscope images, the carbon nanotubes have relatively thick walls, the nanotube channels are virtually empty, and metallic catalyst particles are located at the tips of the carbon nanotubes. The graphite layers arranged in the nanotube walls are strongly distorted and partially stratified. It should be noted that the carbon nanotubes synthesized at an optimum temperature can consist of two or more multiwalled nanotubes (Fig. 1c) rolled up to form a concentric structure.

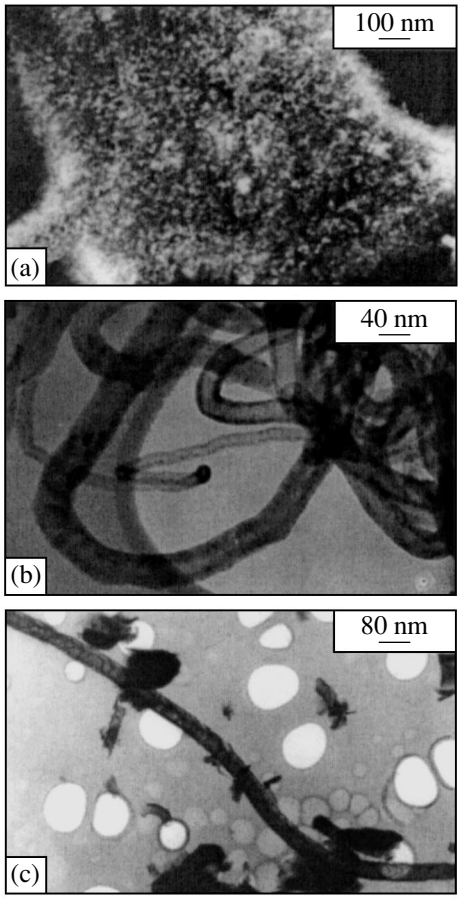

Fig. 1. Micrographs of catalytic nitrogen-containing nanotubes: (a) Jeol-200E scanning electron microscope and (b, c) JEM-2010 transmission electron microscopes.

The composition of the carbon nanotubes under investigation was determined by analyzing the intensities of the x-ray photoelectron spectra with due regard for the photoionization cross sections. The nitrogen content in the catalytic nanotubes was found to be equal to 3%. In the case when the carbon nanotubes were synthesized at higher (or lower) temperatures, the nitrogen content in the product increased to 10%. Figure 2a displays the N 1*s* photoelectron spectrum of the catalytic nanotubes prepared through pyrolysis of acetonitrile. As is clearly seen from Fig. 2a, this spectrum consists

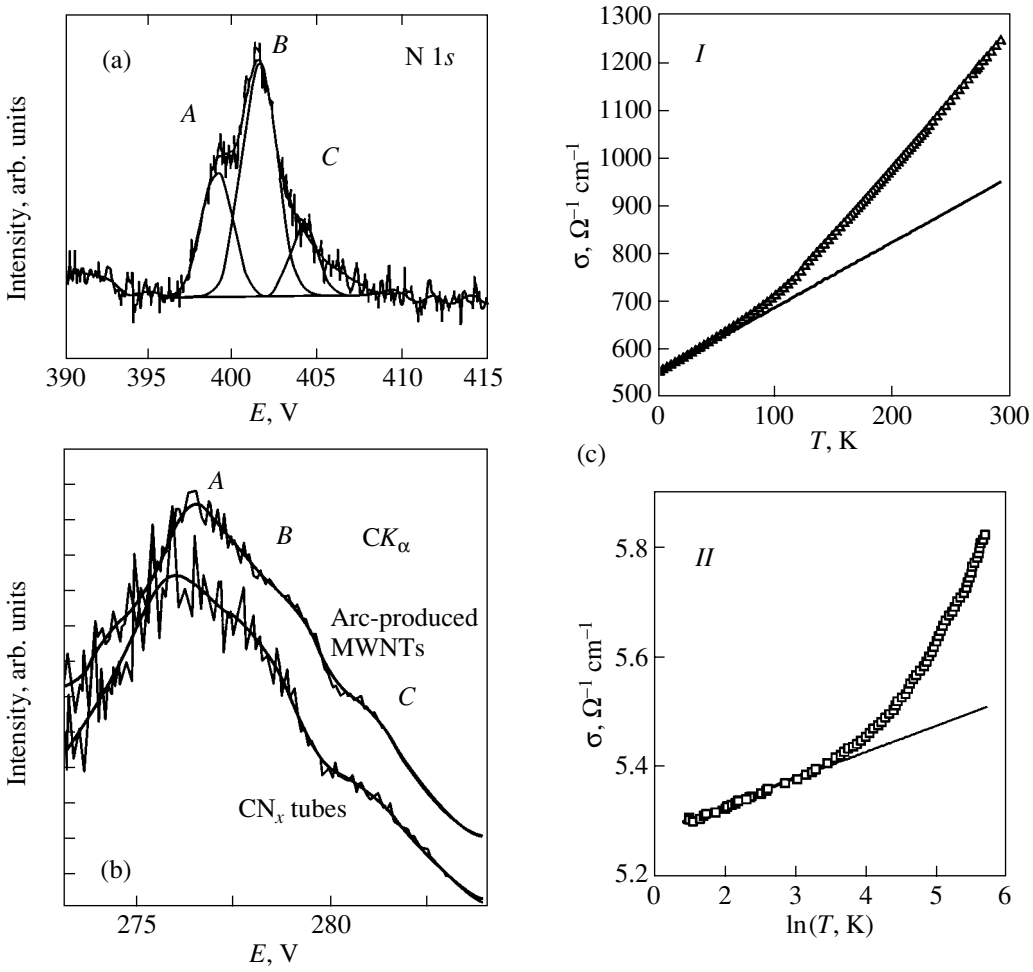

Fig. 2. Spectroscopic and transport properties of carbon nanotubes: (a) N 1*s* x-ray photoelectron spectrum of the catalytic nanotubes prepared by pyrolysis of acetonitrile, (b) CK_α x-ray fluorescence spectra of the carbon nanotubes synthesized through electric-arc evaporation (the upper curve) and catalytic nitrogen-containing carbon nanotubes (the lower curve), and (c) temperature dependences of the electrical conductivity $\sigma(T)$ for samples of (*I*) multi-walled carbon nanotubes produced in an electric arc and (*II*) catalytic nitrogen-containing carbon nanotubes.

of three components with maxima at energies of 398.8 eV (maximum *A*), 401.5 eV (maximum *B*), and 404.2 eV (maximum *C*). This suggests that chemically nonequivalent nitrogen atoms are involved in the nanotube structure. Terrones [5] assumed that nitrogen atoms are incorporated into the carbon network with the formation of a hole-type structure. Each nitrogen atom located in a nanotube layer is bonded to two carbon atoms (the electronic state of the nitrogen atom in the nanotube layer is similar to the electronic state of the nitrogen atom involved in the C_5H_5N pyridine molecule). This chemical state is consistent with the *B* maximum in Fig. 2a. In this figure, the *A* maximum is attributed to the nitrile nitrogen atoms and the *C* maximum is associated with the nitrogen oxidized state.

The electronic state of carbon atoms can be judged from the CK_α x-ray fluorescence spectra of the carbon nanotubes. The CK_α x-ray fluorescence spectra of the electric-arc-produced carbon nanotubes and catalytic nitrogen-containing carbon nanotubes are depicted in Fig. 2b. In both cases, the spectra exhibit three features that can be assigned to electronic transitions from the σ-type energy levels (maximum *A*), the upper σ- and lowest π-type levels (maximum *B*), and the upper occupied π-type energy levels (maximum *C*). The CK_α fluorescence spectrum of the electric-arc-produced carbon nanotubes is in good agreement with the spectrum of graphite. This indicates that the electronic structure of electric-arc-produced carbon nanotubes is similar to the electronic structure of graphite [1]. The CK_α fluorescence spectrum of catalytic nitrogen-containing carbon nanotubes is characterized by a weak short-wavelength shoulder *C* and a more intense maximum *B*. Such a shape of the CK_α fluorescence spectrum suggests a decrease in the carbon π-electron density. This decrease can be explained by the fact that there is a partial carbon hydrogenation with the formation of C–H bonds. The fact that the CK_α fluorescence spectrum of catalytic

nitrogen-containing carbon nanotubes produced by another method can have a different shape [3] indicates that these carbon nanotubes exhibit a different microstructure and, most likely, a different growth mechanism.

The electrical conductivity of the electric-arc-produced and catalytic carbon nanotubes was measured in the temperature range 4.5–300 K (Fig. 2c). For an electric-arc-produced sample consisting of multi-walled carbon nanotubes with a minimum amount of defects, the temperature dependence of the electrical conductivity at temperatures below 50 K exhibits a linear behavior (Fig. 2c, curve *I*): $\sigma(T) = (e^2/2\pi^2\hbar)L_\varphi^{-1}(T)$, where σ is the electrical conductivity of the sample, e is the elementary charge, $\hbar$ is the Planck constant, L_φ is the localization length, and T is the temperature. As is known, this behavior of the temperature dependence of the electrical conductivity is characteristic of three-dimensional effects of weak localization [9]. The localization length L_φ is estimated as $L_\varphi(4.2\text{ K}) = 200$ Å. This suggests that interference effects are predominant in nanotube bundles rather than in an individual nanotube.

For catalytic nitrogen-containing multi-walled carbon nanotubes, the temperature dependence of the electrical conductivity can be described by a logarithmic law (Fig. 2c, curve *II*). This behavior of the temperature dependence of the electrical conductivity corresponds to a two-dimensional localization at temperatures below 50 K due to the presence of defects in nanotubes [10]. It should also be noted that the electrical conductivity of catalytic nitrogen-containing multi-walled carbon nanotubes (Fig. 1) is two orders of magnitude less than that of multi-walled carbon nanotubes synthesized through electric-arc evaporation of graphite (Fig. 2c, curve *I*). This difference is associated with both a higher degree of structure imperfection of catalytic nitrogen-containing carbon nanotubes and a smaller amount of contacts between individual nanotubes in the bulk sample.

4. CONCLUSION

Thus, nitrogen-doped carbon nanotubes can be produced by gas-phase decomposition of acetonitrile with a nickel–cobalt catalyst. The structure and transport properties of nitrogen-containing multi-walled carbon nanotubes substantially differ from those of multi-walled carbon nanotubes synthesized through electric-arc evaporation of graphite.

ACKNOWLEDGMENTS

We would like to thank V.S. Danilovich for his help in scanning electron microscopy of the nanotube samples used in our investigations.

This work was supported by the State Scientific and Technical Program "Fullerenes and Atomic Clusters" (project no. 98055), the Russian Foundation for Basic Research (project nos. 00-03-32463, 00-03-32510, and 00-02-17987), and the International Association of Assistance for the promotion of cooperation with scientists from the New Independent States of the former Soviet Union (project INTAS nos. 97-1400 and 00-237).

REFERENCES

1. A. V. Okotrub, L. G. Bulusheva, A. I. Romanenko, *et al.*, Mol. Mater. **13**, 99 (2000).
2. A. Fonseca, K. Hernadi, P. Piedigrosso, *et al.*, Appl. Phys. A **67**, 11 (1998).
3. L. G. Bulusheva, A. V. Okotrub, I. P. Asanov, *et al.*, J. Phys. Chem. B **105**, 4853 (2001).
4. O. Stephan, P. M. Ajayan, C. Coliex, *et al.*, Science **266**, 1683 (1994).
5. M. Terrones, in *Proceedings of the XV International Winterschool on Electronic Properties of Novel Materials "Molecular Nanostructures," Kirchberg, Austria, 2001*, p. 63.
6. K. Suenaga, M. P. Johansson, N. Hellgren, *et al.*, Chem. Phys. Lett. **300**, 695 (1999).
7. A. V. Okotrub, L. G. Bulusheva, A. I. Romanenko, *et al.*, Appl. Phys. A **71**, 481 (2001).
8. V. D. Yumatov, A. V. Okotrub, and L. N. Mazalov, Zh. Strukt. Khim. **26**, 59 (1985).
9. A. Kawabata, Solid State Commun. **34** (6), 431 (1980).
10. L. Langer, V. Bayot, E. Grivei, *et al.*, Phys. Rev. Lett. **76**, 479 (1996).

Translated by O. Borovik-Romanova

Physics of the Solid State, Vol. 44, No. 4, 2002, pp. 656–658. Translated from Fizika Tverdogo Tela, Vol. 44, No. 4, 2002, pp. 630–633.

PROCEEDINGS OF THE V INTERNATIONAL WORKSHOP "FULLERENES AND ATOMIC CLUSTERS"

(St. Petersburg, Russia, July 2–6, 2001)

Preparation of Single-Walled Nanotubes with the Help of a Ni/Cr-Based Catalyst

V. N. Bezmel'nitsyn*, A. G. Domantovskiĭ*, A. V. Eletskiĭ*, E. V. Obraztsova, A. G. Pernbaum*, K. E. Prikhod'ko*, and S. V. Terekhov****

** Russian Research Centre Kurchatov Institute, pl. Kurchatova 1, Moscow, 123182 Russia*

*** Institute of General Physics, Russian Academy of Sciences, ul. Vavilova 38, Moscow, 117942 Russia*

Abstract— The high-yield synthesis of single-walled carbon nanotubes (SWNTs) is carried out in an electric-arc discharge using the Ni–Cr alloy as a catalyst. A new method of introducing the catalyst into the plasma hot region is used in the synthesis. In this method, the anode with a sandwich structure consists of two longitudinal graphite rods of a rectangular cross section, between which the Ni–Cr alloy in the form of a foil having a thickness approximately equal to 0.2 mm is placed. The obtained samples are investigated using transmission electron microscopy (TEM), Raman spectroscopy, and thermogravimetry. According to the results of TEM observations, SWNTs are tied into bundles with a length of several micrometers and a diameter of about 10 nm. The Raman spectra indicate that the diameter distribution of SWNTs lies between 1.2 and 1.5 nm with a peak at approximately 1.24 nm. The SWNT content in the obtained samples is approximately 20%. Heat treatment at various temperatures with a dosed air supply leads to a noticeable mass loss of the sample and to a change in its composition. For example, thus heating to 600 K causes a mass loss of about 40%, leading to an increase in the content of SWNTs up to 35% without their noticeable destruction. Further heating above 600 K leads to a virtually complete thermal decomposition of SWNTs. *© 2002 MAIK "Nauka/Interperiodica".*

1. INTRODUCTION

The scientific and applied importance of preparing and studying single-walled carbon nanotubes (SWNTs) [1, 2] is primarily due to the their potential application as a basis for nanoelectronic devices [3], electron field emitters [4], devices for gas storage [5], mechanical nanomanipulators [6], etc. However, the practical realization of these potentialities is hampered by the very low efficiency and high production cost inherent in the currently available methods of producing nanotubes [1, 2]. The most popular of these methods is based on the thermal evaporation of graphite electrodes in an electric arc in the presence of a metal catalyst. The metals used as a catalyst have included Fe, Ni, Co, Y, Ce, La, Rh, Pr, and their alloys [1, 2, 7–9]. Since the basic parameters of SWNTs obtained using this method of synthesis are determined to a considerable extent by the type of catalyst used, the list of metals employed as catalysts should be extended. In the present work, we proposed and used a catalyst in the form of a Ni–Cr alloy.

Another important factor determining both the properties of SWNTs and the possibility of synthesizing SWNTs in appreciable amounts is the introduction of the catalyst into the hot region of the plasma arc in which the SWNT synthesis takes place. The most prevalent approach to solving this problem is the filling of a deep cylindrical hole drilled into an anode rod with a mixture of metallic and graphite powders [1, 2]. This mixture must be thoroughly pressed into the hole to prevent sputtering of the powder before its heating. Thus, the procedure of anode preparation is quite complicated, which sets a limit on the output of the SWNT synthesis and increases its cost. In contrast to the traditional approach described above, we used an anode in the form of a sandwich, such that the alloy in the form of a thin foil was placed between two extended graphite rods of a rectangular cross section. This simplified the preparation of the anode and ensured the reproducibility of the properties of the SWNTs being synthesized.

The material obtained using the new type of catalyst and the new way of its introduction into the arc region was studied by Raman spectroscopy, transmission electron microscopy (TEM), and thermogravimetry (TGA). It follows from the results of measurements that the tissuelike material collected from the discharge chamber walls contains 20–25% SWNTs. Heat treatment of samples at a temperature of 600 K and a dosed air supply in combination with acid treatment increases the SWNT content to 35–40%.

2. EXPERIMENT

Soot samples containing SWNTs were obtained in a cylindrical gas-discharge chamber with a volume of 7 l and water-cooled walls. The cathode used was a cylindrical graphite rod with a diameter of 6 mm and a sharpened tip. A consumable anode had a sandwich structure with two graphite rods of a rectangular cross section (7×3.5 mm), between which a thin foil of the

1063-7834/02/4404-0656$22.00 © 2002 MAIK "Nauka/Interperiodica"

catalyst was placed. As catalysts, we tested various metallic alloys and compounds (Ni, Y, YF_3, Fe, Cu, and Cr), as well as their combinations. The best results concerning the SWNT yield were obtained when YNi_2, YF_3Ni_2, and NiCr were used. Most experiments were made using the most suitable Ni–Cr alloy with the weight ratio 80 : 20, which is characterized by good technological properties and a relatively high availability. A 0.2-μm-thick foil constituted about 10% of the weight of the anode material. The introduction of the foil along the gap between the two graphite rods ensured a uniform supply of the catalyst to the plasma region. It should be noted that the use of the catalyst in the form of a thin foil made of the NiCr alloy has obvious technological advantages in producing SWNTs. The dc arc was drawn under a He pressure of 700 Torr, a current of 60 A, and a voltage of 29 to 30 V, the electrode spacing being 4 mm. The voltage and the electrode spacing were stabilized automatically as a result of the displacement of the anode during arc burning [10]. The rate of thermal sputtering of the anode material was on the order of g/h.

A material containing SWNTs was discovered on the discharge chamber walls and on the surface of the cathode. The material coating the chamber walls had a layered tissuelike structure with a porosity at a level of 90%; it could be easily separated from the walls and preserved stability under weak mechanical action. The growth rate for this layer was on the order of 0.1 mm/h. This material was cut into samples with an area of approximately 50 mm^2 and a thickness of 0.5 mm and was investigated using a Raman spectrometer, a transmission electron microscope, and a thermogravimetric analyzer. In addition, the sample was purified by acid treatment.

The TGA of the samples was carried out using the method described in [11]. A sample of the tissuelike material with a weight of 100–200 mg was introduced into a cylindrical vessel of diameter and height equal to 15 mm, where it was heated in air at a rate of 5 K/min in the temperature range from 300 to 900 K. In order to prevent sample inflammation, air was supplied in small doses (0.5 cm^3/s). The sample weight was monitored to within 10 mg.

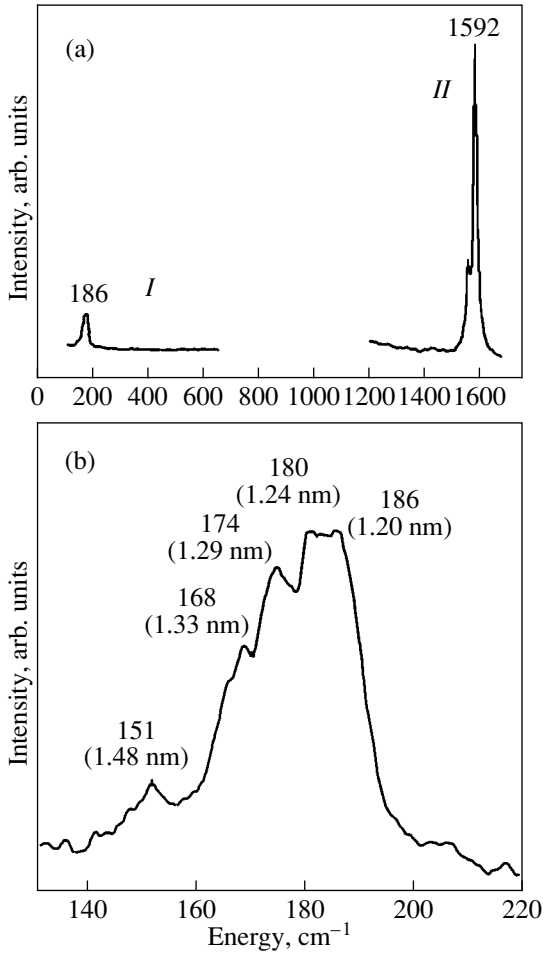

Fig. 1. Raman spectra of SWNT bundles obtained using a Ni/Cr-based catalyst: (a) complete spectrum and (b) enlarged part of the spectrum corresponding to radial breathing modes (*I* marks the radial breathing modes and *II* indicates the tangential modes). The values of nanotube diameters (nm) corresponding to the shift of the Raman line (cm^{-1}) are indicated on the spectrum.

3. DISCUSSION

Figure 1a shows the Raman spectrum of a dirty sample, which was obtained with the help of an Ar^+ laser ($\lambda = 0.5145$ μm). In order to avoid undesirable sample heating, the lasing intensity was maintained at a low level. The Raman spectrum contains two groups of lines, indicating the presence of SWNTs with a diameter distribution in the range from 1.2 to 1.5 nm, whose peak is at 1.24 nm. The first group includes the 1590-, 1566-, and 1551-cm^{-1} lines and belongs to tangential modes typical of SWNTs [12]. The second group of lines lies in the vicinity of 180 cm^{-1} and belongs to radial breathing modes whose frequencies are inversely proportional to the SWNT diameter [13]. This part of the spectrum is shown on a magnified scale in Fig. 1b, where the SWNT diameters corresponding to spectral singularities are indicated.

Figure 2 shows the TEM image of a dirty sample. It can be seen that SWNTs are tied into extended bundles of diameters on the order of 10 nm which consist of a few dozens of nanotubes. In addition to bundles, a large number of carbon particles and amorphous graphite can be observed.

Figure 3 shows typical TGA results. It can be seen that the heat treatment of the sample below 600 K leads to a loss of approximately 40% of its mass. It follows from the results of the Raman spectroscopy that this does not lead to the destruction of nanotubes. However, a further increase in temperature is accompanied by the

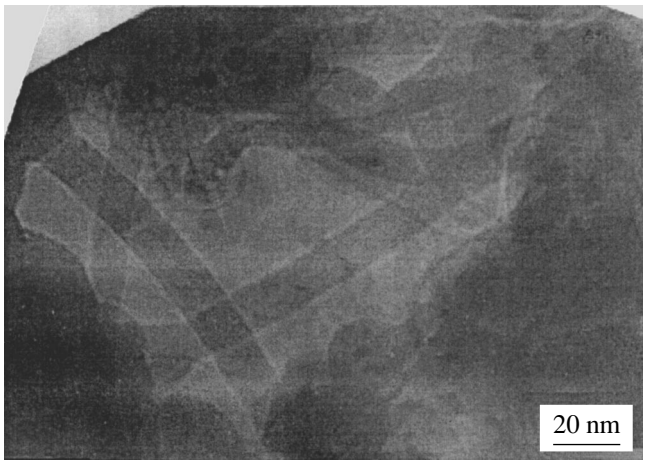

Fig. 2. TEM image of a sample containing SWNT bundles.

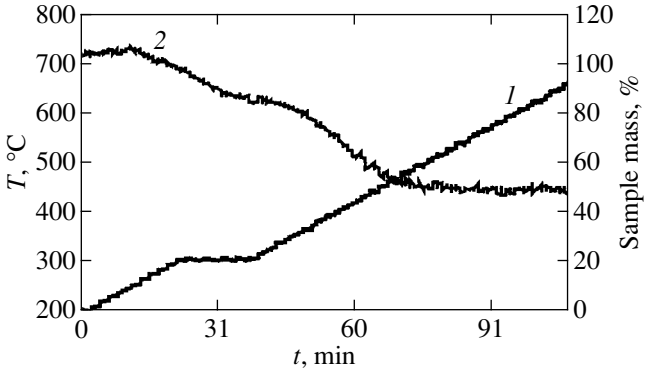

Fig. 3. Results of thermogravimetric analysis of an SWNT-containing sample: curve *1* corresponds to temperature and curve *2* to the sample mass. The heating rate is 5 K/min and the rate of air supply is 0.5 cm^3/s.

thermal decomposition of SWNTs, so that the total loss of the sample mass as a result of heating to 900 K reaches 90%.

The results of measurements described above show that the nanotubes obtained by using a Ni/Cr foil as a catalyst do not differ significantly from the SWNTs obtained by using catalysts on the basis of other metals. However, the application of the sandwich structure of the anode with a catalyst in the form of a thin foil offers indisputable technological advantages. Among other things, this makes it possible to avoid technologically complicated drilling of a deep small-diameter hole into the graphite rod and pressing of powder into the hole, which often lead to the rod breaking. In addition, such a configuration facilitates more complete utilization of the anode rods, which increases the productivity of the SWNT synthesis.

ACKNOWLEDGMENTS

This work was supported by the INTAS, grant no. 97-11894.

REFERENCES

1. R. Saito, G. Dresselhaus, and M. S. Dresselhaus, *Physical Properties of Carbon Nanotubes* (Imperial College Press, London, 1998).
2. A. V. Eletskiĭ, Usp. Fiz. Nauk **167**, 945 (1997) [Phys. Usp. **40**, 899 (1997)].
3. M. Bockrath, D. H. Cobden, P. L. McEuen, *et al.*, Science **275**, 1922 (1997).
4. W. A. de Heer, A. Chatelain, and D. Ugarte, Science **270**, 1179 (1995).
5. A. C. Dillon, K. M. Lones, T. A. Bekkedahl, *et al.*, Nature (London) **386**, 377 (1997).
6. R. Andrews, D. Jacques, A. M. Rao, *et al.*, Appl. Phys. Lett. **75**, 1329 (1999).
7. E. Anglaret, J. L. Sauvajol, S. Rols, *et al.*, in *Electronic Properties of Novel Materials—Progress in Molecular Nanostructures*, Ed. by H. Kuzmany, J. Fink, M. Mehring, and S. Roth (American Inst. of Physics, New York, 1998), AIP Conf. Proc. **442**, 116 (1998).
8. H. Katsuura, Y. Kumazawa, Y. Maniwa, *et al.*, Synth. Met. **103**, 2555 (1999).
9. B. Liu, T. Wädberg, E. Olsson, *et al.*, Chem. Phys. Lett. **30**, 365 (2000).
10. V. N. Bezmelnitsyn, A. V. Eletskii, R. Taylor, and N. G. Shepetov, J. Chem. Soc., Perkin Trans. 2, No. 2, 683 (1997).
11. Z. Shi, Y. Lian, F. Liao, *et al.*, Solid State Commun. **112**, 35 (1999).
12. A. M. Rao, E. Richter, S. Bandow, *et al.*, Science **275**, 187 (1997).
13. R. Saito, T. Takeya, T. Kimura, *et al.*, Phys. Rev. B **57**, 4145 (1998).

Translated by N. Wadhwa

Physics of the Solid State, Vol. 44, No. 4, 2002, pp. 659–662. Translated from Fizika Tverdogo Tela, Vol. 44, No. 4, 2002, pp. 634–637.

PROCEEDINGS OF THE V INTERNATIONAL WORKSHOP "FULLERENES AND ATOMIC CLUSTERS"

(St. Petersburg, Russia, July 2–6, 2001)

Transport and Magnetic Properties of Multiwall Carbon Nanotubes before and after Bromination

A. I. Romanenko[1, 2], O. B. Anikeeva[1, 3], A. V. Okotrub[1], L. G. Bulusheva[1], N. F. Yudanov[1], C. Dong[4], and Y. Ni[4]

[1] *Institute of Inorganic Chemistry, Siberian Division, Russian Academy of Sciences, pr. Akademika Lavrent'eva 3, Novosibirsk, 630090 Russia*

e-mail: romanenk@casper.che.nsk.su

[2] *Novosibirsk State University, ul. Pirogova 2, Novosibirsk, 630090 Russia*

[3] *Novosibirsk State Technical University, Novosibirsk, 630092 Russia*

[4] *National Laboratory for Superconductivity, Institute of Physics, Chinese Academy of Science, Beijing, 100080 China*

Abstract—Bulk samples of oriented carbon nanotubes were prepared by electric arc evaporation of graphite in a helium environment. The temperature dependence of the conductivity $\sigma(T)$, as well as the temperature and field dependences of the magnetic susceptibility $\chi(T, B)$ and magnetoresistance $\rho(B, T)$, was measured for both the pristine and brominated samples. The pristine samples exhibit an anisotropy in the conductivity $\sigma_\parallel(T)/\sigma_\perp(T) > 50$, which disappears in the brominated samples. The $\chi(T, B)$ data were used to estimate the carrier concentration n_0 in the samples: $n_{0ini} \sim 3 \times 10^{10}$ cm^{-2} for the pristine sample, and $n_{0\mathrm{Br}} \sim 10^{11}$ cm^{-2} for the brominated sample. Estimation of the total carrier concentration $n = n_e + n_p$ from the data on $\rho(B, T)$ yields $n_{ini} = 4 \times 10^{17}$ cm^{-3} (or 1.3×10^{10} cm^{-2}) and $n_{\mathrm{Br}} = 2 \times 10^{18}$ cm^{-3} (or 6.7×10^{10} cm^{-2}). These estimates are in good agreement with one another and indicate an approximately fourfold increase in carrier concentration in samples after bromination. © *2002 MAIK "Nauka/Interperiodica".*

1. INTRODUCTION

Being a new type of quasi-one-dimensional object, carbon nanotubes stimulate considerable interest because of their significance in fundamental physics and their application potential. It appears natural to expect the manifestation of new properties connected with cooperative phenomena in bulk samples consisting of carbon nanotubes. Variation of coupling between nanotubes in such samples should give rise to qualitatively novel properties of the material. In our case, the nanotube coupling was varied by chemical bromination. We report here on a study of the electrophysical and magnetic properties of bulk samples of carbon nanotubes, both pristine and modified by bromination.

2. EXPERIMENT

Bulk samples of multiwall carbon nanotubes were prepared by arc evaporation of graphite in a helium environment. The central part of the cathode film contained more than 50 vol % multiwall carbon nanotubes (Fig. 1). We used pristine samples with the maximum nanotube content (~80%) for our experiment. Brominated samples were obtained by maintaining the pristine samples in bromine vapor at room temperature for several weeks. Photoelectron spectroscopy showed the samples thus prepared to have the $CBr_{0.06}$ composition. After bromination, the samples were stored at room temperature for several months until the relaxation processes associated with bromine redistribution over the sample volume stopped. The pristine samples consisted of multiwall carbon nanotubes 50–150 Å in diameter (Fig. 1a) bound in bundles ~500–1500 Å in diameter (Fig. 1b) which were oriented in a bulk sample along the layers perpendicular to the film axis. The samples could be easily split along these layers. Bromination made the sample monolithic, and it could no longer be split along these layers.

The temperature dependence of the sample electrical conductivity anisotropy $\sigma_\parallel(T)/\sigma_\perp(T)$ ($\sigma_\parallel(T)$ and $\sigma_\perp(T)$ are the electrical conductivities along and perpendicular to the layers, respectively) was measured by the Montgomery method within the range 4.2–500 K (Fig. 2). The maximum value $\sigma_\parallel(T)/\sigma_\perp(T) \sim 50$ was observed near room temperature for the pristine sample. No anisotropy was found to exist in the brominated samples ($\sigma_\parallel \sim \sigma_\perp$). Moreover, the room-temperature conductivity of the brominated sample was about four times higher than that measured along the layers in the pristine sample. After bromination, the carrier concentration in single-wall carbon nanotubes was reported to increase [1]. The increase in the conductivity of our

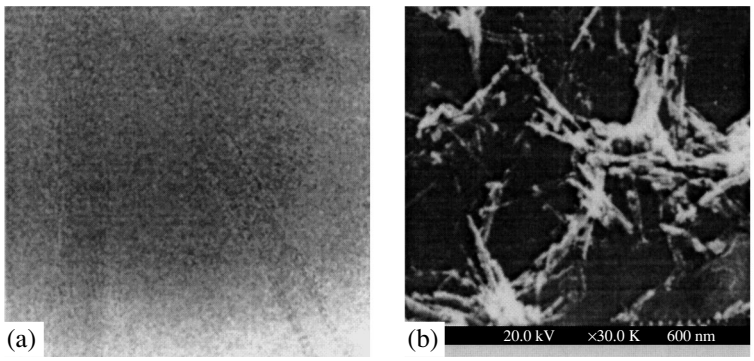

Fig. 1. Images of pristine samples obtained with (a) a high-resolution transmission electron microscope and (b) a scanning electron microscope. The film axis is perpendicular to the figure plane.

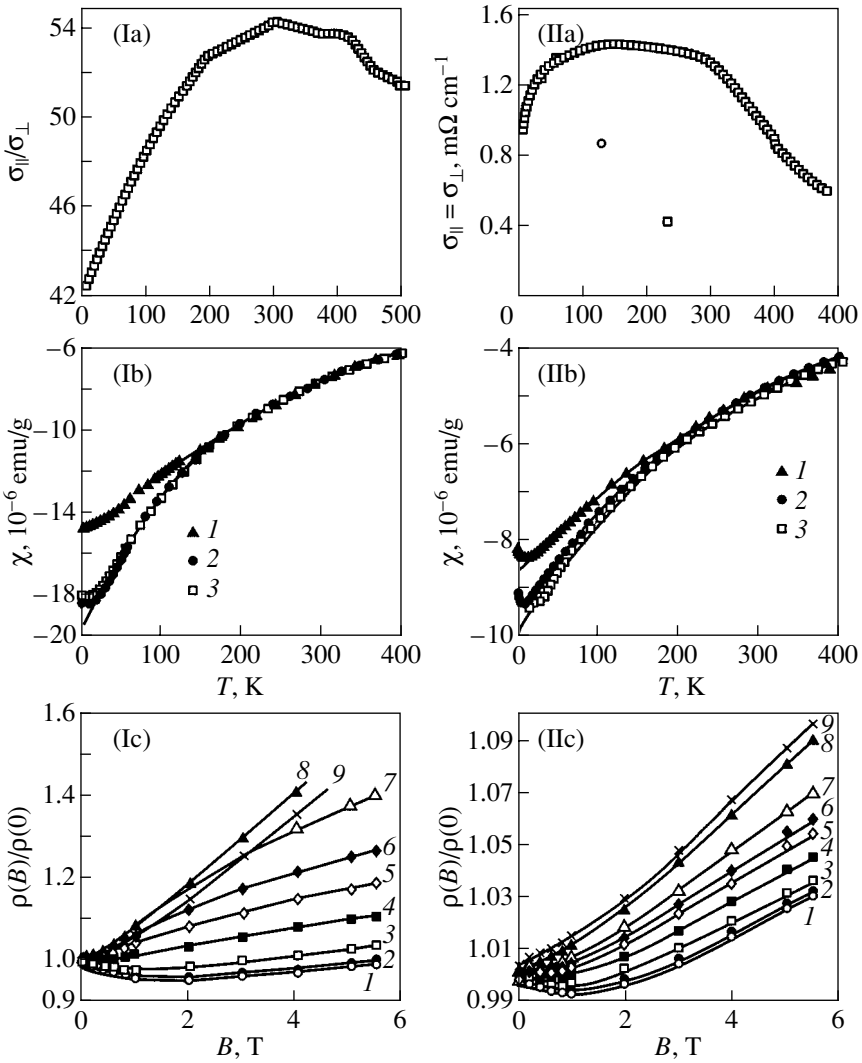

Fig. 2. Temperature dependences of the conductivity anisotropy $\sigma_\parallel(T)/\sigma_\perp(T)$ (Ia), of the conductivity $\sigma_\parallel(T) = \sigma_\perp(T)$ (IIa), and of the magnetic susceptibility $\chi(T)$ measured in different magnetic fields (Ib, IIb), as well as magnetoresistance $\rho(B)$ measured at fixed temperatures (Ic, IIc) in the pristine (Ia–Ic) and brominated (IIa–IIc) samples. In panels Ib and IIb, H is equal to (*1*) 0.01, (*2*) 0.5, and (*3*) 5.5 T; and in panels Ic and IIc, T is equal to (*1*) 4.5, (*2*) 10, (*3*) 25, (*4*) 50, (*5*) 75, (*6*) 100, (*7*) 150, (*8*) 300, and (*9*) 400 K. The continuous lines in Ib and IIb are fits of Eq. (1) to the experimental data obtained in the range 50–400 K. The fitting parameters γ_0 (eV), T_0 (K), and δ (K) for the pristine sample (Ib) are (*1*, *2*) 1.6, 215, and 159; (*3*) 1.7, 327, and 210; and those for the brominated sample (IIb) are (*1*) 1.4, 340, and 252; (*2*) 1.4, 300, and 273; (*3*) 1.5, 435, and 325.

brominated samples consisting of carbon multiwall nanotubes can also be connected with an increase in the carrier concentration. To test this conjecture, we studied the temperature and field dependences of the magnetic susceptibility $\chi(T, B)$ and of the magnetoresistance $\rho(B, T)$ of both the pristine and brominated samples.

The samples intended for magnetic measurements were cut in the form of cylinders, 3 mm in diameter and 10 mm long, of the pristine and brominated samples, with the axis of the cylinder being along that of the deposit axis. The $\chi(T, B)$ relation was measured on an MPMS-5 SQUID magnetometer (Quantum Design, USA). The measurements were performed in the temperature interval 4.5–400 K in three fixed magnetic fields of 0.01, 0.5, and 5.5 T (Fig. 2). The experimental data obtained in the range 50–400 K fit the following relation well (continuous lines in Fig. 2):

$$\chi(T) = \frac{-5.45 \times 10^{-3}\gamma_0^2}{k_B(T + \delta)\{2 + \exp(\eta) + \exp(-\eta)\}}\ \text{emu/g}, \quad (1)$$

which was proposed by Kotosonov for quasi-two-dimensional graphite [2–4]. Later, the applicability of this model to the magnetic susceptibility of carbon multiwall nanotubes was verified both experimentally [5–7] and theoretically [8]. According to this model, the diamagnetic susceptibility is dominated by the concentration of the extrinsic carriers n_0 associated with structural defects. Accordingly, the parameters in Eq. (1) are determined by n_0. In Eq. (1), γ_0 is the band parameter, δ relates to the broadening of the density-of-states function on the Fermi surface caused by carrier scattering from structural defects, and η can be expressed through δ and T_0, where T_0 is the carrier degeneracy temperature. The caption to Fig. 2 lists the values of these parameters obtained by fitting Eq. (1) to the experimental data. Estimation of n_0 made by fitting Eq. (1) to the $\chi(T, B)$ experimental data yielded $n_{0ini} \sim 3 \times 10^{10}$ cm^{-2} and $n_{0\text{Br}} \sim 10^{11}$ cm^{-2} for the pristine and brominated samples, respectively. As seen from the data obtained, bromination increases n_0 by a factor of 3.3. To derive an independent estimate of n_0 from other data, we studied $\rho(B, T)$ in magnetic fields from 0 to 5.5 T at fixed temperatures of 4.5, 10, 25, 50, 75, 100, 150, 300, and 400 K (Fig. 2). The continuous lines in Fig. 2 (Ic, IIc) show the results of approximating the experimental data with the relation

$$\rho(H)/\rho(0) = \frac{\sigma_e\sigma_p(\mu_e + \mu_p)B^2\cos^2\theta}{(\sigma_e + \sigma_p)^2 + (\sigma_e\mu_p - \sigma_p\mu_e)^2B^2\cos^2\theta}, \quad (2)$$

which describes the magnetoresistance of carbon multiwall nanotubes within the two-band model [9]. The magnetic field in our experiment was oriented perpendicular to the nanotube orientation plane ($\theta = 0$). Similar to [9], we assumed that the electron and hole mobilities differ little from each other ($\mu_e \sim \mu_p = \mu$). Using the fitting parameters of Eq. (2), we estimated the concentrations of electrons $\left(n_e = \frac{\sigma}{e\mu(\sigma_e/\sigma_p) + 1}\right)$ and holes $\left(n_p = \frac{\sigma(\sigma_e/\sigma_p)}{e\mu(\sigma_e/\sigma_p) + 1}\right)$. The total carrier concentration $n = n_e + n_p$ was found to be temperature-independent: $n_{ini} = 4 \times 10^{17}$ cm^{-3} (1.3×10^{10} cm^{-2}) and $n_{\text{Br}} = 2 \times 10^{18}$ cm^{-3} (6.7×10^{10} cm^{-2}).

3. DISCUSSION OF RESULTS

As follows from the measurements of the conductivity anisotropy $\sigma_\parallel(T)/\sigma_\perp(T)$ and from electron-microscopy images, the conductivity of samples consisting of more than 80% of carbon multiwall nanotubes is dominated by the conduction along the nanotube bundles in contact with one another. The conductivity of the pristine sample along the layers formed by these bundles is substantially higher than that across the layers, because conduction in the transverse direction occurs over the zigzag channels produced by contacting nanotube bundles belonging to different layers. The number of such contacts in the pristine sample is small enough; this is what brings about the anisotropy in the conductivity and allows easy splitting of the pristine samples along these layers. Bromination creates additional contacts between the nanotube bundles of different layers at the bromine sites. As a result, the conductivity across the layers becomes comparable with that along the layers, the sample can no longer be split, and becomes three-dimensional. In brominated samples, the conductivity along the nanotubes increases about fourfold as a result of the increase in carrier concentration. Estimation of the carrier concentration made from the $\chi(T, B)$ and $\rho(B, T)$ relations also implies about a fourfold increase [a factor of 3.3 from $\chi(T, B)$ data and 5 from $\rho(B, T)$] in the carrier concentration in the brominated samples. The fairly similar values of the carrier concentration obtained from the fitting of the $\chi(T, B)$ and $\rho(B, T)$ relations verify the validity of such estimates and the possibility of their use for intentional modification of samples.

ACKNOWLEDGMENTS

This study was supported by the Russian Research and Development Program "Fullerenes and Atomic Clusters" (project no. 5-1-98), Federal Program "Integration" (project no. K0042), Russian Foundation for Basic Research (project nos. 00-02-17987, 01-02-06500), the Ministry of Education of Russia (project no. E00-3.4-506), Interdisciplinary Integration Pro-

gram of the Siberian Division, Russian Academy of Sciences (project no. 061), and INTAS (grant nos. 97-170, 00-237).

REFERENCES

1. A. M. Rao, P. C. Eklund, S. Bandow, *et al.*, Nature **388**, 257 (1997).
2. A. S. Kotosonov, Pis'ma Zh. Éksp. Teor. Fiz. **43** (1), 30 (1986) [JETP Lett. **43**, 37 (1986)].
3. A. S. Kotosonov, Zh. Éksp. Teor. Fiz. **93** (5), 1870 (1987) [Sov. Phys. JETP **66**, 1068 (1987)].
4. A. S. Kotosonov, Fiz. Tverd. Tela (Leningrad) **33** (9), 2616 (1991) [Sov. Phys. Solid State **33**, 1477 (1991)].
5. A. S. Kotosonov and S. V. Kuvshinnikov, Phys. Lett. A **230**, 377 (1997).
6. A. S. Kotosonov and D. V. Shilo, Carbon **36**, 1649 (1998).
7. A. S. Kotosonov, Pis'ma Zh. Éksp. Teor. Fiz. **70**, 468 (1999) [JETP Lett. **70**, 476 (1999)].
8. A. S. Kotosonov and V. V. Atrazhev, Pis'ma Zh. Éksp. Teor. Fiz. **72** (2), 76 (2000) [JETP Lett. **72**, 53 (2000)].
9. S. N. Song, X. K. Wang, R. P. H. Chang, and J. B. Ketterson, Phys. Rev. Lett. **72**, 697 (1994).

Translated by G. Skrebtsov

Physics of the Solid State, Vol. 44, No. 4, 2002, pp. 663–665. Translated from Fizika Tverdogo Tela, Vol. 44, No. 4, 2002, pp. 638–640.

PROCEEDINGS OF THE V INTERNATIONAL WORKSHOP "FULLERENES AND ATOMIC CLUSTERS"

(St. Petersburg, Russia, July 2–6, 2001)

A Study of the Influence of Structural Imperfection on the Electronic Structure of Carbon Nanotubes by X-ray Spectroscopy and Quantum-Chemical Methods

V. V. Belavin, A. V. Okotrub, and L. G. Bulusheva

Institute of Inorganic Chemistry, Siberian Division, Russian Academy of Sciences, pr. Akademika Lavrent'eva 3, Novosibirsk, 630090 Russia

e-mail: spectrum@che.nsk.su

Abstract—It is demonstrated that the CK_α x-ray fluorescence spectra of carbon nanotubes synthesized by electric-arc evaporation of graphite and the spectra of carbon nanotubes produced using catalytic decomposition of hydrocarbons differ in the intensity of the short-wavelength lines. In order to interpret the obtained data, the electronic structures of perfect and defect-containing nanotubes are calculated in the framework of the tight-binding method with optimized parameters. The density of localized states that correspond to the observed increase in the intensity of the fluorescence spectrum of catalytic nanotubes can be obtained in the case when 15–20% of the total number of carbon atoms are absent in the carbon network. It is shown that defects of this type can bring about a decrease in the band gap of the nanotubes. © *2002 MAIK "Nauka/Interperiodica".*

1. INTRODUCTION

The electronic structure of carbon nanotubes is determined to a large measure by the geometric parameters, such as the nanotube diameter [1], helicity [2], and different-type defects [3–5]. The real structure of nanotubes depends on the method of their synthesis. The most frequently used methods of producing carbon nanotubes are laser evaporation, electric-arc synthesis, and catalytic decomposition of hydrocarbons in the presence of metal nanoparticles. Nanotubes produced by different methods differ in morphology, degree of imperfection, and electronic properties. Investigation into the structure of defects and their effect on the electronic structure is one of the topical directions in the physics of carbon nanotubes.

In this work, we performed x-ray spectroscopic and quantum-chemical investigations into the electronic structure of carbon nanotubes synthesized by electric-arc graphite evaporation [6] and gas-phase decomposition of acetylene with the use of iron and cobalt nanoparticles as a catalyst at a temperature of ~700°C [7].

2. RESULTS AND DISCUSSION

Figure 1a shows the experimental CK_α fluorescence spectra of the electric-arc-produced (curve *2*) and catalytic (curve *3*) nanotubes in comparison with the spectrum of untexturated graphite (curve *1*). The CK_α spectrum characterizes the 2*p* electron density distribution in the valence band of the compound. The measured spectra exhibit three specific features, namely, *A*, *B*, and *C*. The intensity and energy location of these features are virtually identical for the spectra of the electric-arc-produced nanotubes and graphite. This suggests a similarity between the electronic structures of the materials under investigation. The spectrum of catalytic tubes is characterized by an increase in the relative intensity of the short-wavelength line *A*. The *A* maximum in the spectra of graphite materials corresponds to the π system. The changes observed in the spectrum of catalytic nanotubes can be explained in terms of structural imperfections in the carbon network of the nanotube. The carbon network of a nanotube can contain defects in the form of adjacent five- and seven-membered rings (pentagon–heptagon pairs). Partial hydrogenation or the formation of covalent bonds between the layers of multi-walled carbon nanotubes leads to the formation of sp^3-hybridized atoms in the carbon network of the nanotube. The influence of these defects on the shape of the CK_α fluorescence spectra was analyzed in [8, 9]. In the present work, we examined the electronic structure of the (20, 0) nanotube with a periodic defect in the form of a hexagonal hole.

The quantum-chemical calculation was performed in the framework of the semiempirical tight-binding methods [10]. The single-electron parameters were chosen in such a manner that the width and relative positions of the π and σ components of the x-ray emission spectrum of graphite [11] should be reproduced. We calculated the following parameters: E_s = –2.99, E_p = 3.71, $V_{ss\sigma}$ = –4.0, $V_{sp\sigma}$ = 3.7, $V_{pp\sigma}$ = 4.5, and $V_{pp\pi}$ = –2.05. The interactions between the first nearest neighbors were taken into account. Figure 1b displays two

1063-7834/02/4404-0663$22.00 © 2002 MAIK "Nauka/Interperiodica"

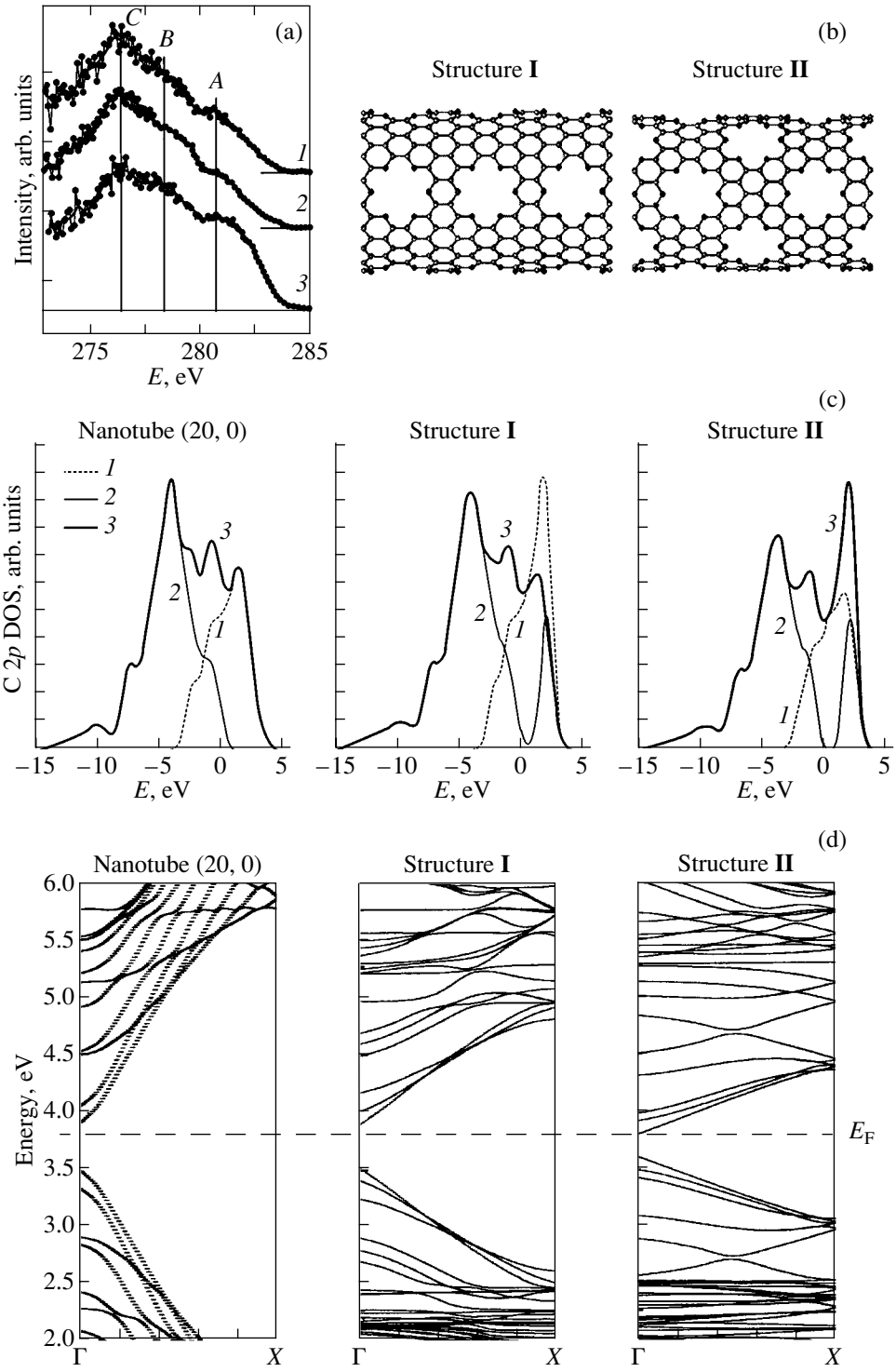

Fig. 1. (a) Experimental CK_α fluorescence spectra of (*1*) graphite and (*2*) electric-arc-produced and (*3*) catalytic carbon nanotubes; (b) structures of the defect-containing carbon nanotubes **I** and **II** with different defect densities; (c) calculated partial C 2*p* electron densities of states in the valence band of a perfect (20, 0) nanotube and defect nanotube structures **I** and **II**: (*1*) π, (*2*) σ, and (*3*) (π + σ) components; and (d) dispersion curves for a perfect zigzag (20, 0) nanotube and defect-containing nanotubes.

considered structures with holes. In structure **I**, the unit cell contains 136 atoms, including 24 twofold-coordinated carbon atoms. In structure **II**, the number of twofold-coordinated carbon atoms in the unit cell is doubled and the total number of carbon atoms involved in the unit cell is 192. The electronic structure is calculated with respect to 21 *k* points in the one-dimensional Brillouin zone.

Figure 1c represents the C 2*p* electron densities calculated for the occupied crystalline orbitals of a perfect (20, 0) nanotube and two defect nanotube structures. The C 2*p* electron density was constructed by summation of the squares of the coefficients for C 2*p* atomic orbitals over all the atoms involved in the unit cell. The π and σ components were obtained separately. The π component is represented by the 2*p* orbitals directed radially to the tube surface. The σ orbitals are directed tangentially to the tube surface. It is seen that the density of states substantially changes upon the introduction of vacancies into the carbon network. The σ component exhibits an additional high-energy maximum at an energy of 2.5 eV due to the localization of the electron density on the dangling bonds of carbon atoms. An insignificant decrease in the intensity of the π component is associated with the decrease in the number of π electrons in the system. If the interactions between the vacancies are ignored, the intensity of the aforementioned high-energy maximum in the σ component can be considered to be proportional to the number of dangling bonds in the unit cell. However, it is evident that, compared to structure **I**, the intensity of this maximum for structure **II** increases by a factor of less than two, even though the number of dangling bonds is doubled. This ratio can be broken as the result of the interaction between electrons of the twofold-coordinated carbon atoms that form the boundaries of the neighboring holes.

The results of calculations of the band structure are represented in Fig. 1d. In the energy range 2.0–2.5 eV, the band structure of the defect-containing nanotubes is characterized by the crystalline orbitals with an insignificant dispersion. The electron density of these orbitals is responsible for the high-energy maximum in the σ component. The formation of holes in the nanotube structure also leads to a change in the band gap due to variations in the efficiency of the interatomic interactions. According to our calculations, the band gap of the perfect (20, 0) nanotube is equal to 0.39 eV; in this case, the valence and conduction bands are doubly degenerate at the Γ point. In structures **I** and **II**, the band gaps decrease to 0.36 and 0.18 eV, respectively. The valence band top and the conduction band bottom in both defect structures are not degenerate at the Γ point.

3. CONCLUSIONS

The above investigation demonstrated that the observed increase in the short-wavelength maximum of the x-ray fluorescence spectrum of the catalytic carbon nanotubes can be caused by the imperfection of the carbon network. The intensity of maximum *A* in the experimental spectrum of the catalytic nanotubes increases by 50% compared to that of the electric-arc-produced nanotubes. The corresponding increase in intensity of the high-energy maximum in the theoretical spectrum is observed when the content of atomic vacancies in the carbon nanotube reaches ~15–20%. The calculation of the band structure showed that the conductivity of defect-containing nanotubes can be higher than that of defect-free nanotubes.

ACKNOWLEDGMENTS

This work was supported by the Russian Scientific and Technical Program “Fullerenes and Atomic Clusters” (project no. 98055), the Russian Foundation for Basic Research (project no. 00-03-32463), and the International Association of Assistance for the promotion of cooperation with scientists from the New Independent States of the former Soviet Union (project INTAS nos. 97-1400 and 00-237).

REFERENCES

1. M. S. Dresselhaus, G. Dresselhaus, and R. Saito, Solid State Commun. **84**, 201 (1992).
2. J. W. Mintmire, D. H. Robertson, and C. T. White, J. Phys. Chem. Solids **54**, 1835 (1993).
3. L. Chico, V. H. Crespi, L. X. Benedict, *et al.*, Phys. Rev. Lett. **76**, 971 (1996).
4. T. Kostyrko, M. Bartkowiak, and G. D. Mahan, Phys. Rev. B **60**, 10735 (1999).
5. H. J. Choi, J. Ihm, S. G. Louie, and L. Cohen, Phys. Rev. Lett. **84**, 2917 (2000).
6. A. V. Okotrub, L. G. Bulusheva, A. I. Romanenko, *et al.*, Appl. Phys. A **71**, 481 (2001).
7. A. Fonseca, K. Hernadi, P. Piedigrosso, *et al.*, Appl. Phys. A **67**, 11 (1998).
8. L. G. Bulusheva, A. V. Okotrub, A. Fonseca, and J. B. Nagy, Synth. Met. **121**, 1207 (2001).
9. L. G. Bulusheva, A. V. Okotrub, I. P. Asanov, *et al.*, J. Phys. Chem. B **105**, 4853 (2001).
10. J. C. Slater and G. F. Koster, Phys. Rev. **94**, 1498 (1954).
11. P. Skytt, P. Glans, D. C. Mancini, *et al.*, Phys. Rev. B **50**, 10457 (1994).

Translated by O. Moskalev

Physics of the Solid State, Vol. 44, No. 4, 2002, pp. 666–667. Translated from Fizika Tverdogo Tela, Vol. 44, No. 4, 2002, pp. 641–642.

PROCEEDINGS OF THE V INTERNATIONAL WORKSHOP "FULLERENES AND ATOMIC CLUSTERS"

(St. Petersburg, Russia, July 2–6, 2001)

Magnetic Properties of Carbon Nanotubes Produced by the Arc-Discharge Method under Different Conditions

A. S. Kotosonov*, D. V. Shilo*, and A. P. Moravskiĭ**

** Research Institute of Structural Graphite Materials, Élektrodnaya ul. 2, Moscow, 111524 Russia*

*** Institute of Problems of Chemical Physics, Russian Academy of Sciences, Chernogolovka, Moscow oblast, 142432 Russia*

e-mail: grafit@aha.ru

Abstract—The diamagnetic susceptibility and EPR signals of multi-walled carbon nanotubes produced at different helium pressures and rates of feed of the graphite anode are studied. It is found that a decrease in the helium pressure and in the feed rate of the graphite anode leads to an increase in the diamagnetic susceptibility and the *g* factor of the EPR signal associated with the carbon nanotubes. The investigation into the magnetic properties within the framework of the band model of quasi-two-dimensional graphite demonstrates that an increase in the diamagnetic susceptibility and in the *g* factor of the EPR signal is due to a decrease in the content of layered defects in the carbon nanotubes. Analysis of the EPR spectra indicates that, in addition to carbon nanotubes, the cathode deposit contains a considerable fraction of polyhedral nanoparticles at helium pressure in a chamber below 200 Torr. A similar situation is observed for cathode deposits obtained at low feed rates of the graphite anode. *© 2002 MAIK "Nauka/Interperiodica".*

1. INTRODUCTION

Theoretical calculations [1] and experimental investigations [2–5] have shown that the electronic structure and magnetic properties of multi-walled carbon nanotubes are sensitive to both the number of layers and the content of layered defects and impurity atoms in nanotubes. It is evident that the content and type of defects in multi-walled carbon nanotubes should be governed, to a large extent, by the conditions of nanotube synthesis.

Earlier [1, 4, 5], it was demonstrated that the temperature dependences of the diamagnetic susceptibility and EPR parameters for multi-walled carbon nanotubes containing 15 layers and more can be adequately described in the framework of the band model of quasi-two-dimensional graphite [6, 7]. Moreover, this model makes it possible to determine the type and content of defects located in graphite layers of multi-walled carbon nanotubes.

In this work, we investigated the magnetic properties of cathode deposits produced by the arc-discharge method at different helium pressures (from 50 to 2000 Torr) and different feed rates of the graphite anode (from 0.8 to 8 mm/min) at an electric-arc current of 65 A.

2. SAMPLES AND EXPERIMENTAL TECHNIQUE

For our measurements, the samples were chosen from the central part of the cathode deposit. The diamagnetic susceptibility was measured on an Oxford Instruments system by the Faraday technique. The error in measuring the susceptibility was no more than 10^{-8} emu/g. The EPR signal was measured on an E-109 Varian spectrometer operating at a frequency of 9.3 GHz. The error in determining the *g* factor was no more than 10^{-4}.

3. RESULTS AND DISCUSSION

The measurements demonstrated that the orientationally averaged diamagnetic susceptibility of the cathode deposit increases from 7.9 to 9.2×10^{-6} emu/g with a decrease in the helium pressure from 2000 to 200 Torr. The correlation between the diamagnetic susceptibility of the cathode deposit and the helium pressure in the deposition chamber is represented in the figure. Analysis of the EPR spectra of the cathode deposits obtained in the aforementioned pressure range showed that the EPR spectrum consists of a singlet associated with multi-walled carbon nanotubes for which the *g* factor increases from 2.015 to 2.021 with a decrease in the helium pressure. This behavior of the magnetic properties suggests that the content of layered defects in multi-walled carbon nanotubes decreases with a decrease in the helium pressure. The experimental temperature dependences of the diamagnetic susceptibility were analyzed theoretically for a number of samples in the framework of the band model of quasi-two-dimensional graphite. It was found that a decrease in the

1063-7834/02/4404-0666$22.00 © 2002 MAIK "Nauka/Interperiodica"

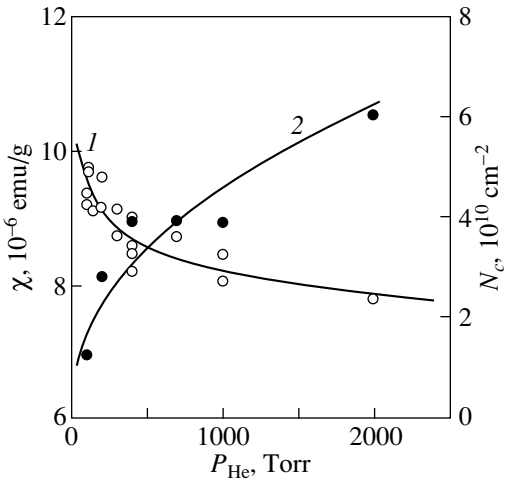

(*1*) Orientationally averaged diamagnetic susceptibility and (*2*) the content of layered defects in multi-walled carbon nanotubes produced at different helium pressures.

helium pressure from 2000 to 200 Torr leads to a decrease in the content of linear defects from 6.1 to 2.8×10^{10} cm^{-2} (see figure). Examination of the EPR spectra of the cathode deposits produced at a helium pressure ranging from 50 to 150 Torr revealed that, in addition to the EPR signal attributed to multi-walled carbon nanotubes, the EPR spectrum exhibits an additional signal (g = 2.01) assigned to nanoparticles. As the helium pressure decreases, the relative intensity of the EPR signal from multi-walled carbon nanotubes decreases, whereas the intensity of the signal associated with nanoparticles increases. Consequently, the fraction of particles in the cathode deposit should increase. This inference was confirmed by high-resolution transmission electron microscopy. It was shown that these samples are characterized by a small amount of multi-walled carbon nanotubes and a large amount of polyhedral nanoparticles.

The influence of the feed rate of the graphite anode on the structure and magnetic properties of the cathode deposits was analyzed for samples prepared at a helium pressure of 500 Torr.

A decrease in the feed rate of the graphite anode leads to an increase in the diamagnetic susceptibility and the g factor of the EPR signal from multi-walled carbon nanotubes due to a decrease in the content of layered defects in the nanoparticles. A theoretical treatment of the temperature dependences of the diamagnetic susceptibility revealed that a decrease in the anode feed rate from 8 to 0.8 mm/min brings about a decrease in the defect content from 6 to 3×10^{10} cm^{-2}. However, the samples prepared at a feed rate of less than 2 mm/min are not homogeneous. In addition to the EPR signal attributed to multi-walled carbon nanotubes, the EPR spectra of these samples at low temperatures (150 K) exhibit an EPR signal with a lower g value. This is caused by the presence of another, more defective form of carbon. According to transmission electron microscopy, these samples, apart from multi-walled carbon nanotubes and polyhedral nanoparticles, contain graphite particles and amorphous carbon.

4. CONCLUSION

The experimental results obtained in this work allowed us to conclude that the magnetic properties of multi-walled carbon nanotubes can be used to control the synthesis of carbon nanotubes with specified properties.

ACKNOWLEDGMENTS

This work was supported by the Russian Scientific and Technical Program "Fullerenes and Atomic Clusters" (project no. 20006) and the Russian Foundation for Basic Research (project no. 99-03-32382).

REFERENCES

1. A. S. Kotosonov and V. V. Atrazhev, Pis'ma Zh. Éksp. Teor. Fiz. **72**, 76 (2000) [JETP Lett. **72**, 53 (2000)].
2. M. Kosaka, T. W. Ebbesen, H. Hiura, *et al.*, Chem. Phys. Lett. **233**, 47 (1995).
3. S. Bandow, J. Appl. Phys. **80**, 1020 (1996).
4. A. S. Kotosonov and S. V. Kuvshinnikov, Phys. Lett. A **230**, 377 (1997).
5. A. S. Kotosonov and D. V. Shilo, Mol. Mater. **13**, 113 (2000).
6. A. S. Kotosonov, Zh. Éksp. Teor. Fiz. **93**, 1870 (1987).
7. A. S. Kotosonov, Carbon **26**, 735 (1988).

Translated by N. Korovin

Physics of the Solid State, Vol. 44, No. 4, 2002, pp. 668–673. From Fizika Tverdogo Tela, Vol. 44, No. 4, 2002, pp. 643–648.

PROCEEDINGS OF THE V INTERNATIONAL WORKSHOP "FULLERENES AND ATOMIC CLUSTERS"

(St. Petersburg, Russia, July 2–6, 2001)

Allotropic Conversion of Carbon-Related Films by Using Energy Beams[1]

H. Naramoto*, Xiaodong Zhu*, Yonghua Xu*, K. Narumi*, J. Vacik*, S. Yamamoto, and K. Miyashita*****

** Advanced Science Research Center, Japan Atomic Energy Research Institute, 1233 Watanuki, Takasaki, Gunma, 370-1292 Japan*

*** Department of Materials Development, Japan Atomic Energy Research Institute, 1233 Watanuki, Takasaki, Gunma, 370-1292 Japan*

**** Gunma Pref. Industrial Technology Research Laboratory; 190 Toriba Maebashi, Gunma, 371-0845 Japan*

Abstract—Energy beams, such as ion and laser beams, were employed to convert carbon allotropes into other ones at a specified position because these energy sources can be controlled precisely in time and space. The ion beam deposition technique employing mass-separated ions proved effective in studying the nucleation process by changing several growth parameters (ion species, incident energies, and substrate temperatures). Immersed nanosized diamonds were found in an sp^3-rich amorphous film prepared with 100-eV $^{12}C^+$ ions at room temperature. Surrounding these nanodiamonds, regularly arrayed small bumps, "petals," were formed around the periphery of bald circles upon cooling. Ar-ion laser illumination is effective in designing the array of high luminescent points on a C_{60} film by careful control of the laser power, and the combination of a micro-Raman spectrometer with a piezoscanning system provides one with a tool for 2-dimensional processing of photosensitive materials. Simultaneous bombardment during C_{60} evaporation results in an interesting pattern formation specific to the simultaneous treatment. The dependence of the surface nanoscale pattern on the ion energy and the substrate temperatures provides one with a new tool for designing nanoscale functional materials. As an extreme, the appearance of hexagonal diamonds was detected with disordered carbon and graphite under the condition of there being a high ratio between the Ne ion beam and the C_{60} thermal beam. © *2002 MAIK "Nauka/Interperiodica".*

Carbon atoms condense in various kinds of chemically bonded forms, and they exhibit remarkably excellent and characteristic properties dependent on bonding nature; this has induced broad research and applications not only in materials science but also in other scientific fields. Because of these potential applications, much attention has been paid to how to convert carbon allotropes into one another in a controlled manner. As is well recognized, the role of catalytic materials is important in the conversion of C_{60} into nanotubes and/or diamond in a more moderate way. The coevaporation of Ni with C_{60} at high temperatures results in a self-organized structure through the competitive process between the segregation of each component and the possible chelate formation [1]. In this case, polymerization of C_{60} and graphitization were also observed. Careful studies have been carried out to elucidate the catalytic behavior depending on the cluster size from the electronic and atomistic points of view [2–4]. These chemical processes are attractive because they are not significantly destructive and are energy-efficient, but if one wants to intend the design of a material to have a specified function, one must rely on other physical processes, such as directional energy beams.

Careful beam tuning in the energy, energy density, and beam size is also useful for changing the bonding nature into another one at a specified area, and this will become a special advantage in the design of materials on a small scale. For example, in the supersaturated mixture between transition metals and C_{60}, they form a uniform mixture or a layered structure without mixing in the low temperature deposition. In this situation, C_{60} molecules will play the role of inert gas atoms, such as Ar atoms, so as to keep Ni clusters separated, but, if the mixture is exposed to intense electronic excitation of energetic ions, C_{60} molecules can be converted into amorphous carbon and the segregation of Ni atoms can be facilitated [5]. The energy beams can be used not only to break up but also to push a limited number of atoms into another quasi-stable phase, which is characteristic in the ion-beam-assisted deposition (IBAD) technique [6–8]. As one of the extremes in IBAD techniques, the ion-beam deposition (IBD) technique has been employed to study the nucleation process of diamonds without the influence of sputtering [9], and it has been shown that the ion species and the incident energy

[1] This article was submitted by the authors in English.

are the dominant parameters for amorphous carbon films with higher sp^3 bonding fractions [10].

In this report, attention will be focused on the appearance of nanoscale topological features combined with the dynamical conversion of C_{60} molecules into other carbon allotropes as a function of the beam energy, the substrate temperature, and the relative amount of the ion beam to the C_{60} molecule beam. As typical examples, the topographic features obtained in IBD and laser processing experiments are illustrated for comparison. The results obtained in this IBAD experiment imply that if an additional parameter is introduced, such as the incident beam direction, the design of the materials will become more facilitated.

1. EXPERIMENTAL

The IBD was performed by employing an accelerator-decelerator system under ultra high vacuum with $^{12}C^+$ ions incident to Si(111) and an Ir(100)/MgO(100) single-crystalline substrate [11]. The typical ion beam parameters are 50–200 eV in energy and around 1 μA in beam current after removal of energetic neutral species. The crystal quality of the Ir(100)/MgO(100) substrate was improved after optimization of the substrate temperature, and the x-ray diffraction analysis and Rutherford Back Scattering (RBS)/channeling analysis show the crystal perfection to be comparable to an Si wafer [12].

The IBAD was made by developing a specially designed chamber, as described in [13]. In this chamber, three different sources (C_{60}, Ne ions, and transition metals) are available. When evaporating C_{60} molecules, energetic Ne^+ ions were introduced in the energy range up to 5 keV. The Ne^+ ion beam is obliquely incident at 60° relative to the surface normal, and the sputtering effect should be considered if one uses ions with a high Z element. The chamber can be evacuated up to 1.2×10^{-6} Pa, and, in the IBAD experiment, the vacuum was maintained at less than 5×10^{-5} Pa. The vapor pressure of C_{60} was maintained constant by controlling the temperature of a Knudsen cell at 370°C, and the simultaneously growing C_{60} film was bombarded with Ne^+ ions in the energy range from 0 to 5 keV. The total amount of incident ions was counted by digitizing the incident current on a target holder. The submicron sized structure after IBAD treatment was analyzed with two kinds of micro-Raman spectrometers by using an Ar-ion laser (Renishaw 2000 with several micron laser spots and a Nanofinder from Tokyo Instruments with a submicron size spot for the 514 nm line). The nanoscale surface characterization was made with an atomic force microscope (JSPM-4200). Optical absorption spectroscopy in the visible and ultraviolet regions was used to assess the optical band gap of the deposited films.

2. RESULTS AND DISCUSSIONS

In the IBD experiment, one can realize a more sophisticated condition for the nucleation study of diamond, for example. The $^{12}CH_x^+$ ($x = 0$–4) ions with different energies (50–200 eV) are incident on two kinds of substrates (Si(111) and Ir(100)/MgO(100)) at different temperatures (room temperature–700°C). In all cases, the amorphous graphite films were formed with the sp^3 main features, but the highest sp^3 fraction (80%) was obtained under the following condition: 100-eV $^{12}C^+$ ions at room temperature on either substrate. It is surprising that the same simultaneous incident with hydrogen atoms as in the experiment using $^{12}CH_x^+$ is effective for the high formation rate of sp^3 bonding. Figure 1 illustrates a set of photographs from IBD carbon films on Ir(100)/MgO(100) synthesized under the highest sp^3 fraction condition. Figure 1a is an optical micrograph (scale, roughly 500 times); it was taken when the film was heated to 400°C under a He flow. In this photo, one can see many bright circles associated with small dots, "flower patterns." The main part of this pattern was formed upon heating, but the regularly arranged dots were found upon cooling. This phenomena was not observed in the IBD films on Si(111) substrates. The IBD films on Si are resistant to heating up to 600°C, and, after 700°C, they started to change into graphite, judging from the Raman analysis. On the contrary, the IBD films on Ir/MgO are not resistant to heating, and, after heating to 400°C, a part of the film starts to be removed. However, the remaining part is of the sp^3 nature. Each flower seems to be formed on crystal imperfections of the substrate crystal with a small dot at the center. Similar flower patterns were also observed on Ir(110)/MgO(110) with (110) symmetry. Figure 1b illustrates the atomic force microscope (AFM) analysis performed on a singe flower among many flower patterns in the same film. The regularly arranged dots around flowers can be observed clearly, and elemental analysis performed on this indicates that the dots are a kind of blister with a small loss of the carbon component. From the above-decribed information, it is reasonable to conclude that regularly arranged dots with a fractal nature are formed through the deformation instability when there is a fast temperature change in the cooling process. The nanodot at the center (roughly 300 nm in diameter) is also interesting, and micro-Raman analysis with a submicron laser spot was performed. The study gives us clear evidence of having found immersed nanodiamonds in the dominant sp^3 amorphous carbon film.

The illumination of C_{60} films on Si with an Ar ion laser resulted in interesting features (not shown for simplicity). By careful tuning of the energy density, it has become possible to prepare high luminescent points of submicron size through the polymerization of C_{60} films. The array of the high luminescent points can be designed easily by using a micro-Raman spectrometer

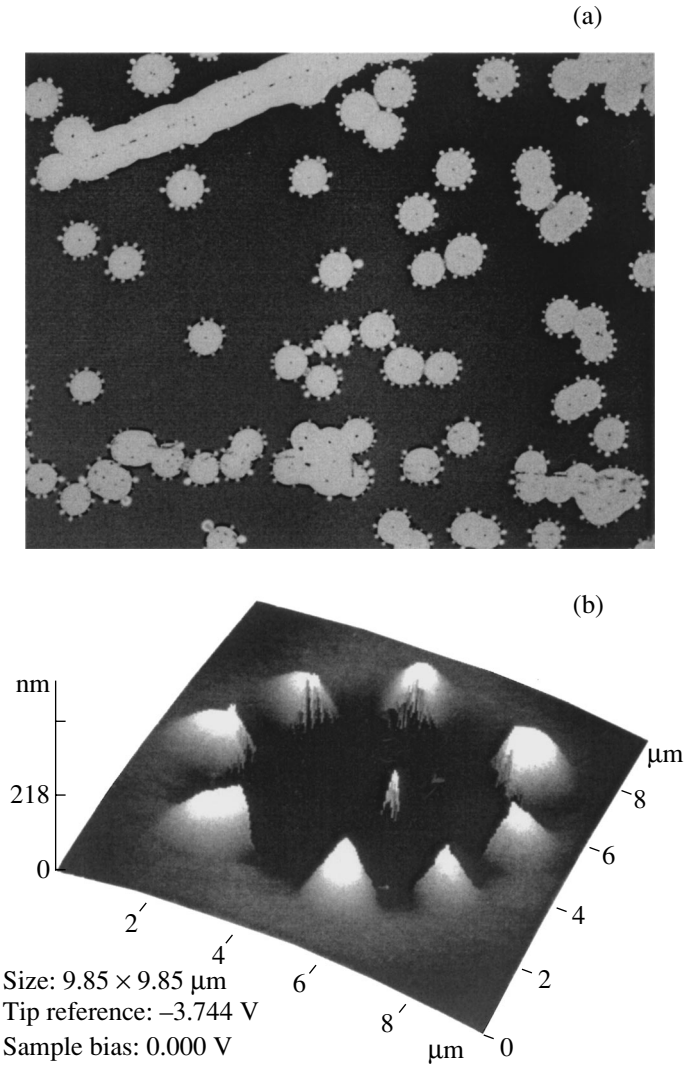

Fig. 1. Surface characterization of sp^3-rich DLC on IR(100)/MgO(100) heated at 700°C under flowing He gas. (a) Optical micrograph (×500). Many "flower" patterns can be seen. (b) AFM image of a flower pattern with a nanodiamond at the center. Regularly arranged small "petals" are formed through the instability in the fast stress-relaxation process.

combined with the AFM stage. Illumination with high energy density or with longer exposure simply induces graphitization. Further studies are scheduled to illustrate polymerization by changing the wavelength of the lasers.

In relation to the carbon allotrope conversion, strong attention was paid to the competitive process between C_{60} evaporation and ion bombardment (IBAD). The main parameters in the IBAD experiment are the Ne^+ ion energies (0–5 keV), the substrate temperatures (room temperature 800°C), and the relative ratio between the Ne^+ ion beam intensity and the C_{60} molecular beam intensity. The Ne^+ ion energy increase improved the quality of the C_{60} film on Si(111) in the sense of its Raman spectrum in the low energy region up to 500 eV, but, in the medium energy region from 600 to 1000 eV, amorphous carbon films with an asymmetric feature in their Raman spectra were formed. In the high energy region from 1600 to 4800 eV, clear graphitization was detected with a more efficient deposition rate of carbon atoms in comparison with the deposition in the medium temperature region. The corresponding analysis of the surface morphology and the optical band gap was carried out by employing AFM observation and optical absorption measurement, respectively. The surface analysis revealed a moundlike structure in the broad energy range from 1000 to 5000 eV, but the details are different (not shown for simplicity). The diameter and the height in the moundlike structure are larger for the high-energy treated films, and, from the correlation analysis, the change in diameter seems to be nonlinear as a function of the Ne^+ ion energy. The optical band gap evaluated shows the maximum around 1600 eV in this study (around

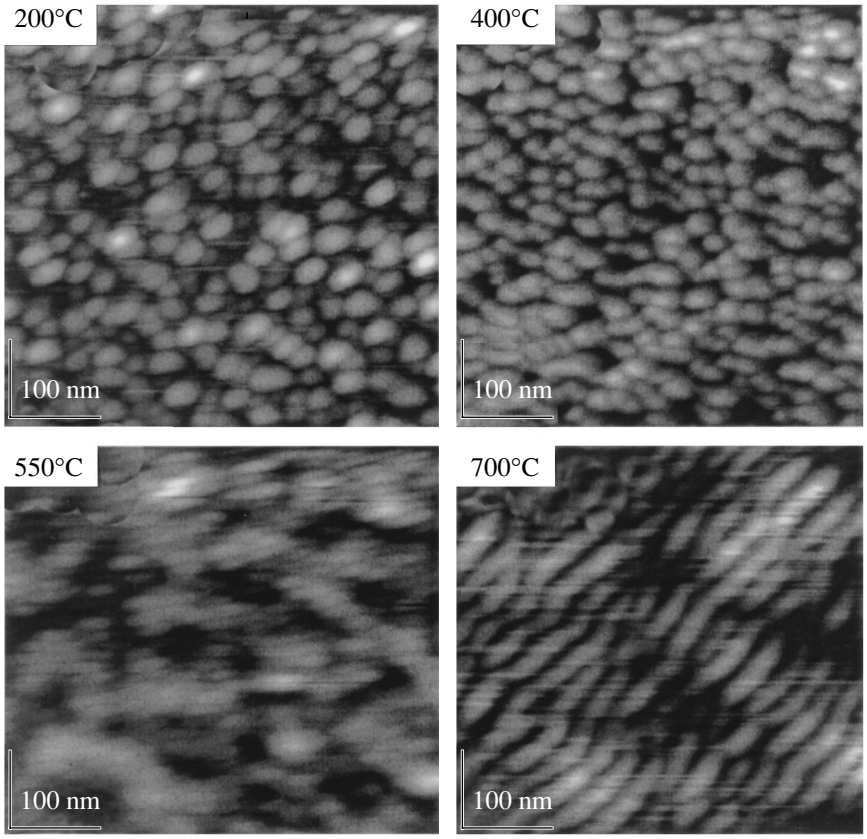

Fig. 2. AFM characterization of carbon films as a function of the deposition temperature. 200°C (top left), 400°C (top right), 550°C (bottom left) and 700°C (bottom right). The Ne^+ ion energy is fixed at 1.5 keV.

1.7 eV), and, in the higher energy region, it goes down to the value corresponding to graphite. In the next, the temperature dependent topological features were analyzed with AFM in the temperature range from 200 to 700°C. Figure 2 is a set of AFM images from IBAD films prepared at different temperatures. In the low temperature region, one can recognize a moundlike structure on a scale of a few tens of nanometers, the same as in the ion energy dependence study, and, in coming close to 550°C, a transition feature with a vague image is observed. A further increase in the substrate temperature to 700°C induces a dramatic change into the ripplelike structure. This arrangement of ripples is correlated to the step structure in the Si substrate after heat treatment. In the IBD experiment with a lesser ion beam intensity, the self-organized dot array of SiC observed along the single step of a Si substrate was observed in the same temperature range, but, in the present case, the resultant intensity of the carbon source after breakage of the C_{60} molecules is dominant. The present result, with additional Raman analysis, shows us that high-temperature deposition induces a graphite ripple structure of a periodic nature. This feature can be used in material design employing the self-organization process.

Further study was made by changing the relative intensity between the Ne^+ ion beam and the C_{60} molecular beam. The decrease in relative intensity resulted in the graphitic feature in the Raman spectrum, but, in the other case, there appeared Raman lines relating to hexagonal diamonds with a rippled surface structure. Figure 3 shows the typical Raman spectrum found in the sample prepared with a high ratio of the Ne^+ beam intensity and C_{60} beam intensity (1.5 keV Ne^+, 700°C). Different from the previous samples described above, the Raman lines are sharp and one can easily recognize the coexistence of hexagonal diamonds and disordered carbon and graphite. The Raman lines at 1157, 1199, and 1326 cm^{-1} can be attributed to hexagonal diamonds [14–17]; the others at 1584 and 1604 cm^{-1}, to disordered carbon and graphite, respectively. The x-ray diffraction analysis mainly manifests the features of hexagonal diamond with 2H-, 8H-, 12H-, and 20H-polytypes. The size of the hexagonal diamonds is estimated to be on the order of 30 nm based on the x-ray diffraction line. Under the present conditions of the ion beam, a great deal of thermal and displacement spikes can be created along the ion trajectories. Rapid quenching of these spikes on the growing surface results in preferential damage of the graphite because diamond is more

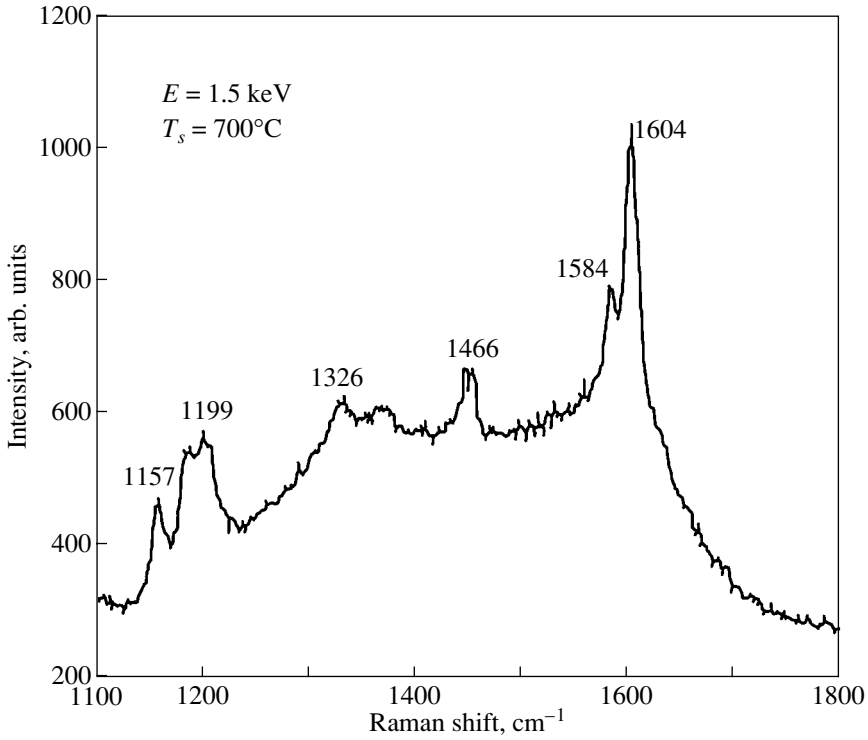

Fig. 3. Raman spectrum in a carbon film prepared with a high ratio between the Ne^+ ion beam and the C_{60} molecular beam (1.5 keV Ne^+, 700°C).

resistant to displacement than graphite. However, this effect is strongly dependent on the substrate temperature. Only in an intermediate temperature range is the probability of relaxation into a diamond site sufficiently large. Otherwise, graphite again becomes the stable phase. In the present work, the temperature dependence of nanocrystalline diamond growth is in good agreement with this argument. Our experiment clearly demonstrates that a substrate temperature as high as 700°C is necessary to form hexagonal diamond. It is said that the irradiation-induced effect produces hexagonal diamonds more easily than the cubic ones due to the similar effect of "shock compression."

3. SUMMARY AND CONCLUSIONS

The systematic IBD experiment revealed nanodiamonds to be immersed in dominant sp^3 amorphous carbon films. C and Ir are immiscible, but the C-implantation together with the introduction of a defect can favor the supersaturated carbon atoms in the subsurface region. Heat treatment can aid further growth from the nucleated embryos. It would be interesting to control the nucleation sites with the help of the ion-beam technique as a further study.

The array of high luminescent points is realized through proper treatment of the C_{60} film with an Ar-ion laser. The present observation can be closely related to the polymerization of the C_{60} film, and further study by changing the wavelength of the illuminating laser is required to clarity the details.

In the IBAD experiment, systematic studies performed by changing the ion energies and substrate temperatures provide us with interesting features of nanopattern formation. The patterns observed can be formed through the dynamical process between the sputtering and deposition. In deposition with an intense Ne^+ ion current, hexagonal diamonds of nanosize were prepared from a C_{60} vapor with simultaneous bombardment of 1.5 keV Ne^+ ions at the proper temperature of 700°C. The Raman features are consistent with the Raman modes predicted from calculations or experimental observation. It is also found that graphite coexists in the sample. Due to the ion-sputtering effect, the surface of the film exhibits regular periodic ripple patterns.

ACKNOWLEDGMENTS

The authors are thankful for the ongoing support of the people in the Advanced Science Research Center, especially, Prof. H. Yasuoka. Several authors, Y.X., J.V., and V.L., are indebted to JAERI Research Fellowships. X.Z. is also thankful for the STA exchange program.

REFERENCES

1. J. Vacik, H. Naramoto, K. Narumi, *et al.*, J. Chem. Phys. **114**, 9115 (2001).
2. C. Cepek, A. Goldoni, and S. Modesti, Phys. Rev. B **53**, 7466 (1996).
3. A. Andriotis, Phys. Rev. B **60**, 4521 (1999).
4. F. Banhart, J.-C. Charlier, and P. M. Ajayan, Phys. Rev. Lett. **84**, 686 (2000).
5. H. Naramoto, J. Vacik, S. Yamamoto, *et al.*, JAERI-Review **2000-024**, 157 (2000).
6. H. Hirai, M. Terauchi, M. Tanaka, and K. Kondo, Phys. Rev. B **60**, 6357 (1999).
7. E. Grossman, G. D. Lempert, J. Kulik, *et al.*, Appl. Phys. Lett. **68**, 1214 (1996).
8. V. I. Merkulov, D. H. Lowndes, G. E. Jellison, Jr., *et al.*, Appl. Phys. Lett. **73**, 2591 (1998).
9. H. Ohno, J. A. van den Berg, S. Nagai, and D. G. Armour, Nucl. Instrum. Methods Phys. Res. B **148**, 673 (1999).
10. Z. Tang, Z. J. Zhang, K. Narumi, *et al.*, J. Appl. Phys. **89**, 1959 (2001).
11. H. Naramoto, Y. H. Xu, X. D. Zhu, *et al.*, Mater. Res. Soc. Symp. Proc. **647**, O-518-1 (2001).
12. H. Naramoto, S. Yamamoto, and K. Narumi, Nucl. Instrum. Methods Phys. Res. B **161–163**, 534 (2000).
13. X. D. Zhu, Y. H. Xu, H. Naramoto, and K. Narumi, private communication.
14. F. P. Bundy and J. S. Kasper, J. Chem. Phys. **46**, 3437 (1967).
15. T. Yagi, W. Utsumi, M. Yamakata, *et al.*, Phys. Rev. B **46**, 6031 (1992).
16. M. Nshishitani-Gamo, T. Tachibana, K. Kobayashi, *et al.*, Diamond Relat. Mater. **7**, 783 (1998).
17. B. R. Wu and J. Xu, Phys. Rev. B **57**, 13355 (1998).

Physics of the Solid State, Vol. 44, No. 4, 2002, pp. 674–676. Translated from Fizika Tverdogo Tela, Vol. 44, No. 4, 2002, pp. 649–651.

PROCEEDINGS OF THE V INTERNATIONAL WORKSHOP "FULLERENES AND ATOMIC CLUSTERS"

(St. Petersburg, Russia, July 2–6, 2001)

Acoustic and Acoustoelectronic Properties of Carbon Nanotube Films

G. D. Mansfeld, Yu. V. Gulyaev, Z. Ya. Kosakovskaya, S. G. Alekseev, and V. V. Saraĭkin

Institute of Radio Engineering and Electronics, Russian Academy of Sciences, ul. Mokhovaya 11, Moscow, 101999 Russia

e-mail: tube@mail.cplire.ru

e-mail: mans@mail.cplire.ru

Abstract—The effect of spontaneous nanotube doping by substrate atoms was discovered using acoustic resonator microwave spectroscopy. The acoustoelectric effect involving surface acoustic waves was observed in nanotube films. The possibility of using nanotube films for efficient acoustic-wave excitation in solids by electrostriction was analyzed. © *2002 MAIK "Nauka/Interperiodica".*

1. INTRODUCTION

The discovery of carbon nanotubes and of new efficient methods of their preparation has stimulated considerable interest in new materials [1]. In our preceding paper [2], resonator acoustic microwave spectroscopy [3] was used to find the density, sound velocity, and acoustic-wave damping coefficient in carbon nanotube films. It was revealed that the sound velocity varies strongly with time, and an explanation of this observation was attempted in terms of the heretofore unknown effect of spontaneous nanotube doping by atoms of the substances making up the substrate. Additional atoms can decrease the density of a nanotube film and change its elasticity. This paper presents additional arguments for this nature of the effect. In addition, this paper reports the preliminary results of our investigation into acoustoelectronic effects involving surface acoustic waves (SAW) in layered structures containing carbon nanotube films.

The experimental studies were conducted on nanotubes prepared by a novel technique, electron beam evaporation of pure graphite in vacuum [4]. In experiments with composite resonators, carbon films were deposited on the surface of YAG or quartz plates. The films used in the SAW experiments were prepared on the YZ-cut surface of lithium niobate ($LiNbO_3$). It is known that the electrostriction effect can be employed to advantage in exciting acoustic waves in nonpiezoelectrics by applying a dc electric field to a crystal medium [5, 6], with the wave generation effect being proportional to the dc field strength. If an electrode is made of a thin nanotube film, very strong electric fields can be readily excited near the tops of the nanotubes because of the very small diameters of the spheres making up the tube tops. Thus, one can reach a strong increase in the efficiency of excitation and of detection of acoustic waves due to the electrostriction effect.

2. STUDY OF THE SELF-DOPING EFFECT

The effect of spontaneous doping was studied by resonator microwave spectroscopy, IR spectroscopy, mass spectrometry, and tunneling electron microscopy. In the first case, a composite microwave resonator of volume acoustic waves was constructed. It consisted of a YAG plate and a zinc oxide film (with platinum electrodes), which was deposited on one of the YAG surfaces. A carbon film to be studied was deposited on the other side of the plate. The structure represented a multifrequency microwave resonator with resonance peaks lying in the 1.5–2 GHz interval. The distances between the peaks and their widths were measured before and after the carbon film deposition. These measurements yielded 2.05 ± 0.05 g/cm^3 for the density of the film material (for graphite, this value is close to 2.2 g/cm^3). The measured velocity of sound was 2×10^6 cm/s, which corresponds to the elastic modulus c_{33} of the order of 1 TPa and is consistent with calculations [1]. However, two weeks thereafter, the velocity measured on the same film was found to be 8×10^5 cm/s. It was conjectured that the acoustic properties of the films change because of their being spontaneously doped by atoms of the substrate material. By penetrating inside the tubes or into the space between them, the excess atoms would considerably affect the effective elasticity and density of the film.

To check this conjecture, we studied the variation of the chemical composition of the nanotube films with time. The chemical composition of the nanotube films on YAG was studied by IR spectroscopy and secondary-

1063-7834/02/4404-0674$22.00 © 2002 MAIK "Nauka/Interperiodica"

ion mass spectrometry. It was established that the IR spectrum of a nanotube film stored for two weeks in air at room temperature exhibits bands characteristic of YAG (Fig. 1a). The mass-spectrometric investigation of the depth profile of film composition showed that nanotube films do indeed absorb aluminum and yttrium atoms from the substrate and that the concentration of these atoms reaches a maximum near the ends of the tubes (Fig. 1b).

We also started SAW studies of the acoustoelectronic properties of carbon nanotube films. The nanotube carbon films were deposited between interdigitated transducers, and the acoustoelectric effect was measured. The acoustoelectric voltage was measured across the indium Ohmic contacts. This voltage, in accordance with the Weinreich relation, was proportional to the acoustic wave power. It turned out, however, that the magnitude of the voltage and its sign depend considerably on time and that this dependence has a random nature. The data obtained in this study are preliminary.

3. APPLICATION OF NANOTUBE FILMS TO THE EXCITATION OF VOLUME ACOUSTIC WAVES

The electrostriction effect inherent in all dielectrics can be used to excite acoustic waves. In this case, it can be associated with the induced piezoelectric effect, which is proportional to the dc bias field by the relation

$$e_{ijk} = \chi_{ijkl} E_l. \quad (1)$$

Here, χ_{ijkl} are the components of the electrostriction constant tensor and E_l is the dc bias field.

As already mentioned, extremely strong electric fields can be generated in the immediate vicinity of the tops of carbon nanotubes because of their small diameter. This makes it possible to increase the efficiency of electroacoustic capacitor transducers based on the electrostriction effect. We estimated the electric field near the nanotube top by solving the Laplace equation for the electric potential, with the tube considered to be one half of a conducting ellipsoid. Next, we calculated the electric field generated by bundles of nanotubes, which were treated subsequently as elementary spherical radiators. The acoustic field generated by an array of such radiators was calculated in the $D/\lambda \gg 1$ limit (D is the transducer diameter).

The excitation of acoustic waves by a nanotube array can be described using the effective piezoelectric modulus:

$$\tilde{\beta} = 2\pi a^2 \chi n_x n_y \gamma^2 E_0. \quad (2)$$

Here, χ is the electrostriction constant, a is the effective radiator diameter, $n_x n_y$ is the number of radiators per unit area, and γ is the field enhancement factor due to the smallness of the radiator diameter.

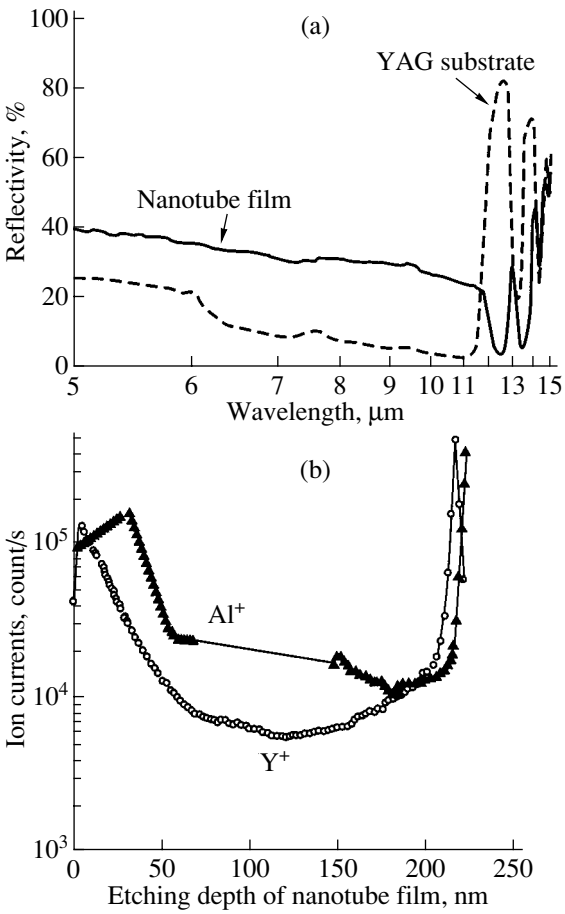

Fig. 1. (a) IR reflectance spectra of nanotube carbon films after two weeks of storage and (b) the depth profile of aluminum and yttrium in the film.

Note that the quantity $\tilde{\beta}$ in Eq. (2) is proportional to γ^2. Therefore, one also takes into account the increase in the effective piezoelectric modulus due to the ac electric field near the dielectric surface being enhanced by the smallness of the radiator diameter.

Estimates show that, for $n_x = n_y = 10^6$, $\gamma = 33$, $a = 5$ nm, and $D = 7$ mm, the effective electromechanical coupling coefficient for YAG plates is about 10% for fields on the order of 100 V/cm. Reaching such high electromechanical coupling constants with conventional metallic electrodes would require fields 10^4–10^5 times higher.

Thus, we have shown that the variation of the acoustic properties of nanotube carbon films with time may be associated with spontaneous nanotube doping by atoms of the substrate material.

It has also been shown that strong dc and ac electric fields created near the tops of the nanotubes because of their small diameter can be used for efficient generation of acoustic waves.

ACKNOWLEDGMENTS

This study was supported by the Russian Foundation for Basic Research (project nos. 99-02-17602, 01-02-18017) and the Ministry of Industry and Science of the Russian Federation (program "Fullerenes and Atomic Clusters," project no. 99034).

REFERENCES

1. A. V. Eletskiĭ, Usp. Fiz. Nauk **167**, 945 (1997) [Phys. Usp. **40**, 899 (1997)].
2. G. D. Mansfeld, S. G. Alekseev, Yu. V. Gulyaev, *et al.*, Ultrason. Symp. Proc. **1**, 561 (1999).
3. G. D. Mansfeld, Ultrason. Symp. Proc. **2**, 655 (1994).
4. Z. Ya. Kosakovskaya, L. A. Chernozatonskiĭ, and E. A. Fedorov, Pis'ma Zh. Éksp. Teor. Fiz. **56** (1), 26 (1992) [JETP Lett. **56**, 26 (1992)].
5. Yu. V. Gulyaev, Fiz. Tverd. Tela (Leningrad) **9** (6), 1816 (1967) [Sov. Phys. Solid State **9**, 1425 (1967)].
6. K. O. Boltar', I. M. Kotelyanskiĭ, and G. D. Mansfeld, Akust. Zh. **23** (4), 544 (1977) [Sov. Phys. Acoust. **23**, 311 (1977)].

Translated by G. Skrebtsov

Physics of the Solid State, Vol. 44, No. 4, 2002, pp. 677–680. From Fizika Tverdogo Tela, Vol. 44, No. 4, 2002, pp. 652–654.

PROCEEDINGS OF THE V INTERNATIONAL WORKSHOP "FULLERENES AND ATOMIC CLUSTERS"

(St. Petersburg, Russia, July 2–6, 2001)

Synthesis of Graphite Monolayer Stripes on a Stepped Ni(771) Surface[1]

A. M. Shikin, G. V. Prudnikova, V. K. Adamchuk, W.-H. Soe*, K.-H. Rieder*, S. L. Molodtsov, and C. Laubschat****

Institute of Physics, St. Petersburg State University, St. Petersburg, 198904 Russia

** Institut für Experimentalphysik, Freie Universität Berlin, Berlin, D-14195 Germany*

*** Institut für Oberflächen- und Mikrostrukturphysik, Technische Universität Dresden, Dresden, D-01062 Germany*

Abstract—Graphite stripes on a stepped Ni(771) substrate were grown *in situ* by cracking propylene followed by annealing at optimal temperatures between 450 and 590°C. The samples were studied by means of C 1*s* and Ni 3*p* core-level photoemission and high resolution electron energy loss spectroscopy. The C 1*s* spectra reveal a dominant graphite-like character. The phonon spectra measured in the direction parallel and perpendicular to the steps display certain differences, which can be explained on the basis of size-limited effects. © *2002 MAIK "Nauka/Interperiodica".*

In the recent past, a large number of experimental studies related to the quantization of electronic states in low-dimensional structures in the direction perpendicular to the surface have been published (see, for instance, [1–4]). On the other hand, much less attention has been paid to the search for and study of systems where size-limited effects can be observed in the direction parallel to the surfaces. The latter can likely be explained by the difficulties involved in the formation of this kind of system. One of the possibilities of preparing them is through *in situ* deposition of the investigated materials onto stepped surfaces of monocrystals of various metals. In this way, stripes of deposited substances with well-defined thicknesses and widths may be grown on top of the terrace surfaces.

The present work is devoted to analyzing the conditions for synthesis of graphite stripes formed by the cracking of carbon-containing gases on top of vicinal Ni(771) surfaces. The *in situ* grown samples were studied by means of C 1*s* and Ni 3*p* core-level photoemission (PE) and high resolution electron energy loss spectroscopy (HREELS) of phonon excitations measured in directions parallel and perpendicular to the steps at the Ni(771) substrate. It was found that such a system is characterized by graphite stripes with (i) monolayer thicknesses (monolayer graphite stripes, MGS), since the cracking is terminated when the whole Ni(771) substrate is covered by C atoms [5–9], and (ii) fixed width defined by the regularly stepped character of Ni(771).

[1] This article was submitted by the authors in English.

1. EXPERIMENTAL DETAILS

C 1*s* and Ni 3*p* core-level PE and HREELS spectra were taken for different annealing temperatures (T_{ann}) beginning from T_{ann} lower than the cracking temperature up to the temperatures at which the destruction of the graphite stripes is observed. The core-level PE spectra were measured for the normal emission geometry using an x-ray source with AlK_α radiation ($h\nu$ = 1486.6 eV) and a CLAM-II analyzer. The HREELS experiments were conducted in a setup equipped with a 127° deflector at a primary electron energy (E_p) of 17.5 eV. The electron incident angles were set to 60° and 75° relative to the normal to the vicinal Ni(771) terraces with (110) orientation and a width of about 12.3 Å [10, 11]. The detection angle was varied from 0° to 65° relative to the direction of the elastically reflected peak.

The Ni(771) substrate was preliminary cleaned by repeated cycles of Ar sputtering, treatment in oxygen and hydrogen atmospheres, and thermal annealing at 700°C until a sharp low energy electron diffraction (LEED) pattern characteristic of vicinal Ni(771) surfaces was obtained [10, 11]. Similar to the monolayer graphite (MG)/Ni(111) system [8, 9], the graphite overlayer (i.e., graphite monolayer stripes) was formed by a 5-min cracking of propylene(C_3H_6) at a sample temperature of about 500°C and a pressure of 1×10^{-6} mbar. In the course of the measurements, the samples were annealed at different temperatures, from 400 and 700°C. The base pressure in the CLAM and HREELS spectrometers during experiments was better than 2×10^{-10} mbar.

1063-7834/02/4404-0677$22.00 © 2002 MAIK "Nauka/Interperiodica"

2. EXPERIMENTAL RESULTS AND DISCUSSION

A series of C 1*s* core-level PE spectra measured under normal emission for systems prepared by the cracking of propylene and following annealings at temperatures between 450 and 650°C is shown in Fig. 1a. For comparison, a C 1*s* spectrum of natural monocrystalline graphite is also presented in the bottom of the figure. The spectra taken after annealing between $450 < T_{ann} < 575$°C are characterized by a single pronounced peak at a binding energy (BE) of about 284.9 eV (marked $C^{(1)}$ in the figure), which is very close to the C 1*s* BE (284.5 eV, dotted line) characteristic of monocrystalline graphite. Similar C 1*s* spectra were obtained for the monolayer of graphite on top of Ni(111) [6] or for the graphite monolayer on the (111) surface of La-carbide [12], where the above small core-level energy shift was related to the bonding between the MG and the substrates. Obviously, an analogous situation occurs in the case of graphite coverage on Ni(771), where the interaction of the graphite layer (i.e., graphite monolayer stripes) with the Ni substrate is confirmed by an energy shift of the graphite-derived phonon modes, as obtained in the HREELS experiment.

With an increase in the annealing temperature, the intensity of the C 1*s* peak decreases. Simultaneously, a new feature appears at a BE of about 283.4 eV (marked $C^{(2)}$ in the figure), which is very close to the values typical of carbides of *d* metals and rare earths [12, 13]. LEED patterns at these annealing temperatures reveal a (4×1) overstructure which is usually ascribed to the formation of carbide-like constructions on the surface of Ni(771) [10, 11]. Corresponding changes in the intensities of the above-discussed C-derived features (C $1s^{(1)}$ and C $1s^{(2)}$) and of the Ni 3*p* core-level signal upon an increase in T_{ann} are shown in Fig. 1b. From an analysis of the presented data, we can conclude that, after annealing at temperatures above 600–620°C, the graphite overlayer is almost completely destroyed and a part of it is transformed into a carbide-like surface compound. The observed slight increase in the intensity of the Ni 3*p* signal supports the above conclusion: at $T_{ann} > 620$°C, the Ni atoms are no longer covered uniformly by the graphite layer.

Similar conclusions can be derived from an analysis of the intensities of the elastically reflected electron beam and the energy-loss peak ascribed to the longitudinal optical (*LO*) graphite-originating phonon mode measured by HREELS. The corresponding data for different annealing temperatures, which are strongly influenced by the degree of ordering of the graphite-derived

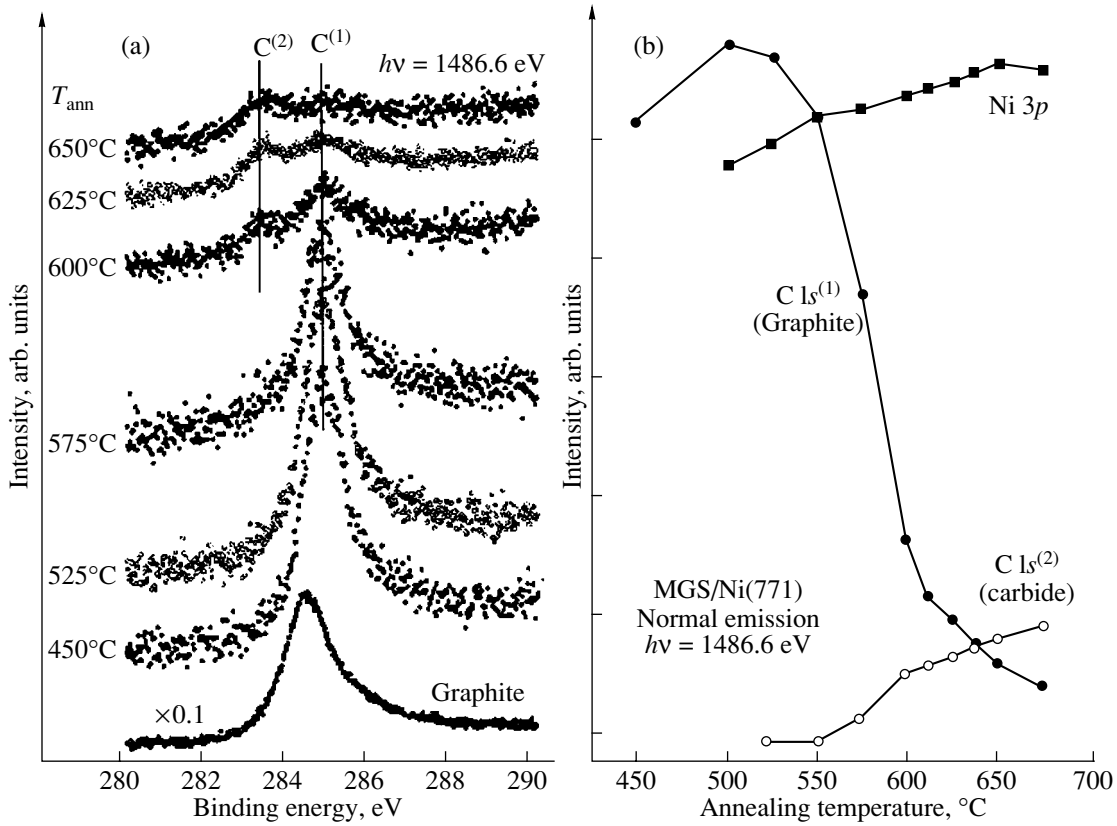

Fig. 1. (a) C 1*s* core-level PE spectra taken for the MGS/Ni(771) system after annealing at different temperatures. (b) PE intensity of graphite- (solid circles) and carbide- (open circles) derived components in C 1*s* spectra, as well as of the Ni 3*p* core-level peak (solid quadrates), depending on the annealing temperatures.

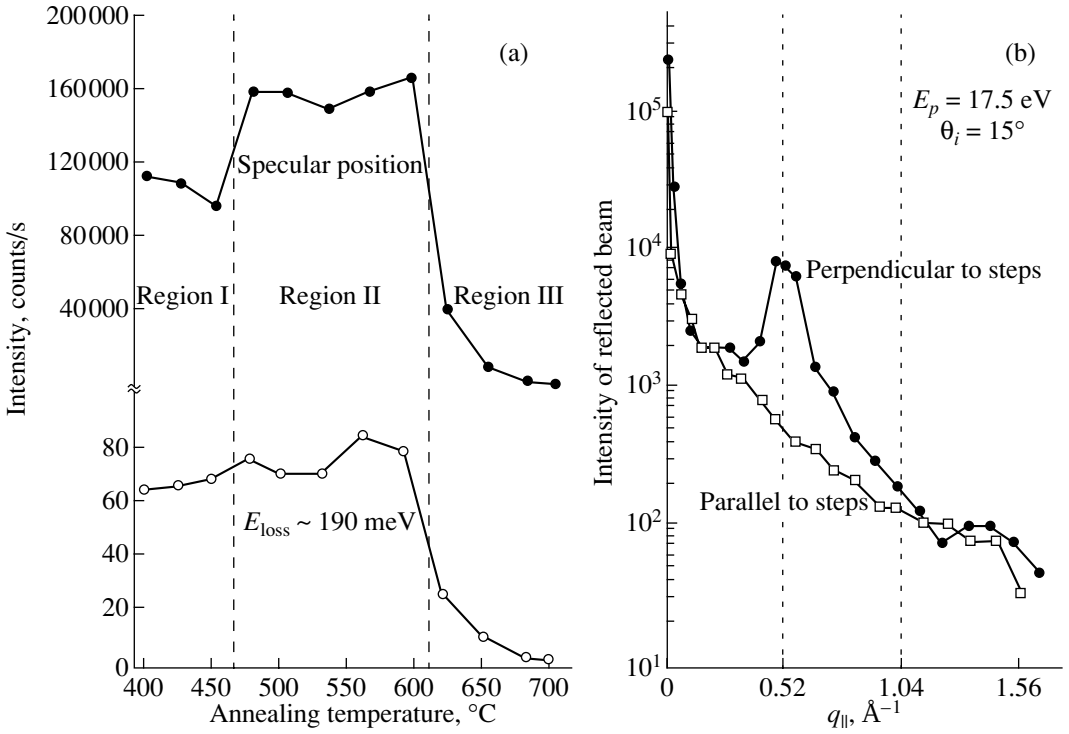

Fig. 2. (a) HREELS intensity of the elastically reflected beam (specular position, solid circles) and of the graphite-derived *LO*-phonon mode peak (energy loss $E_{loss} \approx 190$ meV, open circles) depending on the annealing temperatures. (b) Polar-angle dependence of the reflected peak intensity measured in the directions parallel (open quadrates) and perpendicular (solid circles) to the Ni(771) steps. θ_i is the primary electron incidence angle.

surface and the presence of C atoms in the graphite phase at the surface, are presented in Fig. 2a. As was already shown in the PE measurements, after increasing the annealing temperature to above 600–620°C, the graphite-derived features become suppressed also in the HREELS experiment. The *LO* graphite mode vanishes from the spectra, and all other graphite-derived energy-loss features decrease sharply. At the same time, a decrease in the signal of the elastically reflected peak is observed. The maximum intensity of the reflected beam and graphite-derived phonon modes (only results for the *LO* mode are shown in the figure) are reached in the range $475 < T_{ann} < 590$°C, which demonstrates the formation of mostly ordered structures at these annealing temperatures.

Intensities of the reflected peak measured at different polar angles relative to the elastic peak direction in the directions parallel and perpendicular to the Ni(771) steps are shown in Fig. 2b. The results are plotted as functions of the parallel momentum transfer, $q_{\|}$. For the measurements in the direction parallel to the steps, a monotonic decrease in the intensity of the reflected peak is monitored in the whole region of the presented values of the momentum transfer. In contrast to that, in the direction perpendicular to the steps, a rather sharp peak is observed at a polar angle corresponding to $q_{\|} \approx 0.52$ Å^{-1} in the scattering geometry used in this experiment. Assuming a diffraction origin of this peak, we can find the value of the corresponding period in real space to be equal to 12.1 Å, which is very close to the width of terraces periodically arranged on the stepped Ni(771). Hence, the presented HREELS results provide convincing evidence that the grown graphite overlayer on Ni(771) forms stripes of a certain fixed width located on top of vicinal terraces.

Dispersion of the graphite-derived phonon modes in the MGS/Ni(771) system after annealing between 530 and 590°C, which were measured in the directions parallel (open symbols) and perpendicular (solid symbols) to the steps, are presented in Fig. 3. Corresponding angle-resolved phonon spectra can be found in [14]. Crosses in Fig. 3 denote features characterized by a weak signal-to-noise ratio in spectra measured in the direction perpendicular to the steps. Solid lines correspond to the averaged data for phonon modes measured in the direction parallel to the steps. The measured phonon spectra and the corresponding phonon dispersions in the direction parallel to the steps are very similar to those observed for natural monocrystalline graphite [15] and the graphite monolayer on top of Ni(111) [5, 8, 9]. As for the MG/Ni(111) structure, the corresponding phonon modes in the MGS/Ni(771) system are shifted toward the region of lower energy losses, as compared to their positions in monocrystalline graphite due to interaction with the Ni substrate [5, 8, 9].

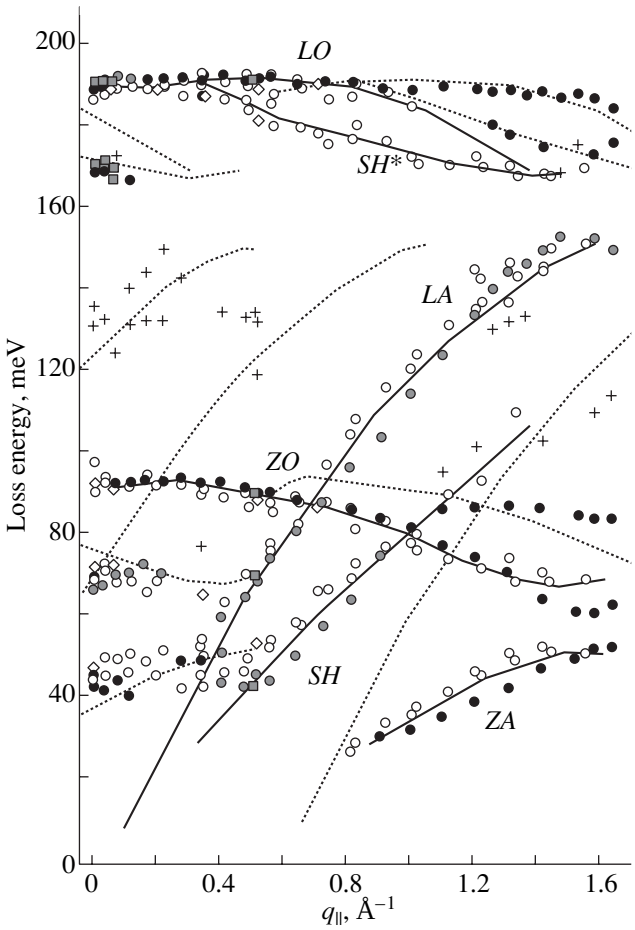

Fig. 3. Dispersions of graphite-derived phonon modes in the directions parallel (open symbols) and perpendicular (solid symbols) to the steps for the MGS/Ni(771) system after annealing at temperatures between 530 and 590°C. Dotted lines denote dispersion curves shifted by a $q_{\|}$-value multiple of 0.52 Å^{-1} relative to the original ones characteristic of the directions parallel to steps (solid lines).

In the case of measurements in the direction perpendicular to the steps, the phonon spectra are characterized by a number of additional features. These features are mainly observed for large values of the parallel momentum transfer and are situated in the energy-loss regions of about 90 and 200 meV. On the basis of the data presented in Fig. 3, we attempted to interpret these features using a series of unmodified graphite-derived phonon modes measured in the direction parallel to the steps and shifted relative to the initial ones by values of $q_{\|}$ as a multiple of 0.52 Å^{-1}. These curves are shown by dotted lines in Fig. 3. Analyzing the presented data, one can conclude that, in first approximation, almost all additional features can be assigned to these dotted curves.

The observed differences in the phonon dispersions in the directions perpendicular and parallel to the steps reveal certain size-limited effects in the system graphite stripes on Ni(771). Detailed analysis of the nature of these phenomena will be given in a forthcoming publication [16].

In summary, graphite stripes on the Ni(771) substrate were grown by the cracking of propylene followed by annealing at optimal temperatures in the range between 450 and 590°C. The C 1*s* spectra in this temperature region reveal a dominant graphite-like character. The binding energy of the C 1*s* peak is shifted, however, relative to its position in bulk monocrystalline graphite due to the interaction of graphite stripes with the Ni substrate. The elastically reflected beam in the HREELS experiment has a maximum intensity for these annealing temperatures, which testifies to the formation of a mostly structurally ordered system. The phonon spectra measured in the direction parallel and perpendicular to the Ni(771) steps reveal certain differences, which can be explained on the basis of size-limited effects.

ACKNOWLEDGMENTS

This work was supported by the Program "Fullerenes and Atomic Clusters" and performed in cooperation with the St. Petersburg State University, the Freie Universität Berlin, and the Technische Universität Dresden.

REFERENCES

1. F. J. Himpsel, J. E. Ortega, G. J. Mankey, and R. F. Willis, Adv. Phys. **47**, 511 (1998).
2. J. E. Ortega, F. J. Himpsel, G. J. Mankey, and R. F. Willis, Phys. Rev. B **47**, 1540 (1993).
3. T.-C. Chiang, Surf. Sci. Rep. **39**, 181 (2000).
4. J. J. Paggel, T. Miller, and T.-C. Chiang, Science **283**, 1709 (1999).
5. T. Aiyawa, R. Souda, Z. Ishiyawa, *et al.*, Surf. Sci. **237**, 194 (1990).
6. A. Nagashima, N. Tejima, and C. Oshima, Phys. Rev. B **50**, 17487 (1994).
7. C. Shelton, H. R. Patil, and J. M. Blakely, Surf. Sci. **43**, 493 (1974).
8. A. M. Shikin, D. Farias, and K.-H. Rieder, Europhys. Lett. **44**, 44 (1998).
9. A. M. Shikin, D. Farias, V. K. Adamchuk, and K.-H. Rieder, Surf. Sci. **424**, 155 (1999).
10. R. Koch, O. Haase, M. Borbonus, and K.-H. Rieder, Phys. Rev. B **45**, 1525 (1992).
11. O. Haase, R. Koch, M. Borbonus, and K.-H. Rieder, Ultramicroscopy **42–44**, 541 (1992).
12. A. M. Shikin, V. K. Adamchuk, S. Siebentritt, *et al.*, Phys. Rev. B **61**, 7752 (2000).
13. L. I. Johanson, Surf. Sci. Rep. **21**, 177 (1995).
14. W. H. Soe, A. M. Shikin, F. Moresco, *et al.*, submitted to Phys. Rev. B.
15. S. Siebentritt, R. Pues, K.-H. Rieder, and A. M. Shikin, Phys. Rev. B **55**, 7927 (1997).
16. A. M. Shikin, S. A. Gorovikov, V. K. Adamchuk, O. Rader, and W. Gudat (in press).

Physics of the Solid State, Vol. 44, No. 4, 2002, pp. 681–682. Translated from Fizika Tverdogo Tela, Vol. 44, No. 4, 2002, pp. 656–657.

PROCEEDINGS OF THE V INTERNATIONAL WORKSHOP "FULLERENES AND ATOMIC CLUSTERS"

(St. Petersburg, Russia, July 2–6, 2001)

Noble-Metal Intercalation under the Graphite Monolayer on Ni(111)

A. G. Starodubov, M. A. Medvetskiĭ, A. M. Shikin, G. V. Prudnikova, and V. K. Adamchuk

Institute of Physics, St. Petersburg State University, ul. Pervogo Maya, Petrodvorets, 198904 Russia

Abstract—Noble metals were intercalated under a graphite monolayer formed on the (111) nickel single-crystal surface. The valence-band electronic structure of the systems thus obtained was studied by angle-resolved photoelectron spectroscopy. Intercalation of noble metals was shown to weaken carbon bonding to the substrate. © *2002 MAIK "Nauka/Interperiodica".*

Hexagons constructed of carbon atoms are building blocks of a large variety of molecules and solids. Graphite and a large class of fullerenes are typical examples of such compounds. The properties of these hexagons largely determine the characteristics of the compounds based on them and, thus, are of considerable interest.

Experimental isolation and analysis of one such cell meets with difficulties, and experiments on preparation of a graphite monolayer (GM) on the surface of transition metals may be considered the first step in this direction. In this case, we deal already with a single, more or less ordered graphite layer located on a metal substrate. The Ni(111) face may serve as such a substrate. The lattice misfit between this face and the graphene cell is less than 2% [1]. In these conditions, one succeeds in forming a monolayer with preferentially oriented graphite hexagons. Nevertheless, the GM obtained in this way was shown [2] to be strongly effected by the substrate. In this work, we consider intercalation as a means of reducing this effect to a minimum and, thus, of obtaining a system which, while being practically isolated from the influence of the substrate, would nonetheless exhibit electronic properties characteristic of graphite.

In this work, the GM bonding to the substrate was studied by angle-resolved photoelectron spectroscopy (ARPES). We analyzed the energy position of the π states responsible for the interaction along the surface normal. In addition to a high surface sensitivity, ARPES possesses the advantage of being close to the only experimental technique capable of providing information on specific points in the Brillouin zone, i.e., of obtaining energy band dispersion. Angle-resolved photoelectron (PE) spectra were measured with a commercial ADES-4000 photoelectron spectrometer (VG Scientific). The He-I and He-II resonance lines (photon energies of 21.2 and 40.8 eV, respectively) were used for excitation. The probing depth reached with these photons was about 10 and 5 Å, respectively. This means that the PE spectra obtained corresponded to the electronic states of a thin surface layer formed by the GM and the uppermost substrate atomic layer.

The GM was formed on the Ni(111) surface by propylene (C_3H_6) cracking at a substrate temperature of 500°C and a gas pressure of 1×10^{-6} Torr for 5 min, which corresponds to an exposure of 300 L. A similar technology of GM preparation on Ni(111) was employed in [3]. Thermally activated dissociation of propylene molecules produces a continuous graphite coating, which, as pointed out in [2], substantially reduces the surface reactivity and, thus, precludes the formation of subsequent layers. The quality of the crystal structure of the graphite film was checked by low-energy electron diffraction (LEED). Noble metals were deposited from helical W sources bearing a weight of the metal [4]. The amount of material adsorbed was monitored on a quartz balance.

The absence of shifts of the graphite-like states in the PE spectra measured immediately after the adsorbate deposition implies that noble metal atoms on the GM/Ni(111) surface virtually do not affect the GM–substrate interaction. Further heating of the system resulted in a shift of the GM π states, which we associate with the onset of thermally activated intercalation.

By measuring the PE response at different electron emergence angles relative to the principal symmetry directions, which were chosen based on LEED data, we obtained a set of spectra for use in constructing dispersion relations for the main valence-band states. We were primarily interested in the π states, whose energy shift was considered to be a measure of the variation of the GM binding to the substrate.

The figure presents dispersion of the π states of the GM/Ag/Ni(111) system in the Γ–M direction of the surface Brillouin zone. Also shown for comparison are similar relations for the GM/Ni(111) system and sin-

1063-7834/02/4404-0681$22.00 © 2002 MAIK "Nauka/Interperiodica"

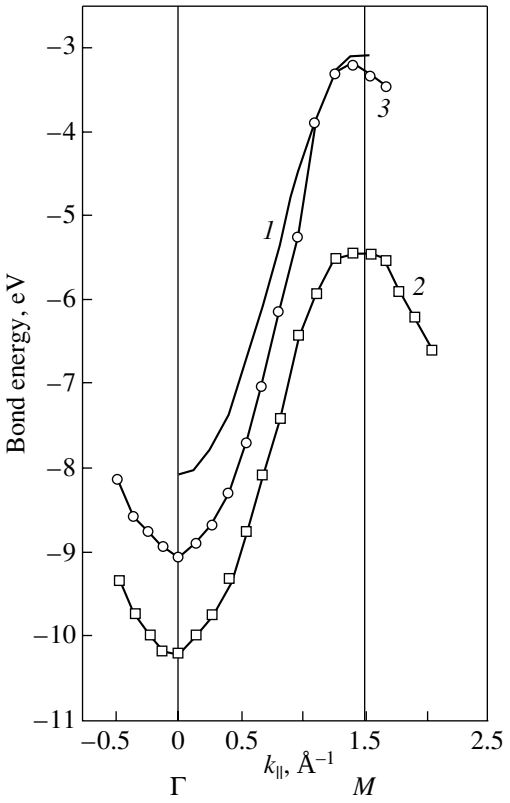

Dispersion of the graphite π states in the Γ–*M* direction of the surface Brillouin zone for (*1*) bulk graphite, (*2*) the graphite monolayer on Ni(111), and (*3*) the GM/Ag/Ni(111) system. The vertical lines bound the Γ–*M* region. The starting angular response of the PE spectra was obtained when working with a helium lamp in the standard He-II regime, which corresponds to the photon energy $h\nu$ = 40.8 eV. Plotted along the horizontal axis is the wave-vector component $k_{\|}$ in the direction parallel to the sample surface.

gle-crystal graphite [5]. We readily see that the branch of π states of the GM/Ag/Ni(111) system is shifted, relative to that of GM/Ni(111), toward the Fermi level into the region characteristic of single-crystal graphite, whose interlayer coupling is known to be due to weak van der Waals interaction. We believe that the observed shift toward the bound energies characteristic of single-crystal graphite, which is about 1 eV at the Γ point, results from the intercalation of silver atoms. Incorporation of silver atoms inhibits the hybrid π–*d* bonds and, as a consequence, weakens the coupling between the graphite layer and the substrate.

A similar situation occurs when atoms of other noble atoms (Au, Cu) are used as intercalates, with the effect being even more pronounced. In particular, copper intercalation also shifts the energies of the π states to values characteristic of single-crystal graphite. Moreover, the bond energy in the vicinity of point *M* reaches a level which is only slightly lower than that observed in bulk graphite. Thus, intercalation of the GM/Ni(111) system by noble metals produces a graphite layer whose properties reproduce, in the limiting case, those of a substrate-free GM.

ACKNOWLEDGMENTS

This study was supported by the “Fullerenes and Atomic Clusters” program, project no. 98052.

REFERENCES

1. R. Rosei, S. Modesti, F. Sette, *et al.*, Phys. Rev. B **29**, 3416 (1984).
2. A. Nagashima, N. Tejima, and C. Oshima, Phys. Rev. B **50**, 17487 (1994).
3. D. Farias, A. M. Shikin, K.-H. Rieder, and Yu. S. Dedkov, J. Phys.: Condens. Matter **11**, 8453 (1999).
4. A. M. Shikin, G. V. Prudnikova, V. K. Adamchuk, *et al.*, Phys. Rev. B **62**, 13202 (2000).
5. R. C. Tartar and S. Rabii, Phys. Rev. B **25**, 4126 (1982).

Translated by G. Skrebtsov

Physics of the Solid State, Vol. 44, No. 4, 2002, pp. 683–685. Translated from Fizika Tverdogo Tela, Vol. 44, No. 4, 2002, pp. 658–660.

PROCEEDINGS OF THE V INTERNATIONAL WORKSHOP "FULLERENES AND ATOMIC CLUSTERS"

(St. Petersburg, Russia, July 2–6, 2001)

Amino-Acid Derivatives of Fullerene C_{60} Behave as Lipophilic Ions Penetrating through Biomembranes

I. M. Andreev*, V. S. Romanova, A. O. Petrukhina**, and S. M. Andreev*****

** Timiryazev Institute of Plant Physiology, Russian Academy of Sciences, ul. Botanicheskaya 25, Moscow, 127276 Russia*

*** Nesmeyanov Institute of Organoelement Compounds, Russian Academy of Sciences, ul. Vavilova 28, Moscow, 117813 Russia*

**** Institute of Immunology, Federal Scientific Center, Moscow, Russia*

Abstract—It was found using potential-sensitive probes that the water-soluble amino-acid derivatives of fullerene C_{60}, such as C_{60}–Pro, C_{60}–ε aminocapronic acid, and C_{60}–Arg, possess a pronounced membranotropic activity. The first two cause concentration-dependent dissipation of the membrane potential ($\Delta\psi$) of the symbiosomes of the nodules of the yellow lupine generated in the presence of ATP and Mg^{2+} ions. In contrast to the first two derivatives, C_{60}–Arg, which carries a strong positive charge at the physiological pH, has no effect on the dissipation of $\Delta\psi$ in this model. On the contrary, this derivative caused a noticeable dissipation of the K^+ diffusion potential ("minus" inside) generated on the membrane of human erythrocytes with the help of the K^+ ionophore of valinomycin. The regularities obtained indicate that the derivatives of C_{60} are transported across biological membranes as lipophil ions, thus causing depolarization of the membranes. © *2002 MAIK "Nauka/Interperiodica".*

At present, an explosive development is observed in the physics and chemistry of carbon clusters such as fullerenes and carbon nanotubes, which is due to the perspectives on their application in nanotechnology and microelectronics. The investigations in the biology of fullerenes are only in the incipient stage; no regions of efficient application have yet to be found in this field, but exploratory studies are in progress in many countries. To date, a number of biological effects have been detected in water-soluble derivatives of C_{60}. Investigations of pharmacokinetics show that they possess a very low toxicity and can be removed from an organism at an acceptable rate. Some of them were proved to possess chemotactic and antioxidant properties and exhibit antiviral activity; in particular, they inhibit protease of AIDS by building into the active center of a ferment. Being irradiated in the presence of oxygen, fullerene compounds are capable of break down DNA chains, causing a cytotoxic effect on tumor cells. Fullerene derivatives containing a central metallic atom inside the molecule are considered to be very promising, especially in radiotherapy. They are more stable than the chelate complexes that are used at present. Note that the fullerene itself possesses neither cytotoxicity nor genotoxicity.

The possible application of fullerene derivatives in biology and medicine requires that they be transported to cell targets. In this connection, a very important part is played by the membranotropic properties of these compounds, namely, their ability to penetrate across biological membranes. There exists information concerning this problem [1, 2], but in essence, these properties of fullerenes have been studied insufficiently.

In this work, which was performed on preparations of nitrogen-fixing units isolated from root nodules of yellow lupine [3] and on human erythrocytes, we investigated the membranotropic properties of three amino-acid derivatives of fullerene, namely, C_{60}–Asp, C_{60}–Pro, and C_{60}–Arg. These derivatives were synthesized using the previously published method [4]. They possessed a relatively high solubility in aqueous solutions and biological activity [5, 6]. Taking into account the magnitude of pK_a of the proton-acceptor groups of amino-acid residuals in these conjugates, it is quite unlikely that the first two compounds are anions in the range of physiological values of pH, whereas C_{60}–Arg, on the contrary, carries a positive charge. The above-mentioned isolated nitrogen-fixing units known as symbiosomes were used in this work for studying membranotropic properties, since they are capable of generating a membrane potential $\Delta\psi$ ("plus" on the inner surface of the membrane) on their outer, so-called peribacteroid, membrane (PBM) in the presence of ATP and Mg^{2+} ions in the incubation mixture owing to the functioning of the electrogenic H^+–ATPase in this membrane [3]. The kinetics of the MgATP-dependent generation of $\Delta\psi$ on the PBM of symbiosomes registered with a potential-sensitive probe such as oxonol VI [7] is shown in Fig. 1b, curve *1*. It can be seen that after the stationary level of $\Delta\psi$ on the PBM is achieved, an addition of C_{60}–Asp to symbiosomes initiates a rela-

1063-7834/02/4404-0683$22.00

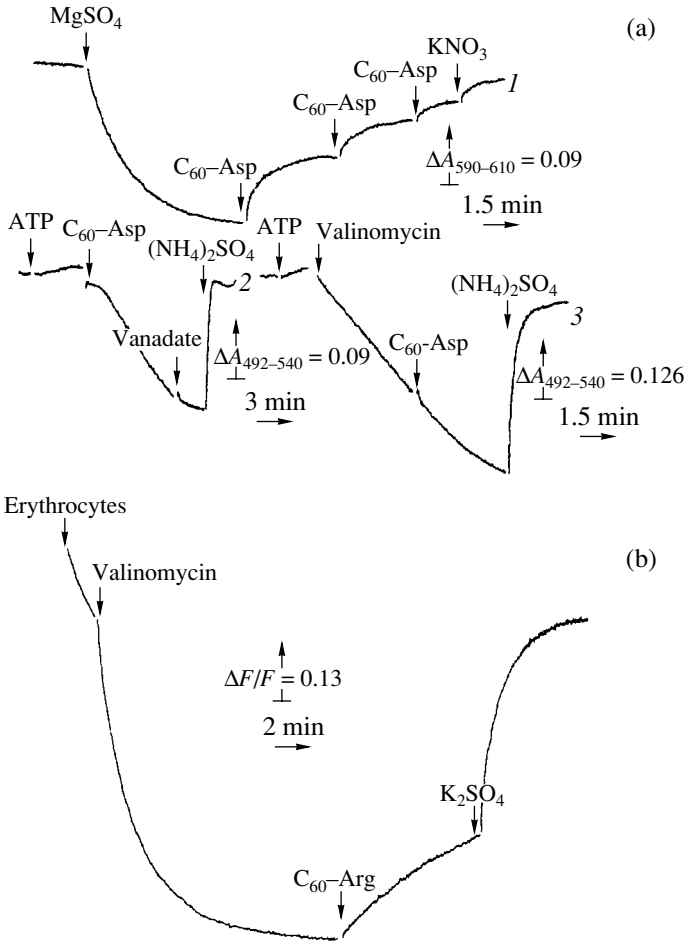

Fig. 1. (a) Curve *1*: Kinetics of the MgATP-dependent generation of the membrane potential on the PBM of symbiosomes of yellow lupine and the dissipation of this potential in the presence of C_{60}–Asp. The symbiosomes were incubated in a medium containing 0.4 M of sorbite, 20 mM of HEPES-BTP (pH 7.0), 1 mM of ATP, and 1 μM of oxonol VI. The arrows indicate the time instants at which $MgSO_4$ (3 mM), C_{60}–Asp (130 μM), and KNO_3 (20 mM) were added. Curve *2*: Kinetics of the MgATP-dependent acidification of the peribacteroid space of symbiosomes that was initiated by the addition of 50 μM of C_{60}–Asp to them. The incubation medium had the same composition as in the case of curve *1* but contained 3 mM of $MgSO_4$ and 12 μM of acridine orange instead of ATP and oxonol VI, respectively. The arrows indicate the time instants at which ATP (1 mM), C_{60}–Asp (50 μM), sodium vanadate (200 μM), and $(NH_4)_2SO_4$ (5 mM) were added. Curve *3*: Kinetics of the Mg–ATP-dependent acidification of the peribacteroid space of the symbiosomes in the same medium but in the presence of 1 μM of valinomycin. The arrows indicate the time instants at which ATP (1 mM) and C_{60}–Asp (50 μM) were added. The spectrophotometric measurements were performed on a Hitachi 557 spectrum photometer in the two-wave mode (in the ranges of 590–610 and 492–540 nm for oxonol VI and acridine orange, respectively). (b) Kinetics of the generation of K^+ diffusion potential on the membrane of human erythrocytes initiated with the addition of valinomycin to them, and the dissipation of this potential in the presence of C_{60}–Arg. The erythrocytes were incubated in a medium containing 0.48 M of sorbitol, 20 mM of HEPES-BTP (pH 7.6), 3 mM of $MgSO_4$, and 1 μM diS–C_3–(5). The arrows indicate the instants at which valinomycin (1 μM), 300 μM of C_{60}–Arg, and 25 mM of K_2SO_4 were added. The measurements of the fluorescence of the potential-sensitive probe diS–C_3–(5) were carried out at 670 nm using a Hitachi 850 fluorescence spectrum photometer with $\lambda_{exc} = 622$ nm.

tively rapid discharge of the membrane potential; this effect increases with increasing concentration of the introduced fullerene derivative. According to our observations, this depolarizing effect is also characteristic of another amino-acid derivative of fullerene, namely, C_{60}–Pro, which is likely to also carry a negative charge in the range of physiological values of pH (no data are given). The revealed effect of C_{60}–Asp and C_{60}–Pro on the magnitude of the membrane potential gives grounds to assume that the compounds selected behave as lipophilic anions capable of penetrating across the PBMs of symbiosomes. The validity of this assumption is confirmed by the results of other experiments, in which we used a ΔpH indicator (acridine orange) [8] to trace the kinetics of the MgATP-dependent acidification of the peribacteroid space of symbiosomes. The data

given in the figure show that C_{60}–Asp added into the incubation mixture containing ATP and Mg^{2+} ions initiates this process (curve *2*) but leaves its kinetics unaltered (curve *3*) when it is triggered with the help of the K^+ ionophore of valinomycin, which catalyzes the escape of K^+ ions from the symbiosomes and thereby ensures dissipation of the MgATP-induced membrane potential on the PBM. These results permit us to conclude that C_{60}–Asp and C_{60}–Pro are transported across the symbiosome membrane as lipophilic anions, cause dissipation of $\Delta\psi$, and thereby stimulate MgATP-dependent formation of ΔpH on the PBM. Moreover, the last effect caused by the above fullerene derivatives indicates that the elimination of the membrane potential on the symbiosome membrane in their presence is completely caused by their capability of penetrating in the form of anions across the hydrophobic barrier of the membrane rather than by the suppression of the activity of the proton pump. It is also important to note that the addition of C_{60}–Arg to the symbiosomes instead of C_{60}–Asp or C_{60}–Pro virtually did not change the kinetics of the processes of generation of $\Delta\psi$ or ΔpH on the PBM (no data are given).

Based on the above data, we can expect that the permeability of biological membranes for C_{60}–Arg should manifest itself in the dissipation by this compound of the membrane potential of another polarity as well. This hypothesis has been tested in another series of experiments, which were performed on human erythrocytes using a high-sensitivity probe such as diS–C_3–(5) [9]. As can be seen from Fig. 1b, the introduction into the suspension of erythrocytes in the potassium-free medium of valinomycin initiates the generation on their membrane of a K^+ diffusion potential ("minus" inside erythrocytes) due to the elimination of K^+ ions from the cells, which is reflected in the decreasing fluorescence of this dye. However, the time dependence of this fluorescence gradually reverted after addition of C_{60}–Arg to erythrocytes, and the initial rate of this response reaction increased with increasing concentration of this compound (no data are given). The very rapid recovery of the initial level of fluorescence of the dye was observed after subsequent introduction into the incubation zone of potassium sulfate because of a significant decrease under these conditions of the magnitude of the transmembrane gradient of K^+ ions at the erythrocyte membrane. On the contrary, the kinetics of the generation of the K^+ diffusion potential on this membrane did not changed after addition to erythrocytes of C_{60}–Asp and C_{60}–Pro, which are negatively charged, in our opinion, amino-acid derivatives of fullerene at the chosen values of pH (no data are given).

On the whole, the results of the above experiments permit us to make a general conclusion that the amino-acid derivatives of fullerene used in this work are capable of penetrating in their ionized form across biological membranes and, thereby, cause membrane depolarization.

ACKNOWLEDGMENTS

This work was supported in part by the Russian Foundation for Basic Research, project no. 00-04-48317a.

REFERENCES

1. R. A. Kotelnikova, A. I. Kotelnikov, G. N. Bogdanov, *et al.*, FEBS Lett. **389**, 111 (1996).
2. R. V. Besanson, E. Bienvenue, M. Delinger, *et al.*, J. Phys. Chem. **98**, 3492 (1994).
3. I. Andreev, P. Dubrovo, V. Krylova, *et al.*, J. Plant Physiol. **151**, 563 (1997).
4. V. S. Romanova, V. A. Tsyryapkin, Yu. A. Lyakhovetskiĭ, *et al.*, Izv. Ross. Akad. Nauk, Ser. Khim. **43**, 1151 (1994).
5. M. E. Vol'pin, Z. N. Parnes, and V. S. Romanova, Izv. Ross. Akad. Nauk, Ser. Khim., No. 5, 1050 (1998).
6. M. E. Vol'pin, E. M. Blavtseva, V. S. Romanova, *et al.*, Mendeleev Commun. 129 (1995).
7. H.-J. Appell and B. Bersch, Biophys. Acta **903**, 480 (1987).
8. M. G. Palmgren, Ann. Biochem. **192**, 316 (1991).
9. P. J. Sims, A. S. Waggoner, C.-H. Wang, and J. F. Hoffman, Biochemistry **13**, 3315 (1974).

Translated by S. Gorin

Physics of the Solid State, Vol. 44, No. 4, 2002, pp. 686–691. Translated from Fizika Tverdogo Tela, Vol. 44, No. 4, 2002, pp. 661–666.

METALS AND SUPERCONDUCTORS

Small-Angle Neutron Scattering and the Mössbauer Effect in Nitrogen Austenite

V. M. Nadutov*, V. M. Garamus, and A. Kh. Islamov*****

** Institute of Metal Physics, National Academy of Sciences of Ukraine, pr. Vernadskogo 36, Kiev, 03680 Ukraine*

*** GKSS Research Center, Geesthacht, Germany*

**** Joint Institute for Nuclear Research, Dubna, Moscow oblast, 141980 Russia*

Received June 15, 2001

Abstract—Small-angle neutron scattering (SANS) in Fe–19%Cr–19%Mn–0.9%N and Fe–18%Cr–10%Mn–16%Ni–0.5%N (wt %) high-nitrogen austenites is investigated. The neutron diffraction patterns and Mössbauer spectra are measured and analyzed. The SANS curves are approximated in the framework of the Guinier and Porod models. The nature of small-angle neutron scattering in nitrogen austenite is explained in terms of microinhomogeneities whose structure depends on the alloying with nickel. The mean size and shape of inhomogeneities are evaluated. The effect of low-temperature annealing of the Fe–19%Cr–19%Mn–0.9%N austenite on small-angle neutron scattering and the parameters of the Mössbauer spectra is analyzed. © *2002 MAIK "Nauka/Interperiodica".*

1. INTRODUCTION

Numerous investigations have demonstrated that the mechanical properties of austenitic stainless steels are substantially improved upon alloying with nitrogen. Nitrogen austenitic steels possess high toughness and resistance to corrosion of different types [1]. These materials are of considerable practical interest.

The microstructure and atomic distribution in a solid solution are important factors affecting the corrosive and mechanical properties of materials. The Mössbauer investigation of the Fe–18%Cr–10%Mn–16%Ni–0.5%N (wt %) austenite revealed that the spectra exhibit a complex hyperfine structure due to an inhomogeneous local atomic order [2]. However, according to the inelastic neutron scattering data obtained in [3] for the Fe–18%Cr–10%Mn–16%Ni–(0–0.5)%N austenite, the local vibrational mode of nitrogen atoms is symmetric in shape and the intensity of this mode increases linearly with an increase in the nitrogen concentration. This suggests that nitrogen atoms are characterized by a homogeneous distribution over the lattice [3].

The small-angle neutron scattering (SANS) technique is widely used for revealing and analyzing inhomogeneities and phase preprecipitates [4, 5]. In our earlier work [6], we observed small-angle neutron scattering in the Fe–18%Cr–10%Mn–16%Ni–0.5%N austenite and attributed it to scattering by nitride-free inhomogeneities with a fractal structure and a rough interface. We assume that these properties of the inhomogeneity structure in the austenitic phase are associated with the presence of nitrogen and nickel. A strong Ni–N [7] or N–N [8] repulsion can lead to an inhomogeneous atomic order in austenite containing nickel and nitrogen and, correspondingly, to an inhomogeneous magnetic order, which, in turn, can ensure the contrast required for observations of small-angle neutron scattering.

In the present work, we performed a comparative SANS investigation of the nickel-free Fe–Cr–Mn–N austenite and nickel-containing Fe–Cr–Mn–Ni–N austenite in order to exclude the effect of one of the elements on the microstructure of the γ phase. The phase composition of the Fe–Cr–Mn–N steel and the changes observed in the short-range atomic order upon low-temperature annealing were examined using neutron diffraction and Mössbauer spectroscopy.

2. EXPERIMENTAL TECHNIQUE

The austenitic steels Fe–19%Cr–19%Mn–0.9%N and Fe–18%Cr–10%Mn–16%Ni–0.5%N (wt %) were chosen as the objects of investigation. The steel compositions are listed in Table 1. Samples in the form of

Table 1. Compositions of austenitic steels

N	C	Mn	Cr	Mo	Ni	S	Ti	Si	B	Al	Cu	P	Fe
0.9	0.04	19.1	18.68	0.06	0.45	<0.01	<0.01	0.45	<0.0004	0.0011	0.06	0.016	The rest [9]
0.5	–	10.0	18.0	–	16.0	–	–	–	–	–	–	–	The rest

1063-7834/02/4404-0686$22.00 © 2002 MAIK "Nauka/Interperiodica"

plates were annealed at temperatures of 1125°C (Fe–19%Cr–19%Mn–0.9%N) and 1100°C (Fe–18%Cr–10%Mn–16%Ni–0.5%N) and were then quenched into water. A number of Fe–19%Cr–19%Mn–0.9%N austenite samples were additionally heat treated at 250°C for 150 h, 300°C for 180 h, and 350°C for 250 h.

The SANS measurement were carried out on a MURN time-of-flight spectrometer installed on an IBR-2 pulsed reactor (Frank Laboratory of Neutron Physics, Joint Institute for Nuclear Research, Dubna). The experimental conditions and the resolution functions for the SANS measurements were described in [10]. The SANS experiments were performed in an axially symmetric geometry (collimator and sample shapes and a recording system). The recording system involved eight toroidal detectors. The neutron intensity at the sample was equal to 10^7 cm^{-2} s^{-1}. The spectrum of incident thermal neutrons was described by a Maxwellian distribution with the mean wavelength $\langle\lambda\rangle$ = 1.1 Å. The measurements were performed in the neutron wavelength ranges 1.1–3.1 Å for the Fe–19%Cr–19%Mn–0.9%N austenite and 1.1–8.5 Å for the Fe–18%Cr–10%Mn–16%Ni–0.5%N austenite. No Bragg diffraction reflections were observed in these wavelength ranges. The neutron beam intensity was calibrated against the vanadium reference sample. The parameters and invariant of the scattering pattern were calculated with due regard for the resolution function of the spectrometer. The statistical error for the measured curves did not exceed 6%.

The neutron diffraction was measured on a DN-2 time-of-flight diffractometer installed on the same reactor. The experimental conditions, data collection, and correction for the integrated intensity were described in [11]. The diffraction data were processed according to the automatic program [12] by the Rietveld method with the use of the MRIYA program [13].

The transmission Mössbauer spectra were recorded at room temperature on a MS-1101É high-speed spectrometer operating in a constant-acceleration mode at the Institute of Metal Physics, National Academy of Sciences of Ukraine (Kiev). A ^{57}Co(Cr) gamma-ray source was used in the experiments. The spectra were approximated using the standard program based on the least-squares technique with a combination of Lorentzian and Gaussian lines. The velocities were calibrated against α-Fe and sodium nitroprusside. The linewidth in the spectrum of sodium nitroprusside did not exceed 0.19–0.20 mm/s.

3. RESULTS

Small-angle neutron scattering is observed in both austenites. The slopes of the SANS curves for nickel-containing and nickel-free austenites differ noticeably (Fig. 1). The low-temperature annealing does not lead to a radical change in the scattering pattern (Fig. 2).

According to the neutron diffraction and Mössbauer data, the samples under investigation have a single-phase austenitic structure (Fig. 3). The spacings of the face-centered cubic lattices for Fe–Cr–Mn–N and Fe–Cr–Mn–Ni–N austenites are equal to 0.35893 and 0.3604 nm, respectively. The low-temperature annealing of the Fe–Cr–Mn–N samples leaves the shape and location of the diffraction lines unchanged and does not lead to the formation of a new phase.

Analysis revealed that the absorption Mössbauer spectra consist of three partial spectra: singlet *0* and doublets *0*' and *1* (Fig. 4), which correspond to different

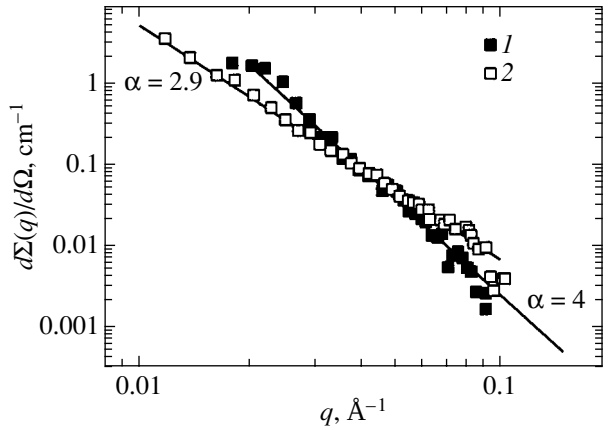

Fig. 1. Differential SANS cross sections for (*1*) Fe–19%Cr–19%Mn–0.9%N and (*2*) Fe–18%Cr–10%Mn–16%Ni–0.5%N (wt %) austenites after homogenization and subsequent quenching. Experimental data are given after subtraction of the background. Solid lines are the approximating curves (α is the exponent). Variations in experimental data can be associated with the statistical error and properties of the chosen approximations.

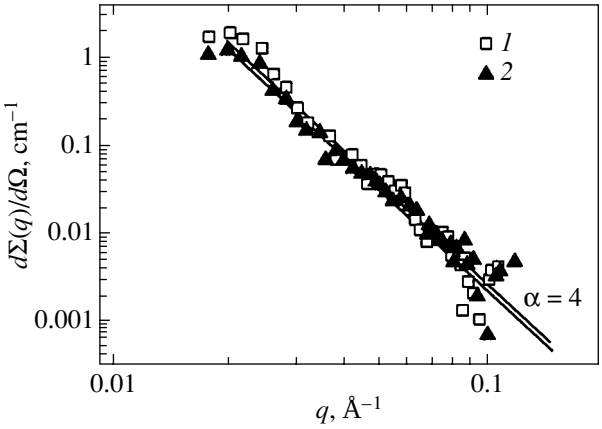

Fig. 2. Differential SANS cross sections for the Fe–19%Cr–19%Mn–0.9%N (wt %) austenite after annealing (*1*) at 250°C for 150 h and (*2*) at 350°C for 250 h. Experimental data are given after subtraction of the background. Solid lines are the approximating curves (α is the exponent).

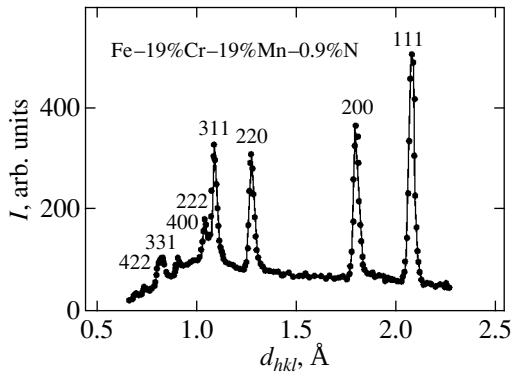

Fig. 3. Neutron diffraction pattern of the Fe–19%Cr–19%Mn–0.9%N (wt %) austenite after homogenization at 1125°C for 0.5 h and subsequent quenching.

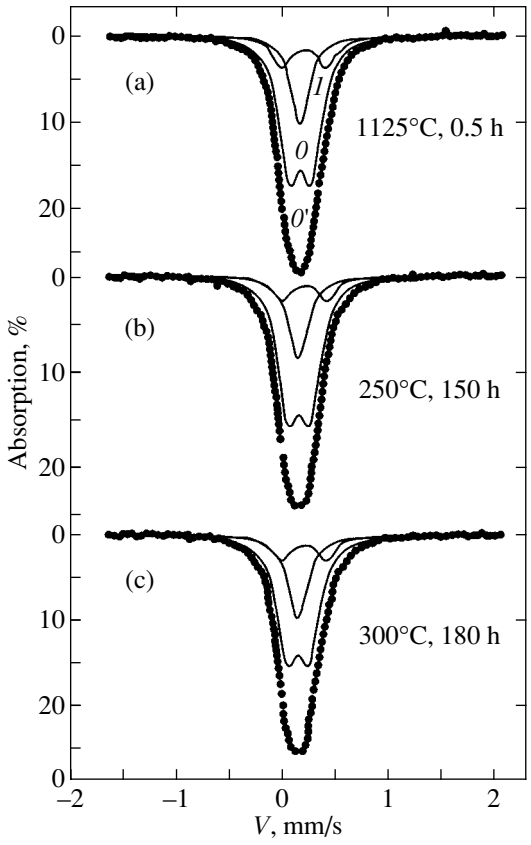

Fig. 4. Mössbauer spectra of the Fe–19%Cr–19%Mn–0.9%N (wt %) austenite after (a) homogenization at 1125°C for 0.5 h and subsequent quenching, (b) annealing at 250°C for 150 h, and (c) annealing at 300°C for 180 h.

atomic environments in the γ phase. Component *0* is associated with Fe atoms whose first coordination sphere contains no alloying elements. Doublet *1* with a positive isomer shift with respect to the singlet (Table 2) is assigned to Fe atoms with the nearest environment involving at least one N atom and other alloying elements. Doublet *0*' with a quadrupole splitting smaller than that of doublet *1* (Table 2) is attributed to Fe atoms that have substitutional atoms as the nearest neighbors and whose nearest interstices contain no N atoms. The isomer shifts and quadrupole splittings of components in the Mössbauer spectra of alloyed austenite were examined thoroughly in [2].

4. DISCUSSION

The observed small-angle neutron scattering indicates that the austenitic phase of the studied compounds contains inhomogeneities or preprecipitates. In the range of large scattering vectors **q**, the differential SANS cross section for the nickel-free Fe–19%Cr–19%Mn–0.9%N austenite is smaller than that for the nickel-containing Fe–18%Cr–10%Mn–16%Ni–0.5%N austenite (Fig. 1). This means that the introduction of nickel leads to an increase in the volume fraction of inhomogeneities in the austenitic phase and, hence, to an enhancement of neutron scattering in austenite.

This situation can be easily predicted, because iron–nickel austenite is characterized by an inhomogeneous atomic order. The nearest environment of atoms of a particular sort varies from site to site, which leads to an inhomogeneous magnetic structure (see [14] and references therein) due to the existence of two electronic states of Fe atoms [15]. According to Hatherly *et al.* [15], these states correspond to the ferromagnetic and antiferromagnetic exchange interactions for which the second moments of the exchange integral have opposite signs and are as follows: $J^{(2)}_{\text{Fe–Fe}} = -9$ meV, $J^{(2)}_{\text{Fe–Ni}} = 39$ meV, and $J^{(2)}_{\text{Ni–Ni}} = 59$ meV.

Magnetic inhomogeneities in nickel-containing austenite strongly depend on the concentration of C or N interstitial atoms (see, for example, [2, 14] and references therein). Since neutrons are scattered not only by nuclei but also by their magnetic moments, the magnetic inhomogeneities make an additional contribution to small-angle neutron scattering in the nickel-containing austenite, whereas this contribution in the nickel-free Fe–19%Cr–19%Mn–0.9%N austenite is substantially smaller.

As is seen from Fig. 1, the SANS curves for nickel-containing and nickel-free austenites are characterized by different slopes. This suggests that inhomogeneities have different microstructures. With the aim of analyzing the slopes of the scattering curves and describing the microinhomogeneities, we used the universally accepted two-phase models. Moreover, it was assumed that the microstructure of the studied system can be represented as a set of particles embedded into a matrix. The particles have a colloidal size and the scattering density ρ, and the matrix is characterized by the scattering density ρ_s.

Table 2. Mössbauer parameters for the Fe–19%Cr–19%Mn–0.9%N (wt %) austenite

Treatment	δ_0, mm/s	Γ_0, mm/s	$\delta_{0'}$, mm/s	$\Delta_{0'}$, mm/s	$\Gamma_{0'}$, mm/s	δ_1, mm/s	Δ_1, mm/s	Γ_1, mm/s	$S_1/\Sigma S_i$, %
1125°C, 0.5 h	–0.193	0.201	–0.193	0.197	0.224	–0.154	0.418	0.228	14.3–16.7
250°C, 150 h	–0.193	0.230	–0.193	0.212	0.253	–0.153	0.431	0.227	12.8–15.4
300°C, 180 h	–0.192	0.229	–0.190	0.205	0.241	–0.147	0.436	0.216	13.2–14.2

Note: δ_i is the isomer shift with respect to α-Fe, Δ_i is the quadrupole splitting, Γ_i is the width of the resonance line (±0.01 mm/s), and $S_1/\Sigma S_i$ stands for the minimum and maximum relative areas of doublet *1* for six different variants of the fitting.

First, we consider the Guinier approximation that describes the differential neutron scattering cross section $d\Sigma(q)/d\Omega$ in the range of the small scattering vectors $q = 4\pi\sin\Theta/\lambda$, where 2Θ is the scattering angle [16]. The Guinier approximation for a given q is valid at $qR_g < 1$, where R_g is the radius of gyration of a particular scattering inhomogeneity. Analysis shows that, in the range of small q, the corresponding portions in the SANS curves for both austenites cannot be represented in terms of the Guinier model. This implies the fulfillment of the inequality $qR_g > 1$, from which it follows that the mean inhomogeneity size exceeds 100 Å.

In the range of large scattering vectors, the SANS curves can be approximated within the Porod model which describes scattering by inhomogeneities or preprecipitates with smooth surfaces [17, 18], that is,

$$d\Sigma(q)/d\Omega = Aq^{-\alpha} + B. \quad (1)$$

Here, $\alpha = 4$, $A = 2\pi\Delta\rho^2 S$ is the Porod constant characterizing the total surface area of inhomogeneities, S is the specific interfacial area in the inhomogeneity–matrix system, B is the residual incoherent background, and $\Delta\rho^2 = (\rho - \rho_s)^2$ is the contrast.

The SANS curve for the nickel-containing Fe–18%Cr–10%Mn–16%Ni–0.5%N austenite does not exhibit a Porod portion. The scattering spectrum of this compound can be approximated by a power law with an exponent $\alpha < 4$, which indicates the occurrence of fractal structures [19]. Fractal-like inhomogeneities have a rough diffuse interface with the surrounding matrix.

In the scattering vector range $q = 0.01$–0.1 (Fig. 1), the calculated fractal dimension D is equal to 2.9 ± 0.2. This fractal dimension was considered in detail in [6]. The value of $D < 3$ indicates a bulk fractal for which the mass M and the linear size l of the inhomogeneity are related by the formula $M = M_0 l^D$, where M_0 is a constant. The existence of a surface fractal also cannot be ruled out, because the inequality $3 \le D < 4$ is satisfied to within the experimental error. Reasoning from the scattering vector range, the size of the objects is estimated at 10–350 Å.

The existence of fractal-like structures in the nitrogen nickel-containing austenite suggests an inhomogeneity of atomic and magnetic densities. Since nitrides in this austenite are not identified by diffraction techniques, the fractal properties can be associated with vacancy clusters or micropores and also with magnetic inhomogeneities arising from alloying of iron steels with nickel and interstitial elements [2, 14, 20]. The contributions of the structural and magnetic inhomogeneities can be separated using polarized neutrons. These contributions can also be reliably separated with the use of x-ray small-angle scattering measurements.

The slope of the SANS curves for the Fe–19%Cr–19%Mn–0.9%N austenite corresponds to $\alpha = 4$. This means that the inhomogeneities are of another nature and that the objects with fractal properties are absent. These data confirm the assumption that the alloying of austenite with nickel can be responsible for the fractality.

Analysis of the results demonstrates that the SANS curves for the Fe–19%Cr–19%Mn–0.9%N austenite in the initial state and after annealing involve Porod portions. The smallest scattering vector q_p at which the Porod approximation becomes valid is equal to 0.03 Å^{-1} (Fig. 1). As follows from the slope of the SANS curves ($\alpha = 4$), all inhomogeneities in the Fe–19%Cr–19%Mn–0.9%N austenite have a smooth interface.

The smooth abrupt interface between inhomogeneities and the matrix in the Fe–19%Cr–19%Mn–0.9%N austenite can be associated with the nitride phase preprecipitates. Since these preprecipitates are not identified using diffraction methods (Fig. 2), it can be assumed that they are characterized by a high degree of dispersion and a small volume fraction.

The Mössbauer measurements also revealed only the austenitic phase without indication of any other phase. The three spectral components (Fig. 4) reflect different nearest environments of Fe atoms with N atoms and (or) with Mn and Cr substitutional atoms in the γ phase. Since additional components corresponding to nitride phase precipitates are absent in the spectrum, microobjects in austenite contain a small fraction of iron and are paramagnetic. Therefore, we can assume that the preprecipitates responsible for small-angle neutron scattering in nickel-free austenite (Figs. 1, 2) are enriched with chromium, manganese, and nitrogen and serve as nuclei of nitrides of these elements.

It should be noted that the SANS curves for the Fe–19%Cr–19%Mn–0.9%N austenite in the range of scattering vectors $q \sim 0.02$ deviate from linear behavior irrespective of heat treatment (Figs. 1, 2). We believe

Table 3. SANS parameters for the Fe–19%Cr–19%Mn–0.9%N austenite

Treatment	A, 10^{-7} cm^{-1} Å^{-4}	Q, 10^{-6} cm^{-1} Å^{3}	K, 10^{-4} cm^{-1} Å^{2}
1125°C, 0.5 h	2.26 ± 0.08	17.4 ± 0.8	10.4 ± 0.7
250°C, 150 h	2.38 ± 0.1	19.0 ± 0.9	11.5 ± 0.8
350°C, 250 h	1.77 ± 0.07	13.3 ± 0.8	8.0 ± 0.7

Table 4. Characteristic sizes of inhomogeneities in the Fe–19%Cr–19%Mn–0.9%N austenite

Treatment	R', Å	$\langle R\rangle$, Å	R_P, Å
1125°C, 0.5 h	200	190 ± 30	74 ± 5
250°C, 150 h	200	190 ± 30	76 ± 5
350°C, 250 h	200	190 ± 30	75 ± 5

that this feature can be associated with structural inhomogeneities of a size less than 100 Å. The use of neutrons with longer wavelengths could make it possible to obtain a more pronounced pattern and to apply successfully the Guinier approximation in the given range of the **q** vectors.

When processing the data, the neutron scattering cross section was integrated over three scattering vector intervals. The Porod approximation (1) was used in the interval $[q_P, \infty]$. The numerical and analytical integration was performed in the interval $[q_{min}, q_P]$. In the interval $[0, q_{min}]$, the scattering cross section was assumed to be constant; i.e., $d\Sigma(q)/d\Omega = d\Sigma(q_{min})/d\Omega$.

Thus, we determined the following parameters: the total surface area of inhomogeneities A according to formula (1) [17]; the Porod invariant $Q = \int_0^\infty q^2(d\Sigma(q)/d\Omega)dq$, which characterizes the total volume of inhomogeneities $N\nu$ (where N is the number of inhomogeneities and ν is the specific volume of inhomogeneity); and the chord distribution parameter $K = q(d\Sigma(q)/d\Omega)dq$, which is related to the mean chord of inhomogeneity [18].

The results of calculations are listed in Table 3. The parameters A, Q, and K for the initial quenched steel do not differ from those for the steel annealed at 250°C. The annealing at a temperature of 350°C leads to a decrease in the integral parameters A, Q, and K as compared to those for the initial state. This change can be explained by the decrease in the contrast $\Delta\rho^2$ or in the geometric size of inhomogeneities, viz., the total surface area, the total volume, and the mean chord of precipitates.

The size and shape of inhomogeneities in the Fe–19%Cr–19%Mn–0.9%N austenite were evaluated from the parameters A, Q, and K in the framework of the following three approaches.

(1) Under the assumption that the inhomogeneities are only slightly prolate or oblate in shape, the mean size of inhomogeneities was estimated from the expression $q_P R' > 6$, which relates the mean radius R' of inhomogeneities and the smallest scattering vector at which the Porod approximation becomes valid [17]. It was found that, for all samples of the Fe–19%Cr–19%Mn–0.9%N steel, the characteristic mean radius R' of preprecipitates is of the order of 200 Å (Table 4).

(2) For inhomogeneities with a constant scattering length, the mean radius $\langle R\rangle$ was calculated using the chord distribution function: $\langle R\rangle = \pi KQ^{-1}$ [16]. The calculated inhomogeneity radii $\langle R\rangle$ are given in Table 4. It can be seen that these radii are in agreement with the data on R'.

(3) The ratio between the A parameter and the Q invariant, i.e., the surface-to-volume ratio of inhomogeneities, gives the so-called Porod radius $R_P = 3/\pi QA^{-1}$. As follows from Table 4, the radii R_P are less than the radii R' and $\langle R\rangle$. The small value of R_P confirms the validity of the above interpretation of the specific feature in the SANS curves for the nickel-free austenite in the range of scattering vectors $q \sim 0.02$. The observed difference in the radii R', $\langle R\rangle$, and R_P suggests that the inhomogeneities have a nonspherical shape.

The averaged ratio $R_{max}/R_{min} \approx 2$ between the maximum and minimum sizes of the inhomogeneities under investigation was derived from the ratios R'/R_P and $\langle R\rangle/R_P$. The estimated ratio $R_{max}/R_{min} \approx 2$ indicates that the inhomogeneities can be slightly prolate or oblate in shape.

The results of calculations performed within different approaches demonstrate that the radii R', $\langle R\rangle$, and R_P for the quenched samples do not differ from those for the annealed samples (Table 4). Therefore, the decrease in the parameters A, Q, and K (Table 3) is caused by the decrease in the contrast $\Delta\rho^2$ between the inhomogeneities and the surrounding matrix. This can be associated with the redistribution of interstitial atoms upon heating.

The redistribution of atoms in austenite was established from analysis of the Mössbauer spectra (Fig. 4). The isomer shifts δ_i, the quadrupole splittings Δ_i the linewidths Γ_i, and the relative areas $S_i/\Sigma S_i$, which were determined from the poorly resolved components in the absorption spectrum of paramagnetic austenite, are strongly correlated. For this reason, the precise determination of the hyperfine interaction parameters and their change upon annealing is complicated. However, the changes in the parameters of doublet *1* (Fig. 4) attributed to Fe atoms with interstitial atoms in their nearest environment are larger than the error of determination (Table 2). This suggests that the atoms in austenite are redistributed upon heating.

It should be noted that the results obtained in this work can serve as a starting point for the understanding of the role played by the ageing in the change in the

fatigue characteristics of the Fe–19%Cr–19%Mn–0.9%N steel [9] and guide the way to further investigations.

5. CONCLUSION

Thus, the neutron diffraction and Mössbauer spectroscopic data demonstrated that the Fe–18%Cr–10%Mn–16%Ni–0.5%N austenite alloyed with nickel and the nickel-free Fe–19%Cr–19%Mn–0.9%N austenite are in a single-phase state. Annealing of the Fe–19%Cr–19%Mn–0.9%N austenite at temperatures of 250 and 350°C leaves the phase composition unchanged.

It was revealed that small-angle neutron scattering occurs in both compounds. However, the differential scattering cross section for the Fe–19%Cr–19%Mn–0.9%N austenite is smaller than that for the Fe–18%Cr–10%Mn–16%Ni–0.5%N austenite. The scattering curve for the Fe–19%Cr–19%Mn–0.9%N austenite contains a Porod portion corresponding to inhomogeneities with a smooth abrupt interface. The fractal-like inhomogeneities characterized by a rough diffuse interface with the matrix were observed only in the nickel-containing Fe–18%Cr–10%Mn–16%Ni–0.5%N.

The size of inhomogeneities with a fractal structure in the Fe–18%Cr–10%Mn–16%Ni–0.5%N austenite falls in the range 10–350 Å. The inhomogeneities observed in the Fe–19%Cr–19%Mn–0.9%N austenite have a nonspherical shape and a characteristic size of 200 Å, irrespective of subsequent annealing. It was found that the annealing of the Fe–19%Cr–19%Mn–0.9%N austenite at 350°C results in a change in the contrast due to atomic redistribution.

ACKNOWLEDGMENTS

We would like to thank N.D. Afanas'ev (Izhevsk) for smelting of the nitrogen austenitic steel containing nickel, Prof. J. Foct and Prof. J.-B. Vogt (Lille University) for providing the austenitic steel used in our investigations and for their participation in discussions of the results, A.I. Beskrovnyiĭ (Dubna) for helpful discussions of the diffraction data, and S. Borbeli (Budapest) for the experimental verification of a number of points in the SANS curve at the Budapest Neutron Center and for discussions of the experimental results.

The SANS measurements were performed at the Frank Laboratory of Neutron Physics (Joint Institute for Nuclear Research, Dubna), project no. IV.1.31. This work was supported in part by the Lille University (France) and the GKSS Research Center (Germany).

REFERENCES

1. F. B. Pickering, in *Proceedings of the II International Conference on High Nitrogen Steels, Lille, 1988*, p. 10.
2. V. M. Nadutov, Mater. Sci. Eng. A **254**, 234 (1998).
3. V. G. Gavrilyuk, V. M. Nadutov, S. A. Danilkin, *et al.*, Mater. Sci. Eng. A **203**, 300 (1995).
4. G. Kostorz, J. Appl. Crystallogr. **24**, 444 (1991).
5. G. Kostorz, in *Modern Aspects of Small-Angle Scattering*, Ed. by H. Brumberger (Kluwer, Dordrecht, 1995), NATO ASI Ser., Ser. C **451**, 255 (1995).
6. V. M. Nadutov, L. A. Bulavin, and V. M. Garamus, Mater. Sci. Eng. A **264**, 286 (1999).
7. P. Rochegude and J. Foct, in *Proceedings of the 1st International Conference on High Nitrogen Steels, Lille, France, 1988*, Ed. by J. Foct and A. Hendry (Inst. of Metals, London, 1989).
8. A. G. Balanyuk, V. N. Bugaev, V. M. Nadutov, and A. L. Sosinov, Phys. Status Solidi B **207**, 3 (1998).
9. J. B. Vogt, A. Messai, and J. Foct, ISIJ Int. **36** (7), 862 (1996).
10. Yu. M. Ostanevich, Macromol. Chem., Macromol. Symp. **15**, 91 (1988); E. P. Kozlova, Yu. M. Ostanevich, and L. Cher, Nucl. Instrum. Methods **169**, 597 (1980).
11. A. M. Balagurov, G. M. Mironova, and V. G. Simkin, World Scientific **21**, 263 (1990).
12. V. B. Zlokazov, Comput. Phys. Commun. **85**, 4151 (1995).
13. V. B. Zlokazov and V. V. Chernyshov, J. Appl. Crystallogr. **25**, 4471 (1992).
14. V. G. Gavrilyuk and V. M. Nadutov, Fiz. Met. Metalloved. **56** (3), 555 (1983).
15. M. Hatherly, Y. Hirokawa, R. D. Lawde, *et al.*, Proc. Phys. Soc. London **84**, 55 (1964).
16. A. Guinier and G. N. Fournet, *Small-Angle Scattering of X-rays* (Wiley, New York, 1955).
17. G. Porod, Kolloid. Z. **125**, 51 (1952).
18. L. A. Feigin and D. I. Svergun, in *Structural Analysis by Small-Angle X-ray and Neutron Scattering* (Plenum, New York, 1987).
19. P. W. Schmidt, in *The Fractal Approach to Heterogeneous Chemistry*, Ed. by D. Avnir (Wiley, New York, 1989), p. 67.
20. J. Foct, P. Rochegude, and C. Cordier-Robert, Hyperfine Interact. **45**, 359 (1989).

Translated by O. Borovik-Romanova

Physics of the Solid State, Vol. 44, No. 4, 2002, pp. 692–703. Translated from Fizika Tverdogo Tela, Vol. 44, No. 4, 2002, pp. 667–677.

METALS AND SUPERCONDUCTORS

Model of a Polaron Superconductor

E. K. Kudinov

Ioffe Physicotechnical Institute, Russian Academy of Sciences, ul. Politekhnicheskaya 26, St. Petersburg, 194021 Russia
e-mail: kudinov@ekk.ioffe.rssi.ru

Received July 5, 2001

Abstract—This paper studies the mechanism of superconductivity in the case where the electrons are strongly coupled to lattice vibrations and, therefore, are in the state of small polarons. The consideration is based on the Holstein model with zero lattice-vibration dispersion and represents a consistent realization of the BCS approach (with no need arising for boson introduction). The ground state and the excitation spectrum are found. The current states are studied and the criterion of their stability is formulated. The superconducting transition temperature is shown to increase without limit with increasing electron–phonon coupling constant. This is accompanied by an exponential decrease in the critical current. Some fundamental properties of high-temperature superconductors are shown to follow directly from this model. © *2002 MAIK "Nauka/Interperiodica".*

1. INTRODUCTION

As far back as in 1981, long before the discovery of high-temperature superconductivity, A. Aleksandrov and Yu. Ranninger proposed [1, 2] a model for a bipolaron superconductor based on the theory of small polarons [3–5] (in particular, on the onset of attraction between electrons and the possibility of formation of electron pairs localized at a lattice site).[1] Although no superconductor similar to substances that could be suspected of being of a polaron nature was known at that time (primarily "dirty" dielectrics of the type of NiO, TiO_2, etc.), those works turned out to be prophetic, because it is the properties of the latter materials that the high-temperature superconductors (HTSC) discovered in 1981 possessed. In our opinion, the significance of works [1, 2], irrespective of the results they claimed, consists in that the hypothesis of the polaron nature of HTSCs was treated from the very beginning on par with other hypotheses.

An additional incentive to investigate the polaron mechanism of superconductivity was provided by the recent observation of a colossal magnetoresistance (which has a considerable application potential) in a number of manganates (which are close in structure to known HTSCs). This has stimulated numerous studies of their properties (see, e.g., [6–10]), which revealed that their specific features are associated, to a considerable extent, with the strong coupling of electrons with lattice vibrations (the polaron effect). Note that the giant isotope effect discovered in these compounds [11], whose extreme manifestation is the transition from the conducting to dielectric state induced by isotopic substitution [12], is also observed in HTSCs [13]. It is the properties of the small polaron that permit one to find a natural explanation for such an effect.

The closeness in structure between the manganates and high-temperature superconductors offers the hope that strong electron–vibration coupling (EVC) and the polaron effects play an essential part in the nature of the above phenomena also in the HTSCs.

The present paper deals with a study of the superconductivity mechanism within the Holstein model [3, 4]. The BCS formalism is used in the strong EVC limit, where the polaron effect makes the band width smaller than the characteristic coupling energy. Due to its simplicity, this model allows for comprehensive analysis; in particular, it offers the possibility of considering the crossover from the strong to weak coupling case under continuous variation of the parameters, as well as of revealing a number of characteristics of the superconducting state which remain veiled under weak-coupling conditions.

2. MODEL HAMILTONIAN

We address the simplest model [3, 4], in which electrons interact with ion vibrations of a crystal lattice consisting of N ions. Its Hamiltonian can be written as

$$H_{ep} = H_v - g\sum_{\mathbf{m}}\sum_{\sigma} n_{\mathbf{m},\sigma}x_{\mathbf{m}} + \sum_{\mathbf{m},\mathbf{g},\sigma} J(\mathbf{g})a^{+}_{\mathbf{m},\sigma}a_{\mathbf{m}+\mathbf{g},\sigma},$$
$$H_v = \sum_{\mathbf{m}}\left(\frac{p^2_{\mathbf{m}}}{2M} + \frac{M\omega^2 x^2_{\mathbf{m}}}{2}\right), \quad (1)$$

where $p_{\mathbf{m}}$ and $x_{\mathbf{m}}$ are the momentum and coordinate, respectively, of an ion localized near the lattice site **m**; $a^{+}_{\mathbf{m},\sigma}$ and $a_{\mathbf{m}+\mathbf{g},\sigma}$ are electron operators; $n_{\mathbf{m},\sigma} = a^{+}_{\mathbf{m},\sigma}a_{\mathbf{m},\sigma}$; σ is a spin index; M is the ion mass;, ω is the

[1] Note that this idea was put forward by V.I. Sugakov in a discussion of a paper submitted to the All-Union conference on the theory of the solid state (Moscow, December 1963). However, it did not attract the attention of the audience at the time.

ion vibration frequency;[2] and g is the EVC constant. $\sum_{\mathbf{m}}$ is the sum over all lattice sites, and $\sum_{\mathbf{g}}$ is the sum over the nearest neighbors of site $\mathbf{m}$. $J(\mathbf{g})$ determines the electron band width in the rigid lattice. The quantity $M\omega^2$ has the meaning of the elastic constant and does not depend on the ion mass. The EVC originates from the potential energy of electron interaction with ions, and therefore, g is likewise independent of M. The number of electrons is $N_e \leq 2N$. The electron field operators ψ_σ^+, ψ_σ are defined as

$$\psi_\sigma(\mathbf{r}) = \sum_{\mathbf{m}} \varphi_{\mathbf{m}}(\mathbf{r}) a_{\mathbf{m},\sigma}, \tag{2}$$

where $\varphi_{\mathbf{m}}(\mathbf{r})$ is a set of orthonormal Wannier-type functions.

We neglect the effects associated with the magnetic field, because it appears more reasonable to treat them within a phenomenological theory (of the Landau–Ginzburg type).

A possible realization of this model is a system of identical cation–anion complexes located at lattice sites [14]. The complex consists of four anions sitting at the vertices of a rhombus centered on a cation (Fig. 1). The electrons migrate over the complexes. Assuming deformation to affect the length of the rhombus diagonal only, one can choose the coordinate of one of the vertices as the characteristic of strain $x_{\mathbf{m}}$ and reckon the strain from the equilibrium position in the absence of the electron. The canonical transformation

$$U = \prod_{\mathbf{m}} \exp\left(i\frac{x_0}{\hbar} \sum_{\sigma} n_{\mathbf{m},\sigma} p_{\mathbf{m}} \right), \quad x_0 = \frac{g}{M\omega^2} \tag{3}$$

(a particular case of the Lang–Firsov transformation [5]) removes the terms linear in $x_{\mathbf{m}}$ in Eqs. (1) and transforms the operators a^+, a into

$$\begin{aligned} \tilde{a}^+_{\mathbf{m},\sigma} &= \exp(i\beta p_{\mathbf{m}}) a^+_{\mathbf{m},\sigma}, \\ \tilde{a}_{\mathbf{m},\sigma} &= \exp(-i\beta p_{\mathbf{m}}) a_{\mathbf{m},\sigma}, \quad \beta = \frac{x_0}{\hbar}. \end{aligned} \tag{4}$$

The operators $n_{\mathbf{m},\sigma}$ remain invariant under the transformation defined by Eqs. (3). Therefore, we have

$$\begin{aligned} \tilde{H}_{\mathrm{ep}} &= H_{\mathrm{v}} - E_p \sum_{\mathbf{m}} (n_{\mathbf{m}\uparrow} + n_{\mathbf{m}\downarrow})^2 \\ &+ \sum_{\mathbf{m},\mathbf{g}} J(\mathbf{g}) \tilde{a}^+_{\mathbf{m},\sigma} \tilde{a}_{\mathbf{m}+\mathbf{g},\sigma}, \end{aligned} \tag{5}$$

[2] We neglect here the vibration dispersion, because otherwise the formalism would loose its clarity; at the same time, the inclusion of dispersion would not change the general pattern of the phenomenon seriously.

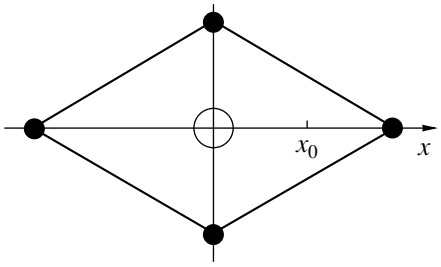

Fig. 1. Cation–anion complex. The empty circle refers to the cation; the filled ones, to the anions.

where $\tilde{H}_{\mathrm{ep}} = UH_{\mathrm{ep}}U^{-1}$ and $E_p = g^2/2M\omega^2$ is the polaron energy shift. The transformed operator $\tilde{a}^+_{\mathbf{m}}$ creates an electron at site $\mathbf{m}$ and the optimum strain. In the case of a strong enough EVC, where $\eta \equiv |J|/2E_p < 1$, such a complex represents a small polaron. The Hamiltonian of Eq. (5) can be recast to the form

$$\begin{aligned} &\tilde{H}_{\mathrm{ep}} = H_0 + V + H_1, \quad H_0 = H_{\mathrm{v}} - E_p \sum_{\mathbf{m}\sigma} n_{\mathbf{m}\sigma}, \\ &V = \sum_{\mathbf{m},\mathbf{g}} J(\mathbf{g}) \exp(i\beta(p_{\mathbf{m}} - p_{\mathbf{m}+\mathbf{g}})) a^+_{\mathbf{m},\sigma} a_{\mathbf{m}+\mathbf{g},\sigma}, \\ &H_1 = -2E_p \sum_{\mathbf{m}} n_{\mathbf{m}\uparrow} n_{\mathbf{m}\downarrow}. \end{aligned} \tag{6}$$

In Eq. (6), we regained the operators a^+, a. Note that EVC gives rise to attraction H_1 of the Hubbard type.

For $J = 0$, transformation (3) exactly diagonalizes the Hamiltonian, such that, under strong-coupling conditions $\eta < 1$, one can construct the perturbation theory in J. For $J = 0$, the states are degenerate; their energies depend only on three variables: the numbers of empty sites and of those that have one and two electrons. To lowest order in J, the eigenfunctions are linear combinations of the zeroth approximation functions (i.e., eigenfunctions Ψ_s of the Hamiltonian $H_0 + H_1$). The latter functions have the form

$$\Psi_s = \Phi_s X_s. \tag{7}$$

Here, Φ_s is the electron function representing the product of a certain number of operators $a^+_{\mathbf{m},\sigma}$ multiplied by the electronic vacuum function and X_s can be written as

$$X_s = \prod_{\mathbf{m}} \psi_{i_{\mathbf{m}}}(x_{\mathbf{m}}),$$

where $\psi_i(x)$ is the function of a harmonic oscillator with quantum number i.

In this approximation, the lowest energy states are solutions of the secular equation in the subspace of the zeroth approximation functions $\{\Psi_0\}$ with $X_s = X_0$,

where $i_{\mathbf{m}} = 0$ for all $\mathbf{m}$. The matrix elements of the Hamiltonian (6) will contain the operators $\exp(\pm i\beta p_{\mathbf{m}})$ only through their expectation values in the state described by X_0, which can be written as[3] (see [3, 4, 14])

$$\langle X_0|\exp(\pm i\beta p_{\mathbf{m}})|X_0\rangle = \exp\left(-\frac{M\hbar\omega}{4}\beta^2\right) = \exp\left(-\frac{E_p}{2\hbar\omega}\right) \equiv \Lambda^{1/2}. \quad (8)$$

Whence it follows that, in this approximation, the lowest energy states of the system are described by an effective Hamiltonian of the Hubbard type:

$$H_e = \sum_{\mathbf{m},\mathbf{g},\sigma} J^*(\mathbf{g}) a^+_{\mathbf{m},\sigma} a_{\mathbf{m}+\mathbf{g},\sigma} - E_p \sum_{\mathbf{m},\sigma} n_{\mathbf{m},\sigma} - 2E_p \sum_{\mathbf{m}} n_{\mathbf{m}\uparrow} n_{\mathbf{m}\downarrow}, \quad (9)$$

where $J^* = J\Lambda = J\exp(-E_p/\hbar\omega)$. Thus, EVC results in renormalization of the constant $J \longrightarrow J^*$ (band narrowing), in a downward energy shift by $-E_p$, and in a single-site attraction characterized by an energy $-2E_p$ (the lattice analog of the δ-function attraction potential employed in the BCS model). Now, we add the Coulomb interaction to Hamiltonian (5):

$$H_{ee} = \sum_{\{\mathbf{m}_i\}\sigma,\sigma'} \sum A(\mathbf{m}_1, \mathbf{m}_2, \mathbf{m}_3, \mathbf{m}_4) \times a^+_{\mathbf{m}_1,\sigma} a^+_{\mathbf{m}_2,\sigma'} a_{\mathbf{m}_3,\sigma'} a_{\mathbf{m}_4,\sigma}. \quad (10)$$

After transformation (3), the following operator will appear in Eq. (10) under the summation sign:

$$\hat{B}(\mathbf{m}_1, \mathbf{m}_2, \mathbf{m}_3, \mathbf{m}_4) = \exp(i\beta p_{\mathbf{m}_1}) \times \exp(i\beta p_{\mathbf{m}_2}) \exp(-i\beta p_{\mathbf{m}_3}) \exp(-i\beta p_{\mathbf{m}_4}). \quad (11)$$

In the subspace $\{\Psi_0\}$, it is equal to the expectation value $\langle X_0|\hat{B}|X_0\rangle$, which will bring about multiplication of A by Λ^p, with $p = 1, 2, 3, 4$. For terms with $\mathbf{m}_1 = \mathbf{m}_4$, $\mathbf{m}_2 = \mathbf{m}_3$ and $\mathbf{m}_1 = \mathbf{m}_3$, $\mathbf{m}_2 = \mathbf{m}_4$ (the Coulomb and exchange terms, which are not connected with real electron transfer from one site to another), we have $p = 0$; i.e., they do not change under the transformation. All the other terms are related to the electron transfer, $p \neq 0$ for them, and the highest power $p = 4$ corresponds to the term $a^+_{\mathbf{m}\uparrow} a^+_{\mathbf{m}\downarrow} a_{\mathbf{m}'\downarrow} a_{\mathbf{m}'\uparrow}$ describing pair transfer. (The terms with $p = 2, 3$ are not significant in our consideration.) In what follows, we shall address the strong EVC case, where $E_p/\hbar\omega$ is large and Λ falls off exponentially with increasing g. In this case, it is reasonable to retain in H_{ee} only terms with $p = 0$. Assuming neither magnetic nor charge order to set in our system, we drop the corresponding terms in Eq. (10) and retain only the Hubbard repulsion term:

$$H_{ee0} = 2A_0 \sum_{\mathbf{m}} n_{\mathbf{m}\uparrow} n_{\mathbf{m}\downarrow}, \quad A_0 = A(0, 0, 0, 0) > 0. \quad (12)$$

The value of A_0 is determined by the structure of the cation–anion complex and can differ appreciably from the Hubbard energy (a few electronvolts) of a bare ion. Thus, in the $\{\Psi_0\}$ subspace, Hamiltonian (6) is equivalent to the Hubbard Hamiltonian:

$$H = H_H + \bar{V}, \quad H_H = 2W \sum_{\mathbf{m}} n_{\mathbf{m}\uparrow} n_{\mathbf{m}\downarrow}, \quad \bar{V} = \sum_{\mathbf{m},\mathbf{g},\sigma} J^*(\mathbf{g}) a^+_{\mathbf{m},\sigma} a_{\mathbf{m}+\mathbf{g},\sigma}, \quad (13)$$

where $W = -E_p + A_0$. Here, we have dropped the term proportional to E_p in the Hamiltonian; for a fixed average number of electrons N_e, that term is equal to the constant $-E_pN_e$. The parameter W is the difference between quantities that are not small (for strong EVC), and, therefore, its magnitude and sign can be arbitrary. (Note that we always have $|W| < E_p$.) Hamiltonian (1) has two dimensionless parameters: η (which does not depend on the ion mass M) and the adiabaticity parameter (AP) $\nu = |J|/\hbar\omega \propto M^{1/2}$. This perturbation theory is applicable in the "antiadiabatic" limit $\nu < 1$. In the adiabatic limit $\nu > 1$, the effective parameters of Hamiltonian (3) change [15] but the exponential factors $\exp(-E_p/\hbar\omega)$ are retained.

In the case of strong EVC, the factor $\exp(-E_p/\hbar\omega)$ in the expression for J^* results in a substantial increase in its sensitivity to variations in the isotopic composition, while E_p (and, hence, W) remains only weakly dependent on the isotopic composition.

We assume $n < 1$, where $n = N_e/N$. The $n > 1$ case reverses to the case of $n < 1$ as one crosses over from electrons to holes. In what follows, we shall consider the case of Hubbard attraction $W < 0$[4] in the "strong-coupling" limit[5]:

$$|W| \gg |J^*|, \quad |W| \gg \hbar\omega, \quad (14)$$

where the band term $\bar{V}$ is a small correction to the Hubbard term H_H.

[3] The quantity E_p in [14] is one half the quantity E_p introduced by Holstein in [3, 4] and used in this work.

[4] The Hubbard model with attraction was considered in [16]. The polaron model reduces the Hubbard model only to the lowest order in J. To higher orders, one has to take into account the operator character of the quantities $\exp(\pm i\beta p)$ (see Appendix 1).

[5] We use quotation marks, because this is how one frequently refers to the models in which the condition opposite to Eq. (14) is realized.

3. THE GROUND STATE

The crucial factor in the problem under study is that the ground state of the Hamiltonian $H_{\rm H}$ in Eqs. (13) is strongly degenerate. For $W < 0$, $N_e/2$ lattice sites in this state are occupied by pairs and the remaining ones are empty. Its energy is $E_0(N_e) = -|W|N_e$ and does not depend on the location of the occupied sites. The degeneracy is $C^N_{N_e/2}$-fold, and the entropy and heat capacity at $T = 0$ are nonzero (we recall that $n \le 1$):

$$S_0 = -Nk\left(\frac{n}{2}\ln\frac{n}{2} + \left(1-\frac{n}{2}\right)\ln\left(1-\frac{n}{2}\right)\right),$$
$$C_0 = \frac{Nk}{2}\ln\frac{2-n}{n}. \tag{15}$$

Therefore, the Nernst principle fails in the system under consideration. This excess degeneracy means that $H_{\rm H}$ does not fully define the system (for instance, its spatial dimension is not defined: the system can be realized in a space of arbitrary dimension n).

This uncertainty can be removed by adding the term λV_r to $H_{\rm H}$, which lifts the above degeneracy. However, the characteristic features of the ground state of the system with the Hamiltonian $H_{\rm H} + \lambda V_r$ depend substantially on the actual form of V_r, such that, for $\lambda \longrightarrow 0$, the extreme ground states can also be different for different V_r.

In our case, the part of V_r is played by the band term $\bar{V}$ ($\lambda = 1$). For V_r, one could accept a term of the type of a "localized-pair transfer,"

$$\sum_{\mathbf{m},\,\mathbf{m}',\,\mathbf{m}\neq\mathbf{m}'} A(\mathbf{m},\mathbf{m}')a^+_{\mathbf{m}\uparrow}a^+_{\mathbf{m}\downarrow}a_{\mathbf{m}'\downarrow}a_{\mathbf{m}'\uparrow}. \tag{16}$$

This would have led us to the bipolaron pattern [1, 2]. However, in the Holstein model of Eqs. (1) considered here, which disregards the vibration dispersion, the quantity A, as already mentioned, is of the order $\exp(-4E_p/\hbar\omega)$. By applying perturbation theory in J to Hamiltonian (6), one can also obtain, in second order, a term of the type of Eq. (16), which turns out to be proportional to $\exp(-2(E_p + |W|)/\hbar\omega)$ (see Appendix 1). Therefore, under strong-coupling conditions, term (16) is exponentially small compared to the band term, which is proportional to $\exp(-E_p/\hbar\omega)$ and whose contribution to the energy is proportional to $\exp(-2E_p/\hbar\omega)$: in other words, the bipolaron mechanism does not operate here. (Taking the vibration dispersion into account may favor realization of the bipolaron situation.)

Let us introduce the chemical potential μ into Hamiltonian (13):

$$\tilde{H} = H - \mu\hat{N}_e = H_{\rm H} + \bar{V} - \mu\hat{N}_e. \tag{17}$$

The characteristic thermodynamic function for Hamiltonian (17) will be the potential $\Omega(T, \mu) = E - \mu N_e$, where $E(T, N_e)$ is the thermodynamic average of the Hamiltonian H in Eqs. (13). Because our system assumes an off-diagonal long-range order (ODLRO), the number of particles is not fixed and N_e should be interpreted as the average number of particles. For $T \longrightarrow 0$, Ω and E tend to the ground-state averages of $\tilde{H}$ and H, respectively. Crossing over to the $\mathbf{k}$ representation, we obtain

$$\tilde{H} = \sum_{\mathbf{k}\sigma}(\varepsilon_{\mathbf{k}} - \mu)a^+_{\mathbf{k}\sigma}a_{\mathbf{k}\sigma} + \frac{2W}{N}\sum_{\{k\}}\delta_{\mathbf{k}_1-\mathbf{k}_2,\,\mathbf{k}_4-\mathbf{k}_3}a^+_{\mathbf{k}_1\uparrow}a_{\mathbf{k}_2\uparrow}a^+_{\mathbf{k}_3\downarrow}a_{\mathbf{k}_4\downarrow}. \tag{18}$$

Here, $\sum_{\mathbf{k}}$ denotes summation over the Brillouin zone,

$$\varepsilon_{\mathbf{k}} = \sum_{\mathbf{g}} J^*(\mathbf{g})e^{i\mathbf{k}\mathbf{g}}, \tag{19}$$

and, without loss of generality, one can impose the condition

$$\sum_{\mathbf{k}}\varepsilon_{\mathbf{k}} = 0. \tag{20}$$

In Eq. (18), only the terms that satisfy the conditions $\mathbf{k}_1 = \mathbf{k}_2$, $\mathbf{k}_3 = \mathbf{k}_4$, or $\mathbf{k}_1 + \mathbf{k}_3 = \mathbf{k}_2 + \mathbf{k}_4 = 2\mathbf{q}$ are significant in the subsequent consideration. Here, $2\mathbf{q}$ has the meaning of the momentum of a Cooper pair. We shall look for the ground-state eigenfunction of Hamiltonian (18) in the BCS form:

$$\Psi^{\{\mathbf{q}\}}_{\rm BCS} = \prod_{\mathbf{k}}(u_{\mathbf{k}} + e^{i\chi(\mathbf{k})}v_{\mathbf{k}}a^+_{\mathbf{k}+\mathbf{q}\uparrow}a^+_{-\mathbf{k}+\mathbf{q}\downarrow})|0\rangle,$$
$$u^2_{\mathbf{k}} + v^2_{\mathbf{k}} = 1, \tag{21}$$

where $u_{\mathbf{k}}$ and $v_{\mathbf{k}}$ are variational parameters (positive numbers) and $\chi(\mathbf{k})$ is an arbitrary real function of $\mathbf{k}$.

The expectation value $\Omega^{(0)}$ of the $\tilde{H}$ operator for the $\Psi^{\{0\}}_{\rm BCS}$ state is expressed through the expectation values of the operator combinations

$$\bar{n}_{\mathbf{k}\uparrow} = \bar{n}_{-\mathbf{k}\downarrow} = v^2_{\mathbf{k}}, \quad \overline{a^+_{\mathbf{k}\uparrow}a^+_{-\mathbf{k}\downarrow}} = e^{-i\chi(\mathbf{k})}u_{\mathbf{k}}v_{\mathbf{k}} \tag{22}$$

and is equal to

$$\left\langle\Psi^{\{0\}}_{\rm BCS}\middle|\tilde{H}\middle|\Psi^{\{0\}}_{\rm BCS}\right\rangle = \sum_{\mathbf{k}}(\varepsilon_{\mathbf{k}} - \mu)2v^2_{\mathbf{k}} + \frac{2W}{N}\left(\sum_{\mathbf{k}}v^2_{\mathbf{k}}\right)^2 + \frac{2W}{N}\left|\sum_{\mathbf{k}}e^{-i\chi(\mathbf{k})}u_{\mathbf{k}}v_{\mathbf{k}}\right|^2. \tag{23}$$

For $W < 0$, quantity (23) reaches a minimum when $\chi(\mathbf{k}) = \text{const}$ [17]; i.e., there is a phase coherence in $\mathbf{k}$ space characteristic of the BCS approach (in what fol-

lows, we assume $\chi = 0$). We denote $u_{\mathbf{k}} = \cos\theta_{\mathbf{k}}$ and $v_{\mathbf{k}} = \sin\theta_{\mathbf{k}}$. Then,

$$n = \frac{1}{N}\sum_{\mathbf{k}} 2v_{\mathbf{k}}^2 = \frac{1}{N}\sum_{\mathbf{k}}(1-\cos 2\theta_{\mathbf{k}}),$$
$$r = \frac{1}{N}\sum_{\mathbf{k}} u_{\mathbf{k}}v_{\mathbf{k}} = \frac{1}{2N}\sum_{\mathbf{k}}\sin 2\theta_{\mathbf{k}}. \quad (24)$$

Here, $n = N_e/N$ is the average electron concentration and

$$r = \frac{1}{2N}\overline{\sum_{\mathbf{k}}(a_{\mathbf{k}\uparrow}^{+}a_{-\mathbf{k}\downarrow}^{+} + a_{-\mathbf{k}\downarrow}a_{\mathbf{k}\downarrow})}$$

is the ODLRO parameter (we note that it is defined only if the above phase coherence exists). Equation (23) takes the form

$$\Omega^{(0)} = \sum_{\mathbf{k}}(\varepsilon_{\mathbf{k}}-\mu)(1-\cos 2\theta_{\mathbf{k}}) + \frac{1}{2}WNn^2 + 2WNr^2. \quad (25)$$

Using Eqs. (24), from the necessary condition of the minimum $\partial\Omega^{(0)}/\partial\theta_{\mathbf{k}} = 0$ for $\mu = \text{const}$, we obtain

$$\cos 2\theta_{\mathbf{k}} = \pm\frac{\varepsilon_{\mathbf{k}}-\mu+Wn}{\sqrt{(\varepsilon_{\mathbf{k}}-\mu+Wn)^2+Q^2}},$$
$$\sin 2\theta_{\mathbf{k}} = \mp\frac{Q}{\sqrt{(\varepsilon_{\mathbf{k}}-\mu+Wn)^2+Q^2}}. \quad (26)$$

The minimum is attained for the upper sign. The values of n and r at which the minimum is reached are related to μ and the Hamiltonian parameters through

$$n = \frac{1}{N}\sum_{\mathbf{k}}\left(1-\frac{\varepsilon_{\mathbf{k}}-\mu+Wn}{\sqrt{(\varepsilon_{\mathbf{k}}-\mu+Wn)^2+Q^2}}\right), \quad (27)$$

$$Q = -\frac{1}{N}\sum_{\mathbf{k}}\frac{WQ}{\sqrt{(\varepsilon_{\mathbf{k}}-\mu+Wn)^2+Q^2}}. \quad (28)$$

We have denoted here $Q = 2|W|r$. A nontrivial solution $Q \neq 0$ exists only for $W < 0$ (we will consider only this case in what follows). The quantity $\Omega^{(0)}$ and the ground-state energy $E^{(0)} \equiv \langle H\rangle$ of Hamiltonian (13) are related through $\Omega^{(0)} = E^{(0)} - \mu N_e$. Taking into account Eq. (20), we obtain the following expression for $E^{(0)}$ at the minimum:

$$E^{(0)} = -N_eE_p - N(1-n)\mu + \frac{1}{2}N\frac{Q^2}{|W|} - N|W|\frac{n(2-n)}{2} - \sum_{\mathbf{k}}\sqrt{(\varepsilon_{\mathbf{k}}-\bar{\mu})^2+Q^2}. \quad (29)$$

We denoted $\bar{\mu} = \mu + |W|n$. Equation (29) contains the polaron energy shift $-N_eE_p$, which was dropped in Eqs. (13). In the limit as $\varepsilon_{\mathbf{k}} \longrightarrow 0$, Eqs. (27) and (28) yield

$$\mu = -|W|, \quad \sqrt{\bar{\mu}^2 - Q^2} = |W|,$$
$$Q^2 = W^2n(2-n). \quad (30)$$

Substituting Eqs. (30) into Eq. (29), we come to $E^{(0)}|_{\varepsilon\to 0} = E_0 = -N_e(E_p + |W|)$ and $\Omega^{(0)}|_{\varepsilon\to 0} = 0$.[6] In the strong-coupling case of Eq. (14), one may restrict oneself in Eqs. (27)–(29) to expansion to the lowest [second, because of Eq. (20)] order in ε. We thus obtain

$$E^{(0)} \approx E_0 - \Delta E^{(0)}, \quad (31)$$

$$\Delta E^{(0)} = N\frac{Q^2(\varepsilon \longrightarrow 0)}{2W^2}\frac{\mathscr{E}}{|W|} = N\frac{n(2-n)}{2}\frac{\mathscr{E}}{|W|}, \quad (32)$$

$$\mathscr{E} = \frac{1}{N}\sum_{\mathbf{k}}\varepsilon_{\mathbf{k}}^2 = \sum_{\mathbf{g}} J^{*2}(\mathbf{g}) > 0; \quad (33)$$

i.e., inclusion of the band term reduces the energy. The difference ΔE_{sn} between energy (31) and that of the normal state ($Q = 0$) can be written as

$$\Delta E_{\text{sn}} = -N_e|W|\frac{2-n}{2} + O(J^*, J^{*2}/|W|); \quad (34)$$

i.e., in the strong-coupling case, the energy of the state with $Q \neq 0$ is always lower than that of the normal state. The electron distribution $n_{\mathbf{k}}$ in $\mathbf{k}$ in the ODLRO state is

$$n_{\mathbf{k}} \equiv 2v_{\mathbf{k}}^2 = n\left(1-(2-n)\frac{\varepsilon_{\mathbf{k}}}{|W|}\right) + O(J^{*2}/W^2) \quad (35)$$

and differs from $n_{\mathbf{k}} = \text{const}$ only in small terms of order $\sim J^*/|W|$. As follows from band theory, $\varepsilon_{\mathbf{k}}$ is an analytic function of $\mathbf{k}$ and, therefore, $n_{\mathbf{k}}$ is also an analytic function. In the opposite, weak-coupling case of $|J^*| \gg |W|$, the function $n_{\mathbf{k}}$ has the form of a stepwise Fermi function broadened analytically in the vicinity of the Fermi surface (as in the models of BCS, Éliashberg, etc.).

The characteristic features of the state under consideration are already seen clearly at this stage. For instance, phase fluctuations, causing breakdown of the phase coherence, are accompanied, according to Eq. (23), by a change in energy on the order of $|W|$; therefore, one may expect the phase transition temper-

[6] Equations (27) and (28) for Hamiltonian (13) were derived for $W < 0$ in [16]. Thereafter, the authors of [16] deviate, however, from the BCS approach by invoking the Bose operators and the results they obtained differ substantially from those presented below.

ature T_c to be of the order of $|W|$ and the critical current to be small because of the polaron-induced band narrowing.

4. WAVE FUNCTION

Using the properties of the Fermi operators, one can cast the ground-state wave function (21) for $\mathbf{q} = 0$ and $\chi = \text{const} \neq 0$ as [18, 19]

$$\Psi^{(0)}_{\text{BCS}}(\chi) = \left(\prod_{\mathbf{k}} u_{\mathbf{k}}\right)\exp\left(\sum_{\mathbf{k}} e^{i\chi}\frac{v_{\mathbf{k}}}{u_{\mathbf{k}}}a^{+}_{\mathbf{k}\uparrow}a^{+}_{-\mathbf{k}\downarrow}\right)|0\rangle. \quad (36)$$

This state is degenerate with the only degeneracy parameter χ. Crossing over to the Wannier functions and taking into account Eqs. (26) and (30), as well as that $u > 0$ and $v > 0$, we find that, for $\varepsilon \longrightarrow 0$, the $\Psi^{(0)}_{\text{BCS}}$ function tends to

$$\prod_{\mathbf{m}}\left(\sqrt{\frac{2-n}{2}} + e^{i\chi}\sqrt{\frac{n}{a}}a^{+}_{\mathbf{m}\uparrow}a^{+}_{\mathbf{m}\downarrow}\right)|0\rangle. \quad (37)$$

As for the ground-state eigenfunctions of the Hamiltonian H_{H}, they can be written as

$$\prod_{\mathbf{m}}\left(\sqrt{\frac{2-n}{2}} + e^{i\chi_{\mathbf{m}}}\sqrt{\frac{n}{2}}a^{+}_{\mathbf{m}\uparrow}a^{+}_{\mathbf{m}\downarrow}\right)|0\rangle. \quad (38)$$

The degeneracy parameter is a set of N numbers $\chi_{\mathbf{m}}$. The volume of the subspace of functions (37) is much less than that of the space of functions (38); therefore, the Nernst principle holds for Eq. (37). Introducing operators $\hat{R}(\mathbf{m})$,

$$\hat{R}(\mathbf{m}) = \frac{1}{2}\sum_{\mathbf{G}} S(\mathbf{G})(a^{+}_{\mathbf{m}\uparrow}a^{+}_{\mathbf{m}-\mathbf{G}\downarrow} + a^{+}_{\mathbf{m}-\mathbf{G}\uparrow}a^{+}_{\mathbf{m}\downarrow}),$$
$$S(\mathbf{G}) = e^{i\chi}\sum_{\mathbf{k}}\frac{v_{\mathbf{k}}}{u_{\mathbf{k}}}e^{i\mathbf{k}\mathbf{G}}, \quad (39)$$

($\sum_{\mathbf{G}}$ is the sum over lattice sites), Eq. (36) can be recast as

$$\Psi^{(0)}_{\text{BCS}} = \text{const}\prod_{\mathbf{m}}\exp\hat{R}_{\mathbf{m}}|0\rangle. \quad (40)$$

The quantity $v_{\mathbf{k}}/u_{\mathbf{k}}$ is a periodic function of $\mathbf{k}$ and analytical on the real axis for all $\mathbf{k}$ directions. Therefore, as $|\mathbf{G}| \longrightarrow \infty$, $S(\mathbf{G})$ decays exponentially (more exactly, faster than any power of $1/|\mathbf{G}|$). When acting on a vacuum $|0\rangle$, the operator $\exp\hat{R}_{\mathbf{m}}$ creates an electronic cluster centered on site $\mathbf{m}$, and the contribution to it due to the states with indices $\mathbf{m} + \mathbf{G}$ falls off exponentially for $|\mathbf{G}| \longrightarrow \infty$ with a characteristic scale length of the order of the lattice constant a_0. In the weak-coupling case, the ground-state wave function has a form and properties similar to those of Eq. (40), but its characteristic decay length is of the order of the correlation length $\sim\hbar v_{\text{F}}/kT_c \gg a_0$.[7] In both cases, the correlators of the $\langle A(\mathbf{r})B(\mathbf{r}')\rangle$ type decrease faster than any power of $|\mathbf{r} - \mathbf{r}'|^{-1}$ as $|\mathbf{r} - \mathbf{r}'| \longrightarrow \infty$ [19].

Thus, the ground-state wave function of a superconductor is created by the action of the product $\prod_{\mathbf{m}}$ of the above-mentioned electronic clusters on a vacuum. We note that Kohn [20] argued that such a structure of the wave function (but without ODLRO) is typical of the dielectric state and is not based on model concepts. The arguments were specified in [21]. It has been demonstrated using a number of examples [19] that such a structure characterizes rather the Mott localization and is inherent not only in the dielectric state but also in BCS-type superconductor models.

5. CURRENT STATES

Consider the case where the parameter $\mathbf{q}$ in Eq. (21) is other than zero. The result of the minimization is given by Eqs. (27)–(29), in which one has to make a replacement,

$$\varepsilon_{\mathbf{k}} \longrightarrow \frac{1}{2}(\varepsilon_{\mathbf{k}+\mathbf{q}} + \varepsilon_{\mathbf{k}-\mathbf{q}}) \equiv \varepsilon(\mathbf{k}, \mathbf{q}). \quad (41)$$

Expansion (31) assumes the form

$$\langle H\rangle^{(\mathbf{q})} = E^{(\mathbf{q})} = E_0 - N\frac{n(2-n)}{2}\frac{\mathscr{E}(\mathbf{q})}{|W|}, \quad (31a)$$

$$\mathscr{E}(\mathbf{q}) = \frac{1}{4N}\sum_{\mathbf{k}}(\varepsilon_{\mathbf{k}+\mathbf{q}} + \varepsilon_{\mathbf{k}-\mathbf{q}})^2$$
$$= \frac{1}{2}\sum_{\mathbf{g}} J^{*2}(\mathbf{q})(1 + \cos 2\mathbf{q}\mathbf{g}). \quad (33a)$$

Obviously enough, $\mathscr{E}(\mathbf{q})$ is a periodic function of $\mathbf{q}$ with a period equal to one half the reciprocal lattice vector. The particle flux operator $\hat{\mathbf{I}}$ is given by the relation of the band theory

$$\hat{\mathbf{I}} \equiv \frac{1}{m}\int_{\mathscr{V}} d\mathbf{r}\sum_{\sigma}(\psi^{+}_{\sigma}(\mathbf{r})\hat{\mathbf{p}}\psi_{\sigma}(\mathbf{r}) - \hat{\mathbf{p}}\psi^{+}_{\sigma}(\mathbf{r})\psi_{\sigma}(\mathbf{r}))$$
$$= \frac{1}{\hbar}\sum_{\mathbf{k}}\frac{\partial\varepsilon_{\mathbf{k}}}{\partial\mathbf{k}}(\hat{n}_{\mathbf{k}\uparrow} + \hat{n}_{\mathbf{k}\downarrow}), \quad (42)$$

where $\mathscr{V}$ is the volume of the system. It is assumed that the operators $\psi^{+}_{\sigma}(\mathbf{r})$ and $\psi_{\sigma}(\mathbf{r})$ meet boundary conditions (for instance, cyclic boundary conditions) which make the momentum operator $\hat{\mathbf{p}} = -i\hbar\nabla$ Hermitian in the volume of the system.

[7] One will have, naturally, to ignore the traditional momentum cutoff.

Let a sample be a right circular cylinder of length L with its axis oriented along a unit vector $\mathbf{e}_0$ ($\mathbf{e}_0^2 = 1$), and let a particle flow pass through the bases. Then, the average flux $\bar{\mathbf{I}}$ is directed along $\mathbf{e}_0$ and $\bar{I} = \mathbf{e}_0 LI$, where I is the total particle flux through the cylinder cross section. Recalling the results obtained in Section 3 and taking into account Eq. (41) and $\mathbf{q} = q\mathbf{e}_0$, one readily sees that current I in state (21) can be written in the lowest order in ε as

$$I(q) = -\frac{N}{L}\frac{Q^2(\varepsilon \longrightarrow 0)}{2W^2}\frac{1}{\hbar}\frac{\partial}{\partial q}\frac{\mathscr{E}(q, \mathbf{e}_0)}{|W|} = -\frac{N}{L}\frac{n(2-n)}{2}\frac{1}{\hbar}\frac{\partial}{\partial q}\frac{\mathscr{E}(q, \mathbf{e}_0)}{|W|}, \quad (43)$$

$$\mathscr{E}(q, \mathbf{e}_0) = \frac{1}{2}\sum_{\mathbf{g}} J^{*2}(\mathbf{g})[1 + \cos 2q(\mathbf{e}_0\mathbf{g})];$$

i.e., it is proportional to the derivative of the energy of Eq. (31a) with respect to q. Introducing the notation $E^{(q\mathbf{e}_0)} = E(q)$, we obtain from Eqs. (31a) and (43)

$$I(q) = \frac{1}{\hbar L}\frac{\partial}{\partial q}E(q). \quad (44)$$

Thus, for a given configuration (orientation of the current relative to the crystal axes), the current state of the system is characterized by the scalar parameter q ($-\infty < q < +\infty$) and its energy is a function of q.

Equation (44) is a particular case of a general thermodynamic relation.[8] It is based on the assumption of the existence of a thermodynamically equilibrium current state (and does not make use of any ideas concerning the nature of the phenomenon). A direct consequence of this assumption is the existence of a thermodynamic parameter q characterizing such a state. The current I is given by Eq. (44). The condition of stability of the equilibrium current state is

$$\left(\frac{\partial I}{\partial q}\right)_S > 0. \quad (45)$$

[Note that the solution to the problem of the critical current in a film [24] obtained in terms of the Landau–Ginzburg theory is based essentially on the thermodynamic relations (44) and (45).] In our case, we have

$$I(q) = \frac{Nn(2-n)}{2L\hbar|W|}\sum_{\mathbf{g}} J^{*2}(\mathbf{g})(\mathbf{e}_0\mathbf{g})\sin[2q(\mathbf{e}_0\mathbf{g})], \quad (46)$$

$$\frac{dI}{dq} = \frac{Nn(2-n)}{L\hbar|W|} \times \sum_{\mathbf{g}} J^{*2}(\mathbf{g})(\mathbf{e}_0\mathbf{g})^2\cos[2q(\mathbf{e}_0\mathbf{g})] > 0. \quad (47)$$

In the approximation used, the boundary of stability is determined by the $\varepsilon_{\mathbf{k}}$ relation. The current $I(q)$ is a bounded and analytic function of q within the $-\infty < q < +\infty$ region; therefore, regions of instability, where $\partial I/\partial q < 0$, always exist for any values of the parameters of the problem. The maximum of the modulus of the electric current J_c is, in order of magnitude,

$$|J_c| = Se\bar{n}\left(\frac{J^*}{W}\right)^2\frac{a_0|W|}{\hbar}, \quad \bar{n} = na_0^{-3}, \quad S = N^{2/3}a_0^2, \quad (48)$$

where a_0 is the lattice constant.

6. EXCITATION SPECTRUM

We first find the excitation spectrum above the $\mathbf{q} = 0$ ground state, obtained in the preceding pages, using the self-consistent field (SCF) approach. We introduce the model Hamiltonian

$$H(0) = \sum_{\mathbf{k}\sigma}(\varepsilon_{\mathbf{k}} - \mu)a^+_{\mathbf{k}\sigma}a_{\mathbf{k}\sigma} + \frac{2W}{N}\sum_{\{\mathbf{k}, \mathbf{k}'\}} n_{\mathbf{k}\uparrow}n_{\mathbf{k}'\downarrow} + \frac{2W}{N}\sum_{\{\mathbf{k}, \mathbf{k}'\}} a^+_{\mathbf{k}\uparrow}a^+_{-\mathbf{k}\downarrow}a_{-\mathbf{k}'\downarrow}a_{\mathbf{k}'\uparrow}. \quad (49)$$

The earlier estimate of the renormalization factor $\exp(-E_p/\hbar\omega)$ of the quantity J entering $\varepsilon_{\mathbf{k}}$ is inapplicable near the phase transition, because the transition temperature is of the order $|W| \gg \hbar\omega$. Using the SCF formalism, the renormalization can be defined as the SCF average

$$J\langle \exp(i\beta p_{\mathbf{m}})\exp(-i\beta p_{\mathbf{m}+\mathbf{g}})\rangle = J^*(T),$$

which was determined by the self-consistency condition. The major contribution is due to averaging over noninteracting vibrations, which yields

$$J^*(T) = J\exp\left(-\frac{E_p}{\hbar\omega}\frac{1}{1 - \exp(-\hbar\omega/kT)}\right) \quad (50)$$

(temperature-induced band narrowing [25]), while the self-consistency procedure will entail only small corrections $\sim(J^*/E_p)^2$.

We introduce the SCF quantities $\bar{n}_{\mathbf{k}\sigma}$ and $\overline{a^+_{\mathbf{k}\uparrow}a^+_{-\mathbf{k}\downarrow}}$:

$$n_{\mathbf{k}\uparrow}n_{\mathbf{k}'\downarrow} \longrightarrow \bar{n}_{\mathbf{k}\uparrow}n_{\mathbf{k}'\downarrow} + n_{\mathbf{k}\uparrow}\bar{n}_{\mathbf{k}'\downarrow} - \bar{n}_{\mathbf{k}\uparrow}\bar{n}_{\mathbf{k}'\downarrow}, \quad (51)$$

[8] The author has to refer to his own paper [22] (see also [23]), because he could not locate a similar treatment in the literature. Such a treatment could have appeared as far back as the times of Kamerlingh Onnes (1911). Appendix 2 presents a brief exposition of [22].

$$a^+_{\mathbf{k}\uparrow}a^+_{-\mathbf{k}\downarrow}a_{-\mathbf{k}'\downarrow}a_{\mathbf{k}'\uparrow} \longrightarrow \overline{a_{-\mathbf{k}'\downarrow}a_{\mathbf{k}'\uparrow}}a^+_{\mathbf{k}\uparrow}a^+_{-\mathbf{k}\downarrow} + \overline{a^+_{\mathbf{k}\uparrow}a^+_{-\mathbf{k}\downarrow}}a_{-\mathbf{k}'\downarrow}a_{\mathbf{k}'\uparrow} - \overline{a_{-\mathbf{k}'\downarrow}a_{\mathbf{k}'\uparrow}}\,\overline{a^+_{\mathbf{k}\uparrow}a^+_{-\mathbf{k}\downarrow}}. \quad (52)$$

(Subtraction of the products of the averages is necessary for correct determination of the ground-state energy.) We set all quantities to be real and $\bar{n}_{\mathbf{k}\uparrow} = \bar{n}_{\mathbf{k}\downarrow}$. Then, the SCF Hamiltonian takes the form

$$H_M(0) = \sum_{\mathbf{k}\sigma}(\varepsilon_{\mathbf{k}} - \mu)n_{\mathbf{k}\sigma} - \frac{|W|}{N}\sum_{\mathbf{k}'\sigma'}\bar{n}_{\mathbf{k}'\sigma'}\sum_{\mathbf{k}\sigma}n_{\mathbf{k}\sigma} - \frac{2|W|}{N}\sum_{\mathbf{k}'}\overline{a_{-\mathbf{k}'\downarrow}a_{\mathbf{k}'\uparrow}}\sum_{\mathbf{k}}(a^+_{\mathbf{k}\uparrow}a^+_{-\mathbf{k}\downarrow} + a_{-\mathbf{k}\downarrow}a_{\mathbf{k}\uparrow}).$$

Following the standard procedure, we obtain an excitation Hamiltonian of the form

$$H_{\text{ex}} = E^{(0)} + \sum_{\mathbf{k}}\zeta_{\mathbf{k}}(\alpha^+_{\mathbf{k}}\alpha_{\mathbf{k}} + \beta^+_{\mathbf{k}}\beta_{\mathbf{k}}), \qquad \zeta_{\mathbf{k}} = \sqrt{(\varepsilon_{\mathbf{k}} - \bar{\mu})^2 + Q^2}. \quad (53)$$

This procedure can be performed for the state described by Eq. (21) with $\mathbf{q} \neq 0$. The result has the form of Eq. (53), where $E^{(0)}$ is replaced by $E^{(\mathbf{q})}$ and $\zeta_{\mathbf{k}}$ by

$$\zeta(\mathbf{k};\mathbf{q}) = \sqrt{(\varepsilon(\mathbf{k},\mathbf{q}) - \bar{\mu})^2 + Q^2} \pm \frac{\varepsilon_{\mathbf{k}+\mathbf{q}} - \varepsilon_{\mathbf{k}-\mathbf{q}}}{2}. \quad (54)$$

Equations (53) and (54) are valid for $W < 0$ and an arbitrary relation between J^* and $|W|$. [The criterion of stability given by Eq. (45) is in no way connected with the properties of the excitation spectrum $\zeta(\mathbf{k})$.]

In the strong-coupling case of Eq. (14), the quantities ζ are positive for all $\mathbf{k}$ an $\mathbf{q}$ and, in the $\varepsilon \longrightarrow 0$ limit, taking into account Eq. (30), can be written as

$$\zeta_0 = \sqrt{\bar{\mu}^2 + Q^2} = |W|. \quad (55)$$

The ground-state stability rests, within the approach used, on the $\zeta > 0$ condition. According to Eqs. (31a) and (33a), the correction to the energy due to the current is of the order of $\sim J^{*2}/|W|$; i.e., it is small compared to the energy ($\sim|W|$) associated with ODLRO. Breakdown of criterion (45) brings about rearrangement of the current system (for instance, the formation of a vortex structure) but not destruction of the ODLRO (type-II superconductor [26]).

In the weak-coupling limit, substantial changes occur in the immediate vicinity of the Fermi surface and critical phenomena are initiated by excitations of negative energy, $\zeta(\mathbf{k};\mathbf{q}) < 0$. Such excitations arise when the following condition (Landau criterion) is met: $q > q_c = 2\Delta/\hbar v_F$, where Δ is the gap parameter and v_F is the velocity at the Fermi surface. The energy associated with the critical current, $\sim\hbar^2 q_c k_F/m$, turns out to be of the order of Δ. In this case, one should expect the ODLRO to be destroyed by the current (type-I superconductor, Silsbee's rule). Reaching beyond the scope of this model (for instance, an explicit inclusion of magnetic field) may change the situation.

Using the variational principle of Bogolyubov–Feynman [27, 28], one can find the free energy in the approximation corresponding to the SCF approach. For $\varepsilon \longrightarrow 0$, we obtain such expressions for the entropy $S(T)$ and heat capacity $C(T)$:

$$S = 2Nk\frac{|W|}{kT}\exp\left(-\frac{|W|}{kT}\right), \qquad C = 2Nk\frac{|W|}{kT}\left(\frac{|W|}{kT} - 1\right)\exp\left(-\frac{|W|}{kT}\right). \quad (56)$$

At low temperatures ($kT < |W|$), the Nernst principle obviously holds and C is always positive. One can readily verify that the heat capacity is also positive for a finite $\varepsilon_{\mathbf{k}}$ that is small compared to $|W|$.

7. PHASE TRANSITION

Using the results obtained in Section 5, one can derive the SCF relations defining μ and Q for a finite temperature:

$$n = \frac{1}{N}\times\sum_{\mathbf{k}}\left(1 - \frac{\varepsilon_{\mathbf{k}} - \bar{\mu}}{\sqrt{(\varepsilon_{\mathbf{k}} - \bar{\mu})^2 + Q^2}}\tanh\frac{\sqrt{(\varepsilon_{\mathbf{k}} - \bar{\mu})^2 + Q^2}}{2kT}\right), \quad (57)$$

$$Q = |W|\frac{1}{N}\times\sum_{\mathbf{k}}\frac{Q}{\sqrt{(\varepsilon_{\mathbf{k}} - \bar{\mu})^2 + Q^2}}\tanh\frac{\sqrt{(\varepsilon_{\mathbf{k}} - \bar{\mu})^2 + Q^2}}{2kT}. \quad (58)$$

In the strong-coupling approximation, one can ignore terms $\sim J^{*2}/W^2$ and set $\varepsilon = 0$. This yields

$$\frac{1}{|W|} = \frac{1}{\sqrt{\bar{\mu}^2 + Q^2}}\tanh\left(\frac{\sqrt{\bar{\mu}^2 + Q^2}}{2kT}\right), \qquad \bar{\mu} = -(1-n)|W|. \quad (59)$$

The transition temperature T_c is defined by the expression

$$\frac{kT_c}{|W|} = \frac{1}{2}\frac{1-n}{\operatorname{arctanh}(1-n)} + O\left(\frac{J^{*2}}{W^2}\right) \quad (60)$$

(Fig. 2). The maximum $T_c = |W|/2$ is reached at $n = 1$. Only the small correction in Eq. (60) is sensitive to isotope substitution.

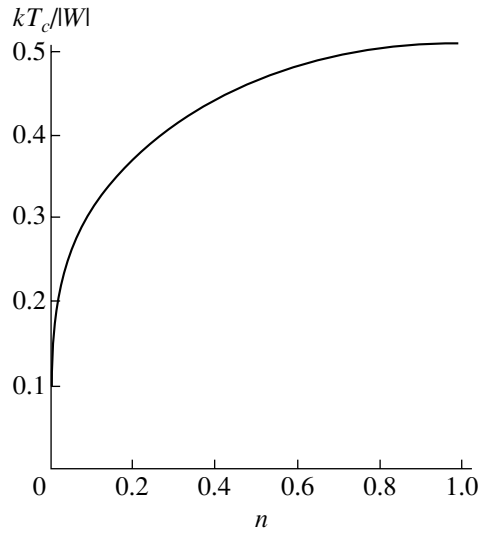

Fig. 2. Transition temperature plotted vs. electron concentration.

8. DISCUSSION OF RESULTS

The above consideration permits the following conclusions:

(1) The mechanism studied is qualitatively similar to the BCS approach; in both cases, the Fermi singularity in $n_{\mathbf{k}}$ vanishes. The Cooper instability against electron–electron attraction plays a dominant role. The difference bears only a quantitative character; more specifically, in the case of weak coupling, the break in the immediate vicinity of the Fermi surface smooths out, while in the strong-coupling case, the rearrangement extends over the whole Brillouin zone and $n_{\mathbf{k}}$ is nearly constant within it.

(2) In the strong-coupling limit, T_c is of the order of $|W|/k$. Note the substantial difference from the boson models, where T_c tends to zero as $|W| \longrightarrow \infty$ because the corresponding coupling constant is proportional to $\sim|W|^{-1}$.

(3) The attainable values of the current in a finite band are limited in magnitude [see Eq. (48)], and all phenomena associated with diamagnetic currents show a tendency to saturation with increasing magnetic field. Therefore, the thermodynamic critical field H_c in this limit is determined by the paramagnetic effect [29]: $H_c \propto |W|/\mu_0$, where μ_0 is the Bohr magneton.

The exponential band narrowing should correspond to small critical currents (low values of the first critical field H_{c1} and large penetration depths). The energy associated with the loss of current stability is small compared to kT_c (see Section 6). (A similar situation is observed in He^4, where the critical velocity estimated from the transition temperature is three orders of magnitude higher than the experimental value.) In the case of very narrow bands, the paramagnetic effect should, perhaps, be taken into account.

Thus, in the strong-coupling case, a superconductor exhibits the properties of a type-II superconductor, in which the paramagnetic limit can be reached. For $|W| \longrightarrow \infty$, a state with zero critical current and a high-temperature type-II transition is realized without any ordering.[9] It should be stressed that the high transition temperature is reached in this model at the expense of reduction of the characteristic currents (and of the magnetic fields induced by them).

(4) Different properties of the model depend differently on the isotopic composition. In the strong-coupling limit, T_c is determined by the magnitude of the polaron energy shift (which is ion-mass independent) and does not depend on the isotopic composition. The isotopic dependence of T_c becomes manifest with decreasing coupling [see Eq. (60)]. At the same time, the phenomena associated with electron transport exhibit an isotopic dependence because the electronic band narrows in proportion to $\propto \exp(-E_p/\hbar\omega)$; this dependence becomes progressively stronger with increasing EVC (the dependence on EVC has an exponential character).

(5) As the parameter $|W|$ varies continuously from negative to positive values (the Hubbard model with repulsion), it appears natural to expect the onset of a dielectric, magnetically ordered state for large enough $W > 0$.

Note that the simplest strong-coupling polaron model of the superconductor considered above exhibits two characteristic features of the HTSCs: (i) the lower critical field is small, while the upper critical field is very high [see item (3) above] (this was established at the very early stages of research), and (ii) the isotopic effect has a differentiated character [13] [item (4)]. The model also contains a possibility of describing the experimentally observed transition to a magnetically ordered state with varying composition [item (5)].

This paper did not touch on the fundamental issue of the realization of the case of single-site attraction $W < 0$. To clarify this situation, it would be expedient to investigate "small" models (the pair of electron–ion complexes shown in Fig. 1), with due inclusion of real polarization mechanisms.

ACKNOWLEDGMENTS

The author expresses warm gratitude to Yu.A. Firsov, A.V. Gol'tsev, L.I. Korovin, S.A. Ktitorov, and B.N. Shalaev for valuable discussions.

[9] The limiting transition should be correctly defined (see Section 3). The possibility of the onset of such a state was mentioned in [30, 31]. In this work, in contrast to [30], this state is a limiting state and does not form a phase.

APPENDIX 1

As follows from the results presented in Section 2, electron transfer between an empty and a single-electron state of a site entails the overcoming of an energy barrier E_p. In contrast, the barrier to be overcome for a electron transferring between an empty and a two-electron state is $4E_p$. Hubbard repulsion in Eq. (12) lowers this barrier. We estimate the corresponding contribution to the energy. A perturbation analysis carried to second order in J yields the following expression for the parameter $A(\mathbf{m}, \mathbf{m}') \equiv J^2\Xi$ in the term of the effective Hamiltonian in Eq. (16) describing the transfer of a pair as a whole from site $\mathbf{m}$ to site $\mathbf{m}'$:

$$\Xi = \sum_{s_1=0}^{\infty}\sum_{s_2=0}^{\infty}\frac{1}{2|W| + \hbar\omega(s_1+s_2)} \quad \text{(A1.1)}$$
$$\times\langle 0|\exp[i\beta(p_1-p_2)]|s_1, s_2\rangle\langle s_1, s_2|\exp[i\beta(p_1-p_2)]|0\rangle.$$

We have

$$\frac{1}{2|W| + \hbar\omega(s_1+s_2)} \equiv \int_0^{\infty}\exp[-(2|W| + \hbar\omega(s_1+s_2))\lambda]d\lambda.$$

Therefore,

$$\Xi = \int_0^{\infty} e^{-2|W|\lambda}\sum_{s_1=0}^{\infty}\exp(-\hbar\omega s_1\lambda)\langle 0|\exp(i\beta p_1)|s_1\rangle$$
$$\times\langle s_1|\exp(i\beta p_1)|0\rangle\sum_{s_2=0}^{\infty}\exp(-\hbar\omega s_2\lambda)$$
$$\times\langle 0|\exp(-i\beta p_2)|s_2\rangle\langle s_2|\exp(-i\beta p_2)|0\rangle d\lambda.$$

Let us go over to the second-quantized operators

$$p_i = i\sqrt{\frac{M\hbar\omega}{2}}(b_i^+ - b_i), \qquad i\beta p_i = -\gamma(b_i^+ - b_i), \quad \gamma = \sqrt{\frac{E_p}{\hbar\omega}} \quad \text{(A1.2)}$$

and introduce the function

$$S(\lambda) = \sum_{s_1=0}^{\infty} e^{-\hbar\omega s_1\lambda}\langle 0|\exp(-\gamma(b_1^+ - b_1))|s_1\rangle$$
$$\times\langle s_1|\exp(-\gamma(b_1^+ - b_1))|0\rangle.$$

We recast $\exp(-\hbar\omega s\lambda)\langle 0|\exp(i\beta p)|s\rangle$ as $\langle 0|\exp(\lambda H_c)\exp(i\beta p)\exp(-\lambda H_c)|s\rangle$, $H_c = \hbar\omega b^+ b$. Denoting $p(\lambda) = \exp(\lambda H_c)p\exp(-\lambda H_c)$, we represent $S(\lambda)$ in the form

$$S(\lambda) = \langle 0|e^{-\gamma[b^+(\lambda) - b(\lambda)]}e^{-\gamma(b^+ - b)}|0\rangle$$

(the subscripts on b and b^+ are dropped). Using the well-known relations for the Hermite polynomials [32] (see also [14]), we obtain

$$S(\lambda) = \exp[-\gamma^2(1 + e^{-\hbar\omega\lambda})].$$

The quantity Ξ can now be written as

$$\Xi = \int_0^{\infty} e^{-2|W|\lambda}(S(\lambda))^2 d\lambda \quad \text{(A1.3)}$$
$$= \frac{1}{\hbar\omega}\int_0^{\infty}\exp[-(2|W|/\hbar\omega)z]\exp\left(-2\frac{E_p}{\hbar\omega}(1+e^{-z})\right)dz.$$

Estimation by the steepest-descent method made for $E_p, |W| \gg \hbar\omega$ yields

$$\Xi = \sqrt{\frac{\pi}{|W|\hbar\omega}}\exp\left(-\frac{2E_p}{\hbar\omega}\right) \times\exp\left(-\frac{2|W|}{\hbar\omega}\left(1 - \ln\frac{|W|}{E_p}\right)\right). \quad \text{(A1.4)}$$

In comparison with the contribution due to the band term $\Delta E^{(0)}$ of Eq. (32) (which is proportional to $\sim\exp(-2E_p/\hbar\omega)$), one can see that there is an additional exponential smallness $\exp(-2|W|/\hbar\omega\alpha)$, where $\alpha > 1$.[10] In the Hubbard model without EVC, this term would be of the order of $\Delta E^{(0)}$.

APPENDIX 2

THERMODYNAMICS OF THE CURRENT STATE

The elementary work done on a current system is equal to [33]

$$\Delta\mathcal{A} = -\frac{1}{c}\int_{\mathcal{V}}\mathbf{j}(\mathbf{r})\Delta\mathbf{A}\,d\mathbf{r}, \quad \text{(A2.1)}$$

where $\mathbf{j}(\mathbf{r})$ is the current density in the system and $\Delta\mathbf{A}$ is the change in the vector potential (VP) effected by an external source. Indeed, the work $\Delta\mathcal{A}$ performed in time Δt by an external force field $\mathbf{F}$ on a particle moving with velocity $\mathbf{v}$ is $\Delta\mathcal{A} = \mathbf{F}\cdot\mathbf{v}\Delta t$ [whence it also follows that Eq. (A2.1) does not contain the electronic charge].

Assuming the existence of an equilibrium current state (ECS), let us find $\Delta\mathcal{A}$ for a cylindrical conductor (Fig. 3) of length L and with a cross section S which is connected through electrodes (*2*, *2*') to a circuit with a variable emf source *3*. The internal resistance of the source is assumed to be large (the current source). The cylinder axis is aligned with x. The effect of the magnetic field created by the current flowing in the circuit on the conductor is assumed to be excluded.

[10] If the Hubbard repulsion energy $2A_0$ is zero, this quantity is equal to $\exp(-2E_p/\hbar\omega)$ and $\Xi \propto \exp(-4E_p/\hbar\omega)$, similar to the localized-pair direct-interaction term (see Section 2).

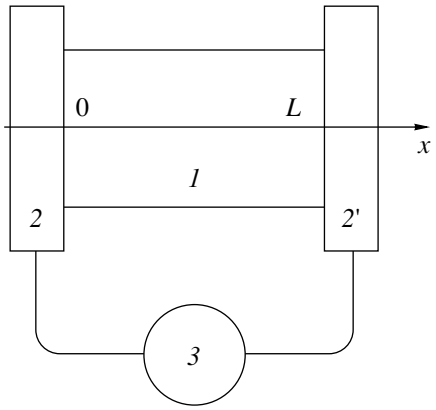

Fig. 3. Superconducting cylinder (*1*) connected to a circuit with an emf source (*3*). The area of the electrodes (*2*, *2*') is assumed to be large enough for the field E to be nonzero only in the gap between them.

Let an equilibrium current J_x set in the circuit. (In accordance with the invoked assumption, the potential difference ΔU across the electrodes *2* and *2*' is zero.) Starting from the instant $t = 0$, the source maintains a field $E \neq 0$ in the region between the electrodes and performs work on the conductor. The VP depends linearly on the time [$\mathbf{A}(t) = -c\mathbf{E}t$] and is directed along x. At time t_1, the control is stopped, ΔU becomes zero, and the system transfers to the ECS with a current that is different from its initial value. The process is reversible for $E \longrightarrow 0$, $t_1 \longrightarrow \infty$, and Et_1 being finite (and small). The change in the VP in this process is $\Delta\mathbf{A} = -c\mathbf{E}t_1$, and the work performed is

$$\Delta\mathcal{A} = LJ_xEt_1, \quad LJ_x \equiv \int_{\mathcal{V}} j_x(\mathbf{r})d\mathbf{r}. \qquad \text{(A2.2)}$$

(In a normal conductor, $J_x = 0$ and $\Delta\mathcal{A} = 0$ in such a process.) Setting $-eEt_1 = \hbar\Delta q = \Delta A$ and $(-1/e)J_x = I$ (the particle flux), we have

$$\Delta\mathcal{A} = \hbar LI\Delta q. \qquad \text{(A2.3)}$$

The quantity q (with dimensions of L^{-1}) is a thermodynamic parameter characterizing the ECS; the average energy E is a function of q; and the fundamental thermodynamic identity has the form

$$dE(S, q) = TdS + \hbar LIdq, \qquad \text{(A2.4)}$$

where S is the entropy. Whence it follows that $I = (\hbar L)^{-1}(\partial E/\partial q)s$ (I and q are thermodynamically conjugate). One readily obtains the condition of ECS stability,

$$\left(\frac{\partial^2 E}{\partial q^2}\right)_S \equiv \hbar L\left(\frac{\partial I}{\partial q}\right)_S > 0. \qquad \text{(A2.5)}$$

One may choose the current I for the thermodynamic parameter. It is this case that is realized in practice. The characteristic function for it will be $W(S, I) = E - \hbar LIq$ (an analog of the enthalpy).

The function $E(S, q)$ characterizing the equilibrium current state under ODLRO conditions can be defined for the configuration of Fig. 3 by conventional methods employed in statistical mechanics, namely, by fixing the gauge of the kinetic energy (for instance, taking it in the form $\hat{\mathbf{p}}^2/2m$) and imposing the condition[11] $\phi_{S_2} - \phi_{S_1} = Lq$ on the phase ϕ of the anomalous mean $F(\mathbf{r}) = \langle\psi_\sigma(\mathbf{r})\psi_{-\sigma}(\mathbf{r})\rangle \equiv \Lambda(\mathbf{r})\exp i\phi(\mathbf{r})$. One can readily verify that the Fourier expansion of $F(\mathbf{r})$ will retain only terms of the kind $\langle a_{-\mathbf{k}+\mathbf{q}-\sigma}a_{\mathbf{k}+\mathbf{q}}\sigma\rangle$, $\mathbf{q} = q\mathbf{e}_0$. The quantity q is a characteristic of a macroscopic state. This procedure can easily be generalized to a solid of an arbitrary shape.

This consideration is also valid in the case where magnetic fields (both those generated by the current in the sample and external ones) are taken into account. In doing this, one should fix the gauge of the vector potential [22].

REFERENCES

1. A. Alexandrov and J. Ranninger, Phys. Rev. B **23** (4), 1796 (1981).
2. A. Alexandrov and J. Ranninger, Phys. Rev. B **24** (3), 1164 (1981).
3. T. Holstein, Ann. Phys. **8**, 325 (1959).
4. T. Holstein, Ann. Phys. **8**, 343 (1959).
5. I. G. Lang and Yu. A. Firsov, Zh. Éksp. Teor. Fiz. **43**, 1843 (1962) [Sov. Phys. JETP **16**, 1301 (1963)].
6. J. van der Brink, W. Stekelenburg, D. I. Khomskii, *et al.*, cond-mat/9802146.
7. M. Quijada, J. Cerne, J. R. Simpson, *et al.*, cond-mat/9803201.
8. K. H. Kim, J. H. Jung, and T. W. Noh, cond-mat/9804167.
9. A. S. Alexandrov and A. M. Bratkovsky, cond-mat/9806030.
10. Unjong Yu and B. I. Min, cond-mat/9906263.
11. Guo-meng Zhao, K. Conder, H. Keller, and K. A. Miller, Nature **381**, 676 (1996).
12. N. A. Babushkina, L. M. Belova, V. I. Ozhogin, *et al.*, cond-mat/9805315.
13. Guo-meng Zhao, M. B. Hunt, H. Keller, and K. A. Miller, Nature **385**, 236 (1997).
14. Yu. A. Firsov and E. K. Kudinov, Fiz. Tverd. Tela (St. Petersburg) **39** (12), 2159 (1997) [Phys. Solid State **39**, 1930 (1997)].

[11] It might seem necessary to impose a condition on the modulus of F at the ends. It can be shown, however, that the above consideration is equivalent to the case of a toroidal sample with current excitation by a linearly varying magnetic flux, where such boundaries do not exist at all. Note also that the values of q are quantized: $q = 2\pi n/L$, where n is an integer.

15. Yu. A. Firsov and E. K. Kudinov, Fiz. Tverd. Tela (St. Petersburg) **43** (3), 431 (2001) [Phys. Solid State **43**, 447 (2001)].
16. P. Nozieres and S. Schmitt-Rink, J. Low Temp. Phys. **59**, 195 (1985).
17. P. W. Anderson, Phys. Rev. **112**, 1900 (1958).
18. J. R. Schrieffer, *Theory of Superconductivity* (Benjamin, Reading, 1964; Nauka, Moscow, 1970).
19. E. K. Kudinov, Fiz. Tverd. Tela (St. Petersburg) **41** (9), 1582 (1999) [Phys. Solid State **41**, 1450 (1999)].
20. W. Kohn, Phys. Rev. A **133** (1), 171 (1964).
21. R. Resta and S. Sorella, cond-mat/9808151.
22. E. K. Kudinov, Fiz. Tverd. Tela (Leningrad) **30** (9), 2594 (1988) [Sov. Phys. Solid State **30**, 1493 (1988)].
23. E. K. Kudinov, Fiz. Tverd. Tela (Leningrad) **26** (10), 3122 (1984) [Sov. Phys. Solid State **26**, 1880 (1984)].
24. P. G. de Gennes, *Superconductivity of Metals and Alloys* (Benjamin, New York, 1966; Mir, Moscow, 1968).
25. J. Yamashita and T. Kurosawa, Phys. Chem. Solids **5**, 34 (1958).
26. A. A. Abrikosov, Zh. Éksp. Teor. Fiz. **32** (6), 1442 (1957) [Sov. Phys. JETP **5**, 1174 (1957)].
27. R. P. Feynman, *Statistical Mechanics: A Set of Lectures* (Benjamin, Reading, 1972; Mir, Moscow, 1975).
28. S. V. Tyablikov, *Methods in the Quantum Theory of Magnetism* (Nauka, Moscow, 1965; Plenum, New York, 1967).
29. A. Clogston, Phys. Rev. Lett. **9**, 266 (1962).
30. B. K. Chakraverty, J. Phys. (Paris) **37**, C4-353 (1976).
31. A. V. Ivanov and E. K. Kudinov, Fiz. Tverd. Tela (Leningrad) **31** (6), 14 (1989) [Sov. Phys. Solid State **31**, 922 (1989)].
32. *Higher Transcendental Functions (Bateman Manuscript Project)*, Ed. by A. Erdelyi (McGraw-Hill, New York, 1953; Nauka, Moscow, 1966), Vol. 2.
33. L. D. Landau and E. M. Lifshitz, *Course of Theoretical Physics*, Vol. 8: *Electrodynamics of Continuous Media* (Nauka, Moscow, 1982; Pergamon, New York, 1984).

Translated by G. Skrebtsov

Physics of the Solid State, Vol. 44, No. 4, 2002, pp. 704–708. Translated from Fizika Tverdogo Tela, Vol. 44, No. 4, 2002, pp. 678–682.

SEMICONDUCTORS AND DIELECTRICS

Electronic Structure of $FeSi_2$

S. I. Kurganskiĭ and N. S. Pereslavtseva

Voronezh State University, Universitetskaya pl. 1, Voronezh, 394693 Russia

e-mail: phssd18@main.vsu.ru

Received March 19, 2001; in final form, July 10, 2001

Abstract—The electronic structure of volume and film iron disilicides with crystal structure of the type of α leboit and fluorite was calculated using the linearized augmented plane-wave formalism. Joint and local partial densities of electronic states, x-ray emission spectra in different series of all inequivalent atoms of these phases, and photoelectron spectra for different excitation energies were obtained. γ-$FeSi_2$ was found to be, unlike α-$FeSi_2$, an unstable phase in both the volume and film realizations. X-ray $L_{2,3}$ emission spectra of silicon in the iron group disilicides $NiSi_2$, $CoSi_2$, and $FeSi_2$ were compared. $NiSi_2$, $CoSi_2$, and α-$FeSi_2$ exhibit transformation of the maximum in the near-Fermi region of the Si $L_{2,3}$ spectra as one crosses over from a bulk to a film sample. This transformation is closely connected with phase stability and may serve as a criterion of thermodynamic stability of the iron-group transition-metal disilicides. © *2002 MAIK "Nauka/Interperiodica".*

1. INTRODUCTION

Among the rich variety of materials used in present-day micro- and nanoelectronics technologies, of particular interest are compounds exhibiting high melting points, low electrical resistivity, and good conductivity. In addition, these materials should be easily workable. Among the most promising in this respect are the silicides of transition metals. The high temperature stability of both the crystal and electronic properties of these compounds makes them virtually irreplaceable in the production of contacts, Schottky barriers, and heterostructures. For this reason, investigation of the electronic properties of transition-metal silicides is currently a topical issue in solid-state physics [1].

This paper presents the results of a theoretical investigation into the electronic structure of disilicides of the iron-group transition metals, namely, α-$FeSi_2$, γ-$FeSi_2$, $CoSi_2$, and $NiSi_2$. These compounds possess all the above-mentioned properties. A fairly complete idea of the valence-band electronic structure was obtained, however, only for the cobalt and nickel disilicides. These materials have been well investigated experimentally ($CoSi_2$ [2–6], $NiSi_2$ [3–10]); we have studied the valence-band structure of the film phases of $CoSi_2$ [11] and $NiSi_2$ [12]. The α-leboit and the γ phase have attracted very scant interest; indeed, α-$FeSi_2$ has been studied primarily by experimental techniques [2, 13–16] (although an attempt at calculating the densities of states of a bulk sample was made in [13]), and for γ-$FeSi_2$, photoelectron spectra of a film were measured in [16, 17] and the densities of electronic states of the bulk material were calculated in [18]. In this work, we carried out a comprehensive calculation of the electronic structure of α-$FeSi_2$ and γ-$FeSi_2$ films and bulk materials, which have not been studied theoretically in a systematic way until now, and compared the calculated electronic structure and spectral properties of the iron disilicide with the available data on the nickel and cobalt disilicides.

2. METHOD OF CALCULATION

The electronic structure of films was calculated by the film version of the linearized augmented plane wave (LAPW) formalism. This method is described in considerable detail in [19] and was discussed by us briefly in [11]. The valence-band structure of bulk materials was calculated using the volume version of the LAPW formalism [20].

3. RESULTS AND DISCUSSION

3.1. Densities of Electronic States

Figures 1 and 2 present local partial densities of states (LPDOS) of atoms of α-$FeSi_2$ and γ-$FeSi_2$, which provide the main contribution to the valence band of these materials, namely, LPDOS of the iron *d* states and of the silicon *s* and *p* states. The solid lines specify the LPDOS of atoms in bulk samples, which virtually do not differ from those of atoms in the inner film layers, and the dashed lines are the LPDOS of the iron atoms closest to the surface and of the silicon near-surface atoms in the films. We readily see that the iron *d* states are localized in energy and that the density of these states reaches a maximum about 2 eV below the Fermi level (E_F) for the α phase and 1.5 eV below E_F for γ-$FeSi_2$. The distribution of the silicon *s* and *p* states of α-leboit in the valence band has the following form: in the bulk, the density of the *s* states is the highest in the region 7–14 eV below E_F and the density of the *p* states is the highest 1–6 eV below E_F. As one crosses over to

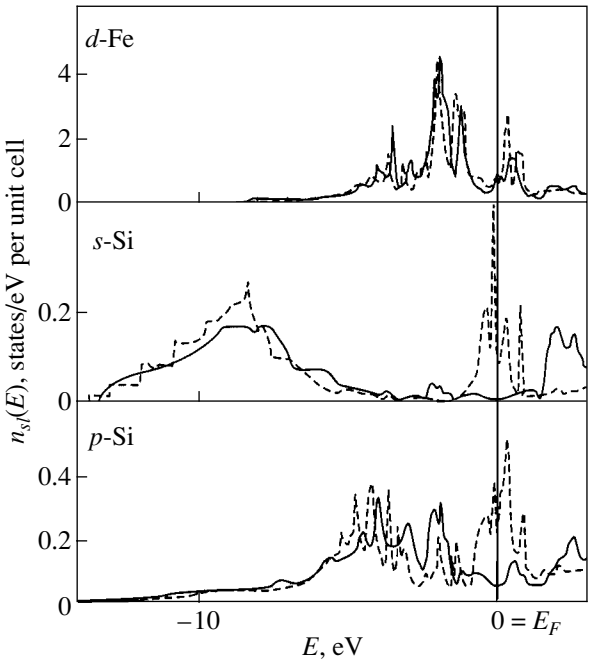

Fig. 1. LPDOS of atoms in α-$FeSi_2$. Solid lines show the LPDOS of the bulk phase, and dashed lines show those of the iron atoms closest to the surface and of the surface silicon atoms in films.

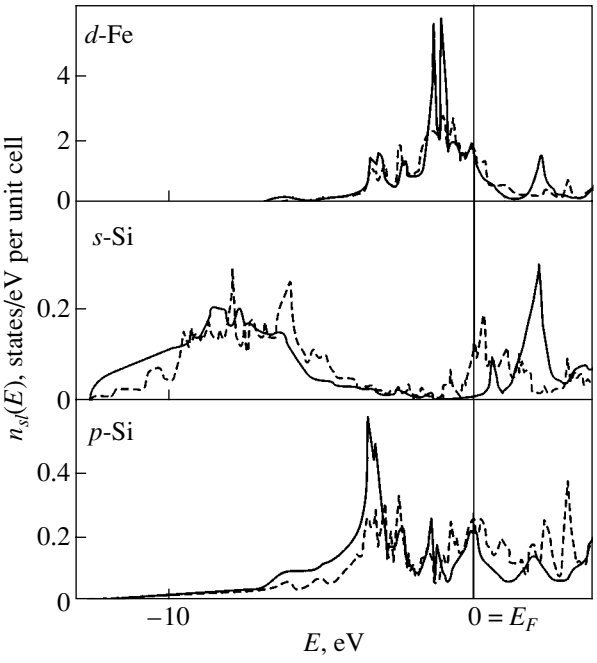

Fig. 2. LPDOS of atoms in γ-$FeSi_2$. Solid lines show the LPDOS of the bulk phase, and dashed lines show those of the iron atoms closest to the surface and of the surface silicon atoms in films.

near-surface film atoms, the density increases considerably in the range 0–1 eV below E_F. For the γ phase, the regions of the highest concentration of the silicon *s* and *p* states lie 6–13 and 1–6 eV below E_F, respectively.

The magnetic properties of the γ phase as related to its electronic structure is an interesting issue. DOS calculations of the bulk γ phase made by Christensen [18] yielded $0.3\mu_B$ for the magnetic moment of the iron atoms. A later study [17] also came to the conclusion that this phase is a magnet. On the other hand, it is known [21] that if the Fe–Si system contains more than 40% Si, the iron atoms in this compound bear no magnetic moment. In γ-$FeSi_2$, the silicon-to-iron ratio is 2 : 1; i.e., the silicon content is more than 66%. These two mutually contradictory results initiated a spin-polarization calculation of the electronic structure of the γ phase in order to determine the magnetic moment on the iron atoms of this silicide. As input data for a self-consistent calculation, we used the magnetic moment of iron atoms in the bulk material quoted in [18]: $\mu^{Fe}_{FeSi_2} = 0.3\mu_B$. However, reaching self-consistency in the occupation numbers brought about the disappearance of spin splitting in the energy bands. Thus, our calculations suggest that γ-$FeSi_2$ is a paramagnet, as is α-$FeSi_2$ also. Therefore, the data presented in this paper refer to the paramagnetic phases of these compounds.

One of the main distinctions of the valence-band structure of the γ phase from that of the α-leboit is the substantially increased density of states directly at the Fermi level, a feature characteristic of both a film and a bulk material. This implies that this phase is unstable. However, whereas some authors [16, 18] maintain that both bulk and film samples of γ-$FeSi_2$ are unstable, others [17] are of the opinion that the films can be stabilized. Because we have not been able to locate any other data in support of the results of [17], we believe that annealing could bring about a change in the lattice parameter or the formation of a thin oxide film on the surface, introduce impurity atoms, or produce a considerable deviation from stoichiometry, which was missed by the authors of [17]. Such changes in the crystal structure of a film should inevitably cause a shift of the Fermi level. In the case of γ-$FeSi_2$, even a very small shift of the Fermi level, as seen from the calculations, should substantially reduce the density of states at E_F and, as a consequence, stabilize the system. Our reasoning is supported by the fact that the study of the γ phase in [17] revealed a nonzero magnetic moment on the iron atoms in this compound. As for our calculations, they did not reveal, as already mentioned, any Fe magnetic moment in γ-$FeSi_2$. This may suggest that a phase of some other compound, in which the iron/silicon ratio was certainly larger than in γ-$FeSi_2$, 1 : 2 [21], was formed in the course of preparation or in the attempt at stabilization of the γ-$FeSi_2$ film [17]. Thus, our calculations of the electronic structure of the γ phase and the results of other studies [16, 18] strongly question the possible existence of stable γ-$FeSi_2$.

3.2. Photoelectron Spectra

Figure 3 compares the calculated photoelectron spectra of bulk and film iron disilicides with the experimental data [2, 14–17] available for different excitation energies $\hbar\omega$. The main maximum of these spectra derives from the *d* states of iron. As the excitation energy varies from 12 to 1253 eV, the position of this peak changes from 1.84 to 1.89 (1.16 to 1.21) and from 1.68 to 1.78 (1.26 to 1.42) eV below E_F in the bulk and film α (γ) phases, respectively. A second feature in the photoelectron spectra lies 2.5–4 eV below E_F. At low excitation energies (less than 50 eV), this feature is derived primarily from the *s* and *p* states of silicon and the *d* states of iron. As the excitation energy increases, the role of the silicon *s* and *p* states in the formation of this feature becomes progressively less noticeable, because the photoionization cross section increases with an excitation energy for the silicon *s* and *p* states that is considerably slower than that for the *d* states of Fe. In contrast to α-$FeSi_2$, the photoelectron spectra of γ-$FeSi_2$ at low incident photon energies reveal, in addition to these two features, one that is observed at 0–1 eV below E_F for $\hbar\omega < 30$ eV, derives primarily from silicon *s* and *p* states, and disappears with increasing excitation energy. Thus, at high incident photon energies, the pattern of the photoelectron spectra of iron disilicide is determined, in actuality, only by the iron *d* states.

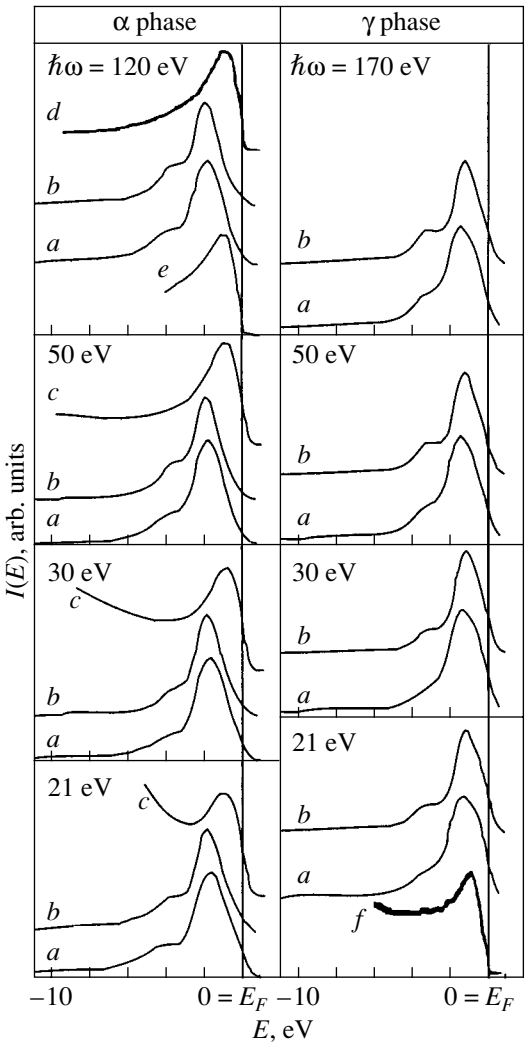

Fig. 3. Photoelectron spectra of α-$FeSi_2$ and γ-$FeSi_2$. Curves *a* and *b* present calculations for film and bulk samples; curves *c* and *d* are experiment [2] and [15] for the bulk crystal, respectively, and curves *e* and *f* are experiment [16] and [17] for the film, respectively.

3.3. X-ray Emission Spectra

Figure 4 presents Si $L_{2,3}$ x-ray emission spectra of iron-group disilicides. The character of these spectra is of considerable interest. The fact is that studies of iron-group disilicides ($NiSi_2$, $CoSi_2$) have revealed a change in the intensity of the peak near the Fermi level as one crosses over from a bulk sample to a film [3–8]. This phenomenon is connected with the fact that the charge transfer from silicon to the metal atoms in the film is different from that in the bulk material. The mechanism of this process was discussed by us in considerable detail in [11, 12].

In accordance with the dipole selection rules, the Si $L_{2,3}$ spectra reflect the distribution of the Si *s* and *d* states in the valence band. We first consider these spectra for bulk α-$FeSi_2$ and γ-$FeSi_2$. As follows from the calculations, the maxima at ~8.2 (8.9) and 2 (1) eV below E_F in the Si $L_{2,3}$ spectra of α-leboit (γ phase) are due to the *s* states. The *d* states become manifest as a small feature in the $L_{2,3}$ spectrum of the γ phase in the region 3.5 eV below E_F. The relative intensity of this feature is weak, because the matrix element for the transition probability for *s* states is larger by about an order of magnitude than that for the *d* states. This peak in the $L_{2,3}$ spectrum of silicon is also observed in other transition-metal disilicides of the iron group ($NiSi_2$, $CoSi_2$) which have the same crystal lattice (CaF_2 type [22]). The absence of this feature in the silicon $L_{2,3}$ spectrum of α-leboit is apparently connected with the fact that the crystal structure of this compound differs substantially from that of fluorite. As seen from Fig. 4, the Si $L_{2,3}$ spectra of the bulk sample (curves *a*) are very similar to those of the inner atoms of the film (curves *b*). However, in the $L_{2,3}$ spectra of silicon in γ-$FeSi_2$, we were not able to detect the transformation of the maximum in the near-Fermi region expected to occur in going from the bulk (*a*) to the film (*b*) sample characteristic of other iron-group disilicides with the same crystal structure ($NiSi_2$ [3–8], $CoSi_2$ [3–6]). However, the absence of such a peak transformation near the Fermi level could be anticipated. The matter is that as one crosses over from $NiSi_2$ to $CoSi_2$ to $FeSi_2$, the num-

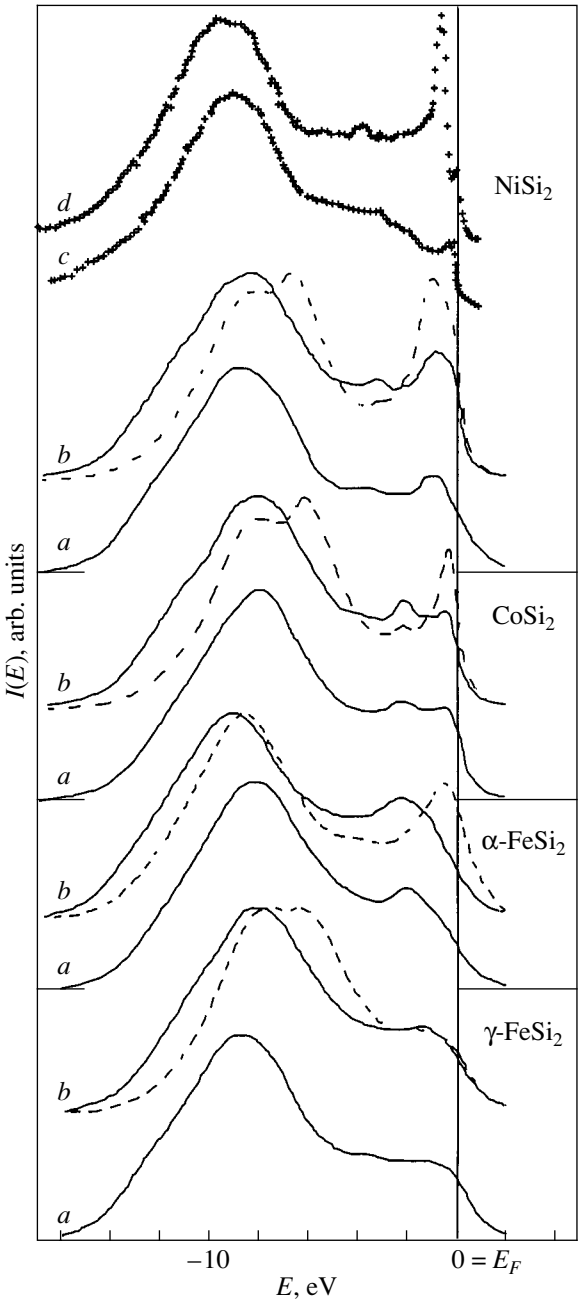

Fig. 4. X-ray Si $L_{2,3}$ emission spectra of iron-group disilicides for (*a*) a bulk sample and (*b*) film sample (the solid line indicates the inner layer; the dashed line, surface atoms); curves (*c* and *d*) are experimental data [3, 4] for the bulk and film samples, respectively.

ber of valence electrons per unit cell in the film decreases. This decrease gives rise to a shift of the Fermi level, as a result of which the density of states immediately below E_F decreases substantially. Indeed, while this effect of peak transformation near E_F is clearly pronounced in $NiSi_2$ [3–8, 12], it is much weaker in $CoSi_2$ [3–6, 11] and, by our calculations, is altogether absent in γ-$FeSi_2$. However, the maximum in the near-Fermi region of the Si $L_{2,3}$ spectra was found to transform slightly as one crosses over from a bulk to a film sample of α-$FeSi_2$, which came for us as a surprise, because α-leboit radically differs in crystal structure from $NiSi_2$ and $CoSi_2$ [22]. On the other hand, the α-$FeSi_2$ disilicide, as well as the disilicides of nickel and cobalt, is a stable phase, in contrast to γ-$FeSi_2$. We believe that the above effect of transformation is a property of stable phases of iron-group transition-metal disilicides.

4. CONCLUSIONS

One can thus formulate the following conclusions:

(1) The valence band of film and bulk disilicides of iron derives primarily from the *d* states of iron and *s* and *p* states of silicon.

(2) The shape and the energy position of the main DOS features of the bulk material and of the inner atoms in a film almost coincide for both the α and the γ phase.

(3) Iron atoms in the α-$FeSi_2$ and γ-$FeSi_2$ disilicides bear zero magnetic moment.

(4) The high density of states at the Fermi level in γ-$FeSi_2$ compared to the α-leboit implies instability of this compound in both the bulk and film structures.

(5) At low excitation energies (less than 50 eV), the structure of photoelectron spectra of both bulk and film iron disilicides is determined by the *d* states of iron and the *s* and *p* states of silicon. At higher incident photon energies, the pattern of the spectrum is governed, in effect, only by the *d* states of iron.

(6) An analysis of the Si $L_{2,3}$ spectra of bulk and film samples of α-$FeSi_2$ and γ-$FeSi_2$ showed that these spectra have practically the same structure in the bulk phase and in the inner film layer.

(7) The shape of the $L_{2,3}$ spectra of silicon atoms is mainly due to the *s* states of silicon. The contribution of the silicon *d* states to the $L_{2,3}$ spectrum is seen distinctly only as a small peak at 3.5 eV below the Fermi level for silicon atoms in the bulk γ phase.

(8) As one goes over from a bulk to a film sample, the transformation of the peak in the near-Fermi region of the $L_{2,3}$ spectra of silicon, which is characteristic of the $NiSi_2$ and $CoSi_2$ iron-group disilicides, was observed only in α-$FeSi_2$. No such transformation was found for γ-$FeSi_2$.

REFERENCES

1. V. L. Ginzburg, Usp. Fiz. Nauk **169** (4), 419 (1999).
2. J. H. Weaver, A. Francioni, and V. L. Moruzzi, Phys. Rev. B **29** (6), 3293 (1984).
3. J. J. Jia, T. A. Calcott, W. L. O'Brien, *et al.*, Phys. Rev. B **46** (15), 9446 (1992).

4. H. Nakamura, M. Iwami, M. Hirai, *et al.*, Phys. Rev. B **41** (17), 12092 (1990).
5. P. J. W. Weijs, H. van Leuken, R. A. de Groot, *et al.*, Phys. Rev. B **44** (15), 8195 (1991).
6. E. P. Domashevskaya and Yu. A. Yurakov, J. Electron Spectrosc. Relat. Phenom. **96**, 195 (1998).
7. É. P. Domashevskaya, Yu. A. Yurakov, V. M. Andreeshchev, and S. M. Karal'nik, Metallofizika **2** (5), 24 (1980).
8. S. V. Vlasov, É. P. Domashevskaya, A. G. Narmonev, *et al.*, Metallofizika **9** (3), 97 (1987).
9. P. J. W. Weijs, G. Wiech, W. Zahorowski, and K. H. J. Buschov, Phys. Scr. **41** (4), 629 (1990).
10. P. J. W. Weijs, M. T. Czyzyk, J. F. van Acker, *et al.*, Phys. Rev. B **41** (17), 11 899 (1990).
11. S. I. Kurganskiĭ and N. S. Pereslavtseva, Fiz. Tverd. Tela (St. Petersburg) **42** (8), 1499 (2000) [Phys. Solid State **42**, 1542 (2000)].
12. N. S. Pereslavtseva and S. I. Kurganskiĭ, Fiz. Tverd. Tela (St. Petersburg) **41** (11), 2075 (1999) [Phys. Solid State **41**, 1906 (1999)].
13. S. Eisebitt, J.-E. Rubensson, M. Nicodemus, *et al.*, Phys. Rev. B **50** (24), 18330 (1994).
14. B. Egert and G. Pazner, Phys. Rev. B **29** (4), 2091 (1984).
15. F. Sirotti, M. De Santis, and G. Rossi, Phys. Rev. B **49** (16), 11134 (1994).
16. F. Sirotti, M. De Santis, X. Jin, and G. Rossi, Phys. Rev. B **48** (11), 8299 (1993).
17. N. Onda, J. Henz, E. Muller, *et al.*, Appl. Surf. Sci. **56/58**, 421 (1992).
18. N. E. Christensen, Phys. Rev. B **42** (11), 7148 (1990).
19. H. Krakauer, M. Posternak, and A. J. Freeman, Phys. Rev. B **19** (4), 1706 (1979).
20. D. D. Koelling and G. O. Arbman, J. Phys. F **5** (11), 2041 (1975).
21. I. N. Shabanova, V. I. Kormilets, L. D. Zagrebin, and N. S. Terebova, Zh. Strukt. Khim. **39** (6), 1098 (1998).
22. G. V. Samsonov, L. A. Dvorina, and B. M. Rud', *Silicides* (Metallurgiya, Moscow, 1979).

Translated by G. Skrebtsov

Physics of the Solid State, Vol. 44, No. 4, 2002, pp. 709–713. Translated from Fizika Tverdogo Tela, Vol. 44, No. 4, 2002, pp. 683–687.

SEMICONDUCTORS AND DIELECTRICS

Study of the Component Distribution in Si/Ge_xSi_{1-x}/Si Heterostructures Grown by Molecular Beam Epitaxy

V. G. Kesler, L. M. Logvinskiĭ, V. I. Mashanov, O. P. Pchelyakov, and V. V. Ul'yanov

Institute of Semiconductor Physics, Siberian Division, Russian Academy of Sciences, pr. Akademika Lavrent'eva 13, Novosibirsk, 630090 Russia

e-mail: kesler@isp.nsc.ru

Received January 30, 2001; in final form, July 13, 2001

Abstract—This paper reports on a study of the depth profile of components in GeSi heterostructures grown on low-temperature silicon (LTSi: $T_{gr} \sim 350$–400°C) and porous silicon by molecular-beam epitaxy. An excess Ge concentration was found by Auger electron spectroscopy depth profiling at the Ge_xSi_{1-x}/LTSi interface, which decreased in all samples subjected to annealing. The Ge diffusion activation energy was calculated to be $E_a \approx 1.6$ eV in this case. An enhanced Ge concentration was also detected by x-ray photoelectron spectroscopy at the Si cap surface. Possible reasons for the surface enrichment of the silicon layer and of the Ge_xSi_{1-x} film interface by germanium are considered, and the relation between the component distribution and the structural features of plastically strain-relieved layers are discussed. © *2002 MAIK "Nauka/Interperiodica".*

1. INTRODUCTION

While epitaxial growth of gallium arsenide on silicon has been dealt with in many studies, the problem of preparing films that would not be inferior in quality to the bulk material of the substrate remains unsolved. The preparation of defect-free GaAs films on Si is hampered by two main factors, namely, the large lattice mismatch between the film and the substrate and the difference between the lattice types.

This problem can be solved by using buffer layers or so-called alternate substrates whose surface is coated by layers with a lattice parameter close to that of the film. Such substrates should meet the requirements of zero mechanical strain and low defect density. To obtain these properties, intermediate buffer layers of Ge and of its solid solutions with silicon are introduced between the silicon substrate and the GaAs epitaxial layer. To improve the quality of the buffer layer, it is proposed to use the so-called compliant substrate in the form of an epitaxial silicon membrane film deposited on a porous silicon (PS) layer [1]. Another approach to solving this problem lies in introducing buffer layers of low-temperature silicon (LTSi) grown at a temperature of ~350–400°C. The growth of Ge_xSi_{1-x} solid solutions on Si(001) substrates coated by a low-temperature silicon buffer layer is a new method producing heterostructures with a low density of grown-in dislocations [2–4]. The depth profile and the inhomogeneities in the distribution of the main components near the film–substrate interface, capable of affecting the mechanical stress distribution and defect formation, play an important role in obtaining multilayer germanium–silicon heterosystems.

This paper reports on a study of the depth distribution of components in heterostructures and analyzes the interface structure and how it is affected by the preparation conditions and heat treatments used.

2. EXPERIMENTAL TECHNIQUE

The heterostructures were grown by molecular beam epitaxy (MBE) on a Katun-S setup. A molecular beam of silicon was produced by means of an electron-beam evaporator, and a crucible source was used to prepare the molecular beam of germanium. To improve surface morphology, a buffer silicon layer was grown at 700°C on a preliminarily cleaned Si substrate. We call this layer high-temperature silicon (HTSi). The growth rates of the silicon and of the solid-solution buffer layers were 0.07 and 0.09 nm/s, respectively. In the course of the Si and Ge_xSi_{1-x} growth, we observed a diffraction pattern from the (100)-2×1 superstructure in the form of long streaks, with point reflections superposed on them at Ge_xSi_{1-x} thicknesses in excess of 150 nm, which indicated the development of a rough surface. Solid-solution layers were coated by a 5-nm-thick Si layer in most cases. After this, the surface became smooth again. The heterostructures thus grown (Fig. 1) were subjected to isochronous annealing at temperatures of 700–800°C. In contrast to [1], we grew the main $Ge_{0.3}Si_{0.7}$ solid solution at the same temperatures as the LTSi. The type of the structural defects and their spatial distribution were determined on the same samples by transmission electron microscopy (TEM) on a JEM-4000EX (JEOL) electron microscope [5]. The degree of heteroepitaxial strain relaxation was measured with a triple-crystal x-ray diffractometer in a double-crystal arrangement with a Si(004) monochromator

1063-7834/02/4404-0709$22.00

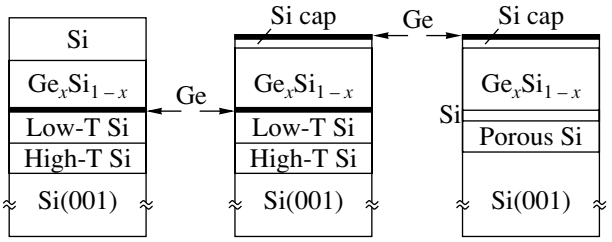

Fig. 1. Si/Ge_xSi_{1-x}/LTSi and Si/Ge_xSi_{1-x}/PS heterostructures. The arrows identify the germanium-enriched regions.

or was determined from the misfit dislocation density in the case of low-intensity reflection peaks. The main parameters of the grown layers are listed in the table.

The depth profiles of the components were measured using two mutually complementary methods, namely, x-ray photoelectron spectroscopy (XPS) and Auger electron spectroscopy (AES) combined with layer-by-layer Ar^+ ion sputtering. These methods differ considerably in elemental sensitivity; indeed, the sensitivity of XPS to germanium is practically an order of magnitude higher than that of AES. The experiments were carried out on the setup (RIBER) at the Surface Science Center.

Ion sputtering was done with a 3-keV Ar^+ ion beam. The ion incidence angle to the surface normal was 64° and 74° for the XPS and AES measurements, respectively. The ion beam diameter was about 1 mm. To obtain a plane sputtered-crater bottom in XPS depth profiling (which is required to achieve the maximum resolution in depth), the area scanned was $\sim 10 \times 7$ mm.

Excitation of the photoelectron spectrum was done with a 1486.6-eV x-ray beam (AlK_α radiation). The x-ray beam diameter was about 5 mm. The depth profiles were constructed using the Ge2*p*/Ge3*d* and Ge2*p*/Si2*p* photoelectron peak intensity ratios. By using signal intensity ratios, we substantially reduced the effect of instrumental distortions originating from instrument parameter instabilities. In addition, the difference between the electron escape depths λ corresponding to the germanium 2*p* and 3*d* peaks, which is due to the difference between the electron kinetic energies (270 and 1457 eV, respectively), also contributed favorably to the measurements. Because the signal comes from the layer depth determined by λ, it is obvious that in the case of a thin surface layer of germanium, the Ge3*d* peak intensity will start to decrease earlier when this layer is being milled off than the intensity of the Ge2*p* peak. Thus, use of the Ge2*p*/Ge3*d* peak intensity ratio permitted us to substantially improve the depth resolution of the technique and made it possible to perform a more detailed study of the near-surface Ge distribution.

Because layer-by-layer XPS analysis requires ion-beam scanning of a large area, which dramatically reduces the sputtering rate, the XPS depth profiling was limited to investigation of the near-surface region of the heterostructures. In view of the large layer thicknesses, the interfaces were studied by AES layer-by-layer analysis, which permitted us to construct compositional depth profiles of the heterostructures as a whole. The experiments were carried out on several sets of samples differing in the conditions of preparation and heat treatment (see table).

The Ge*LMM* and Si*KLL* Auger transitions were excited by a primary 5-keV electron beam with a 150-nA current. The diameter of the primary electron beam was ~5–10 μm. The intensity of the Ge*LMM* and Si*KLL* peaks was measured simultaneously with the ion milling.

3. RESULTS OF THE EXPERIMENTS AND THEIR DISCUSSION

3.1. Investigation of the Film Structure

TEM measurements show the structural defects in all the samples studied to be primarily 60° dislocations with the Burgers vectors $\mathbf{b} = \frac{a}{2}\langle 110\rangle$, which glide along the {111} inclined planes. The nonannealed samples are dominated by long misfit dislocations (up to 100 μm) with a linear density of $(1–3) \times 10^2$ cm^{-1}. Grown-in dislocations were not detected by TEM in these samples, which indicates their low density in the initial stage of

Parameters of the Si/Ge_xSi_{1-x}/LTSi and Si/Ge_xSi_{1-x}/PS heterostructures

Sample	Buffer thickness (nm) and type	Ge_xSi_{1-x} thickness, nm	*x* (measuring method)	Si cap thickness, nm	Anneal temperature,* °C
2–3	50 (LTSi)	100	0.3 (XPS, AES)	5	–
3–3	50 (LTSi)	100	0.25 (XPS, AES)	5	700
6	50 (LTSi)	150	0.27 (XPS, AES)	10	700, 800
7	50 (LTSi)	80	0.19 (AES)	75	700, 800
3741	17 (PS)	100	0.33 (AES)	5	–
3742	17 (PS)	100	0.29 (AES)	5	700

* All anneals 1 h long.

plastic relaxation ($<10^5$ cm^{-2}). After the films were annealed at 800°C for one hour, the residual elastic strains in the 100-nm-thick films became slightly lower compared to what is quoted in [3, 4], although the degree of plastic relaxation did not change significantly. The degree of plastic relaxation was observed to increase only with increasing film thickness. In particular, for a thickness of 300 nm, plastic relaxation was found to be close to 100%.

3.2. Investigation of the Near-Surface Region in Heterostructures

We studied heterostructures 2–3, 3–3, and 6 (see table). XPS measurements revealed the presence of Ge about 0.15 monatomic layers thick on the starting surface (i.e., on the Si cap layer) even before the ion sputtering (Fig. 2). The Ge content was estimated by the technique used to determine the surface coating described in [6]. An XPS layer-by-layer analysis showed the Ge concentration to fall off rapidly in the bulk of the Si cap layer (Fig. 2). The observed character of Ge distribution is apparently connected with surface segregation of Ge, which takes place during the silicon layer growth on the Ge_xSi_{1-x} solid solution. Information on experimental and theoretical studies of Ge segregation in Si is available in the literature [7–14]. However, the segregation processes that occur in MBE of germanium–silicon heterostructures remain poorly studied.

We studied samples with different Si layer thicknesses (5 nm for samples 2–3 and 3–3 and 10 nm for sample 6), thus permitting us to follow the dependence of the Ge distribution in the near-surface region of the heterostructures on the cap layer thickness. Figure 2 presents XPS depth profiles of the near-surface region of samples with different Si layer thicknesses, namely, 5 and 10 nm. For convenience, the profiles are matched at the cap/solid-solution interface. While germanium is also present on the surface of the thicker cap layer, its concentration in the bulk of silicon is lower than that in the first sample.

XPS spectra obtained at different times of the ion sputtering procedure (Fig. 3) show that the shape and position of the Ge2*p* peak from the surface are changed compared to those from the bulk of the Si layer, which indicates the surface Ge to be oxidized (when the samples were transferred from the growth chamber to the analysis chamber in air).

3.3. Study of the Ge_xSi_{1-x}/LTSi and Ge_xSi_{1-x}/PS Interfaces

The most interesting subjects of the present study were the Ge_xSi_{1-x}/LTSi and Ge_xSi_{1-x}/PS interfaces, i.e., the transitional regions to the compliant substrate, which strongly affect the heterostructure characteristics.

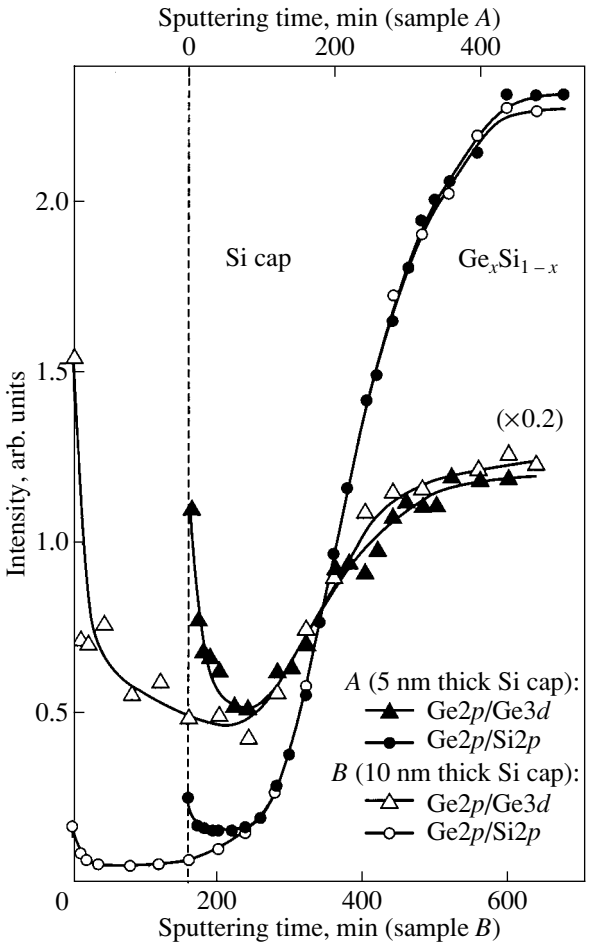

Fig. 2. XPS depth profiles of the near-surface region of heterostructures with a Si cap layer of different thicknesses: (*A*) 5 and (*B*) 10 nm matched at the Si/Ge_xSi_{1-x} interface. The dashed line shows the surface of the sample with a 5-nm-thick silicon layer. Plotted on the vertical axis are the Ge2*p*/Ge3*d* and Ge2*p*/Si2*p* peak intensity ratios.

In addition to the above features in the component distribution, we found a region of enhanced Ge concentration at the solid-solution/LTSi interface (Fig. 4). This effect was observed with a good reproducibility in all lots of samples with an LTSi buffer (samples 2–3, 3–3, 6, 7, see table) and was not detected in structures with a porous buffer (samples 3741, 3742, see table). Annealing resulted in a broadening of the Ge concentration peak at the interface with LTSi, which is shown in Fig. 4, and permits one to follow the evolution of the interface region caused by diffusion during the heat treatment. Increasing the annealing temperature to 800°C brought about a further decrease in the magnitude of the Ge peak until it vanished altogether.

Layer-by-layer AES analysis has a finite resolution determined by a set of factors, which includes, in particular, the finite electron escape depth, interface roughness, and the influence of the ion beam on a sample

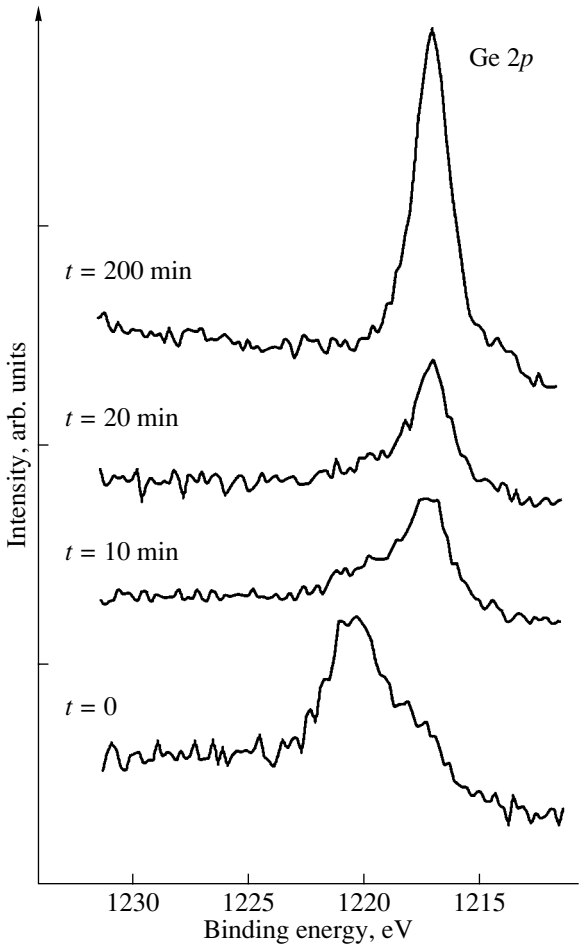

Fig. 3. X-ray photoelectron spectra (Ge2*p* peak) from the near-surface region in the Si/Ge_xSi_{1-x}/LTSi heterostructure for different ion sputtering times.

[15]. This results in a broadening of the originally sharp interfaces and of the concentration depth profile. The depth resolution of the method under the above experimental conditions was about 4 nm. This value was obtained in depth-profiling thin Ge layers (10 ML) in silicon. Thus, taking into account the finite resolution of the method, one may expect that the real Ge interface concentration to be higher than that observed in the depth profiles and that the enrichment to be localized in a narrower region.

The enrichment by germanium of the Ge_xSi_{1-x}/LTSi interface may be due to the so-called shutter effect, which is associated with the design feature of the crucible germanium sources. It originates from the germanium melt cooling after the shutter has been opened, which gives rise to a rapid decrease in the flux and a decrease in the germanium percent content in the solid-solution film as the film increases in thickness in the initial stage of growth.

The variation in the concentration with annealing temperature permits one to estimate the effective activation energy of Ge diffusion in the interface region. A calculation made by the technique described in [16] yielded $E_a \approx 1.6$ eV. This value is less by nearly 1 eV than the activation energies of Ge diffusion in the Ge_xSi_{1-x} solid solutions ($0.3 < x < 0.7$) quoted in the literature [17–19]. This discrepancy may be caused by the fact that the conditions at the Ge_xSi_{1-x}/LTSi interface of the heterostructures studied are such as to make the diffusion mechanisms more complicated. The heterodiffusion may be affected by such factors as the mechanical stress field, concentration gradients of the main solid-solution constituents and point defects, and enhanced diffusion over the cores of grown-in dislocations. These dislocations form in the course of nucle-

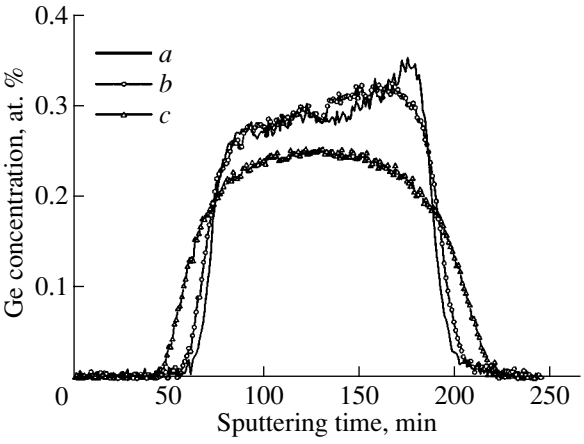

Fig. 4. AES depth profiles of the Si/Ge_xSi_{1-x}/LTSi heterostructure (a) before annealing and (b, c) after annealing for one hour at 700 and 800°C, respectively.

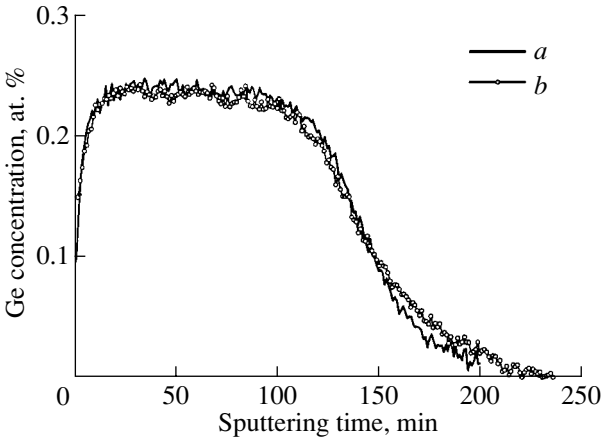

Fig. 5. AES depth profile of the Si/Ge_xSi_{1-x}/PS heterostructure (a) before annealing and (b) after annealing at T = 700°C for one hour.

ation and development of the misfit dislocation network, to whose formation the enrichment of the low-temperature Si layer by point defects may contribute to a large extent [5].

AES depth profiling of structures buffered by porous silicon, Si/Ge_xSi_{1-x}/PS (samples 3741, 3742; see table), showed that the growth of a solid solution on PS does not produce a germanium-enriched interface layer between the solid solution and porous silicon. These samples are characterized by a strongly broadened concentration distribution profile near the Ge_xSi_{1-x}/PS interface (Fig. 5), with some germanium depletion being observed in the region where a Ge concentration peak was detected in structures grown on low-temperature Si. Subsequent annealing resulted in additional diffusion broadening of the interface (Fig. 5). Investigation of the possible mechanisms responsible for this phenomenon, in particular, of Ge diffusion in PS, requires further study.

4. CONCLUSIONS

Thus, we have obtained information on the composition and structure of germanium–silicon heterosystems grown by MBE on low-temperature and porous Si and studied their behavior in heat treatments employed to obtain strain-relieved structures. It was shown that the heterosystems have germanium-enriched regions (i) on the surface of the silicon cap layer and (ii) at the solid-solution/LTSi buffer interface.

The activation energy obtained for Ge diffusion at the Ge_xSi_{1-x}/LTSi interface is indicative of conditions which make the diffusion mechanisms more complicated. The acceleration of diffusion is possibly due to the complex structure of the interface region sandwiched between the solid-solution and the low-temperature silicon layers.

The experimental data obtained can be applied to advantage to technologies involving the formation of alternate substrates based on GeSi heterosystems.

ACKNOWLEDGMENTS

This study was supported by the Russian Foundation for Basic Research, project nos. 00-02-17638, 00-02-17461, and 00-15-96806.

REFERENCES

1. A. K. Gutakovskiĭ, S. I. Romanov, O. P. Pchelyakov, *et al.*, Izv. Ross. Akad. Nauk, Ser. Fiz. **62** (2), 255 (1998).
2. H. Chen, L. W. Guo, Q. Cui, *et al.*, J. Appl. Phys. **79** (2), 1167 (1996).
3. J. H. Li, C. S. Peng, Y. Wu, *et al.*, Appl. Phys. Lett. **71** (21), 3132 (1997).
4. J. H. Li, C. S. Peng, Z. H. Mai, *et al.*, J. Appl. Phys. **86** (3), 1292 (1999).
5. Yu. B. Bolkhovityanov, A. K. Gutakovskii, V. I. Mashanov, *et al.*, Thin Solid Films **392**, 98 (2001).
6. O. Millo, A. Many, and Y. Goldstein, J. Vac. Sci. Technol. A **7** (4), 2688 (1989).
7. K. Nakagawa and M. Miyao, J. Appl. Phys. **69**, 3058 (1991).
8. S. Fukatsu, K. Fujita, H. Yaguchi, *et al.*, Appl. Phys. Lett. **59** (17), 2103 (1991).
9. Z. Lu, J.-M. Baribeau, and D. Lockwood, J. Appl. Phys. **76** (6), 3911 (1994).
10. S. Zaima and Y. Yasuda, J. Cryst. Growth **162** (1–2), 105 (1996).
11. D. J. Godbey, J. V. Lill, J. Deppe, and K. D. Hobart, Appl. Phys. Lett. **65** (6), 711 (1994).
12. D. J. Godbey and M. G. Ancona, Surf. Sci. **395** (1), 60 (1998).
13. G. G. Gernigan, P. E. Tompson, and C. L. Silvestre, Appl. Phys. Lett. **69** (13), 1894 (1996).
14. Yun Li, G. G. Hembree, and J. A. Venables, Appl. Phys. Lett. **67** (2), 276 (1995).
15. S. Hofmann, Rep. Prog. Phys. **61**, 827 (1998).
16. A. Zalar, S. Hofmann, and P. Panjan, Vacuum **48**, 625 (1997).
17. J. C. Phillips and J. A. van Vechten, Phys. Rev. Lett. **30** (6), 220 (1973).
18. M. C. Joncour, M. N. Carasse, and K. Burgeat, J. Appl. Phys. **58** (9), 3373 (1985).
19. N. V. Nomerotskiĭ, O. P. Pchelyakov, and E. M. Trukhanov, Poverkhnost, No. 2, 57 (1993).

Translated by G. Skrebtsov

Physics of the Solid State, Vol. 44, No. 4, 2002, pp. 714–719. Translated from Fizika Tverdogo Tela, Vol. 44, No. 4, 2002, pp. 688–693.

SEMICONDUCTORS AND DIELECTRICS

Electronic Structure and Simulation of the Dielectric Function of β-$FeSi_2$ Epitaxial Films on Si(111)

N. G. Galkin*, A. M. Maslov*, and A. O. Talanov**

** Far East State Technical University, ul. Sukhanova 8, Vladivostok, 690600 Russia*

*** Institute of Automatics and Control Processes, Far East Division, Russian Academy of Sciences, Vladivostok, 690041 Russia*

e-mail: galkin@iacp.dvo.ru

Received April 13, 2001; in final form, July 21, 2001

Abstract—The optical functions of iron disilicide (β-$FeSi_2$) thin epitaxial films are calculated from the reflectance spectra in the energy range 0.1–6.2 eV with the use of the Kramers–Kronig (KK) integral relations. A comparison of the results of calculations from the transmittance and reflectance spectra and the data obtained from the reflectance spectra in terms of the Kramers–Kronig relations indicates that the fundamental transition at an energy of 0.87 ± 0.01 eV is a direct transition. An empirical model is proposed for the dielectric function of β-$FeSi_2$ epitaxial films. Within this model, the specific features in the electronic energy-band structure of the epitaxial films are described in an analytical form. It is shown that the maximum contributions to the dielectric function and the reflectance spectrum in the energy range 0.9–1.2 eV are made by the 2*D* M_0-type second harmonic oscillator with an energy of 0.977 eV. This oscillator correlates with the second direct interband transition observed in the energy-band structure of β-$FeSi_2$. *© 2002 MAIK "Nauka/Interperiodica".*

1. INTRODUCTION

Semiconducting iron disilicide (β-$FeSi_2$) is one of the most extensively studied and promising materials for use in silicon technology of integrated circuits and optoelectronic devices [1–5]. As follows from analysis of the transmittance and reflectance spectra, β-$FeSi_2$ is a direct-band-gap semiconductor with a band gap of 0.87 eV [1, 2]. However, theoretical calculations have demonstrated that iron disilicide is a quasi-direct-gap semiconductor [3–5] for which the energies of the indirect and direct interband transitions differ by 0.04–0.06 eV. The real and imaginary parts of the dielectric function of β-$FeSi_2$ have been experimentally determined for epitaxial films [2, 3, 5] and bulk single-crystal samples [5]. The results obtained for the high-energy features in the electronic energy-band structure of β-$FeSi_2$ are in good agreement. At the same time, there are discrepancies regarding the amplitude and fine structure, specifically in the vicinity of the fundamental transition. This disagreement is associated with a defect structure of epitaxial films (lattice strains, dislocations, and grain boundaries). Some authors carried out theoretical calculations of the energy-band structure of single-crystal β-$FeSi_2$ (with the inclusion of lattice deformations [4] and without regard for such deformations [3, 5]) and optical functions. It was shown that strains arising in the β-$FeSi_2$ crystal lattice can lead to a change in the type of fundamental transition. Unfortunately, the effect of extrinsic defects (for example, an ordered dislocation network in the film) on the optical properties and the energy-band structure of β-$FeSi_2$ epitaxial films has defied calculation. At present, there is a need to investigate thoroughly and simulate the optical properties of β-$FeSi_2$ epitaxial films with a defect structure for the purpose of designing optoelectronic devices based on β-$FeSi_2$/Si heterostructures.

In the present work, we grew thin epitaxial films of β-$FeSi_2$, calculated the optical functions, and determined the energies of the first interband transitions by two different methods. Moreover, we derived an empirical model of the dielectric function of the β-$FeSi_2$ epitaxial film, calculated the model parameters, determined the contribution from oscillators to the dielectric function, and compared the results of calculations with the experimental reflectance spectrum.

2. EXPERIMENTAL TECHNIQUE

Iron disilicide (β-$FeSi_2$) films on silicon substrates were grown in a VARIAN ultrahigh vacuum chamber at a pressure of 2×10^{-10} Torr. The chamber was equipped with an Auger electron analyzer, a manipulator with four degrees of freedom, a holder for three samples, a bank of sources (Cr, Fe, Mg, and Si), and a quartz thickness gauge. In the experiments, *n*-type Si(111) plates ($5 \times 18 \times 0.35$ mm in size) with a resistivity of 5 Ω cm served as substrates. The Si(111)-(7×7) atomically clean silicon surface was prepared by high-temperature annealing at a temperature of 1250°C for 2 min. The surface condition was monitored by Auger electron spectroscopy. The phase composition of the grown films was determined by characteristic electron-energy-

1063-7834/02/4404-0714$22.00 © 2002 MAIK "Nauka/Interperiodica"

loss spectroscopy. Chemically pure iron (99.99%) was used as an iron source. The deposition rate of iron was equal to 0.5–0.6 nm/min.

The β-$FeSi_2$ films were grown by the seed-layer technique, which provided the appropriate conditions for the epitaxial growth of β-$FeSi_2$ on the Si(111) substrate [6]. After the formation of the seed layer, iron was deposited onto a hot (480°C) substrate followed by annealing at a temperature ranging from 600 to 650°C for 20–30 min. As a result, we obtained 30- and 50-nm-thick β-$FeSi_2$ continuous epitaxial films.

The transmittance (T) and reflectance (R) spectra of the samples prepared were recorded on SPECORD 71IR and MDR-3 spectrophotometers in the energy range 0.089–1.2 eV at room temperature. Moreover, the reflectance spectra in the energy range 1.55–6.2 eV at room temperature were measured on a SPECORD UV-VIS spectrophotometer. The main optical functions for β-$FeSi_2$ thin films on Si(111) in the transparent region were calculated from the reflectance and transmittance spectra in the framework of the film–substrate bilayer model [7]. The optical functions ε_1, ε_2, $\mathrm{Im}(\varepsilon)^{-1}$, and σ_{opt} for β-$FeSi_2$ thin films in the energy range 0.1–6.2 eV were calculated from the reflectance spectra in terms of the Kramers–Kronig (KK) integral relations. In order to simulate the optical functions, we derived an empirical model of the dielectric function for β-$FeSi_2$ epitaxial films.

3. THE EMPIRICAL MODEL OF THE DIELECTRIC FUNCTION FOR β-$FeSi_2$

The calculated spectra $\varepsilon(E)$ were analyzed in the framework of an empirical model that is based on the dielectric function model [8, 9] and adapted to β-$FeSi_2$ epitaxial films. Within the dielectric function model, the dielectric function $\varepsilon(E)$ is represented as the sum of the free harmonic oscillators. For each oscillator, the features in the energy-band structure of β-$FeSi_2$ films are described in an analytical form within the approximation of parabolic bands and constant transition matrix elements in the vicinity of the critical points.

Detailed theoretical investigations into the energy-band structure [3] have demonstrated that, for the most part, the energy gap separates the nonbonding and antibonding Fe 3d states with a small admixture of the 3p and 3d states of iron and silicon. It was revealed that a certain mixing of the Fe d, Fe p, and Si p states occurs at the valence band top and the conduction band bottom. Consequently, the optical transitions are not forbidden transitions. The band gap in the β-$FeSi_2$ semiconductor can be either direct [5] or indirect [3, 4]. At the same time, the second interband transition must necessarily be direct and slightly different from the first interband transition [3–5]. The direct band gap is located at a point with low symmetry (along the $Z\Gamma$ line [5] in Fig. 1), whereas the wider direct band gap (0.82–0.86 eV) is observed at the Y point of the Brillouin zone

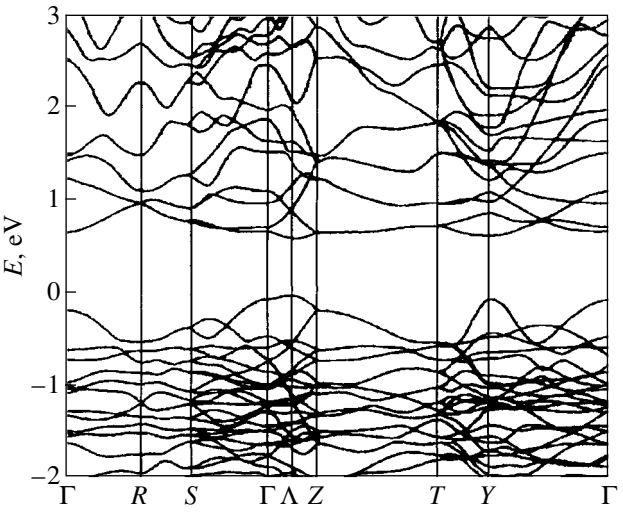

Fig. 1. Electronic energy-band structure calculated by the LMTO method for β-$FeSi_2$ along the directions with a high symmetry in the vicinity of the band gap [5].

[5]. These transitions should exhibit critical points of the three-dimensional (3D) M_0 type. The density of states in the vicinity of the fundamental transition and the oscillator strength of this transition are very small [3–5]. As a result, the reflectance spectrum shows no maximum in the energy range of the fundamental transition. According to theoretical calculations, the first maximum in the reflectance spectrum of β-$FeSi_2$ is observed in the energy range 1.65–1.80 eV [5] and correlates with d–p interband transitions from electronic states in the valence band of iron and silicon to electronic states in the conduction band and vice versa. However, the reflectance spectra of the epitaxial and polycrystalline β-$FeSi_2$ films contain the first maximum in the energy range 0.9–1.05 eV [1, 5]. Therefore, it is in this energy range that the direct interband transition with a large oscillator strength should occur in the energy-band structure of β-$FeSi_2$. The second maximum in the reflectance spectra of β-$FeSi_2$ epitaxial films is observed at 1.9–2.0 eV [5]. As follows from theoretical calculations [3–5], direct interband transitions with critical points of the 3D M_2 and 3D M_1 types [10] and with large oscillator strengths should be observed in the vicinity of the Y, Z, and Γ points [5] (Fig. 1), which stem from the negative band-edge curvature.

At these energies, the energy bands are characterized by an insignificant bending. As a consequence, the three-dimensional M_1-type critical point transforms into the two-dimensional (2D) M_0-type critical point. Therefore, the decomposition of the first two peaks in the reflectance spectrum in the energy range 0.78–2.2 eV can be represented as the sum of electronic transitions of the 3D M_0 (one oscillator) and 2D M_0 (two oscillators) types. In the energy range 2.5–6.2 eV, the reflectance spectrum shows a maximum at 4.5–5.0 eV

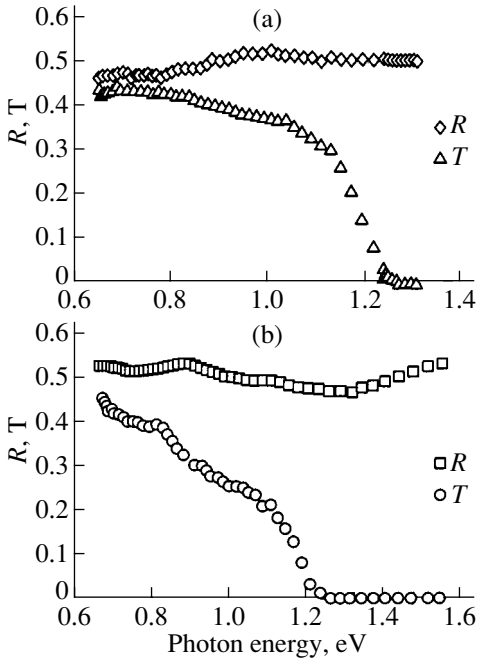

Fig. 2. Transmittance (*T*) and reflectance (*R*) spectra of the β-$FeSi_2$/Si(111) system for different film thicknesses: (a) 30 and (b) 50 nm.

[5]. This suggests that the interband transitions exhibit a large oscillator strength at these energies. On this basis, the dielectric function can be represented as the sum of contributions from three transitions or more, including damped harmonic oscillators (DHO) (a broadened critical point of the 2*D* M_1 type [8]). We assume that all the harmonic oscillators are characterized by a Lorentzian-type broadening [8, 9].

The proposed model is derived for numerical fitting of the dielectric function of the β-$FeSi_2$ epitaxial film in the energy range 0.1–6.2 eV. This model includes six free harmonic oscillators and 19 parameters. These latter are six strength parameters (A_0, $B_1^{(1)}$, $B_1^{(2)}$, $C_2^{(3)}$, $C_2^{(4)}$, and $C_2^{(5)}$), six energies (E_0, $E_0^{(1)}$, $E_2^{(2)}$, $E_2^{(3)}$, $E_2^{(4)}$, and $E_2^{(5)}$), six broadening parameters (Γ_0, $\Gamma_0^{(1)}$, $\Gamma_2^{(2)}$, $\Gamma_2^{(3)}$, $\Gamma_2^{(4)}$, and $\Gamma_2^{(5)}$), and one additive constant ε_∞. The ε_∞ additive constant is not an rf permittivity of the β-$FeSi_2$ epitaxial films but accounts for the effect of all high-energy transitions above 6.2 eV. The fitting was performed by minimizing the root-mean-square error σ_0 for both the real and imaginary parts of the dielectric function $\varepsilon(\omega) = \varepsilon_1(\omega) + i\varepsilon_2(\omega)$ [11]. This error is defined by the expression

$$\sigma_0^2 = \sum_N [(\varepsilon_{1,m} - \varepsilon_{1,d})^2 + (\varepsilon_{2,m} - \varepsilon_{2,d})^2]/\sum_N [\varepsilon_{1,d}^2 + \varepsilon_{2,d}^2],$$

where the subscripts *m* and *d* refer to the model and experimental data, respectively, and *N* is the number of experimental points.

4. EXPERIMENTAL RESULTS, SIMULATION, AND DISCUSSION

Auger electron spectroscopy indicates that the surface of all the β-$FeSi_2$ films under investigation is enriched with silicon. This is explained by the silicon segregation during the growth of β-$FeSi_2$. In this case, the island growth is ruled out because the silicon loss peak associated with the excitation of a bulk plasmon (at 17.1 eV) [12] is absent in the characteristic electron-energy-loss spectra. On the other hand, the spectra of β-$FeSi_2$ films of different thicknesses contain the bulk plasmon excitation loss peak at 20.5–21.0 eV at different energies of the primary electron beam (300–900 eV). This energy of plasmon excitation loss corresponds to the density of valence electrons in the β-$FeSi_2$ semiconductor [13]. Consequently, the β-$FeSi_2$ films are comparable to the bulk single crystals in both their atom and electron densities.

As-prepared iron disilicide semiconductor films 30–50 nm thick are smooth with a mirror luster. According to atomic force microscopy, the thickness inhomogeneity of these films is equal to 10–16 nm. Therefore, all the β-$FeSi_2$ films are continuous and can be examined using optical spectroscopy with the aim of calculating the optical functions, provided the reflectance spectrum is corrected in the energy range above 2 eV [14].

Figure 2 shows the transmittance and reflectance spectra of 30- and 50-nm-thick β-$FeSi_2$ films on the silicon substrate. It can be seen that an increase in the β-$FeSi_2$ layer thickness leads to a decrease in the transmittance of the film–substrate system in the energy range 0.65–1.2 eV. The reflectance spectra of these films are similar in shape, and the corresponding reflection coefficients are close in magnitude. The dependence of the absorption coefficient on the photon energy for the 30-nm-thick β-$FeSi_2$ epitaxial film (Fig. 3a) was determined by solving a system of transcendental equations [7]. The grown samples are characterized by linear portions in the dependence $(\alpha h\nu)^2$ on the photon energy [10] in the range 0.84–1.1 eV (Fig. 3b). By extrapolating the linear portions to the point of intersection with the energy axis, we obtained the direct band gap E = 0.87 eV and the second direct interband transition energy E = 0.97–0.99 eV. In the energy range below 0.87 eV, the behavior of the absorption coefficient cannot be not described by the contribution from the indirect transition with a lower energy and, as a rule, is attributed to absorption by defects in β-$FeSi_2$ films [1]. Our data on the band gap and the type of second interband transition are in agreement with the results obtained by Bost and Mahan [1] and Onda *et al.* [15], who determined the film parameters either by calculating the transmittance and reflectance spectra or

from analysis of the photoreflectance spectra. The fact that the second direct interband transition occurs at an energy of 0.98 ± 0.01 eV is quite consistent with the results of band-structure calculations for both the bulk β-$FeSi_2$ sample [16] and thin β-$FeSi_2$ epitaxial films [16]. The spectra of the absorption coefficient calculated in terms of the Kramers–Kronig integral relations also indicate that the direct fundamental transition should take place at an energy of 0.87 eV (Fig. 3b).

The spectral dependences of the energy loss function $\mathrm{Im}(\varepsilon)^{-1}$ (Fig. 4a) and the optical conductivity σ_{opt} (Fig. 4b) for a 30-nm-thick β-$FeSi_2$ epitaxial film provide additional information on the energy loss distribution of electrons interacting with incident radiation. It can be seen that the spectral dependence of the energy loss function exhibits three local maxima at 1.4, 2.65, and 4.3 eV. The energy positions of these maxima in the energy loss spectrum coincide with those of the minima observed in the spectrum of the optical conductivity. The optical conductivity is a macroscopic parameter and characterizes the absorption of electromagnetic radiation by charge carriers [17]. Consequently, the peaks associated with the energy absorption by charge carriers (at 1.25, 1.6, and 3.7 eV) alternate with the peaks due to electron energy loss. This allows us to distinguish the groups of main oscillators and to apply the dielectric function model to the decomposition of the integrated spectra of the complex dielectric function into the sum of the six spectra of effective free harmonic oscillators.

Let us now consider the calculated data on the fundamental and high-energy interband transitions, which were obtained by numerical simulation of the dielectric function for β-$FeSi_2$. Figure 5 shows the results of numerical simulation (dashed lines) and the experimental spectra $\varepsilon_1(E)$ (open circles) and $\varepsilon_2(E)$ (open squares) processed in terms of the Kramers–Kronig relations. The table presents the parameters determined by the numerical fitting through the minimization of the root-mean-square errors. The root-mean-square error in the simulation is equal to 2.62%. The overall simulated spectrum of the dielectric function is in close agreement with the experimental spectrum in the energy range 0.9–5.5 eV. A small difference between these spectra in the energy range 0.1–0.9 eV can be associated with a more complex structure of the electronic transitions from nonbonding states of iron and silicon, because these transitions are inadequately described within the model of a 3*D* M_0-type harmonic oscillator. This is indicated, for example, by a small oscillator strength (strength parameter) and a considerable broadening parameter of this oscillator (see table). A certain discrepancy is also observed at energies in the range 5.5–6.2 eV and, most likely, can be due to a complex structure of the interband transitions from the Fe–Si *p–d* bonding states to the conduction band in β-$FeSi_2$ epitaxial films. It should be noted that the second effective oscillator with an energy of 0.977 eV is character-

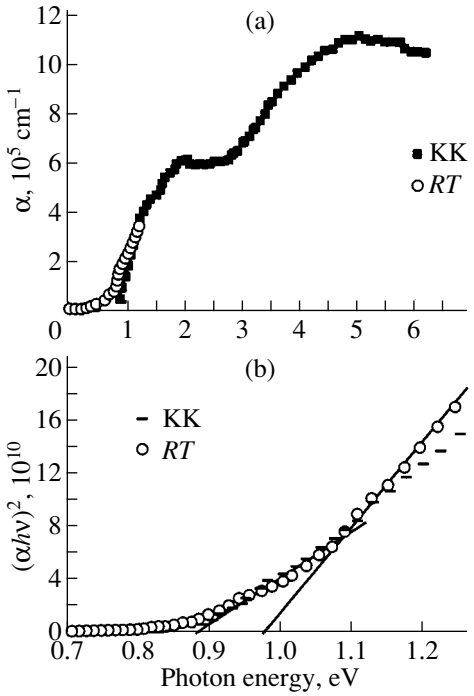

Fig. 3. Spectral dependences of (a) the absorption coefficient and (b) the square of the product of the absorption coefficient by the photon energy for a 30-nm-thick β-$FeSi_2$ epitaxial film. Points represent the results of the calculations from the transmittance and reflectance spectra (*RT*) and the data obtained using the Kramers–Kronig integral relations (KK).

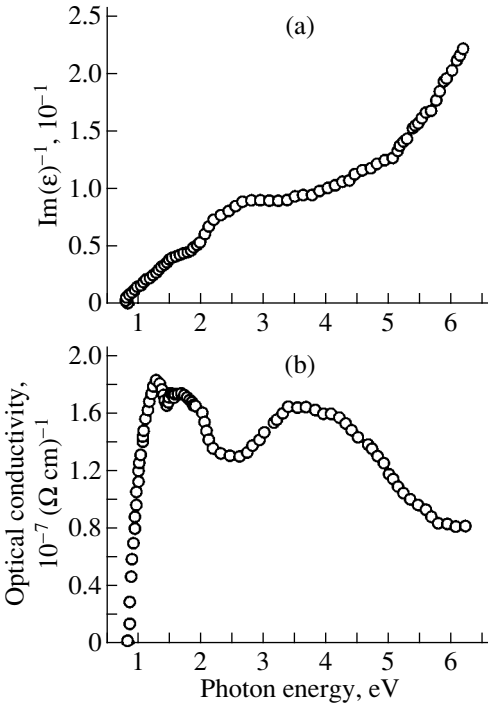

Fig. 4. Spectral dependences of (a) the energy-loss function $\mathrm{Im}(\varepsilon)^{-1}$ and (b) the optical conductivity σ_{opt} for a 30-nm-thick β-$FeSi_2$ epitaxial film.

Parameters of six free harmonic oscillators for the β-$FeSi_2$ epitaxial film

Critical point type	Parameter	Numerical value	Critical point type	Parameter	Numerical value
	E_0 (eV)	0.80		$E_2^{(3)}$ (eV)	3.5
$3D\ M_0$	A_0 (eV)$^{1.5}$	1×10^{-10}	$2D\ M_1$ (DHO)	$C_2^{(3)}$	2.155
	Γ_0 (eV)	0.69		$\Gamma_2^{(3)}$ (eV)	1.293
	$E_1^{(1)}$ (eV)	0.977		$E_2^{(4)}$ (eV)	4.25
$2D\ M_0$	$B_1^{(1)}$	12.33	$2D\ M_1$ (DHO)	$C_2^{(4)}$	0.339
	$\Gamma_1^{(1)}$ (eV)	0.0358		$\Gamma_2^{(4)}$ (eV)	0.605
	$E_1^{(2)}$ (eV)	1.777		$E_2^{(5)}$ (eV)	5.59
$2D\ M_0$	$B_1^{(2)}$	6.879	$2D\ M_1$ (DHO)	$C_2^{(5)}$	1.142
	$\Gamma_1^{(2)}$ (eV)	1.333		$\Gamma_2^{(5)}$ (eV)	2.24
			Contribution from high-energy transitions	ε_∞	0.505
			Root-mean-square error, %	σ_0	2.63

ized by a large strength parameter and insignificant broadening. These data are at variance with the results of theoretical calculations performed in [3–5]. The second harmonic oscillator correlates with the second direct interband transition at an energy of 1.0 ± 0.02 eV. The numerical simulation demonstrated that the electronic structure of β-$FeSi_2$ epitaxial films in the energy range 0.90–1.2 eV differs substantially from the ideal electronic structure used in theoretical calculations [3–5] for β-$FeSi_2$ single crystals. The strength parameters of the third and fourth oscillators are also relatively large (see table); hence, they make a considerable contribution to the dielectric function in the energy range 1.5–2.5 eV. Since the fifth and sixth oscillators are characterized by smaller strength parameters and a more pronounced broadening, they should contribute to the dielectric function to a lesser degree. The effect of all the high-energy interband transitions observed at energies above 6.2 eV is taken into account by the additive constant $\varepsilon_\infty = 0.505$.

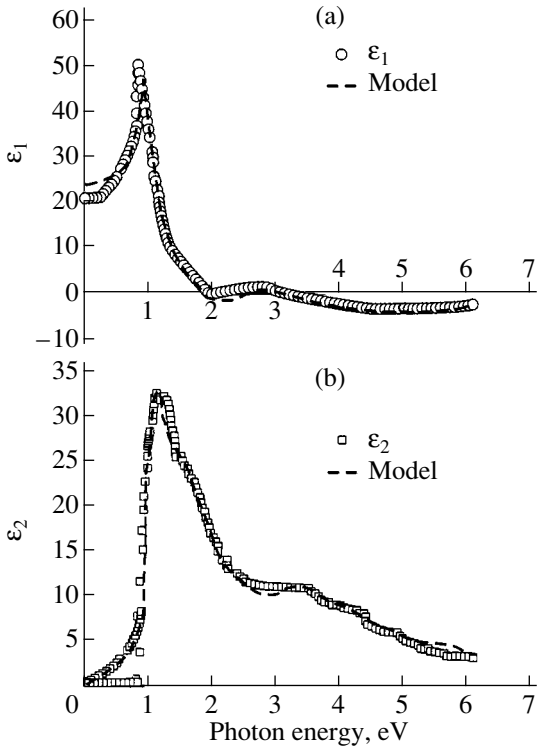

Fig. 5. (a) Real ε_1 and (b) imaginary ε_2 parts of the dielectric function for the β-$FeSi_2$ epitaxial film. Dashed lines represent the simulated spectra $\varepsilon(E)$.

The reflection coefficient measured at close-to-right angles of incidence can be represented in the following form [10]:

$$R(E) = \left[\frac{\{[\varepsilon_1(E) + i\varepsilon_2(E)]^{0.5} - 1\}}{\{[\varepsilon_1(E) + i\varepsilon_2(E)]^{0.5} + 1\}}\right]^2.$$

Figure 6 displays the theoretical reflectance spectrum $R(E)$ (dashed line), which was derived from the simulated spectra of the dielectric function, and the experimental reflectance spectrum (open circles). As can be seen, the dielectric function model proposed in this work adequately describes the experimental dependence of the reflection coefficient for β-$FeSi_2$ films over the entire range of photon energies (0.1–6.2 eV). A

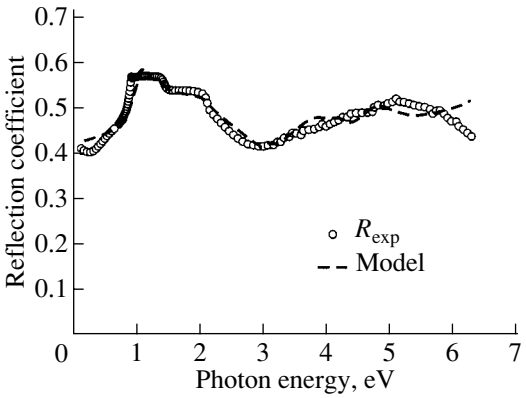

Fig. 6. Model dependence of the reflection coefficient on the photon energy (dashed line) and the experimental reflectance spectrum (circles) for the β-$FeSi_2$ epitaxial film.

small disagreement is observed when simulating the shape of high-energy peaks (3.5–6.2 eV) rather than their amplitudes.

5. CONCLUSION

Thus, the β-$FeSi_2$ continuous thin epitaxial films on the Si(111) substrate were grown by the seed-layer technique. We investigated the electronic structure of these films and calculated the optical functions. The results of calculations from the transmittance and reflectance spectra and the data obtained from the reflectance spectra in terms of the Kramers–Kronig relations demonstrated that the direct fundamental transition occurs at an energy of 0.87 ± 0.01 eV. The semiempirical model of the dielectric function for β-$FeSi_2$ epitaxial films was derived reasoning from an analysis of the reflectance spectra of β-$FeSi_2$ films and theoretical data available in the literature on the energy-band structure of β-$FeSi_2$ single crystals. The integrated spectra were decomposed into the six spectra of free harmonic oscillators, and their parameters were determined. It was shown that the second 2*D* M_0-type harmonic oscillator with an energy of 0.977 eV makes the dominant contribution to the dielectric function and the reflectance spectrum in the energy range 0.9–1.2 eV. This oscillator correlates with the second direct interband transition in the energy-band structure of β-$FeSi_2$.

ACKNOWLEDGMENTS

This work was supported by the Russian Foundation for Basic Research (project no. 00-02-81000Bel2000_a) and the Program "Basic Research in the Field of Electronics and Radio Engineering," the Ministry of Education of the Russian Federation (project KG 98.7).

REFERENCES

1. M. C. Bost and J. E. Mahan, J. Appl. Phys. **58** (7), 2696 (1985).
2. K. Radermacher, R. Carius, and S. Mantl, Nucl. Instrum. Methods Phys. Res. B **84** (2), 163 (1994).
3. N. E. Christensen, Phys. Rev. B **42** (11), 7148 (1990).
4. L. Miglio and G. Malegori, Phys. Rev. B **52** (3), 1448 (1995).
5. A. B. Filonov, D. B. Migas, V. L. Shaposhnikov, *et al.*, J. Appl. Phys. **83** (8), 4410 (1998).
6. X. Chen, L. Wang, Q. Chen, *et al.*, Appl. Phys. Lett. **68** (20), 2858 (1996).
7. N. G. Galkin, A. M. Maslov, and A. V. Konchenko, Thin Solid Films **311** (1), 230 (1997).
8. S. Adachi, Phys. Rev. B **38** (17), 12345 (1988).
9. S. Adachi and K. Sato, Jpn. J. Appl. Phys. **31**, 3907 (1992).
10. R. A. Smith, *Semiconductors* (Cambridge Univ. Press, Cambridge, 1978; Mir, Moscow, 1982).
11. C. C. Kim, J. W. Garland, H. Abad, and P. M. Raccah, Phys. Rev. B **45** (20), 11749 (1992).
12. N. Lieske and R. Hezel, Phys. Status Solidi B **92** (1), 159 (1979).
13. X. Wallart, H. S. Zeng, J. P. Nys, and G. Dalmai, Appl. Surf. Sci. **56–58** (2), 472 (1992).
14. N. G. Galkin, A. M. Maslov, A. V. Konchenko, *et al.*, Opt. Spektrosk. **85** (4), 658 (1998).
15. N. Onda, H. Sirringhaus, S. Goncalves-Conto, *et al.*, Appl. Surf. Sci. **73** (1), 124 (1993).
16. S. J. Clark, H. M. Al-Allak, S. Brand, and R. A. Abram, Phys. Rev. B **58** (16), 10389 (1998).
17. R. K. Ahrenkiek, J. Opt. Soc. Am. **61** (2), 1851 (1971).

Translated by O. Borovik-Romanova

Physics of the Solid State, Vol. 44, No. 4, 2002, pp. 720–726. Translated from Fizika Tverdogo Tela, Vol. 44, No. 4, 2002, pp. 694–699.

SEMICONDUCTORS AND DIELECTRICS

Energy Fluctuations in Optical Transitions in Cu*Hal* Crystals

P. M. Valov and V. I. Leĭman

St. Petersburg State Technological University of Plant Polymers, ul. Ivana Chernykh 4, St. Petersburg, 198095 Russia
e-mail: valeri_leiman@omnisp.ru

Received April 11, 2001; in final form, July 30, 2001

Abstract—This paper reports on a comprehensive study of fundamental-absorption spectra of CuCl and CuBr nanocrystals measured in the temperature range extending from 80 K up to the melting point. The temperature dependences of the energy E, oscillator strength f, and temperature-broadening coefficient σ of optical-transition spectral to excitonic states were determined. A new approach to the calculation of the shape and temperature-broadening of absorption spectra, based on quantum statistics, was employed. The crystal is treated as a quantum statistical ensemble. The set of atoms involved in the electronic transition initiated by a photon absorption is taken as an element of the ensemble. Energy fluctuations of electronic states occurring in the elements of the ensemble give rise to temperature broadening of the optical-transition spectra. The temperature dependence of the χ coefficient of thermodynamic fluctuations of the $Z_{1,2}$ and Z_3 exciton states was found. A theoretical substantiation of the Urbach rule was obtained in terms of the model proposed. © *2002 MAIK "Nauka/Interperiodica".*

1. INTRODUCTION

Publication of new data on the temperature dependence of absorption spectra of semiconductor nanocrystals (NCs) of CuCl [1] and CuBr has reinstated the question of interpretation of the shape and temperature-induced broadening of optical absorption spectra. Studies of the melting–crystallization phase transitions in NCs of CuCl [2] and CuBr established the temperature region where one could investigate the fundamental absorption spectra of these systems. Size-quantization effects do not yet manifest themselves in NCs with dimensions of 10 nm and larger, and they are close in their parameters to single crystals [1, 3]. In contrast to CuBr, the absorption band of the Z_3 exciton in CuCl lies below the $Z_{1,2}$ band [4]. Increasing the temperature brings about a positive shift in energy of the exciton and interband transitions. The temperature-induced broadening of absorption spectra is accompanied by a change in the oscillator strength of optical transitions. The long-wavelength tail of the absorption spectra of Cu*Hal*, as of many other systems [5], follows the Urbach rule. To determine the temperature dependence of the optical-transition parameters in Cu*Hal*, one has to determine the shape of the absorption spectra.

Calculations of absorption spectra in well-known theoretical works (see, e.g., [6–12]) have been performed primarily for the region of the long-wavelength decay to validate the Urbach rule. The results obtained in those works do not permit one to calculate the whole absorption band on a unified basis and make a comparison with experimental data.

This paper puts forward a new approach to the interpretation of the shape and temperature dependence of the absorption spectra of crystals. This approach is based on applying Fermi–Dirac quantum statistics. The crystal as a whole is treated as a quantum ensemble consisting of small crystal regions—the elements of the ensemble. Thermal lattice vibrations give rise to fluctuations of the energy states in an ensemble element and, accordingly, of the optical transition energy. We calculated the shape of the exciton and band-to-band transitions with due account of these fluctuations and determined the temperature dependences of the optical-transition parameters in Cu*Hal* NCs. The long-wavelength tail in the absorption spectra calculated within this model is in agreement with the Urbach rule.

2. FUNDAMENTAL ABSORPTION IN Cu*Hal* NANOCRYSTALS

Earlier, we presented the fundamental absorption spectra of CuCl NCs [1]. Figure 1 displays similar absorption spectra of CuBr NCs. The NCs studied had an average diameter of about 10 nm. The measurements were carried out at temperatures ranging from 300 K up to the melting point. As the temperature increases, both systems exhibit a considerable positive energy shift of the $Z_{1,2}$ and Z_3 exciton absorption bands (in CuCl, this effect is slightly more pronounced than in CuBr).

The temperature broadening of the exciton absorption bands is accompanied by a change (a decrease for the $Z_{1,2}$ exciton and an increase for the Z_3 exciton) in the oscillator strength of the optical transition. A nodal point appears in the long-wavelength tail of the $Z_{1,2}$ exciton absorption band in CuCl and CuBr NCs at an energy E_U, at which the absorption coefficient remains temperature-independent up to NC melting. The nodal point lies at 3.24 eV in CuCl [1] and at 3.00 eV in CuBr.

1063-7834/02/4404-0720$22.00

Below E_U, the absorption spectra of CuCl [1] and CuBr (Fig. 1) fall off exponentially, which is in accord with the Urbach rule. The shape and the observed temperature broadening of the fundamental absorption band and of the long-wavelength tail are governed, most likely, by the same mechanism. This paper proposes a quantum statistical approach for use in calculating the absorption spectra and their temperature-induced variations.

3. MODEL

In accordance with the principles underlying the statistical theory [13], a large system (for instance, a crystal) may be treated as a canonical quantum ensemble consisting of smaller systems—elements of the ensemble (EEs). The choice of the EEs is determined by the problem under study, namely, determination of the effect of temperature on optical absorption spectra. In this case, one has to choose, as an EE, the set of atoms that participate in the electronic transition initiated by the absorption of a photon. In the electron transfer model [14, p. 70], the primary photon absorption event consists in electron transfer to a neighboring atom. Then, the EE will contain atoms of the first coordination shell, with possible involvement of the atomic fields of the second and third coordination shells.

There are two types of elements of which quantum statistical ensembles can consist: bosons and fermions. We assume the EE in the model under study to be the fermion, because the interaction in it is dominated by electrons. In accordance with the definition of the canonical ensemble, the EEs virtually do not interact with one another, because they are excited at different times and at different points of the crystal. They can exchange energy with the remainder of the crystal as with a bath. As a result, the EE ground-state energy will fluctuate. Each EE has a set of energy levels which coincides, at $T = 0$, with that of the crystal. Being a part of the crystal, the EEs do not have translational degrees of freedom.

In terms of the Fermi–Dirac statistics, the distribution of energy E in an ensemble of fermions is given, in the case of no degeneracy, by the relation [13]

$$n(E, T) = \left(e^{\frac{(E-\mu)}{kT}} + 1\right)^{-1}. \quad (1)$$

In this ensemble, μ is the equilibrium position of the EE energy (the crystal ground state) and, as in metals at $T = 0$, is the upper occupied level of the crystal, i.e., the top of the valence band ($\mu = E_V$). When the crystal is heated, the E_V level can change its position as a result of lattice expansion.

According to thermodynamic theory, the EE energy fluctuations can consist of two parts, namely, of the entropy term (due to electron redistribution over the EE levels) and the external work (associated with a change in EE volume and bringing about a shift of the energy

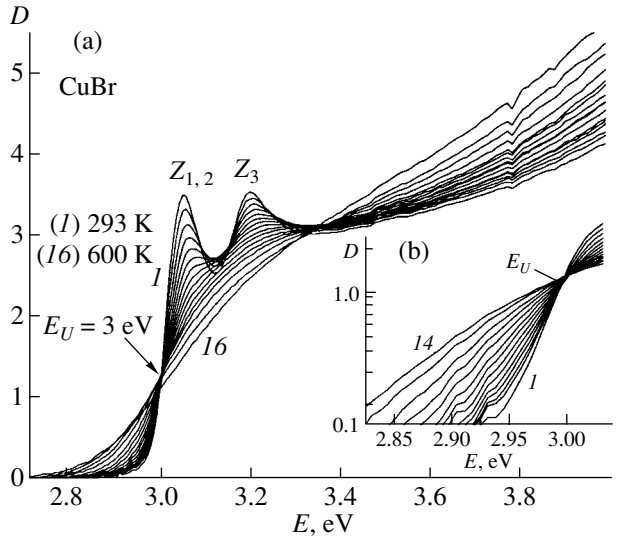

Fig. 1. Fundamental absorption spectra of CuBr NCs measured at different temperatures. Inset shows the long-wavelength tail drawn on the E–log$D$ scale; E_U is the nodal-point energy in the absorption spectra of the $Z_{1,2}$ exciton.

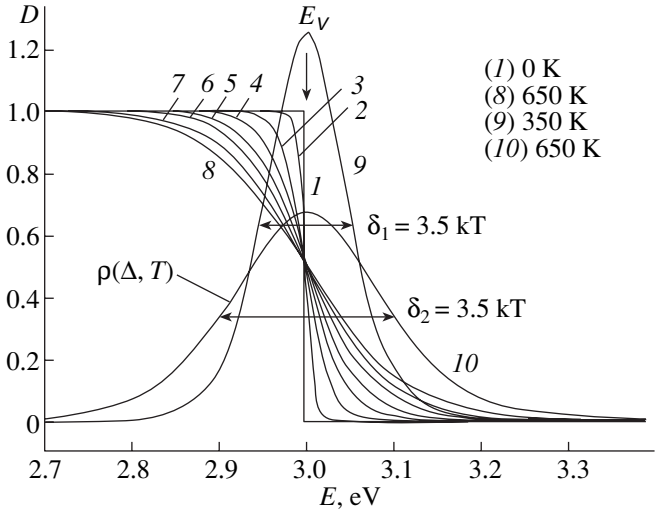

Fig. 2. Fluctuation-induced broadening of the crystal valence-band density of states (*1–8*) calculated using Eq. (1), and the probability distribution function in energy fluctuations for the valence-band top (*9*, *10*) calculated from Eq. (3) for $\sigma\Delta = E - E_V$.

levels [13, p. 47]). In the case of dielectrics and semiconductors with $E_g \gg kT$ (E_g is the band gap width), energy exchange with the bath cannot initiate electron redistribution over empty levels, as is the case with metals. However, thermal fluctuations of the EE volume may cause a shift Δ of the valence-band maximum E relative to the equilibrium position E_V ($\Delta = E - E_V$). Figure 2 presents the $n(E, T)$ distribution for $\mu = E_V$ (calculated for the temperature range 0–650 K) and thermally

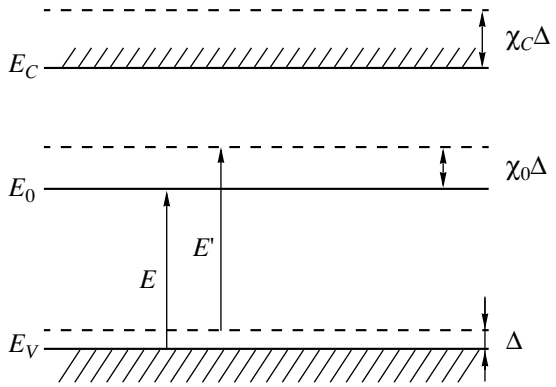

Fig. 3. Energy level shift in an element of the ensemble caused by fluctuations in its volume. E_V, E_C, and E_0 are the energies of the valence-band top, conduction-band bottom, and local level, respectively.

broadened density-of-states curves for the valence-band top for 350 and 650 K.

A volume fluctuation of an EE will shift the whole level system in it, including the conduction-band minimum E_C or a local state E_0 in the band gap (Fig. 3). Obviously enough, the shift of the higher lying electronic states Δ_l in an EE will be proportional to that of the ground state Δ:

$$\Delta_l = \chi_l\Delta, \tag{2}$$

where χ_l is the coefficient of thermodynamic fluctuations of the state E_l, which determines the factor by which the fluctuations of the electronic state l are larger than those of the ground state. The χ coefficient depends on the electronic-state configuration and, in the general case, can be different for a compressed and a stretched EE.

The modulus of the energy derivative of the distribution of Eq. (1) is the function $\rho(\Delta, T)$ characterizing the density-of-states broadening at the valence-band top of the crystal. One can also define the $\rho(\Delta, T)$ function as the distribution of the energy fluctuation probability Δ for the ground state in a fermion ensemble as a function of crystal temperature. This interpretation of the derivative of the function of Eq. (1) is well substantiated, because the level shift Δ is associated with thermal fluctuations of the EE volume. Taking into account Eq. (2), one can relate the probability of the optical-transition energy fluctuations Δ_{opt} to the probability of the fluctuation Δ. To do this, one has to make a replacement $\Delta = \sigma\Delta_{opt}$ in Eq. (1), where σ is a parameter connected with the coefficient χ (the latter will be defined later). As a result, the probability of thermodynamic fluctuations of optical transition energy in an EE will be written as

$$\rho(\Delta_{opt}, T) = \left(e^{\frac{\sigma\Delta_{opt}}{kT}} + 1\right)^{-2} e^{\frac{\sigma\Delta_{opt}}{kT}} \frac{\sigma}{kT}. \tag{3}$$

For the transition from the valence band to a local level E_0 (Fig. 3),

$$\begin{aligned}\Delta_{opt} = E' - E &= (E_0 + \chi_0\Delta) - (E_V + \Delta) \\ &- (E_0 - E_V) = (\chi_0 - 1)\Delta.\end{aligned} \tag{4}$$

Equation (4) yields the relation used for the above-mentioned replacement in the derivative of Eq. (1):

$$\Delta = \frac{1}{\chi_0 - 1}\Delta_{opt} = \sigma\Delta_{opt}, \quad \sigma = \frac{1}{\chi_0 - 1}. \tag{5}$$

To describe optical transitions from the valence to the conduction band, one will have to replace χ_0 in Eqs. (5) for σ by χ_C. In the general case, the coefficient σ for a transition from the ground state (1) to an excited state (2) is given by

$$\sigma = \frac{1}{\chi_2 - \chi_1}, \tag{6}$$

where χ_1 and χ_2 are the corresponding coefficients for the ground and excited states. The less χ_1 and χ_2 differ from one another, the larger the parameter σ and, according to Eq. (3), the smaller the temperature-induced fluctuations of the optical transition energy.

4. TEMPERATURE-INDUCED BROADENING OF THE ABSORPTION SPECTRUM OF A LOCAL CENTER AND OF THE INTERBAND ABSORPTION EDGE

To derive the temperature dependence of absorption spectra for $T > 0$, the reduced density-of-states spectrum $g(E, T)$, which for $T = 0$ is given by a function $g(E, 0)$, should be averaged (as in [6]) over all possible fluctuations of the optical-transition energy Δ defined by Eq. (3). (For convenience, we drop the label "opt".) Thus, we have

$$g(E, T) = \frac{\int_{-\infty}^{+\infty} \rho(\Delta, T) g[(E - \Delta), 0]\, d\Delta}{\int_{-\infty}^{+\infty} \rho(\Delta, T)\, d\Delta}. \tag{7}$$

If the density of states at the band edges is cut off sharply, the spectrum of the reduced density of states for band-to-band transitions is a step $g_1(E, 0) = \mathrm{St}(E_g - E)$ (for $E < E_g$, the St function is zero, and for $E > E_g$, St = 1). The averaging in Eq. (7) yields the following expression for $g_1(E, T)$:

$$g_1(E, T) = \left(e^{\frac{\sigma(E_g - E)}{kT}} + 1\right)^{-1}. \tag{8}$$

This relation was experimentally observed earlier for absorption spectra in interband transitions in the (hexagonal) ZnS system [5].

The density of states for local centers can be presented in the form of a delta function, $g_2(E, 0) = \delta(E_0 - E)$. Due to averaging in Eq. (7), the density-of-states spectrum $g_2(E, 0)$ is broadened and, for a temperature T, is given by the relation

$$g_2(E, T) = \left(e^{\frac{\sigma(E_0 - E)}{kT}} + 1\right)^{-2} e^{\frac{\sigma(E_0 - E)}{kT}} \frac{\sigma}{kT}. \quad (9)$$

For $E_i - E$ (index i denotes g or 0) larger than $2.5kT$, the low-energy absorption tail in Eqs. (8) and (9) can be approximated by the relation

$$g_i(E, T) \sim e^{-\frac{\sigma(E_i - E)}{kT}} \quad (10)$$

defining the Urbach rule [5]. It should be pointed out that the high-energy tail in the absorption spectra of a local center also follows the Urbach rule.

One can use averaging in Eq. (7) to find the temperature-induced broadening for an arbitrary spectrum of the reduced density of states for optical transitions.

5. DETERMINATION OF FUNDAMENTAL ABSORPTION PARAMETERS FOR Cu*Hal* NANOCRYSTALS

It was shown earlier [1] that the absorption curve for interband transitions in CuCl NCs has two steps associated with transitions from different valence subbands. Therefore, the experimental exciton absorption bands were derived from fundamental absorption spectra by subtracting the calculated band-to-band absorption curves $\alpha(E, T)$, which were represented as a sum of two temperature-broadened steps similar to those described by Eq. (8):

$$\alpha(E, T) = f_1\left(e^{\frac{(E_{1g} - E)}{kT}} + 1\right)^{-1} + f_2\left(e^{\frac{(E_{2g} - E)}{kT}} + 1\right)^{-1}, \quad (11)$$

where E_{1g}, E_{2g}, f_1, and f_2 are the energies and oscillator strengths of transitions from the lower and upper valence subbands, respectively. (The coefficients σ in Eq. (11) for these transitions were taken equal to unity.) The optical-transition parameters were determined by comparing the experimental exciton spectra with calculations.

The exciton absorption bands were calculated using Eq. (9) and by assuming that they are due to absorption by local centers. In this case, the absorption [$\alpha_1(E, T)$ for the $Z_{1,2}$ exciton and $\alpha_2(E, T)$ for the Z_3 exciton] can be written as

$$\alpha_1(E, T) = f_{01}\left(e^{\frac{\sigma_1(E_1 - E)}{kT}} + 1\right)^{-2} e^{\frac{\sigma_1(E_1 - E)}{kT}} \frac{\sigma_1}{kT}, \quad (12)$$

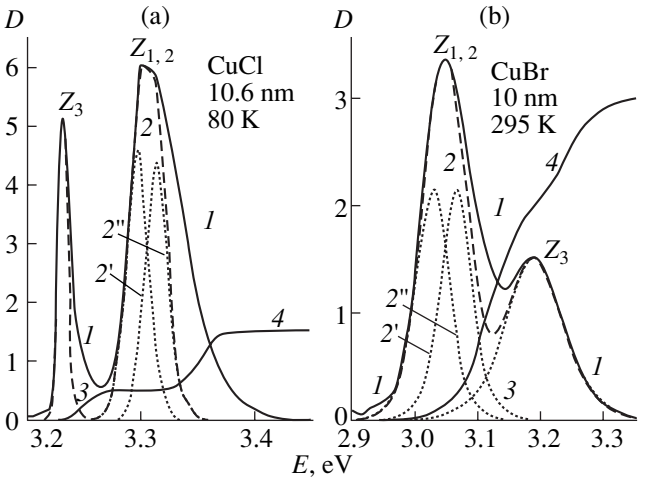

Fig. 4. Decomposition of experimental absorption spectra of NCs of (a) CuCl (80 K) and (b) CuBr (293.5 K). The exciton absorption spectra (curves *1*) were obtained by subtracting the calculated interband absorption [curves *4*, calculation using Eq. (11)] from the experimental spectrum. The exciton absorption spectrum (*2*, *2*", *3*) was calculated using Eqs. (12) and (13).

$$\alpha_2(E, T) = f_{02}\left(e^{\frac{\sigma_2(E_2 - E)}{kT}} + 1\right)^{-2} e^{\frac{\sigma_2(E_2 - E)}{kT}} \frac{\sigma_2}{kT}, \quad (13)$$

where E_1, E_2, f_{01}, and f_{02} are the energies and relative oscillator strengths of transitions to the $Z_{1,2}$ and Z_3 excitonic states, respectively. It was found that E_1 and E_2 are temperature-dependent.

In Eqs. (12) and (13),

$$\sigma_1 = \frac{1}{\chi_1 - 1}, \quad \sigma_2 = \frac{1}{\chi_2 - 1}, \quad (14)$$

where χ_1 and χ_2 are the corresponding coefficients of thermodynamic fluctuations for the $Z_{1,2}$ and Z_3 excitons, respectively.

Figure 4 illustrates the separation of the exciton absorption curves from the fundamental absorption of CuCl and CuBr NCs and the calculation of the exciton bands as being due to local-center absorption. First, we subtracted the interband absorption (curves *4*), calculated using Eq. (11), from the experimental $D(E, T)$ absorption curves. The remaining exciton absorption (curves *1*) was approximated by Eqs. (12) and (13). By fitting the long-wavelength exciton-band tail, the corresponding parameters σ_1 and σ_2 were found (for the $Z_{1,2}$ and Z_3 excitons, respectively). In fitting the calculated to experimental curves at the maximum, we chose the energies (E_1, E_2) and oscillator strengths (f_{01}, f_{02}). The absorption band of the $Z_{1,2}$ exciton (curves *2*) consists of two overlapping bands (curves *2*', *2*") with a splitting of 0.017 eV for CuCl and 0.036 eV for CuBr which were calculated from Eq. (12) using the same parame-

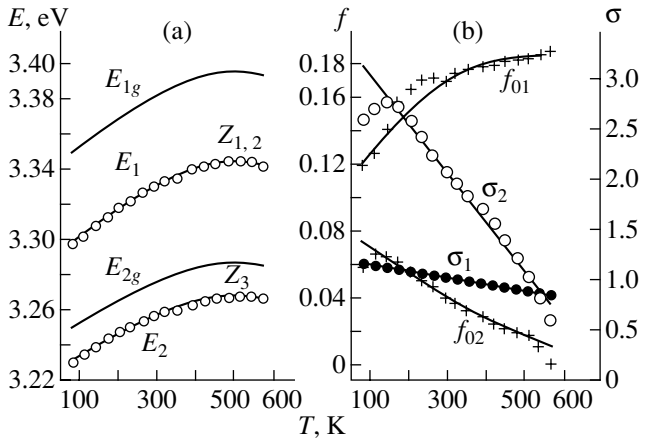

Fig. 5. Temperature dependences (a) of the energies E_{1g} and E_{2g} (interband transitions), E_1 and E_2 (absorption band maxima for the $Z_{1,2}$ and Z_3 excitons), and (b) of the oscillator strengths f_{01} and f_{02}, as well as of the parameters σ_1 and σ_2 [points are the selection made in the calculation; solid lines are extrapolation using Eqs. (17) and (19)] for CuCl NCs.

ter σ_1. The experimental spectra are broader on the high-energy side compared to the calculations. This may be due to the thermodynamic coefficients χ (which define, according to Eq. (5), the parameter σ) being different in the cases of compression and stretching. Superposition of the exciton energy on the band states could also produce an effect. The discrepancy between the calculated and experimental spectra decreases with increasing temperature.

We calculated exciton absorption spectra with the corresponding best-fit parameters f_0, σ, E_1, and E_2 for each temperature separately. In this way, we obtained parameters for all temperatures and their approximating temperature relations. The results for the CuCl NCs are shown in Fig. 5. The parameters of the temperature-induced shift of the exciton transitions E_1 and E_2 are approximated by the relations

$$E_1 = E_{01}(1 + Q(T)), \quad E_2 = E_{02}(1 + 0.9Q(T)), \quad (15)$$

$$Q(T) = 0.65kT - 115(kT)^3, \quad (16)$$

where $E_{01} = 3.282$ eV and $E_{02} = 3.217$ eV. The oscillator strength f_{01} for optical transitions to the $Z_{1,2}$ exciton state increases by a factor of 1.5 (Fig. 5b) when the crystal is heated from 80 to 573 K (the onset of melting). The parameter f_{02} for transitions to the Z_3 exciton state increases slightly when the crystal is heated from 83 to 150 K, to decrease subsequently to zero as the temperature continues to increase. The temperature dependences of the parameters f_{01} and f_{02} can be approximated by the relations

$$\begin{aligned} f_{01} &= 0.086(1 + Q_1(T)), \\ f_{02} &= 0.087(1 - Q_2(T)), \end{aligned} \quad (17)$$

$$\begin{aligned} Q_1(T) &= 72kT - 220(kT)^{1.5}, \\ Q_2(T) &= 22kT - 1700(kT)^3. \end{aligned} \quad (18)$$

The larger part of the temperature dependences of the parameters σ_1 and σ_2 (Fig. 5b) decays linearly with increasing temperature and can be approximated as

$$\sigma_1 = 1.22 - 7.5kT, \quad \sigma_2 = 3.55 - 57kT. \quad (19)$$

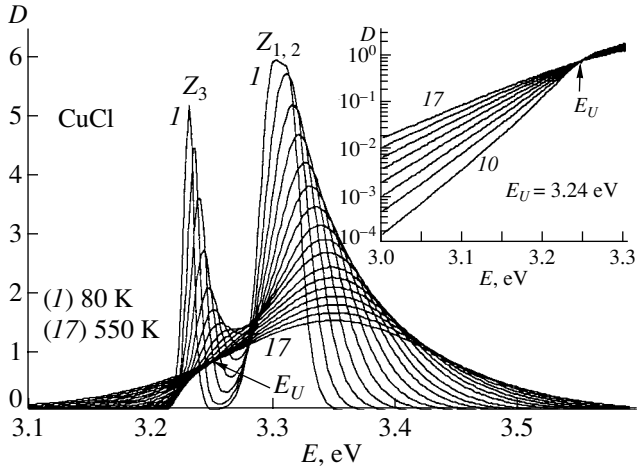

Fig. 6. Absorption spectra of a local center calculated with the parameters of the $Z_{1,2}$ and Z_3 excitons in CuCl NCs.

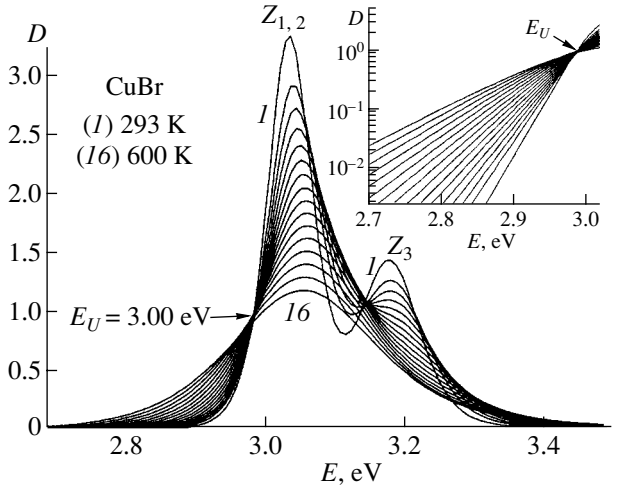

Fig. 7. Absorption spectra of a local center calculated with the parameters of the $Z_{1,2}$ and Z_3 excitons in CuBr NCs.

The temperature-induced shift of the band-to-band transition energy can be described in a way similar to Eqs. (15):

$$E_{1g}(T) = E_{01g}(1 + Q(T)),$$
$$E_{2g}(T) = E_{02g}(1 + Q(T)), \quad (20)$$

where the parameters E_{01g} = 3.333 eV and E_{02g} = 3.236 eV. Fitting the oscillator strengths for the band-to-band transitions yielded

$$f_1(T) = 1.50 + 3.73kT,$$
$$f_2(T) = 0.58 - 7.4kT. \quad (21)$$

The temperature-induced variations of the optical-transition parameters for CuBr NCs can be described by relations similar to those derived for CuCl.

Figures 6 and 7 sum up the calculations of all exciton absorption spectra for CuCl and CuBr NCs, which were made taking into account Eqs. (15)–(21). The temperature-induced variations of the calculated absorption bands and of the long-wavelength tail agree well with the experimental spectra of CuCl [1] and CuBr (Fig. 1) NCs. The presence of the nodal point in the calculated spectra (Figs. 6, 7) in the exciton absorption tail at the energy E_U is accounted for by the temperature-induced shift of the $Z_{1,2}$ exciton energy in the systems under study. The behavior of absorption in the calculated spectra below E_U is consistent with the Urbach rule (see insets to Figs. 6, 7).

In accordance with Eqs. (5), the $\sigma(T)$ relations obtained for CuCl and CuBr NCs can be used to derive the temperature-induced variation of the thermodynamic fluctuation coefficients χ for the exciton states. The temperature dependences obtained for χ are close to exponentials,

$$\chi = \chi_0 + \alpha_1 \exp(\alpha_2 kT). \quad (22)$$

The corresponding parameters for the $Z_{1,2}$ exciton in CuCl are χ_0 = 1.64, a_1 = 0.2, and a_2 = 20. For CuBr, χ_0 = 1.55, a_1 = 0.026, and a_2 = 60. For the Z_3 exciton in CuCl, χ_0 = 1.35, a_1 = 0.005, and a_2 = 110. For CuBr, these parameters were determined within a narrow temperature interval; their approximate values are χ_0 = 2.14, a_1 = 0.025, and a_2 = 50. Figure 8 plots temperature dependences of χ for the excitonic states in NCs of CuCl and CuBr (the regions where the values of χ for CuBr were not determined are dotted). The larger the energy separation between a valence-band state and the corresponding exciton state, the larger the coefficient χ. In CuCl NCs, the fluctuations of the Z_3 exciton state grow considerably more strongly with increasing temperature than those of the $Z_{1,2}$ exciton. The amplitude of fluctuations of the $Z_{1,2}$ states is nearly two times (χ_1 = 1.8 at 80 K) that of the ground state. In the case of CuBr, the energy of transition to the Z_3 state is higher than that to the $Z_{1,2}$ state and, accordingly, the fluctuations of the Z_3 state are larger. At the maximum temperature (immediately before melting), the fluctuation amplitudes of the Z_3 exciton states are more than twofold those of the crystal ground state.

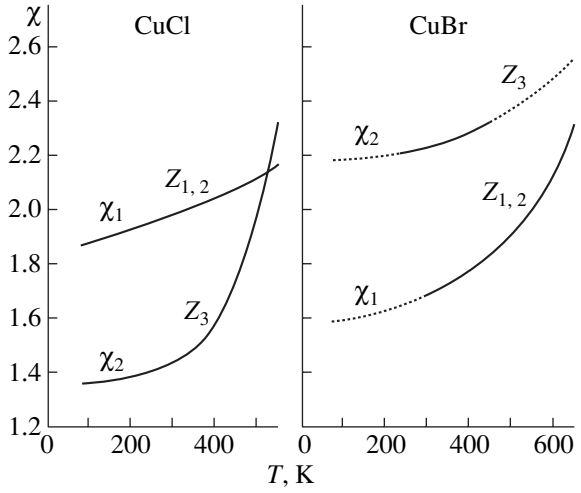

Fig. 8. Temperature dependence of the thermodynamic fluctuation coefficients χ for energy states of the $Z_{1,2}$ and Z_3 excitons in CuCl and CuBr NCs.

6. CONCLUSIONS

Thus, the model proposed for the calculation of the temperature broadening of absorption spectra, which is based on the application of Fermi–Dirac quantum statistics to the crystal, demonstrated its efficiency for the specific example of CuCl and CuBr NCs. We succeeded in establishing, for the first time, the temperature dependences of the parameters of optical transitions to exciton states. The exciton-absorption line shape is described fairly well in terms of thermodynamic fluctuations of the crystal energy states. The nodal point in the long-wavelength tail of the absorption spectra of Cu*Hal* NCs, which is also observed to exist in many systems [5], is due to the temperature-induced shift of the exciton state energy. The long-wavelength absorption tail in the calculated exciton absorption spectra is consistent with the Urbach rule. The parameter σ in the Urbach relation has been given an interpretation different from the one accepted earlier (see, e.g., [11, 12]). The parameter σ is determined by the difference between the ground- and excited-state fluctuations in an optical transition.

The reduced density of states for the band-to-band transition edge in Cu*Hal* crystals, as well as in ZnS [5], is described well by a distinct step (for $T \longrightarrow 0$). As the temperature is increased, the step broadens toward the band gap. The absorption tail is also consistent with the Urbach rule.

The proposed model for the interpretation of the shape and temperature-induced broadening of absorption spectra is also applicable to impurity centers (*F*

centers). It can also be employed in calculations of the temperature broadening of the absorption edge for disordered systems (melts, amorphous dielectrics, or oxide glasses). In all cases, the absorption tail at high temperatures should follow the Urbach rule.

ACKNOWLEDGMENTS

This study was supported by the Russian Foundation for Basic Research (project no. 00-15-96750.

REFERENCES

1. P. M. Valov, L. V. Gracheva, V. I. Leĭman, and T. A. Negovorova, Fiz. Tverd. Tela (St. Petersburg) **36** (6), 1743 (1994) [Phys. Solid State **36**, 954 (1994)].
2. P. M. Valov and V. I. Leĭman, Fiz. Tverd. Tela (St. Petersburg) **41** (2), 310 (1999) [Phys. Solid State **41**, 278 (1999)].
3. A. I. Ekimov, Phys. Scr. T **39**, 217 (1991).
4. M. Cordona, Phys. Rev. **129** (1), 69 (1963).
5. M. V. Kurik, Phys. Status Solidi A **8** (1), 9 (1971).
6. D. L. Dexter, Nuovo Cimento Suppl. **7**, 245 (1958).
7. D. L. Dexter, Phys. Rev. Lett. **19**, 1383 (1967).
8. H. Sumi and Y. Toyozava, J. Phys. Soc. Jpn. **31** (2), 342 (1971).
9. V. D. Kagan, Fiz. Tverd. Tela (Leningrad) **17** (9), 2578 (1975) [Sov. Phys. Solid State **17**, 1717 (1975)].
10. A. S. Ioselevich, Zh. Éksp. Teor. Fiz. **81** (4), 1508 (1981) [Sov. Phys. JETP **54**, 800 (1981)].
11. M. Schreiber and Y. Toyozava, J. Phys. Soc. Jpn. **51** (5), 1528 (1982); **51**, 1537 (1982); **51**, 1544 (1982).
12. A. V. Sherman, Phys. Status Solidi B **145** (1), 319 (1988).
13. L. A. Girifalco, *Statistical Physics of Materials* (Wiley, New York, 1973; Mir, Moscow, 1975).
14. R. S. Knox, *Theory of Excitons* (Academic, New York, 1963; Mir, Moscow, 1966).

Translated by G. Skrebtsov

Physics of the Solid State, Vol. 44, No. 4, 2002, pp. 727–731. Translated from Fizika Tverdogo Tela, Vol. 44, No. 4, 2002, pp. 700–704.

SEMICONDUCTORS AND DIELECTRICS

Shallow Thermal Donors in Nitrogen-Doped Silicon Single Crystals

V. V. Voronkov, G. I. Voronkova, A. V. Batunina, V. N. Golovina, L. V. Arapkina, N. B. Tyurina, A. S. Gulyaeva, and M. G. Mil'vidskiĭ

State Rare-Metal Research Institute, Bol'shoĭ Tolmachevskiĭ per. 5, Moscow, 109017 Russia

e-mail: icpm@mail.girmet.ru

Received April 11, 2001; in final form, August 6, 2001

Abstract—Czochralski-grown nitrogen-doped silicon crystals contain shallow thermal donors (STD) which are not present in reference crystals. In the course of annealing at 600 or 650°C, the STD concentration reaches saturation and this concentration scales with nitrogen content N as $N^{1/2}$. This implies that an STD includes only one nitrogen atom and that the most likely model of the STD defect is the NO_m complex of an interstitial nitrogen atom with *m* oxygen atoms. The number *m* is estimated as, on the average, $m = 3$ from data on the temperature dependence of the equilibrium constant for the complex formation reaction © *2002 MAIK "Nauka/Interperiodica".*

1. INTRODUCTION

Shallow single thermal donors, with an ionization energy from 35 to 37 eV, were observed in Czochralski-grown silicon single crystals both immediately in the as-grown state and after subsequent heat treatments performed over a broad temperature range [1–8]. These defects are identified with several sharp peaks in the IR region, and they can contribute substantially to the carrier concentration. The nature of the shallow thermal donors (STDs) observed after a low-temperature anneal (near 470°C) remains unclear [2, 3, 7, 8]. There may exist several types of centers of different chemical nature but with closely lying shallow levels. On the other hand, STDs were observed in the post-growth state and after annealing at moderate temperatures of 600–700°C only in crystals that were doped with nitrogen and had a high oxygen concentration [1, 4–6]. In these cases, the STDs are certainly nitrogen–oxygen complexes and their properties attract considerable interest. The moderate-temperature region used to create the nitrogen STDs is remarkable in that, in silicon samples not doped with nitrogen, one observes fast annealing of conventional (double) oxygen thermal donors and generation of so-called new (second-kind) oxygen thermal donors (NTDs) [9, 10]. The NTDs form, however, only after a relatively long anneal (compared with the fast STD generation in samples containing a nitrogen impurity), and, for this reason, thermal donors of the above two types are well separated. Moreover, according to [11], NTD formation is completely suppressed in the presence of the nitrogen impurity even after a prolonged anneal. Hence, the STD generation at 600–700°C can be studied simply by following the carrier concentration, without application of optical techniques. Useful information is provided primarily by comparing samples with different nitrogen concentrations over a broad range of doping levels. Such data permit one to draw a conclusion as to the chemical composition of the STD defects.

2. EXPERIMENT

This study was performed on samples of three silicon crystals 150 mm in diameter which were Czochralski grown under identical conditions. Two of them were doped with nitrogen by introducing silicon nitride into the melt, and the third served as a reference sample. The original nitrogen concentration in the melt was $N_0^* = 10^{18}$ cm^{-3} for the first crystal and 10^{17} cm^{-3} for the second. The nitrogen impurity distribution coefficient *K* [12] is much less than unity, $K = 7 \times 10^{-4}$, and, therefore, nearly all the nitrogen remains in the melt in the course of growth. The nitrogen concentration in the melt *N** grows with increasing fraction *g* of the solidified silicon, and the concentration of nitrogen in the crystal ($N = KN^*$) reproduces this variation:

$$N = KN_0^*/(1-g). \quad (1)$$

This concentration increases noticeably along the crystal length; in our case, the increase is about fivefold as one goes from the beginning to the end of the crystal.

The other crystal characteristics are as follows: the oxygen content is almost uniform over the length and radius and close to 7×10^{17} cm^{-3} (when using the optical calibration coefficient 2.45×10^{17} cm^{-2}), the carbon content is below the optical sensitivity threshold (3×10^{15} cm^{-3}), and the boron dopant concentration is 5×10^{14} cm^{-3} or less.

1063-7834/02/4404-0727$22.00 © 2002 MAIK "Nauka/Interperiodica"

Rectangular samples, 12 mm long and 3 mm wide, were prepared from original wafers (1 mm thick) cut from different parts of the crystal. The samples were isothermally annealed at different temperatures (for the most part, at 600 or 650°C). The room-temperature carrier concentration (in some cases, of the electrons n_r, and in the other, of the holes, p_r) was derived from Hall effect measurements. To check the energy position of the thermodonor level, the temperature dependence of the Hall effect down to the liquid-helium temperature was measured on some samples.

The concentration of the STDs (shallow single donors), denoted subsequently by N_s, was calculated as $N_s = N_B + n_r$ (for the *n*-type samples) or as $N_s = N_B - p_r$ (for the *p*-type samples). To determine the boron acceptor concentration N_B, some samples prepared in the post-growth state were annealed at 900°C for five or ten minutes to remove the grown-in thermal donors. These samples always exhibited *p*-type conductivity, and in this case, using a standard technique [13], N_B and the residual concentration of the compensating donors (which was usually low) were determined separately from Hall effect measurements performed from room temperature down to 15 K.

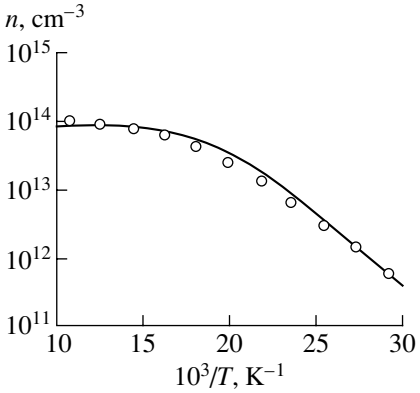

Fig. 1. Temperature dependence of the electron concentration from Hall measurements performed down to the liquid-nitrogen temperature. The sample with nitrogen concentration $N = 2 \times 10^{15}$ cm^{-3} was heat-treated at 600°C for four hours. The low-temperature part of this curve corresponds to a shallow donor level $E_c - 36$ meV.

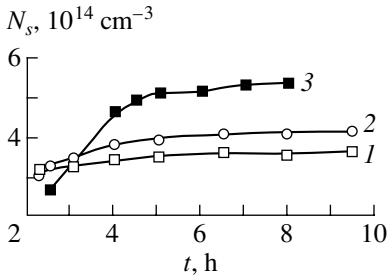

Fig. 2. STD concentration vs. annealing time at 600°C. Nitrogen concentration N (10^{14} cm^{-3}): (*1*) 8, (*2*) 11, and (*3*) 17.

3. RESULTS

Figure 1 illustrates the temperature dependence of the electron concentration $n(T)$ as derived from Hall measurement data obtained on a sample with a relatively high nitrogen content after heat treatment at 600°C. The decrease in n at low temperatures is caused by electron trapping on a shallow level $E_c - 36$ meV, which is in agreement with the position of the STD donor levels known from optical measurements [1–8].

Typical kinetic curves $N_s(t)$ (the dependence of the STD concentration on annealing time) for samples with different nitrogen concentrations are displayed in Fig. 2 (annealing at 600°C). In the original (post-growth) state, these samples usually had *n*-type conductivity due to the presence of grown-in thermal donors: the conventional (double) oxygen thermal donors and STDs. At 600°C, however, double thermal donors disappear fairly rapidly (in half an hour) and the samples are rendered *p* type. In this stage, the concentration of STDs is lower than the acceptor concentration N_B. As the anneal time increases, the conduction recovers to the *n* type due to the increasing N_s concentration. N_s reaches saturation after about six hours of annealing. In the samples prepared from the reference crystal, annealing at 600 or 650°C rapidly resulted in *p* conductivity, with the concentration of holes being close to that of the boron acceptors. Hence, STDs are not generated in the absence of the nitrogen impurity within this temperature interval.

The dependence of the concentration N_s (in the saturation stage) on the nitrogen impurity concentration N is shown in Fig. 3. These data were obtained for two anneal temperatures (600 and 650°C) and represent the main result of the present work. It was found that N_s is proportional not to the nitrogen concentration N but rather to the square root of N.

4. DISCUSSION OF RESULTS

It is well known that nitrogen in silicon prepared by float-zone melting (i.e., with a low oxygen content) exists at room temperature primarily in the molecular form N_2. This relates both to samples with implanted nitrogen [14] and to crystals doped in the melt [15]. The most probable form of the molecular state is a complex of two nitrogen interstitials [16]. As the temperature increases, the molecular nitrogen N_2 dissociates partially into two interstitials atoms; however, close to 650°C, the molecular species should still be dominant.

This statement is corroborated by data [17] on the nitrogen diffusion coefficient D in float-zoned silicon obtained at 1000–1100°C. The prefactor in the $D(T)$ dependence was found to be anomalously high (2.7×10^3 cm^2/s), whereas for the interstitial impurities in silicon, it is only ~0.1 cm^2/s [18]. This anomalously high value finds ready explanation if we assume that nitrogen diffusion occurs through the transport of rapidly

diffusing nitrogen interstitials (with the diffusion coefficient D_1), which make up only a small fraction of the total nitrogen concentration N. The concentrations of the two species of nitrogen—C_1 (of labile atomic interstitials) and C_2 (of low-mobility molecular interstitials)—are related through the law of mass action

$$C_1^2/C_2 = \rho \exp(-E/kT), \quad (2)$$

where ρ is equal, in order of magnitude, to the density of interstitial sites (5×10^{22} cm^{-3}) and E is the molecule dissociation energy. When the molecular species is dominant, C_2 is close to $N/2$ and C_1 can be written as

$$C_1 \approx (\rho N/2)^{1/2} \exp(-E/2kT). \quad (3)$$

The diffusive flux of the impurity (i.e., of the interstitials) is $-D_1 dC_1/dx$. It is expressed through the gradient of the total concentration (dN/dx) in accordance with Eq. (3). On the other hand, this flux is $-DdN/dx$, where D is the effective (measured) diffusion coefficient. Hence, $D = 0.5D_1C_1/N$. The total prefactor of this expression includes a factor associated with the diffusion coefficient D_1 (having a normal value) and an additional factor $(\rho/8N)^{1/2}$, which is equal, in order of magnitude, to 10^3 (for the actual nitrogen concentration in the diffusion experiment).

Thus, the anomalously large prefactor in the $D(T)$ relation argues for the relatively weak dissociation of molecular nitrogen at temperatures below 1100°C and, the more so, in our temperature interval (below 700°C). Theoretical calculations of the energies of different nitrogen species [19, 20] suggest a still more categorical statement, namely, that the molecular species remains dominant up to the melting point.

Hence, in view of Eq. (2), one can maintain that the square-root dependence of the STD concentration on the total nitrogen concentration N (Fig. 3) implies the existence of one nitrogen interstitial in each STD defect. The concentration C_1 of the nitrogen interstitials in equilibrium with the molecular species scales as $N^{1/2}$ (actually, this relation should be corrected for the STD contribution to the total concentration N, but the $N^{1/2}$ dependence holds qualitatively if N is not too low). Atomic nitrogen reacts with oxygen to form STD complexes NO_m; their equilibrium concentration is proportional to C_1, and, hence, it scales as $\sim N^{1/2}$. This model of STD defects is consistent with the calculation of the electronic properties of the NO_m complexes [21], which suggests that these complexes should be shallow donors for $m > 1$.

The STD family includes several types of NO_m complexes with different oxygen index m. The equilibrium concentration of each such complex N_{sm} is expressed through the reagent concentrations C_1 (of atomic nitrogen) and C (of oxygen) related by the law of mass action, which is similar to Eq. (2):

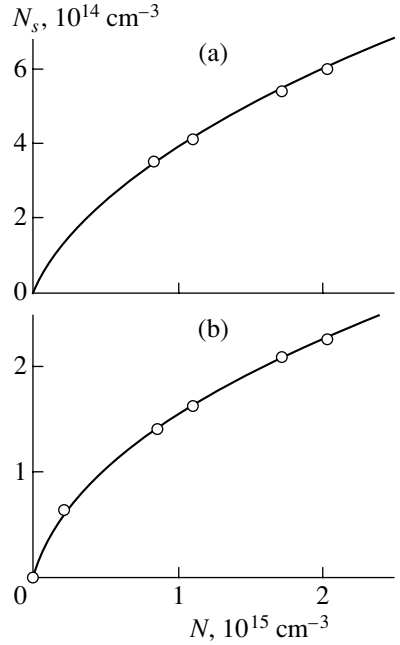

Fig. 3. STD concentration in the saturation stage (for the anneal time interval 4–8 h) plotted vs. nitrogen content in samples annealed at (a) 600 and (b) 650°C. Solid lines are calculated using Eq. (7).

$$C_1 C^m / N_{sm} = \rho^m \exp(-E_m/kT), \quad (4)$$

where E_m is the energy of dissociation of the NO_m complex into atoms.

We assume that the STD concentration in the saturation stage corresponds to complete equilibrium, where both equilibrium relations, Eqs. (2) and (4), hold for all members of the STD family providing the major contribution to N_s. To express the concentration of each STD defect N_{sm} in terms of the total nitrogen and oxygen concentrations, one should bear in mind that a part of the molecular nitrogen in silicon with a high oxygen concentration (obtained by the Czochralski method), similar to atomic nitrogen, is bound to oxygen and forms, most likely, electrically inactive complexes N_2O [14, 22]. This effect manifests itself in the formation of satellite IR peaks close to the vibration-mode peaks of the molecular species N_2. Thus, molecular nitrogen exists in two species, N_2 and N_2O, and the ratio of their concentrations at temperatures near 650°C is unknown. However, this does not complicate the model noticeably if we assume that the concentrations of the above two species C_2 (for the N_2 state) and C_2^* (for the N_2O state) have equilibrium values:

$$C_2 C / C_2^* = \rho \exp(-E^*/kT), \quad (5)$$

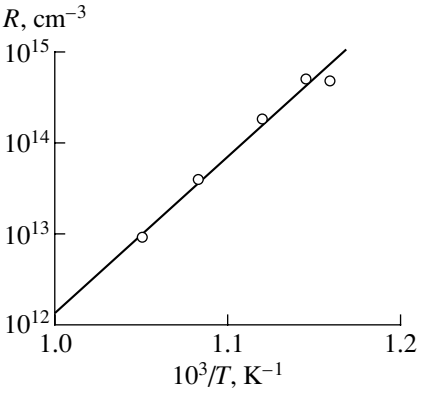

Fig. 4. Temperature dependence of the equilibrium constant R characterizing formation of STDs (NO_m complexes).

where E^* is the N_2O-complex dissociation energy into N_2 and an oxygen atom.

The total nitrogen concentration N now includes the contribution from both molecular species (N_2 and N_2O) and from all STD defects (NO_m complexes with different m):

$$N = 2(C_2 + C_2^*) + N_s. \quad (6)$$

Combining Eqs. (2) and (4)–(6) yields a general equation relating the concentration N_s (which is the sum of all individual contributions N_{sm} of the complexes with different m) to the total nitrogen-impurity concentration N:

$$N_s^2/(N - N_s) = R(C). \quad (7)$$

Here, R is the equilibrium constant and the quantity $\sqrt{R}$ is expressed through a sum over all STD defects with different m. In particular, if STDs with one given m are dominant, then

$$R(C) = \frac{0.5\rho(C/\rho)^{2m}\exp(\varepsilon_m/kT)}{1 + (C/\rho)\exp(E^*/kT)}, \quad (8)$$

where $\varepsilon_m = 2E_m - E$ is a combination of the dissociation energies defined above. In a general case of several types of STD defects with different m present in comparable concentrations, one may retain Eq. (8) but consider the number m in this expression as an average oxygen index for the NO_m complexes.

The equilibrium constant R was determined from the best fit of Eq. (7) to the curves in Fig. 3. The corresponding calculations are shown by solid lines in Fig. 3. The equilibrium constant determined in this way is $R = 5 \times 10^{14}$ cm^{-3} for 600°C and 5.7×10^{13} cm^{-3} for 650°C.

If the total nitrogen concentration N is large compared to R, nitrogen exists predominantly as the molecular species N_2 or N_2O and the fraction of the electrically active (donor) species NO_m is small. However, for low concentrations ($N \ll R$), the donor species NO_m becomes dominant; i.e., the electrical activity of the nitrogen impurity is nearly 100%. In the concentration range under study, the donor species, though not dominant, provide an appreciable contribution into the total nitrogen concentration.

4.1. The Temperature Dependence of the Equilibrium Constant and the Average Number of Oxygen Atoms in the STD

Most of the data were obtained for the anneal temperatures 600 and 650°C. For some other temperatures (590, 620, 680°C), the STD concentration in the saturation region was measured only for one or two nitrogen concentrations. This was enough to determine the equilibrium constant R using Eq. (7). The temperature dependence of R thus obtained is displayed in Fig. 4. It is well fitted by the standard exponential Arrhenius equation, with an activation energy of 3.3 eV and a prefactor 4.5×10^{-5} cm^{-3}. According to Eq. (8), the $R(T)$ function reduces to an exponential if one of the molecular complexes (N_2 or N_2O) is dominant. If N_2 dominates, the prefactor in $R(T)$ is $0.5\rho(C/\rho)^{2m}$; in the opposite case, it is $0.5\rho(C/\rho)^{2m-1}$. The dependence on the oxygen concentration is a power law (of the type C^q), and the numerical value of the prefactor corresponds to the power $q = 5.5$. The above two expressions for this factor yield different relations of the exponent q with the oxygen index m ($q = 2m$ or $q = 2m - 1$), but the values of m derived from them differ by only 0.5. Therefore, the estimated average index lies within a relatively narrow interval, from 2.75 to 3.25. One may thus conclude that the family of STDs consists predominantly of the NO_2, NO_3, and NO_4 complexes. This conclusion is consistent with the electrical properties of the NO_m complexes (shallow donors for $m > 1$) predicted in [21].

4.2. Possible Kinetics of STD Generation

Thus far, we have used only the equilibrium parameters of the defects participating in STD generation; the above analysis does not depend on the actual reactions leading to the formation of the NO_m complexes. The type of the reactions involved influences only the characteristic time during which the equilibrium is established. The simplest mechanism is the dissociation of molecular nitrogen and the subsequent reaction of the rapidly diffusing nitrogen interstitials with oxygen giving rise to the formation of NO complexes (which, according to [21], are electrically inactive). Further growth to NO_2 and larger complexes (to the STD state) can proceed through the diffusion of oxygen atoms.

The characteristic time τ of oxygen attachment in the case of a diffusion-controlled reaction is given by the well-known expression

$$1/\tau = 4\pi r D_O C, \quad (9)$$

where D_O is the oxygen diffusion coefficient [23] and r is the radius of capture (of the order of the interatomic distance). For instance, at 600°C, $D_O = 3.3 \times 10^{-16}$ cm^2/s and the characteristic attachment time τ is about 2.5 h. This estimate is consistent with the experimentally measured time required to reach saturation (a few hours at 600°C).

The initial stage of STD formation (the formation of the NO complexes) can also proceed without dissociation of molecular nitrogen N_2, if the dissociation energy is sufficiently high. In this case, the N_2 molecule can react with the rapidly diffusing oxygen dimer O_2 to produce two NO complexes. These complexes should be mobile enough to migrate to a considerable distance from each other in the course of heat treatment.

5. CONCLUSIONS

Thus, the data obtained and analyzed in this work show that the shallow single thermal donors (STDs) generated at moderate anneal temperatures (near 650°C) are complexes of oxygen and nitrogen impurities, NO_m. Such a complex contains one interstitial nitrogen atom and m oxygen atoms. The STD family apparently includes several types of complexes with the number m varying from two to four (on the average, three).

The relation between the STD concentration (N_s) in the saturation stage and the total nitrogen concentration N in the crystal was established. The total nitrogen content N can be calculated from the measured value of N_s using a simple expression,

$$N = N_s + N_s^2/R. \quad (10)$$

The equilibrium constant R was determined only for one value of the oxygen concentration C. However, R depends on C according to a power law C^q with the exponent $q = 5.5$, which permits one to calculate R for other values of C.

The electrical activity of the nitrogen impurity originates from the donor defects NO_m; it is fairly high for nitrogen concentrations below 10^{15} cm^{-3} (after annealing at moderate temperatures). At still lower nitrogen concentrations, this impurity may nearly fully become electrically active.

REFERENCES

1. M. Suezawa, K. Sumino, H. Harada, and T. Abe, Jpn. J. Appl. Phys. **25** (10), L859 (1986).
2. H. Navarro, J. Griffin, J. Wever, and L. Genzel, Solid State Commun. **58**, 151 (1986).
3. J. A. Griffin, J. Hartung, J. Weber, *et al.*, Appl. Phys. A **48** (1), 41 (1989).
4. A. Hara, T. Fukuda, T. Miyabo, and I. Hirai, Appl. Phys. Lett. **54** (7), 626 (1989).
5. A. Hara, M. Aoki, M. Koizuka, and T. Fukuda, J. Appl. Phys. **75** (6), 2929 (1994).
6. D. Yang, R. Fan, L. Li, *et al.*, Appl. Phys. Lett. **68** (4), 487 (1996).
7. R. C. Newman, J. C. Tucker, N. G. Semaltianos, *et al.*, Phys. Rev. B **54** (10), R6803 (1996).
8. R. C. Newman, M. J. Ashwin, R. E. Pritchard, and J. H. Tucker, Phys. Status Solidi B **210**, 519 (1998).
9. P. M. Grinshteĭn, G. V. Lazareva, E. V. Orlova, *et al.*, Fiz. Tekh. Poluprovodn. (Leningrad) **12** (1), 68 (1978) [Sov. Phys. Semicond. **12**, 68 (1978)].
10. A. Kanamori and M. Kanamori, J. Appl. Phys. **50** (12), 8095 (1979).
11. D. Yang, R. Fan, L. Li, *et al.*, J. Appl. Phys. **80** (3), 1493 (1996).
12. Y. Yatsurugi, N. Akijama, Y. Endo, and T. Nozaki, J. Electrochem. Soc. **120** (7), 975 (1973).
13. J. S. Blakemore, *Semiconductor Statistics* (Pergamon, Oxford, 1962; Mir, Moscow, 1964).
14. H. J. Stein, Mater. Res. Soc. Symp. Proc. **59**, 523 (1986).
15. T. Abe, H. Harada, N. Ozawa, and K. Adomi, Mater. Res. Soc. Symp. Proc. **59**, 537 (1986).
16. F. B. Rasmussen, S. Oberg, R. Jones, *et al.*, Mater. Sci. Eng. B **36**, 91 (1996).
17. T. Ito and T. Abe, Appl. Phys. Lett. **53** (1), 39 (1988).
18. B. I. Boltaks, *Diffusion and Point Defects in Semiconductors* (Nauka, Leningrad, 1972).
19. H. Sawada and K. Kawakami, Phys. Rev. B **62** (3), 1851 (2000).
20. H. Kageshima, A. Taguchi, and K. Wada, Appl. Phys. Lett. **76** (25), 3718 (2000).
21. G. P. Ewels, R. Jones, S. Oberg, *et al.*, Phys. Rev. Lett. **77** (5), 865 (1996).
22. P. Wagner, R. Oeder, and W. Zulehner, Appl. Phys. A **46** (2), 73 (1988).
23. J. Mikkelsen, Mater. Res. Soc. Symp. Proc. **59**, 19 (1986).

Translated by G. Skrebtsov

Physics of the Solid State, Vol. 44, No. 4, 2002, pp. 732–737. Translated from Fizika Tverdogo Tela, Vol. 44, No. 4, 2002, pp. 705–710.

DEFECTS, DISLOCATIONS, AND PHYSICS OF STRENGTH

Structural Mechanisms of Plastic Deformation in Nanocrystalline Materials

V. A. Pozdnyakov and A. M. Glezer

Institute of Metal Physics and Functional Materials, Bardin Central Research Institute of Ferrous Metallurgy, Vtoraya Baumanskaya ul. 9/23, Moscow, 107005 Russia

e-mail: Glezer@imph.msk.ru

Received June 4, 2001; in final form, July 16, 2001

Abstract—A model of the initial stage of plastic deformation in nanomaterials is proposed. Within this model, the plastic deformation occurs through grain boundary microsliding (GBM). The accommodation processes accompanying the formation of GBM regions are considered. The relationships describing the regularities in the deformation behavior of nanomaterials and the dependence of the flow stress on the grain size are derived, and the temperature dependence of the GBM resistance stress is calculated. It is demonstrated that the results obtained are in good agreement with the experimental data. *© 2002 MAIK "Nauka/Interperiodica".*

1. INTRODUCTION

Nanocrystalline materials (the grain size D is of the order of 10 nm) possess a number of unusual mechanical properties compared to conventional materials [1, 2]. This is associated with the scale effects due to small grain sizes and considerable fractions of a disordered material contained in grain boundaries [2–4].

Electron microscopic investigations of nanocrystalline materials indicate either that dislocations are absent or that their density is negligibly small in the bulk of grains [1–4]. Extrinsic dislocations are observed in the grain boundaries. When the grain size in the nanocrystalline material is less than a limiting value (10–20 nm), no dislocations appear at any stage of deformation and fracture of samples [4]. The grain boundaries are the most important structural units of nanocrystalline materials and determine their macroscopic properties in many respects. Nanocrystalline materials can be produced by a number of techniques, such as nanopowder compaction, mechanical fusing, nanocrystallization of amorphous alloys, and high-rate plastic deformation. Depending on the preparation technique, the nanomaterial formed can have a grain structure with different degrees of structural nonequilibrium, misorientation spectrum, defectiveness, and chemical composition of the grain boundaries.

Siegel [5] investigated a number of nanocrystalline materials with the use of high-resolution electron microscopy and revealed that the width of grain boundaries does not exceed 1 nm and their structure corresponds to that of grain boundaries in usual polycrystals. In nanocrystalline materials prepared through crystallization of amorphous alloys, Lu [6] observed specific (as a rule, faceted) grain boundaries. In submicrocrystalline nanomaterials obtained by high-rate plastic deformation, Valiev and Islamgaliev [7] experimentally observed high internal stresses induced by grain boundaries with a nonequilibrium structure. These authors assumed that the grain boundary phase can be formed in these compounds. Moreover, amorphous interlayers were found in nanocrystalline materials based on silicon carbide and silicon nitride [2]. The structure and properties of boundaries in nanocrystalline materials can differ considerably from those in polycrystalline analogs. However, a number of aspects regarding the structure and state of grain boundaries in nanocrystalline materials remain unclear.

Nanocrystalline materials possess a high strength but very low plasticity. Apparently, this is associated with the fact that the generation and motion of dislocations are suppressed at the expense of small grain size. Investigations into the mechanical properties of nanocrystalline materials have demonstrated that the Hall–Petch relationship for the yield strength $\sigma_y = \sigma_0 + kD^{-1/2}$ also holds in the nanometer range of grain sizes; however, the dependence $\sigma_y(D)$ is substantially weaker than that for conventional materials [8]. It was found that the deformation behavior of nanocrystalline materials exhibits other anomalies: the dependence of the yield strength reaches saturation, or the value of σ_y decreases with a decrease in the grain size [1–4]. The currently available experimental data on the mechanical properties of nanocrystalline materials are scarce and refer primarily to the dependence of the hardness or the yield strength on the grain size. In recent years, there appeared the works dealing with the temperature and concentration dependences of the flow stress in nanocrystalline materials [9, 10]. This information can be more useful for the elucidation of the deformation mechanisms in the materials under consideration.

The models proposed for describing the mechanical behavior of nanocrystalline materials can be divided

1063-7834/02/4404-0732$22.00 © 2002 MAIK "Nauka/Interperiodica"

into several groups. The first group involves the models that consider the development of a dislocation structure in nanograins [11, 12]. The models of the second group include the disclination and (or) dislocation description of nonequilibrium boundaries and a network of grain boundaries as a whole and make it possible to evaluate their effect on the yield strength in nanocrystalline materials [13, 14]. Within the models of the third group, the grain boundaries are treated as an independent phase and the yield strength of this two-phase material is expressed in terms of the rule of mixtures through the mechanical characteristics of intragranular and grain boundary phases [15]. The investigations concerned with the simulation of the grain boundary structure and plastic deformation in nanocrystalline materials belong to the fourth group [16, 17]. In particular, Schiotz *et al.* [17] simulated the plastic deformation processes in nanocrystalline materials and established that the inverse Hall–Petch relationship holds true. It was found that the plastic deformation occurs along the grain boundaries through the formation of numerous elementary shears.

It seems likely that the grain boundary sliding is the most probable mechanism of plastic deformation in nanocrystalline materials at low temperatures. This is also evident from a number of experimental works. In our earlier work [18], we proposed a model of the initial stage of the plastic flow occurring in nanocrystalline materials through the grain boundary microsliding (GBM). We determined the conditions for a change in the deformation mechanism with a decrease in the grain size—the crossover from the generation of dislocation loops in the grain boundaries to the grain boundary sliding—and considered the specific features in the deformation behavior of nanocrystalline materials. More recently, Hahn and Rabmanabhan [19] proposed one more model of deformation in nanocrystalline materials on the basis of grain boundary sliding. However, this model disregarded the limitations imposed on the sliding due to triple junctions and kinks in the grain boundaries.

The aim of the present work was to advance the model proposed in [18]. We analyzed the possible microstructural mechanisms of shear processes in grain boundaries of nanomaterials and considered the formation of regions of shear transformations similar to those responsible for heterogeneous plastic deformation in amorphous alloys [20]. Moreover, we calculated the dependences of the flow stress on the grain size and temperature for nanocrystalline materials.

2. PLASTIC DEFORMATION ASSOCIATED WITH GRAIN BOUNDARY MICROSLIDING

Without defining a particular structure of grain boundaries, we consider the low-temperature grain-boundary sliding processes in a nanocrystalline material. First, we introduce a grain boundary parameter that characterizes the ability of the grain boundary to undergo structural transformations leading to sliding over the boundary under shear stress. Let this parameter be the shear stress $\tau_s^{(i)}(T)$ of resistance to free (unconstrained) sliding over a planar grain boundary of the *i*th type at the temperature *T*. The index *i* refers to two unit vectors, namely, the vector θ of mutual grain misorientation [8] and the normal $\mathbf{n}$ to the grain boundary plane, i.e., $i = \theta, \mathbf{n}$. The shear stress $\tau_s^{(i)}$ is determined by the structure and state of the boundaries, the number of impurities, and the temperature *T*. When the external (allowed in the boundary plane) shear stress τ_a reaches the stress $\tau_s^{(i)}$, the sliding occurs over a grain boundary of the *i*th type.

As a rule, grain boundaries have a faceted structure; i.e., they consist of planar regions bounded by lines of kinks, edges, and junctions of grain boundaries. Grain boundary sliding over particular grain boundary facets with $\tau_s^{(i)} < \tau_a$—grain boundary microsliding—can occur at low-temperature deformation. In the general case, the strain associated with the grain boundary microsliding does not only reduce to pure shear but involves the dilatation component and is described by the strain tensor ε_{ik}^0. Therefore, there arises the problem of the stressed–strained state of an isotropic linear elastic medium with a system of randomly arranged planar GBM regions with the mean proper strain $\varepsilon_{ik}^0(\tau_a)$.

Now, we introduce the Cartesian coordinate system X_i (i = 1, 2, and 3) related to a sample and consider the case of a uniaxial tension (compression) with the load axis aligned along the X_3 axis. Under external stress, the grain boundary microsliding occurs in certain regions of grain boundaries. The formation of N GBM regions with the volumes Ω_s and the proper strains ε_{ik}^{0s} gives rise to a plastic strain in the sample:

$$\varepsilon_{ik} = \sum_{s=1}^{N} \varepsilon_{ln}^{0s} m_{il}^s m_{kn}^s \Omega_s / V, \tag{1}$$

where V is the sample volume and m_{il}^s stands for the cosines of the angles between the axes of the coordinate system related to the sth region and the axes of the basic coordinate system. The summation is performed over repeated indices.

The strain of the material in the bounded region induces the stress field $\sigma_{ik}^s(\mathbf{r})$, which can be represented by the expression [21]

$$\sigma_{ik}^s(\mathbf{r}) = -C_{ijkl} \times \left\{ \int_\Omega C_{pqmn} \varepsilon_{mn}^{0s}(\mathbf{r}') G_{kp,\,ql}(\mathbf{r} - \mathbf{r}')\, d\mathbf{r}' + \varepsilon_{kl}^{0s}(\mathbf{r}) \right\}. \tag{2}$$

Here, $\Omega_s = \omega_s \sigma S_s$ is the volume of the sth GBM region, S_s is the area of the sth GBM region, ω_s is the numerical coefficient determined by the region shape, δ is the effective thickness of the grain boundary, C is the elastic constant tensor, and G is the tensor Green's function in the elasticity theory.

In the case of pure shear grain boundary microsliding, the shear $\mathbf{u}^s(\mathbf{r})$ in the sth region of the boundary with the normal $\mathbf{n}^s$ leads to the plastic strain

$$\varepsilon_{ik}^s = (2\delta)^{-1}(u_i^s u_k^s + u_k^s u_i^s) = (m_{ik}^s + m_{ki}^s)\gamma^s/2. \quad (3)$$

Here, each coefficient m_{ik}^s is the product of two direction cosines of the angle between the normal $\mathbf{n}^s$ to the plane of the sth GBM region and the kth basis vector and the angle between the GBM direction $\mathbf{m}^s$ in this plane and the ith basis vector, $\gamma^s = u^s/\delta$, and u^s is the shear averaged over the area S_s.

The GBM regions can involve one or several facets (or faces) of the grain boundary and, hence, have different sizes L_s. Under the assumption of a continuous distribution of GBM regions over sizes, spatial arrangements, and orientations, the strain tensor of the material has the form

$$\varepsilon_{ik} = \varepsilon_{ik}^0 + (N/8\pi) \times \int_Y (n_k m_i + n_i m_k)\gamma\omega L^2 \delta \sin\varphi \Gamma(y) N(L) dY. \quad (4)$$

Here, ε_{ik}^0 is the strain tensor without grain boundary microsliding, i.e., the elastic strain tensor; the second term is the plastic strain tensor; the integral is taken over the combination of variables $Y = \{\varphi, \psi, \gamma, L\}$; $N(L)$ and $\Gamma(\gamma)$ are the distribution functions of GBM regions over sizes and shears, respectively; $n_i = (\sin\varphi\cos\phi, \sin\varphi\sin\varphi, \cos\varphi)$; φ is the angle between n and X_3; ϕ is the angle between the X_1X_3 and nX_3 planes; and N is the number of GBM regions with any size and orientation per unit volume.

By analogy with the problem of deformation of a material with a large number of cracks [22], we can use the vector quantity with the components $\Omega_i = m_i\Omega\gamma = m_i\omega\delta L^2\gamma$, where the mean values of the ω, L, and γ parameters are introduced. In this case, the determination of the dependence of $\mathbf{\Omega}$ on the external stress $\boldsymbol{\sigma}_a$ ($\Omega_i = I_{ikl}\sigma_{akl}$, where the tensor $\mathbf{I}$ is governed by the mechanism of grain boundary microsliding and the character of loading of a particular GBM region) is the final stage in the solution of the posed problem.

3. THE MODEL OF THE INITIAL STAGE OF PLASTIC DEFORMATION

Let us average the GBM resistance stress τ_s over an ensemble of grain boundaries in a nanocrystalline material. For the uniaxial tension (compression) at $\sigma_a/2 > \tau_s$, the grain boundary microsliding arises in the nanocrystalline material; i.e., there appear the first GBM regions (in the grain boundaries) whose planes are oriented at an angle of approximately 45° to the load axis. According to relationship (4), a further increase in the external stress σ_a results in an increase in the concentration N and the size L of the GBM regions, i.e., in an increase in their volume fraction $f = \omega\delta L^2 N$. As follows from relationship (4), the plastic strain of the nanocrystalline material along the load axis is determined by the volume fraction f and the equilibrium mean shear strain γ in the GBM regions, that is,

$$\varepsilon = mf\gamma, \quad (5)$$

where m is the mean orientational factor.

Now, we derive the relationship between the shear strain γ and the external stress. The shear stresses allowed in the plane with the normal $\mathbf{n}^s$ along the $\mathbf{m}^s$ direction due to the stress field $\boldsymbol{\sigma}_p$ can be represented as $\tau_p^s = \mathbf{n}^s\sigma_p\mathbf{m}^s$. The quantity γ^α for the αth GBM region can be obtained from the following condition of mechanical equilibrium at each point r_α inside this region ($r_\alpha \in \Omega_\alpha$):

$$\tau_a^\alpha + \tau^\alpha(r^\alpha) + \sum_\beta \tau^{\alpha\beta} + \tau_i = \tau_s^\alpha. \quad (6)$$

Here, $\tau^\alpha(r^\alpha)$ is the proper internal shear stress [formula (2)] in the αth region, $\tau^{\alpha\beta}$ is the shear stress induced by the βth region in the αth region, and τ_i are the improper internal stresses unrelated to the GBM regions. We assume that the GBM region has the form of an oblate ellipsoid with the principal semiaxes $a = b = L/2$ and $c = \delta/2$ ($c \ll a$ and b), $\omega = 4\pi/3$, and the shear strain is uniform in Ω_α. The GBM regions can be treated as planar inclusions with the proper strain ε^{0s}. From formula (2) for the internal shear stresses [21], we obtain the proper internal shear stress in the GBM region with the shear strain γ^α:

$$\tau^\alpha = -A(\delta/L)G\gamma^\alpha, \quad (7)$$

where $A = \pi(2 - \nu)/4(1 - \nu)$, ν is the Poisson ratio, and G is the shear modulus of the material. In a nanocrystalline material containing a system of randomly distributed ellipsoidal inclusions with the volume density f, the mean internal stress $\langle\tau\rangle$ in an inclusion, with due regard for the image fields [21], is defined as $\langle\tau\rangle = (1 - f)\tau^\alpha$. Substitution of the equilibrium shear strain γ into relationship (5) gives the expression describing the initial stage of the plastic deformation in the nanocrystalline material, that is,

$$\sigma_a = \sigma_s + AG\delta(1 - f)\varepsilon/fLm^2, \quad (8)$$

where $(\sigma_a - \sigma_s)m = \tau_a - \tau_s$.

In the case when γ exceeds the critical shear strain γ^* in the course of deformation in the nanocrystalline material, an increase in the internal stresses associated with the development of GBM regions will be accompanied by the accommodation processes resulting in stress relaxation. The formation of dislocations on linear topographic defects of grain boundaries (kinks, junctions, and edges of grain boundaries) and the plastic rotation of grains are the possible accommodation processes. It is known that lattice dislocations can be formed through the coalescence of grain boundary dislocations in specific grain boundaries [8]. In arbitrary grain boundaries, this process becomes possible due to the transformation of structural units of the boundary. When the grain boundary microsliding occurs in the adjacent grain-boundary faces (facets) or the orientation of the intergranular shear vector changes with an increase in the area of the GBM region, there is a grain-boundary plastic strain misfit in junctions and kinks. This induces a stress field similar to the field of the effective dislocation at the junction with the Burgers vector $\mathbf{b}^* = \mathbf{u}_1 - \mathbf{u}_2$. In this case, the possible accommodation mechanism is associated with the formation (and displacement) of a lattice dislocation in the region of a linear defect in the grain boundary. The deformation criterion for the realization of this mechanism can be the condition when the magnitude b^* reaches the magnitude of the Burgers vector of the lattice dislocation (or when the shear strain γ reaches the critical shear strain γ^*). At small grain sizes, the formed dislocations cannot move into the grain bulk due to the large expenditures of energy required to overcome the image [23] or line-tension [18] forces. The plastic rotation of grains can serve as another possible mechanism of accommodation of grain boundary misfits at junctions. If the misfit with the vector $\mathbf{b}^*$ is formed in a junction or kink of the grain boundary upon grain boundary microsliding, the grain rotation through the angle $\phi = \zeta b^*/D$ (where ζ is the constant) eliminates this misfit. It was found that, for hexagonal grains, $\zeta = \sqrt{3}/2$ [24].

For $\varepsilon > \varepsilon^* = mf\gamma^*$, the arising internal stresses relax and their contribution to further strain hardening of the nanocrystalline material becomes negligible. However, there appears another contribution caused by the stress field of formed defects. The density of dislocations that are generated in the grain boundary and provide the joint grain-boundary plastic strain and the relaxation of arising stresses can be evaluated within the approach proposed in [25] for analyzing the strain in plastically inhomogeneous materials. According to this approach, the dislocation density is determined from the formula $\rho = kf(\gamma - \gamma^*)/bL_f$, where L_f is the mean facet size and k is a numerical coefficient of the order of unity. The corresponding stresses are represented by the expression $\sigma_i = \alpha Gb\rho^{1/2}$, where $\alpha \approx 1$.

The total area of the grain boundaries per unit volume is defined as $S_v = q/D$, where $q \approx 3$ is the numerical coefficient [8]. By assuming that the area (per unit volume) of grain boundaries involved in the grain boundary sliding at the initial deformation stage is proportional to S_v, i.e., $(f/\delta) = hS_v$, we obtain the plastic strain of the material:

$$\varepsilon = m\delta h(q/D)\gamma(\sigma_a), \tag{9}$$

where the coefficient h at $\sigma_a/2 > \tau_s$ takes on a finite value h = const and can increase with an increase in ε according to relationship (4). Within the linear approximation, we have $h = h_0 + h_1\varepsilon$. As a result, the expressions describing the deformation behavior have the form

$$\sigma_a = \sigma_s + AG(D/L)(1 - \delta qh/D)\varepsilon/qhm^2,$$
$$\varepsilon < \varepsilon^* = mqh(\delta/D)\gamma^*, \tag{10}$$
$$\sigma_a = \sigma_a(\varepsilon^*) = \alpha G[kb(\varepsilon - \varepsilon^*)/m\zeta D]^{1/2}, \quad \varepsilon > \varepsilon^*,$$

where $\zeta < 1$ is the numerical parameter relating L_f and D.

Let us consider the dependence of the yield strength on the size grain for the nanocrystalline material. The yield strength σ_y is defined as the stress corresponding to the specified plastic strain ε_y taken, for example, to be equal to 0.2%. For microcrystalline materials, the relationships $(D \sim 1\ \mu\text{m})$ $\varepsilon^* \ll \varepsilon_y$ and $\sigma(\varepsilon^*) \approx \sigma_s$ are satisfied and the standard Hall–Petch relationship can be derived from expressions (10). For nanocrystalline materials, the value of $\varepsilon^* \approx 10^{-3}$–$10^{-2}$ can exceed the plastic strain corresponding to the yield strength. In this case, $\sigma_y(D)$ is determined by the first expression (10). For $L = \zeta_1 D$ (where ζ_1 is the constant), as follows from expressions (10), the yield strength at $f \ll 1$ does not depend on the grain size and the Hall–Petch relationship with the weak dependence $\sigma_y(D)$ is fulfilled in the presence of accommodation processes. This inference is in agreement with the experimental data obtained by Nieman *et al.* [26]. When L is proportional to D^p $(p < 1)$ or L is independent of D, the yield strength represented by the first expression (10) for the nanocrystalline material increases with an increase in the grain size. This agrees with the experimental results reported in [2–4].

4. THE STRUCTURAL MECHANISM AND KINETICS OF GRAIN BOUNDARY MICROSLIDING

According to modern concepts, an arbitrary grain boundary can be treated as a limited set of structural units that coincide with the Voronoi–Bernal polyhedra proposed for describing the structure of liquids and amorphous materials [27]. It can be assumed that the grain boundary microsliding under shear stresses should occur through the transformation of structural units of grain boundaries upon the formation of shear transformation microregions in the grain boundary structure. The GBM resistance stress in an arbitrary grain boundary is determined by the critical stress for

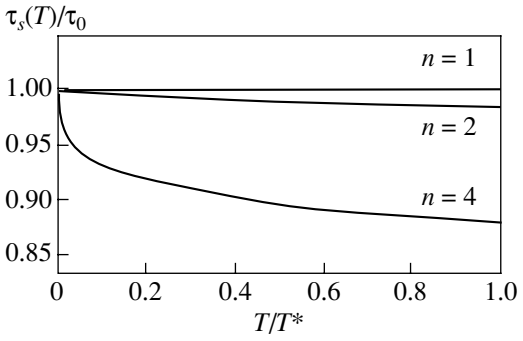

Fig. 1. Temperature dependences of the GBM resistance stress at $n = 1$, 2, and 4.

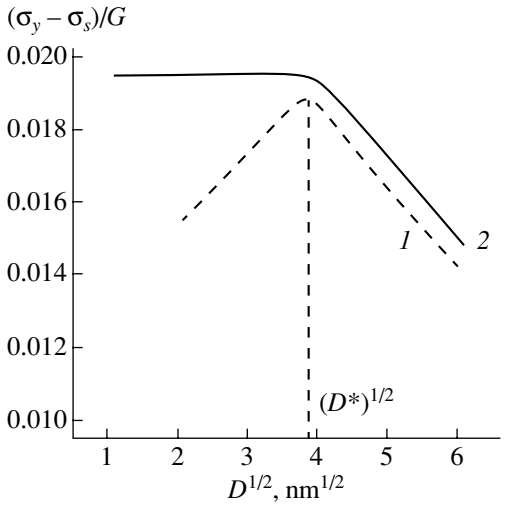

Fig. 2. Dependences of the yield strength σ_y on the square root of the grain size D for a nanocrystalline material at (*1*) $L = \text{const}(D)$ and (*2*) $L = \zeta_1 D$.

the transformation of structural units of the boundary. These elementary shear regions are similar to regions of shear transformations that are responsible for the development of heterogeneous plastic deformation in amorphous alloys at low temperatures [20].

In this case, the rate of free sliding over the grain boundary is defined by the formula

$$\dot{U} = \nu\chi u_0 \exp(-\Delta G/kT), \qquad (11)$$

where ν is the frequency of the normal vibrational mode of a shear microregion along the activation trajectory [28], χ is the volume fraction of nuclei of shear microregions in the grain boundary, u_0 is the mean shear in these microregions, and ΔG is the free energy of formation of a shear transformation microregion with critical parameters.

Analysis of different mechanisms of elementary shear processes demonstrates that the energy of formation of shear microregions in the grain boundary can be written as

$$\Delta G(\tau_a) = \zeta\tau_0\Omega_m[1 - (\tau_a/\tau_0)]^n, \qquad (12)$$

where ζ and n are the numerical parameters, τ_0 is the athermic grain boundary sliding stress (ideal shear strength of the boundary), and Ω_m is the volume of the shear transformation microregion.

If the volume fraction of GBM regions only slightly varies in the course of deformation and $L \sim D$, the strain rate of the nanocrystalline material at the initial stage can be represented by the expression

$$\dot{\varepsilon} = \nu\chi u_0 \exp[-\Delta G(\tau_a - \tau_i)/kT]/D, \qquad (13)$$

where τ_i are the total internal shear stresses in the GBM region. Hence, from formula (13), we obtain the first expression (10) for the flow stress with an explicit temperature dependence of the GBM resistance stress,

$$\tau_s(T) = \tau_0\{1 - [(kT/\zeta\tau_0\Omega_m)\ln(\nu\chi u_0/D\dot{\varepsilon})]^{1/n}\}. \qquad (14)$$

Figure 1 shows the dependences $\tau_s(T)$ at different values of n and the following parameters: $D = 10$ nm, $\varepsilon = 10^{-4}$ s^{-1}, $\Omega_m = 4.3 \times 10^{-28}$ m^3, $\nu = 10^{12}$ s^{-1}, $u_0 = 0.2$ nm, and $\chi = 0.4$.

At $n = 2$, the dependence of the activation energy for shear transformation microregions on the stress is similar to the dependence of the energy of generation of shear transformations in amorphous alloys [20]. Consequently, relationships (13) and (14) at $n = 2$ describe the deformation kinetics in a nanocrystalline material whose grain boundaries are in the amorphous state. The temperature dependence of the GBM resistance stress and, correspondingly, the yield strength of the nanocrystalline material should satisfy relationship (14) up to a certain temperature T^*, above which other deformation modes become energetically more favorable.

5. DISCUSSION

Let us now examine in greater detail the dependence of the flow stress on the grain size for a nanomaterial, which is determined from expressions (10). Two different cases are possible depending on the procedure of preparation of nanocrystalline materials with various grain sizes: the quantity L either is linearly related to D or is independent of D. The size L should be proportional to the mean size of facets (or faces) of the grain boundary and, hence, to the grain size D. However, when the grain size changes upon recrystallization annealings, the proportionality between the facet and grain sizes can be violated by an additional faceting. In the nanocrystalline material, the grain boundary microsliding can proceed over faces of several adjacent grains and the size L will be independent of D. It is convenient to introduce the characteristic grain size D^*, which is expressed through the quantity ε^* (its value corresponds to the condition $\varepsilon^* = \varepsilon_y$): $D^* = hqh\delta\gamma^*/\varepsilon_y$.

The dependence $\sigma_y(D)$ is determined only by the first expression (10) at $D < D^*$ and only by the second expression (10) at $D \gg D^*$. For $qm = 1.5$, $h = 0.2$, $\delta = 0.5$, $\gamma^* = 0.3$, and $\varepsilon_y = 0.3\%$, we obtain $D^* = 15$ nm. The dependences $\delta_y(D)$ for the cases under consideration are plotted in Fig. 2. Note that the value of τ_0 depends on the state of the grain boundary and, hence, can also vary with an increase in D.

6. CONCLUSION

In this work, we considered the initial stage of plastic deformation in a nanocrystalline material, i.e., the microyield defined as the deformation stage at which separate plastic flow regions are formed in the elastic matrix. However, owing to an extremely large grain boundary area per unit volume of the nanocrystalline material, these processes produce a plastic strain of several percent. For this deformation stage, we calculated the dependences of the flow stress on the grain size and temperature. The GBM resistance stress was determined in terms of flow stresses of amorphous metal alloys. The critical stress of the structural transformation in the grain boundary should be close to the cohesion strength of boundaries and, hence, further tension should lead to fracture. However, the compression or cyclic loading can result in a further development of deformation. As the load increases, the number and area of GBM regions increase, these regions merge together, and the percolation crossover to the macroplastic flow stage occurs at a critical volume fraction of the regions.

REFERENCES

1. H. Gleiter, Prog. Mater. Sci. **33** (4), 223 (1989).
2. R. A. Andrievskiĭ and A. M. Glezer, Fiz. Met. Metallogr. **88** (1), 50 (2000).
3. R. A. Andrievskiĭ and A. M. Glezer, Fiz. Met. Metallogr. **89** (1), 91 (2000).
4. V. G. Gryaznov and L. I. Trusov, Prog. Mater. Sci. **37** (4), 289 (1993).
5. R. W. Siegel, J. Phys. Chem. Solids **55** (10), 1097 (1994).
6. K. Lu, Mater. Sci. Eng., R **16**, 161 (1996).
7. R. Z. Valiev and R. K. Islamgaliev, Fiz. Met. Metallogr. **85** (3), 161 (1998).
8. A. N. Orlov, V. N. Perevezentsev, and V. V. Rybin, *Grain Boundaries in Metals* (Metallurgiya, Moscow, 1980).
9. V. V. Shpeĭzman, V. I. Nikolaev, B. I. Smirnov, *et al.*, Fiz. Tverd. Tela (St. Petersburg) **40** (7), 1264 (1998) [Phys. Solid State **40**, 1151 (1998)].
10. V. V. Shpeĭzman, V. I. Nikolaev, B. I. Smirnov, *et al.*, Fiz. Tverd. Tela (St. Petersburg) **40** (9), 1639 (1998) [Phys. Solid State **40**, 1489 (1998)].
11. G. A. Malygin, Fiz. Tverd. Tela (St. Petersburg) **37** (8), 2281 (1995) [Phys. Solid State **37**, 1248 (1995)].
12. C. S. Pande, R. A. Masumura, and R. W. Armstrong, Nanostruct. Mater. **2** (3), 323 (1993).
13. A. A. Nazarov, A. E. Romanov, and R. Z. Valiev, Nanostruct. Mater. **6** (5–8), 775 (1995).
14. S. G. Zaĭchenko and A. M. Glezer, Fiz. Tverd. Tela (St. Petersburg) **39** (11), 2023 (1997) [Phys. Solid State **39**, 1810 (1997)].
15. D. A. Konstantinidis and E. C. Aifantis, Nanostruct. Mater. **10**, 1111 (1998).
16. P. Keblinski, S. R. Phillpot, D. Wolf, and Y. Gleiter, Nanostruct. Mater. **9**, 651 (1997).
17. J. Schiotz, F. D. Di Tolla, and K. W. Jacobsen, Nature **391** (6667), 561 (1998).
18. V. A. Pozdnyakov and A. M. Glezer, Pis'ma Zh. Tekh. Fiz. **21** (1), 31 (1995) [Tech. Phys. Lett. **21**, 13 (1995)].
19. H. Hahn and K. A. Rabmanabhan, Philos. Mag. B **76** (4), 553 (1997).
20. A. S. Argon, Acta Metall. **27** (1), 47 (1979).
21. T. Mura, *Micromechanics of Defects in Solids* (Martinus Nijhoff, The Hague, 1982).
22. R. L. Salganik, Izv. Akad. Nauk SSSR, Mekh. Tverd. Tela **4**, 149 (1973).
23. V. G. Gryaznov, I. A. Polonsky, and A. E. Romanov, Phys. Rev. B **44** (1), 42 (1991).
24. V. N. Perevezentsev and V. V. Rybin, Fiz. Met. Metalloved. **51** (3), 649 (1981).
25. M. F. Ashby, Philos. Mag. **21**, 170 (1970); **21**, 399 (1970).
26. G. W. Nieman, J. R. Weertman, and R. W. Siegel, J. Mater. Res. **6** (5), 1012 (1991).
27. A. P. Sutton and V. Vitek, Philos. Trans. R. Soc. London, Ser. A **309**, 1 (1983).
28. U. F. Kocks, A. S. Argon, and M. F. Ashby, Prog. Mater. Sci. **19** (1), 1 (1975).

Translated by O. Borovik-Romanova

Physics of the Solid State, Vol. 44, No. 4, 2002, pp. 738–743. Translated from Fizika Tverdogo Tela, Vol. 44, No. 4, 2002, pp. 711–716.

DEFECTS, DISLOCATIONS, AND PHYSICS OF STRENGTH

On the Mechanism of Deformation in Submicrocrystalline Titanium

M. M. Myshlyaev* and S. Yu. Mironov**

** Baĭkov Institute of Metallurgy and Materials Technology, Russian Academy of Sciences, Leninskiĭ pr. 49, Moscow, 119911 Russia*

*** Institute of Problems of Metal Superplasticity, Russian Academy of Sciences, ul. Khalturina 39, Ufa, 450001 Bashkortostan, Russia*

Received May 22, 2001; in final form, August 27, 2001

Abstract—The mechanical behavior and structural evolution of submicrocrystalline titanium in the course of deformation are investigated at room temperature. The possible mechanisms of deformation are analyzed. It is proved that the dislocation motion inside grains is responsible for the plastic flow. © *2002 MAIK "Nauka/Interperiodica".*

1. INTRODUCTION

Nanocrystalline and submicrocrystalline materials have been extensively studied in recent years because they are of considerable scientific and practical interest. The scientific interest expressed in these materials is associated with the hypothesis of possible changes in the mechanism of deformation when grains reach submicrometer and nanometer sizes. This hypothesis is based on the fact that, at a sufficiently small size of grains in a material, the number of atoms in the bulk of grains becomes comparable to the number of atoms located in the grain boundary and the grain boundary phase either strongly affects or even determines the properties of the material.

One of the first works in this field was done by Chokshi *et al.* [1], who revealed a substantial increase in the diffusion creep rate of copper and palladium after their transformation into the nanocrystalline state. Subsequently, these data, however, were not confirmed experimentally [2]. Furthermore, in [2–6], it was shown that the Hall–Petch relationship holds only for very small grain sizes. This result casts some doubt on the aforementioned hypothesis. On the other hand, the results obtained in a number of recent works indicate either that the dislocation theory of deformation at very small crystallite sizes [7] should be essentially modified or that the main mechanism of deformation in these materials is associated either with the Coble diffusion creep [8, 9] or with grain boundary sliding [10].

The available experimental data on the properties of these materials are scarce and contradictory and, hence, call for further investigation. In this respect, we made an attempt to analyze the possible mechanisms of deformation in submicrocrystalline materials by using technically pure titanium with a mean grain size of 0.4–0.6 μm as an example.

2. MATERIALS AND EXPERIMENTAL TECHNIQUE

In this work, we used technically pure titanium (BT1-00). The contents of impurities were as follows (wt %): ~0.443 Al, ~0.0965 Fe, ~0.073 N, ~0.068 O, and ~0.0385 C.

The submicrocrystalline state was achieved through large plastic deformations on an EU-100 universal testing machine with a permanent change in the axis of strain according to the procedure described in [11]. After this treatment, the mean grain size was equal to 0.4–0.6 μm. Samples were cut from the central part of the prepared materials by the electric-spark method.

The samples were annealed in order to obtain the submicrocrystalline structures free of excess dislocation density and the structures with different grain sizes. The annealing temperature varied from 425 to 800°C, and the annealing time ranged from 0.33 to 20 h. As a result, we obtained a set of structures with the mean grain size varying from 0.4 to 58 μm.

The mechanical tensile test and the tensile test with stress relaxation were performed with a Shenck trebel testing machine at room temperature and a deformation rate of 1 mm/min. All the experiments were carried out using an extensometer with a gauge length of 15 mm. Planar samples with a working part $18 \times 3.5 \times 1.5$ mm in size were used in the measurements. All the samples were annealed prior to testing.

In order to construct the true stress–true strain (S–φ) curves, the extension of a number of samples was discontinued and the minimum cross-sectional area was measured with a slide gauge. In this case, the samples remained in tension grips under a permanent load. After each measurement, the samples were again subjected to extension to the point of fracture. The minimum cross-sectional area of the samples was used for calculating

1063-7834/02/4404-0738$22.00

the true stress S and the true strain φ at different deformation stages.

The microhardness was measured on a PMT-3M instrument with the use of a Vickers pyramidal indenter at a load of 100 g and a loading time of 10 s. The number of indentations was equal to 50.

The apparent activation volume was determined from the experimental data on stress relaxation according to the method proposed in [12]. In the case of stress relaxation, the relaxation time was 5 min.

The evolution of the structure in the course of plastic deformation was examined by transmission electron microscopy under a JEM 2000EX microscope with the use of foils cut from different regions of the samples subjected to deformation.

3. RESULTS

The initial portions of the stress–strain (σ–ε) curves for submicrocrystalline titanium samples are depicted in Fig. 1a. As can be seen, all the curves exhibit a sharp yield point and a yield (Lüders) plateau at the initial stage of the plastic deformation. A decrease in the grain size leads to a lowering of the sharp yield point and an increase in the length of the Lüders plateau. For some samples with a minimum grain size (0.4 μm), the yield plateau immediately goes into a neck and the stage of uniform deformation is absent. The plastic deformation of these samples is inhomogeneous (unstable).

The S–φ curves for samples with a submicrocrystalline structure are shown in Fig. 1b. It is seen that an increase in the degree of strain results in a considerable increase in the strength of the samples. This indicates that the tensile samples undergo strain hardening. It should be noted that this hardening is almost identical for all the samples and does not depend on the strain.

The dependences of the conventional yield strength, the microhardness H_V, and the apparent activation volume of the strain V^* on the grain size are plotted in Figs. 2a–2c. It can be seen that, within the limits of experimental error, the dependences of the strength characteristics are adequately described by the Hall–Petch relationship and the activation volume does not depend on the grain size and the degree of strain and is equal to $\sim 30b^3$, where b is the magnitude of the Burgers vector.

Figure 3a shows the histogram of the grain size distribution for the sample with a mean grain size of 0.4 μm and a maximum strength. Note that, although the sample is predominantly composed of submicrograins, there is a fraction of grains (~2%) whose size exceeds 1 μm. As can be seen from Fig. 3b, this fraction of large-sized grains makes a noticeable contribution (~37%) to the total volume of the sample.

The micrographs represented in Figs. 4a–4d illustrate the structural evolution of this sample. It is seen that the structure of the sample in the initial unstrained state (Fig. 4a) predominantly consists of relatively

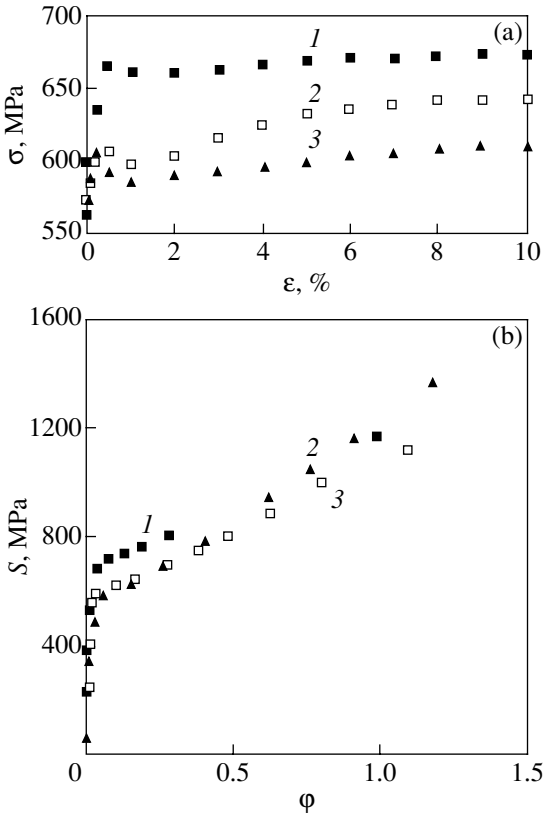

Fig. 1. Stress–strain curves in (a) relative and (b) true coordinates for submicrocrystalline samples with different mean grain sizes: (*1*) 0.4, (*2*) 0.5, and (*3*) 0.6 μm.

equiaxial polyhedral grains without a preferred direction in their arrangement. The contrast inside the grains is virtually uniform. The grains have straight-line boundaries, and thickness extinction contours are often observed in the images of the boundaries. Some grains involve dislocations. A strain of 5% (Fig. 4b) leads to the formation of elongated grains, the disappearance of thickness extinction contours at the boundaries, a substantial increase in the dislocation density, the appearance of bend extinction contours, and a noticeable variation in the contrast inside the grains. A further increase in the degree of strain to 10% (Fig. 4c) and then to 25% (Fig. 4d) results in the formation of the structure with a pronounced orientation (metallographic texture).

The transformation of the initial structure with equiaxial grains into a structure with elongated grains can also be traced in Fig. 5. The results presented in this figure allow us to make the following inferences: (1) grains of different sizes become elongated, (2) the content of elongated grains increases with an increase in the strain, and (3) the larger the grain, the faster its elongation.

Some features in the intragranular and grain boundary structures of dislocations at different deformation stages are shown in Figs. 6a–6c. As is seen from Fig. 6a, the developed dislocation structure is formed in

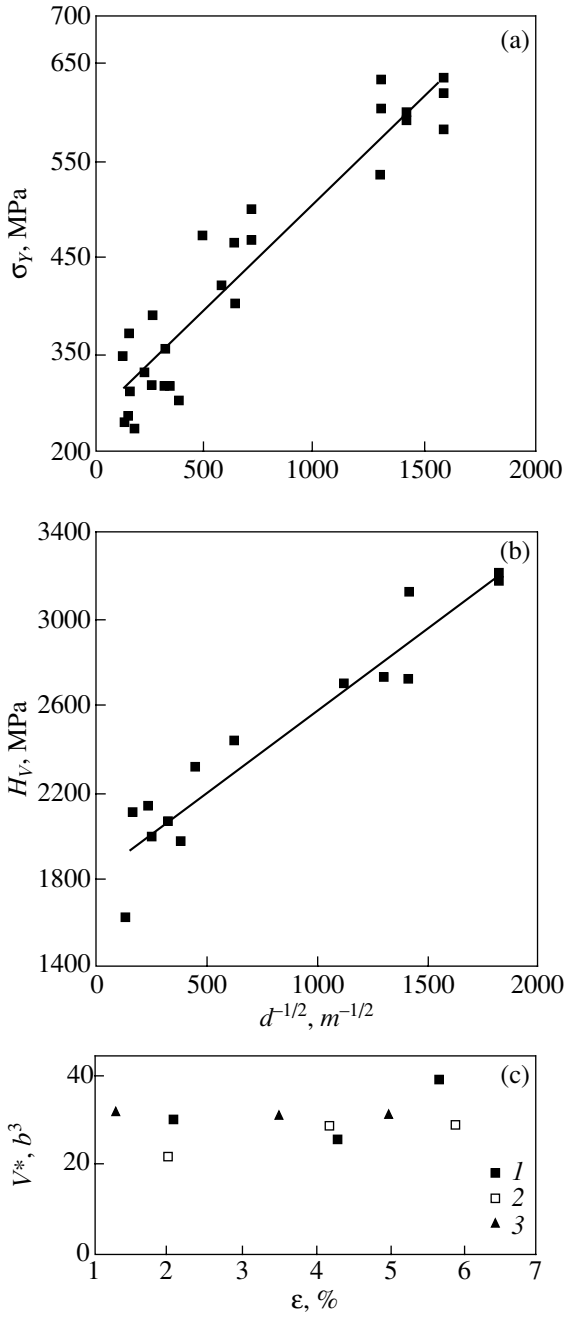

Fig. 2. Dependences of (a) the conventional yield strength, (b) the Vickers microhardness, and (c) the apparent activation volume on the grain size of samples. Mean grain size, μm: (*1*) 0.5, (*2*) 2.5, and (*3*) 58.

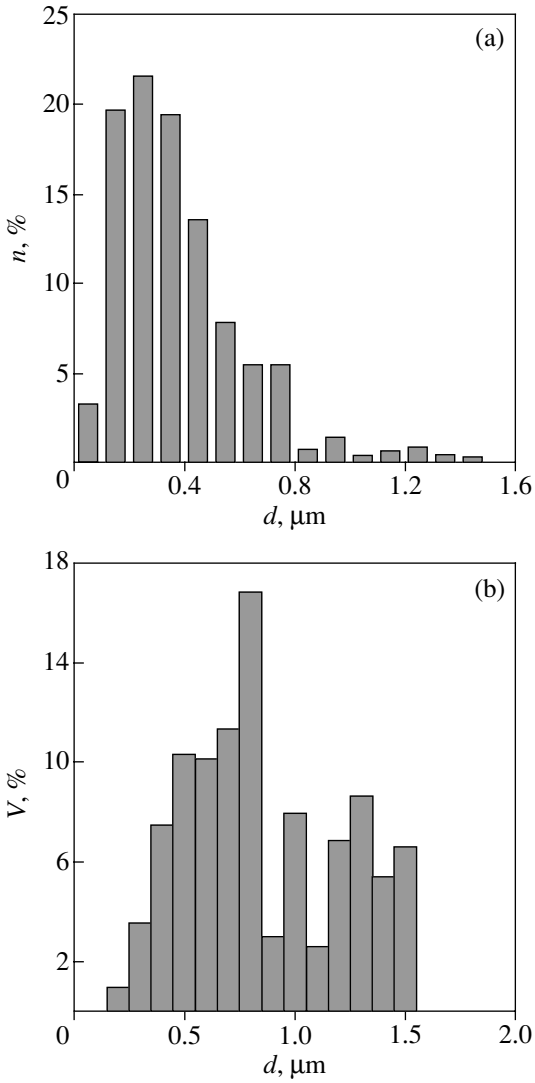

Fig. 3. Histograms of (a) the grain size distribution and (b) the distribution of the contributions from fractions of grains with different sizes to the total volume for the sample with a mean grain size of 0.4 μm and a maximum strength.

grains with sizes larger than 0.5 μm. This structure is characterized by a considerable dislocation density and involves dislocation subboundaries. Grains with smaller sizes (Fig. 6b) have no subboundaries. However, these grains also exhibit a high dislocation density. Lattice dislocations are observed in the grain boundaries shown in Fig. 6c. The density of these dislocations is also relatively high.

4. DISCUSSION

Let us consider the dislocation glide, twinning, Coble diffusion creep, and grain boundary sliding as possible mechanisms of deformation in the material under investigation. As a rule, the first two processes are observed during plastic flow of titanium under similar temperature–rate conditions [13] and the possible occurrence of the second two processes is determined by specific features of the submicrocrystalline state [8–10]. However, let us first consider specific features of the material under investigation.

Under the assumption that all grains have an identical size of 0.4 μm and a spherical shape and that the boundary width is equal to 2*b* (0.5 nm), the volume fraction occupied by the grain boundaries is estimated at ~0.7%. Consequently, for the studied material, the

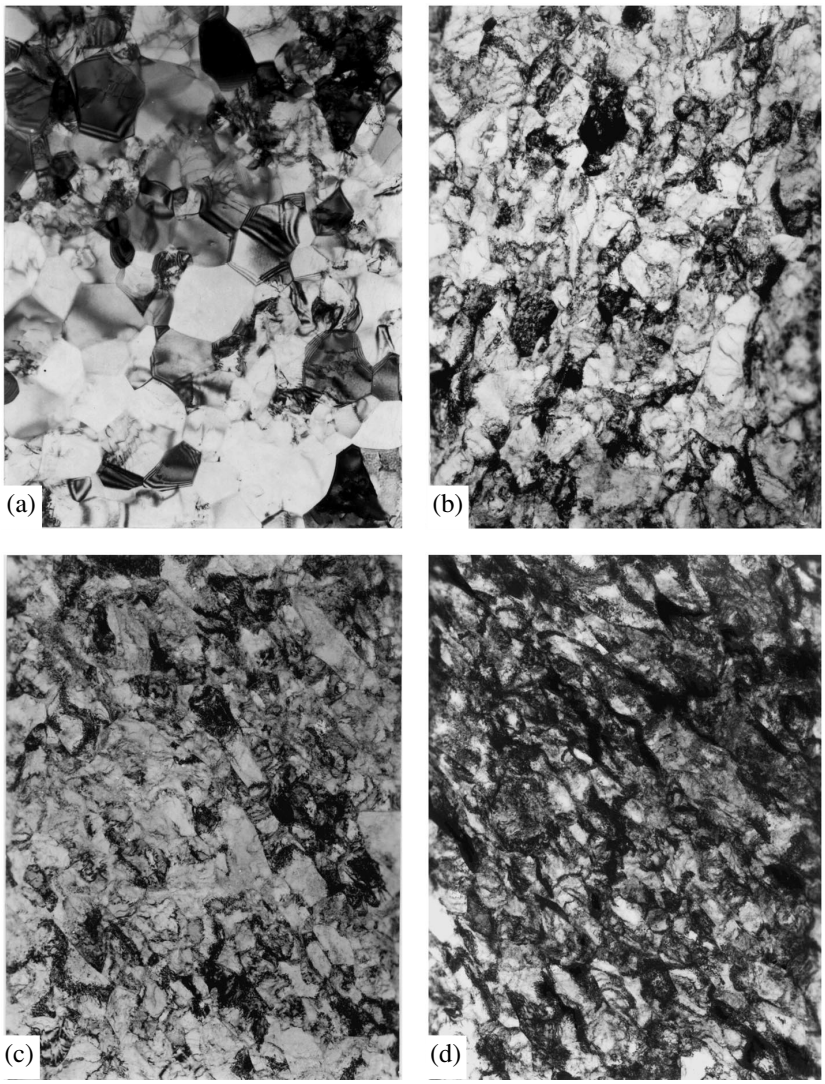

Fig. 4. Structural evolution of submicrocrystalline titanium in the course of deformation. ε (%): (a) 0, (b) 5, (c) 10, and (d) 25.

assumption that the number of atoms located in the grain boundaries is comparable to the number of atoms in the bulk of grains is incorrect. Moreover, the actual volume occupied by the grain boundaries is considerably less than the estimated volume, because our sample contains grains with sizes larger than 1 μm (Fig. 3a). As is seen from Fig. 3b, these grains occupy a substantial (~37%) volume of the sample. Therefore, it can be assumed that the mechanism of deformation in this region of the sample is identical to that in the material with a mean grain size of 1 μm; i.e., we are dealing here with intragranular dislocation glide [13]. Thus, even preliminary examinations of the histogram of the grain size distribution demonstrate that the realization of the other aforementioned deformation mechanisms is doubtful, whereas the dislocation glide mechanism is quite probable in a rather large part of the sample.

Now, we turn our attention to the discussion of the experimental results. There are at least five arguments in favor of a rather intensive intragranular dislocation glide. The first (and most illustrative) argument is the formation of a developed dislocation substructure with a high dislocation density inside the grains (Figs. 6a, 6b). As can be seen from Fig. 6b, an appreciable dislocation density is inherent even in grains with sizes of ~0.2 μm. It should be noted that the developed dislocation structure in submicrograins was also observed in [14–16]. The elongation of grains (even with the smallest sizes) and the formation of the metallographic texture (Figs. 4, 5) can be treated as the second argument in support of the high-rate dislocation glide inside the grains. Similar processes were also noted in [14–16]. The presence of the sharp yield point and the Lüders plateau in the stress–strain curves for the submicrocrystalline samples under investigation (Fig. 1a) is the third

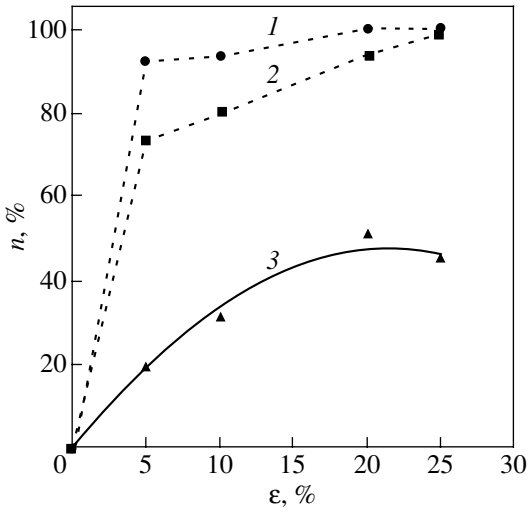

Fig. 5. Dependences of the content of elongated grains on the strain for grain sizes (*1*) $d < 0.5$, (*2*) $d = 0.5$–1, and (*3*) $d > 1$ μm.

argument for the dislocation mechanism of deformation. This finding is in agreement with the data obtained by Salishchev *et al.* [16, 17], who also observed the yield plateau at the initial stage of the deformation of submicrocrystalline samples. There exist different hypotheses providing explanations for these findings [18, 19]; however, all of them are based on a sharp increase in the density of mobile dislocations in grains. The strain hardening accompanying the plastic flow of submicrocrystalline titanium (Fig. 1b) serves as the fourth argument confirming the intragranular dislocation glide. The independence of the apparent activation volume on the grain size and the degree of strain (Fig. 2c) and the good agreement between this volume and the data available in the literature [13] suggest that the thermoactivation mechanism of deformation consists in overcoming interstitial impurity atoms by dislocations. This can be considered the fifth argument. Thus, the occurrence of the high-rate intragranular dislocation glide during the deformation of submicrocrystalline titanium is beyond question.

Let us now analyze other deformation mechanisms. The careful investigation into the microstructure of the strained submicrocrystalline samples revealed no twins. According to the available data on the suppression of twinning with a decrease in the grain size in the titanium structure [13], we can argue that no twinning occurs in the studied samples.

The elongation of grains (including grains with the smallest sizes) (Figs. 4, 5), a noticeable strain hardening (Fig. 1b), and a considerable density of dislocations in the boundaries and boundary regions of grains (Fig. 6c) suggest that, even though the grain boundary sliding takes place, it does not contribute significantly to the total plastic deformation. It is quite possible that the grain boundary sliding plays only an accommodating role (the so-called induced grain boundary sliding [20]) and provides joint deformation in the polycrystal.

The activation volume of the diffusion process is equal to $\sim b^3$. This is at variance with the experimental data (Fig. 2c). Moreover, as for the grain boundary sliding, the strain hardening observed in submicrocrystalline titanium and the occurrence of undissociated or slightly dissociated lattice dislocations in the grain boundaries (this is unlikely in the case of high-rate vacancy diffusion along the grain boundaries) disagree

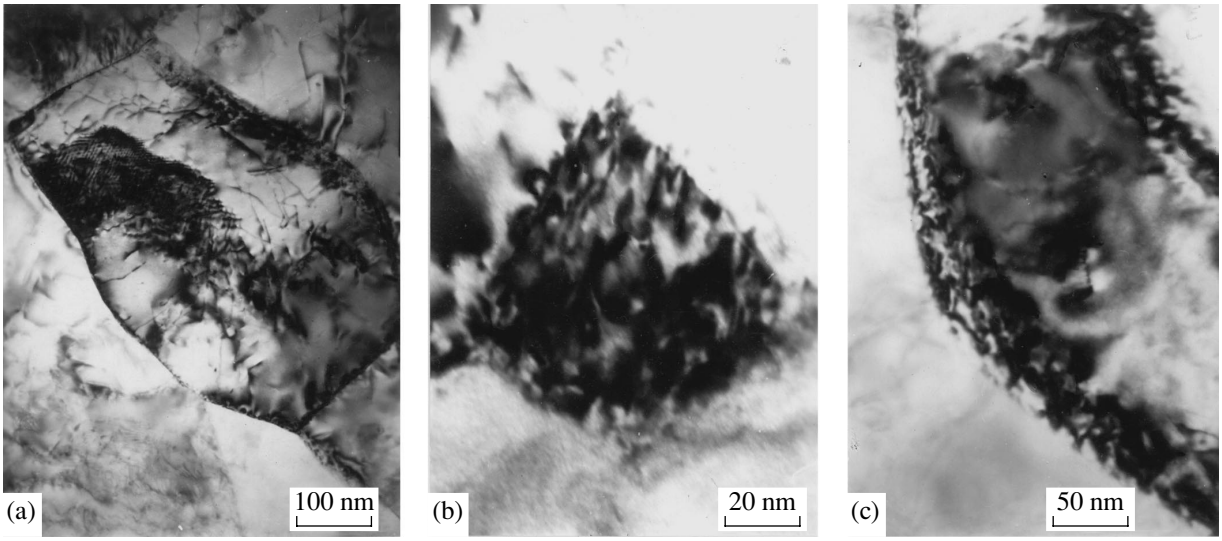

Fig. 6. Specific features in the dislocation structure of strained submicrocrystalline titanium: (a) formation of dislocation subboundaries in grains with a size of larger than 0.5 μm, (b) high dislocation density in grains with a size of smaller than 0.5 μm, and (c) lattice dislocations in dislocation boundaries in grain boundaries.

with the diffusion creep. All these factors, taken together, allow us to conclude that the diffusion creep cannot be considered the main deformation mechanism.

Thus, we can make the inference that the transformation of coarse-grained titanium into the submicrocrystalline state does not affect the deformation mechanism and that the intragranular dislocation glide is responsible for the plastic flow in the submicrocrystalline titanium studied in the present work. This conclusion is confirmed by the fact that the Hall–Petch relationship adequately describes the dependences of the yield strength and the microhardness on the grain size in the submicrometer range (Figs. 2a, 2b).

On this basis, the influence of the grain size on the mechanical properties of submicrocrystalline titanium can be explained in the framework of four models: (i) the planar dislocation pileup model proposed by Hall [21] and Petch [22] and then developed by Cottrell and Armstrong [23, 24], (ii) the Conrad strain hardening model [25], (iii) the Meyers–Ashworth composite model [26], and (iv) the Ashby model of geometrically necessary dislocations [27]. The choice of the most appropriate model calls for further investigation.

ACKNOWLEDGMENTS

This work was supported by the Russian Foundation for Basic Research, project no. 01-02-16505.

REFERENCES

1. A. N. Chokshi, A. Rosen, J. Karch, and H. Gleiter, Scr. Metall. **23** (10), 1679 (1989).
2. G. W. Nieman, J. R. Weertman, and R. W. Siegel, Scr. Metall. Mater. **24** (1), 145 (1990).
3. G. W. Nieman, J. R. Weertman, and R. W. Siegel, Scr. Metall. **23** (12), 2013 (1989).
4. J. S. C. Jang and C. C. Koch, Scr. Metall. **24** (8), 1599 (1990).
5. J. R. Weertman and P. G. Sanders, Solid State Phenom. **35–36**, 249 (1994).
6. P. G. Sanders, J. A. Eastman, and J. R. Weertman, Acta Mater. **45** (10), 4019 (1997).
7. R. Scattergood and C. Koch, Scr. Metall. Mater. **27**, 1195 (1992).
8. R. A. Masumura, P. M. Hazzledine, and C. S. Pande, Acta Mater. **46** (13), 4527 (1998).
9. H. S. Kim, Y. Estrin, and M. B. Bush, Acta Mater. **48**, 493 (2000).
10. H. Conrad and J. Narayan, Scr. Mater. **42**, 1025 (2000).
11. G. A. Salishchev, O. R. Valiakhmetov, R. M. Galeev, and S. P. Malysheva, Fiz. Met. Metallogr. **81** (4), 86 (1996).
12. V. I. Dotsenko, Phys. Status Solidi B **93**, 11 (1979).
13. H. Conrad, Prog. Mater. Sci. **26**, 123 (1981).
14. G. A. Salishchev, K. G. Farkhutdinov, and V. D. Afanas'ev, Metally, No. 2, 116 (1993).
15. S. Yu. Mironov, S. P. Malysheva, R. M. Galeev, *et al.*, Fiz. Met. Metallogr. **87** (3), 247 (1999).
16. G. A. Salishchev, R. G. Zaripova, A. A. Zakirova, *et al.*, Fiz. Met. Metallogr. **89** (3), 100 (2000).
17. G. Salishchev, R. Zaripova, R. Galeev, and O. Valiakhmetov, Nanostruct. Mater. **6**, 913 (1995).
18. A. H. Cottrell and B. A. Bilby, Proc. Phys. Soc. London, Ser. A **62**, 49 (1949).
19. W. G. Johnston, J. Appl. Phys. **33** (9), 2716 (1962).
20. R. Z. Valiev, V. G. Khaĭrullin, and A. D. Sheikh-Ali, Izv. Vyssh. Uchebn. Zaved., Fiz. **34** (3), 93 (1991).
21. E. O. Hall, Proc. Phys. Soc. London, Sect. B **64**, 747 (1951).
22. N. J. Petch, J. Iron Steel Inst., London **147**, 25 (1953).
23. A. H. Cottrell, *Dislocations and Plastic Flow in Crystals* (Clarendon, Oxford, 1953; Metallurgizdat, Moscow, 1958).
24. R. W. Armstrong, in *Ultrafine-Grain Metals: Proceedings of the 16th Sagamore Army Materials Research Conference, Raquette Lake, 1969*, Ed. by J. J. Burke and V. Weiss (Syracuse Univ. Press, Syracuse, 1970; Metallurgiya, Moscow, 1973).
25. H. Conrad, in *Ultrafine-Grain Metals: Proceedings of the 16th Sagamore Army Materials Research Conference, Raquette Lake, 1969*, Ed. by J. J. Burke and V. Weiss (Syracuse Univ. Press, Syracuse, 1970; Metallurgiya, Moscow, 1973).
26. M. A. Meyers and E. Ashworth, Philos. Mag. A **46** (5), 737 (1982).
27. M. F. Ashby, Philos. Mag. **21**, 399 (1970).

Translated by O. Borovik-Romanova

Physics of the Solid State, Vol. 44, No. 4, 2002, pp. 744–746. Translated from Fizika Tverdogo Tela, Vol. 44, No. 4, 2002, pp. 717–719.

MAGNETISM AND FERROELECTRICITY

Relaxation under Pulsed Magnetization Reversal of Monocrystalline Films of $(Bi,Lu)_3(Fe,Ga)_5O_{12}$ with (210) Orientation

V. V. Randoshkin, A. M. Saletskiĭ, and N. N. Usmanov

Moscow State University, Vorob'evy gory, Moscow, 119899 Russia

Received June 5, 2001

Abstract—The photoresponse method is used for studying the relaxation process under pulsed magnetization reversal of monocrystalline films with the composition $(Bi,Lu)_3(Fe,Ga)_5O_{12}$ with (210) orientation depending on the amplitude and duration of the remagnetizing pulse. Magnetization reversal occurs through the formation, motion, and destruction of an end domain wall. © *2002 MAIK "Nauka/Interperiodica".*

Among bismuth-containing monocrystalline garnet ferrite films (BCMGFF), films grown by the liquid-phase epitaxy method from supercooled solution in melt on $Gd_3Ga_5O_{12}$ substrates with the composition $(Bi,Lu)_3(Fe,Ga)_5O_{12}$ are the materials that exhibit the strongest Faraday rotation [1]. Unfortunately, the velocity of domain walls (DWs) in these materials is low when substrates with the (111) crystallographic orientation are used [2]. The DW velocity in films with the above-indicated composition and grown on substrates with (210) orientation is higher [3]. It should be noted that films with the composition $(Bi,Y,Lu,Pr)_3(Fe,Ga)_5O_{12}$ with (210) orientation are characterized by a still higher speed of response [4]. However, the Pr^{3+} ions introduce considerable damping, while the Y^{3+} ions, together with the Bi^{3+} ions, create a high orthorhombic and uniaxial magnetic anisotropy. Films with the $(Bi,Lu)_3(Fe,Ga)_5O_{12}$ composition occupy an intermediate position, which makes it possible to trace the variation of dynamic properties of BCMGFF upon a transition from films with the lowest damping [2, 5–7], whose properties are virtually isotropic in their plane, to the most anisotropic films, whose damping parameter depends on the direction of the DW motion in the plane of the film [8, 9].

This work aims at an analysis of relaxation during pulsed magnetization reversal of BCMGFF with the $(Bi,Lu)_3(Fe,Ga)_5O_{12}$ composition with (210) orientation using the photoresponse method.

Experiments were made on a universal magnetooptical device [3], which made it possible to observe the process of magnetization reversal with the help of high-speed laser photography. The Faraday effect was used to visualize the domain structure. The source of illumination was a laser with $\lambda \cong 638$ nm. The sample was placed between a polarizer and an analyzer whose transmission axes formed an angle suitable for observation of the domain structure in terms of amplitude contrast. The role of a photodetector was played by a photoelectric multiplier (PEM). A signal from the PEM was fed to the inputs of an analog-to-digital converter and a dual-trace oscilloscope. A static magnetic (bias) field H_b was created by a coil. A pulsed laser with a light-pulse duration of 10 ns was used for observing dynamic domains. The source of current pulses was synchronized with the laser with the help of a pulse generator G5-67.

We present here the results obtained for a sample with the following parameters: film thickness $h \cong 11$ μm, tilt angle of the easy magnetization axis (EMA) $\theta \cong 46°$, saturation magnetization $4\pi M_s \cong 43$ G, dimensionless Gilbert damping parameter $\alpha \cong 0.0135$, and uniaxial magnetic anisotropy constant $K_u \cong 1050$ erg/cm^3.

The dimensionless damping parameter was determined from the ferromagnetic resonance (FMR) line width. The FMR signal contained two lines indicating the inhomogeneity of BCMGFF. It should be noted that, in view of the MGFF inhomogeneity, the above value of parameter α may be overestimated. The value of $H_K - 4\pi M_s$, where $H_K = 2K_u/M_s$ is the field of uniaxial magnetic anisotropy, was also determined according to the FMR data from the resonance fields corresponding to the external magnetic field orientation perpendicular and parallel to the plane of the film. The value of $4\pi M_s$ was calculated from the field corresponding to the collapse of cylindrical magnetic domains (disregarding the effect of the EMA tilting).

Figure 1 contains a scheme of a magnetic-field pulse and a photoresponse signal. In the initial state, the sample was magnetized by a bias field exceeding the saturation field H_s of the sample. The pulsed magnetic field was applied in the opposite direction. The rise time and fall time of the magnetic-field pulse were 7 and 40 ns, respectively.

1063-7834/02/4404-0744$22.00

As in [10], the photoresponse signal (Fig. 1) was characterized by the following parameters: magnetization reversal delay τ_{df}, rise time of the photoresponse signal (magnetization reversal rate) τ_f, delay of photoresponse signal decay τ_{db}, and fall time of the photoresponse signal τ_b. In addition, we measured the time τ_{sm} of the sample being in the magnetized (single-domain) state. The magnetization time τ_m was defined as $\tau_m = \tau_{df} + \tau_f$, while the time τ_r of relaxation to the initial state was defined as $\tau_r = \tau_{db} + \tau_b$. The duration τ of the photoresponse signal was determined at a level of 0.05; the time τ_{sm} of the sample being in the magnetized state, at a level of 0.95; and the rise time and fall time of the pulse were defined between levels of 0.1 and 0.9.

Curve *1* in Fig. 2 shows the time τ_{sm} of the sample being in the magnetized state as a function of the amplitude of the magnetic field pulse H_p, which was obtained for a fixed duration of the magnetic field pulse τ_p = 1050 ns. The value of τ_{sm} increases with H_p, since the time of sample magnetization decreases (curve *2* in Fig. 2) while the delay of the photoresponse signal decay after the termination of the magnetic field pulse increases (curve *3* in Fig. 2). The increase in τ_{sm} with H_p is associated to a greater extent with an increase in τ_{db} than with a decrease in τ_m.

The value of τ_m decreases due to both the decrease in the magnetization reversal delay τ_{df} and the increase in the magnetization reversal rate.

Figure 3 shows the time τ_{sm} of the sample being in the magnetized state as a function of the magnetic pulse duration τ_p, which is measured for fixed values of H_p. For a small amplitude of the magnetic field pulse insignificantly exceeding the value required for the film transition to the single-domain state, the $\tau_{sm}(\tau_p)$ dependence is linear and represented by a straight line with a slope of 45° to the abscissa axis (line *1* in Fig. 3). This corresponds to a trivial increase in τ_{sm} as a result of the increase in the magnetic pulse duration. For a larger amplitude of the magnetic pulse, the shape of the $\tau_{sm}(\tau_p)$ curve changes (curves *2–4* in Fig. 3): it acquires an initial segment on which the value of τ_{sm} increases more sharply. This reflects the fact that τ_{db} increases with H_p (curve *3* in Fig. 2). It should be noted that, in a certain range of amplitudes, the initial segment on the $\tau_{sm}(\tau_p)$ curve is displaced towards the ordinate axis. In this amplitude range, τ_{db} is proportional to the time of action of the pulse from the instant τ_m. For large values of H_p, not only the slope but also the position of the initial segment on the $\tau_{sm}(\tau_p)$ curve is independent of H_p. This reflects the fact that the value of τ_{db} attains saturation upon an increase in H_p (curve *3* in Fig. 2).

The observation of magnetization reversal in the BCMGFF under investigation with the help of high-speed photography revealed that the process begins with the formation of an end domain wall (EDW), which subsequently moves across the thickness of the film, and the EDW velocity is a linear function of H_p in a certain range of amplitudes. The fact that the final segment on curves *2–4* in Fig. 3 is displaced upwards relative to the straight line *1* by the same value τ_d indicates that there is a qualitative change in the magnetization-reversal mechanism for the BCMGFF. Apparently, for small values of H_p and quite large values of τ_p, the EDW reaches the opposite surface of the film but does not disappear. After the end of a magnetic pulse, the structure of the EDW experiences a rearrangement (which is responsible for the relaxation delay) and then the EDW moves in the opposite direction and is destroyed in a layer with a lower uniaxial anisotropy.

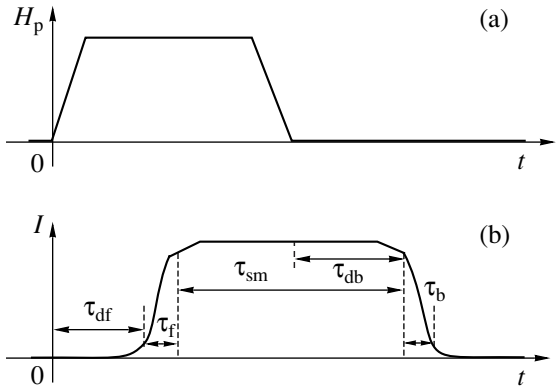

Fig. 1. Schematic diagram of (a) a remagnetizing pulse and (b) a photoresponse signal.

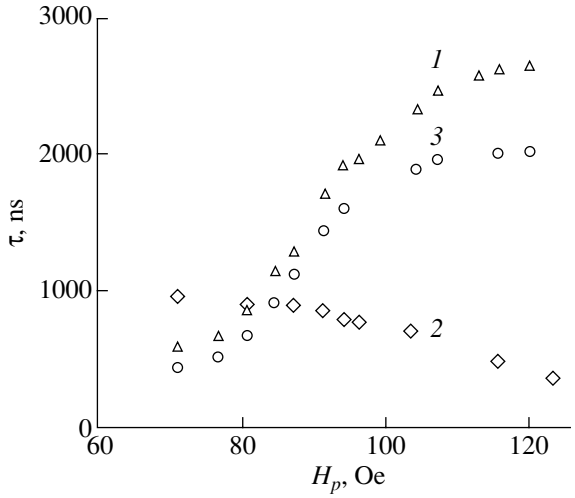

Fig. 2. Time τ_{sm} of a sample being in the magnetized state (triangles), sample magnetization time τ_m (diamonds), and delay τ_{db} of the photoresponse signal decay after the cessation of a magnetic field pulse (circles) as functions of the magnetic pulse amplitude H_p for a fixed duration of the magnetic field pulse $\tau_p \cong 1050$ ns.

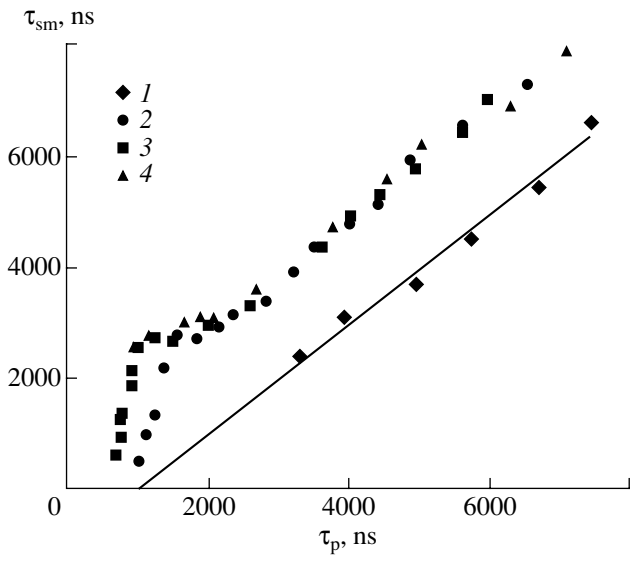

Fig. 3. Dependence of the time τ_{sm} of residence of a sample in the magnetized state on the duration τ_p of the magnetic pulse for fixed values of remagnetizing pulse amplitude H_p, Oe: (*1*) 45, (*2*) 79, (*3*) 107, and (*4*) 129.

For large values of H_p and appreciable τ_p, the EDW reaches the opposite surface of the film and is destroyed; consequently, an extra time τ_d is required for its generation. Since the final segments of curves *2–4* in Fig. 3 coincide, this time is independent of H_p, because the relaxation process is determined by the bias field.

Thus, we have demonstrated that the pulsed magnetization reversal of BCMGFF of composition $(Bi,Lu)_3(Fe,Ga)_5O_{12}$ with (210) orientation through the formation and motion of the EDW leads to a jumpwise change in the time of residence of the film in the magnetized state, the jump magnitude being independent of H_p.

REFERENCES

1. V. V. Randoshkin and A. Ya. Chervonenkis, *Applied Magnetooptics* (Énergoatomizdat, Moscow, 1990).
2. V. E. Bakhteuzov, T. A. Kim, V. V. Randoshkin, *et al.*, Zh. Tekh. Fiz. **55** (6), 1227 (1985) [Sov. Phys. Tech. Phys. **30**, 707 (1985)].
3. N. N. Usmanov, E. N. Il'icheva, and A. G. Shishkov, Vestn. Mosk. Univ., Ser. 3: Fiz., Astron. **36** (5), 74 (1995).
4. V. V. Randoshkin, V. I. Chani, M. V. Logunov, *et al.*, Pis'ma Zh. Tekh. Fiz. **15** (14), 42 (1989) [Sov. Tech. Phys. Lett. **15**, 553 (1989)].
5. V. V. Randoshkin, Proc. SPIE **1307**, 10 (1990).
6. V. V. Randoshkin, Proc. SPIE **1469**, 796 (1991).
7. V. V. Randoshkin, Tr. Inst. Obshch. Fiz. Akad. Nauk **35**, 49 (1992).
8. V. V. Randoshkin and Yu. N. Sazhin, Zh. Tekh. Fiz. **66** (8), 83 (1996) [Tech. Phys. **41**, 790 (1996)].
9. V. V. Randoshkin, Fiz. Tverd. Tela (St. Petersburg) **39** (8), 1421 (1997) [Phys. Solid State **39**, 1260 (1997)].
10. M. V. Lagunov and V. V. Randoshkin, Zh. Tekh. Fiz. **55** (6), 1199 (1985) [Sov. Phys. Tech. Phys. **30**, 686 (1985)].

Translated by N. Wadhwa

Physics of the Solid State, Vol. 44, No. 4, 2002, pp. 747–751. Translated from Fizika Tverdogo Tela, Vol. 44, No. 4, 2002, pp. 720–723.

MAGNETISM AND FERROELECTRICITY

The Origin of Frustration of Magnetic Coupling in the $NiFeCrO_4$ Ferrite

L. G. Antoshina, A. N. Goryaga, and D. A. Chursin

Moscow State University, Vorob'evy gory, Moscow, 119899 Russia

Received June 18, 2001

Abstract—The magnetostriction of the $NiFeCrO_4$ ferrite is investigated for the first time. It is found that the frustration of magnetic coupling occurs only in the *B* sublattice of the $NiFeCrO_4$ ferrite, whereas the *A* sublattice has a usual magnetic structure. The inference is made that the frustration of magnetic coupling in the *B* sublattice is caused not only by the negative direct *BB* exchange interaction $Cr_B^{3+}-Cr_B^{3+}$ but also by the positive indirect *AB* exchange interaction $Fe_A^{3+}-O^{2-}-Cr_B^{3+}$. Reasoning from the experimental data and an analysis of the exchange interactions in the $NiFeCrO_4$ ferrite sample, it is demonstrated for the first time that the magnetic moments of Fe_A^{3+} ions in this ferrite deviate from collinearity. It is established that, at low temperatures, the *B* sublattice of the $NiFeCrO_4$ ferrite is responsible for the total magnetic moment $n_{0\text{exp}}$. © *2002 MAIK "Nauka/Interperiodica".*

1. INTRODUCTION

Ferrites with a spinel structure are the most suitable objects for the formation of a frustrated magnetic structure. The frustrated magnetic structure in ferrites with a spinel-type structure is usually formed through dilution of both ferrite sublattices with nonmagnetic ions [1]. However, Coey [2] proved that even a few exchange interactions differing in sign and magnitude suffice to give rise to a frustrated magnetic structure in spinel ferrites. Recently, Muraleedharan *et al.* [3] and Mohan *et al.* [4] revealed a frustrated magnetic structure in ferrite–chromites containing Cr_B^{3+} ions in sufficient amounts, which, according to the authors' opinion, should lead to the frustration of magnetic coupling.

Mössbauer investigations performed by Srivastava *et al.* [5] revealed a frustrated magnetic structure in the $NiFeCrO_4$ ferrite–chromite. These authors made the assumption that the frustration is caused by the presence of Cr^{3+} ions in octahedral sites of the $NiFeCrO_4$ ferrite. It was of interest to elucidate whether the presence of Cr_B^{3+} ions in the $NiFeCrO_4$ ferrite is the sole cause of the formation of a frustrated magnetic structure or if there exist other factors responsible for the frustration of magnetic coupling.

Earlier [6], we analyzed the anomalous temperature dependences of the spontaneous magnetization $\sigma_s(T)$ for ferrite–chromites and made the inference that a necessary condition for the appearance of the *N*-type (according to Néel) anomalous dependence is the formation of a frustrated magnetic structure in at least one of the ferrite sublattices. In this respect, we have been interested in clarifying whether a similar situation is observed in the $NiFeCrO_4$ ferrite with a compensation point [1].

The question as to which of the sublattices of the $NiFeCrO_4$ ferrite is responsible for the magnetic moment at 0 K remains open to date. For example, Kulkarni *et al.* [7] assigned the magnetic moment to the *A* sublattice of the $NiFeCrO_4$ ferrite. Srivastava *et al.* [8] and McGuire and Greenwald [9] assumed that the *B* sublattice of the ferrite is responsible for the magnetic moment. As is known, the $NiFeCrO_4$ ferrite–chromite is characterized by the $Fe[NiCr]O_4$ cation distribution. By assuming the Néel spin distribution and taking into account that all the ions have only spin magnetic moments ($\mu_{Fe^{3+}} = 5\mu_B$, $\mu_{Ni^{2+}} = 2\mu_B$, and $\mu_{Cr^{3+}} = 3\mu_B$) at $T = 0$ K, the theoretical magnetic moment $n_{0\text{theor}}$ of the $NiFeCrO_4$ ferrite–chromite should be equal to zero [9]. However, it was experimentally found that the magnetic moment $n_{0\text{exp}}$ of this sample at $T = 0$ K is equal to $0.4\mu_B$ [9]. Since the strong negative direct exchange interaction between Cr_B^{3+} ions brings about the formation of a noncollinear magnetic structure in the *B* sublattice, it is not improbable that the *A* sublattice can appear to be responsible for the magnetic moment of the $NiFeCrO_4$ ferrite–chromite at $T = 0$ K. In this respect, it is important to answer questions as to why the theoretical magnetic moment $n_{0\text{theor}}$ is less than the experimental value $n_{0\text{exp}}$ for this compound ($n_{0\text{theor}} < n_{0\text{exp}}$) and as to which of the ferrite sublattices is responsible for the magnetic moment at 0 K.

In order to elucidate the nature of the magnetic moment of the $NiFeCrO_4$ ferrite–chromite, we investi-

1063-7834/02/4404-0747$22.00 © 2002 MAIK "Nauka/Interperiodica"

gated the magnetization, coercive force, and magnetostriction of this compound.

2. SAMPLE PREPARATION AND EXPERIMENTAL TECHNIQUE

The $NiFeCrO_4$ sample was synthesized according to the ceramic technique. The first annealing was carried out at a temperature of 1000°C for 4 h, and the second annealing was performed at 1350°C also for 4 h. Both annealings were carried out in air with subsequent slow cooling. X-ray diffraction analysis demonstrated that the sample synthesized has a single-phase composition and a spinel structure. The magnetization was measured using the ballistic technique in magnetic fields up to 11 kOe in the temperature range 80–600 K. The remanent magnetization σ_r and the coercive force H_c were determined from the hysteresis loop measurements. The magnetostriction was measured by the tensometric method in magnetic fields up to 12 kOe in the temperature range 80–400 K.

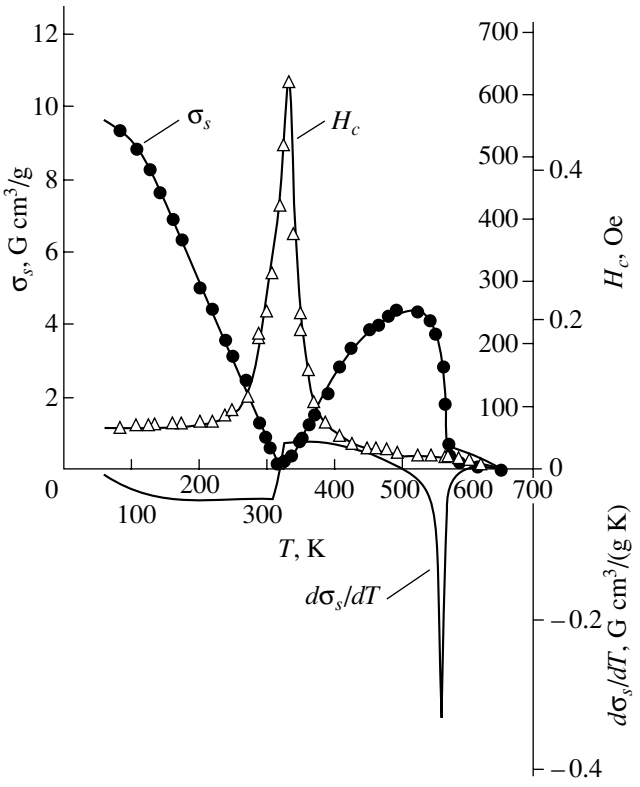

Fig. 1. Temperature dependences of the spontaneous magnetization $\sigma_s(T)$, the coercive force $H_c(T)$, and the derivative of the spontaneous magnetization $(d\sigma_s/dT)(T)$ for the $NiFeCrO_4$ sample.

3. RESULTS AND DISCUSSION

Figure 1 shows the temperature dependences of the spontaneous magnetization $\sigma_s(T)$, the coercive force $H_c(T)$, and the derivative of the spontaneous magnetization $(d\sigma_s/dT)(T)$. It is seen from Fig. 1 that the dependence $\sigma_s(T)$ is represented by an *N*-type curve, the compensation temperature T_c is equal to 325 K, and the Curie temperature T_C is 575 K. By extrapolating the dependence $\sigma_s(T)$ to $T = 0$ K, we determined the spontaneous magnetization σ_{0s}, from which, in turn, we found the experimental magnetic moment $n_{0exp} = 0.40 \pm 0.01\ \mu_B$. This result is in good agreement with the data reported in [9].

As can also be seen from Fig. 1, the temperature dependence of the derivative of the spontaneous magnetization $|(d\sigma_s/dT)(T)|$exhibits a sharp maximum in the vicinity of the Curie temperature T_C. This behavior of the dependence $(d\sigma_s/dT)(T)$ near the T_C temperature is characteristic of a conventional ferrimagnet with the *Q*-type dependence $\sigma_s(T)$. This proves that, at $T > T_c$, the *A* sublattice in which the frustrated magnetic structure is absent is responsible for the magnetic moment of the $NiFeCrO_4$ ferrite. However, at $T < T_c$, the dependence $(d\sigma_s/dT)(T)$ is virtually constant. As a rule, this situation is observed for ferrites with a frustrated magnetic structure [10, 11]. Therefore, judging from the behavior of the dependences $\sigma_s(T)$ (the *N*-type curve) and $(d\sigma_s/dT)(T)$, we can assume that the octahedral sublattice is responsible for the magnetic moment of the $NiFeCrO_4$ ferrite–chromite at 0 K.

The longitudinal $\lambda_\parallel$ and transverse $\lambda_\perp$ magnetostrictions of the $NiFeCrO_4$ sample were investigated for the first time in the present work. By using the data on $\lambda_\parallel$ and $\lambda_\perp$, we calculated the volume magnetostriction $\omega = \lambda_\parallel + 2\lambda_\perp$. It is known that the longitudinal $\lambda_\parallel$ and transverse $\lambda_\perp$ magnetostrictions of a ferromagnet with a nonfrustrated magnetic structure obey the Akulov rule $\lambda_\parallel = -2\lambda_\perp$. As a consequence, the volume magnetostriction ω should be equal to zero.

Figure 2 displays the temperature dependences of the volume magnetostriction $\omega(T)$ calculated for the magnetic field $H = 12$ kOe and the measured susceptibility of the paraprocess $\chi_p(T)$ in a magnetic field in the range 6–10 kOe. It can be seen that, below the compensation temperature T_c, the negative volume magnetostriction ω drastically increases in magnitude with a decrease in the temperature and becomes equal to $\approx -193 \times 10^{-6}$ at $T = 93$ K. Above T_c, the volume magnetostriction ω is virtually zero. This finding is consistent with the Akulov rule and, thus, confirms once more the inference that the magnetic structure in the *A* sublattice is not frustrated. As is seen from Fig. 2, a sharp increase in the magnitude of $\omega(T)$ below the T_c temperature is attended by a drastic increase in the susceptibility of the paraprocess $\chi_p(T)$. This indicates that the true

magnetization of the sample increases in a magnetic field.

It is found that the longitudinal $\lambda_{\parallel}$, transverse $\lambda_{\perp}$, and volume ω magnetostrictions exhibit a substantially different behavior at temperatures below and above the compensation point T_c.

The isotherms of the magnetization $\sigma(H)$, the longitudinal magnetostriction $\lambda_{\parallel}(H)$, the transverse magnetostriction $\lambda_{\perp}(H)$, and the volume magnetostriction $\omega(H)$ measured at a temperature $T < T_c$ are depicted in Fig. 3. As can be seen from Fig. 3, the values of $\lambda_{\parallel}(T)$ and $\lambda_{\perp}(T)$ are negative and anomalous: the magnitude of $\lambda_{\parallel}$ is approximately ten times larger than that of $\lambda_{\perp}$. The absence of saturation in the curves $\omega(H)$ and $\sigma(H)$ indicates that a paraprocess associated with a decrease in the degree of noncollinearity in the *B* sublattice of the $NiFeCrO_4$ ferrite occurs at low temperatures.

Similar isotherms $\sigma(H)$, $\lambda_{\parallel}(H)$, $\lambda_{\perp}(H)$, and $\omega(H)$ measured at a temperature $T > T_c$ are shown in Fig. 4. As regards the longitudinal $\lambda_{\parallel}$ and transverse $\lambda_{\perp}$ magnetostrictions, the Akulov rule holds in virtually all magnetic fields: $\lambda_{\parallel} = -2\lambda_{\perp}$; hence, the volume magnetostriction ω is approximately equal to zero. It can be seen that no saturation is observed in the dependences $\lambda_{\parallel}(H)$, $\lambda_{\perp}(H)$, and $\sigma(H)$. These findings allow us to make the inference that the nature of the paraprocess at $T > T_c$ differs from that at $T < T_c$. It seems likely that the paraprocess at $T > T_c$ is due to an increase in the degree of noncollinearity in the *B* sublattice of the $NiFeCrO_4$ ferrite.

Therefore, the results obtained in the investigation into the magnetic and magnetostriction properties of the Fe[NiCr] ferrite demonstrated that the frustration of magnetic coupling occurs only in the *B* sublattice of this compound, whereas the *A* sublattice has a usual magnetic structure. Moreover, it was found that the *B* sublattice is responsible for the magnetic moment $n_{0\text{exp}}$ of the ferrite under investigation.

This inference is supported by a similar behavior of the isotherms of the longitudinal $\lambda_{\parallel}(H)$ and transverse $\lambda_{\perp}(H)$ magnetostrictions at $T < T_c$ for the $NiFe_{1.1}Cr_{0.9}O_4$ ferrite–chromite with the $Fe[NiFe_{0.1}Cr_{0.9}]O_4$ cation distribution, in which the magnetic moment at low temperatures is determined by the *B* sublattice [12].

It is of interest to elucidate the origin of frustrated magnetic coupling in the $NiFeCrO_4$ ferrite–chromite. Since the frustrated magnetic structure in the ferrite–chromite sample can be caused either by dilution of the ferrite with nonmagnetic ions [1] or by exchange interactions differing in sign and magnitude [2], it is necessary to analyze the exchange interactions between ions entering into the composition of this ferrite.

According to Goodenough [13], the following exchange interactions can occur in the ferrite–chromite sample under investigation: (i) the indirect intersublattice exchange interactions Fe_A^{3+}–O^{2-}–Cr_B^{3+} and Fe_A^{3+}–O^{2-}–Ni_B^{2+}; (ii) the indirect intrasublattice exchange interactions Ni_B^{2+}–O^{2-}–Ni_B^{2+}, Ni_B^{2+}–O^{2-}–Cr_B^{3+}, and Cr_B^{3+}–O^{2-}–Cr_B^{3+}; and (iii) the direct exchange Cr_B^{3+}–Cr_B^{3+}. As a rule, the intrasublattice exchange interac-

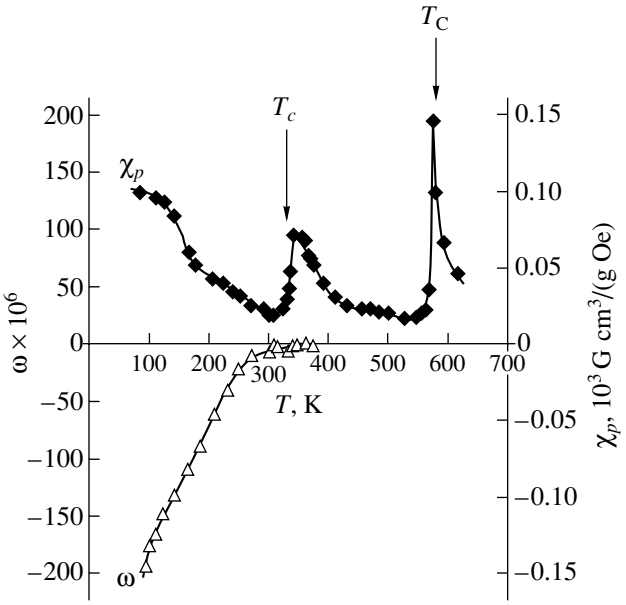

Fig. 2. Temperature dependences of the volume magnetostriction $\omega(T)$ calculated for the magnetic field H = 12 kOe and the measured susceptibility of the paraprocess $\chi_p(T)$ in a magnetic field in the range 6–10 kOe for the $NiFeCrO_4$ sample.

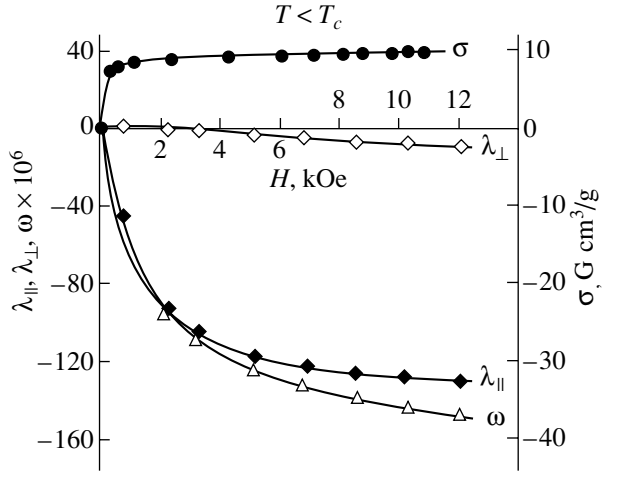

Fig. 3. Isotherms of the magnetization $\sigma(H)$, the longitudinal magnetostriction $\lambda_{\parallel}(H)$, the transverse magnetostriction $\lambda_{\perp}(H)$, and the volume magnetostriction $\omega(H)$ for the $NiFeCrO_4$ sample at T = 123.5 K.

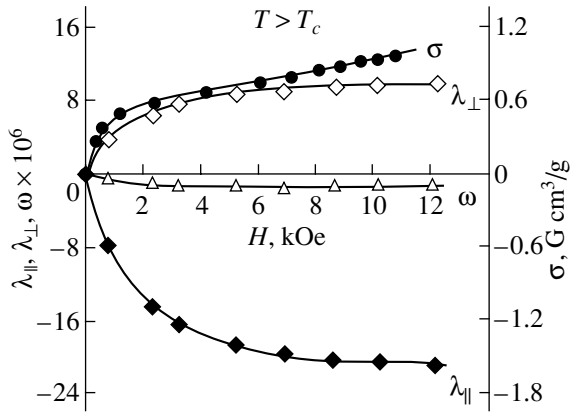

Fig. 4. Isotherms of the magnetization σ(*H*), the longitudinal magnetostriction $\lambda_\parallel(H)$, the transverse magnetostriction $\lambda_\perp(H)$, and the volume magnetostriction ω(*H*) for the $NiFeCrO_4$ sample at $T = 343.5$ K.

tions in the *A* sublattice of the ferrite with a spinel structure can be ignored.

The Fe_A^{3+} cation ($t_{2g}^3 e_g^2$) has a magnetic d_{z2} orbital and forms the p_σ bond with a *p* orbital of oxygen. In turn, the Cr_B^{3+} cation ($t_{2g}^3 e_g^0$) has magnetic t_{2g} orbitals and forms the p_π bond with the same oxygen orbital. Consequently, the indirect intersublattice exchange interaction Fe_A^{3+}–O^{2-}–Cr_B^{3+} due to the p_σ–p_π bond is positive and not very strong [13]. The indirect intersublattice exchange interaction Fe_A^{3+}–O^{2-}–Ni_B^{2+} between the $Fe_A^{3+}(t_{2g}^3 e_g^2)$ and $Ni_B^{2+}(t_{2g}^6 e_g^2)$ cations is associated with the p_σ–p_σ bond. Hence, it can be assumed that this interaction is negative and strong (as judged from the high Curie temperature $T_C = 575$ K for the studied ferrite).

The positive intrasublattice *BB* exchange interaction between the Ni^{2+} ($t_{2g}^6 e_g^2$) cations that are located at octahedral sites and form the p_π–p_π bond is relatively weak. Since the e_g orbital is magnetic in the Ni_B^{2+} ($t_{2g}^6 e_g^2$) cation and the t_{2g} orbital is magnetic in the Cr_B^{3+} ($t_{2g}^3 e_g^0$) cation, the intrasublattice exchange interaction Ni_B^{2+}–O^{2-}–Cr_B^{3+} due to the p_σ–p_π bond is negative and relatively strong. The intrasublattice exchange Cr_B^{3+}–Cr_B^{3+} between the Cr_B^{3+} ($t_{2g}^3 e_g^0$) cation is direct, strong, and negative. The negative indirect intrasublattice exchange interaction Cr_B^{3+}–O^{2-}–Cr_B^{3+} is very weak and, as a rule, is ignored.

Thus, it was shown for the first time that, in the $NiFeCrO_4$ ferrite, the sufficiently strong positive indirect *AB* exchange interaction Fe_A^{3+}–O^{2-}–Cr_B^{3+} counteracts the strong negative indirect *AB* exchange interaction Fe_A^{3+}–O^{2-}–Ni_B^{2+}; as a result, the magnetic moments of Fe_A^{3+} cations deviate from collinearity. Therefore, we can argue that the experimental total magnetic moment n_{0exp} of the $NiFeCrO_4$ ferrite is due to the formation of a noncollinear magnetic structure in the *A* sublattice.

The negative intrasublattice *BB* exchange interactions Ni_B^{2+}–O^{2-}–Cr_B^{3+} and Cr_B^{3+}–Cr_B^{3+} are considerably weaker than the intersublattice *AB* exchange interactions. The former two types of interactions make a smaller contribution to the total magnetic moment of the sample under investigation but lead to the formation of a noncollinear magnetic structure in the *B* sublattice. Apparently, the degree of noncollinearity in the *B* sublattice decreases in response to an external magnetic field at low temperatures. This provides an explanation for the absence of saturation in the isotherms of the magnetization σ(*H*), the longitudinal magnetostriction $\lambda_\parallel(H)$, and the transverse magnetostriction $\lambda_\perp(H)$.

From the above discussion, we can state that the formation of a frustrated magnetic structure in the *B* sublattice is caused not only by the negative direct intrasublattice exchange Cr_B^{3+}–Cr_B^{3+} but also by the positive indirect intersublattice exchange Fe_A^{3+}–O^{2-}–Cr_B^{3+} whose contribution is greater than that of the direct exchange. This assumption can be confirmed by the fact that the pure nickel chromite $Ni[Cr_2]O_4$ does not exhibit a frustrated magnetic structure. Therefore, the presence of Cr_B^{3+} ions in large amounts when the positive *AB* exchange Fe_A^{3+}–O^{2-}–Cr_B^{3+} is absent does not result in the frustration of magnetic coupling in the $NiCr_2O_4$ chromite.

Thus, the results obtained in the above investigation into the magnetization and magnetostriction of the $NiFeCrO_4$ ferrite–chromite allowed us to draw the conclusion that the frustrated magnetic structure can occur only in the *B* sublattice.

REFERENCES

1. C. P. Poole and H. A. Farach, Z. Phys. B **47**, 55 (1982).
2. J. M. D. Coey, J. Appl. Phys. **49** (3), 1646 (1978).
3. K. Muraleedharan, J. K. Srivastava, V. R. Marathe, and R. Vijayaragharan, J. Magn. Magn. Mater. **49**, 333 (1985).
4. H. Mohan, I. A. Shaikh, and R. G. Kulkarni, Physica B (Amsterdam) **217**, 292 (1996).

5. J. K. Srivastava, K. Muraleedharan, and R. Vijayaraghavaran, Phys. Status Solidi B **140**, K47 (1987).

6. L. G. Antoshina, A. N. Goryaga, and V. V. San'kov, Fiz. Tverd. Tela (St. Petersburg) **42** (8), 1446 (2000) [Phys. Solid State **42**, 1488 (2000)].

7. J. A. Kulkarni, K. Muraleedharan, J. K. Srivastava, *et al.*, J. Phys. C **18**, 2593 (1985).

8. J. K. Srivastava, K. Le Dang, and P. Veillet, J. Phys. C **19**, 599 (1986).

9. T. K. McGuire and S. W. Greenwald, in *Solid State Physics in Electronics and Telecommunication*, Ed. by M. Desirant and J. L. Michiels (Academic, New York, 1960), Vol. 1 (3), p. 50.

10. L. G. Antoshina and E. N. Kukudzhanova, Fiz. Tverd. Tela (St. Petersburg) **40** (8), 1505 (1998) [Phys. Solid State **40**, 1366 (1998)].

11. L. G. Antoshina, A. N. Goryaga, E. N. Kukudzhanova, and I. A. Fil'gus, Zh. Éksp. Teor. Fiz. **111** (5), 1732 (1997) [JETP **84**, 948 (1997)].

12. L. G. Antoshina, A. N. Goryaga, and R. R. Annaev, Fiz. Tverd. Tela (St. Petersburg) **42** (11), 2048 (2000) [Phys. Solid State **42**, 2109 (2000)].

13. J. B. Goodenough, *Magnetism and the Chemical Bond* (Interscience, New York, 1963; Metallurgiya, Moscow, 1968).

Translated by O. Borovik-Romanova

Physics of the Solid State, Vol. 44, No. 4, 2002, pp. 752–758. Translated from Fizika Tverdogo Tela, Vol. 44, No. 4, 2002, pp. 724–730.

MAGNETISM AND FERROELECTRICITY

The Influence of Magnetoelastic Coupling of Exchange Spin Waves on the Spectrum of Magnetoacoustic Vibrations in Planar Structures

A. S. Bugaev and V. B. Gorsky

Moscow Physicotechnical Institute, Institutskiĭ proezd 9, Dolgoprudnyĭ, Moscow oblast, 141700 Russia

Received July 12, 2001

Abstract—The influence of coupling between exchange spin waves and acoustic waves on the spectrum of magnetoelastic vibrations in planar structures (such as a ferrite film–dielectric substrate structure) is investigated theoretically. A strong magnetoelastic coupling is observed in a narrow spectrum of magnetoacoustic modes that corresponds to the phase matching of the exchange magnetostatic and acoustic modes. An explanation is offered for the experimental results obtained earlier by the authors, according to which the linear excitation of exchange acoustic and dipole exchange acoustic modes occurs in a spectral range corresponding to the resonance magnetoelastic coupling of exchange modes irrespective of the degree of pinning of surface spins in the ferrite film. It is demonstrated that the exchange acoustic and dipole exchange acoustic modes can be excited in films with free surface spins due to a substantial transformation of the structure of normal modes of the magnetization vector and elastic displacements in the range of the phase matching of the exchange spin and acoustic modes.

1. INTRODUCTION

The coupling between magnetostatic (spin) and acoustic waves was first considered for the case of bulk crystals. It was demonstrated that, in spatially inhomogeneous magnetic fields, these waves efficiently transform into each other in the range of wave phase matching [1].

The coupling of dipole magnetostatic waves with fast acoustic modes in a planar structure (such as a ferrite film–dielectric substrate structure) was treated theoretically and experimentally in [2, 3]. Special mention should be made of the works by Filimonov [4] and Filippov *et al.* [5], who theoretically proved that dipole magnetostatic waves can independently interact with both fast acoustic modes and higher bulk (exchange) magnetostatic modes.

Earlier [6, 7], we investigated the coupling of exchange spin waves and dipole exchange spin modes with acoustic modes in yttrium iron garnet (YIG) films with pinned surface spins. All the aforementioned works [4–7] dealt with films involving pinned surface spins, because, otherwise, the excitation of higher bulk modes becomes impossible. This can be explained by the fact that the distribution of ac magnetization over the film thickness is symmetric with respect to the midplane of the film [8, 9] and that the integral of overlap of the ac magnetization distribution with an external magnetic field (quasi-homogeneous over the film thickness) or with a dipole field of the lowest bulk (dipole) mode is equal to zero.

More recently [10, 11], we demonstrated that, even in films with free surface spins, the exchange acoustic and hybrid dipole–exchange–acoustic modes are efficiently excited in a narrow spectrum of magnetoacoustic modes that corresponds to the phase matching of exchange spin waves and acoustic modes. This effect was attributed to substantial distortions of the spatial distributions of the ac magnetization and elastic displacements of normal magnetoacoustic modes in a planar structure with strong magnetoacoustic coupling. In the present work, we thoroughly analyzed the influence of magnetoelastic coupling of higher bulk exchange modes on the spectrum of normal modes of the magnetic and elastic systems in a planar structure.

2. BASIC EQUATIONS, APPROXIMATIONS, AND BOUNDARY CONDITIONS

The aim of this work was to analyze the magnetoacoustic wave spectrum that should be observed under the conditions when the phase matching of higher bulk exchange modes and acoustic modes becomes possible. First, we will derive dispersion relations for magnetoelastic modes in a planar structure such as the ferrite film–dielectric substrate (Fig. 1). Primary emphasis will be placed on the coupling of exchange magnetostatic waves with transverse acoustic waves, because, in real crystals, this coupling is one order of magnitude stronger than the coupling with longitudinal waves. Gulyaev and Zil'berman [12] thoroughly treated the coupling of dipole magnetostatic waves with acoustic waves and proved that the degeneracy of two transverse acoustic modes with different polarizations is removed in the presence of magnetoacoustic coupling and that

1063-7834/02/4404-0752$22.00

only one wave is efficiently coupled with the magnetostatic wave.

According to [10], the energy density of a magnetoelastic wave is defined by the relation

$$E(\mathbf{r}, t) = -(\mathbf{H}_e\mathbf{M}) - \frac{1}{2}(\mathbf{H}_m\mathbf{M}) + \frac{1}{2}\alpha\left(\frac{dM_i}{dx_i}\right)^2 + E_{ma}(u_{lm}, \mathbf{M}) + E_a. \quad (1)$$

Here, the first term is the Zeeman energy density in the external field $\mathbf{H}_e$, $\mathbf{M}(\mathbf{r}, t)$ is the magnetization vector, and the second term is the energy density of the interaction between magnetic dipoles. In the second term, the quantity $\mathbf{H}_m$ is given by

$$\mathbf{H}_m = -\nabla\varphi,$$

$$\varphi = \frac{1}{4\pi}\int_V d^3\mathbf{r}'\mathbf{M}_i(\mathbf{r}', t)\frac{d}{dx_i'}\frac{1}{|\mathbf{r} - \mathbf{r}'|}. \quad (2)$$

The third term determines the energy of the inhomogeneous exchange interaction. The energy of anisotropy, which is described by the fourth term, makes the main contribution to the energy of the magnetoacoustic coupling. Hereafter, we will use a linear approximation in which the anisotropy energy takes the form

$$E_{ma}(u_{lm}, \mathbf{M}) = E_{ma}^0(\mathbf{M}) + b_{iklm}M_iM_ku_{lm}, \quad (3)$$

where b_{iklm} is the magnetoelastic constant tensor.

The last term in relation (1) is the elastic energy density

$$E_a = \frac{1}{2}\left(\rho\left(\frac{du_i}{dt}\right)^2 + c_{iklm}u_{ik}u_{lm}\right). \quad (4)$$

Here, ρ is the density of the crystal and c_{iklm} is the elastic constant tensor.

By solving simultaneously the equations of motion for the magnetization vector and the elastic medium and seeking solutions in the form of traveling plane waves m and $u \sim \exp(i\omega t - i\mathbf{kr})$, we obtain the following dispersion relation:

$$\omega^2 - \gamma_2\Big((H_{\text{intz}} + 4\pi M\alpha k^2) + 2b_{44}M^2(-ik_z) \times\left(-ik_z\frac{2b_{44}M}{c_{44}(k^2 - \omega^2/v^2)}\right)\Big) \times\Big((H_{\text{intz}} + 4\pi M\alpha k^2) + 2b_{44}M^2(-ik_z) \times\left(-ik_z\frac{2b_{44}M - Mh_{\text{dip}x}/m_x}{c_{44}[k^2(1 + (1 + c_{12}/c_{44})k_r^2/k^2) - \omega^2/v^2]}\right) - Mh_{\text{dip}x}/m_x\Big) = 0. \quad (5)$$

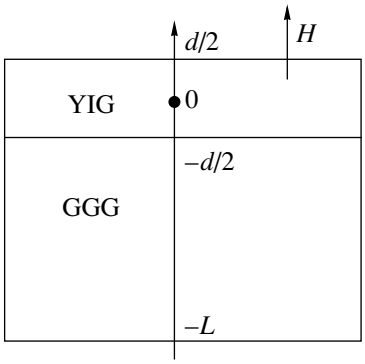

Fig. 1. A geometry of the structure under investigation.

Here, H_{int} is the internal constant magnetic field (for a ferrite film magnetized normally to the surface, $H_{\text{int}} = H_e - 4\pi M$); m is the high-frequency component of the magnetization vector; v is the acoustic wave velocity; γ is the gyromagnetic ratio; h_{dip} is the high-frequency component of the demagnetizing field in the ferrite film, which is determined by the spatial distribution $\mathbf{m}(r)$; and k_r is the projection of the wave number onto the film plane. Within the approximation $k_r \ll k$, we obtain a simpler standard expression,

$$(\omega - \gamma H_{\text{intz}} - \omega_{\text{dip}}(k) - \gamma 4\pi M\alpha k^2) \times (k^2 - \omega^2/v^2) = \gamma M\eta k^2,$$

where $\eta = 4b_{44}^2M^2/c_{44}$, b_{44}, and c_{44} are the diagonal elements of the magnetostriction tensor and elastic constant tensor, respectively, and $\omega_{\text{dip}}(k)$ is the dispersion dependence of the dipole magnetostatic waves (given, for example, in [1, 5]).

The attenuation is included by introducing additional complex terms into the equations of motion for the magnetization vector and the elastic displacement vector. As a result, the dispersion relation takes the form

$$(\omega - \omega_m(k) - i\omega\alpha_m)(\omega - \omega_a(k) - i\omega\alpha_a) = \mu_{ma}, \quad (6)$$

where $\omega_m(\mathbf{k})$ and $\omega_a(\mathbf{k})$ represent the dispersion relations for magnetostatic and acoustic waves, respectively; α_m and α_a account for the attenuation of magnetostatic and acoustic waves; and the quantity $\mu_{ma} \approx (1/2)\gamma M\eta vk$ characterizes the coupling between the magnetostatic and acoustic waves. The wave attenuation is described by the relation

$$\omega'' = \frac{\omega\alpha_a(\omega - \omega_a(\mathbf{k})) + \omega\alpha_a(\omega - \omega_m(\mathbf{k}))}{(\omega - \omega_a(\mathbf{k})) + (\omega - \omega_m(\mathbf{k}))}. \quad (7)$$

The dispersion dependence is most pronounced in the range of the phase matching of the acoustic and exchange modes in which $\omega_a(k) \approx \omega_m(k)$, that is,

$$(\omega - \omega_m(\mathbf{k}))(\omega - \omega_a(\mathbf{k})) = \mu_{ma}''. \quad (8)$$

In this case, the effective magnetoelastic coupling constant that accounts for the attenuation is defined as

$$\mu''^{-1}_{ma} = \mu^{-1}_{ma}\left[1 + \left(\frac{\omega\alpha_m - \omega\alpha_a}{(\omega - \omega_a(k)) + (\omega - \omega_m(k))}\right)^2\right]. \quad (9)$$

The boundary conditions used are as follows: (1) the standard magnetostatic boundary conditions, which allow for continuity of the transverse and longitudinal components of the magnetic induction vector and magnetic field vector, respectively; (2) the exchange boundary conditions, which determine the degree of pinning of surface spins; and (3) the acoustic boundary conditions, which account for the absence of elastic stresses at the structure–air boundaries and the continuity of elastic displacement and stress at the film–substrate interface.

Of special note are the boundary conditions at the boundaries of the ferrite film, that is,

$$\frac{dm}{dz} + bm = 0. \quad (10)$$

In this case, we have $b \longrightarrow 0$ for free spins at the boundary and $b \longrightarrow \infty$ for completely pinned spins. Our prime interest here is in the case of $b \longrightarrow 0$, with emphasis on the condition $b \approx k_r$ when the coupling between the dipole and exchange components is exactly equal to zero [13].

In order to calculate the distributions of the ac magnetization and elastic displacements over the thickness of the structure, the solution for the magnetic potential inside the ferrite film is sought as a combination of six waves:

$$\varphi(\mathbf{r}, t) = \sum_{j = 1\ldots6} A_j \exp(i(\omega t - kx))\exp(-ik_{jz}z). \quad (11)$$

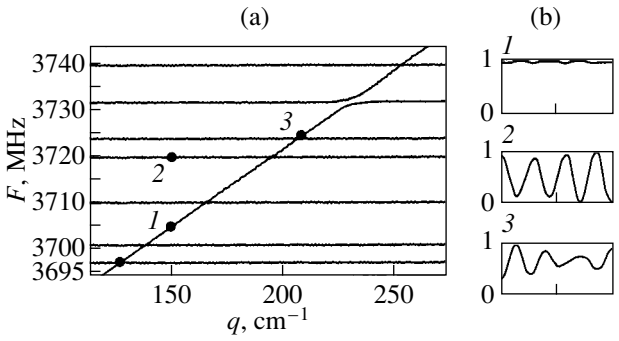

Fig. 2. (a) Spectrum of magnetoelastic vibrations in a 3.1-μm-thick yttrium iron garnet film on a 100-μm-thick gadolinium gallium garnet substrate and (b) distributions of the ac magnetization over the film thickness for (*1*) dipole, (*2*) exchange, and (*3*) hybrid dipole–exchange–acoustic modes. The numerals in panels a and b of the figure indicate the same modes.

The quantities k_j and A_j are derived by solving the dispersion relation (5) and the set of boundary conditions, respectively.

Consequently, the magnetization distribution $m(z)$ over the film thickness for each excited magnetoacoustic mode can be represented as a combination of three standing waves. The excitation efficiency I of the magnetoacoustic mode is determined by the integral of overlap between the function describing $m(z)$ and the external high-frequency electromagnetic field h_{em} whose distribution can be considered to be quasi-homogeneous in the range of magnetoacoustic mode excitation. As a result, the intensity of the magnetoacoustic mode, which should be observed experimentally, can be estimated from the formula

$$I \cong \frac{\int_{-d/2}^{d/2} m(z)h_{\text{em}}dz}{\sum_{i = 1\ldots6} E_i\Delta\omega_i/\omega}, \quad (12)$$

where $\Delta\omega_i$ determines the loss of the ith component and can be obtained from relation (7); E_i is the energy of the ith component, which is determined by expression (1); and d is the thickness of the ferrite film.

3. RESULTS OF NUMERICAL CALCULATIONS

It is known that, in the absence of magnetoelastic coupling in films with free surface spins, the spectrum of magnetoacoustic modes consists of the lowest bulk dipole magnetostatic mode, higher bulk exchange modes (for films with a thickness of less than 10–15 μm), and transverse and longitudinal acoustic modes. In the present work, we consider only the transverse mode with a polarization identical to that of the magnetostatic modes, because this transverse mode is most strongly coupled with magnetostatic modes.

The calculated dispersion dependences for a 3.1-μm-thick yttrium iron garnet film on a 100-μm-thick gadolinium gallium garnet (GGG) substrate are displayed in Fig. 2a. The value of η was taken equal to 0.001. The magnetic field was assumed to be 1405 Oe. For this magnetic field, the phase matching range should be observed in the vicinity of a frequency of 3725 MHz. Actually, the divergent dispersion curves characteristic of coupled waves are clearly seen in Fig. 2a. Figure 2b shows the distributions of ac magnetization over the thickness of the ferrite film both for the dipole and exchange modes at $q = 215$ cm^{-1} and for the hybrid dipole–exchange–acoustic mode excited in the range where the dispersion curves of dipole, exchange, and acoustic modes cross one another. In order to identify the dispersion curves, we calculated the magnetic-to-acoustic-energy and dipole-to-exchange-energy ratios for the vibrational mode [from formulas (1)–(5)],

Spectra of magnetoacoustic modes excited in a magnetic field of 1405 Oe at the wave numbers in the film plane $q = 150.00$ cm^{-1} (upper part) and $q = 212.00$ cm^{-1} (lower part)

Vibrational mode	F_{res}, MHz	E_{dip}/E_{exch}	E_{ac}/E_{mag}	Δf, MHz	I, rel. units
Acoustic	3697.43	0.013	27.0	0.3	0.001
Exchange	3700.63	0.001	0.18	1.3	0.0003
Dipole	3705.04	300.0	0.02	1.5	0.6603
Acoustic	3710.61	0.02	23.0	0.4	0.003
Exchange	3719.67	0.0001	0.54	1.0	0.0003
Acoustic	3724.39	0.0004	8.2	0.4	0.0003
Acoustic	3733.00	0.0019	4.5	0.5	0.0003
Acoustic	3740.40	0.0008	3.0	0.6	0.00001
Vibrational mode	F_{res}, MHz	E_{dip}/E_{exch}	E_{ac}/E_{mag}	Δf, MHz	I, rel. units
Acoustic	3697.43	0.02	28.0	0.3	0.001
Exchange	3700.64	0.001	0.17	1.3	0.0003
Acoustic	3710.59	0.05	24.0	0.4	0.005
Exchange	3719.68	0.003	0.54	1.0	0.01
Acoustic	3724.30	0.20	3.1	0.7	0.07
Dipole (hybrid)	3726.17	88.0	0.07	1.4	0.59
Acoustic	3733.04	0.1	4.4	0.5	0.001
Acoustic	3740.40	0.001	3.0	0.6	0.001

Note: The vibrational mode is determined from the ratio of the dipole, exchange, and acoustic energies. F_{res} is the resonance frequency, E_{dip}/E_{exch} is the dipole-to-exchange-energy ratio, E_{ac}/E_{mag} is the acoustic-to-magnetic-energy ratio, Δf is the width of the resonance curve, and I is the relative intensity of the mode excited in a homogeneous microwave field.

the wave attenuation (the width of the resonance curve), and the relative intensity of vibrational modes excited with an electromagnetic field. The calculated values of these parameters are listed in the table. In our calculations, we assumed that the loss in the magnetic system corresponds to the width of the ferromagnetic resonance curve (1.5 MHz), whereas the loss in the acoustic system is determined by the width of the absorption curve (0.2 MHz). The calculations were performed for two projections of the wave number onto the film plane: (i) $q = 150$ cm^{-1}, when all the modes are well-separated from one another and can easily be identified, and (ii) $q = 212$ cm^{-1}, when the dipole, exchange, and acoustic modes are simultaneously involved in the coupling at frequencies close to $f = 3725$ MHz.

Figure 3 depicts calculated absorption spectra that should be observed experimentally. According to calculations, the excited exchange acoustic modes have a very low intensity. As can be seen from the calculated spectrum (Fig. 3a), these modes are excited at frequencies of 3701 and 3710 MHz. Experimentally, their excitation should be observed only in the case when the exchange acoustic mode occurs in the vicinity of a dipole mode, i.e., when the dipole component makes a sufficiently large contribution to the latter mode. It is clearly seen from Fig. 3b that the hybrid dipole–exchange–acoustic modes are excited at frequencies close to $f = 3725$ MHz.

In experiments, the magnetoelastic coupling in an external magnetic field most clearly manifests itself in periodic oscillations of the resonance frequencies and intensities of the magnetoacoustic modes observed in the range of phase matching of the exchange spin and

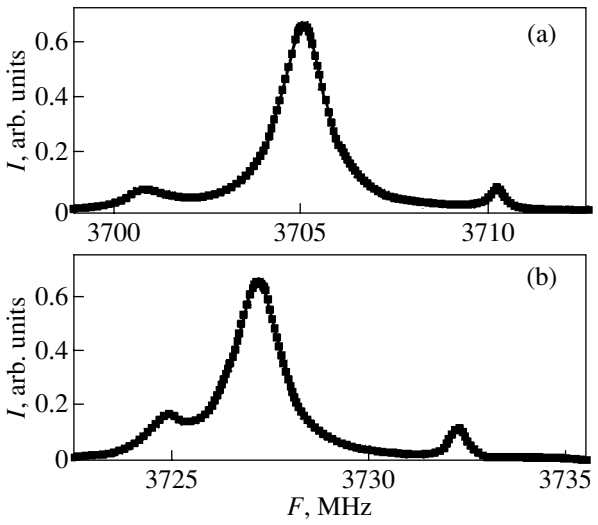

Fig. 3. Calculated spectra of vibrational modes presumably observed in circular-disk resonators at q = (a) 150 and (b) 212 cm^{-1}.

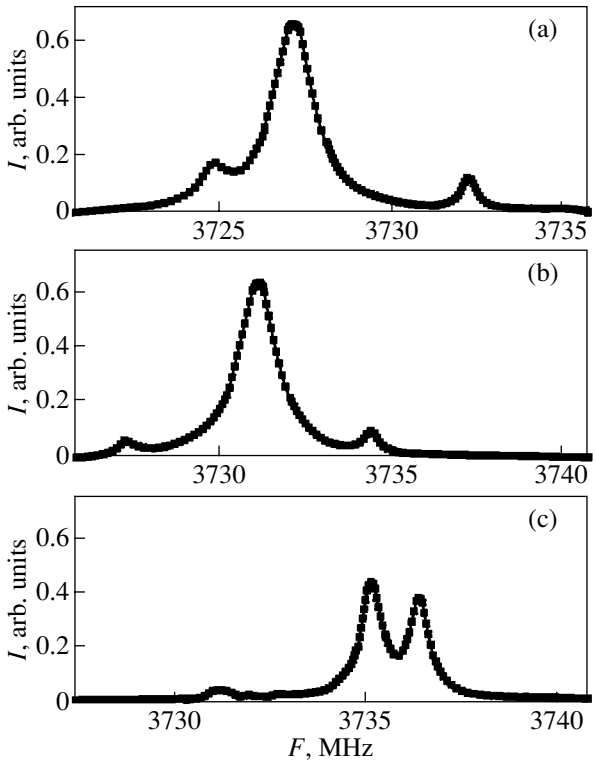

Fig. 4. Calculated spectra of vibrational modes presumably excited in a circular-disk resonator at $q = 240$ cm^{-1} in different magnetic fields: (a) 1405, (b) 1407, and (c) 1408.7 Oe.

acoustic modes. Let us now consider this effect in more detail. Figure 4 displays the calculated spectra of magnetoacoustic modes [the dependences of the absorbed power on the microwave field frequency $P(f)$] at different external magnetic fields H_e. In the absence of magnetoelastic coupling, the intensities of magnetostatic vibrations are virtually independent of H_e and the resonance frequencies f_i of all the magnetostatic vibrations vary proportionally with the external magnetic field H_e. It is worth noting that, in the initial portion of the magnetostatic wave spectrum, where the external magnetic field H_e changes insignificantly, the dependence $f_i(H_e)$ exhibits a nearly linear behavior. In the presence of the magnetoelastic coupling, the aforementioned proportional change in the resonance frequencies of the magnetoacoustic vibrations with variations in the external magnetic field H_e is accompanied by periodic changes in the resonance frequencies and intensities of magnetoacoustic vibrations in the phase matching range of the spin and acoustic waves. The period of these changes is determined by the difference in frequency of the adjacent Lamb modes. This difference is inversely proportional to the thickness of the planar structure.

The oscillating changes observed in the spectrum can be associated with the fact that the resonance frequencies of the acoustic modes are virtually independent of the magnetic field, whereas the resonance frequencies of the magnetostatic modes are proportional to the external magnetic field strength. This can be easily explained in terms of any *i*th exchange magnetostatic vibration whose wave number in the frequency range covered is of the order of the wave number of the acoustic mode. We assume that, at the initial instant, the resonance frequency of the exchange vibration coincides with none of the natural frequencies of the acoustic modes. It follows that, for this vibration, the magnetization distribution $m_i(z)$ is virtually symmetric with respect to the midplane of the ferrite film and the intensity is close to zero. As the magnetic field strength increases, the resonance frequency of the *i*th exchange vibration increases and, at a certain instant of time, approaches the resonance frequency of the *j*th acoustic mode. As a result, the exchange acoustic vibration manifests itself in the spectrum, because the $m_i(z)$ distribution becomes asymmetric with the respect to the midplane of the ferrite film due to a hybridization with the acoustic mode. Thus, the direct coupling of exchange vibrations with acoustic modes is the first reason for the observed oscillations of the spectrum. It should be noted that, in the case when the resonance frequency of the exchange vibration coincides with the resonance frequency of the acoustic vibration, the vibrational modes can either diverge or intersect depending on the magnetostriction coupling.

The second reason for the observed oscillations of the spectra is the dipole coupling of the exchange acoustic vibrations with dipole magnetostatic vibrations. Indeed, the coupling with the acoustic mode leads to a change in the location of the exchange magnetostatic vibration in the spectrum of magnetoacoustic vibrations. For example, if the resonance frequency of the exchange acoustic vibration approaches the resonance frequency of one of the dipole vibrations, the dipole component appears in the $m(z)$ distribution and the hybrid dipole–exchange–acoustic mode is excited. For a sufficiently strong interaction between the dipole fields of the exchange acoustic and dipole vibrations, when the resonance frequency of the dipole vibration coincides with the resonance frequency of the exchange acoustic vibration, there occurs a characteristic divergence of the vibrational modes; otherwise, this is attended by changes in the intensity, shape, and width of the resonance curves of the dipole magnetostatic and exchange acoustic vibrations. With a further increase in the magnetic field strength, this situation should be reproduced when the resonance frequency of the dipole magnetostatic vibration coincides with the resonance frequency of the next Lamb mode.

Now, we analyze similar changes in the vibrational spectrum represented in a more convenient form used in experiments; in other words, we consider the vibrational spectrum as a function of the magnetic field and examine the dependences of the resonance magnetic field and the intensity of excited modes on the fre-

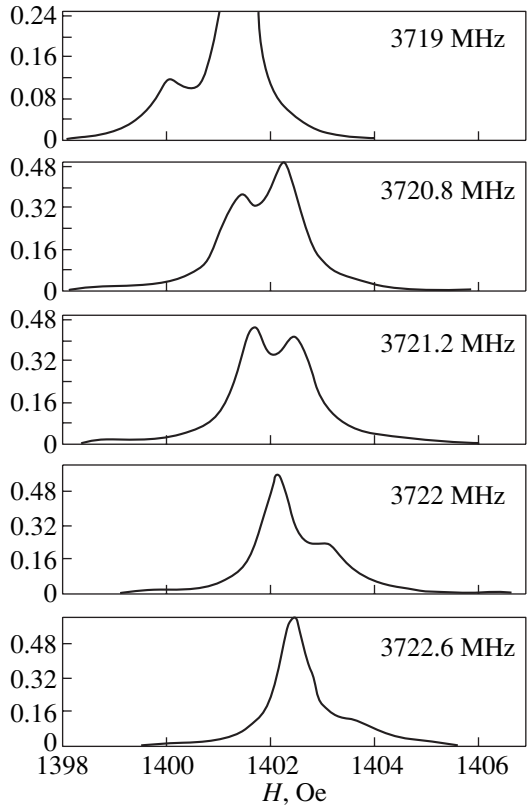

Fig. 5. Evolution of the vibrational spectrum as a function of the magnetic field with variations in the excitation frequency at $q = 220$ cm^{-1}. The exchange acoustic mode is characterized by a more pronounced frequency dependence. When the excitation conditions for this mode and the dipole mode coincide, the hybrid dipole–exchange–acoustic modes are excited ($f = 3721.2$ MHz).

quency as a parameter. It is assumed that the difference between the adjacent resonance frequencies of the acoustic modes is considerably larger than the width of the acoustic resonance curve. This is true for experiments with planar structures such as the YIG film–GGG substrate, because the acoustic loss in gadolinium gallium garnet in the frequency range 2–8 GHz corresponds to $\Delta f \approx 0.05$–0.15 MHz, whereas the difference between the frequencies of the adjacent transverse acoustic resonances for 450-μm-thick planar structures is of the order of 3.5 MHz. Unlike the preceding case, efficient excitation at a specified excitation frequency f is observed only for one (ith) acoustic mode whose resonance frequency f_{res}^{i} is closest to the microwave field frequency f, because the width of the acoustic resonance curve is substantially less than the difference between the frequencies of the adjacent acoustic resonances. For the exchange modes associated with the acoustic system, the acoustic component makes a minimum contribution when $f \approx (f_{\text{res}}^{i} + f_{\text{res}}^{i+1})/2$. The resonance magnetic fields of magnetoacoustic modes at these frequencies are close to the field strengths in the absence of the magnetoacoustic coupling. As the excitation frequency approaches one of the natural frequencies of the acoustic modes, the contribution of the acoustic component to the vibration increases and the dependence of the resonance frequency on the magnetic field strength becomes weaker or, what is the same, the frequency dependence of the resonance magnetic field becomes stronger. When the resonance magnetic field of this exchange acoustic vibration coincides with the resonance magnetic field of one of the dipole vibrations, the dipole exchange acoustic modes are

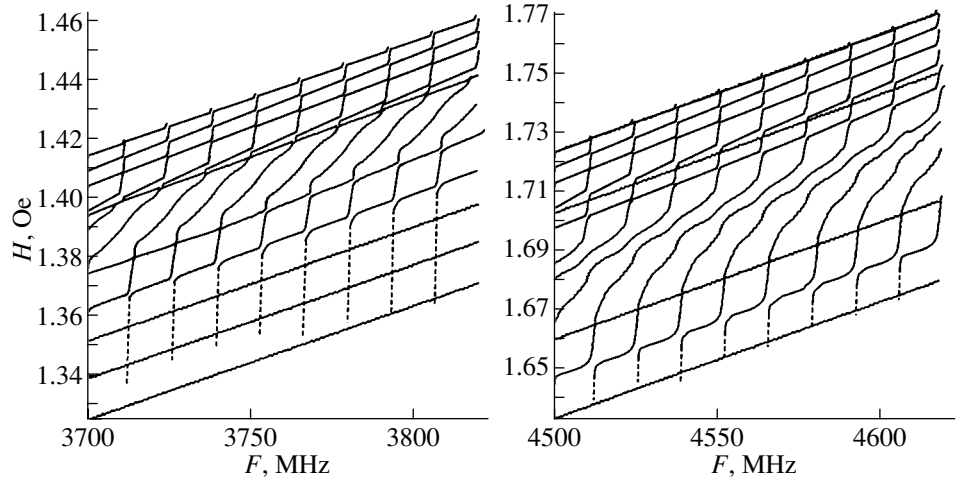

Fig. 6. Frequency dependences of the resonance magnetic fields of magnetoacoustic vibrations in two frequency ranges. The range of strong coupling between the exchange and acoustic modes shifts away from the origin of the magnetostatic wave spectrum with an increase in the frequency.

excited (Fig. 5). The coupling between the vibrational modes occurs through their dipole fields. If this coupling is sufficiently strong, the characteristic divergence of vibrational modes takes place. Figure 6 displays the calculated frequency dependences of the resonance magnetic fields for magnetoelastic modes at $q = 220$ cm^{-1}. For magnetic vibrations unrelated to the acoustic system, the dependences $H_{res}(f)$ are represented by lines with the slope γ. In the absence of the magnetoelastic coupling, the acoustic modes should be represented in the form of vertical equidistant straight lines. A comparison of Figs. 6a and 6b clearly demonstrates that the range of coupling with acoustic modes shifts away from the origin of the magnetostatic wave spectrum with an increase in the excitation frequency.

4. CONCLUSION

Thus, it was demonstrated that a considerable transformation of the vibrational spectrum due to a radical change in the structure of coupled magnetoacoustic modes is observed in the range of phase matching of the higher bulk exchange magnetostatic and acoustic modes. As a result, the linear excitation of exchange acoustic modes becomes possible regardless of the degree of pinning of surface spins. When the excitation conditions for the exchange acoustic modes and dipole modes coincide, there occurs excitation of hybrid dipole–exchange–acoustic modes.

The coupling of dipole modes with the elastic system through the exchange component is many orders of magnitude stronger than the direct coupling between the dipole and acoustic modes. The dispersion dependences exhibit a characteristic divergence of the dispersion branches of the dipole, exchange, and acoustic modes.

The discreteness of the elastic excitation spectrum of the planar structure and the different dependences of the acoustic and magnetic wave spectra on the magnetic field strength are responsible for the frequency oscillations observed in the spectrum represented as a function of the magnetic field; correspondingly, the oscillations in the spectrum represented as a function of the frequency are observed with a change in the magnetic field. Owing to the very strong magnetoelastic coupling, the magnetoacoustic modes can be efficiently excited in the ranges of frequencies and magnetic fields well away from the range of the phase matching of exchange acoustic waves.

REFERENCES

1. W. Strauss, in *Physical Acoustics: Principles and Methods*, Vol. 4, Part B: *Applications to Quantum and Solid State Physics*, Ed. by W. P. Mason (Academic, New York, 1968; Mir, Moscow, 1970).
2. A. S. Bugaev, Yu. V. Gulyaev, P. E. Zil'berman, and Yu. A. Filimonov, Fiz. Tverd. Tela (Leningrad) **23** (9), 2647 (1981) [Sov. Phys. Solid State **23**, 1552 (1981)].
3. Yu. V. Gulyaev, P. E. Zil'berman, G. T. Kazakov, *et al.*, Pis'ma Zh. Éksp. Teor. Fiz. **34** (9), 500 (1981) [JETP Lett. **34**, 477 (1981)].
4. Yu. A. Filimonov, Author's Abstract of Candidate's Dissertation (1982).
5. B. N. Filippov, V. D. Boltachev, and Yu. G. Lebedev, Fiz. Met. Metalloved. **49** (6), 1150 (1980).
6. V. B. Gorsky and A. V. Pomyalov, Pis'ma Zh. Tekh. Fiz. **15** (7), 61 (1989) [Sov. Tech. Phys. Lett. **15**, 273 (1989)].
7. A. S. Bugaev and V. B. Gorsky, Radiotekh. Élektron. (Moscow), No. 1, 1 (1992).
8. M. Sparks, Phys. Rev. B **1** (9), 3831 (1970).
9. Yu. V. Gulyaev, A. S. Bugaev, and P. E. Zil'berman, Pis'ma Zh. Éksp. Teor. Fiz. **30** (9), 600 (1979) [JETP Lett. **30**, 565 (1979)].
10. A. S. Bugaev and V. B. Gorsky, in *Abstracts of 1997 IEEE International Ultrasonic Symposium*, PFF-1 p. 97.
11. A. S. Bugaev and V. B. Gorsky, in *Extended Abstracts of International Conference on Solid State Device and Materials, Yokohama, Japan, 1994*, p. 823.
12. Yu. V. Gulyaev and P. E. Zil'berman, Izv. Vyssh. Uchebn. Zaved., Fiz. **31** (11), 6 (1988).
13. A. V. Lugovskoĭ and P. E. Zil'berman, Fiz. Tverd. Tela (Leningrad) **24** (2), 458 (1982) [Sov. Phys. Solid State **24**, 259 (1982)].

Translated by O. Borovik-Romanova

Physics of the Solid State, Vol. 44, No. 4, 2002, pp. 759–762. Translated from Fizika Tverdogo Tela, Vol. 44, No. 4, 2002, pp. 731–733.

MAGNETISM AND FERROELECTRICITY

Magnetic Structure of the $NiCr_2O_4$ Nickel Chromite

A. N. Goryaga, L. G. Antoshina, A. I. Kokorev, and D. A. Chursin

Moscow State University, Vorob'evy gory, Moscow, 119899 Russia

Received April 16, 2001; in final form, July 25, 2001

Abstract—The magnetic properties of the $NiCr_2O_4$ chromite are investigated and compared with similar properties of the $NiFe_{1.1}Cr_{0.9}O_4$ nickel ferrite–chromite material. It is found for the first time that the tetrahedral (*A*) sublattice of the $NiCr_2O_4$ chromite is responsible for the total magnetic moment. Moreover, it is revealed that the $NiCr_2O_4$ chromite exhibits a giant magnetostriction of the paraprocess ($\lambda_{para} \sim 200 \times 10^{-6}$) and an anomalously large volume magnetostriction ($\omega \sim 500 \times 10^{-6}$) at a temperature of 4.2 K in magnetic fields up to ~50 kOe. The inference is made that the observed paraprocess is caused by an increase in the degree of noncollinearity of the magnetic moments induced in the octahedral (*B*) sublattice of the $NiCr_2O_4$ chromite in an external magnetic field. © *2002 MAIK "Nauka/Interperiodica".*

1. INTRODUCTION

Although the ferrimagnetic nickel chromite $NiCr_2O_4$ has long been a subject of investigation [1–4], the nature of the magnetic properties of this compound at low temperatures is still not clearly understood. In particular, it remains unclear which of the $NiCr_2O_4$ sublattices—the tetrahedral sublattice *A* or the octahedral sublattice *B*—is responsible for the experimental magnetic moment $n_{0\,\mathrm{exp}}$ at 0 K and why the experimental magnetic moment is substantially less than the theoretical value: $n_{0\,\mathrm{exp}} \ll n_{0\,\mathrm{theor}}$. McGuire and Greenwald [3] and Jacobs [4] assumed that, in the case when the magnetic moment arises from the octahedral sublattice *B*, the low value of $n_{0\,\mathrm{exp}}$ is determined by the spin noncollinearity observed in this sublattice due to a considerable negative *BB* exchange interaction between Cr_B^{3+} cations.

In the present work, we experimentally investigated the magnetic properties of the $NiCr_2O_4$ chromite and made an attempt to elucidate the nature of its magnetic structure.

Delorme [1] was the first to establish the fact that the crystal structure of the $NiCr_2O_4$ chromite at room temperature has a tetragonal distorted lattice with the unit-cell parameter ratio $c/a = 1.04$. It was assumed that the observed distortions of the spinel structure can be associated with the Jahn–Teller Ni^{2+} ions located at the tetrahedral sites. Hence, it can be expected that the $NiCr_2O_4$ chromite should possess a pronounced magnetic anisotropy due to the aforementioned distortions. Moreover, proper allowance must be made for the fact that the Curie temperature T_C of the $NiCr_2O_4$ chromite is close to the liquid-nitrogen temperature. In particular, Lotgering [2] showed that the Curie temperature T_C of $NiCr_2O_4$ is equal to 80 ± 5 K.

Making allowance for the above findings, we measured the magnetic properties of the $NiCr_2O_4$ nickel chromite at a temperature of 4.2 K in magnetic fields up to 50 kOe. It is obvious that precisely these measurements can provide reliable experimental data on the spontaneous magnetization σ_{s0} of the compound under investigation and, consequently, ensure correct determination of the magnetic moment $n_{0\mathrm{exp}}$.

2. SAMPLE PREPARATION AND EXPERIMENTAL TECHNIQUE

The $NiCr_2O_4$ sample was synthesized according to the ceramic technique. X-ray diffraction analysis demonstrated that, at $T = 293$ K, the sample synthesized has a tetragonal distorted lattice with the unit-cell parameter ratio $c/a = 1.025$.

Measurements of the magnetization σ and the coercive force H_c were performed on a vibrating-coil magnetometer at a temperature of 4.2 K. The longitudinal $\lambda_\parallel$ and transverse $\lambda_\perp$ magnetostrictions were measured by the tensometric method. In both cases, the permanent magnetic field was induced using a superconducting solenoid.

3. RESULTS AND DISCUSSION

Figure 1 depicts the experimental isotherms of the magnetization σ, longitudinal magnetostriction $\lambda_\parallel$, and transverse magnetostriction $\lambda_\perp$ of the $NiCr_2O_4$ chromite sample at a temperature of 4.2 K. It can be seen that the isotherm $\sigma(H)$ does not exhibit saturation in strong magnetic fields. In our opinion, this behavior of the magnetization cannot be explained by the insufficiently strong magnetic fields that are incapable of overcoming the magnetic anisotropy forces in nickel chromites, because the coercive force H_c of the $NiCr_2O_4$ chromite

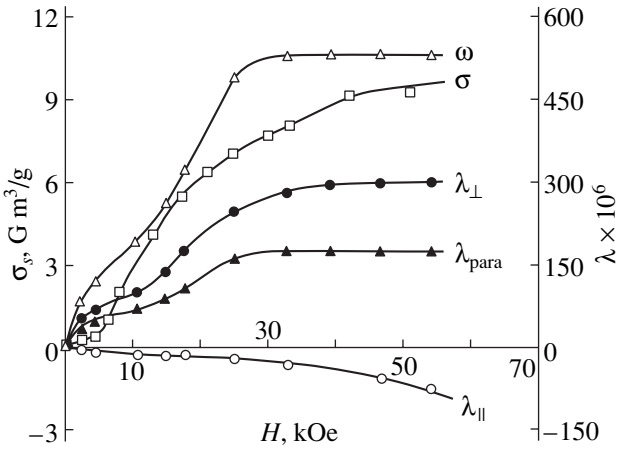

Fig. 1. Experimental isotherms of the magnetization σ, longitudinal magnetostriction $\lambda_{\parallel}$, and transverse magnetostriction $\lambda_{\perp}$ and calculated isotherms of the magnetostriction of the paraprocess λ_{para} and volume magnetostriction ω for the $NiCr_2O_4$ chromite at $T = 4.2$ K.

at 4.2 K is found to be equal to only 12.7 kOe. Therefore, we can state with assurance that the observed behavior of the magnetization is associated with a paraprocess, i.e., the true magnetization σ_i. Since this paraprocess cannot be described by a linear function, it is impossible to obtain an exact value of the spontaneous magnetization through linear extrapolation of the curve $\sigma(H)$ to zero magnetic field ($H = 0$).

In our case, the spontaneous magnetization σ_s was determined by the thermodynamic coefficient method [5]. According to this method, the behavior of the magnetization σ can be described by the equation

$$\alpha\sigma + \beta\sigma^3 = H, \qquad (1)$$

where $\sigma = \sigma_s + \sigma_i$ and α and β are the thermodynamic coefficients, which are dependent on the temperature and pressure. Equation (1) can be rewritten in the following form:

$$\alpha + \beta\sigma^2 = H/\sigma. \qquad (2)$$

In this method, the experimental results are represented as the curve $(H/\sigma(\sigma^2))$. Then, the spontaneous magnetization σ_s^2 is determined by extrapolating the curve $(H/\sigma(\sigma^2))$ to zero magnetic field ($H = 0$).

As a rule, the thermodynamic coefficient method is used in data processing of the magnetization measured in ferro- and ferrimagnetic materials in the vicinity of the Curie temperature. Moreover, this method is applied to the description of the magnetization of weak band ferromagnets in the low-temperature range (below the Curie point), because these materials possess a weak magnetization σ [6]. From the aforesaid, it follows that the thermodynamic coefficient method can be used in our case, because nickel chromites at 4.2 K are also characterized by a weak magnetization σ.

We plotted the curve $H/\sigma(\sigma^2)$ and found that the spontaneous magnetization σ_s of the nickel chromite sample at 4.2 K is approximately equal to 1.51 G cm^3/g. This value of σ_s, which we determined for 4.2 K, can be treated, to sufficient accuracy, as the spontaneous magnetization σ_{s0} at 0 K. By using the obtained value of σ_s, we determined the experimental magnetic moment: $n_{0exp} \approx 0.06\ \mu_B$. Such a low value of n_{0exp} indicates that the magnetic moments of the *A* and *B* sublattices of the $NiCr_2O_4$ chromite are close in magnitude.

The experimental magnetic moments n_{0exp} of the $NiCr_2O_4$ chromite, which were determined by McGuire and Greenwald [3], Jacobs [4], and the authors of the present work, are equal to 0.2, 0.35, and 0.06 μ_B, respectively. As can be seen, the $n_{0\,exp}$ value obtained in our work is substantially less than those determined in [3, 4]. This can be explained by the fact that, in [3, 4], the linear extrapolation of the curve $\sigma(H)$ to zero magnetic field was performed from comparatively stronger magnetic fields; consequently, these authors obtained the magnetization $\sigma = \sigma_s + \sigma_i$ (rather than σ_s); i.e., the magnetization of the paraprocess σ_i was added to the spontaneous magnetization σ_s.

The theoretical magnetic moment $n_{0\,theor}$ was calculated from the cation distribution in $Ni[Cr_2]O_4$ (by assuming there to be collinear spin ordering in both sublattices) and was found to be equal to 3 μ_B, provided the magnetic moments of cations involved in this compound, namely, Ni_A^{2+} ($3d^8$) and Cr^{3+} ($3d^3$), at $T = 0$ K are equal to $\mu_{Ni^{2+}} = 3\ \mu_B$ and $\mu_{Cr^{3+}} = 3\ \mu_B$, respectively. It should be noted that the magnetic moment of Ni_A^{2+} cations located at the tetrahedral sites is induced not only by the spin magnetic moment but also by an incompletely frozen orbital magnetic moment. In this case, the octahedral sublattice of the $NiCr_2O_4$ nickel chromite is responsible for the total magnetic moment.

Reasoning from the obtained data on the magnetization, we could not answer the question as to which of the sublattices of the $NiCr_2O_4$ nickel chromite is responsible for the experimental total magnetic moment. For this purpose, we measured the longitudinal $\lambda_{\parallel}$ and transverse $\lambda_{\perp}$ magnetostrictions of the $NiCr_2O_4$ nickel chromite and compared these characteristics with those of the $Fe[NiFe_{0.1}Cr_{0.9}]O_4$ nickel ferrite–chromite, in which, according to the data reported in [3, 4], the octahedral sublattice is responsible for the experimental total magnetic moment $n_{0\,exp}$.

The longitudinal $\lambda_{\parallel}$ and transverse $\lambda_{\perp}$ magnetostrictions of the $NiCr_2O_4$ chromite were also measured at 4.2 K in magnetic fields up to 55 kOe (Fig. 1). It was revealed that the dependences $\lambda_{\parallel}(H)$ and $\lambda_{\perp}(H)$ exhibit an anomalous behavior. As can be seen from Fig. 1, the

magnitude of the $\lambda_\perp$ magnetostriction is substantially larger than that of $\lambda_\parallel$ ($|\lambda_\perp| \gg |\lambda_\parallel|$); i.e., the Akulov rule is completely violated for the technical magnetostriction λ_{techn},

$$\lambda_{\parallel techn} = -2\lambda_{\perp techn}. \quad (3)$$

By using the experimental values of $\lambda_\parallel$ and $\lambda_\perp$, we calculated the magnetostriction of the paraprocess λ_{para} from the following formulas:

$$\lambda_\parallel = \lambda_{\parallel techn} + \lambda_{para}, \quad (4)$$

$$\lambda_\perp = \lambda_{\perp techn} + \lambda_{para}. \quad (5)$$

Then, we constructed the isotherm $\lambda_{para}(H)$ (Fig. 1). It is seen from Fig. 1 that the $NiCr_2O_4$ chromite exhibits a giant positive magnetostriction of the paraprocess ($\lambda_{para} \sim 200 \times 10^{-6}$ at $H = 54$ kOe). In our opinion, the fact that the magnitude $|\lambda_\parallel|$ is substantially less than the magnitude $|\lambda_\perp|$ can be explained by the high value of λ_{para}. Consequently, the $NiCr_2O_4$ chromite should also possess a considerable volume magnetostriction ω. According to the formula

$$\omega = \lambda_\parallel + 2\lambda_\perp, \quad (6)$$

we calculated the volume magnetostriction ω and constructed the isotherm $\omega(H)$ (Fig. 1). As would be expected, beginning with weak magnetic fields, this chromite is characterized by a sufficiently large positive volume magnetostriction ($\omega \sim 5 \times 10^{-4}$ in the magnetic field $H = 54$ kOe).

Therefore, if the assumption is made that the octahedral sublattice of the $NiCr_2O_4$ nickel chromite is responsible for the total magnetic moment, the applied external magnetic field should bring about a decrease in the spin noncollinearity in this sublattice. In turn, this should result in a negative magnetostriction of the paraprocess λ_{para} and a negative volume magnetostriction ω. Thus, if a similar behavior of the magnetostrictions λ_{para} and ω is observed in the $Fe[NiFe_{0.1}Cr_{0.9}]O_4$ nickel ferrite–chromite under the action of an external magnetic field, we can state with assurance that, in the $NiCr_2O_4$ nickel chromite, the octahedral sublattice is responsible for the total magnetic moment.

Since the $Fe[NiFe_{0.1}Cr_{0.9}]O_4$ ferrite–chromite has a high Curie temperature ($T_C \sim 570$ K) and a relatively weak magnetic anisotropy, it would suffice to investigate the behavior of the longitudinal $\lambda_\parallel$ and transverse $\lambda_\perp$ magnetostrictions of this compound at a temperature of 80 K in magnetic fields as high as 12 kOe.

The experimental values of $\lambda_\parallel$ and $\lambda_\perp$ (Fig. 2) were used to calculate the isotherms $\lambda_{para}(H)$ and $\omega(H)$. It can be seen that the results obtained for the $Fe[NiFe_{0.1}Cr_{0.9}]O_4$ ferrite–chromite are in contradiction with those for the $Ni[Cr_2]O_4$ chromite. For example, the $Fe[NiFe_{0.1}Cr_{0.9}]O_4$ ferrite–chromite in strong magnetic fields exhibits negative magnetostrictions λ_{para} and ω,

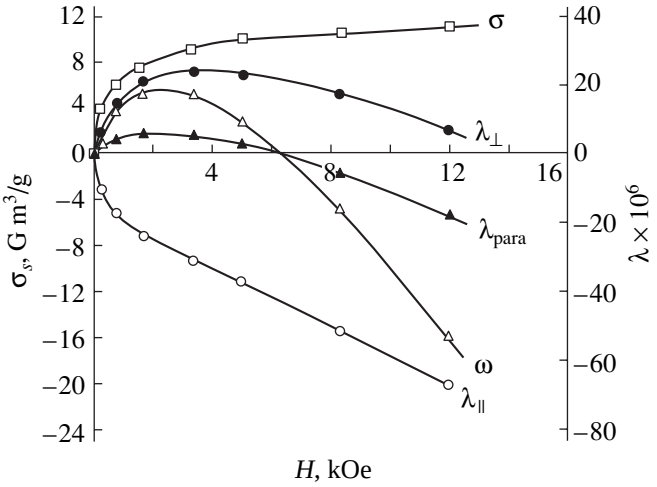

Fig. 2. Experimental isotherms of the magnetization σ, longitudinal magnetostriction $\lambda_\parallel$, and transverse magnetostriction $\lambda_\perp$ and calculated isotherms of the magnetostriction of the paraprocess λ_{para} and volume magnetostriction ω for the $NiFe_{1.1}Cr_{0.9}O_4$ ferrite–chromite sample at $T = 80$ K.

and their magnitudes are substantially less than those for the nickel chromite. A comparison of these results allows us to conclude that, in the $NiCr_2O_4$ chromite, the applied external magnetic field should bring about an increase in the spin noncollinearity in the octahedral sublattice. However, this situation can be observed only in the case when the tetrahedral sublattice of this chromite is responsible for the total magnetic moment.

Thus, we revealed that the magnetic moment M_A of the tetrahedral sublattice in the $NiCr_2O_4$ chromite is greater than the magnetic moment M_B of the octahedral sublattice.

Analysis of the exchange interactions demonstrated that, in the $NiCr_2O_4$ chromite, the formation of a noncollinear magnetic structure in the *B* sublattice is due to a negative direct *BB* exchange interaction Cr_B^{3+}–Cr_B^{3+} which counteracts the negative indirect *AB* exchange interaction Ni_A^{2+}–O^{2-}–Cr_B^{3+}. The observed well-pronounced paraprocess can be caused by the fact that the applied magnetic field, in addition to the negative *BB* exchange interaction, contributes to an increase in the degree of noncollinearity in the *B* sublattice. Since the magnetic moment of the tetrahedral sublattice in the $NiCr_2O_4$ chromite is greater in magnitude than that of the octahedral sublattice ($|M_A| > |M_B|$), the total magnetic moment M_s should increase.

In conclusion, we should note that, in the $NiCr_2O_4$ chromite, the completed orbits of the tetrahedral Ni_A^{2+} and octahedral Cr_B^{3+} cations are characterized by the

$e_g^4 t_{2g}^4$ and $t_{2g}^3 e_g^0$ electronic configurations, respectively. Therefore, the indirect intersublattice interaction $Ni_A^{2+} - O^{2-} - Cr_B^{3+}$ in the $NiCr_2O_4$ chromite can occur only through weak π bonds. Apparently, this can be one of the main reasons why the $NiCr_2O_4$ chromite has a relatively low Curie temperature.

REFERENCES

1. C. Delorme, C. R. Hebd. Seances Acad. Sci. **241**, 1588 (1955).
2. F. K. Lotgering, Philips Res. Rep. **11**, 218 (1956).
3. T. K. McGuire and S. W. Greenwald, in *Solid State Physics in Electronics and Telecommunication:* Part 1. *Magnetic and Optical Properties*, Ed. by M. Desirant and J. L. Michiels (Academic, New York, 1960), Vol. 3.
4. J. S. Jacobs, J. Phys. Chem. Solids **15**, 54 (1960).
5. K. P. Belov and A. N. Goryaga, Fiz. Met. Metalloved. **2** (1), 3 (1956).
6. E. P. Wohlfarth, Phys. Status Solidi A **25** (1), 285 (1974); J. Phys. C **2** (1), 68 (1969).

Translated by O. Borovik-Romanova

Physics of the Solid State, Vol. 44, No. 4, 2002, pp. 763–768. Translated from Fizika Tverdogo Tela, Vol. 44, No. 4, 2002, pp. 734–738.

MAGNETISM AND FERROELECTRICITY

Dynamics of Nonlinear Precession of Magnetization in a Garnet Ferrite Film of the (100) Type

A. M. Shutyĭ and D. I. Sementsov

Ul'yanovsk State University, ul. L'va Tolstogo 42, Ul'yanovsk, 432700 Russia

e-mail: shuty@mail.ru

Received April 24, 2001

Abstract—The dynamics of steady-state resonant magnetization precession setting in under a transverse magnetic bias field in a garnet ferrite film of the (100) type is investigated on the basis of numerical solution of the equation describing the motion of magnetization. The existence of a steady-state dynamic mode in which the magnetization performs undamped spiral motion, as well as of large-amplitude nutation with a period being a multiple of the period of precession, is discovered. *© 2002 MAIK "Nauka/Interperiodica".*

1. INTRODUCTION

The attainment of large-angle uniform resonant precession of magnetization in magnetically ordered crystals requires the fulfillment of conditions under which first- and second-order Suhl instabilities caused by three- and four-magnon interactions cannot occur. One of such conditions is that the precession frequency be chosen such that it coincides with the minimum possible spectral frequency $\omega(k)$ of spin waves, i.e., such that it corresponds to the bottom of the spin-wave band [1–5]. For a transversely magnetized thin layer, the fundamental (homogeneous) mode of the spin-wave spectrum corresponds to the bottom of the band and can be separated by a considerable frequency interval from the first (inhomogeneous) spin-wave mode [6, 7]. It is for this reason that no resonance saturation at the fundamental mode takes place upon an increase in the high-frequency (HF) field amplitude in films placed in a transverse bias field in the case of $\omega = \omega_{min}$ for $k = 0$ [8, 9] and the features of nonlinear dynamics of magnetization are manifested even for the uniform precession of magnetization.

The results of investigation of the features of nonlinear precession in a garnet ferrite film of the (111) type that are associated, in particular, with the nutation of magnetization and the frequency-doubling effect are presented in [10, 11]. It is shown that an increase in the HF field amplitude may lead to bifurcations in the magnetization precession, which lead to a sharp change in the precession amplitude and to bistable states. In resonance studies and in applications of garnet ferrites, films of the (100) type are widely used, since the easy magnetization axis of such films can be made perpendicular to the plane of the film without any difficulty and this orientation has the lowest sensitivity to various types of composition inhomogeneity, to stresses, and to temperature variations [12]. In this work, we present the results of numerical analysis of the equations of motion of magnetization, which reveal peculiarities in the nonlinear resonant precession that are inherent in this type of films and indicate a noticeable difference from precession in the (111)-type films.

2. GENERAL EQUATIONS AND RELATIONS

Epitaxial garnet ferrite films are monocrystalline layers with a cubic crystal lattice. We assume that the crystallographic axis [100] coincides with the x axis and is normal to the film surface, while the [010] and [001] axes coincide with the y and z axes, respectively; the polar and azimuthal angles (θ and ψ) of the magnetization vector **M** are reckoned from the x and y axes, respectively. In the case under investigation, the free-energy density is

$$F = -\mathbf{M}(\mathbf{H} + \mathbf{h}) + (K_u - 2\pi M^2)\sin^2\theta + \frac{1}{4}K_1(\sin^2 2\theta + \sin^4\theta\sin^2 2\psi), \quad (1)$$

where K_u and K_1 are the growth-induced and crystallographic anisotropy constants, respectively. The equilibrium angles θ_0 and ψ_0 are found from the conditions $\partial F/\partial\theta = 0$ and $\partial F/\partial\psi = 0$. The dynamic behavior of the magnetization in an external static (**H**) and high-frequency (**h**) magnetic fields, which will be henceforth assumed to be orthogonal ($\mathbf{H} \perp \mathbf{h}$), is described by the Landau–Lifshitz equation written in the spherical system of coordinates [2]:

$$\dot{\psi}M\sin\theta = \gamma\frac{\partial F}{\partial\theta} + \frac{\lambda}{M}\frac{1}{\sin\theta}\frac{\partial F}{\partial\psi},$$
$$\dot{\theta}M = \frac{\lambda}{M}\frac{\partial F}{\partial\theta} - \gamma\frac{1}{\sin\theta}\frac{\partial F}{\partial\psi}, \quad (2)$$

1063-7834/02/4404-0763$22.00 © 2002 MAIK "Nauka/Interperiodica"

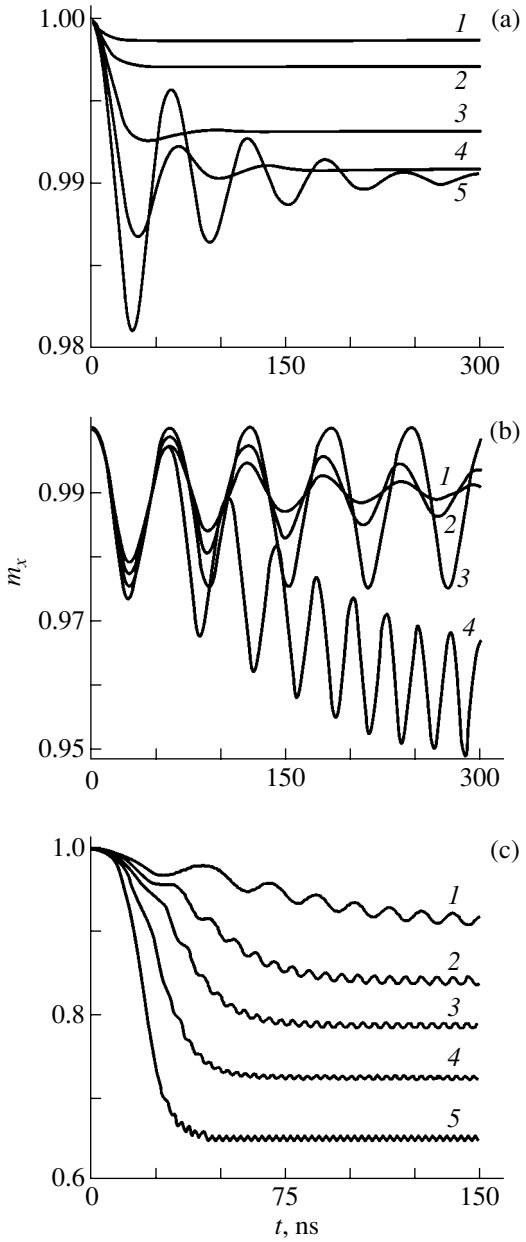

Fig. 1. Time dependence of the normal component of the magnetic moment ($m_x = M_x/M$) settling in a steady-state precession orbit upon the application of a HF field with amplitude $h = 0.5$ Oe and frequency $\omega_r/2\pi = 1$ GHz for different values of constant K_1 (erg/cm^3) and static field H (Oe): (a) $K_1 = 100$, $H = 678$ (curves *1*); $K_1 = 50$, $H = 684$ (*2*); $K_1 = 0$, $H = 690$ (*3*); $K_1 = -30$, $H = 693$ (*4*); $K_1 = -50$, $H = 695.5$ (*5*); (b) $K_1 = -55$, $H = 696$ (*1*); $K_1 = -60$, $H = 696.7$ (*2*); $K_1 = -65$, $H = 697$ (*3*); $K_1 = -70$, $H = 698$ (*4*); and (c) $K_1 = -80$, $H = 699$ (*1*); $K_1 = -100$, $H = 701$ (*2*); $K_1 = -120$, $H = 704$ (*3*); $K_1 = -150$, $H = 707$ (*4*); $K_1 = -200$, $H = 713$ (*5*).

where γ is the gyromagnetic ratio and λ is the damping parameter. Solving these equations allows us to find the time dependence of angles ψ and θ for given applied-field directions and time dependence of the external field. The resonant precession frequency ω_r is given by the relation

$$\omega_r = \gamma H_{\text{eff}} = \frac{\gamma}{M\sin\theta}(F_{\theta\theta}F_{\psi\psi} - F_{\theta\psi}^2)^{1/2}, \qquad (3)$$

where the second derivatives of the free-energy density are taken for the equilibrium angles θ_0 and ψ_0.

A detailed analysis of the magnetization precession, which is an essentially nonlinear effect, can be carried out only on the basis of a numerical solution to Eqs. (2) taking into account the basic parameters determining the state of the magnetized film. The subsequent analysis will be carried out for values of the static field **H** that ensure the equilibrium orientation of vector **M** along the normal to the film surface ($\theta_0 = 0$) for given values of constants K_u and K_1. In this case, the resonance frequency is found to be $\omega_r = \gamma H_{\text{eff}}(0)$, where the effective field is given by

$$H_{\text{eff}}(0) = H - 4\pi M + 2(K_u + K_1)/M. \qquad (4)$$

We assume that the HF field is linearly polarized and lies in the *yz* plane; i.e., $\mathbf{h} \perp \mathbf{H}$.

3. NUMERICAL ANALYSIS

It can be seen from Eqs. (2) that both the bias field and the anisotropy field considerably affect the magnetic-moment precession. The parameters of growth-induced anisotropy of a specific sample with a fixed crystallographic anisotropy can be changed by thermal annealing [12]. Our analysis revealed, however, that in the case under investigation, the precession amplitude of the magnetic moment, the characteristics of its nutation, and the character of the steady-state dynamic modes setting in are mainly determined by the magnitude of the crystallographic anisotropy field. This is due to the fact that the derivative of the free-energy density with respect to the azimuthal angle is independent of constant K_u (although the growth-induced and crystallographic anisotropy constants appear symmetrically in the effective field). For this reason, we assume that the growth-induced anisotropy constant is fixed. In our calculations, we will use the parameters of a garnet ferrite film $Y_{2.9}La_{0.1}Fe_{3.9}Ga_{1.1}O_{12}$ grown on a gadolinium gallium garnet substrate for which the angle of resonant precession was determined to be $\phi \simeq 20°$–$25°$ [13], namely, $4\pi M = 214.6$ G, $\gamma = 1.755 \times 10^7$ (Oe s)$^{-1}$, $\lambda = 3 \times 10^6$ s^{-1}, and $K_u = -10^3$ erg/cm^3.

Figure 1 shows the time dependences of the normal component $m_x = M_x/M$ of the magnetic moment passing into the steady-state precession orbits that correspond to the HF field with amplitude $h = 0.5$ Oe and frequency $\omega_r/2\pi = 1$ GHz for different values of the crystallographic anisotropy constant K_1. In order to satisfy the resonance conditions, the value of the static field H is determined from Eq. (4). The curves in the figure show that, for $K_1 = 100$, 50, and 0 erg/cm^3 and the corre-

sponding values of the field $H \approx 678$, 684, and 690 Oe (curves *1–3* in Fig. 1a), the FMR mode with a small precession amplitude $\langle\phi\rangle = \arccos\langle m_x\rangle$, which increases upon a decrease in parameter K_1, becomes steady quite rapidly ($\tau \gtrsim 50$ ns) in the film. A certain increase in the thickness of the dynamic curves indicates enhancement of nutation of the magnetic moment vector, which is mainly caused by the linear polarization of the HF field in the plane of precession and is absent in the case of circular polarization of the HF field [1, 2]. A further decrease in the anisotropy constant [$K_1 = -30$, -50 erg/cm^3 for $H \approx 693$, 695.5 Oe (curves *4*, *5* in Fig. 1a) and $K_1 = -55$, -60 erg/cm^3 for $H \approx 696$, 696.7 Oe (curves *1*, *2* in Fig. 1b)] leads to the emergence of damped oscillations of the precession angle ϕ at the initial stage after the application of the HF field, which is reflected in the figure in the oscillations of m_x. As a result, the time of the steady-state precession mode setting in increases considerably. This time interval increases upon a decrease in parameter K_1, and a special steady-state dynamic mode (curve *3* in Fig. 1b) is realized for a certain value of $K_c \approx -65$ erg/cm^3 (and, accordingly, for $H \approx 697$ Oe); in this mode, the magnetic moment moves in a spiral trajectory from a position close to the film normal to a position with a certain maximum angle ϕ_m, then moves back, and so on. It should be noted that this dynamic mode is characterized by a practically zero transient period and starts immediately after the application of the HF field. For $K_1 = -70$ erg/cm^3 and $H \approx 698$ Oe (curve *4* in Fig. 1b), as well as for $K_1 = -80$, -100, -120, -150, -200 erg/cm^3 and $H = 699$, 701, 704, 707, 713 Oe, respectively (curves *1–5* in Fig. 1c), i.e., for decreasing $K_1 < K_c$ and the corresponding resonance fields, the averaged value of the precession angle $\langle\phi\rangle$ increases, while the spiral motion of vector **M** in the interval of angles ϕ depending on K_1 ($\phi_n \le \phi \le \phi_m$) is preserved. In this case, the oscillations of the precession angle should be regarded as large-amplitude nutation of the magnetization vector, whose period is a multiple of the period of the HF field and, hence, of the precession period; this distinguishes this nutation from those considered earlier. The amplitude of this nutation decreases upon a decrease in the value of K_1 and, accordingly, upon an increase in the static field H, while the nutation frequency increases (Fig. 1c).

Figure 2 shows the projections m_α ($\alpha = x, y, z$) on the *zy* plane (panels a, b) and *xz* (panel c) of the magnetic moment moving from its initial position ($\theta = 0$) under the action of the HF field $h = 0.5$ Oe for $\omega_r/2\pi = 1$ GHz and the anisotropy constant $K_1 = -100$ erg/cm^3 (panel a) and $K_1 = K_c$ (panels b, c). As before, the field H is chosen in accordance with Eq. (4). In the case depicted in Fig. 2a, the magnetic moment moves towards a stationary orbit in a spiral trajectory with a variable pitch, being held in the vicinity of several intermediate orbits.

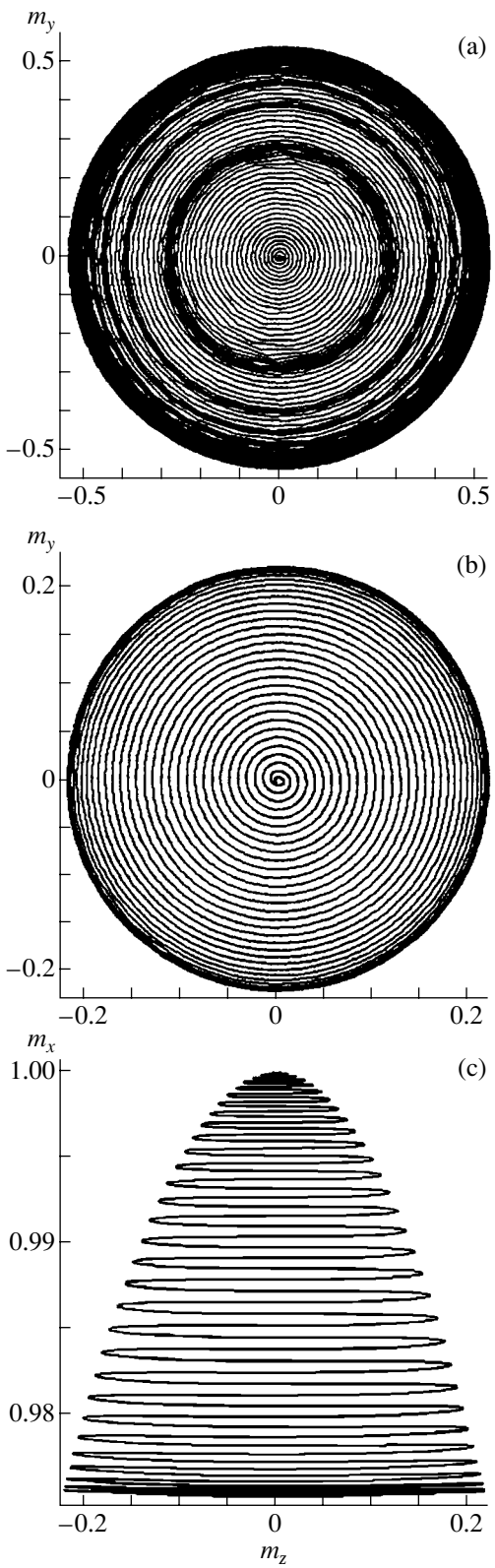

Fig. 2. Trajectories of vector **M** (a) settling in a steady-state orbit for $K_1 = -100$ erg/cm^3 and (b, c) occurring in a phase of increasing precession angle of the oscillatory mode for $K_1 = K_c \approx -65$ erg/cm^3; $h = 0.5$ Oe and $\omega_r/2\pi = 1$ GHz.

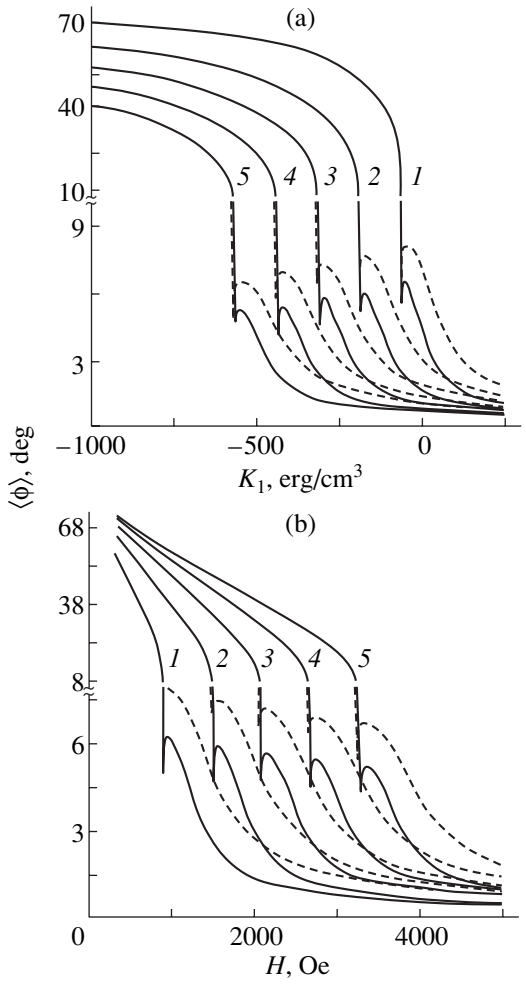

Fig. 3. Resonance precession angle $\langle\phi\rangle$ (a) as a function of anisotropy constant K_1 for different values of frequency ω_r (GHz) and resonance field H (Oe): $\omega_r/2\pi = 1$, $H = 730$ (curves *1*), $\omega_r/2\pi = 3$, $H = 1450$ (*2*), $\omega_r/2\pi = 5$, $H = 2160$ (*3*), $\omega_r/2\pi = 7$, $H = 2880$ (*4*), and $\omega_r/2\pi = 9$, $H = 3590$ (*5*); and (b) as a function of static field H for $K_1 = -100$ (*1*), –200 (*2*), –300 (*3*), –400 (*4*), and –500 erg/cm^3 (*5*); $h = 0.5$ (solid curves) and 1 Oe (dashed curves).

It should be noted that this does not take place in the case of a strong anisotropy field. In the case presented in Figs. 2b and 2c, the magnetic moment under the action of a linearly polarized HF field moves in a spiral from a position close to the film normal to an orbit corresponding to the maximum precession angle ϕ_m and then, rotating in the same direction, returns to the initial position (the former motion corresponds to monotonically descending segments of curve *3* in Fig. 1b; the latter, to monotonically ascending segments of this curve). A small change in angle $\langle\phi\rangle$ occurring in the precession orbit corresponding to the maximum amplitude (Fig. 2c) can be explained by the magnetic moment nutation due to anisotropy of the effective field and by the linear polarization of the HF field leading to the frequency doubling effect [1, 2].

Figure 3 shows the dependences of the resonant precession angle $\langle\phi\rangle$ on the crystallographic anisotropy constant K_1 (panel a) and on the static field H (panel b) for the HF field amplitude $h = 0.5$ Oe (solid curves) and 1 Oe (dashed curves). The $\langle\phi\rangle(K_1)$ dependences were obtained for frequencies $\omega_r/2\pi = 1$, 3, 5, 7, and 9 GHz and resonance field values $H \simeq 730$, 1450, 2160, 2880, and 3590 Oe (curves *1–5* in Fig. 3a). The $\langle\phi\rangle(H)$ curves were calculated for fixed values of the anisotropy constant $K_1 = -(100–500)$ erg/cm^3 (curves *1–5* in Fig. 3b); the resonant precession frequency was, in accordance with Eq. (3), in the interval $\omega_r/2\pi = 0–13$ GHz. The curves depicted in Fig. 3a show that, for positive and close-to-zero negative values of K_1, the amplitude of precession is small and depends to a considerable extent on the HF field amplitude. For large (in absolute value) negative K_1, the precession amplitude attains several tens of degrees and is virtually independent of the HF field **h**. In this region, the normal position of magnetization is unstable and vector **M** spontaneously passes to a stable limit cycle determined by the values of the static field and anisotropy field. The two regions indicated above are separated by an interval within which a weakly manifested maximum and minimum of the $\langle\phi\rangle(K_1)$ curve are observed. For the frequency-dependent value $K_1 = K_c$ close to the value corresponding to the minimum just mentioned, spiral motion of the magnetization vector with an angular amplitude $\phi_m \approx 2\langle\phi\rangle_{\min}$ takes place. As the frequency ω_r increases together with the bias field, the negative K_c increases in magnitude. For $K_1 > K_c$ (in the vicinity of K_c), the time of the steady mode setting in is long, since strongly damped oscillations of the precession angle ϕ take place at the initial stage. For $K_1 < K_c$, large-amplitude nutation of the magnetic moment with a period being a multiple of the precession period ω_r occurs along with a sharp increase in the angular amplitude $\langle\phi\rangle$; for this reason, the averaging of the angular amplitude in this case was carried out over a large time interval. The $\langle\phi\rangle$(H) dependence calculated for fixed values of K_1 (Fig. 3b) is similar in many respects to the $\langle\phi\rangle(K_1)$ dependence: it is also characterized by two regions with large and small precession angles, respectively, and for each value of constant K_1, there exists a field value H_c corresponding to the spiral mode of the magnetization vector precession, i.e., to the mode in which $0 \le \phi \le \phi_m$.

Figure 4 shows the dependence of the averaged angle of precession with frequency $\omega_r/2\pi = 1$ GHz on the HF field amplitude for different values of the crystallographic anisotropy constant: $K_1 = 100$, 0, –30, –60, –63.5, –65, –67, and –70 erg/cm^3 (curves *1–8*); the bias field H has its resonance value. It can be seen that for the frequency chosen and for $K_1 \gtrsim 0$, the $\langle\phi\rangle(h)$ dependence is close to linear and the precession amplitude tends to zero as the value of h vanishes. As a result of

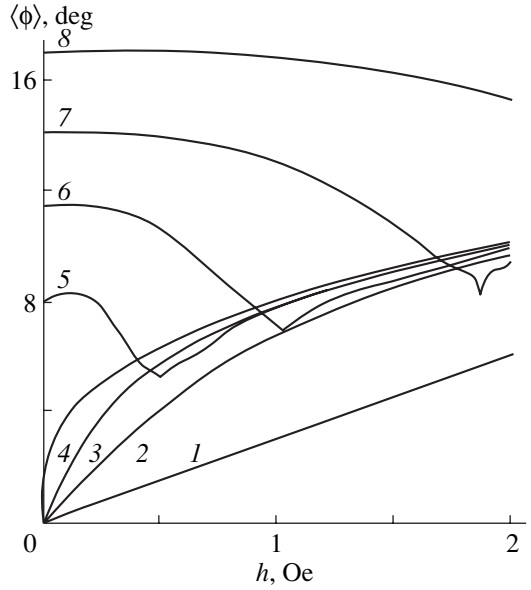

Fig. 4. Dependence of the average resonant precession angle on the HF field amplitude for different values of the anisotropy constant K_1 (erg/cm^3): 100 (*1*), 0 (*2*), –30 (*3*), –60 (*4*), –63.5 (*5*), –65 (*6*), –67 (*7*), and –70 (*8*); $\omega_r/2\pi$ = 1 GHz.

the sign reversal and the subsequent decrease in constant K_1, the dependence just mentioned becomes nonlinear and then nonmonotonic. The minimum in the $\langle\phi\rangle(h)$ dependence corresponds to a precession mode with spiral motion in the range $0 \le \phi \le \phi_m$ and shifts towards higher values of h upon a decrease in the anisotropy constant. It is also worth noting that for large (in absolute value) negative K_1, the precession amplitude becomes independent of h in the region of weak HF fields. As mentioned above, in this range of parameters, the position of the magnetic moment normal to the film surface is unstable and an attractor corresponding to precession about the film normal arises, with its radius being determined by the values of K_1 and H.

4. CONCLUSIONS

The above analysis leads to the following conclusions. Under the FMR conditions, magnetization precession modes differing considerably in amplitude and in the character of nutation are realized in garnet ferrite films of the (100) type depending on the relation between the bias field and the crystallographic anisotropy field. In particular, for large values of constant K_1 (for fixed values of the static field H), steady-state precession rapidly sets in with a small amplitude and an insignificant nutation whose frequency is a multiple of the precession frequency. As the value of constant K_1 decreases, the time of steady-state precession setting in increases due to the emergence of damped oscillations of the precession angle. When the oscillation decay time becomes infinitely long, a special steady-state dynamic mode is realized, which is characterized by a spiral motion of magnetization between the orbit with the maximum precession angle ϕ_m and a position close to the normal to the film surface ($\phi_n = 0$). Upon further decrease in the crystallographic anisotropy constant, the precession angle turns out to be confined to the interval $\phi_n \le \phi \le \phi_m$, where ϕ_n is nonzero. Thus, large-amplitude nutation arises, with its period being a multiple of the period of precession. In this case, there are no steady-state orbits of precession and the magnetization vector draws around the surface of a spherical layer during its motion. As the magnitude of the negative constant K_1 increases (for a fixed H), angle ϕ_n increases faster than ϕ_m does, which leads to a decrease in the amplitude and period of nutation, and attractors independent of the HF field are formed corresponding to precession about the normal to the film.

For the sake of comparison, we will briefly consider the results of analysis of the precession of the magnetic moment vector in garnet ferrite films of the (111) type [10, 11]. In films of this type, in the case of a weak bias field and the HF field amplitude exceeding the critical value, the magnetization is tilted towards one of three directions not coinciding with the normal around which precession sets in with an average amplitude $\phi \lesssim 3°$. An increase in the field H leads to a precession mode around the film normal with a maximum amplitude of $\phi \approx 30°$ and to a significant contribution to nutation of the third harmonic of the fundamental frequency ω_r. Modes with dynamic bistability (i.e., with two stable steady-state precession orbits with different amplitudes) and bifurcations leading to a sharp change in the precession amplitude and to modes with complex trajectories of the moving magnetization vector with a period of a multiple of the HF field period have also been observed.

In films of the (100) type, no bifurcation of the magnetization precession, leading to dynamic bistability or to sharp changes in the precession amplitude, takes place. In such films, a smooth transition between different modes of precession takes place upon a gradual variation in the anisotropy constant of the film or in the magnitude of the bias field. In contrast to the (111)-type films, nutation contains practically no harmonics of the fundamental frequency ω_r of precession and is characterized by a period which is a multiple of the period of the HF field.

REFERENCES

1. Ya. A. Monosov, *Nonlinear Ferromagnetic Resonance* (Nauka, Moscow, 1971).
2. A. G. Gurevich, *Magnetic Resonance in Ferrites and Antiferromagnets* (Nauka, Moscow, 1973).
3. Yu. V. Gulyaev, P. E. Zil'berman, S. A. Nikitov, and A. G. Temiryazev, Fiz. Tverd. Tela (Leningrad) **28** (9), 2774 (1986) [Sov. Phys. Solid State **28**, 1553 (1986)].

4. S. M. Rezende and F. M. de Aguiar, Proc. IEEE **78** (6), 893 (1990).
5. G. A. Melkov and A. Yu. Taranenko, Fiz. Tverd. Tela (Leningrad) **28** (2), 570 (1986) [Sov. Phys. Solid State **28**, 318 (1986)].
6. S. S. Mikhaĭlovskiĭ and N. M. Salanskiĭ, Izv. Akad. Nauk SSSR, Ser. Fiz. **36** (7), 1496 (1972).
7. V. V. Tikhonov and A. V. Tolmachev, Fiz. Tverd. Tela (St. Petersburg) **36** (1), 185 (1994) [Phys. Solid State **36**, 101 (1994)].
8. P. E. Zil'berman, A. G. Temiryazev, and M. P. Tikhomirova, Zh. Éksp. Teor. Fiz. **108** (1), 281 (1995) [JETP **81**, 151 (1995)].
9. A. G. Temiryazev, M. P. Tikhomirova, and A. V. Maryakhin, in *Proceedings of the XVI Conference on Novel Magnetic Materials for Microelectronics, NMMM-XVI, Moscow, 1998*, Vol. 1, p. 270.
10. A. M. Shutyĭ and D. I. Sementsov, Fiz. Tverd. Tela (St. Petersburg) **42** (7), 1268 (2000) [Phys. Solid State **42**, 1306 (2000)].
11. A. M. Shutyĭ and D. I. Sementsov, Zh. Éksp. Teor. Fiz. **118** (3), 110 (2000) [JETP **91**, 531 (2000)].
12. A. M. Balbashov and A. Ya. Chervonenkis, *Magnetic Materials for Microelectronics* (Énergiya, Moscow, 1979).
13. B. Neite and H. Doetsch, Proc. SPIE **1018**, 115 (1989).

Translated by N. Wadhwa

Physics of the Solid State, Vol. 44, No. 4, 2002, pp. 769–773. Translated from Fizika Tverdogo Tela, Vol. 44, No. 4, 2002, pp. 739–744.

MAGNETISM AND FERROELECTRICITY

Self-Polarization and Migratory Polarization in Thin Lead Zirconate–Titanate Films

I. P. Pronin*, E. Yu. Kaptelov*, E. A. Tarakanov*, T. A. Shaplygina*, V. P. Afanas'ev, and A. V. Pankrashkin****

** Ioffe Physicotechnical Institute, Russian Academy of Sciences, ul. Politekhnicheskaya 26, St. Petersburg, 194021 Russia*
e-mail: pronin@inprof.ioffe.ru

*** St. Petersburg State Electrical Engineering University, St. Petersburg, 197376 Russia*

Received July 5, 2001

Abstract—This paper reports on a study of the electrical properties of 0.7–1-μm-thick textured PZT ferroelectric films prepared by rf magnetron sputtering of a $PbZr_{0.54}Ti_{0.46}O_3$ target which additionally contained 10 mol % lead oxide. Such films are shown to feature a combination of a self-polarized state and migratory polarization. The totality of the data obtained suggest that the films had *n*-type conduction. As shown by the laser beam modulation technique, the polarization was distributed nonuniformly in depth, with most of the poled state localized near the lower interface of the thin-film ferroelectric capacitor. The mechanism underlying the onset of this self-polarization is related to the charging of the lower interface of the structure by electrons, which occurs during the cooling following the high-temperature treatment of the PZT film, and to poling of the bulk of the film by the charged interface. This mechanism of the self-polarization of ferroelectric films is believed to have a universal character. *© 2002 MAIK "Nauka/Interperiodica".*

1. INTRODUCTION

Polarized ferroelectric films of lead-containing oxides, in particular, of the lead zirconate–titanate $PbZr_{1-x}Ti_xO_3$ (PZT), enjoy broad application in the development of active elements for use in micromechanical devices and piezo- and pyroelectric sensors used for a variety of purposes [1–4]. The efficiency of thin ferroelectric films in such devices is determined by a number of factors, in particular, by the film polarization and the conditions of formation of the ferroelectric phase. In particular, one can prepare films which become polarized (self-polarized) directly after their preparation without application of an external polarizing electric field [5–8]. This excludes the labor-consuming operation of their poling.

It is known that the pyroelectric coefficients of such self-polarized films may reach levels characteristic of films poled by the application of an external field. Such a situation is observed with tetragonal PZT films ($x > 0.5$) [9–12]. At the same time, self-polarization in rhombohedral films of these solid solutions is inhibited [3, 10–12]. The part played by either an excess of lead (above its stoichiometric content in the film) or by its deficiency in the onset of the polarized state is stressed to be significant [13, 14]. Macroscopic polarization in a ferroelectric layer may reverse direction with changing lead content [13].

The mechanism by which the self-polarized state sets in in thin films remains unclear. In [10], for instance, the self-polarized state is assumed to be intimately connected with the built-in electric field. A built-in field capable of poling a ferroelectric film may originate from electron capture by interface traps, from dipole defects present, or again from an asymmetric distribution of weakly mobile (bound) charged defects [15–17]. A Schottky barrier, which forms at the lower interface of a thin-film ferroelectric capacitor, is also considered a possible physical reason for the generation of a polarizing field [12]. On the other hand, a strong built-in field was observed to exist in a PZT film after reactive ion etching of the upper platinum electrode in an SF_6 and O_2 environment [18].

This work was aimed at revealing the mechanisms underlying the onset of the self-polarized state through a study of the electric properties of thin PZT films containing a lead excess.

2. TECHNOLOGY OF PREPARATION OF PZT FILMS AND METHODS OF THEIR CHARACTERIZATION

Thin films were prepared by rf magnetron sputtering of a $PbZr_{0.54}Ti_{0.46}O_3$ target additionally containing 10 mol % lead oxide [19]. The films were deposited on "cold" substrates maintained at a temperature of about 130°C. The substrates were glass-ceramic and single-crystal silicon plates with a lower thin-film platinum electrode deposited on a titanium buffer, which served to improve adhesion. The films were 0.7–1-μm thick. Amorphous PZT films were crystallized into the perovskite phase at temperatures from 520 to 550°C in air.

1063-7834/02/4404-0769$22.00

The upper electrode, whose diameter varied from 130 to 300 μm, was also a platinum film.

The film crystal structure was studied by x-ray diffraction using a DRON-2 diffractometer. The depth profile of the elemental composition was measured by Auger spectroscopy (ÉKO-3 spectometer). Dielectric hysteresis loops were obtained in a modified Sawyer–Tower circuit. The depolarization currents in the samples were measured with a V7-30 electrometer. The depth profiles of the polarization in the films were studied by measuring the frequency-dependent pyroelectric current by means of laser beam modulation (LIMM) [20–23].

3. CRYSTAL STRUCTURE AND ELEMENTAL COMPOSITION OF PZT FILMS

X-ray diffraction analysis showed the films under study to have polycrystalline perovskite structure, with the crystallites oriented predominantly in the [111] direction (Fig. 1). The films were found to have phase homogeneity within the sensitivity of this method. However, microstructural analysis [23] detected inclusions of a phase with an excess lead concentration at the upper and lower film interfaces, as well as at the boundaries of grains, which were 20–50 nm in size. Excess lead content was also observed to exist in the elemental depth profiles, which were obtained using layer-by-layer Auger electron spectroscopy of the ion-milled ferroelectric film (Fig. 2). The lead content is seen clearly to be enhanced at both the upper and lower PZT film interfaces. In view of the results reported in [13, 14, 24–26], an analysis of these data suggests that the excess lead makes up a separate lead oxide phase (PbO).

4. STUDY OF THE HYSTERESIS LOOPS AND DEPOLARIZATION CURRENTS

Figure 3a presents a typical asymmetric hysteresis loop of PZT films containing an excess of lead oxide, which was obtained by applying a small ac voltage to the film after the perovskite phase had formed in the course of heat treatment. The loop shift along the horizontal axis suggests the existence of a fairly high built-in electric field of 30–40 kV/cm in the film. On successively applying a positive (Fig. 3b) and a negative (Fig. 3c) dc voltage of 15 V relative to the lower electrode, the shape of the hysteresis loops changes and becomes dependent on the voltage polarity. Obviously enough, the asymmetry of the loops relative to the vertical axis is a consequence of the existence of an internal field, which is seen clearly to coincide in direction with the electric field produced by applying a positive potential to the upper platinum electrode of the ferroelectric thin-film capacitor.

Note that the shape of all hysteresis loops (Fig. 3) is asymmetric and resembles that of a hard-poled piezoceramic, whose distortion is related to the migratory polarization "$-P_2$" [27, 28]. It is well known that the migratory polarization "$-P_2$" originates from the depolarization field appearing in a prepoled sample and is associated with charge motion within the grains. The migratory polarization "$-P_2$" is directed counter to the polarization P_r induced by an external electric field and can be very stable even under the application of a strong ac field capable of reorienting the P_r [27].

Application of a similar approach to PZT films permits one to conclude that the displacement field derived from the hysteresis loops is nothing other than migratory polarization, which cancels the polarization (Figs. 3b, 3c) or self-polarization (Fig. 3a) of the thin film. This is in accord with the above assumption that the displacement of a hysteresis loop associated with

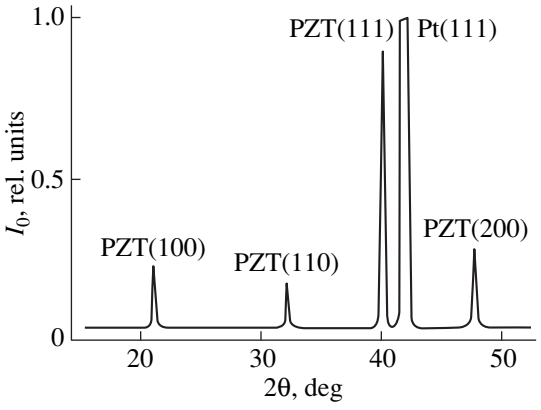

Fig. 1. X-ray diffraction pattern of a 1-μm-thick polycrystalline PZT film prepared on a glass-ceramic substrate with a platinum electrode and an adhesion-improving titanium buffer and annealed in air at 520°C for 10 min.

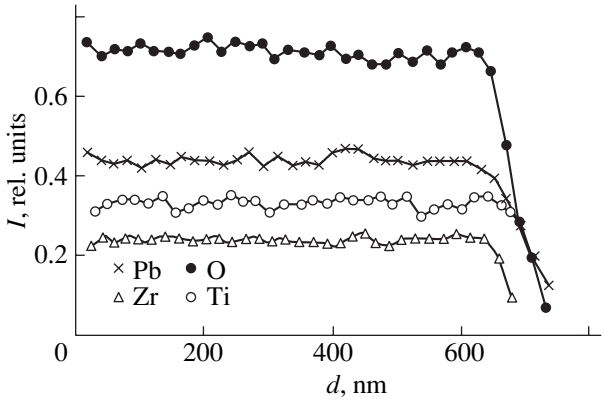

Fig. 2. Elemental depth profiles of a PZT film prepared by sputtering a lead-enriched target of $PbZr_{0.54}Ti_{0.46}O_3$ + 10 mol % PbO and heat-treated in air at 550°C.

the presence of an internal built-in field actually reflects the existence of a self-polarized state in such films [9–11, 14, 19]. The only difference is that using the migratory polarization to describe the polarized state of a thin ferroelectric film facilitates understanding of the fact that, in the "static state," there is no real internal field in a film. One may thus believe that self-polarization is intimately connected with migratory polarization. The results reported below identify their origin more clearly.

Measurements of the depolarization currents (curve *1* in Fig. 4) made on polarized samples showed that if the latter are heated rapidly (curve *2*) to a temperature close to the Curie point, the current plot exhibits two portions corresponding to different current directions. The low-temperature part of the curve reflects depolarization of the spontaneously polarized state, and the high-temperature (slowly falling-off) portion is due to the relaxation of the migratory polarization. Similar relations were observed in bulk piezoceramic samples, which could be characterized by a combination of the residual polarization P_r with the migratory polarization "$-P_2$" [27].

Because the migratory polarization in a ferroelectric is associated with charge motion, determination of the type of carriers present in the films under study is important. The majority carriers in PZT are known to be either electrons (*n* type), which are due to oxygen vacancies, or holes (*p* type), whose presence is usually related to lead vacancies. Lead vacancies form, as a rule, in films deposited on a substrate at a high temperature or crystallized at a high temperature, i.e., in the conditions where the lead deficiency is caused by the high volatility of the lead oxide. It may be conjectured that the hysteresis loops are shifted in this case along the horizontal axis toward positive voltages [3, 4]. By contrast, the negative loop displacement is usually assigned to a perovskite film being rendered *n* type when deposited in a medium with a low oxygen partial pressure [5, 6].

In our case, when a target with a lead excess is sputtered on a cold substrate and the perovskite phase is subsequently produced, oxygen vacancies form in the film. This may result from the lead becoming oxidized to the α-PbO phase, which has an oxygen excess [29] because of the oxygen being absorbed from the PZT perovskite phase [30]. An additional argument for the presence of oxygen vacancies may be the value of the activation energy, which is derived from the temperature dependence of conductivity *G* measured at 1 MHz (Fig. 5). The activation energy *W*, calculated from the relation $G = \text{const}\exp(-W/kT)$ and determined from the slope of a plot of the logarithm of the conductivity vs. inverse temperature obtained above 260°C, was found to be 0.22 eV (Fig. 5). This figure corresponds to the depth of the levels formed by oxygen vacancies and lying within the range 0.19–0.48 eV in the band gap of the PZT perovskite structure [31].

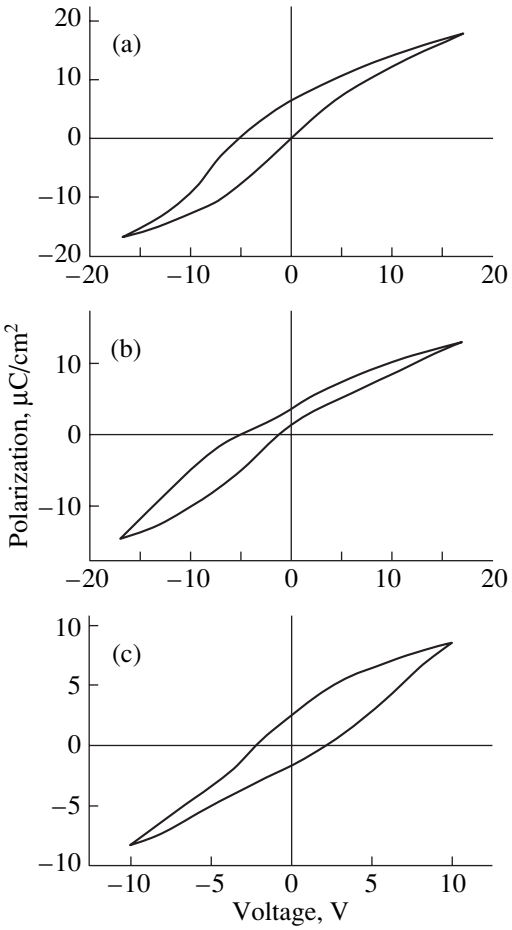

Fig. 3. Dielectric hysteresis loops of a 1-μm-thick PZT film obtained (a) directly after preparation, (b) following polarization with a +15 V voltage, and (c) after polarization by −15 V at room temperature for 10 min.

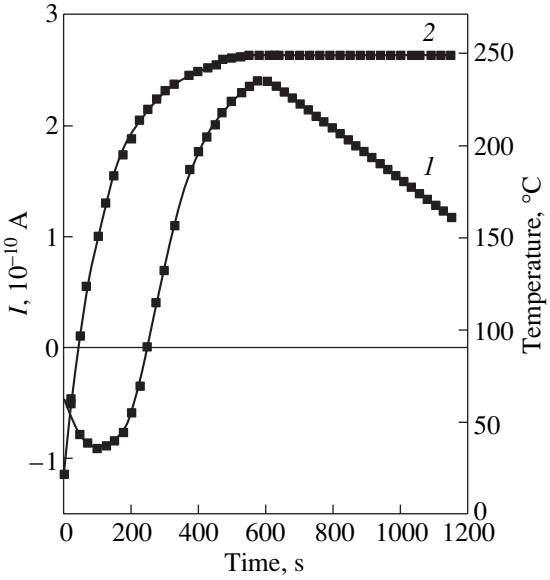

Fig. 4. Depolarization current vs. time plot (curve *1*) under fast heating to 250°C (described by curve *2*) of a film polarized by +15 V at room temperature for 10 min.

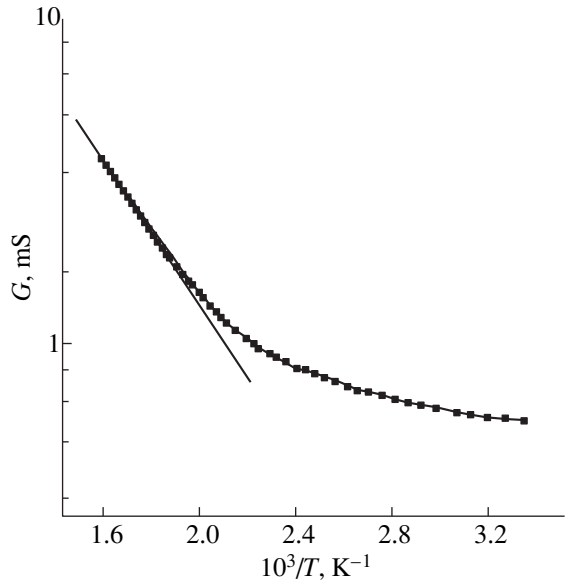

Fig. 5. Temperature dependence of the film conductivity G obtained at a frequency of 1 MHz.

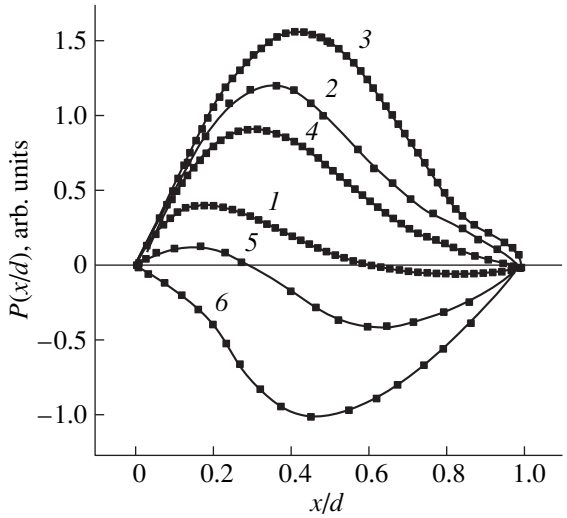

Fig. 6. Depth profile of the polarization obtained by LIMM. (*1*) Self-polarized state; (*2*, *3*) positive voltage (+8 and +15 V, respectively) applied to the film; (*5*, *6*) same for negative voltage of –8 and –15 V, respectively; and (*4*) film polarized with +15 V and then aged for 24 h.

5. MEASUREMENT OF THE FREQUENCY-DEPENDENT PYROELECTRIC CURRENT

The technique employed to measure and process the frequency-dependent pyroelectric response under IR laser irradiation of a sample is described in considerable detail in [22]. The signals were computer-processed under the assumption of the polarization vanishing both at the lower and upper interfaces of the structure. A rising positive voltage of up to +15 V and a negative voltage varying down to –15 V were successively applied to the plates of a thin-film ferroelectric capacitor. The sample was maintained at each voltage at room temperature for 0.5 h. The measurements were performed 1 h after the removal of the polarizing voltage. The calculated depth profile of the polarization is plotted (in arbitrary units) in Fig. 6.

Curve *1* in Fig. 6 is the depth profile of the self-poled state in the film. Judging from the pattern of the curve, throughout about half of the film volume, the self-polarization is produced by the negative charge at the lower interface of the structure. The dominant role of the lower interface is in accord with the assumptions made in [12], where this phenomenon was studied by measuring the piezoelectrically induced strain in thin PZT films. As one approaches the upper interface of the structure, the curve passes through zero and a weakly polarized state of the opposite sign sets in the upper part of the film.

As is evident from Fig. 6, the degree of sample polarization is not high, 10–15% of the polarization induced by applying a 15-V dc voltage across the capacitor plates (see curves *1*, *3*). As follows from a comparison of curves *3* and *4*, the film undergoes a fast relaxation of the polar state; indeed, the residual polarization decreased to 50–60% of the initial level in about 10^5 s. Such a pronounced aging effect is characteristic of piezoelectric materials with a high concentration of mobile charges, whose migration brings about partial screening of the poled state.

It is worth noting that the $P(x/d)$ curves that were obtained on a sample poled by applying +15 and –15 V (curves *3*, *6*) are asymmetric relative to the horizontal axis. This asymmetry indicates that the field of –15 V is not capable of switching the polarization in an appreciable part of the film volume adjoining the lower electrode. This implies, in turn, that the local field generated by the charges at the lower interface of the structure can be quite high (in this case, not lower than 150 kV/cm).

6. DISCUSSION OF RESULTS

Thus, our studies suggest that the introduction of a substantial excess of lead oxide into a PZT film gives rise to (1) oxygen vacancy formation and, as a consequence, to *n*-type conduction in the film; (2) negative charging of the lower interface of a ferroelectric thin-film capacitor and the formation of migratory polarization; (3) the onset of a self-poled state near the lower film interface; and (4) the formation of a poled state near the upper interface of the structure, which is weak compared to that near the lower interface and is directed counter to it.

The results obtained in this work permit one to suggest the following scenario of the onset of self-polarization in such PZT films. When a PZT film crystallized into the perovskite structure at 520–550°C is being cooled, electrons of the oxygen vacancies present in the film begin to occupy the near-surface (localized) states

of the lower interface. Below the Curie temperature, the field generated by these electrons polarizes the region of the film close to the lower interface. To be capable of polarizing a PZT film, this field may be quite weak, because the coercive fields are comparatively weak in the vicinity of the Curie point. The high concentration of localized states at the lower interface may be traced to a number of reasons, the most significant of them, in our opinion, being crystal structure distortions, the presence of defects and foreign inclusions (for instance, of the PbO phase), chemical interaction, interdiffusion, etc. Note that the charging of the lower interface in a thin-film capacitor implies the formation of migratory polarization in the ferroelectric film, because, in this case, the interface plays the part of a grain boundary.

Cooling the sample to room temperature increases the spontaneous polarization in accordance with its temperature dependence. This enhances the depolarization field, which, in turn, brings about an increase in the migratory polarization "$-P_2$."

We note that dielectric hysteresis loops permit one to determine the magnitude of the bias field induced by the migratory polarization. However, in an inhomogeneously polarized film (the case we have here), the bias field is an averaged quantity.

It may be conjectured that the mechanism of charging of the lower interface by carriers (electrons, as in our case, or holes if the main structural defects are vacancies of lead or of other ions occupying octahedral sites in a cubic crystal) and the onset of self-polarization are of a universal character for thin-film perovskite ferroelectrics.

The formation of a polarized state near the upper interface, which is weak compared to that near the lower interface, does not lend itself to unambiguous interpretation. It is conceivable that part of the electrons reach the upper interface of the structure to become captured there by traps produced by lead oxide inclusions. Checking this conjecture would require, however, additional investigations.

ACKNOWLEDGMENTS

This study was supported by the Ministry of Education of the Russian Federation, project no. E00-3.4-350.

REFERENCES

1. D. L. Polla, Microelectron. Eng. **29**, 51 (1995).
2. R. W. Whatmore, Ferroelectrics **225**, 179 (1999).
3. G. Gerlach, G. Suchaneck, R. Kohler, and T. Sandner, Ferroelectrics **230**, 109 (1999).
4. D. F. Jenkins, W. W. Clegg, G. Velu, *et al.*, Ferroelectrics **224**, 259 (1999).
5. N. F. Foster, J. Appl. Phys. **40**, 420 (1969).
6. A. V. Gorish, V. P. Dudkevich, M. F. Kupriyanov, A. E. Panich, and A. V. Turik, *Piezoelectric Instrument-Making*, Vol. 1: *Physics of Ferroelectric Ceramics* (Izd. Zhurnala "Radiotekhnika", Moscow, 1999).
7. M. Adachi, T. Matsuzaki, N. Yamada, *et al.*, Jpn. J. Appl. Phys. **26**, 550 (1987).
8. R. Kohler, N. Neumann, N. Heβ, *et al.*, Ferroelectrics **201**, 83 (1997).
9. G. Suchaneck, R. Kohler, P. Padmini, *et al.*, Surf. Coat. Technol. **116**, 1238 (1999).
10. M. Schreiter, R. Bruchhaus, D. Pitzer, and W. Wersing, in *Proceedings of the Eleventh IEEE International Symposium on Applications of Ferroelectrics (ISAF XI'98), Montreux, Switzerland, 1998*, p. 181.
11. R. Bruchhaus, D. Pitzer, M. Schreiter, and W. Wersing, J. Electroceram. **3** (2), 151 (1999).
12. A. L. Kholkin, K. G. Brooks, D. V. Taylor, *et al.*, Integr. Ferroelectr. **22**, 525 (1998).
13. M. Kobune, H. Ishito, A. Mineshige, *et al.*, Jpn. J. Appl. Phys. **37**, 5154 (1998).
14. V. P. Afanasjev, A. A. Petrov, I. P. Pronin, *et al.*, J. Phys.: Condens. Matter **13** (39), 8755 (2001).
15. D. Dimos, W. L. Warren, M. B. Sinclair, *et al.*, J. Appl. Phys. **76** (7), 4305 (1994).
16. G. E. Pike, W. L. Warren, D. Dimos, *et al.*, Appl. Phys. Lett. **66** (4), 484 (1995).
17. W. L. Warren, B. A. Tuttle, D. Dimos, *et al.*, Jpn. J. Appl. Phys., Part 1 **35** (2B), 1521 (1996).
18. E. G. Lee, J. K. Lee, J.-Y. Kim, *et al.*, J. Mater. Sci. Lett. **18**, 2025 (1999).
19. V. P. Afanas'ev, S. V. Bogachev, N. V. Zaĭtseva, *et al.*, Zh. Tekh. Fiz. **66** (6), 160 (1996) [Tech. Phys. **41**, 607 (1996)].
20. S. B. Lang, Ferroelectrics **106**, 269 (1990).
21. S. B. Lang, Ferroelectrics **118**, 343 (1991).
22. G. Suchaneck, Th. Sandner, R. Kohler, *et al.*, in *Proceedings of the Eleventh IEEE International Symposium on Applications of Ferroelectrics (ISAF XI'98), Montreux, Switzerland, 1998*, p. 187.
23. V. P. Afanas'ev, G. N. Mosina, A. A. Petrov, *et al.*, Pis'ma Zh. Tekh. Fiz. **27** (11), 56 (2001) [Tech. Phys. Lett. **27**, 467 (2001)].
24. Zh. Song, W. Ren, L. Zhang, and Ch. Lin, Thin Solid Films **353**, 25 (1999).
25. K. Yamakawa, O. Arisumi, K. Okuwada, *et al.*, in *Proceedings of the Eleventh IEEE International Symposium on Applications of Ferroelectrics (ISAF XI'98), Montreux, Switzerland, 1998*, p. 159.
26. Zh.-J. Wang, R. Maeda, and K. Kikuchi, Jpn. J. Appl. Phys., Part 1 **38** (9B), 5342 (1999).
27. K. Okazaki, *Ceramic Engineering for Dielectrics* (Tokyo, 1969).
28. Yu Xu, *Ferroelectric Materials and Their Applications* (North-Holland, Amsterdam, 1991).
29. P. V. Kovtunenko, *Physical Chemistry of Solid State. Crystals with Defects* (Vysshaya Shkola, Moscow, 1993).
30. O. F. Lutskaya and E. A. Kognovitskaya, Neorg. Mater. **35** (3), 348 (1999).
31. T. Kala, Phase Transit. **36**, 65 (1991).

Translated by G. Skrebtsov

Physics of the Solid State, Vol. 44, No. 4, 2002, pp. 774–778. Translated from Fizika Tverdogo Tela, Vol. 44, No. 4, 2002, pp. 745–749.

MAGNETISM AND FERROELECTRICITY

Lead Titanate Ferroelectric Films on Single-Crystal Silicon

A. S. Sidorkin*, A. S. Sigov, A. M. Khoviv*, O. B. Yatsenko*, and V. A. Logacheva***

** Voronezh State University, Universitetskaya pl. 1, Voronezh, 394693 Russia*

*** Moscow State Institute of Radio Engineering, Electronics, and Automation, pr. Vernadskogo 78, Moscow, 117454 Russia*

e-mail: sidorkin@dom.vsu.ru

Received May 14, 2001; in final form, July 30, 2001

Abstract—This paper reports on the results of investigations into the phase transformations observed in Pb/Ti/Si and Ti/Pb/Si thin-film heterostructures upon layer-by-layer magnetron sputtering of lead and titanium onto a single-crystal silicon substrate and subsequent annealing in an oxygen atmosphere. It is shown that the dielectric properties of lead titanate films depend on the order of sputtering of lead and titanium metal layers onto the surface of single-crystal silicon. The ferroelectric properties are revealed in 3000-nm-thick lead titanate films prepared by two-stage annealing of the Pb/Ti/Si thin-film heterostructure (with the upper lead layer) at T_1 = 473 K and T_2 = 973 K for 10 min. These films are characterized by the coercive field E_c = 4.8 kV/cm and the spontaneous polarization P_s = 16.8 μC/cm^2. The lead titanate films produced by annealing of the Ti/Pb/Si thin-film heterostructure (with the upper titanium layer) do not possess ferroelectric properties but exhibit properties of a conventional dielectric. © *2002 MAIK "Nauka/Interperiodica".*

1. INTRODUCTION

A radically new approach currently being developed in functional electronics implies that elements produced in a single technological cycle with the use of multifunctional materials should exhibit an important fundamental property, namely, a nonlinear dependence of the characteristics on external action. Among these materials are thin films of lead titanate ($PbTiO_3$). Many properties of $PbTiO_3$ films (for example, the high remanent polarization, low coercive field, high permittivity, low dielectric loss, high breakdown voltage, and good acoustic characteristics) are widely used in power-independent memory elements, dynamic random-access memory devices, capacitors, waveguides, and different-type acoustooptic devices intended for modifying the spectral composition, amplitude, and direction of propagation of light signals [1–3].

The properties of lead titanate thin films are governed, to a large extent, by the film structure (grain size, degree of porosity, film–substrate interface condition, etc.), which, in turn, depends on the preparation conditions. This leads to a considerable difference between the parameters of the bulk and film samples and to a substantial scatter in the characteristics of the films produced using different techniques. For example, Byun *et al.* [4] prepared lead titanate films with a perovskite structure through metal–organic chemical vapor deposition (MOCVD) at T = 450°C and revealed that the dielectric properties of these films depend on the substrate type. It was found that the $PbTiO_3$ film grown on a silicon substrate possesses a low permittivity (ε = 78). By contrast, the $PbTiO_3$ film grown on a substrate prepared from silicon with a TiO_2 sublayer is characterized by a relatively high permittivity (ε = 120). According to Auger electron spectroscopy, the latter film has a stoichiometric composition, and the presence of the TiO_2 sublayer on the film–substrate boundary prevents interdiffusion of silicon and lead. For a $PbTiO_3$ film in the $Pt/PbTiO_3/Pt/SiO_2/Si$ heterostructure, the permittivity ε is equal to 150 and the capacitance–voltage characteristic does not take on a butterfly shape typical of ferroelectric films in metal/ferroelectric/metal structures [4].

The lead titanate films produced using the sol–gel technique with deposition onto $LaNiO_3$ conducting films [5] possess ferroelectric properties characterized by the remanent polarization P_r = 9.0 μC/cm^2 and the coercive field E_c = 40 kV/cm. For a $PbTiO_3$ bulk single-crystal sample, these parameters are as follows: P_r = 75 μC/cm^2 and E_c = 6.75 kV/cm. Yoon *et al.* [6] prepared $PbTiO_3$ films on an indium–tin oxide (ITO) conducting layer through metal–organic chemical vapor deposition. According to the current–voltage and capacitance–voltage measurements, these films in an $Au/PbTiO_3/ITO$ metal–dielectric–metal capacitor exhibit properties of conventional dielectrics. The authors explained the results of these electrical measurements in terms of the stoichiometric composition (according to Auger spectroscopy) and good surface morphology of the lead titanate film under investigation.

The lead titanate films prepared by annealing of the Ti/Pb/Si(100) heterostructure in our earlier work [7] did not exhibit pronounced ferroelectric properties, even though they consisted of titanate phases. In the present work, we demonstrated that the microstructure,

phase composition, and dielectric properties of the lead titanate films produced by oxidizing the aforementioned thin-film structures depend on the order of sputtering of metal layers onto the surface of single-crystal silicon.

2. EXPERIMENTAL TECHNIQUE

The thin-film metal composites were prepared by magnetron sputtering of titanium and lead metal layers from two different magnetrons in a single experimental cycle. The chamber was preliminarily evacuated to a pressure of 0.33×10^{-2} Pa. Argon was used as a sputtering gas. The sputtering rate of titanium at the operating pressure $P = 0.16$ Pa and the anode current $I = 0.7$ A was equal to 0.55 nm/s, and the sputtering rate of lead at $P = 0.27$ Pa and $I = 0.2$ A was as high as 2.5 nm/s. Separate sputtering of titanium and lead metals made it possible to obtain structures of the specified thickness with different sequences of metal layers deposited onto the silicon substrate. The ÉKÉF-500 Si(100) single crystals were used as substrates. The objects of investigation were Pb/Ti/Si and Ti/Pb/Si thin-film heterostructures with metal layers ~500 nm thick.

The lead–titanium (titanium–lead) thin-film structures were heat treated in a quartz reactor in a resistance furnace at $T_1 = 473$ K and $T_2 = 973$ K. The duration of each annealing stage was 10 min, and the oxygen flow rate was equal to 40 l/h. The phase composition of the studied films was determined by x-ray diffraction analysis on a DRON-3M diffractometer (CuK_α radiation) in the angle range 20°–65°. The surface morphology of lead titanate films and the film–substrate interface were examined using scanning electron microscopy (SEM). In order to measure the electrical properties of lead titanate films, the upper nickel electrode was applied by magnetron sputtering under vacuum through a mask with 1-mm holes and the lower contact with a silicon plate was provided by an indium–gallium eutectic alloy. The dielectric hysteresis loops were measured at a voltage of 0.5 V and a frequency of 50 Hz.

3. RESULTS AND DISCUSSION

3.1. Dependence of the phase composition and the structure of lead titanate films on the sequence of metal layers deposited onto the substrate. Figures 1a and 1b show the micrographs of cross-sectional cleavages of the initial (prior to annealing) Pb/Ti/Si and Ti/Pb/Si thin-film heterostructures prepared by magnetron sputtering onto the surface of single-crystal silicon. The lead titanate films with the lower titanium layer are characterized by a better adhesion to the silicon surface as compared to the films with the lower lead layer. The lead titanate films with the upper lead layer have a coarse-grained structure with a grain size of ~1000 nm. In the Ti/Pb/Si heterostructure, the grained surface of coarse-grained lead is smoothed by the upper titanium layer. The x-ray diffraction pattern of the initial Pb/Ti/Si heterostructure (Fig. 2a) contains only reflections of lead with the preferred orientation along the [111] direction. The absence of titanium reflections in this diffraction pattern suggests that titanium has a fine-dispersed x-ray amorphous (for x-ray powder diffraction analysis) structure. The x-ray diffraction pattern of the Ti/Pb/Si heterostructure (Fig. 2b) with the upper titanium layer exhibits additional reflections of lead along the [200] and [220] directions, which indicates a disturbance of the lead texture.

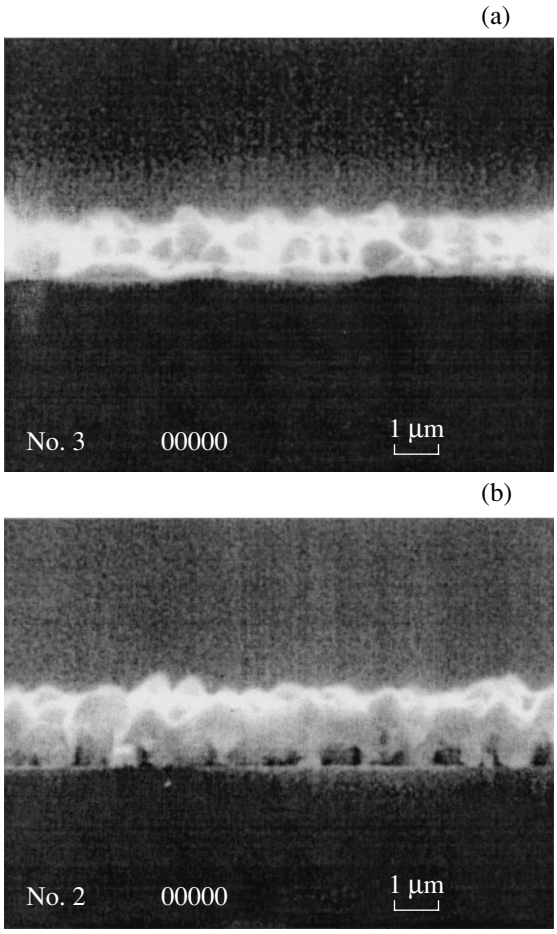

Fig. 1. Micrographs of cross-sectional cleavages of the (a) Pb/Ti/Si and (b) Ti/Pb/Si thin-film heterostructures after magnetron sputtering.

The initial structures were annealed under identical conditions: the initial annealing ($T_1 = 473$ K) resulted in the stabilization of the initial structures, and the final annealing ($T_2 = 973$ K) brought about the formation of oxide films with a complex composition. The x-ray diffraction pattern of the lead titanate film produced by annealing of the Pb/Ti/Si thin-film heterostructure is displayed in Fig. 3. The main set of (101), (110), (111), (002), and (102) reflections corresponds to the $PbTiO_3$ tetragonal phase. It should be noted that, after short-term annealing for 10 min ($T = 973$ K), the reflections

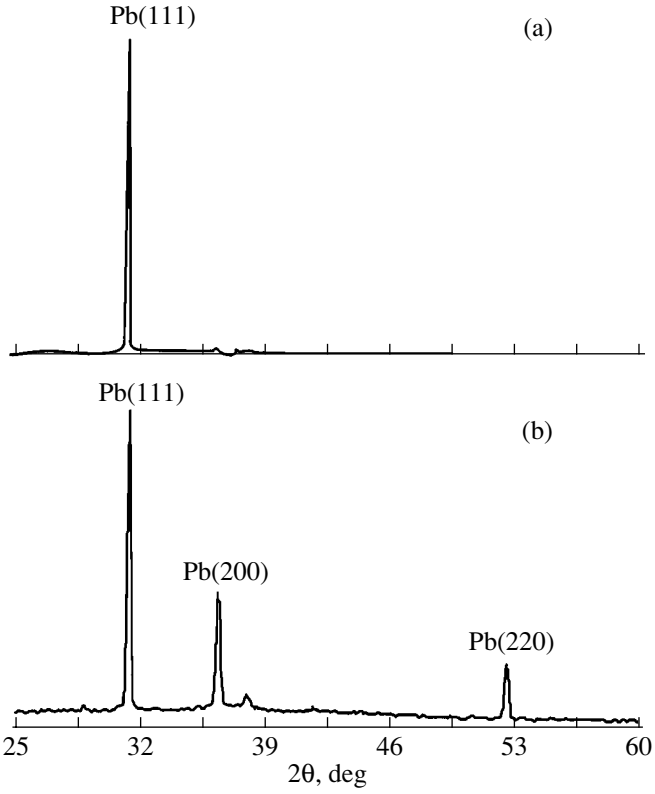

Fig. 2. X-ray diffraction patterns of the (a) Pb/Ti/Si and (b) Ti/Pb/Si thin-film heterostructures prior to annealing.

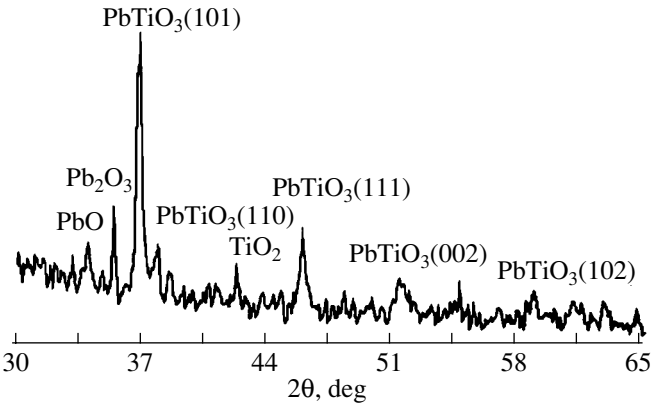

Fig. 3. X-ray diffraction pattern of the Pb/Ti/Si thin-film heterostructure after annealing in an oxygen atmosphere at T_1 = 473 K and T_2 = 973 K for 10 min.

attributed to the Pb_3O_4 and PbO lead oxides and one low-intensity (~10%) reflection assigned to the TiO_2 titanium oxide with a rutile structure remain in the x-ray diffraction pattern. Figure 4 shows the micrograph of the cross-sectional cleavage of the $PbTiO_3$ film obtained on a single-crystal silicon substrate after annealing of the Pb/Ti/Si thin-film heterostructure. According to the SEM data, the film thickness is equal to 3280 nm and the mean grain size is ~580 nm. Judging from the micrograph, the $PbTiO_3$ film has a polycrystalline (without craters and cracks) structure in which nearly rectangular grains are oriented in a random manner. It can be seen that the transition layer (~1000 nm thick) is formed on the film–substrate boundary due to interdiffusion of titanium and silicon. The absence of the reflections associated with titanium silicide phases suggests that the transition layer consists of a titanium–silicon solid solution.

The annealing of the Ti/Pb/Si structure under the same conditions brings about the formation of lead titanate films in which the main phase is the Pb_2O_3 oxide. The x-ray diffraction pattern of the Ti/Pb/Si thin-film heterostructure after annealing at T_2 = 973 K (Fig. 5) exhibits reflections attributed to lead titanate with a tetragonal structure [(100), (110), and (111)], the $PbTi_2O_7$ pyrochlore [(301)], and the TiO_2 rutile. The micrograph of the film cleavage is displayed in Fig. 6. As is seen, the structure and morphology of this film differ substantially from those of the lead titanate film prepared through the oxidation of the Pb/Ti/Si thin-film heterostructure. The structure of the former film involves two weakly bound layers. No indication of interdiffusion between lead and silicon is observed at the abrupt film–substrate interface. No grains of particular shape are formed in the film. Therefore, the annealing temperature T_2 = 973 K is not sufficiently high to provide the formation of the film containing lead titanate as the main phase.

Figure 7 displays the x-ray diffraction pattern of the Ti/Pb/Si thin-film heterostructure after additional annealing at T = 1173 K for 10 min. The main peak is observed in the range $2\theta = 36°–39°$ and corresponds to the Pb_2O_3 oxide. It can be seen that, as the annealing temperature increases, the main peak is split into the (101) and (110) reflections assigned to $PbTiO_3$, the other reflections of lead titanate become narrower, and their intensities increase. The last circumstance indicates that the degree of crystallinity of the studied film increases with a rise in the annealing temperature to 1173 K. Therefore, the formation of the lead titanate film during annealing of the Ti/Pb/Si thin-film heterostructure occurs at an annealing temperature 200 K above the temperature of formation of the lead titanate film during annealing of the Pb/Ti/Si heterostructure. It should be noted that the studied film contains TiO_2 in addition to lead titanate with a tetragonal structure.

Analysis of the phase composition and structure of the lead titanate films formed through the oxidation of Pb/Ti/Si and Ti/Pb/Si thin-film heterostructures revealed that the reactivity of the thin-film heterostructure during the interaction of lead and titanium metal layers (primarily, with oxygen and silicon and, then, with each other) is determined by the sequence of these layers. The reactivity of the Pb/Ti/Si structure is higher

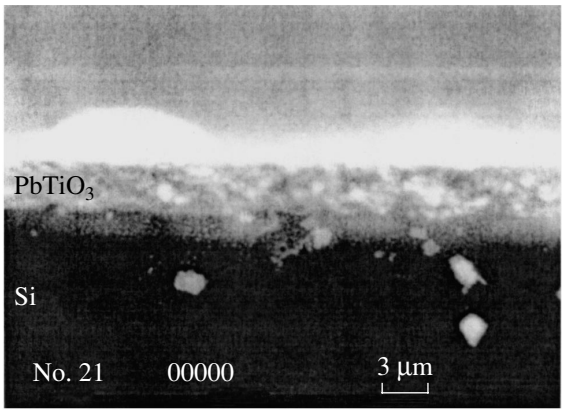

Fig. 4. Micrograph of the cross-sectional cleavage of the Pb/Ti/Si thin-film heterostructure after annealing in an oxygen atmosphere at T_1 = 473 K and T_2 = 973 K for 10 min.

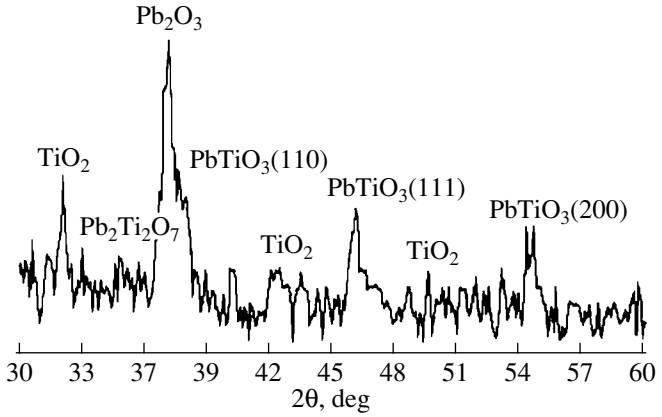

Fig. 5. X-ray diffraction pattern of the Ti/Pb/Si thin-film heterostructure after annealing in an oxygen atmosphere at T_1 = 473 K and T_2 = 973 K for 10 min.

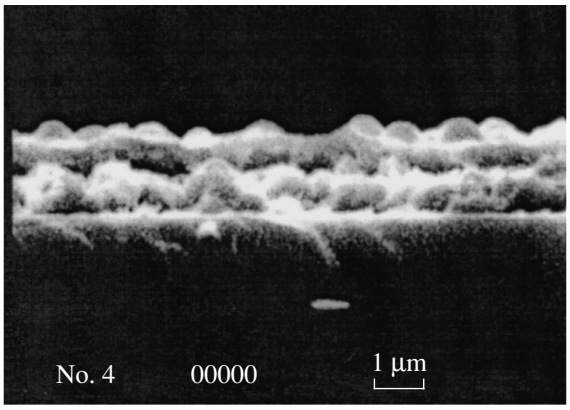

Fig. 6. Micrograph of the cross-sectional cleavage of the Ti/Pb/Si thin-film heterostructure after annealing in an oxygen atmosphere at T_1 = 473 K and T_2 = 973 K for 10 min.

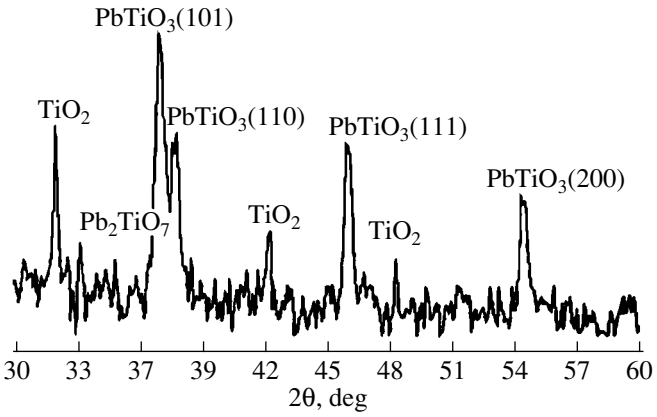

Fig. 7. X-ray diffraction pattern of the Ti/Pb/Si thin-film heterostructure after annealing in an oxygen atmosphere at T_1 = 473 K and T_2 = 973 K for 10 min and subsequent annealing at T_3 = 1173 K for 10 min.

than that of the Ti/Pb/Si structure. The interaction of the titanium layer with the silicon surface during heating is accompanied by the generation of stresses at the interface. The interface stresses arise both from the lattice mismatch and different symmetries of titanium and silicon crystals and from the difference between the thermal expansion coefficients of the contacting layers. The interface stresses activate the structures of interacting layers, favor the breaking of bonds, and facilitate the diffusion of silicon atoms into the titanium film. Upon the interaction of titanium with silicon, lattice strains also arise in crystal regions adjacent to the titanium–silicon interface and activate interactions throughout the heterogeneous thin-film structure [8].

In the case when single-crystal silicon is in contact with the lead layer (the system with the upper titanium layer in the thin-film heterostructure), lead itself does not interact with silicon and efficiently suppresses all types of interaction between titanium and silicon. Upon heating, ductile lead does not give rise to stresses similar to those generated by titanium in the system. Therefore, the system with the lead layer on single-crystal silicon in the thin-film heterostructure (the case of the upper titanium layer) should be heated to substantially higher temperatures in order to obtain the phases already formed in the thin-film heterostructure with the titanium layer on single-crystal silicon (the case with the upper lead layer).

3.2. Dielectric properties of lead titanate films. The dielectric hysteresis loops of the Pb/Ti/Si heterostructures subjected to annealing were measured with the use of a Sawyer–Tower hysteresis scheme. The hys-

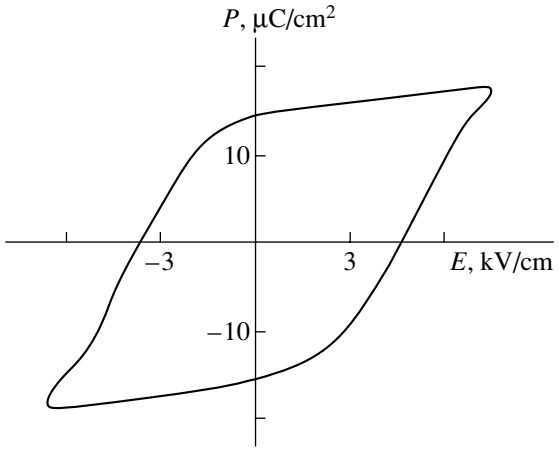

Fig. 8. Dielectric hysteresis loop of the Pb/Ti/Si thin-film heterostructure after annealing in an oxygen atmosphere at T_1 = 473 K and T_2 = 973 K for 10 min.

teresis loops obtained have the form characteristic of ferroelectrics (Fig. 8). Analysis of the hysteresis loops, specifically for 3280-nm-thick films, gave the coercive field E_c = 4.8 kV/cm and the spontaneous polarization P_s = 16.8 μC/cm^2. Note that the spontaneous polarization of these films is higher than those of 1000-nm-thick lead titanate films prepared using a modified sol–gel technique with deposition onto platinum (P_s = 3.5 μC/cm^2) [9] and 380-nm-thick lead titanate films produced through metal–organic chemical solution deposition onto Pt(111)/Ti/SiO_2/Si(100) (P_s = 13.62 μC/cm^2) [10].

The lead titanate films produced by annealing of the Ti/Pb/Si thin-film heterostructures do not exhibit ferroelectric properties even at the annealing temperature T = 1173 K despite the fact that, according to x-ray powder diffraction analysis, the $PbTiO_3$ lead titanate is the main phase in these films.

4. CONCLUSIONS

The results obtained in the above investigation allowed us to make the following inferences. The composition, crystal structure, and electrical properties of the lead titanate films subjected to annealing are governed by the sequence of lead and titanium layers prepared by magnetron sputtering onto single-crystal silicon, all other factors being the same. In the lead–titanium–silicon structure, lead oxides formed at the upper interface not only permit unobstructed penetration of oxygen into the lower layers but even transfer oxygen to titanium, for example, due to reduction of lead oxide with metallic titanium. Since the oxidation occurs in an oxygen atmosphere, the lead oxidation and oxygen transfer proceed repeatedly. Part of titanium remains in the metallic state due to the oxidation of the upper lead layer, on the one hand, and the diffusion of silicon atoms into the titanium layer which suppresses the oxygen diffusion, on the other. As a result, the formation temperature of titanate decreases and the $PbTiO_3$-based heterostructures with lead oxides and clearly pronounced ferroelectric properties are formed. In the titanium–lead–silicon structure, titanium and lead oxides are almost independently formed on single-crystal silicon and then interact to form lead titanate. Consequently, the final heterostructure involves lead titanate and titanium oxide and, as a whole, is characterized by the dielectric properties.

Thus, by changing the sequence of lead and titanium layers deposited onto single-crystal silicon, it is possible to promote or inhibit the action of oxygen and silicon and to exercise control over the composition, structure, and properties of the lead titanate films formed during annealing of the heterostructures.

ACKNOWLEDGMENTS

This work was supported by the “Nonlinear Dielectric Films for Nanotechnology” grant of the Netherlands Research Organization (NWO) and the Russian Foundation for Basic Research, project no. 01-02-16828.

REFERENCES

1. X. Meng, Z. Huang, H. Ye, *et al.*, Mater. Res. Soc. Symp. Proc. **541**, 723 (1999).
2. A. Okada, J. Appl. Phys. **48** (7), 2905 (1997).
3. T. L. Ren, L. T. Zhang, L. T. Liu, and Z. J. Li, J. Phys. D **33** (15), L77 (2000).
4. C. Byun, J. W. Jang, Y. J. Cho, *et al.*, Thin Solid Films **324**, 94 (1998).
5. A. Li, D. Wu, C. Z. Ge, *et al.*, Thin Solid Films **375**, 220 (2000).
6. Y. S. Yoon, S. S. Yom, T. W. Kim, *et al.*, Appl. Surf. Sci. **93**, 285 (1996).
7. A. S. Sidorkin, A. S. Sigov, A. M. Khoviv, *et al.*, Fiz. Tverd. Tela (St. Petersburg) **42** (4), 727 (2000) [Phys. Solid State **42**, 745 (2000)].
8. S. Murarka, *Silicides for VLSI Applications* (Academic, New York, 1983; Mir, Moscow, 1986).
9. P. A. Shcheglov, S. A. Men’shikh, L. F. Rybakova, and Yu. Ya. Tamashpol’skiĭ, Neorg. Mater. **36** (4), 470 (2000).
10. F. M. Pontes, J. H. G. Rangel, E. R. Leite, *et al.*, Thin Solid Films **366**, 232 (2000).

Translated by O. Borovik-Romanova

Physics of the Solid State, Vol. 44, No. 4, 2002, pp. 779–788. Translated from Fizika Tverdogo Tela, Vol. 44, No. 4, 2002, pp. 750–757.

LATTICE DYNAMICS AND PHASE TRANSITIONS

A Semiclassical Vibronic Model of Charge Ordering in Crystals of Biferrocene Derivatives: Mössbauer Spectra

S. I. Klokishner and O. S. Reu

Moldova State University, ul. Matteevicha 60, Chisinau, MD-2009 Moldova

e-mail: sophia@usm.md

Received June 14, 2001

Abstract—A microscopic model of phase transitions in biferrocene derivatives is proposed. This model allows for the presence of interacting mixed-valence cations and counteranions in the crystal structure, electron transfer in cations, and charge oscillations in counteranions. The mutual effect of the mixed ordered phase is investigated, and the Mössbauer spectra of the biferrocenium triiodide and diiodobiferrocenium hexafluoroantimonate crystals are interpreted. An explanation is offered for the coexistence of the localized and delocalized Mössbauer spectra. © *2002 MAIK "Nauka/Interperiodica".*

1. INTRODUCTION

Mixed-valence molecular crystals contain clusters consisting of two or more metal ions with different valences that are joined into a molecular system. Each cluster involves a tunneling electron or a hole. The physical properties of mixed-valence crystals are governed by competition between intracluster and intercluster interactions. Sufficiently strong intercluster interaction suppresses electron tunneling and gives rise to cooperative phenomena in crystals of biferrocene derivatives containing binuclear clusters of low-spin iron [1, 2] and in crystals of hydroxy carboxylates $[M_3O(O_2CCH_3)_6(L)_3]S$ involving trinuclear mixed-valence complexes (where M is a transition metal, such as iron or manganese; L is the ligand; and S is the solvate molecule) [3, 4]. The spectra of these crystals in different spectral ranges exhibit an unusual temperature behavior. This behavior suggests that the redistribution of electron density with an increase in temperature is a specific feature of the cooperative phenomena. In the charge-ordered phase, an extra electron is completely or partly localized and a superposition of the spectra characteristic of cluster ions in fixed oxidation states is observed at low temperatures. An increase in temperature leads to a disturbance in the charge ordering. As a result, the observed spectra are characterized by the averaged parameters, which, in turn, indicate a complete delocalization of electrons. It was found that, for crystals of biferrocene derivatives and hydroxy carboxylates, the temperatures corresponding to the averaging of the Mössbauer spectra coincide with the temperatures of jumps in the heat capacities [1–4].

In the first works devoted to the vibronic model of charge ordering [5–8], the authors used the Piepho–Krausz–Schats approximation [9]. Within this approximation, it is assumed that each ion in a cluster has one singlet state interacting with a totally symmetric mode of the nearest environment. The intercluster dipole–dipole interaction was chosen as a cooperative interaction. Subsequently, this theory was developed in a direction approaching the model concepts and real systems. In 1993, Rabah *et al.* [10] demonstrated that, in biferrocene compounds, the spectrum of the lowest one-particle states for each fragment of a Fe(II)–Fe(III) low-spin iron cluster involves two molecular orbitals of the d_{xy} and $d_{x^2-y^2}$ types with close energies. In 1994, the Piepho–Krausz–Schats model was extended to this case by Linares *et al.* [11]. More recently, in addition to the totally symmetric mode interacting with both orbitals d_{xy} and $d_{x^2-y^2}$, Klokishner *et al.* [12] introduced the Piepho mode [13] that modulates the distance between fragments a and b in a dimeric cluster. The theory of charge and structural ordering in mixed-valence biferrocene salts was proposed in [14]. This theory allowed for the mixing of the d_{xy} and $d_{x^2-y^2}$ orbitals by a nontotally symmetric vibration. It should be noted that all the aforementioned works were reduced to a model that accounts for only mixed-valence cations consisting of two iron ions with different valences, four adjacent cyclopentadienyl rings, and a substituent atom X (X = I, Br, Cl, H, etc.) in the crystal structure of biferrocene derivatives [15]. However, these crystals are built up either of stacks of mixed-valence cations and their surrounding stacks of counteranions (I_3^-, I_2Br^-, Br_2I^-, etc.) [15] or of stacks in which mixed-valence cations alternate with counteranions. In this case, counteranions have either two electron-transfer-coupled electronic

1063-7834/02/4404-0779$22.00 © 2002 MAIK "Nauka/Interperiodica"

states X_A^-–Y–X_B and X_A–Y–X_B^- or two stable equilibrium positions between which anions jump. Charge oscillations in the anion and the cation–anion interaction lead not only to a change in the conditions for the electron localization in the mixed-valence cation but also to the ordering of charge or position of the anion depending on its type. The phenomenological theory of phase transitions in biferrocene derivatives with due regard for the interaction between mixed-valence cations and anions was constructed by Kambara *et al.* [16]. However, these authors used the one-orbital model and the Ising-type semiphenomenological Hamiltonian of intercluster interaction and disregarded the interaction of clusters with lattice vibrations. At the same time, the extra electron in the mixed-valence cation and the charge oscillations in the counteranion cause a considerable distortion of the local environment and favor the stabilization of the charge-ordered phase.

In the present work, we proposed a two-orbital semiclassical vibronic model of phase transitions in crystals of biferrocene derivatives. This model includes electron migration in the mixed-valence cation, charge oscillations in the counteranion, and cation–cation and cation–anion cooperative interactions. Since the temperature evolution of the Mössbauer spectra reflects changes in the electronic structure of biferrocene derivative crystals due to phase transitions, special attention is focused on the interpretation of this temperature evolution within the model proposed.

2. HAMILTONIAN OF A CRYSTAL

Biferrocene derivatives whose crystals undergo phase transitions belong to low-spin iron compounds. Since a Fe^{3+} ion in this case can be treated as an ion with a hole in the $d\varepsilon$ shell, the spins are represented as $S(Fe^{2+}) = 0$ and $S(Fe^{3+}) = 1/2$ and the Heisenberg-type exchange inside each mixed-valence cation is absent. The interaction of iron ions in the cation can be described within the model taking into consideration only the electron transfer. Let us assume that the spectrum of the lowest electronic states of the Fe(II)–Fe(III) cation with localized electrons contains two orbitals of the d_{xy} and $d_{x^2-y^2}$ types [10] which are separated by the energy gap

$$\Delta = E(d_{xy}) - E(d_{x^2-y^2}). \tag{1}$$

Now, we designate the orbitals as $\varphi_i(d_{x^2-y^2})$ and $\psi_i(d_{xy})$ (where $i = a$ and b) and introduce the transfer parameters $p = \langle\varphi_a \| \varphi_b\rangle$ and $p_1 = \langle\psi_a \| \psi_b\rangle$, which are related to these orbitals [11]. The transfer integrals $\langle\varphi_a \| \psi_b\rangle$ between the states of different symmetry are ignored [11]. Furthermore, we introduce the transfer parameter $\beta = \langle\Phi_A \| \Phi_B\rangle$ relating the states Φ_A and Φ_B in the counteranion.

The Hamiltonian of a crystal consisting of interacting cations and counteranions can be written in the form

$$\begin{aligned} H = &\sum_{\mathbf{n}} H_{\mathbf{n}}^C + \sum_{\mathbf{m}} H_{\mathbf{m}}^A + \sum_{\mathbf{n}} H_{eL}^{C\mathbf{n}} + \sum_{\mathbf{m}} H_{eL}^{A\mathbf{m}} \\ &+ \sum_{\mathbf{n}} H_L^{C\mathbf{n}} + \sum_{\mathbf{m}} H_L^{A\mathbf{m}} + V_{dd}^{CC} + V_{dd}^{CA}. \end{aligned} \tag{2}$$

Eight terms of this Hamiltonian will be represented below. In the basis set of the states $\varphi_i\Phi_j$ and $\psi_i\Phi_j$ (where $i = A$ and B), the electronic Hamiltonians of the cation and anion have the form

$$\begin{aligned} \mathbf{H}_{\mathbf{n}}^C &= \begin{pmatrix} pI_{\mathbf{n}}^C & 0 \\ 0 & p_1 I_{\mathbf{n}}^C \end{pmatrix} \otimes \boldsymbol{\sigma}_x^{C\mathbf{n}} + \frac{\Delta}{2}\begin{pmatrix} -I_{\mathbf{n}}^C & 0 \\ 0 & I_{\mathbf{n}}^C \end{pmatrix} \otimes I_{\mathbf{n}}^C, \\ H_{\mathbf{m}}^A &= \beta\begin{pmatrix} \boldsymbol{\sigma}_x^{A\mathbf{m}} & 0 \\ 0 & \boldsymbol{\sigma}_x^{A\mathbf{m}} \end{pmatrix} \otimes I_{\mathbf{m}}^A. \end{aligned} \tag{3}$$

Here, σ_x and σ_z are the Pauli matrices, $\otimes$ is the symbol of the direct product of matrices, and I is the 2-by-2 unit matrix. The third term in relationship (2) describes the interaction between the extra electron of each cation and the asymmetric (out-of-phase) mode [9] $q_{C\mathbf{n}} = [q_{A_1}^{\mathbf{n}a} - q_{A_1}^{\mathbf{n}b}]/\sqrt{2}$ [here, $q_{A_1}^{\mathbf{n}i}$ ($i = a$ and b) are the totally symmetric displacements of ions in the nearest environment of the a and b centers of the cation]; that is,

$$H_{eL} = v_C q_{C\mathbf{n}} \boldsymbol{\tau}_{\mathbf{n}}^C, \quad \tau_{\mathbf{n}}^C = \begin{pmatrix} I_{\mathbf{n}}^C & 0 \\ 0 & I_{\mathbf{n}}^C \end{pmatrix} \otimes \boldsymbol{\sigma}_z^{C\mathbf{n}}, \tag{4}$$

where v_C is the vibronic coupling parameter for the cation. In formula (4), the constants of the interaction with the φ_i and ψ_i orbitals are taken equal to each other. For biferrocene salts, this assumption was proved by calculations performed in [11]. The $q_{C\mathbf{n}}$ mode is assumed to be local, and the dispersion of vibrations is disregarded. Moreover, it is assumed that free vibrations of the **n**th cation at the frequency ω_C are harmonic; that is,

$$H_L^{C\mathbf{n}} = \frac{\hbar\omega_C}{2}\left(q_{C\mathbf{n}}^2 - \frac{\partial^2}{\partial q_{C\mathbf{n}}^2}\right). \tag{5}$$

In a similar manner, we can write the operator $H_{eL}^{A\mathbf{m}}$ of the interaction between the counteranion and its antisymmetric mode mixing the tunneling states $\Phi_\pm$ =

$(1/\sqrt{2})(\Phi_A \pm \Phi_B)$ and also the Hamiltonian $H_L^{A\mathbf{m}}$ for free vibrations of the anion:

$$H_{eL}^{A\mathbf{m}} = v_A q_{A\mathbf{m}} \boldsymbol{\sigma}_{\mathbf{m}}^A, \quad \boldsymbol{\sigma}_{\mathbf{m}}^A = \begin{pmatrix} \boldsymbol{\sigma}_z^{A\mathbf{m}} & 0 \\ 0 & \boldsymbol{\sigma}_z^{A\mathbf{m}} \end{pmatrix} \otimes I_{\mathbf{m}}^A, \quad (6)$$

$$H_L^{A\mathbf{m}} = \frac{\hbar\omega_A}{2}\left(q_{A\mathbf{m}}^2 - \frac{\partial}{\partial q_{A\mathbf{m}}^2}\right). \quad (7)$$

Finally, V_{dd}^{CC} and V_{dd}^{CA} are the cation–cation and cation–anion dipole–dipole interaction operators defined as

$$V_{dd}^{CC} = -\frac{1}{2}\sum_{\mathbf{n},\,\mathbf{n}'} K_{CC}(\mathbf{n}-\mathbf{n}')\boldsymbol{\tau}_{\mathbf{n}}^C\boldsymbol{\tau}_{\mathbf{n}'}^C,$$
$$V_{dd}^{CA} = -\frac{1}{2}\sum_{\mathbf{n},\,\mathbf{m}} K_{CA}(\mathbf{n}-\mathbf{m})\boldsymbol{\tau}_{\mathbf{n}}^C\boldsymbol{\sigma}_{\mathbf{m}}^A, \quad (8)$$

where

$$K_{CC}(\mathbf{n}-\mathbf{n}') = d_0^2 R_{\mathbf{nn}'}^{-3}(3\cos^2\theta_{\mathbf{nn}'} - 1),$$
$$K_{CA}(\mathbf{n}-\mathbf{m}) = d_0 D_0 R_{\mathbf{nm}}^{-3}(3\cos^2\theta_{\mathbf{nm}} - 1). \quad (9)$$

Here, $R_{\mathbf{nn}'}$ is the distance between the **n**th and **n**'th cations, $R_{\mathbf{nm}}$ is the distance between the **n**th cation and **m**th anion, and $\theta_{\mathbf{nn}'}$ and $\theta_{\mathbf{nm}}$ are the polar angles of the $\mathbf{R}_{\mathbf{nn}'}$ and $\mathbf{R}_{\mathbf{nm}}$ vectors, respectively. Since the mean distance between anions is large compared to those between cations or a cation and an anion, the anion–anion interaction is ignored. In expressions (9), $d_0 = eR_{ab}/2$ is the dipole moment of the cation with a completely localized electron, $D_0 = qr_{AB}/2$ is the dipole moment either of the anion with a completely localized charge or of the anion occupying an equilibrium position (depending on the anion type), and, correspondingly, r_{AB} is the distance either between the anion fragments or between two stable equilibrium positions of the anion. In the latter case, $R_{\mathbf{nn}'}$ is the distance between the cation and the midpoint of the segment r_{AB} connecting two equilibrium positions of the anion.

3. THE MOLECULAR-FIELD APPROXIMATION IN THE SEMICLASSICAL VIBRONIC MODEL

We now turn to the molecular-field approximation and replace the quantities $\tau_{\mathbf{n}}^C\tau_{\mathbf{n}'}^C$ and $\tau_{\mathbf{n}}^C\sigma_{\mathbf{m}}^A$ in the interaction Hamiltonians according to the equalities

$$\tau_{\mathbf{n}}^C\tau_{\mathbf{n}'}^C = \bar{\tau}\tau_{\mathbf{n}}^C + \bar{\tau}\tau_{\mathbf{n}'}^C - \bar{\tau}^2,$$
$$\tau_{\mathbf{n}}^C\sigma_{\mathbf{m}}^A = \bar{\tau}\sigma_{\mathbf{m}}^A + \bar{\tau}\tau_{\mathbf{n}}^C - \bar{\tau}\bar{\sigma}. \quad (10)$$

The parameters $d_0\bar{\tau}$ and $D_0\bar{\sigma}$ characterize the mean dipole moments of the cation and the anion. In this case, the quantities $\bar{\tau}$ and $\bar{\sigma}$ play the role of dimensionless order parameters and are defined by the formulas

$$\bar{\tau} = \frac{\mathrm{Sp}[\exp(-\tilde{H}/kT)\boldsymbol{\tau}_{\mathbf{n}}^C]}{\mathrm{Sp}[\exp(-\tilde{H}/kT)]},$$
$$\bar{\sigma} = \frac{\mathrm{Sp}[\exp(-\tilde{H}/kT)\boldsymbol{\sigma}_{\mathbf{n}}^A]}{\mathrm{Sp}[\exp(-\tilde{H}/kT)]}. \quad (11)$$

Here, $\tilde{H}$ is the molecular-field Hamiltonian of the crystal, which can be expanded as the sum of the single-site Hamiltonians:

$$H_{\mathbf{n}}^C = H_{\mathbf{n}}^C + H_{eL}^{C\mathbf{n}} + H_L^{C\mathbf{n}} - K_C\bar{\tau}\boldsymbol{\tau}_{\mathbf{n}}^C, \quad (12)$$

$$H_{\mathbf{m}}^A = H_{\mathbf{m}}^A + H_{eL}^{A\mathbf{m}} + H_L^{A\mathbf{m}} - \frac{1}{2}K_{CA}\bar{\tau}\boldsymbol{\sigma}_{\mathbf{m}}^A. \quad (13)$$

Here, the quantities

$$K_C = \sum_{\mathbf{n}'} K_{CC}(\mathbf{n}-\mathbf{n}'), \quad K_{CA} = \sum_{\mathbf{m}} K_{CA}(\mathbf{n}-\mathbf{m})$$

are the structure parameters, which depend on the mutual arrangement of cations and anions in the crystal lattice. These parameters differ for biferrocene derivative crystals that are formed by individual stacks of cations and anions and those formed by stacks in which cations alternate with anions.

According to the molecular-field approximation, it is necessary to determine the eigenvalues of Hamiltonians (12) and (13) at arbitrary values of the order parameters $\bar{\tau}$ and $\bar{\sigma}$, i.e., at an arbitrary temperature. Then, these eigenvalues should be substituted into relationships (11). The set of self-consistent equations thus obtained determines the dependences $\bar{\tau}(T)$ and $\bar{\sigma}(T)$. However, a nonadiabatic pseudo-Jahn–Teller vibronic problem with Hamiltonians (12) and (13) can be solved only numerically. For this reason, the set of self-consistent equations for the order parameters cannot be obtained in an explicit form. To overcome this difficulty, hereafter, we will resort to the adiabatic approximation in the framework of the molecular-field method and disregard the kinetic energy of the nuclei in Hamiltonians (12) and (13). Within this approximation, the energies of the cation and the anion are the adiabatic potentials. This approximation was used earlier in [5–8]. It was shown that the temperature dependences of the parameters for the charge-ordered state exhibit physically adequate features for strong, intermediate, and weak vibronic coupling. The spurs in relationships (11) are conveniently calculated in terms of the follow-

ing adiabatic functions diagonalizing Hamiltonians (12) and (13):

$$\psi^C_{1,2} = \left[\frac{1}{2}\left(1 \mp \frac{f_C(q_C)}{W(q_C)}\right)\right]^{1/2}\varphi_a \pm \left[\frac{1}{2}\left(1 \pm \frac{f_C(q_C)}{W(q_C)}\right)\right]^{1/2}\varphi_b,$$

$$\psi^C_{3,4} = \left[\frac{1}{2}\left(1 \mp \frac{f_C(q_C)}{W_1(q_C)}\right)\right]^{1/2}\psi_a \pm \left[\frac{1}{2}\left(1 \pm \frac{f_C(q_C)}{W_1(q_C)}\right)\right]^{1/2}\psi_b, \quad (14)$$

$$\Phi_{1,2} = \left[\frac{1}{2}\left(1 \mp \frac{f_A(q_A)}{W_2(q_A)}\right)\right]^{1/2}\Phi_A \pm \left[\frac{1}{2}\left(1 \pm \frac{f_A(q_A)}{W_2(q_A)}\right)\right]^{1/2}\Phi_B,$$

where

$$W(q_C) = [p^2 + f_C^2(q_C)]^{1/2};$$

$$W_1(q_C) = [p_1^2 + f_C^2(q_C)]^{1/2};$$

$$W_2(q_A) = [\beta^2 + f_A^2(q_A)]^{1/2},$$

$$f_C(q_C) = K_C\bar{\tau} + \frac{1}{2}K_{CA}\bar{\sigma} - V_C q_C,$$

$$f_A(q_A) = \frac{1}{2}K_{CA}\bar{\tau} - V_A q_A.$$

The corresponding adiabatic potentials take the form

$$U^C_{1,2}(q_C) = \frac{\hbar\omega_C}{2}q_C^2 \pm W(q_C),$$

$$U^C_{3,4}(q_C) = \frac{\hbar\omega_C}{2}q_C^2 + \Delta \pm W_1(q_C), \quad (15)$$

$$U^A_{1,2}(q_A) = \frac{\hbar\omega_A}{2}q_A^2 \pm W_2(q_A).$$

In the semiclassical approximation, the summation over vibronic states in relationships (11) is replaced by integration over the vibrational coordinates q_C and q_A. As a result, we obtain the following set of self-consistent equations for the order parameters $\bar{\tau}$ and $\bar{\sigma}$:

$$\bar{\sigma} = \frac{\int_{-\infty}^{\infty}\exp\left[-\frac{\hbar\omega q_A^2}{2kT}\right]\sinh\left(\frac{W_2(q_A)}{kT}\right)\frac{f_A(q_A)}{W_2(q_A)}dq_A}{\int_{-\infty}^{\infty}\exp\left[-\frac{\hbar\omega q_A^2}{2kT}\right]\cosh\left(\frac{W_2(q_A)}{kT}\right)dq_A},$$

$$\bar{\tau} = \frac{\int_{-\infty}^{\infty}\exp\left[-\frac{\hbar\omega_C q_C^2}{2kT}\right]\left[\sinh\left(\frac{W(q_C)}{kT}\right)\frac{1}{W(q_C)} + \exp\left[-\frac{\Delta}{kT}\right]\sinh\left(\frac{W_1(q_C)}{kT}\right)\frac{1}{W_1(q_C)}\right]f_C(q_C)dq_C}{\int_{-\infty}^{\infty}\exp\left[-\frac{\hbar\omega_C q_C^2}{2kT}\right]\left[\cosh\left[\frac{W(q_C)}{kT}\right] + \exp\left[-\frac{\Delta}{kT}\right]\cosh\left(\frac{W_1(q_C)}{kT}\right)\right]dq_C}. \quad (16)$$

This set of equations possesses a number of nontrivial solutions that are determined by the ratios between the vibronic and transfer parameters and the characteristic cation–cation and cation–anion interaction energies.

In [14], it was demonstrated that, within the two-orbital model, a crystal composed only of interacting mixed-valence dimers of low-spin iron can undergo two phase transitions under the conditions when $-1 < \Delta/p \le x^*$ and $1 < p/D \le y^*$ (where D is the characteristic energy of intercluster dipole–dipole interaction and the parameters x^* and y^* are derived numerically). At the same time, one transition occurs at $p/D < 1$ and $\Delta/p > x^*$ or at $\Delta/p < -1$ and $p_1/D < 1$. We assume that there exists one orbital on each center of the cluster, as is the case with the anion. Hence, the system is characterized by one transfer parameter and only one phase transition can take place, provided the transfer parameter is considerably less than the characteristic energy of the intercluster interaction. On this basis, we will analyze the temperature dependences of the order parameters $\bar{\tau}$ and $\bar{\sigma}$ for the system of interacting cations and anions within the framework of the above model including two orbitals on the cation and one orbital on the anion.

For simplicity, we assume that $p \gg p_1$. The validity of this inequality for biferrocene salts was demonstrated using molecular-orbital calculations in [11]. Since the studied compounds are characterized by the parameters $p = 500$ cm^{-1}, $\omega_C = 300$ cm^{-1} [11], and $\omega_A = 150$ cm^{-1} [16], we have $p/\omega_C = 1.7$ and $\omega_A/\omega_C = 0.5$. First, we consider the case when the level with the

energy $-p$ and the wave function $\varphi_- = (\varphi_a - \varphi_b)/\sqrt{2}$ ($\Delta/p > -1$) is the ground state of an isolated mixed-valence cation. Figures 1 and 2 display the family of curves that illustrate how the vibronic interaction affects the temperature dependences of the order parameters $\bar{\tau}(T)$ and $\bar{\sigma}(T)$. It is seen from these figures that the $\bar{\tau}(T)$ and $\bar{\sigma}(T)$ parameters simultaneously vanish at the phase transition temperatures. In the case of weak cooperative interactions ($\beta/K_{CA} = 1$ and $p/K_C = 3$), the charge ordering in a frozen lattice is absent. At all the temperatures, the parameters $\bar{\tau} = \bar{\sigma} = 0$ are the solution to the set of equations (16). The vibronic interaction in the cation ($\nu_C/\hbar\omega_C = 2$) leads to the localization of the extra electron in this cation, and the maximum dipole moment of the cation becomes equal to $0.93d_0$. The localized electron in the cation induces the dipole moment of the anion. However, the parameter $\bar{\sigma}_1$ is considerably less than $\bar{\tau}_1$, because the vibronic coupling parameter ν_A is equal to zero (Fig. 1, curves *1*, *1*'). The opposite situation occurs with curves *2* and *2*' in Fig. 1. At temperatures $T < T_c$ (where T_c is the phase transition temperature), the anion due to the interaction with its odd vibration either has a localized extra charge or occupies a fixed equilibrium position, thus suppressing the electron tunneling in the cation. The temperature dependences of the order parameters $\bar{\tau}$ and $\bar{\sigma}$ for the case when two phase transitions are possible in the rigid lattice at temperatures T_c' and T_c ($T_c' < T_c$) are depicted in Fig. 2 (curves *1*, *1*', *2*, *2*'). The charge-ordered state occurs in the finite temperature range $T_c' < T < T_c$. As the vibronic interaction becomes stronger, the temperature range of the stabilization of the charge-ordered state becomes wider and the order parameters $\bar{\tau}$ and $\bar{\sigma}$ increase (Fig. 2, curves *2*, *2*'). Finally, under the condition when $\nu_A = \nu_C = \hbar\omega_C$, one phase transition instead of two transitions is observed and the order parameters $\bar{\tau}$ and $\bar{\sigma}$ increase. This result can be qualitatively interpreted as follows. Since the transfer parameter p of the ground state ($\Delta/p = -0.45$) exceeds the energy of the cation–cation interaction ($p/K_C = 1.5$), this interaction cannot localize the electron in the cation. At the same time, the ratio β/K_{CA} is equal to 1.5. Therefore, at $\nu_A = \nu_C = 0$ and low temperatures, when only the ground states of the cation and the anion are populated, the crystal is in the disordered state. For the first excited level in the cation, the tunneling splitting p_1 is substantially less than the characteristic energy K_C of the cation–cation interaction. As a consequence, the population of this level leads to an ordering of electrons in cations, the appearance of a nonzero molecular field on each anion, and, hence, an ordering of anions. An increase in the temperature results in a disturbance in the correlation between dipole moments, and the crystal reverts to the disordered state. In the presence of the vibronic interaction, the spacing

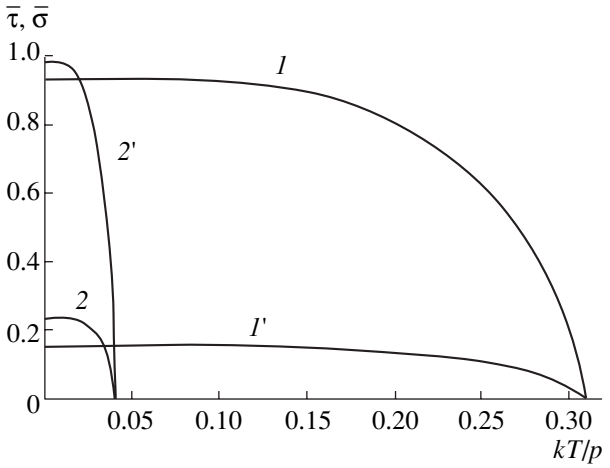

Fig. 1. Temperature dependences of the order parameters (*1*, *2*) $\bar{\tau}$ and (*1*', *2*') $\bar{\sigma}$ at (*1*, *1*') $\nu_A = 0$ and $\nu_C/\hbar\omega_C = 2$ and (*2*, *2*') $\nu_C = 0$ and $\nu_A/\hbar\omega_C = 2$. $p/\hbar\omega_C = 1.7$, $\Delta/p = 0$, $p/K_C = 3$, $\omega_A/\omega_C = 0.5$, $\beta/p = 1$, and $K_{CA}/K_C = 1$.

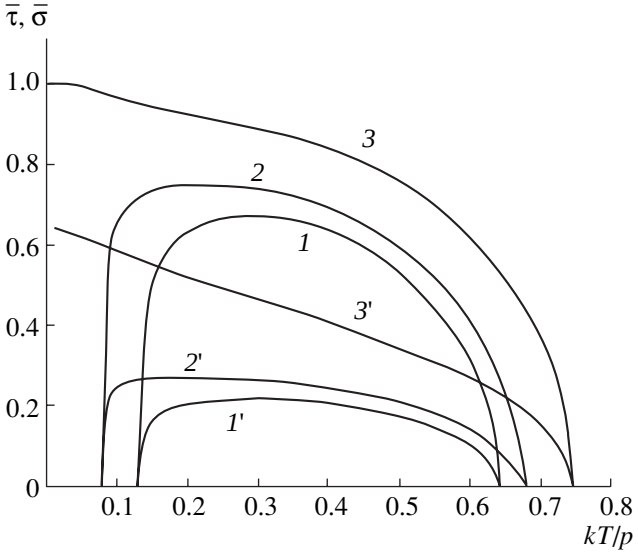

Fig. 2. Temperature dependences of the order parameters (*1*–*3*) $\bar{\tau}$ and (*1*'–*3*') $\bar{\sigma}$ at $\nu_C = \nu_A = (1, 1')$ 0, (*2*, *2*') $0.45\hbar\omega_C$, and (*3*, *3*') $\hbar\omega_C$. $p/\hbar\omega_C = 1.7$, $\Delta/p = -0.45$, $p/K_C = 1.5$, $\omega_A/\omega_C = 0.5$, $\beta/p = 1.5$, and $K_{CA}/K_C = 1.5$.

between the minima of the ground and first excited adiabatic potentials of the cation with the transfer parameters p and p_1 decreases and the range of the existence of the charge-ordered phase increases (Fig. 2, curve *2*). For $\nu_A = \nu_C = \hbar\omega_C$, the minimum of the adiabatic potential $U_4^C(q_C)$ with the transfer parameter p_1 corresponds to the ground state, the conditions for the stabilization of the charge-ordered phase in the crystal appear to be

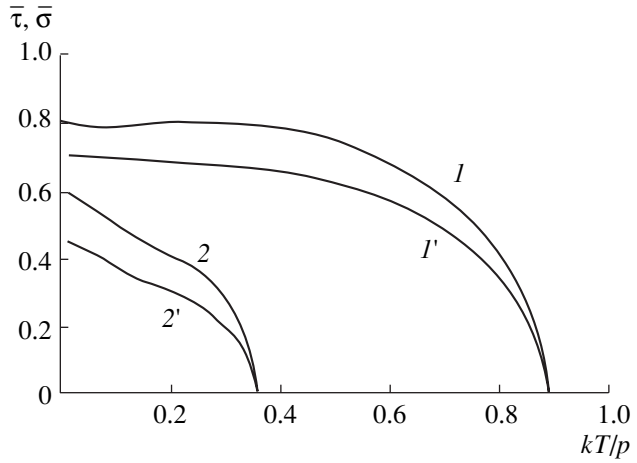

Fig. 3. Temperature dependences of the order parameters (*1*, *2*) $\bar{\tau}$ and (*1*', *2*') $\bar{\sigma}$ at different K_{CA}/K_C ratios: (*1*, *1*') 10 and (*2*, *2*') 6.25. $p/\hbar\omega_C = 1.7$, $v_A/\hbar\omega_C = 0.5$, $v_C/\hbar\omega_C = 1$, $\Delta/p = 0$, $p/K_C = 5$, $\omega_A/\omega_C = 0.5$, and $\beta/p = 1$.

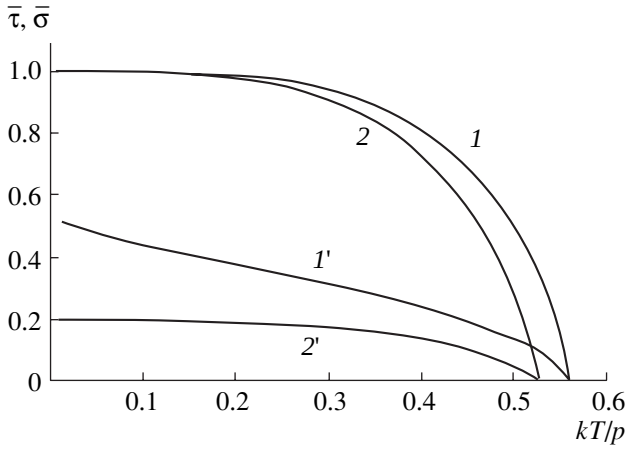

Fig. 4. Temperature dependences of the order parameters (*1*, *2*) $\bar{\tau}$ and (*1*', *2*') $\bar{\sigma}$ at $v_C = v_A = (1, 1')\ \hbar\omega_C$ and (*2*, *2*') 0. $p/\hbar\omega_C = 1.7$, $\Delta/p = -1.5$, $p/K_C = 2$, $\omega_A/\omega_C = 0.5$, $\beta/p = 1.5$, and $K_{CA}/K_C = 1.2$.

considerably milder, and one phase transition occurs in the crystal.

The influence of the cooperative cation–anion interaction is illustrated by the curves plotted in Fig. 3. An increase in the ratio K_{CA}/K_C leads to an increase in the phase transition temperature and the order parameters $\bar{\tau}$ and $\bar{\sigma}$. Both variants depicted in Fig. 3 are calculated at $p/K_C = 5$. This indicates that the strong cation–anion interaction aligns dipole moments of cations with a sufficiently fast electron tunneling in cations. Figure 4 shows the temperature dependences of the order parameters for the ground level with a tunneling splitting $p_1 \ll p$ and the wave function $\psi_- = (\psi_a - \psi_b)/\sqrt{2}$. In this situation, even a very weak cation–cation interaction suppresses the electron tunneling in the cation. Therefore, the charge-ordered phase is stabilized at $p/K_C = 2$ and $\beta/K_{CA} = 1.25$.

4. MÖSSBAUER SPECTRA

The electron delocalization being partly dependent on the temperature is due to the temperature dependence of the molecular field. This effect is referred to as delocalization in a stationary sense [17], because the spectrum is determined by the electron density redistribution inside the mixed-valence cluster with a change in the temperature rather than by the jump frequency of the extra electron. The stationary (spatial) mechanism of temperature transitions of the localization–delocalization type in the Mössbauer spectra of mixed-valence molecular crystals was quantitatively investigated in [7, 8, 18–21]. Now, we apply the theory of stationary localization–delocalization of an extra electron to the calculation of the Mössbauer spectra of biferrocene derivative crystals within the two-orbital vibronic model of charge ordering. For a dimeric cluster with identical nuclei *a* and *b*, the operator for the quadrupole interaction of electron shells with nuclei can be written in the form

$$V(\mathbf{r}, \mathbf{R}) = \frac{e^2 Q_n}{4I(2I-1)} \sum_{k=a,b} \mathbf{q}_k [3\hat{I}_{zk}^2 - I(I+1)], \quad (17)$$

where Q_n is the quadrupole nuclear moment, $\mathbf{q}_k = \sum_i (3z_{ik}^2 - r_{ik}^2)/r_{ik}^5$ is the operator for the electric field gradient acting on the *k*th nucleus, r_{ik} is the radius vector of the *i*th electron (reckoned from the *k*th nucleus), and *I* is the nuclear spin. The isomer shift operator is given by the expression

$$\boldsymbol{\delta} = \frac{2\pi^2 e^2 z_n}{5} \sum_{i,k} \delta(\mathbf{r}_{ik})[R_{\text{ex}}^2 - R_{\text{gr}}^2]. \quad (18)$$

Here, R_{ex} and R_{gr} are the radii of nuclei in the excited and ground states, respectively. The quadrupole splitting and the isomer shift for the cation in a particular state with the wave function $\psi_i^C(q_C)$ are determined by averaging operators (17) and (18) over the electronic coordinates and then by integrating the result over the vibrational coordinate q_C. However, taking into account that, at a given temperature, the system with the highest probability resides in minima of the adiabatic potential sheets, we determine the quadrupole splitting and the isomer shift in minima of each adiabatic potential sheet. The quadrupole splitting for the nucleus of the *a* ion in the state $\psi_i^C(q_C^{i\gamma})$ in the cluster at an arbitrary

temperature is defined by the relationship

$$\Delta E_{Qa}^{(1,2)\gamma} = \frac{e^2 Q_n}{4} \times \left[\left(1 \mp \frac{f_C(q_C^{(1,2)\gamma})}{W(q_C^{(1,2)\gamma})}\right)q + \left(1 \pm \frac{f_C(q_C^{(1,2)\gamma})}{W(q_C^{(1,2)\gamma})}\right)q^*\right],$$
$$\Delta E_{Qa}^{(3,4)\gamma} = \frac{e^2 Q_n}{4} \times \left[\left(1 \mp \frac{f_C(q_C^{(3,4)\gamma})}{W_1(q_C^{(3,4)\gamma})}\right)q + \left(1 \pm \frac{f_C(q_C^{(3,4)\gamma})}{W_1(q_C^{(3,4)\gamma})}\right)q^*\right]. \quad (19)$$

Here, γ is equal to 1 for the adiabatic potentials $U_\alpha^C(q_C)$ (where $\alpha = 1$, 3, and 4) with one minimum at the point $q_C^{(\alpha)1}$. This is true for the adiabatic potential U_4^C, because $p \gg p_1$. The adiabatic potential $U_2^C(q_C)$ has two minima, and, hence, the value of γ can be equal to 1 and 2. The quadrupole splitting for the b nucleus can be obtained by the replacement $q^* \longleftrightarrow q$ and $q \longleftrightarrow q^*$. Here, q and q^* designate the mean electric field gradients at the Fe(III) and Fe(II) ions, i.e., the ions of the cation with the completely localized electron. These quantities are determined directly from experiments with mononuclear complexes (cluster fragments). The isomer shifts for the cations in the states $\psi_i^C(q_C^{i\gamma})$ are represented in a similar manner; that is,

$$\delta_a^{(1,2)\gamma} = \frac{1}{2} \times \left[\left(1 \mp \frac{f_C(q_C^{(1,2)\gamma})}{W(q_C^{(1,2)\gamma})}\right)\delta + \left(1 \pm \frac{f_C(q_C^{(1,2)\gamma})}{W(q_C^{(1,2)\gamma})}\right)\delta^*\right],$$
$$\delta_a^{(3,4)\gamma} = \frac{1}{2} \times \left[\left(1 \mp \frac{f_C(q_C^{(3,4)\gamma})}{W_1(q_C^{(3,4)\gamma})}\right)\delta + \left(1 \pm \frac{f_C(q_C^{(3,4)\gamma})}{W_1(q_C^{(3,4)\gamma})}\right)\delta^*\right], \quad (20)$$

where δ and δ^* are the isomer shifts for the Fe(III) and Fe(II) nuclei. The nucleus is sensitive to the quadrupole splitting and isomer shift of the $\psi_i^C(q_C^{i\gamma})$ state of the cation at the minimum $q_C^{i\gamma}$ in the case when the width of this level is less than the corresponding quadrupole splitting and isomer shift, i.e., when the relaxation is rather slow. Note that the overall Mössbauer spectrum is the sum of the spectra attributed to different states $\psi_i^C(q_C^{i\gamma})$ of the cation at the minima $q_C^{i\gamma}$ of the adiabatic potential in the molecular field. If the relaxation is fast, i.e., the level width is larger than the quadrupole splitting, the nuclei respond only to the averaged parameters. In this case, the contributions from different minima of the adiabatic potentials to the quadrupole splitting and the isomer shift are averaged over equilibrium populations.

The structure of the adiabatic potential minima for the cation in the molecular field is such that, as the temperature increases, the gap between the minima of the potentials $U_3^C(q_C)$ and $U_4^C(q_C)$ ($p \gg p_1$) and the gap between two minima of the sheet $U_2^C(q_C)$ first decrease and vanish at the T_c temperature. At the same time, the adiabatic potential $U_1^C(q_C)$ at $T \longrightarrow T_c$ has a minimum at the point $q_C^{11} = 0$ at which $U_1^C(q_C^{11}) = p$. By assuming that the state $\psi_1^C(q_C^{11})$ relaxes slowly, the quadrupole splitting $\Delta E_{Qi}^{(1,1)1}$ and the isomer shift $\delta_i^{(1,1)1}$ can be calculated from relationships (19) and (20).

Since the minima of the adiabatic potential $U_2^C(q_C)$ rapidly approach each other at $T \longrightarrow T_c$, the contributions from the ψ_2 state at the points q_C^{21} and q_C^{22} to ΔE_{Qi} and δ_i should be averaged over the equilibrium populations of the minima $U_2^C(q_C^{21})$ and $U_2^C(q_C^{22})$. For the quadrupole splitting, this can be described by the expression

$$\Delta E_{Qi}^{(2)} = \frac{\sum_{\gamma=1}^{2} \Delta E_{Qi}^{(2)} \exp[-U_2^C(q_C^{2\gamma})/kT]}{\sum_{\gamma=1}^{2} \exp[-U_2^C(q_C^{2\gamma})/kT]}, \quad i = a, b. \quad (21)$$

The relationship for the isomer shift $\delta_i^{(2)}$ can be written in a similar manner. The quantities $\Delta E_{Qi}^{(3,4)}$ and $\delta_i^{(3,4)}$, which correspond to the U_3^C and U_4^C sheets, can be easily derived by averaging $\Delta E_{Qi}^{(3)1}$, $\Delta E_{Qi}^{(4)1}$, $\delta_i^{(3)1}$, and $\delta_i^{(4)1}$ over the equilibrium populations of the U_3^C and U_4^C sheet minima.

The overall Mössbauer spectrum (i.e., the observed spectrum) is a superposition of Lorentzian curves describing different electronic states of the cluster in the molecular field with due regard for their Boltzmann populations. The temperature evolution of the Mössbauer spectra of biferrocenium triiodide and diiodobiferrocenium hexafluoroantimonate crystals is displayed in Figs. 5 and 6. The spectra were calculated using formulas (19)–(21) with the isomer shift $\delta(Fe^{3+}) = \delta(Fe^{2+}) = 0.48$ mm/s [22] and the vibronic coupling parameter $v_C = 417$ cm^{-1} [11]. The following quadrupole splitting parameters $e^2Q_nq(Fe^{3+})/2$ and

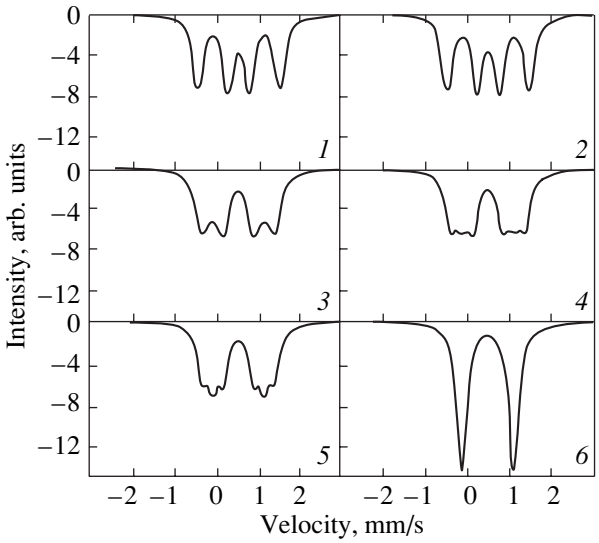

Fig. 5. Temperature evolution of the Mössbauer spectra of the biferrocenium triiodide crystal. Temperature, K: (*1*) 100, (*2*) 200, (*3*) 330, (*4*) 335, (*5*) 338, and (*6*) 342.

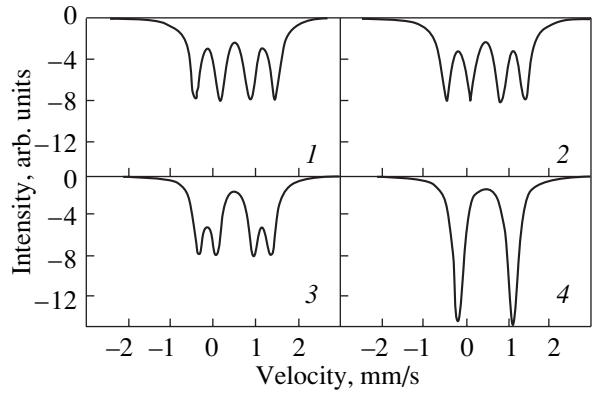

Fig. 6. Temperature evolution of the Mössbauer spectra of the diiodobiferrocenium hexafluoroantimonate crystal. Temperature, K: (*1*) 100, (*2*) 200, (*3*) 263, and (*4*) 265.

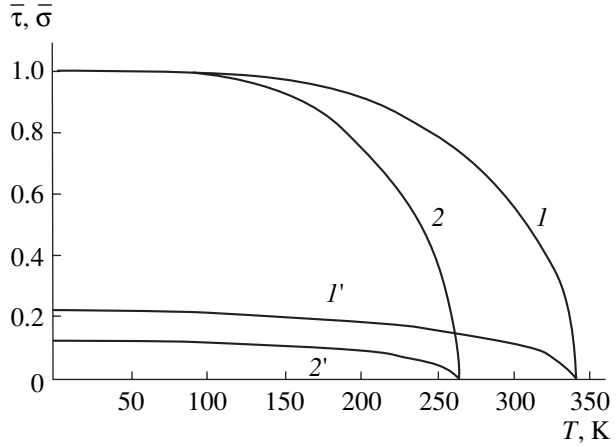

Fig. 7. Temperature dependences of the order parameters $\bar{\tau}$ and $\bar{\sigma}$ for (*1*, *1*') biferrocenium triiodide and (*2*, *2*') diiodobiferrocenium hexafluoroantimonate crystals.

$e^2Q_nq(Fe^{2+})/2$, the molecular field parameters K_C, and the gaps Δ were taken from [22]: $e^2Q_nq(Fe^{3+})/2$ = 0.54 mm/s, $e^2Q_nq(Fe^{2+})/2$ = 2.08 mm/s, K_C = 172 cm^{-1}, and Δ = 322 cm^{-1} for diiodobiferrocenium hexafluoroantimonate and $eQ_nq(Fe^{3+})/2$ = 0.3 mm/s, $eQ_nq(Fe^{2+})/2$ = 2.11 mm/s, K_C = 200 cm^{-1}, and Δ = –81 cm^{-1} for biferrocenium triiodide. The parameters p, ω_A, and ω_C were specified in Section 3, and the transfer parameter β was taken equal to 480 cm^{-1}. The vibronic coupling parameter v_A and the molecular-field parameter K_{CA} for the crystals under consideration were determined by the best fitting of the calculated to experimental phase transition temperatures. The temperature dependences of the order parameters $\bar{\sigma}$ and $\bar{\tau}$ for both crystals are plotted in Fig. 7. We start our discussion with the spectrum of the biferrocenium triiodide crystal. At low temperatures ($T \le 200$ K), the spectrum consists of two doublets with quadrupole splittings characteristic of Fe^{2+} and Fe^{3+} (Fig. 5). As the temperature increases, the lines of the doublets come close together and the quadrupole splittings differ from $\Delta E_Q(Fe^{2+})$ and $\Delta E_Q(Fe^{3+})$. Already at the temperature T = 335 K, the delocalized component with a noticeable intensity appears in the spectrum. Thus, the spectrum involves three doublets, namely, two localized doublets and one delocalized doublet. At $T = T_c$, the spectrum is averaged. These results can be qualitatively explained in terms of the adiabatic potentials (Fig. 8). At low temperatures, only the deepest minimum of the lower adiabatic potential sheet $U_2^C(q_C)$ (Fig. 8a) is populated and the system is localized; i.e., $\psi_2^C(q_C^{21}) \approx \varphi_a(\mathbf{r})$ and $\psi_2^C(q_C^{22}) \approx \varphi_b(\mathbf{r})$. As a consequence, two doublets appear in the Mössbauer spectrum (Fig. 5). With an increase in the temperature (a decrease in the molecular-field parameters), the minima of the U_2^C sheet approach each other in energy (Fig. 8b) and, correspondingly, the lines in the Mössbauer spectrum come closer together. This is accompanied by the population of the minimum of the $U_4^C(q_C)$ adiabatic potential sheet. Therefore, at the temperature T = 335 K, the spectrum contains three doublets: two localized doublets associated with the U_4^C potential sheet and one delocalized doublet attributed to the U_2^C potential sheet. The latter sheet is responsible for the appearance of the delocalized doublet, because the minima of this sheet almost level off at T = 335 K (Fig. 8c). However, at the same temperature, the system remains localized at the minimum of the U_4^C potential sheet. This situation occurs as a consequence of a large difference between the p and p_1 transfer parameters and small values of the order parameters $\bar{\tau}$ and $\bar{\sigma}$ at 335 K. Thus, the proposed model provides a clear physical explanation for the coexistence of the localized and

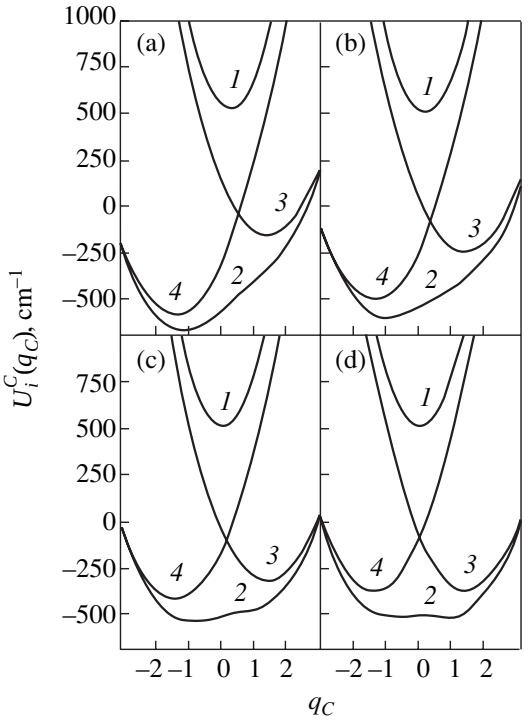

Fig. 8. Temperature evolution of the adiabatic potentials $U_i^C(q_C)$ (i = 1–4) of a cation in the molecular-field approximation for the biferrocenium triiodide crystal. Temperature, K: (a) 100, (b) 300, (c) 335, and (d) 342.

delocalized spectra experimentally observed by Hendrickson's group [23–25].

The temperature evolution of the Mössbauer spectrum of the diiodobiferrocenium hexafluoroantimonate crystal (Fig. 6) differs from that described above. The spectrum contains two doublets over a wide range of temperatures. A change in the temperature leads only to a change in the spacing between the lines of the doublets. At the phase transition temperature, the spectrum transforms into the averaged doublet. As in the above case, the U_2^C potential is characterized by a lower sheet. However, the spacing between the minima of the lower sheet and the minimum of the first excited potential U_4^C is larger than the energy kT_c, so that the population of the minimum of the U_4^C potential sheet and, hence, the intensity of the spectrum attributed to this sheet are negligibly small at all temperatures $T \le T_c$. For this reason, the spectrum at any temperature does not exhibit three doublets.

5. CONCLUSION

The basic results obtained in this work can be summarized as follows. The charge ordering, phase transitions, and their manifestation in the Mössbauer spectra were investigated in crystals of biferrocene derivatives in the framework of the microscopic model proposed. This model accounts for the complex spectrum of tunneling states of the cation and anion, the vibronic interaction of the pseudo-Jahn–Teller type in the cation and anion, and the cation–cation and cation–anion cooperative interactions. It was shown that, in addition to the localized Mössbauer spectra (Fe^{2+} and Fe^{3+}) at low temperatures and the delocalized (averaged) spectra ($Fe^{2.5+}$) at high temperatures, the spectra can contain three doublets. This reflects the coexistence of localized (Fe^{2+} and Fe^{3+}) and averaged ($Fe^{2.5+}$) Mössbauer spectra. The experimental data on the Mössbauer spectra of the biferrocenium triiodide and diiodobiferrocenium hexafluoroantimonate crystals were interpreted.

ACKNOWLEDGMENTS

This work was supported by the Moldova State University.

REFERENCES

1. M. Sorai, A. Nishimori, D. N. Hendrickson, *et al.*, J. Am. Chem. Soc. **109** (14), 4266 (1987).
2. R. J. Webb, P. M. Hagen, R. J. Wittebort, *et al.*, Inorg. Chem. **31** (10), 1791 (1992).
3. V. Kaneko, M. Nakano, M. Sorai, *et al.*, Inorg. Chem. **28** (6), 1067 (1989).
4. Ho G Jang, K. Kaji, M. Sorai, *et al.*, Inorg. Chem. **29** (18), 3547 (1990).
5. S. I. Klokishner, B. L. Kushkuleĭ, and B. S. Tsukerblat, Fiz. Tverd. Tela (St. Petersburg) **34** (3), 832 (1992) [Sov. Phys. Solid State **34**, 445 (1992)].
6. B. S. Tsukerblat, S. I. Klokishner, and B. L. Kushkuley, Chem. Phys. **166** (1), 97 (1992).
7. S. I. Klokishner, B. S. Tsukerblat, and B. L. Kushkuley, New J. Chem. **17** (1–2), 43 (1993).
8. S. I. Klokishner, B. S. Tsukerblat, and B. L. Kushkuley, Phys. Lett. A **179** (6), 429 (1993).
9. S. B. Piepho, E. R. Krausz, and P. N. Schats, J. Am. Chem. Soc. **100** (10), 2996 (1978).
10. H. Rabah, J. Guillin, A. Cereze-Ducouret, *et al.*, Hyperfine Interact. **17** (1), 51 (1993).
11. J. Linares, K. Boukheddaden, and F. Varret, Chem. Phys. **182** (1), 1 (1994).
12. S. Klokishner, J. Linares, and F. Varret, Chem. Phys. **226** (1), 171 (1998).
13. S. B. Piepho, J. Am. Chem. Soc. **110** (25), 6319 (1988).
14. S. Klokishner, K. Boukheddaden, and F. Varret, Phys. Rev. B **60** (1), 150 (1999).
15. T.-Y. Dong, M. J. Cohn, D. N. Hendrickson, and C. G. Pierpont, J. Am. Chem. Soc. **107** (16), 4777 (1985).

16. T. Kambara, D. N. Hendrickson, T.-Y. Dong, and M. J. Cohn, J. Chem. Phys. **86** (4), 2362 (1987).

17. L. A. Blyumenfel'd, V. I. Gol'danskiĭ, M. I. Podgoretskiĭ, and D. S. Chernavskiĭ, Zh. Strukt. Khim. **8** (5), 854 (1967).

18. B. S. Tsukerblat and S. I. Klokishner, Dokl. Akad. Nauk SSSR **305** (1), 144 (1989).

19. A. V. Koryachenco, S. I. Klokishner, and B. S. Tsukerblat, Chem. Phys. **150** (3), 295 (1991).

20. A. V. Koryachenko, S. I. Klokishner, and B. S. Tsukerblat, Fiz. Tverd. Tela (Leningrad) **33** (7), 2176 (1991) [Sov. Phys. Solid State **33**, 1225 (1991)].

21. S. I. Klokishner and B. D. Geĭkhman, Fiz. Tverd. Tela (St. Petersburg) **35** (8), 2239 (1993) [Phys. Solid State **35**, 1113 (1993)].

22. K. Boukheddaden, J. Linares, and F. Varret, Phys. Rev. B **49** (22), 15659 (1994).

23. T.-Y. Dong, D. N. Hendrickson, K. Iwai, *et al.*, J. Am. Chem. Soc. **107** (26), 7996 (1985).

24. T.-Y. Dong, T. Kambara, and D. N. Hendrickson, J. Am. Chem. Soc. **108** (15), 4423 (1986).

25. T.-Y. Dong, T. Kambara, and D. N. Hendrickson, J. Am. Chem. Soc. **108** (19), 5857 (1986).

Translated by O. Borovik-Romanova

Physics of the Solid State, Vol. 44, No. 4, 2002, pp. 789–792. Translated from Fizika Tverdogo Tela, Vol. 44, No. 4, 2002, pp. 758–761.

LOW-DIMENSIONAL SYSTEMS AND SURFACE PHYSICS

Electrical and Thermoelectric Properties of Nanoporous Carbon

V. V. Popov*, S. K. Gordeev, A. V. Grechinskaya**, and A. M. Danishevskiĭ***

** Ioffe Physicotechnical Institute, Russian Academy of Sciences, ul. Politekhnicheskaya 26, St. Petersburg, 194021 Russia*
e-mail: Valeri.Popov@pop.ioffe.rssi.ru
*** Central Research Institute of Materials, St. Petersburg, 191014 Russia*
Received May 18, 2001; in final form, August 2, 2001

Abstract—This paper reports on a study of the temperature dependences of the electrical resistivity, Hall coefficient, and thermopower of nanoporous carbon prepared from polycrystalline carbides (α-SiC, TiC, Mo_2C) and 6*H*-SiC single crystals in the temperature range 1.5–300 K. The structural units responsible for the character of charge transport in these materials are carbon nanoclusters measuring ~10–30 Å. The conductivity in all the samples studied was found to be *p* type with a high carrier concentration ($n_h \sim 10^{20}$ cm^{-3}). The behavior of the transport coefficients at low temperatures is discussed. © *2002 MAIK "Nauka/Interperiodica".*

1. INTRODUCTION

Studies of the various carbon modifications capable of forming structures with manometer-scale dimensions, such as fullerenes, nanotubes, and nanoclusters, have recently attracted considerable interest. The transport properties of macroscopic bulk materials produced by combining such structures will depend both on the properties of the nanostructural constituents themselves and on the methods used to compact them into a sample [1]. One of the new objects with nanostructural constituents combined to form a compact high-porosity material is nanoporous carbon (*npor*-C). It is prepared by chemically reacting carbide compounds (SiC, TiC, Mo_2C). Chemical removal of other than carbon atoms produces a nanocluster carbon framework with an average cluster size of 10–25 Å and a high porosity of up to 70 vol % [2]. The possibility of fabricating mechanically strong pieces of a given shape, combined with the nanoporous structure, makes this material promising for application, for instance, for use in electrodes in electrolytic capacitors with record-high capacitance characteristics [3]. At the same time, the electrical properties of *npor*-C have not been studied in detail. Information on the mechanisms of conductivity and on the character of carrier scattering in these materials is lacking.

This paper reports on a study of the electrical and thermoelectric properties of nanoporous carbon carried out over a broad temperature range. It was found that the difference in transport properties between *npor*-C samples prepared under different technological conditions is primarily of a quantitative nature, whereas the qualitative characteristics of all the samples studied are similar and are apparently due to the properties of their structural elements, more specifically, of carbon nanoclusters.

2. SAMPLE PREPARATION

The *npor*-C material was prepared by chlorinating the starting carbides (α-SiC, TiC, Mo_2C) at temperatures of 700 to 1000°C. Composite samples were produced from a polycrystalline powder of the corresponding carbide. Powder with grain sizes of up to 40 μm was molded into a sample using a temporary binder; next, pyrocarbon was synthesized in the pores to bind the carbide grains into a compact material, after which high-temperature chlorination (950°C) was carried out, and the chlorine was removed in an argon flow. This treatment leaves 8–11% of the nonporous pyrocarbon binder in the samples (denoted subsequently by *B*). Part of the samples prepared from SiC powder were subjected, before chlorination, to high-temperature silicidation (type *A* samples). The pyrocarbon inclusions reacted chemically to produce disordered β-SiC and were subsequently also transformed to nanoporous carbon by chlorination. We also studied *npor*-C samples prepared by chlorination of 6*H*-SiC single crystals shaped as 0.5 to 1-mm-thick plates.

The *npor*-C structure was characterized using x-ray diffraction and small-angle x-ray scattering [4], as well as electron microscopy. It was found that the scattering structural elements—carbon nanoclusters and nanopores—are approximately of the same size. The size of the nanoclusters and pores depends primarily on the type of the starting carbide used, and the degree of their uniformity depends on the grain size of the starting carbide powder, temperature, and rate of the carbonization process, which is determined, in turn, by the rate with which the reaction gases evolve. The nanoclusters in the samples prepared from polycrystalline SiC (*npor*-C⟨*poly*-SiC⟩) are the most uniform in size, the major part of their volume being made up of structural elements 10–15 Å in dimension. In *npor*-C⟨*poly*-TiC⟩

samples, the average size of such nanoparticles is larger, 14–16 Å, and in *npor*-C⟨*poly*-Mo_2C⟩, it is 20–25 Å. The carbonization of *npor*-C from single-crystal 6*H*-SiC takes more time than that from polycrystalline carbides because the reaction gases experience difficulties in escaping (due to its denser structure); as a result, the low rate of the reaction front progression in *npor*-C⟨6*H*-SiC⟩ allows the formation of relatively large quasi-graphite nanoclusters measuring 30–120 Å and greater.

3. RESULTS AND DISCUSSION

The temperature dependences of the electrical resistivity ρ and of the Hall coefficient R are shown in Figs. 1 and 2, respectively, for a number of *npor*-C samples prepared from different carbides under different conditions. The curves in all the figures are labeled according to the sample numbers in the table. Also specified are the type of the starting carbide and the technology of preparation (*A* and *B* for the polycrystalline carbides), as well as the electrical parameters of the samples at 300 K (calculated without regard for the material porosity). The ρ(T) and R(T) relations of most samples are seen to follow a similar pattern, with the resistivity and the Hall coefficient increasing with decreasing temperature. Some samples exhibit saturation of R(T) at low temperatures, and the Hall coefficient of *npor*-C⟨6*H*-SiC⟩ (sample no. 9) is temperature-independent throughout the temperature interval covered. The sign of R corresponds to the *p*-type conduction. The magnetic-field dependences of the Hall voltage are linear for most samples up to H = 30 kOe. Thus, the conduction can be assumed to be primarily of a single-band nature. The hole concentration n_h in the single-band case lies within the range $n_h = 1/eR > 10^{19}$–10^{20} cm^{-3} for the samples studied.

The corresponding Hall mobility μ (T = 300 K) calculated from the expression $\mu = R/\rho$ is about 1 cm^2/V s in the *npor*-C⟨*poly*⟩ samples and is as high as 23 cm^2/V s in one *npor*-C⟨6*H*-SiC⟩ (Samples no. 7).

Figure 3 displays the temperature dependence of thermopower α for a number of *npor*-C samples. The sign of the thermopower corresponds to hole conduction and coincides with that of the Hall coefficient. The α(T) relation is seen to be linear for $T > 50$ K, a feature characteristic of the diffusion thermopower α_d of a degenerate carrier state with one carrier type [5],

$$\alpha_d = \pi^2 k^2 T(1 + r)/3eE_F. \quad (1)$$

Knowing the scattering exponent r and the carrier concentration n_h, and recalling that the Fermi energy is $E_F = \pi^2\hbar^2(3n_h/\pi)^{2/3}/2m^*$, one can estimate the carrier effective mass m^* in the nanoclusters. Assuming $r = -0.5$, which corresponds to scattering from grain (nanocluster) boundaries [5], we obtain $m^* \sim 0.1m_0$ (m_0 is the free-electron mass). A specific feature of the thermopower behavior in *npor*-C is the absence of the phonon-drag maximum in the α(T) dependence observed in both pure and microcrystalline graphite [6] at $T_{max} \sim 90$ K. Indeed, the phonon drag effect manifests itself at low temperatures, where electron interaction

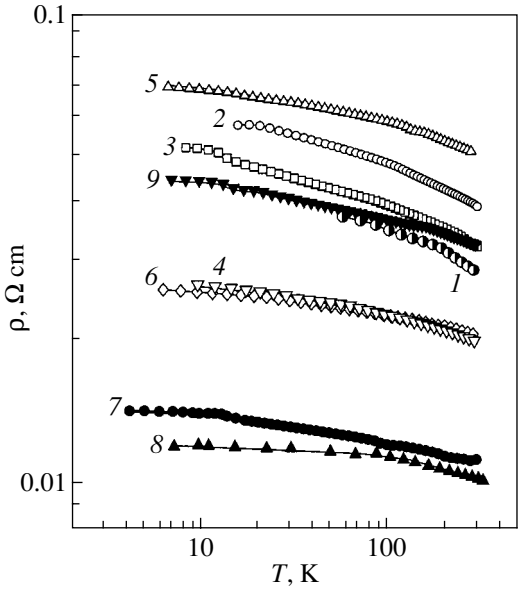

Fig. 1. Temperature dependences of the electrical resistivity of nanoporous carbon. Here and in the other figures, the curves are labeled in accordance with the samples in the table.

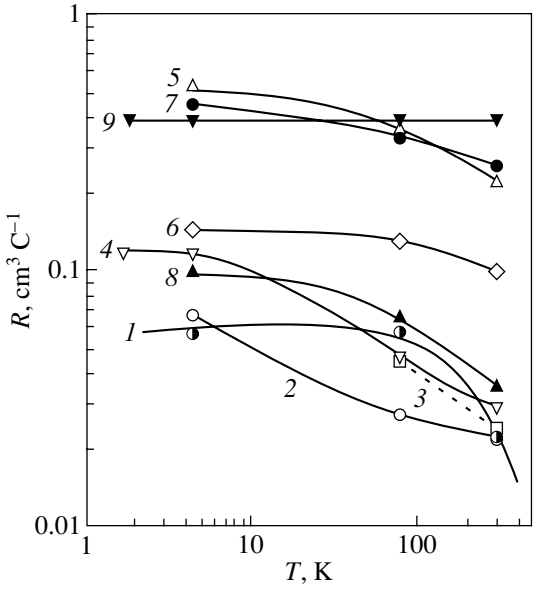

Fig. 2. Temperature dependences of the Hall coefficient of nanoporous carbon.

Characteristics of the *npor*-C samples studied

Sample no.	Starting carbide	R(300 K), cm^3/C	ρ(300 K), Ω cm	μ(300 K) = R/ρ, cm^2/V s
1	SiC-*A*	0.023	0.028	0.82
2	SiC-*A*	0.022	0.038	0.58
3	SiC-*B*	0.024	0.032	0.75
4	SiC-*B*	0.029	0.019	1.5
5	TiC-*B*	0.22	0.51	4.3
6	Mo_2C-*B*	0.1	0.002	5.0
7	6*H*-SiC	0.255	0.011	23
8	6*H*-SiC	0.035	0.01	3.5
9	6*H*-SiC	0.38	0.033	12

with long-wavelength phonons increases and the phonon component α_{ph} adds to the diffusion thermopower: $\alpha = \alpha_d + \alpha_{ph}$. As the cluster dimensions decrease, the phonon spectrum changes and phonon scattering increases, which results in a change in the character of the electron–phonon coupling and the phonon drag effect being suppressed. Suppression of the phonon component was earlier observed in nanocluster PbSe embedded in an opal host [7].

The difference in crystal structure and electrical properties between different modifications of carbon is known to be accounted for by the fact that its atoms can reside in more than one valence state and can form (through *s*–*p* hybridization) bonds of three main types (sp^3, sp^2, and *sp* hybridization). Furthermore, real structures, depending on the actual conditions of their formation, can form structures of intermediate types [8]. Accordingly, the electrical properties of different carbon modifications may vary over a wide range. A comparison of the electrical properties of the studied samples of nanoporous carbon with those of its other modifications shows that the dependence of the electrical resistivity on temperature follows neither the behavior of amorphous carbon, where one observes a strong growth in the resistivity with decreasing temperature ($\rho \sim \exp(T_0/T^n)$, with n lying between 1/2 and 1/4 [9]), nor the metallic course $\rho(T)$ in crystalline graphite [8].

In pure single-crystal graphite, band overlap results in electron–hole anisotropic conduction with a high carrier mobility. In microcrystalline graphite, the Fermi level shifts into the *p* band, such that, at concentrations $n_h \geq 8 \times 10^{18}$ cm^{-3}, one can use the single-band model to describe the transport phenomena [10]. The increase in the hole concentration with decreasing grain size is usually attributed to the increase in the number of surface states acting as electron-trapping centers. Thus, the high hole concentration in nanoporous carbon can be associated with a large free surface and, accordingly, with a high concentration of acceptor states. The low hole mobility is apparently caused by band-structure distortions near the nanocluster boundaries and by the mean free path being constrained to the nanocluster size. Indeed, the hole mobility in the samples prepared from different carbides grows in proportion to the dimensions of the nanoclusters and to the extent to which they fill the sample volume and assumes the largest value in *npor*-C⟨6*H*-SiC⟩, where large quasi-graphite clusters play a substantially larger part. The presence of the pyrocarbon binder in type *B* samples prepared from polycrystalline carbides does not affect the mobility markedly. The carrier mean free path being apparently determined by the crystallite dimensions, the usual mechanisms of its limitation (due to phonons, impurities), which govern the temperature dependence in conventional graphite-based materials, do not play a noticeable role in our case. In these conditions, the temperature dependences of the transport coefficients can be determined by quantum corrections to the conduc-

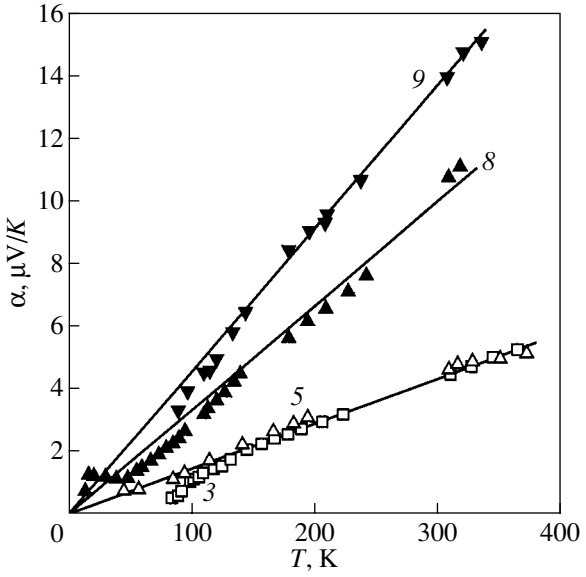

Fig. 3. Temperature dependence of the thermopower of nanoporous carbon.

tivity, whose comprehensive study would require measurement of these coefficients in magnetic fields and at low temperatures.

4. CONCLUSIONS

Thus, our study of the electrical and thermopower properties of nanoporous carbon prepared under the specified technological conditions suggests that the conduction has a *p* character with a high carrier concentration. The main carrier scattering mechanism responsible for the low mobility is associated with the carbon clusters being nanosized. The specific features in the nanocluster structure also account for the suppression of the thermopower component originating from the phonon drag.

ACKNOWLEDGMENTS

This study was supported by the Russian Foundation for Basic Research (project no. 99-02-17984), Russian research program "Fullerenes and Atomic Clusters" (project no. 98-059), INTAS, and the Skeleton Technology Group (Sweden).

REFERENCES

1. M. Baxendale, K. G. Lim, and G. A. J. Amaratunga, Phys. Rev. B **61** (19), 12 705 (2000).
2. S. K. Gordeev and A. V. Vartanova, Zh. Prikl. Khim. (St. Petersburg) **66** (7), 1080 (1994); **66** (9), 1375 (1994).
3. R. G. Avarbé, S. K. Gordeev, A. V. Vartanova, *et al.*, RF Patent No. 2084036, MKlb N0169/00, Byull., No. 19 (1997).
4. R. N. Kyutt, É. A. Smorogonskaya, S. K. Gordeev, *et al.*, Fiz. Tverd. Tela (St. Petersburg) **41** (5), 891 (1999) [Phys. Solid State **41**, 808 (1999)]; Fiz. Tverd. Tela (St. Petersburg) **41** (8), 1484 (1999) [Phys. Solid State **41**, 1359 (1999)].
5. R. D. Bernard, *Thermoelectricity in Metals and Alloys* (Taylor & Francis, London, 1992).
6. L. V. Vovchenko, I. V. Dvorkina, and L. Yu. Matsuĭ, Fiz. Nizk. Temp. **20** (5), 463 (1994) [Low Temp. Phys. **20**, 368 (1994)].
7. L. I. Arutyunyan, V. N. Bogomolov, D. A. Kurdyukov, *et al.*, Fiz. Tverd. Tela (St. Petersburg) **40** (4), 781 (1998) [Phys. Solid State **40**, 719 (1998)].
8. N. B. Brandt, S. M. Chudinov, and Ya. G. Ponomarev, *Semimetals*, Vol. 1: *Graphite and Its Compounds* (North-Holland, Amsterdam, 1988), Modern Problems in Condensed Matter Sciences, Vol. 20.
9. J. J. Hauser, Solid State Commun. **17**, 1557 (1975).
10. M. S. Dresselhaus, Phys. Rev. B **15** (6), 3180 (1977).

Translated by G. Skrebtsov

Physics of the Solid State, Vol. 44, No. 4, 2002, pp. 793–795. Translated from Fizika Tverdogo Tela, Vol. 44, No. 4, 2002, pp. 762–764.

LOW-DIMENSIONAL SYSTEMS AND SURFACE PHYSICS

Electronic States of Dysprosium Submonolayer Films Adsorbed on the W(100) Surface

O. A. Panchenko, S. V. Sologub, B. V. Stetsenko, and A. I. Shchurenko

Institute of Physics, National Academy of Sciences of Ukraine, pr. Nauki 46, Kiev, 03650 Ukraine

Received June 22, 2001

Abstract—The unfilled electronic states of dysprosium submonolayer films absorbed on the W(100) surface are investigated using angle-resolved inverse photoelectron spectroscopy. It is shown that the energy position of the peak at 1.7 eV is independent of the angle of incidence of electrons onto the crystal surface. This specific feature is associated with electron transitions to the Dy 4*f* state located above the Fermi level. A correlation between the change in the energy position of this peak and the change in the work function with an increase in the absorbed dysprosium coverage suggests that the dipole moment of adatoms is affected by the dipole–dipole interaction. *© 2002 MAIK "Nauka/Interperiodica".*

1. INTRODUCTION

Earlier [1, 2], lanthanide submonolayer coatings on the surface of tungsten and molybdenum were studied to develop high-temperature cathodes with a small work function. Further investigations were performed for the purpose of revealing the reasons for the observed change in the work function of different faces of the substrate upon atomic adsorption of rare-earth metals and of elucidating the structure of adsorbed layers and the role played by the 4*f* shell of rare-earth metals [3–7].

It is known from theoretical and experimental works that adsorption on tungsten is accompanied by a transition of divalent lanthanides to the trivalent state. In this case, the *d* electron transferred from the *f* shell is attached to two valence *s* electrons. As a result of this electron transition, the ground state of the rare-earth metal remains unfilled and is located above the Fermi level. Since the *f* shells are isolated from external perturbations, the *f* level can be treated as the core level and its position relative to the Fermi level is determined by both the interaction with the substrate and the interaction between adsorbate atoms.

In this work, the energy location of the *f* state above the Fermi level of dysprosium submonolayer coatings on the W(100) face was investigated using angle-resolved inverse photoelectron spectroscopy.

2. EXPERIMENTAL TECHNIQUE

The experimental results were obtained by measuring the spectra in an isochromate mode. Electrons with the energy E_{kin} impinged on the sample at a specified angle to the normal to the surface. In the spectrum, the intensity of emitted photons with a fixed energy (isochromate) was measured on scanning E_{kin}.

The measurements were performed with a photon-counting spectrometer similar to the spectrometer described earlier in [8]. The photon-counting spectrometer included an electron multiplier with a CaF_2 window. The maximum detection efficiency was 9.8 eV, and the transmission band was 0.6 eV.

The W(100) sample was cleaned from carbon impurities according to the standard technique of annealing in a rarefied oxygen atmosphere. The surface was cleaned with a flash up to $T \approx 2500$ K. The dysprosium source was prepared from a tantalum strip that was previously degassed under vacuum at a temperature above the working temperature. A 1-mm^3 piece of dysprosium was welded onto the depression of the strip. The adsorbate purity was 99.99%. The adsorbate deposition onto the sample was performed at room temperature. The residual pressure in the vacuum chamber was 10^{-11} Torr.

3. RESULTS AND DISCUSSION

Figure 1 shows the isochromate inverse photoelectron emission spectra of the Dy–W(100) system, which were measured for normal incidence of the electron beam and different adsorbate coverages. It is seen that the spectrum of the atomically clean W(100) surface contains a broad peak located approximately 4.4 eV above the Fermi level. This peak is associated with electron transitions to tungsten bulk unfilled states [9]. As the dysprosium coverage increases, the amplitude of the main peak decreases, specific features appear on its sides, and the minimum at 7 eV smoothens. Noticeable differences between the inverse photoelectron emission spectrum of the clean tungsten surface and the spectra of the surface with the deposited adsorbate manifest themselves at the coverage $\theta = 0.1$ of the monolayer (ML) of dysprosium.

1063-7834/02/4404-0793$22.00

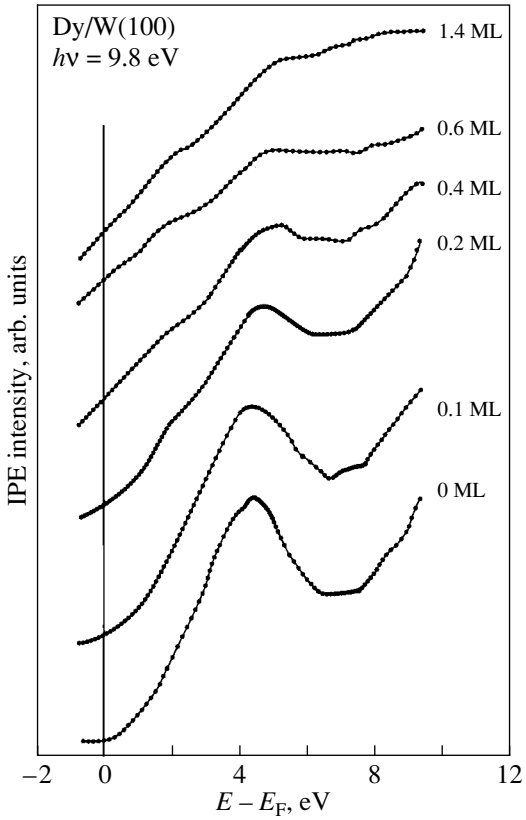

Fig. 1. Inverse photoelectron emission spectra of the W(100) surface covered with adsorbed dysprosium films at different coverages measured for normal incidence of electrons.

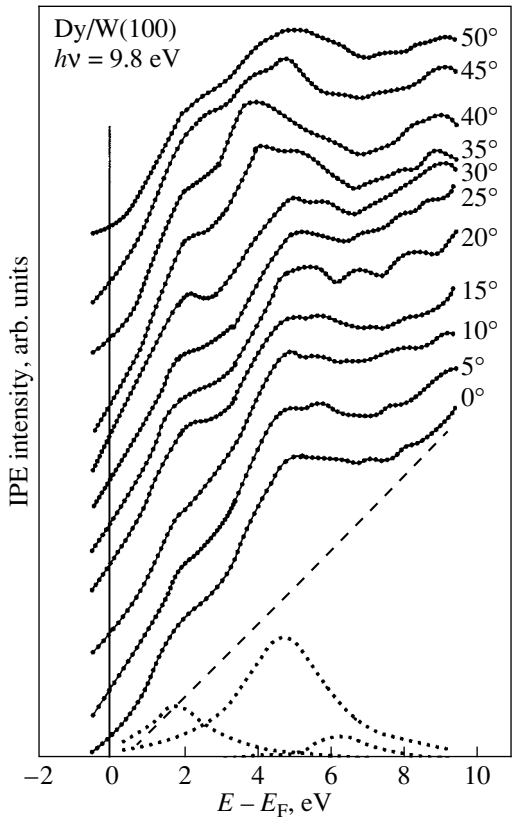

Fig. 2. Inverse photoelectron emission spectra of the W(100) surface (θ = 0.6 ML of Dy) at different angles of incidence of the electron beam onto the substrate. The decomposition of the inverse photoelectron emission spectrum into the Lorentzian peaks and the linear background is illustrated at the bottom of the figure. The dashed line shows the change in the location of the Dy 4*f* level.

Upon the deposition of dysprosium, the inverse photoelectron emission spectrum changed only slightly due to a low probability of radiative transitions to 4*f* levels at a photon energy of 9.8 eV. For this reason, the spectra were decomposed into a structureless background and Lorentzian peaks. The structureless background was approximated by a linear function. An example of the decomposition of the inverse photoelectron emission spectrum for normal incidence of electrons at a coverage of 0.6 ML is shown in Fig. 2 (dotted lines). It can be seen that, apart from the peak associated with the electron transition to band states (4.4 eV), there exist two peaks at energies of 1.7 and 6.2 eV. The latter two peaks correspond to adsorbed dysprosium. Here, we analyze the change in the energy position with variations in the coverage for only one peak whose energy with respect to the Fermi level is equal to 1.7 eV at θ = 0.6 ML. In order to elucidate the nature of the observed peaks, we measured the angle dependence of the inverse photoelectron emission (Fig. 2). The experiment demonstrated that the energy position of the 1.7-eV peak is independent of the angle of incidence of the electron beam onto the surface; i.e., it is independent of the tangential component of the momentum. A comparison with the energy level diagram for atomic

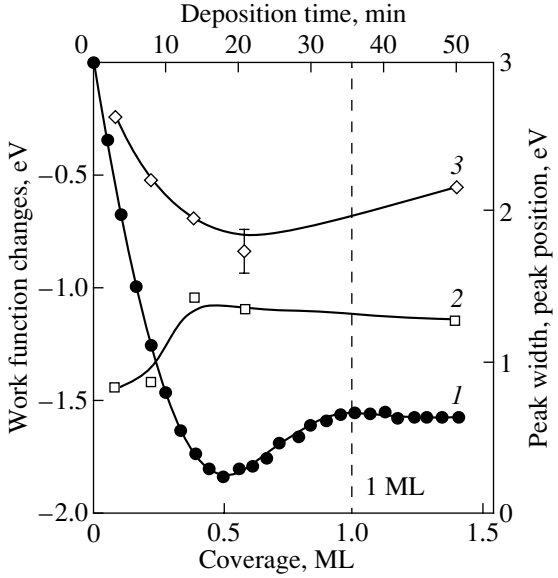

Fig. 3. Changes in the (*1*) work function, (*2*) width, and (*3*) location of the 4*f* level of dysprosium atoms adsorbed on the W(100) face as functions of the dysprosium coverage.

dysprosium gives grounds to assume that this feature is associated with transitions to the ground 4*f* state of the triply charged dysprosium ion $^6H_{15/2}$ [10].

The changes in the energy position and width of the studied feature with respect to the Fermi level with an increase in the dysprosium coverage on the surface is illustrated in Fig. 3. The root-mean-square error in the determination of the energy position is shown for one of the points in Fig. 3. In order to calculate its value, several inverse photoelectron emission spectra, which were measured under identical conditions, were decomposed into peaks and a structureless background. Note that, as the coverage increases to half the monolayer, the level under investigation approaches the Fermi level. This dependence correlates with the change in the work function with variations in the adsorbate coverage (Fig. 3). A further increase in the dysprosium coverage leads to an increase in both the work function and energy of the level. According to the concept of adsorption of electropositive atoms [11], the dipole moment of adatoms decreases in the region 0–0.5 ML due to the dipole–dipole interaction. This process should be accompanied by a decrease in the distance between the adatoms and the surface and can lead to a shift of the Dy 4*f* level toward the Fermi level. Another argument in support of this inference is the observed increase in the width of the energy level (Fig. 3). In actual fact, as the adatom approaches the metal surface, the probability of the electron transition from the 4*f* state to the substrate bulk increases, which leads to broadening of the energy levels of adatoms. A similar mechanism was considered earlier in [12].

It should be noted that, upon the adsorption of electropositive elements on the W(100) surface, the specific feature of the electron density of unfilled states was also observed in the vicinity of E_f with the use of angle-resolved inverse photoelectron emission spectroscopy [13, 14]. However, in contrast with the Dy–W(100) system, the energy position of this feature varies depending on the angle of incidence of the electron beam but remains unchanged with an increase in the adsorbate coverage. This difference reflects the role played by the 4*f* states of the rare-earth metals in the course of adsorption.

4. CONCLUSION

Thus, the inverse photoelectron emission spectroscopic investigation of the dysprosium adsorption on the W(100) surface experimentally revealed the unfilled Dy 4*f* states above the Fermi level. The data obtained confirm the inference that the dipole moment of adatoms decreases as the result of the dipole–dipole interaction. Further consideration of the shifts of 4*f* states with variations in the adsorbate coverage calls for theoretical estimations.

REFERENCES

1. O. K. Kultashev and S. E. Rozhkov, in *Rare-Earth Metals and Alloys*, Ed. by E. M. Savitskiĭ and V. F. Terekhov (Nauka, Moscow, 1971), p. 57.
2. B. K. Medvedev, N. I. Ionov, and Yu. I. Belyakov, Fiz. Tverd. Tela (Leningrad) **15** (9), 2620 (1973) [Sov. Phys. Solid State **15**, 1743 (1973)].
3. M. A. Shevchenko and S. A. Shakirova, Fiz. Tverd. Tela (Leningrad) **31** (11), 29 (1989) [Sov. Phys. Solid State **31**, 1854 (1989)].
4. V. A. Pleshkov, S. A. Shakirova, and G. A. Rump, Poverkhnost, No. 10, 16 (1990).
5. V. K. Medvedev, T. P. Smereka, S. I. Stepanovskiĭ, *et al.*, Fiz. Tverd. Tela (Leningrad) **33** (12), 3603 (1991) [Sov. Phys. Solid State **33**, 2028 (1991)].
6. V. A. Pleshkov, S. A. Shakirova, and G. A. Rump, Poverkhnost, No. 4, 34 (1991).
7. J. Kolaczkiewicz and E. Bauer, Surf. Sci. **175**, 487 (1986).
8. N. Babbe, W. Drube, I. Schäfer, and M. Skibowski, J. Phys. E **18**, 158 (1985).
9. A. Lamouri and I. L. Krainsky, Surf. Sci. **303**, 341 (1994).
10. K. N. R. Taylor and M. Darby, *Physics of Rare-Earth Solids* (Chapman and Hall, London, 1972; Mir, Moscow, 1974).
11. L. B. Bol'shov, A. P. Napartovich, A. G. Naumovets, and A. G. Fedorus, Usp. Fiz. Nauk **122**, 126 (1977) [Sov. Phys. Usp. **20**, 432 (1977)].
12. H. Ueba, Surf. Sci. **234**, 384 (1990).
13. A. Lamouri and I. L. Krainsky, Surf. Sci. **278**, 286 (1992).
14. A. Lamouri, I. L. Krainsky, A. G. Petukhov, *et al.*, Phys. Rev. B **51** (3), 1803 (1995).

Translated by N. Korovin

Physics of the Solid State, Vol. 44, No. 4, 2002, pp. 796–797. Translated from Fizika Tverdogo Tela, Vol. 44, No. 4, 2002, pp. 765–766.

LOW-DIMENSIONAL SYSTEMS AND SURFACE PHYSICS

Ensembles of Aluminum Islands on the Surface of Strained Poly(ethylene terephthalate) Films

V. I. Vettegren, E. A. Bakulin, and Yu. V. Kovalenko

Ioffe Physicotechnical Institute, Russian Academy of Sciences, ul. Politekhnicheskaya 26, St. Petersburg, 194021 Russia

e-mail: Victor.Vettegren@pop.ioffe.rssi.ru

Received June 13, 2001; in final form, July 16, 2001

Abstract—This paper reports on a study of the size distribution of aluminum islands forming an aluminum-coated poly(ethylene terephthalate) film subjected to tension. The islands are shown to form four statistical ensembles, with the distribution in each of them being thermodynamically optimized and coinciding with the canonic distribution of thermodynamic probability. *© 2002 MAIK "Nauka/Interperiodica".*

1. INTRODUCTION

The distribution $n(y)$ in size y in an ensemble of nonequilibrium objects (soot aggregates in filled rubber, nanodefects on the surface of loaded metals, bacteria, yeast fungi, protein molecules in bacteria, density fluctuations on the surface of polymethyl methacrylate) was found [1–5] to be identical to the canonic distribution of the thermodynamic probability [6]:

$$n(y) = n_0 y^2 \exp(-\beta y \Delta U_0), \quad (1)$$

where ΔU_0 is the formation energy of the object, $\beta \equiv 1/k_B T$, k_B is the Boltzmann constant, T is the temperature, and n_0 is the normalization constant. This implies that the distribution of such objects is thermodynamically optimized, i.e., that the entropy of their arrangement has a maximum value.

This work is a continuation of those studies. It deals with the distribution of aluminum islands forming on the surface of an aluminized poly(ethylene terephthalate) film subjected to tension.

2. EXPERIMENTAL

The samples used were oriented poly(ethylene terephthalate) films 5 μm thick, 15 mm long, and 4 mm wide, on whose surface a 30-nm-thick aluminum layer was deposited. The films were stretched along the orientation axis, and the elongation was measured. Two samples were studied: one of them was stretched to 1.33 times its original length at a temperature of 323 K; the other, to 1.53 times its original length at 373 K. When stretched, the aluminum layer cracked to form islands (Fig. 1). The size distribution of the islands was analyzed with a Neophot 32 optical microscope (Karl Zeiss, Jena). The number of islands on the surface under study was ≈1000–1500, thus ensuring fairly reliable statistics.

3. RESULTS AND DISCUSSION

Figure 1 shows a part of the surface of an aluminum-coated poly(ethylene terephthalate) film stretched (at 373 K) to 1.53 times its original length. The tension axis was horizontal. Aluminum islands with their long axis perpendicular and short axis parallel to the direction of tension are seen to have formed on the surface. The linear size of an island was estimated as the mean of two measurements, one parallel and the other perpendicular to the stretching axis.

The island size distribution for one of the samples is displayed in Fig. 2. The $n(y)$ distribution for the second sample had the same asymmetric pattern. Analysis shows that the distributions can be described as a sum of four relations of the type of Eq. (1) with different

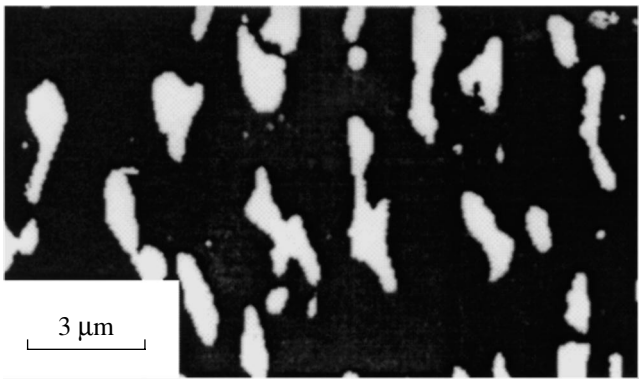

Fig. 1. Image of aluminum islands on the surface of a poly(ethylene terephthalate) film stretched to 1.53 times its original length at 373 K.

1063-7834/02/4404-0796$22.00

energies ΔU_{0i} (Fig. 2):

$$n(y) = \sum_{i=1}^{4} n_{0i} y_i^2 \exp(-\beta y_i \Delta U_{0i}). \quad (2)$$

Hence, the aluminum islands make up four statistical ensembles. The island formation energies for these ensembles were found to be $\Delta U_{01} \approx 0.098$, $\Delta U_{02} \approx 0.033$, $\Delta U_{03} \approx 0.01$, and $\Delta U_{04} \approx 0.003$ kJ/mol. The average island sizes in the four ensembles are $\langle y_1 \rangle = 0.05$, $\langle y_2 \rangle = 0.15$, $\langle y_3 \rangle = 0.45$, and $\langle y_4 \rangle \approx 1.40$ μm, respectively.

Thus, the formation energy and the average island size in the neighboring ensembles differ by a factor of three:

$$\frac{\Delta U_{01}}{\Delta U_{02}} = \frac{\Delta U_{02}}{\Delta U_{03}} = \frac{\Delta U_{03}}{\Delta U_{04}} = \frac{\langle y_2 \rangle}{\langle y_1 \rangle} = \frac{\langle y_3 \rangle}{\langle y_2 \rangle} = \frac{\langle y_4 \rangle}{\langle y_3 \rangle} = 3. \quad (3)$$

The ratio of the average sizes and formation energies of nanodefect ensembles on the surface of loaded metals was also found to be three [2, 5].

The room-temperature values of $\beta \Delta U_{0i}$ do not exceed 0.03. This implies that the ensembles of islands on the surface of poly(ethylene terephthalate) were produced by thermal fluctuations.

At equilibrium, the prefactor in Eq. (1) has the form [1]

$$n_{0i} = \frac{(1 - p_i)^3}{2}, \quad (4)$$

where $p_i \equiv \exp(-\beta \Delta U_{0i})$. Because $\frac{\Delta U_{0i}}{\Delta U_{0i+1}} \approx 3$, the prefactor ratio $\gamma_i \equiv \frac{n_{0i+1}}{n_{0i}}$ for the two adjacent ensembles should be equal to $\gamma_0 = 1/27$ at equilibrium. In real fact, however, the values of γ_i varied from 0.01 to 29; hence, the ensembles of aluminum islands in the samples under study are not at equilibrium. A similar result was obtained for ensembles of nanodefects on the surface of loaded metals [2, 5]; namely, there was no equilibrium between defect ensembles and the extent to which the equilibrium was not reached depended on the actual experimental conditions (the load and duration of its application).

Despite the absence of equilibrium, the shape of the island size distribution is described as a sum of canonical probability distributions (1), each of them being determined by the maximum entropy [6]. A thermodynamically optimized shape of the distribution sets in apparently in a time considerably shorter than the sample loading time (under our conditions, this time was approximately 10 min).

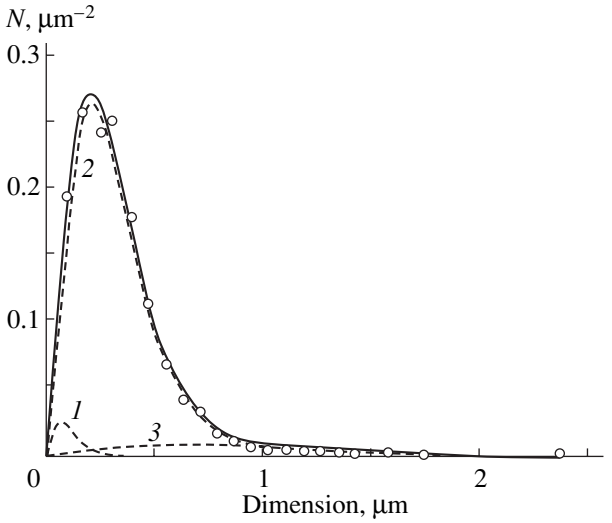

Fig. 2. Size distribution of aluminum islands on the surface of a poly(ethylene terephthalate) film stretched to 1.53 times its original length at 373 K. Solid line is the fitting of the distribution with Eq. (2); dashed line, the island distributions for ensembles *1*, *2*, and *3*.

Thus, it was established that the aluminum islands produced in an aluminum-coated poly(ethylene terephthalate) film under tension form four statistical ensembles. The size distribution of the islands in each ensemble is thermodynamically optimized and has the form of a canonical distribution of thermodynamic probability.

ACKNOWLEDGMENTS

This study was supported by the Ministry of Education of the Russian Federation, project no. E00-4.0-21.

REFERENCES

1. H. G. Kilian, R. Metzler, and B. Zink, J. Chem. Phys. **107** (20), 8697 (1997).
2. H. G. Kilian, V. I. Vettegren, and V. N. Svetlov, Fiz. Tverd. Tela (St. Petersburg) **42** (11), 2024 (2000) [Phys. Solid State **42**, 2083 (2000)].
3. H. G. Kilian, Rubber Chem. Technol. (2002) (in press).
4. H. G. Kilian, M. Koepf, and V. I. Vettegren, Prog. Colloid Polym. Sci. (2002) (in press).
5. H. G. Kilian, V. I. Vettegren, and V. N. Svetlov, Fiz. Tverd. Tela (St. Petersburg) **43** (11), 2107 (2001) [Phys. Solid State **43**, 2199 (2001)].
6. B. L. Lavenda, *Statistical Physics. A Probabilistic Approach* (Wiley, New York, 1991).

Translated by G. Skrebtsov